Konferenzen

105th International
WE-Heraeus-Seminar

Hadronic Processes at Small Angles in Storage Rings

Proceedings

Bad Honnef
February 1–3, 1993

Forschungszentrum Jülich GmbH

Dr. Wilhelm Heinrich Heraeus und Else Heraeus-Stiftung
(WE-Heraeus-Stiftung)

105th International WE-Heraeus-Seminar on

Hadronic Processes at Small Angles in Storage Rings

Proceedings

Physikzentrum, Bad Honnef
February 1–3, 1993

edited by
E. Rössle, Universität Freiburg, Germany
O.W.B. Schult, Forschungszentrum Jülich, Germany

Konferenzen des Forschungszentrums Jülich Band 12 / 1993

ISSN 0938-6521 ISBN 3-89336-112-X

Die Deutsche Bibliothek - CIP-Einheitsaufnahme

WE-Heraeus-Seminar <105, 1993, Honnef>:
Proceedings / 105th International WE Heraeus Seminar on Hadronic Processes at Small Angles in Storage Rings : Physikzentrum, Bad Honnef, February 1 - 3, 1993 / Forschungszentrum Jülich GmbH ; Dr.-Wilhelm-Heinrich-Heraeus- und Else-Heraeus-Stiftung (WE-Heraeus-Stiftung). Ed. by E. Rössle ; O. W. B. Schult. - Jülich : Forschungszentrum, Zentralbibliothek, 1993
(Konferenzen des Forschungszentrums Jülich ; Bd. 12)
ISBN 3-89336-112-X
NE: Rössle, Erwin [Hrsg.]; Physikzentrum <Honnef>; Hadronic processes at small angles in storage rings; Forschungszentrum <Jülich>: Konferenzen des Forschungszentrums ...

Herausgeber und Vertrieb: Forschungszentrum Jülich GmbH
ZENTRALBIBLIOTHEK
Postfach 1913 · D-5170 Jülich
Telefon (02461) 61-5368 · Telefax (02461) 61-6103

Druck: WEKA-Druck GmbH, Linnich

Copyright: Forschungszentrum Jülich 1993

Konferenzen des Forschungszentrums Jülich, Band 12

ISSN 0938-6521

ISBN 3-89336-112-X .

The DR. WILHELM HEINRICH HERAEUS AND ELSE HERAEUS–STIFTUNG was constituted for the furtherance of basic research in physics and associated fields through the financial support and organization of seminars.

Aims and purpose of the 105. WE–Heraeus–Seminar:

Cooler Synchrotron and Storage Rings and their circulating very intense cold beams with high phase space density allow the study – in the nonperturbative QCD regime – of hadronic processes which cannot be investigated by other means. Measurements at small angles including zero degrees permit the study of meson production near and at threshold, in particular in unique spin states, because both polarized beams and polarized, windowless targets can be used. Hadron spectroscopy at small angles allows among other studies crucial measurements of charge–exchange processes and break–up studies for investigation of e.g. the deuteron wave function at high momenta, in a test of quark effects, and studies of the excitations of the nucleon.

The scope of the seminar is to review the first results obtained at Cooler–Storage Rings, to discuss the experimental approaches and the theoretical models and predictions for meson production including strange hadrons and their interactions in nuclear matter in order to develop the best strategy for future work.

Scientific organization:

Prof. Dr. O. Schult	Forschungszentrum Jülich
Prof. Dr. E. Roessle	Universität Freiburg

International Advisory Committee:

Prof. Dr. J. Arvieux	Laboratoire National SATURNE, Saclay, Frankreich
Prof. Dr. J. Cameron	Indiana Uni. Cyclotron Fac., Bloomington, Indiana, USA
Prof. Dr. B. Hoistad	Universität Uppsala, Schweden
Prof. Dr. K. Kilian	Forschungszentrum Jülich
Prof. Dr. B. Schoch	Universität Bonn
Prof. Dr. W. Weise	Universität Regensburg

Venue:

Physikzentrum	Hauptstraße 5 W–5340 Bad Honnef GERMANY Phone +49 (0) 22 24 / 50 68 Fax +49 (0) 22 24 / 71 063

General organization:

Dr. V. Schaefer	WE–Heraeus–Stiftung Postfach 15 53 W–6450 Hanau 1 GERMANY Phone +49 (0) 61 81 / 35 409 Fax +49 (0) 61 81 / 35 651

Program

Monday, 1 February

09:00 – 09:10	Introductory Remarks *V. Schäfer*, WE–Heraeus Stiftung; *O. Schult*, Jülich
	Chairman: *B. Nefkens*, Los Angeles
09:10 – 09:45	**K^+ Production in Nuclei with Subthreshold–Energy Protons** *K. Sistemich*, Jülich
09:50 – 10:25	**Zero–Degree Experiments in the IUCF Cooler Ring: Some Results and Plans** *D.W. Miller*, Bloomington
10:45 – 11:10	Coffee Break
	Chairman: *A. Strzalkowski*, Cracow
11:10 – 11:30	**Coulomb–Hadronic Interference at COSY Energies** *P. Kroll*, Wuppertal
11:40 – 11:55	**COSY–Jülich – A Synchrotron and Storage Ring for Medium Energy Physics** *R. Maier*, Jülich
12:05 – 12:20	**The Internal Cluster Target for COSY** *D. Grzonka*, Jülich
12:30 – 14:00	Lunch
14:00 – 16:00	**Workshop I** Convener: *U. Lynen*, Darmstadt contributions also by: U. Faschingbauer, R. Eßer, B. Nefkens, H.P. Morsch, H.R. Koch
16:00 – 16:40	Coffee Break
	Chairman: *Th. Mayer–Kuckuk*, Bonn
16:40 – 17:00	**Coherent Pion Production at Small Scattering Angels** *F. Osterfeld*, Jülich
17:10 – 17:30	**Zero Degrees Centigrade – or the $d+d \rightarrow \alpha+2\pi$ Reaction in CELSIUS** *C. Bargholtz*, Stockholm
17:40 – 17:55	**Subthreshold K^+ Production in the Proton–Nucleus Interaction below 1 GeV** *V. Koptev*, St. Petersburg
18:05 – 18:20	**Subthreshold Production of K^- Mesons** *H. Müller*, Dresden
18:30	Dinner

Followed by an invitation of the WE–Heraeus–Stiftung to a social gathering in the "Bürgerstube" at the Physikzentrum

Tuesday, 2. February

	Chairman: *R. Maschuw*, Bonn
09:00 – 09:35	**Threshold Measurements at the Experiment COSY–11** *W. Oelert*, Jülich
09:45 – 10:20	**Strangeness Production with Protons and Pions** *C.B. Dover*, Upton
10:30 – 11:10	Coffee Break
	Chairman: *K. Kilian*, Jülich
11:10 – 11:30	**Hadron Production in Proton–Nucleus Collisions** *W. Cassing*, Giessen
11:40 – 11:55	**The pp → dπ^+ Excitation Function at Small Angles** *F. Hinterberger*, Bonn
12:05 – 12:20	**An Internal High Density Storage Cell Target for Polarized Hydrogen** *K. Zapfe*, Hamburg
12:30 – 14:00	Lunch
14:00 – 16:00	**Workshop II** Covener: *W. Weise*, Regensburg contributions also by: J.M. Laget, A. Sibirtsev, B. Kamys, P. Oltmanns
16:00 – 16:40	Coffee Break
	Chairman: *E. Klempt*, Mainz
16:40 – 17:00	**The Structure of Mesons and Nucleons** *J. Speth*, Jülich
17:10 – 17:30	**Magnet Spectrometer for the IUCF Cooler** *G.P.A. Berg*, Bloomington
17:40 – 17:55	**Study of pp, pd and p^{3}He Interactions in Pure Spin States at COSY** *S. Belostotsky*, St. Petersburg
18:05 – 18:20	**Study of Short Range Deuteron Structure at COSY – Theoretical Point of View** *O. Grebenyuk*, St. Petersburg
18:30	Dinner

Wednesday, 3 February

	Chairman: *J.M. Laget*, Saclay
09:00 – 09:35	**Exclusive Deuteron Break–up Study with Polarized Protons and Deuterons at COSY** *V.I. Komarov*, Dubna
09:45 – 10:20	**Physics at Small Angels with the Extracted Beams of SATURNE** *A. Boudard*, Saclay
10:30 – 11:10	Coffee Break
11:10 – 11:30	**Dynamics of Two–Baryon Systems** *B. Metsch*, Bonn
11:40 – 11:55	**p–d Reactions at Intermediate Energies and Deuteron Structure at Small N–N Distances** *G.I. Lykasov*, Dubna
12:05	**Concluding Remarks** *B. Schoch*, Bonn

Contents

K^+ PRODUCTION IN NUCLEI WITH PROTONS AT ENERGIES BELOW THE NN THRESHOLD

K. Sistemich[1], M. Büscher[1], W. Cassing[2], B. Kamys[3], V. Komarov[4], V. Koptev[5], H. Müller[6], and A. Sibirtsev[7]

[1] Institut für Kernphysik, Forschungszentrum Jülich, Postfach 1913, W–5170 Jülich, Germany

[2] Institut für Theoretische Physik, Universität Gießen, Heinrich–Buff–Ring 16, W–6300 Gießen, Germany

[3] Institute of Physics, Jagellonian University, Reymonta 4, 30059 Cracow, Poland

[4] Joint Institute for Nuclear Research, Dubna, P.O.Box 79, Head Post Office, Moscow, Russia

[5] Petersburg Nuclear Physics Institute, 188350 Gatchina, Russia

[6] Institut für Kern– und Hadronenphysik, Forschungszentrum Rossendorf, Postfach 19, O–8051 Dresden, Germany

[7] Institute for Theoretical and Experimental Physics, B. Cheremushkinskaya 25, 117259 Moscow, Russia

The study of the production of hadrons in proton–nucleus collisions at projectile energies below the free nucleon–nucleon threshold allows the investigation of nuclear–medium effects on elementary particle reactions. The subthreshold–K^+ production is especially well suited for the study of such effects since the K^+ mass and consequently the "missing" energy is large at proton energies far below the NN threshold of 1.58 GeV, and since the rescattering of the produced K^+ mesons within the nuclear medium is small, because of its strange–antiquark content. It is planned to investigate this production at COSY–Jülich where high luminosities can be reached with internal targets. Inclusive measurements of the K^+ momentum spectra as well as coincidence studies of kaons in correlation with light particles are envisaged at the 0^0 Facility, integrated into the storage ring . In particular, the search for a theoretically predicted peak structure in the momentum spectrum of correlated deuterons from the process $pN \rightarrow \pi d$ plus $\pi N \rightarrow NK^+\Lambda$ will be performed. If this structure is observed, then the dynamics of the K^+ production is unambiguously determined and the measurement of the K^+–momentum spectrum will provide information on the nuclear–medium effects.

1. Introduction

The study of the K^+–meson production in proton–nucleus collisions at projectile energies below the threshold for the formation in free nucleon–nucleon collisions (NN threshold) is a unique means to probe nuclear–medium effects on elementary particle reactions. In this process the energy of the projectile can only be converted into the meson mass through cooperative effects in the target nucleus. The nuclear contribution may come from the internal momentum of an individual nucleon inside the nucleus (Fermi momentum) with which the projectile interacts, or from the correlated action of more than one target nucleon participating in the process. Thus, the study of the subthreshold–K^+ production can provide information on high–momentum components of the many–body nuclear wave function and on correlations of nucleons inside a nucleus.

The K^+ meson is especially well suited for the study of nuclear medium effects since its mass is large and, thus, its formation requires a strong participation of the nucleus at projectile energies far below the NN threshold. It is equally important that this meson has a weak interaction with nuclear matter: Its momentum will not be changed strongly on the way out of the nucleus, so that the information which it carries on the reaction, is preserved. In fact, the mean free path of K^+ mesons with momenta between 0.1 and 0.8 GeV/c is 2–3 times larger[1] than the radius of ^{12}C.

2. Kinematics of the subthreshold–K^+ production

The threshold for a proton–induced production of a kaon is determined by the need to create the corresponding mass:

$$T_p^{th} = m\,\{1 + (m_p + 0.5\,m)/m_T\},$$

where m is $= m_K + m_\Lambda - m_N$, and m_T is the mass of the system which interacts with the projectile proton, be it a single nucleon, a group of nucleons or the target nucleus as a whole. The values of T_p^{th} are 1.582, 1.127 and 0.747 GeV for $m_T = m_p$, $2\,m_p$ and m_A, respectively, where the first value is the NN threshold and the last one the absolute threshold for a ^{12}C target.

Two alternatives are discussed for the mechanism in the subthreshold–K^+ reaction:
- the primary process, in which the K^+ formation takes place directly in a collision of the projectile with a target nucleon ($pN \rightarrow N\Lambda K^+$) or with a cluster of nucleons, also labeled direct mechanism or first collision model (FCM)
- the secondary process with the formation of an intermediate pion by the projectile proton, and the subsequent creation of the K^+ meson in a second step by this pion ($pN_1 \rightarrow NN\pi$ plus $\pi N_2 \rightarrow K^+\Lambda$), also called two–step mechanism (TSM).

Kinematically, it makes a clear difference whether one or two target nucleons are involved in the K^+–production process. If one single nucleon takes part, its internal momentum enables the K^+ creation and must consequently be high for projectile energies far below the NN threshold, see Fig. 1, curve n=1. If two nucleons take part either as a cluster or in the two–step process, then the Fermi–momentum is exploited twice and can, therefore, be smaller, see Fig. 1, curve n=2.

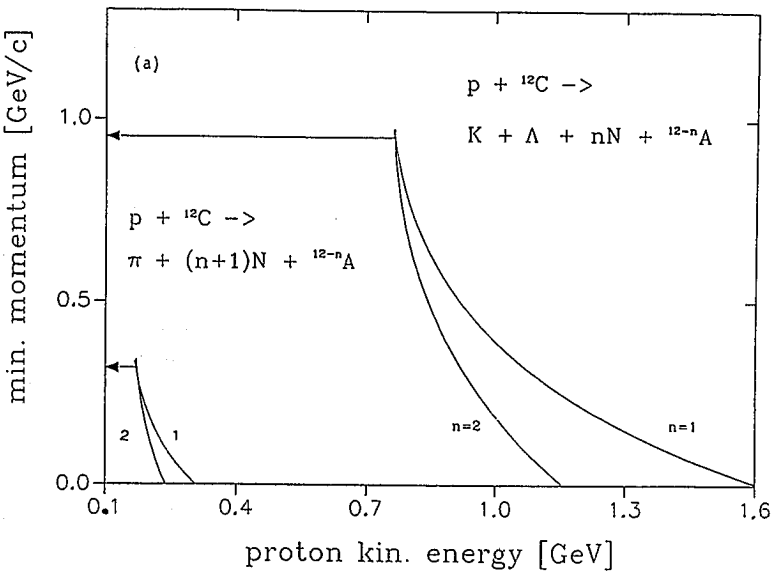

Fig. 1: Minimal intrinsic momentum of a single nucleon (n=1) and the sum of the momenta of two nucleons (n=2) for the production of pions and kaons in ^{12}C as a function of the energy T_p of the projectile proton.

It is obvious that the required Fermi momenta are considerably higher in FCM than in TSM at projectile energies not too far below $T_p = 1.58$ GeV. Close to the absolute threshold, however, both mechanisms require similar momenta of about 1 GeV/c. So, indeed, a region of Fermi momenta can be studied through the K^+ production which is as yet unknown, provided that the expected low cross sections allow the corresponding experiments. The subthreshold–π production would not be similarly sensitive to this momentum regime; here the required minimum momenta at the absolute threshold are close to the average Fermi–momentum of nucleons in ^{12}C and about three times lower than in the case of the K^+–meson production, see left–hand side of Fig. 1.

3. Status of subthreshold–K^+ production studies

The proton–induced K^+ production in different target materials at projectile energies of $0.8 \leq T_p \leq 1.0$ GeV have been measured[2-5] at the synchrocyclotron of the Petersburg Nuclear Physics Institute in Gatchina. Part of the results are shown in Fig. 2. The total cross sections σ_{tot} range[4] from about 0.25 nb for Be at $T_p = 0.8$ GeV to 700 nb for U at $T_p = 1$ GeV, and show a strong dependence on the projectile energy and the target mass. Koptev and coworkers[4] have discussed their results in terms of the alternatives of the direct and two–step mechanism. The data can only be reproduced by calculations in the frame of the primary process (FCM) at a single nucleon if phenomenological momentum distributions are assumed which, at high momenta, deviate[6] considerably from the usually adopted distributions, e.g. see Fig. 3. No quantitative considerations were made for the alternative of a primary process which involves clusters. But it was shown that the energy dependence of σ_{tot} scales fairly well with minimum masses of

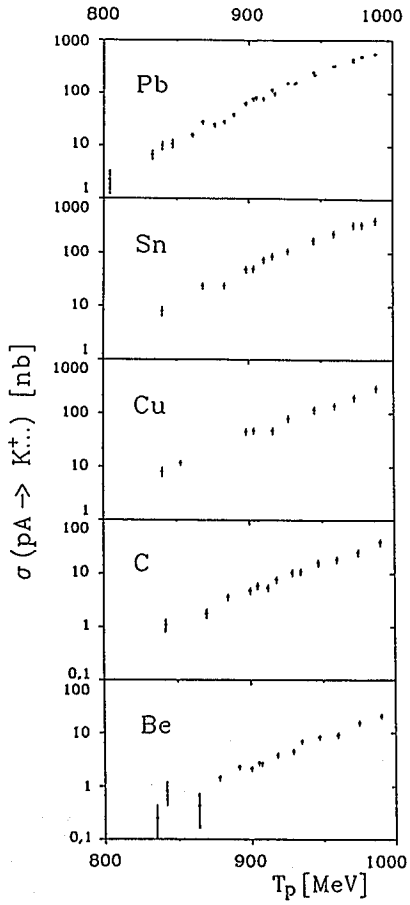

Fig. 2: Total cross sections for the subthreshold K^+ production measured at the PNPI synchrocyclotron[4].

assumed clusters for all target nuclei. At the lower energy limit of their studies, clusters of as many as 6 nucleons had to be assumed. Calculations in terms of the secondary process (TSM) using a Fermi–gas momentum distribution for the nucleons resulted in a good description of the data at the higher projectile energies, and, in particular, of the mass dependence[4] of σ_{tot}.

The authors have pointed out the possible importance of the special process $pN \rightarrow \pi d$ as initial reaction of TSM. This reaction is an energetically favoured entry to the K^+ production since the pions from this channel are formed with high momenta.

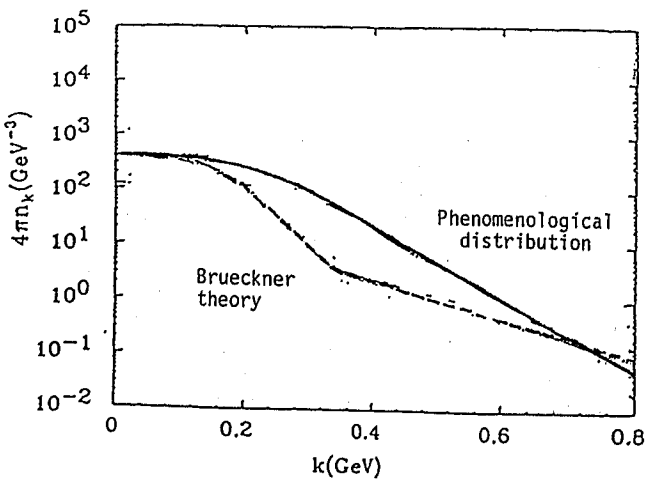

Fig. 3: Comparison of the phenomenological spectral momentum function used in the one–step calculations[4] *of the subthreshold–K^+ production on ^{12}C with the theoretical function*[7].

Fig. 4 elucidates this effect for the proton–induced pion production on H and D targets[8]. In the momentum spectrum of the pions a peak is seen which is connected with the formation of a deuteron. It is broadened in the case of a D target, but nevertheless present. Since a momentum of $p_\pi > 630$ MeV/c is necessary for the K^+ production in the second step of TSM, these high–momentum pions are expected to have strong influence. Koptev et al. estimated their contribution at $T_p = 1$ GeV to about 25% of the subthreshold–K^+ production[4]. It should be pointed out that the d–formation cross section increases[9] in pp reactions with decreasing T_p, so that the influence of the deuteron–correlated processes is expected to rise[5] when T_p approaches the absolute K^+ production threshold for a given target nucleus.

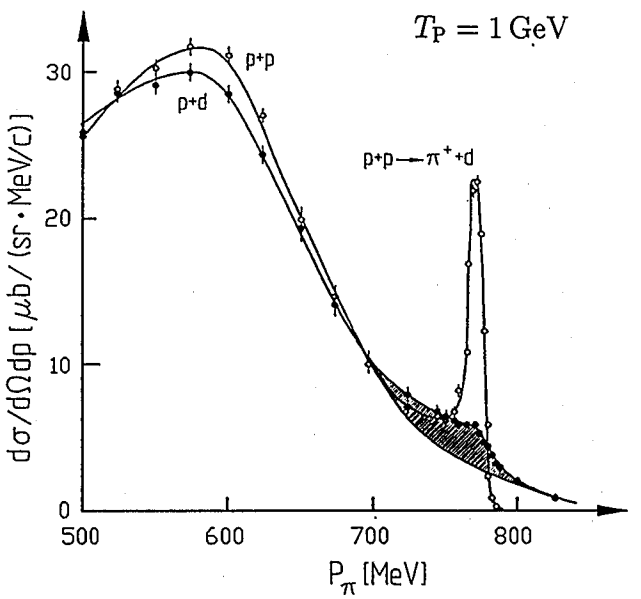

Fig. 4: Spectrum of π^+ mesons from $D(p,\pi^+)X$ and $p(p,\pi^+)X$ measured[8] at 0^0. The shaded area shows that there is clearly an enhancement due to the quasi–free $pp \rightarrow \pi^+d$ reaction in the case of the deuteron target.

Koptev et al. pointed out that their results on total cross sections alone do not yet allow to separate out the contribution of the different reaction mechanisms and to unambiguously deduce information on high–momentum components of the nuclear wave functions or on the existence of correlated–nucleon actions. They stress the need for information on angular and energy spectra of the K^+ mesons and on the correlated emission of kaons and light particles (n, p, d ...).

Studies of the subthreshold–K^+ production in heavy–ion induced reactions have also been performed[10-12], in part at very low energies per nucleon[11]. Results have been published on the reactions Si + Si at 1.6 GeV/u, Ref. 10, Ar + Ti at 0.092 GeV/u, Ref. 11, and Au + Au at 1 GeV/c, Ref. 12. A major goal of these studies is to gain information on the nuclear equation of state via the nuclear–density dependence of the K^+ production.

4. Theoretical studies

It is remarkable that several theoretical investigations have been carried out which reproduce the measured total K^+–production cross sections as well as their dependence on the projectile energy and on the target mass. These studies have provided predictions for quantities like the double differential cross sections $d^2\sigma/d\Omega dp$ for the K^+ production or the cross sections for the production of kaons and correlated light particles. The results of these studies form the basis for planning of experiments on the corresponding quantities. Only if such investigations have been performed full use of the study of the subthreshold–K^+ production for the yield of information about nuclear–medium effects can be made.

Cassing et al.[13-15] used a folding model based on Hartree–Fock distributions of the ground–state momenta for the calculation of the K^+ production probability both in the primary and secondary process. For the primary process the free proton–nucleon cross section for K^+ production was folded with the momentum distribution of the nucleons. In the case of TSM the elementary $\pi N \rightarrow K^+\Lambda$ cross section was folded with the pion momentum distribution, calculated in a first step, and the momentum distribution of the nucleons. The Glauber approximation has been used for the calculation of the number of first–chance nucleon–nucleon collisions. The studies have provided a good description of the total K^+–production cross sections. The contribution of the primary process, FCM, is found to be about a factor of 10 smaller than that of TSM. This is in accordance with the result[4] by Koptev et al. that their data can only be reproduced, when a non–standard momentum distribution for the internal momenta is used, see Fig. 3.

Kopeliovich and Nemchik have pointed out[16] the importance of the inclusion of the binding energies of the nucleons and of short range correlations in such calculations. As Koptev et al. they stress the probable importance of the $pN \rightarrow \pi d$ reaction for the two–step process. It should be noted that Kopeliovich and Niedermayer have discussed[17] the subthreshold–K^+ production in terms of multi–quark clusters.

The expected momentum and angular distributions of the K^+ mesons have been calculated in terms of Cassing's folding model by Kamys et al.[18,19], who extended the code towards an exact treatment of the relativistic kinematics. There are remarkable differences in the results for the FCM and TSM processes, in particular in the angular distributions, see Fig. 5.

Müller and Büscher[20] have studied the K^+ production in correlation with the emission of light particles in the Modified Phase Space Model[21] (MOPS). In this model the pA reactions are taken as a superposition of NN interactions which allow the participation of more than one target nucleon in the K^+–formation process. In a first step the energy of the projectile is assumed to be converted into excitation energy. In a second stage the excited subsystem of the target nucleons decays into different channels for which the probabilities are calculated. Again the necessary energy for K^+ formation at subthreshold projectile energies is available because of the weight of the correlated group of target nucleons in the process, and of the Fermi motion. The deexcitation of the residual nucleus is assumed to take place in a break–up process.

It has been pointed out by the authors that their model treats hadron–hadron and hadron–nucleus collisions on equal footing and does not need a parametrization of elementary cross–sections. The parameters of the model are determined from a description of experimental data other than the subthreshold–K^+ production. For the

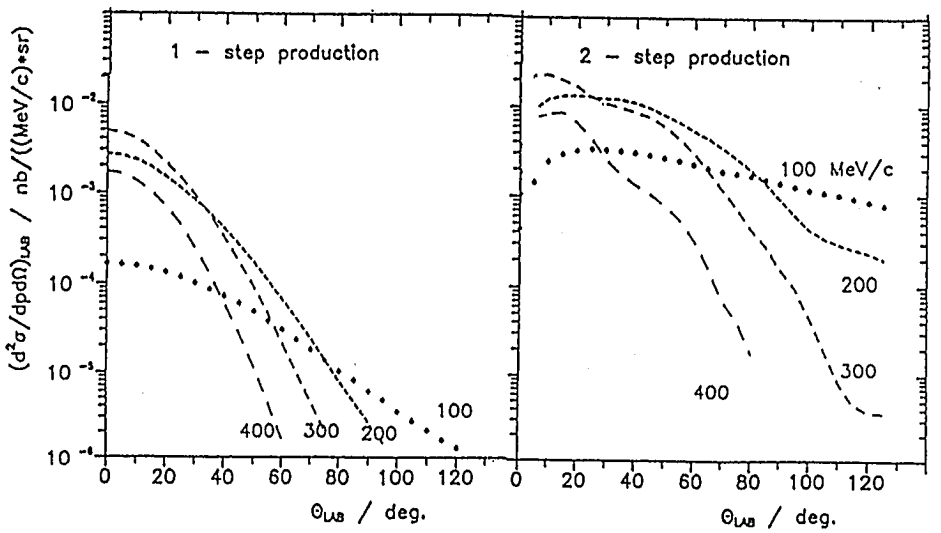

Fig. 5: Angular distributions for the subthreshold–K^+ production at $T_p = 950$ MeV, calculated with the code of Ref. 13 under inclusion of the relativistic kinematics.

K^+–production studies they are taken from an investigation of the overall features of pp collisions in the range of T_p between 0.8 and 11 GeV. A test of the calculations is the K^+ production in pp reactions above threshold which is well reproduced[20]. With these parameters the total cross section for the subthreshold production at 1 GeV on Ni is calculated to 350(25)nb in reasonable agreement with the measured value[4] of about 300 nb for Cu.

These authors have also studied the influence of the particular reaction $pN \rightarrow \pi d$ on the subthreshold–K^+ production in the two–step process. Here, they followed the procedure outlined[13] by Cassing et al. for the two–step mechanism, but included this special process and an exact energy–momentum conservation by an off–shell treatment of the involved nucleons. They found that 2/3 of the K^+–production processes at 1 GeV go via the $pN \rightarrow \pi d$ channel since the ratio $\sigma_{\pi d}/\sigma_{NN\bar{\pi}}$ is relatively large; it even increases with decreasing projectile energy, see section 3.

An especially interesting aspect is the fact that the πd channel is connected with a peak in the momentum distribution of the deuterons which are correlated with the K^+–meson production. Since the deuteron is created in a quasi two–body process it has a well defined momentum, which is only broadened by the Fermi motion of the nucleons. Fig. 6 shows the result of the calculations. The peak in the momentum spectrum of the deuterons is obvious. It may provide a clear signature for the two–step process, see section 5.

In the frame of MOPS also the correlated production of K^+ mesons with other light particles has been studied[22]. The result is shown in Fig. 7. Here, only fragments arising from the projectile–correlated group interaction have been taken into account; a possible

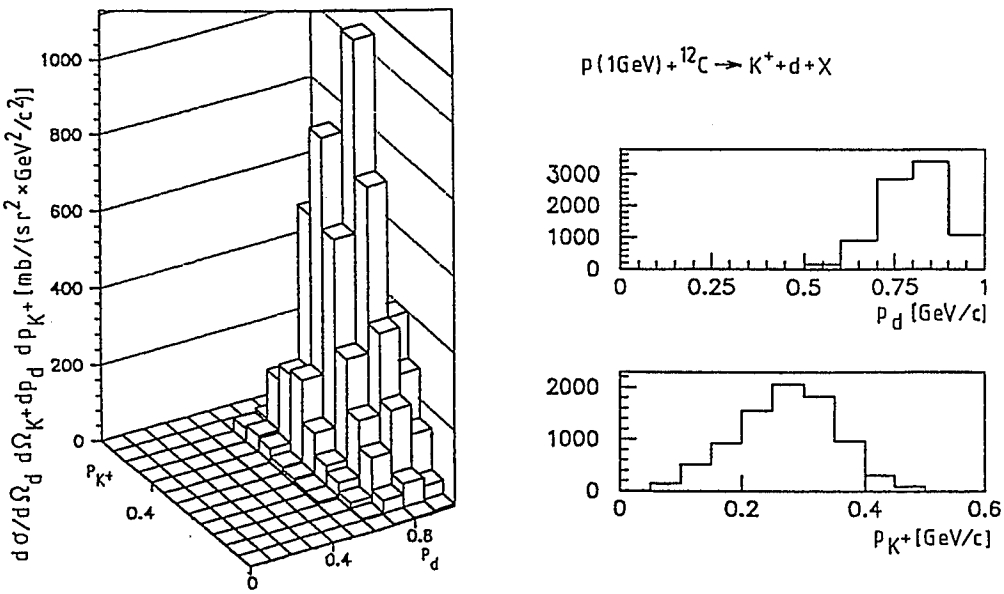

Fig. 6: Correlated K^+ and d spectra calculated by assuming a two–step process with the deuteron emerging from the $pN \rightarrow \pi d$ channel[20].

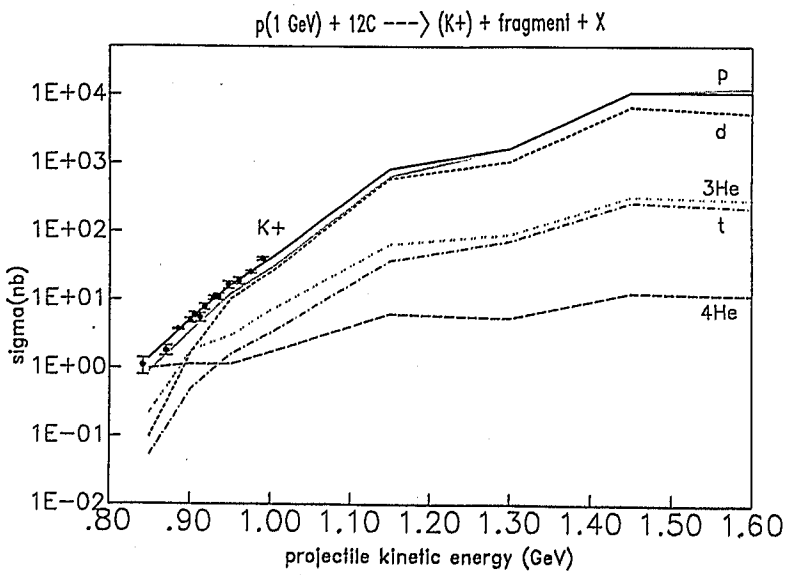

Fig. 7: Cross section for the production of K^+ meson (thick line) calculated in MOPS[20] *compared with the data*[4]*. The contributions involving different fragments are marked.*

disintegration of the residual nucleus is not considered. The protons from the decay of the Λ hyperon are, however, included and cause the "overshoot" of the curve for the K^+p events at energies around the NN threshold. It is interesting to note that the correlated K^+d production plays an important role also in these calculations, but that close to the absolute threshold at 0.747 GeV the contribution of processes involving even heavier particles are dominant for energy reasons.

The subthreshold-K^+ production in pA reactions has also been studied[23 24] by Sibirtsev and Büscher.They used the folding procedure analoguous to the one used by Cassing et al.[13] and took a momentum distribution according to the Fermi–gas model plus a term representing high–momentum components. The calculations treated the nucleons off–shell and have been performed for the primary (FCM) and secondary (TSM) processes. The results for the $p^{12}C$ reaction are shown in Fig. 8. The primary process has been studied including and excluding the high momentum component, curve 1 and 2, respectively. These curves fall short of the measured total cross sections[4]. In particular, there is no way to reproduce the measured cross–sections at low T_p without the high–momentum component. The agreement is better if the two–step process is included, curve 3. The authors also included the $pN \rightarrow \pi d$ channel in their calculations. Curve 4 shows this contribution which is remarkable in the energy range considered, in accordance with the findings of other authors[4,16,20]. It should be noted that both here and in the calculations by Cassing et al.[13-15] the measured total cross sections are not only reproduced for the reaction $p^{12}C$ but also for other target nuclei.

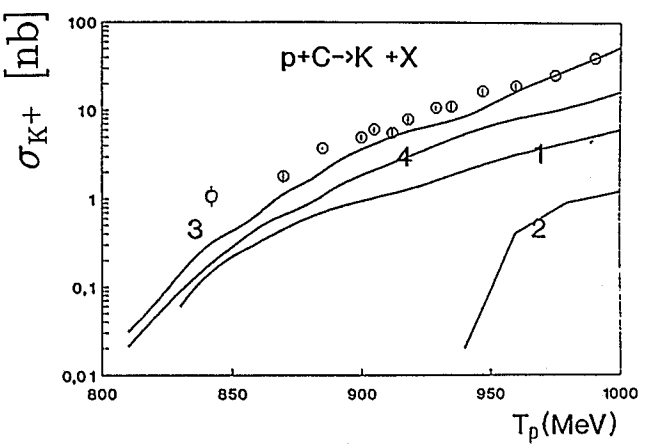

Fig. 8: Calculated[23] total cross sections for the K^+ production in the energy range of Koptev's experiments (circles). Curves 1 and 2 give the results for FCM with and without a high–energy tail of the momentum distribution, respectively. Curves 3 and 4 represent the TSM results for the $pN \rightarrow NN\pi$ and $pN \rightarrow \pi d$ channels, respectively.

Sibirtsev and Büscher also calculated the differential cross sections $d\sigma/d(\cos\Theta_K)$ and $Ed^3\sigma/dp^3$ and have found similar differences between the primary and secondary processes as Cassing et al.[14] as well as Kamys et al.[18]. Their calculations with inclusion of the $pN \rightarrow \pi d$ channel also predict the existence of a relatively narrow peak in the momentum spectrum of the deuterons emitted in correlation with the K^+ mesons, see Fig. 9, curve 1, in good agreement with the result of Müller et al.[20] and with cascade calculations[6] by Koptev. Here, it is interesting to note that this peak "survives" rescattering of the outgoing deuterons in the nucleus, according to the calculations by Sibirtsev and Büscher[23,24] (curve 2) and stands out above the expected deuteron background (curve 3).

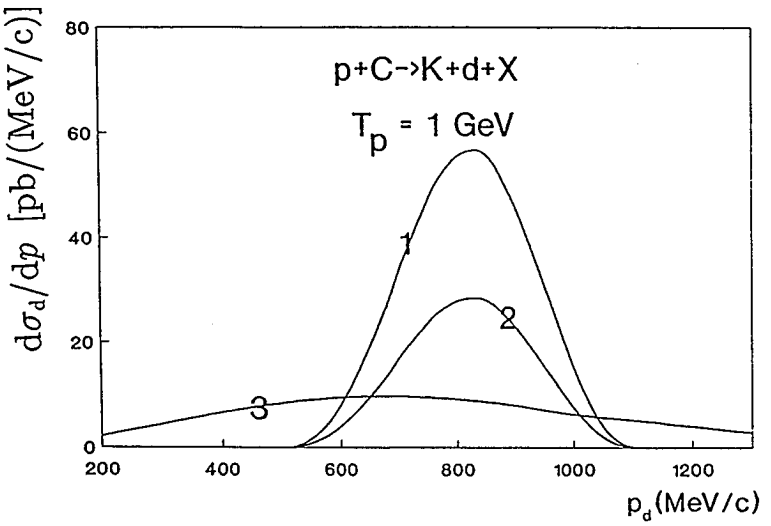

Fig. 9: Expected[23] spectra for deuterons in correlation with K^+ mesons. Curves 1 and 2 describe the original deuteron peak and the one expected after rescattering in the target nucleus, respectively. Curve 3 shows the expected deuteron background from reaction channels other than $pN \rightarrow \pi d$.

5. Envisaged experimental investigations

The results of the work by Koptev et al.[4] have shown that the K^+ production can be investigated at energies far below the NN threshold, so that this process can be used for studies of nuclear–medium effects on elementary reactions. The theoretical investigations by the authors as well as the work by other groups show, however, that the total cross sections alone do not yield information on high–momentum components of the nuclear-wave function and on correlated actions of groups of nucleons, maybe even on the existence of many–quark clusters inside the nucleus. This is mainly due to the fact that the reaction mechanism is not unambiguously known since primary and secondary processes compete. There is an agreement among the results of the different calculation that the two–step process is expected to give a dominant contribution to the total cross section. But these studies are not parameter–free.

More data are needed to identify the reaction mechanism and to allow the extraction of the relevant nuclear–medium information from a comparison of the data with theoretical predictions. Since such predictions are available for the momentum and angular distributions of the K^+ mesons, inclusive measurements of differential cross sections are already of interest, for example a study of the K^+–momentum spectrum from the bombardment of different target nuclei with protons at subthreshold energies. It is favourable to perform these studies at emission angles close to 0^0 with respect to the projectile direction where the cross sections are expected to be highest. A measurement at different angles, e.g. at 0^0 and 90^0, should help to reveal the dominating reaction mechanism. It is essential to perform such measurements at energies as close as possible to the absolute threshold (0.75 GeV for a ^{12}C target), since there the influence of the nuclear medium is especially large, cf. Fig. 1. It is clear, however, that the K^+–production cross sections are low, see Fig. 2, which will limit the possibilities for detailed studies. In fact, measurements of the process in this energy regime with cross

sections in the nanobarn region will only be possible at proton accelerators with high luminosity.

A very interesting result of the theoretical work[4,16,20,23] is the importance of the $pN \rightarrow \pi d$ channel and the prediction of a peak structure in the momentum distribution of the deuterons which are emitted in correlation with the K^+ mesons, see Figs. 6 and 9. Since this peak structure is predicted[23] to "survive" the passage of the deuterons through the target nucleus, it should be possible to experimentally confirm whether it exists and, thus, unambiguously identify the two–step mechanism. (A byproduct of such investigations would be the confirmation of the existence of intermediate pions.) For this purpose, momentum spectra for correlated K^+ mesons and deuterons have to be determined. It is important to note that the calculations[20,23] reveal a predominance of forward emission of the deuterons. Thus, the study of the deuteron momenta under 0^0 with respect to the beam direction would be the best choice.

Besides this test of the importance of the $pN \rightarrow \pi d$ channel for the subthreshold–K^+ production, it is also appealing to study the correlated emission of K^+ mesons with other light particles in order to verify the prediction[22] that these processes contribute strongly at low projectile energies. Again, a predominant emission of the correlated particles in the forward direction is expected.

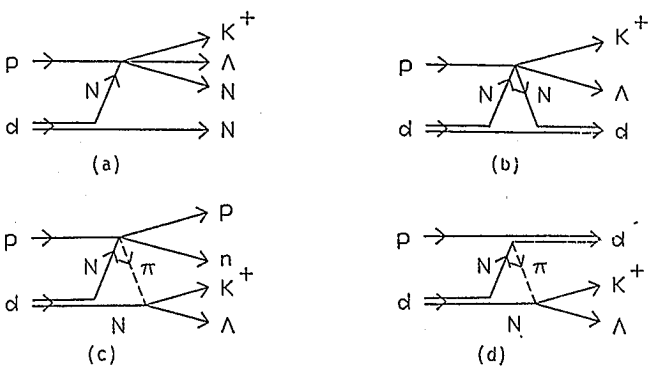

Fig. 10: Graphs for the K^+ production on deuterons. (a,b) and (c,d) correspond to the primary and secondary process, respectively; (b) and (d) illustrate the correlated K^+–d production.

An attractive target is deuterium for which the subthreshold–K^+ production has not yet been studied at all. Experiments with this target should provide the most direct way to identify the mechanisms in the subthreshold–K^+ production. The Feynman graphs for the primary and secondary processes are shown in Fig. 10 where also the processes corresponding to the correlated K^+d productions are included. Since all the subprocesses are relatively well known, all the graphs of Fig. 10 should be accessible to reliable calculations. If an exclusive study of the reaction $pD \rightarrow dK^+\Lambda$ via the measurement of the kaons and deuterons is performed, then any difference between the data from such an experiment and the results of the calculations including the graphs c and d of Fig. 10 is evidence for more exotic processes.

For the envisaged studies of the subthreshold–K^+ production, a proton beam with high luminosity is indispensable. The projectile energies should range from about 0.7 to 1.6 GeV in order to allow measurements between the absolute thresholds for different

targets and the NN threshold. The use of thin targets is mandatory for most of the planned experiments for the following reasons:
- minimization of the break–up of the produced correlated light particles,
- minimal changes of the four momenta of the projectiles and ejectiles on their way through the target,
- avoidance of contaminations from two–step K^+ production processes involving two different target nuclei,
- reduction of background which increases more than linearly with the thickness of the target like that of e^-e^+ pairs from the conversion of π^0–decay photons,
- the use of window free targets; windows would cause severe distortions because of the strong A dependence of the K^+–production cross sections.

The new cooler–synchrotron COSY–Jülich[25] offers very good possibilities for experimental studies of the subthreshold–K^+ production. The energy of the projectiles can be varied at COSY over the whole range of interest. Very thin internal targets can be used like deuterium–gas or cluster targets as well as solid strip targets. Nevertheless, high luminosities can be achieved. For example, with 10^{10} protons of 1 GeV in COSY values of $L \approx 3 \cdot 10^{30}/cm^2\,s$ and $2 \cdot 10^{33}/cm^2$ can be reached with D–gas targets and a ^{12}C–ribbon target of 150 $\mu g/cm^2$ thickness, respectively.

The 0^0 Facility[26 27] for measurements under forward angles of ejectiles which emerge from internal targets at the target position TP2 in the straight experimental section of COSY will enable inclusive K^+–production studies as well as coincidence experiments for kaons and correlated light particles, see Fig. 11. This device will provide a momentum resolution of $\Delta p/p \leq 1\%$. The expected rates have been estimated via simulation calculations, where the results of Ref. 20 for the production probabilities have been used as input data and where the passage of the ejectiles through the separator magnet D2 towards the detectors at the side of this magnet (mainly K^+ mesons and correlated protons) and in forward direction (mainly deuterons) was determined with a raytracing code. The planned detector setup for the identification of the particles of interest in the presence of a large background of pions and of scattered protons have been described elsewhere[26-28].

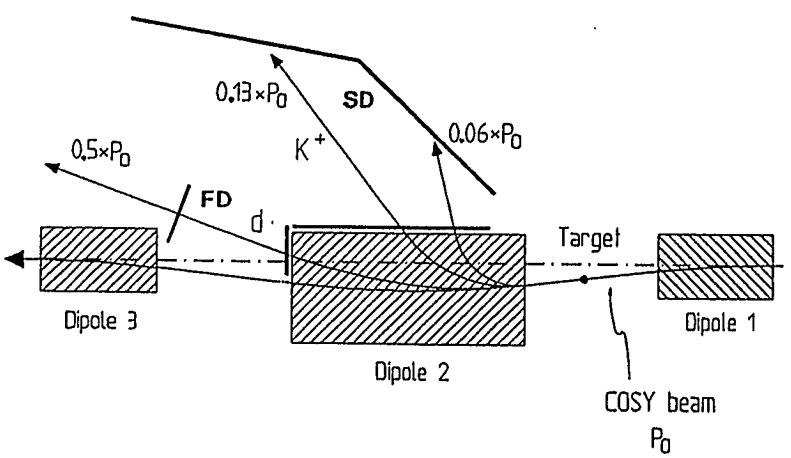

Fig. 11: Schematic plot of the 0^0 Facility which is in preparation for the target place TP2 of COSY–Juelich[25]. FD and SD indicate the forward and side detector, respectively, which consist of multiwire chambers for track reconstruction and of scintillator hodoscopes[26] for TOF and ΔE measurements as well as of Čerenkov counters for background suppression.

References:

1. Kaon Factory Proposal, TRIUMF, Vancouver, B.C., Canada, p. 3–22, 1985

2. N.K. Abrosimov, V.A. Volchenkov, V.A. Gordeev, V.A. Eliseev, E.M. Ivanov, V.P. Koptev, S.P. Kruglov, Yu.A. Malov, S.M. Mikirtych'yants, G.A. Ryabov, G.V. Shcherbakov, Piz'ma Zh. Eksp. Theor. Fiz. **36** (1982) 211

3. N.K. Abrosimov, V.A. Volchenkov, A.B. Gridnev, V.A. Eliseev, E.M. Ivanov, V.P. Koptev, S.P. Kruglov, Yu.A. Malov, S.M. Mikirtych'yants, G.A. Ryabov, G.V. Shcherbakov, JETP Lett. **43** (1986) 270

4. V.P. Koptev, S.M. Mikirtych'yants, M.M. Nesterov, N.A. Tarasov, G.V. Shcherbakov, I.K. Abrosimov, V.A. Volchenkov, A.B. Gridnev, V.A. Eliseev, E.M. Ivanov, S.P. Kruglov, Yu.A. Malov, G.A. Ryabov, Sov. Phys. JETP **67** (1988) 2177

5. V. Koptev, these proceedings

6. V. Koptev, PNPI Gatchina, Leningrad district, Russia, unpublished

7. Xiangdong Ji and J. Engel: Phys. Rev. **C40**, 497 (1989)

8. V.V. Abaev, A.B. Gridnev, V.P. Koptev, S.P. Kruglov, Yu. A. Malov, I.I. Strakovski, G.V. Shcherbakov, Akad. Nauk SSSR **569** (1980), (Preprint LNPI)

9. B.J. Ver West and R.A. Arndt, Phys. Rev. **C25** (1982) 25

10. J. Carroll, Nucl. Phys. **A488** (1988) 203c

11. J. Julien, D. Lebrun, A. Mougeot, P. de Saintignon, N. Alamanos, Y. Cassagnou, C. Le Brun, J.F. Lecolley, R. Legrain, G. Perrin, Phys. Lett. **264** (1991) 269

12. W. Ahner, P. Baltes, Ch. Bormann, D. Brill, R. Brockmann, M. Cieslak, E. Grosse, W. Henning, P. Coczon, B. Kohlmeyer, W. Konrad, D. Miskowiec, Ch. Müntz, H. Oeschler, H. Pöppl, W. Prokopowicz, F. Pühlhofer, R. Renfordt, A. Sandoval, S. Sartorius, R. Schicker, E. Schwab, P. Senger, Y. Shin, J. Stein, K. Stiebing, R. Stock, H. Ströbele, K. Völkel, A. Wagner, W. Walus, Z. Phys. A–Hadrons and Nuclei **341** (1991) 123

13. W. Cassing G. Batko, U. Mosel, K. Niita, O. Schult, Gy. Wolf: Phys. Lett. **B238** (1990) 25

14. W. Cassing, in Proc. Workshop on Strangeness in Nuclei, Cracow, Poland, May 1992, in print

15. W. Cassing, these proceedings

16. B. Kopeliovich and J. Nemchik, Report KFA–Jülich, **Jül–2396** (1990), ISSN 0366–0885

17. B.Z. Kopeliovich and F. Niedermayer, Phys. Rev. **C33** (1986) 2070

18. B. Kamys, W. Cassing, L. Jarczyk, O.W.B. Schult, K. Sistemich, A. Strzalkowski, Ann. Report 1991 of the IKP, KFA Jülich, **Jül–2590** (1992) 30, ISSN 0366–0883

19. B. Kamys, W. Cassing, L. Jarczyk, O.W.B. Schult, K. Sistemich, A. Strzalkowski, Ann. Report 1992 of the IKP, KFA Jülich, in print

20. H. Müller and M. Büscher, in Proc. Workshop on Strangeness in Nuclei, Cracow, Poland, May 1992, in print

21. H. Müller, Z. Physik A–Hadrons and Nuclei **339**, 409 (1991)

22. W. Borgs, M. Büscher, D. Gotta, D. Grzonka, H.R. Koch, W. Oelert, H. Ohm, O.W.B. Schult, H. Seyfarth, K. Sistemich, K.H. Watzlawik, J. Ernst, F. Hinterberger, L. Jarczyk, B. Kamys, St. Kistryn, A. Kozela, J. Smyrski, A. Strzalkowski, S. Dienel, K.–W. Leege, H. Müller, Chr. Schneidereit, S.V. Dshemuchadze, V.I. Komarov, V. Lyachenko, F. Nichitiu, V. Travkin, B.Zh. Zalyhanov, N.I. Zhuravlev, V. Abaev, V. Koptev, P. Birien, W. Cassing, H. Dombrowski, R. Santo: Proposal Nr. 18 to the COSY Program Advisory Committee, Okt. 17, 1991

23. A.A. Sibirtsev and M. Büscher, subthreshold–K^+ production in pA collisions, to be published

24. A.A. Sibirtsev , these proceedings

25. U. Bechstedt, G.P.A. Berg, U. Hacker, H. Hagedoorn, A. Hardt, K. Henn, F. Hinterberger, P. Jahn, K. Kilian, W. Klein, H.R. Koch, M. Köhler, P. Krejcik, G. Kroel, H. Lang, S.A. Martin, K. Matela, T. Mayer–Kuckuk, N. Mosko, H. Poth, D. Prasuhn, H.J. Probst, A. Richert, G. Riepe, M. Rogge, P. von Rossen, T. Sagefka, G. Schug, O.W.B. Schult, B. Seligmann, H. Singer, P. Turek, E. Veiders, G. Wüstefeld, L. Zemlo, Report KFA–Jülich, **Jül–Spez–370** (1986) ISSN 0343–7639

26. V. Abaev, P. Birien, W. Borgs, M. Büscher, H. Dombrowski, S.V. Dshemuchadze, J. Ernst, D. Gotta, D. Grzonka, F. Hinterberger, L. Jarczyk, B. Kamys, St. Kistryn, H.R. Koch, V.I. Komarov, V. Koptev, A. Kozela, V. Lyachenko, H. Müller, F. Nichitiu, W. Oelert, H. Ohm, R. Santo, Chr. Schneidereit, A. Schubert, O.W.B. Schult, H. Seyfarth, K. Sistemich, J. Smyrski, A. Strzalkowski, V. Travkin, B.Zh. Zalyhanov, N.I. Zhuravlev, in Proc. Workshop on Meson Production, Interaction and Decay, Cracow, Poland, May 1991 (World Scientific, Singapore, A. Magiera et al. eds.) 1992, p. 259

27. K. Sistemich, M. Büscher, V. Abaev, U. Bechstedt, P. Birien, W. Borgs, W. Cassing, S. Dienel, H. Dombrowski, S.V. Dshemuchadze, J. Ernst, R. Eßer, D. Gotta, D. Grzonka, A. Hardt, F. Hinterberger, M. Ivanov, L. Jarczyk, B. Kamys, St. Kistryn, H.R. Koch, V.I. Komarov, V. Koptev, A. Kozela, A. Krykin, K.W. Leege, H. Müller, W. Oelert, H. Ohm, R. Santo, Chr. Schneidereit, O.W.B. Schult, H. Seyfarth, V. Shelkov, J. Smyrski, A. Strzalkowski, K.–H. Watzlawik, B.Zh. Zalyhanov, N.I. Zhuravlev, P. Zolnierczuk, in Proc. Workshop on Strangeness in Nuclei, Cracow, Poland, May 1992, in print

28. R. Eßer, H. Ohm, M. Büscher, A. Kiselev, V. Koptev, S. Kopyto, S. Mikirty'chjants, H. Müller, B. Prietschk, B. Rimarzig, G. Shcherbakov, K. Sistemich, these proceedings

ZERO-DEGREE EXPERIMENTS IN THE IUCF COOLER RING: SOME RESULTS AND PLANS

D.W.MILLER*, A.D.BACHER*, J.M.CAMERON*, and J.W.WATSON+

* *Indiana University Cyclotron Facility*
Bloomington, Indiana 47405, U.S.A.

+ *Kent State University, Kent, Ohio 44242, U.S.A.*

Several experiments with reaction particles emitted at 0° have been carried out or are in progress in the "T section" of the IUCF electron-cooled storage ring. In addition, a number of future experiments are planned for the proposed IUCF chicane/spectrometer system in the "S section" of the ring, described in another paper at this workshop. The present paper provides a brief summary of some of these experiments in order to illustrate the wide variety of types of physics studies which are accessible with 0° experiments in a cooler ring.

1. Introduction

The Indiana University Cooler provides many unusual new features for nuclear physics studies in the energy range from 50-500 MeV. These include the opportunity to carry out experiments with carrier-free polarized targets in a high-resolution stored polarized beam, the ability to detect recoils from very thin internal targets, and a counting environment without a localized beam dump.

In such a ring it is possible to carry out experiments in which the nuclear reaction products or recoils are emitted at 0° or at very small angles with respect to the circulating beam. This is feasible provided the emitted products have a substantially lower magnetic rigidity than that of the stored beam. At the Indiana University Cyclotron/Cooler Facility (IUCF), experiments of this type have already been completed in the "T section" of the ring, and more are planned using a chicane/spectrometer system proposed for the "S section" of the ring. (The equipment for the latter system will be described in a separate paper at this workshop by G.P.A. Berg et al.[1])

The present paper gives a brief survey of some of these experiments in progress or planned in the IUCF Cooler ring. With one exception, these experiments all include products emitted at 0° . Spokespersons or contact persons are listed for each experiment; they should be contacted for further details.

It should be mentioned that single-pass 0° experiments have also been performed using the cyclotron and K600 magnetic spectrometer at IUCF, but these will not be discussed here.

2. 0° Experiments Completed or in Progress

2.1 Kinematically Complete Measurements of pp → pnπ⁺ Near Threshold (Spokesperson: W.W. Daehnick, University of Pittsburgh)

The fundamental pion-nucleon vertex has been studied extensively in hadron-induced reactions through NN → NN, Nπ → Nπ, πd → πd, and NN → πd processes at meson factories. The three-body final state in NN → NNπ has received much less attention, particularly near threshold due to experimental difficulties. The three-body final state is especially interesting because of the variety of kinematical conditions and spin-isospin states which can be examined. When studied near threshold, it has the additional advantage of suppressing the delta resonance. The large negative Q values for pion creation also lead to high momentum transfer, so that the reaction samples the N-N system at short distances in a process involving a relatively small number of degrees of freedom. Thus the data should be sensitive to the off-shell characteristics of the NNπ interaction in a fairly direct way. Recent work also suggests sensitivity to heavy meson exchange currents.

Previously published IUCF Cooler Experiments CE01 and CE23 studied the pp → ppπ⁰ reaction near threshold down to $\theta_p = 3°$.[2] The experiment reported here (CE03) measured the pp → pnπ⁺ total cross section (threshold $E_p = 292.30$ MeV) down to and including θ_p and $\theta_n = 0°$, using unpolarized proton beams at 294, 300, 307, 314 and 320 MeV. The experimental layout at the "T site" of the IUCF Cooler is shown in Fig. 1.[3]

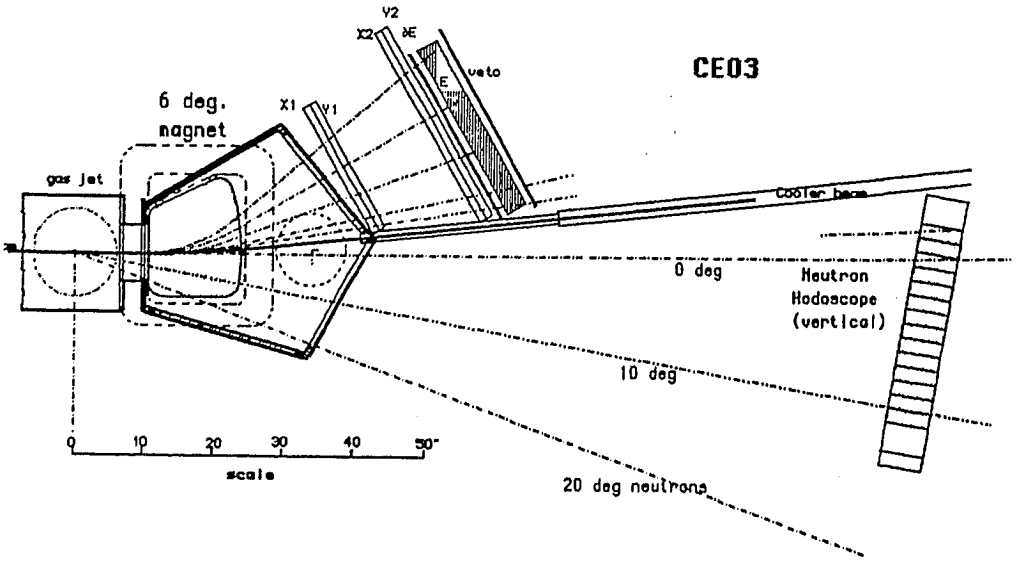

Fig. 1. Experimental layout for measurement of the pp → pnπ⁺ reaction in the T section of the IUCF Cooler ring.

The experiment employed a hydrogen gas-jet target, mounted just ahead of the 6-degree bending magnet, and an unpolarized proton beam providing an average luminosity of $0.8 \times 10^{30} cm^{-2} s^{-1}$. Reaction protons were detected by two large-area position-sensitive multiwire drift chambers (8 planes), a large-area ΔE detector, five 13-cm deep E scintillators, followed by a large-area veto counter. In the neutron arm, a 120 cm wide by 71 cm high neutron hodoscope, utilizing 14 scintillator bars for detecting 40-130 MeV neutrons, was mounted 5 m from the target, and preceded by a large veto detector. The beam luminosity was monitored by detecting forward protons from elastic p-p scattering in the proton arm in coincidence with 90° protons in a position-sensitive detector.

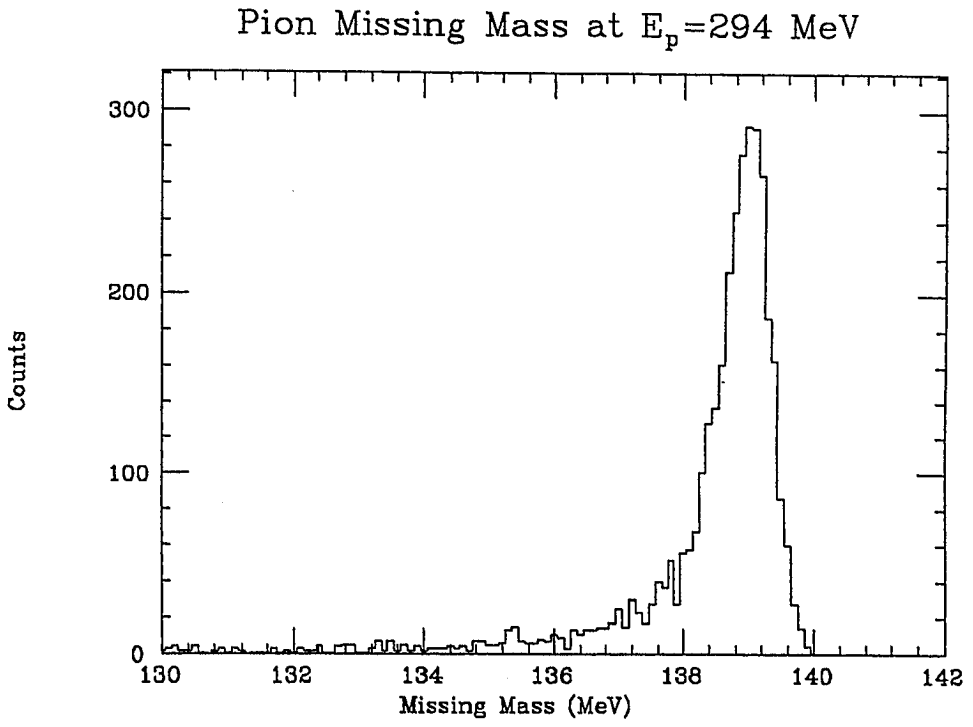

Fig. 2. Pion missing mass in the $pp \rightarrow pn\pi^+$ reaction at 294-MeV bombarding energy.

The efficiency of background rejection in the experiment at all energies including 294 MeV was good. Fig. 2 shows the pion missing mass plotted for 294 MeV after cuts on the reconstructed event vertex and a particle-identification (E-ΔE) cut. At this energy, the differential cross section plotted as a function of the pion emission angle relative to the center of mass of the n-p system, for which the data cover nearly the full range of angles, is isotropic within experimental errors, as expected for s-wave pion emission near

threshold. The total cross section plotted as a function of the dimensionless pion maximum momentum η lies above and parallel to the earlier pp $\rightarrow$ ppπ^0 results at IUCF. The final results, soon to be published, will present absolute differential and total cross sections for each of the energies studied.

2.2 High Momentum-Transfer Reactions Studied using Recoil Detection at 0° (Spokespersons: R.E. Segel, Northwestern University, and R.D. Bent, IUCF)

These experiments (CE06 and CE32) utilize the detection of recoil nuclei produced in high momentum-transfer reactions. In this way cross sections for different reaction channels can be measured simultaneously with the same beam, target, and detection system.

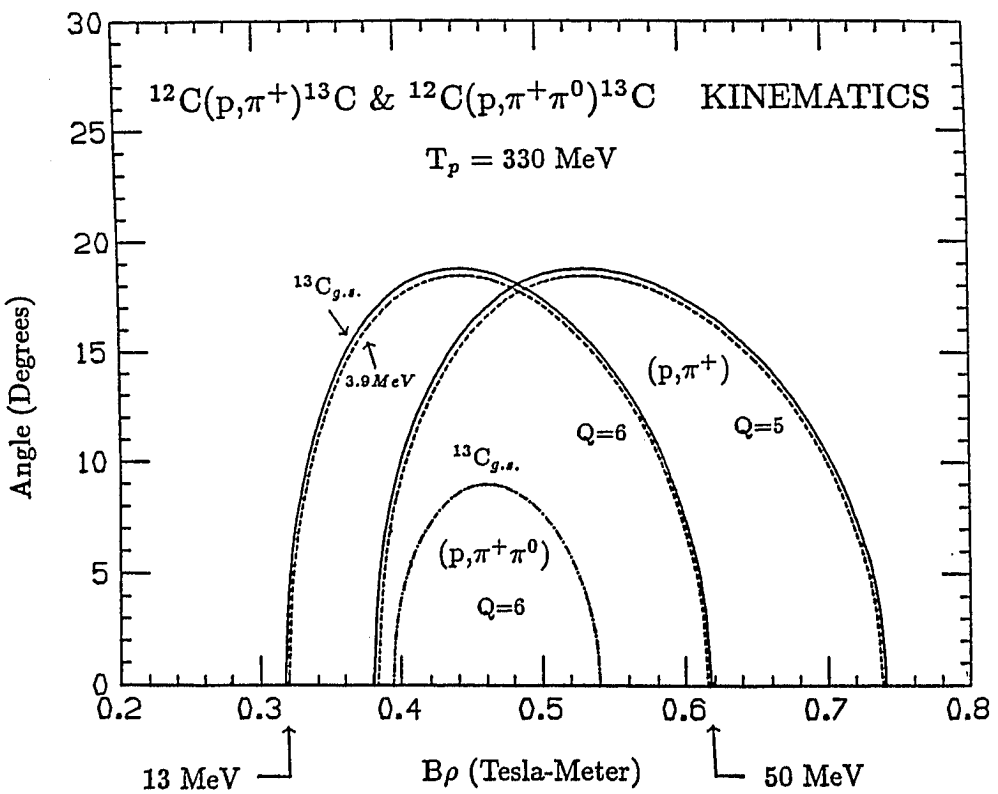

Fig. 3. Angle vs. momentum of the recoil ions from the (p,π^+) and $(p,\pi^+\pi^-)$ reactions on ^{12}C at 330-MeV bombarding energy, for recoil charge states Q = 5 or 6.

For example, one can measure different isospin channels simultaneously to allow quantitative checks of earlier data suggesting deviations from isospin invariance and from pre-

dicted near-threshold cross section behavior in the $^{12}C(p,\pi^+)$ and $^{12}C(p,\pi^0)$ reactions. Further, measurements of the isospin selectivity of the A(p,2π)A+1 reaction should yield information about the relative importance of nonlinear terms in the πN interaction involving the pion field to third and fourth order. The A(p,2π)A+1 reaction is also a possible tool for looking for evidence of a bound or quasi-bound two-pion state in nuclear matter. Finally, sparse photonuclear data at intermediate energies and the difficulties of photonuclear polarization measurements make studies of the inverse ($\vec{p}$,γ) reaction with polarized beams using the recoil technique an attractive alternate approach.

Experiments CE06 and CE32 are designed to determine cross sections for production of mass 13 recoils from the reactions $^{12}C(p,\pi^0)^{13}N$, $^{12}C(p,\pi^+)^{13}C$, $^{12}C(p,\pi^-)^{13}O$, and $^{12}C(p,\pi\pi)$ at proton energies T_p = 160–350 MeV. A sample kinematic plot showing loci for different charge states for one-pion production (in this case π^+) compared to two-pion production is given in Fig. 3; note that the latter is a three-body process and the corresponding events fill the smallest locus. This experiment employs a carbon fiber skimmer target yielding an average luminosity of $\sim 10^{30}cm^{-2}s^{-1}$. It uses the same 6-degree magnet at the Cooler T site as shown in Fig. 1, but a completely different detection system for the recoils. The first detector just clearing the beam is a large-area parallel-grid avalanche detector. It is followed by a 50-cm flight path, and then a ΔE-E detector telescope consisting of a gas proportional counter and 24 silicon micro-strip detectors covering a 65 cm x 10 cm area. Each detector is 5 cm x 5 cm, with 1 mm wide strips 300 μm thick.

Experiments CE06 and CE32 took production data for the above reactions in November-December 1992 and February 1993.

2.3 Measurements of Proton-Neutron Correlation in Elastic Deuteron Breakup at 260 MeV (Spokespersons: B.Ni and J.M.Cameron, IUCF)

A number of important charge-exchange and scattering experiments would be accessible if a good-resolution tagged polarized neutron beam could be produced by breakup of polarized deuterons in the Cooler ring. Some of these will be mentioned in Sec. 3.41. The experiment described here (CE10) was designed in part to determine the feasibility of producing such a tagged polarized neutron beam. In addition, more breakup data are needed to clarify theoretical interpretations of the reaction mechanism of deuteron breakup at medium energies, particularly in comparisons of absolute cross sections for breakup.

Experiment CE10 measured the small-angle proton-neutron angular correlation in the C(d,np), Cu(d,np) and Pb(d,np) reactions at E_d = 260 MeV, using the same 6-degree magnet at the Cooler T site already described. C, Cu and Pb skimmer targets were inserted alternately ahead of this magnet and bombarded by an unpolarized deuteron beam, providing an average luminosity of about $10^{28}cm^{-2}s^{-1}$. The proton arm utilized a proton telescope, consisting of x and y delay-line wire planes sandwiched between a pair of thin scintillators and followed by two NaI(Tl) detectors. This telescope covered the laboratory angular range $\theta_p \sim 0°$ to 6° beam left, with a vertical acceptance of $\Delta\phi_p \sim 3°$. In the neutron arm, an array of six 102 cm x 15 cm x 10 cm plastic scintillator bars were placed 9.5 m from target, centered at 1° intervals from $\theta_n = 0°$ to 5° beam right, each with acceptances $\Delta\theta_n = 0.67°$ and $\Delta\phi_n = 1°$. The position accuracy obtained for (n,p) conversion was about 3.5 cm (out of 102 cm). The proton telescope also simultaneously monitored deuterons, so that it also served as a beam luminosity monitor.

A typical angular correlation for elastic (d,pn) breakup at 260 MeV is shown in Fig. 4 for Cu and C skimmer targets. The results show the angular distribution for neutrons in coincidence with a particular average proton angle bin of $\theta_p = 2°$. The full width at half maximum of the breakup peak at this bombarding energy is $\pm 2°$. The measured absolute cross sections provide encouragement for the production of tagged polarized neutrons in the Cooler ring.

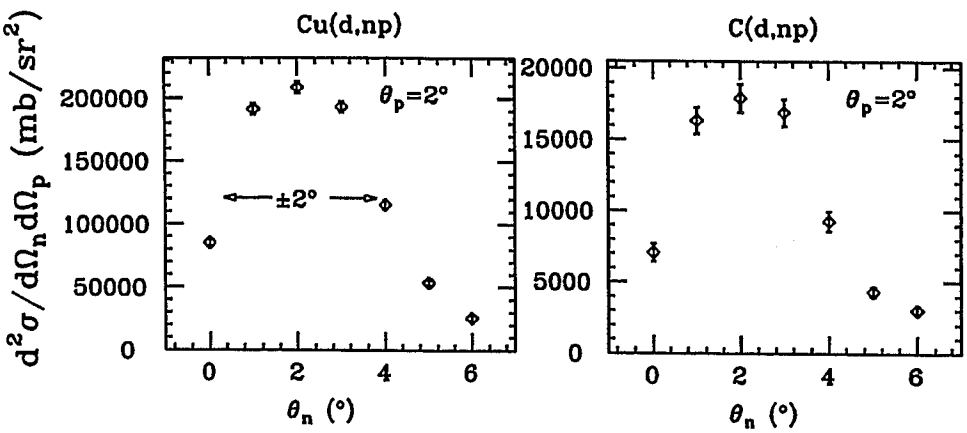

Fig. 4. Typical n-p angular correlation for elastic deuteron breakup at 260 MeV.

2.4 Vector and Tensor Analyzing-Power Measurements in ($\vec{d}$,^{2}He) Reactions (Spokesperson: M.Spraker, IUCF)

In the present discussion, isospin-raising, charge-exchange reactions [(n,p), (d,^{2}He), (t,^{3}He), etc.] are referred to as β^+ reactions, and isospin-lowering reactions [(p,n), (^{3}He,t), etc.] as β^- reactions, because these reactions connect the same nuclei as β^+ and β^- decays. A central feature of the proposed IUCF chicane/spectrometer system will be the capability for studying the β^+ charge-exchange reaction ($\vec{d}$,^{2}He) to complement the extensive work undertaken at IUCF over the past decade on the β^- charge-exchange reaction (p,n). Some of the proposed β^+ charge-exchange studies will be discussed in Sec. 3.4.

Several of the studies of interest require the determination of the final-state spins in the ($\vec{d}$,^{2}He) reaction. In particular, selection of 0^-, 1^- and 2^- final states in spin-dipole, charge-exchange reactions provide important comparisons with theoretical nuclear structure descriptions. Tensor and vector analyzing powers in the ($\vec{d}$,^{2}He) reaction appear to give the desired unique final-state spin selectivity. It is important to calibrate this selectivity experimentally against known states, as well as to make comparisons with theoretical DWIA predictions.

Experiment CE36 has been approved to measure the tensor and vector analyzing powers from 0° to 15° for the 280-MeV ^{12}C($\vec{d}$,^{2}He) reaction leading to spin-dipole states, including the known 1^- and 2^- states in ^{12}B. The overall energy resolution is expected to

be $\leq$ 300 keV. A carbon skimmer target will be placed ahead of the 6-degree magnet in the T section of the ring and bombarded with a polarized deuteron beam, providing an expected average luminosity of about $10^{29}cm^{-2}s^{-1}$. To obtain the desired energy resolution, the 6-degree magnet will be followed by two additional dipoles and three-quadrupoles to deflect and focus the correlated diprotons on to a split Ge detector. The scattering angle will be determined using a 3-plane multiwire chamber (x,y,u) at the exit of the 6° magnet. An identical chamber will be placed at the entrance to the Ge detector to determine the proton entrance point, and a He bag between the two chambers will be employed to reduce energy straggling. The Ge detector is a specially fabricated 7-cm dia. segmented double-detector serving as a ΔE-E system for each proton. A thin plastic scintillator immediately precedes the first wire chamber, and a thin split scintillator precedes the Ge detector to provide timing and coincidence information. A deuteron luminosity monitor is provided simultaneously by ^{12}C(d,d) elastic scattering into scintillators and NaI detectors placed at 5° , 10° , 15° and 20° on the opposite side of the 6-degree magnet. The general layout of this system is shown in Fig. 5.

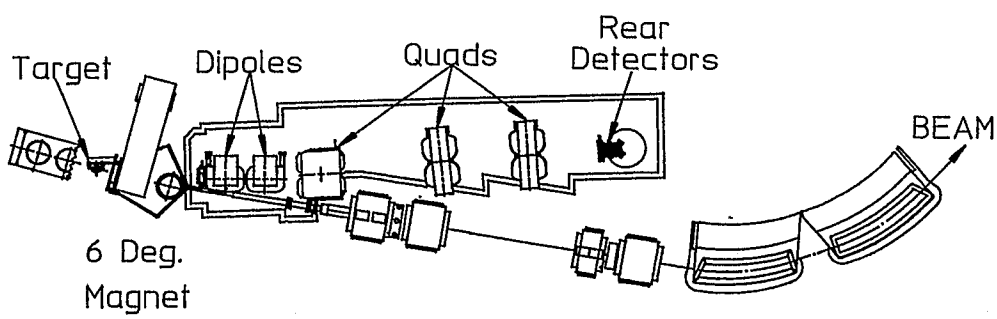

Fig. 5. The general layout of the T section for experiment CE36, showing the additional deflecting and focussing dipoles and quadrupoles, and the location of the Ge detector.

3. 0° Experiments Planned for the Proposed Chicane/Spectrometer

3.1 Chicane/Spectrometer Concept

As mentioned in Sec. 1 and discussed in detail in a later paper[1] at this workshop, it is currently proposed to install a new 3-magnet chicane in the "S" region of the IUCF Cooler ring, with gas jet, microribbon, dust or polarized targets inserted near the entrance or up-stream edge of the second magnet. When combined with a new large-aperture quadrupole, a new septum magnet and the existing K300 spectrometer magnet, a versatile spectrometer system will be provided. In particular, experiments can be carried out detecting particles emitted at 0° lab with magnetic rigidities up to 1.9 Tm when the beam has its maximum rigidity of 3.6 Tm; at larger laboratory angles reaction particles with up to 2.7 Tm rigidity can be detected. The following subsections describe 0° or near-0° experiments planned for the chicane/spectrometer system.

3.2 Examples of Symmetry Studies

3.21 Chiral Symmetry and Pionium (Spokesperson: S.E.Vigdor, IUCF)

π-π scattering lengths are fundamental parameters of chiral-symmetry breaking models. However, previous determinations of these scattering lengths involve indirect final-state interaction analyses of multibody processes. These suffer either from questions about the assumptions of the model employed, or from scatter in the experimental data. However, if a bound $\pi^+\pi^-$ atom can be formed, its $2\gamma/2\pi^0$ decay ratio directly determines the difference of the T = 0 and T = 2 s-wave π-π scattering lengths. The pionium atom is expected to be a large (400 fm) weakly-bound (2 keV) object, and thus very difficult to observe by standard methods. The Cooler provides the unique possibility of searching for bound pionium just above threshold, where the use of low-density targets should cause negligible perturbations of the pionium, once formed.

The planned experiment would be carried out in two phases, initially with a (modified) detection system in the T section, as already described for CE36 (see Fig. 5), and later with the chicane/spectrometer system. Phase 1 will be a high-resolution measurement of the ^{3}He recoil spectrum in the reaction pd $\rightarrow$ ^{3}He $(\pi^+\pi^-)$ to determine the total pionium production cross section about 1 MeV above threshold. In this measurement π^+ and π^- ejectiles deflected in the 6-degree or center chicane magnet will be detected separately to veto their free production in the process. Phase 2 will then entail the measurement of coincident $\gamma\gamma$ decay of pionium atoms tagged by the appropriate ^{3}He recoils.

The final configuration planned for the chicane/spectrometer system will involve a deuterium gas jet target preceding the central chicane magnet. The chicane/spectrometer in the "normal mode" (see Fig. 2 of reference 1) will be set at 0° to detect recoil ^{3}He in the forward cone with an overall resolution of about 70 keV. At 1 MeV above threshold, the spectrometer will accept the full 4π decay solid angle in the center-of-mass system. A cylindrical segmented photon detector around the target will be added to detect the coincident $\gamma\gamma$ decay of the pionium. With efficient vetoing of the free charged pions, pionium production should be clearly identifiable by the ^{3}He kinematic locus, as long as the total cross section for pionium production is at least 1 nb at $\sim$ 1 MeV above threshold.

3.22 Charge Symmetry Breaking in the dd $\rightarrow$ $\alpha\pi^0$ Reaction (Contact Person: W.W.Jacobs IUCF)

IUCF studies of $\vec{n}$-$\vec{p}$ scattering provide evidence for CSB effects arising in part from ρ-ω mixing. Theoretical considerations suggest that the isospin-violating reaction d + d $\rightarrow$ α + π^0 will be sensitive to π-η mixing. Using essentially the same configuration as just described for the pionium search, the chicane/spectrometer system should allow a search for the d + d $\rightarrow$ α + π^0 reaction in a very clean experimental environment. Potential backgrounds due to dd $\rightarrow$ $\alpha\gamma$, dp $\rightarrow$ ^{3}Heγ, dd $\rightarrow$ $\alpha\pi^0\pi^0$ etc. should be suppressed by the use of a contaminant-free target, the high-resolution detection of the recoil α using the chicane/spectrometer system, and a bombarding energy near threshold for dd $\rightarrow$ $\alpha\pi^0$.

The planned measurement is to search for the isospin-violating reaction dd $\rightarrow$ $\alpha\pi^0$ (threshold E_d = 225.5 MeV) at a deuteron bombarding energy of 237 MeV. At this energy

the full center-of-mass solid angle will still appear in the forward α cone accepted by the spectrometer at 0° , allowing the total cross section to be determined directly. A deuterium gas jet target will be employed ahead of the center magnet using the chicane/spectrometer system in the normal mode, just as in the pionium experiment already described. In the present case the cylindrical photon detector will be used to detect photons from π^0 decay for background suppression. It is expected that the kinematic focusing of the recoil ^{4}He nuclei plus this background suppression should should allow the search for this reaction to a total cross section sensitivity level as small as 0.1 pb.

3.3 Examples of Spin-Correlation Studies

3.31 Nucleon-Nucleon Interaction in the Nuclear Medium (Contact Persons: E.J. Stephenson, IUCF; N.S.Chant, Maryland)

Proton-induced reactions leading to the production of discrete states or giant resonances with protons or neutrons as the detected particle have been well described using an effective nucleon-nucleon interaction with a DWIA model. In experiments with both polarized beam and polarized targets, the non-zero target spin should allow determination of amplitudes and phases sensitive to medium modifications of the effective N-N interaction. Spin-correlation measurements of both inelastic proton scattering and $(\vec{p},2p)/(\vec{p},pn)$ knockout reactions using polarized targets are unique to the Cooler and chicane/spectrometer combination. If spin orientations in the S region of the Cooler are managed through Siberian Snake magnets in other parts of the ring, then longitudinally and sideways polarized beams as well as transversely polarized beam would be available for measurements with this system.

Previous measurements of elastic scattering with polarized beam and polarized target[4] have found very small target analyzing power and spin-correlation parameters. To a first approximation, such parameters in the elastic channel tend to be of the order 1/A, where A is the target mass. On the other hand, one should expect larger effects for inelastic scattering, since the core remains inert for both the polarized nucleon and the interaction that creates many single-particle levels. A sample planned experiment is to study the $^{14}N(\vec{p},p')$ reaction at 160 MeV over the angular range from 3° → 50° . This would include the measurement of the spin-correlation parameters C_{NN}, C_{LL} and C_{SL}, and beam and target vector and tensor analyzing powers A_N, $A_{(NN)}$, $A_{(SS)}$ and $A_{(SL)}$. Fig. 6 shows DWIA predictions by Stephenson[5] based on earlier exploratory work by Franey and Love[6]. The solid curve in the upper left panel represents the full cross section, while the contributions calculated from the central (C), spin-orbit (S) and tensor (T) amplitudes are also indicated. The right hand panels show similar information for the spin correlation parameters C_{NN} and C_{SL}, and the lower left panel three of the target tensor analyzing powers, $A_{(NN)}$, $A_{(SS)}$ and $A_{(SL)}$.

This experiment would employ a $^{14}\vec{N}$ polarized target (N mixed with optically-pumped alkali vapor) with the chicane/spectrometer system in the "small-angle mode"[1] to detect inelastic protons. This mode will detect elastic and inelastic protons up to 270 MeV for laboratory angles as low as 3° .

Medium modifications of the effective N-N interaction can also be studied by $(\vec{p},2p)/(\vec{p},pn)$ knockout reactions, incorporating an appropriate DWIA description for com-

parison. Such studies would complement measurements of spin-transfer observables and emitted-nucleon polarizations being carried out at TRIUMF[7]. The experimental arrangement in the IUCF Cooler will include an appropriate polarized target, a large solid-angle wire chamber/plastic/NaI detector array for knockout protons from ($\vec{p}$,2p), or a large acceptance CH_2 converter/drift chamber array for knockout neutrons from ($\vec{p}$,pn).

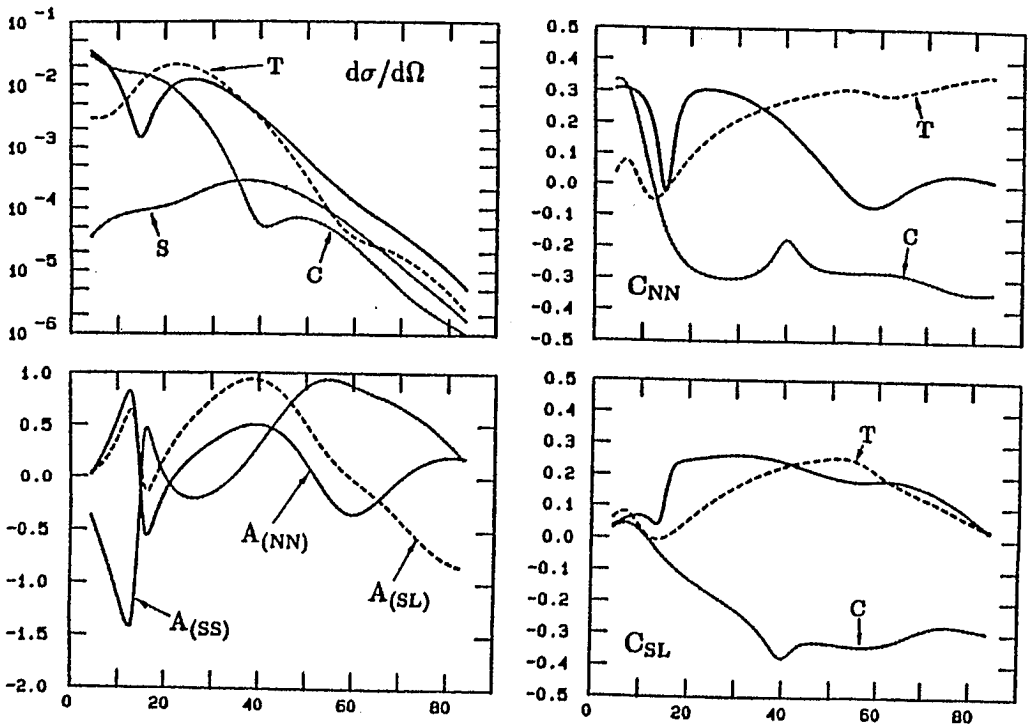

Fig. 6. DWIA predictions for spin correlation parameters, target analyzing powers, and cross sections for the $1^+ \rightarrow 0^+$ T = 1 transition in ^{14}N for 160-MeV inelastic proton scattering.

3.32 Interference between Fermi and Gamow-Teller Transition Amplitudes (Contact Persons: C.D.Goodman and E.J.Stephenson, IUCF)

In the transition from a T = 1/2 nuclear state to its isospin mirror both the Fermi and Gamow-Teller operators can contribute coherently, but, unless both the target and the projectile are polarized, the interference is not observable. Spin-correlation measurements can reveal the interference term and, hence, the relative phase between these two operators. This is not possible with charge-exchange analyzing-power or spin-transfer measurements, and has not been measured in nucleon-nucleon scattering. Sample charge-exchange reactions for studying the relative F/GT phase are $^3\vec{He}(\vec{n},p)T$ and $^{15}\vec{N}(\vec{p},n)^{15}O$. The tagged

neutron capability of the Cooler ring/chicane combination and carrier-free polarized targets are ideally suited for such measurements. Fig. 7 shows a prediction by Stephenson[5] of the spin-correlation parameter C_{LL} for the $^{15}\vec{N}(\vec{p},n)^{15}O$ ground state $(1/2^-)$ to ground state $(1/2^-)$ mixed transition, as a function of the relative phase between the Fermi ($\Delta J^\pi = 0^+$) and Gamow-Teller ($\Delta J^\pi = 1^+$) amplitudes.

A specific experiment of interest in the opposite (β^+) charge-exchange direction is the measurement of the spin-correlation parameter C_{NN} in the $^3\vec{He}(\vec{n},p)T$ reaction at $\theta_p = 0°$ and a neutron energy $E_n = 140$ MeV. This would employ a skimmer target and a polarized deuteron beam of energy $E_d = 290$ MeV to produce the tagged polarized neutrons. The tagging protons would be detected by using the central chicane magnet plus a scintillator array. An optically-pumped $^3\vec{He}$ polarized second target would be employed, similar to the one now in use in the IUCF Cooler, followed by a converter and scintillator telescope to detect the $(\vec{n},p)$ protons.

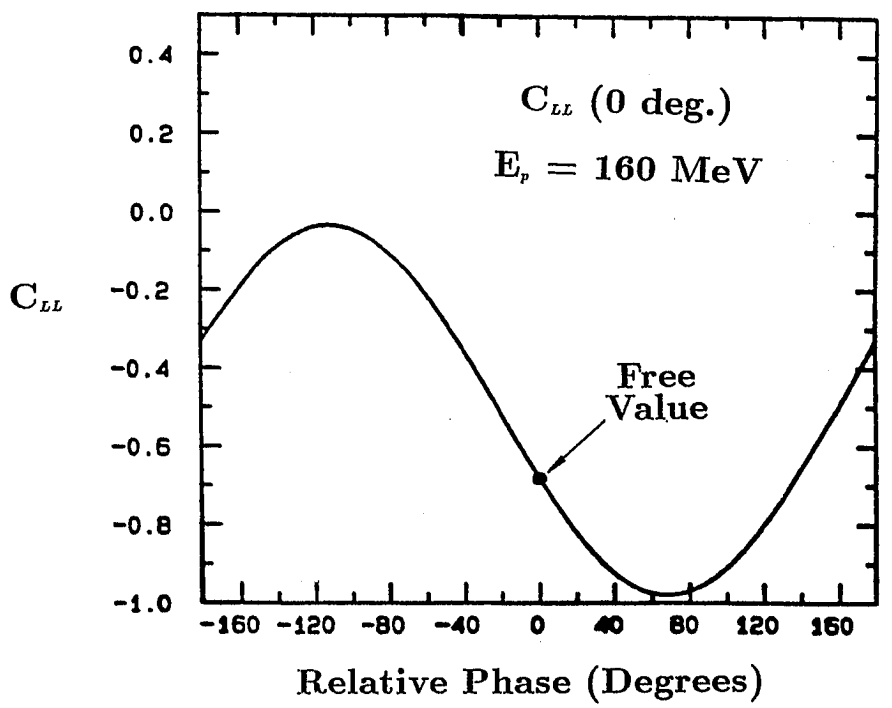

Fig. 7. Predicted spin-correlation parameter C_{LL} at 0° as a function of the relative Fermi/Gamow-Teller phase for the $^{15}\vec{N}(\vec{p},n)^{15}O$ g.s. reaction.

3.4 ($\vec{d}$,^{2}He) Investigations

3.41 Comparison of Isospin-Raising (β^+) with Isospin-Lowering (β^-) Reactions (Contact Persons: J.W. Watson, Kent State; D.W.Miller, IUCF)

Charge-exchange nuclear reactions in the β^- direction have been extensively studied above 100 MeV at IUCF, TRIUMF, and LAMPF using the (p,n) reaction, which has proven at medium energies to be a powerful, quantitative probe of nuclear structure and reaction dynamics.[8,9] β^+ reactions can also be used to shed light on a number of nuclear physics issues that are of current importance. Of special interest is the measurement of β^+ matrix elements to states not accessible in beta decay. For this purpose the (n,p) reaction has been studied at medium energies with secondary neutron beam facilities at TRIUMF, LAMPF/WNR and TSL (Uppsala). However, because two sequential nuclear reactions are required, these (n,p) studies have been severely limited by resolution. With a final charged-particle resolution of about 1 MeV or worse, (n,p) results do not, in general, separate final states (with the exception of a few cases in light nuclei). Further, large quantities of (often separated-isotope) target material are required. By contrast, the (d,^{2}He) reaction [a (d,2p) process in which the two outgoing coincident protons are detected closely correlated in space in a $^1S_0$ state] has some definite advantages over the (n,p) reaction when carried out with polarized beam and an appropriate spectrometer. The ($\vec{d}$,^{2}He) reaction can study much of the same physics as the (n,p) reaction, but with more unique spin-isospin selection, good resolution, substantial count rates, modest quantities of target material and the possibility of uniquely determining nuclear spins (J) of final states from analyzing-power measurements[10], as mentioned in Sec. 2.4.

An important feature of the planned IUCF chicane/spectrometer facility is the capability of studying the ($\vec{d}$,^{2}He) reaction with good resolution at a beam energy of 140 MeV/nucleon. Investigations of several areas of interest are planned. It is important to determine whether the GT quenching factor (the ratio of observed to calculated GT strength) is the same for the β^+ direction as it is for the β^- direction. In nuclei with L-S closed proton cores, the GT resonance is Pauli blocked in the β^+ direction because no $0\hbar\omega$ $\Delta L = 0$, $\Delta S = 1$ transitions are available in the pure shell model. However, ground-state configuration mixing in the target nucleus can open up GT transitions, and the detection of this strength represents a very sensitive test of such mixing. It is also expected that measurements with the (d,^{2}He) reaction can provide important constraints on theoretical calculations of the two-neutrino mode of double beta decay. Finally, (d,^{2}He) measurements also have important applications for astrophysical questions; for example, in calculations of pre-supernova stellar collapse a knowledge of electron-capture rates is of crucial importance.

One cannot overemphasize the importance of good resolution for β^+ measurements. As an example, Fig. 8 illustrates this in studies related to the double beta decay of ^{48}Ca to ^{48}Ti. The crucial state in the intermediate ^{48}Sc nucleus is the $J^\pi = 1^+$ state at 2.52 MeV. In the ^{48}Ca(p,n)^{48}Sc reaction at 135 MeV[9], the 300-keV resolution employed is quite adequate to resolve this crucial state. However, in the ^{48}Ti(n,p)^{48}Sc reaction at 198 MeV[11] the 1.3 MeV resolution is clearly not adequate to extract unambiguous B(GT) values for this transition. The (d,^{2}He) reaction in the IUCF Cooler ring using the chicane/spectrometer system should provide good resolution in the β^+ direction, expected to be $\leq$ 200 keV.

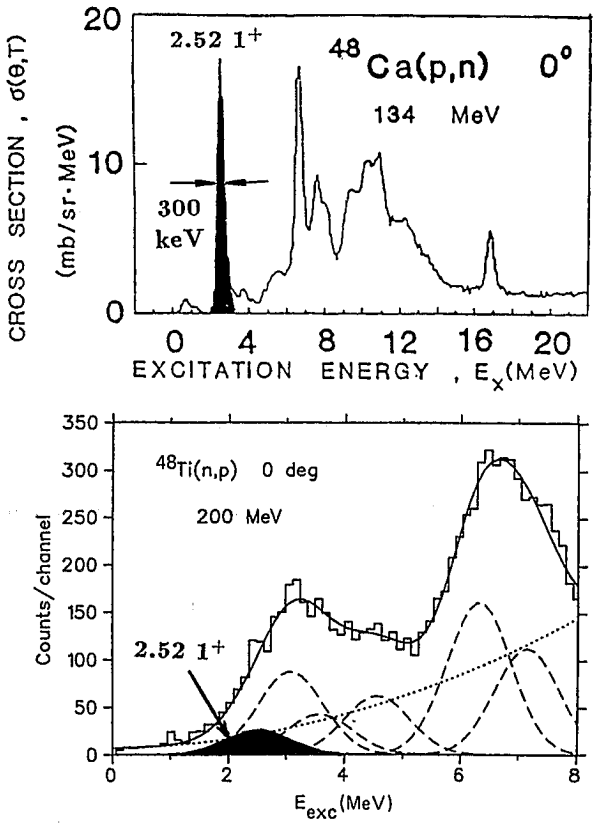

Fig. 8. Illustration of the need for better resolution than currently available in charge-exchange measurements for double beta decay comparisons. Top: ^{48}Ca(p,n) at 134 MeV[9] with 300-keV resolution. Bottom: ^{48}Ti(n,p) at 200 MeV[11] with 1.3-MeV resolution, necessitated by two sequential reactions.

A sample measurement now under consideration would be the high-resolution measurement of ^{16}O($\vec{d}$,^{2}He)^{16}N at $E_d \leq 290$ MeV to determine ground-state configuration mixing in ^{16}O . This would include the measurement of the differential cross section ($d\sigma/d\omega$) and the tensor analyzing power A_{yy} for laboratory angles $0° \leq \theta_{lab} \leq 30°$. The investigation would employ a water vapor jet target and the chicane/spectrometer in its normal mode to detect coincident final-state protons.

3.42 Collective Effects Sensitive to the Spin-Longitudinal Nuclear Response Function (Contact Person: S.E. Vigdor, IUCF)

An important, unresolved issue concerning the nuclear response function is whether there are any significant collective effects associated with the pion field in nuclei. There are theoretical reasons to expect that the pion-exchange ($\vec{\sigma}\cdot\vec{q}$) residual particle-hole interaction in nuclei should be sufficiently attractive at intermediate momentum transfers ($q \sim 2$ - $3m_\pi$) to introduce significant collectivity.[12] This collectivity is predicted to lead to an enhancement and "softening" (i.e. shift toward lower excitation energy) of the isovector spin-longitudinal response of nuclei. Intermediate-energy ($\vec{p}$,$\vec{p'}$) and ($\vec{p}$,$\vec{n}$) spin transfer measurements have not confirmed this predicted longitudinal enhancement, but ambiguities in

the interpretation of the measurements remain. A clearer resolution of the issue might be provided if one could map out the distributions of 0^-, $\Delta T = 1$ strength (i.e., of excitations carrying the pion's quantum numbers) in the continuum. These excitations involve only the isovector spin-longitudinal response, so that their distribution should directly reveal collectivity in this response.

To provide such a map, it is planned to use the unique thin-target and recoil-detection capability of the Cooler and the chicane/spectrometer system to map out the distribution of 0^-, $\Delta T = 1$ strength in the nuclear continuum. This can be accomplished with the $(\vec{d},^2\mathrm{He})$ reaction by using the tensor analyzing power $A_{yy} = 1$ and isotropic decay as signatures of 0^- excitation. The procedure planned is to measure the product of σA_{yy} at lab angles corresponding to a cross section maximum for $\Delta L = 1$ transfer for each excitation-energy bin of the residual system; this will emphasize 0^- strength. Then, a further enhancement of the 0^- strength would be obtained by multiplying the product σA_{yy} by a measure of the decay symmetry of the recoil nuclei when the reaction is initiated by vector polarized deuterons.

A sample measurement would study the $^{40}\mathrm{Ar}(\vec{\mathrm{d}},^2\mathrm{He})^{40}\mathrm{Cl}$ reaction at a bombarding energy $E_d = 290$ MeV and a laboratory ^{2}He detection angle of $\theta_{lab} \sim 5^\circ$. The two measurements required would be the differential cross section $\mathrm{d}\sigma/\mathrm{d}\Omega$ and tensor analyzing power A_{yy} using a tensor-polarized deuteron beam, and the decay anisotropy for ^{40}Cl recoils in coincidence with ^{2}He using a vector-polarized deuteron beam. These measurements will be carried out using an ^{40}Ar gas jet target with the chicane/spectrometer in normal mode to detect the ^{2}He . To detect the ^{40}Cl recoils, Si microstrip detectors located near the target (in the Cooler vacuum) will be employed.

4. Summary and Conclusions

Ten experiments have been summarized, including experiments completed and in progress using the 6-degree magnet in the T section of the IUCF Cooler ring, and experiments planned for the chicane/spectrometer system in the S section of the Cooler ring. These examples indicate the wide variety of interesting physics investigations, from studies of symmetries to investigations of spin correlations, pion production and nuclear structure, which are well adapted to 0° measurements below 500 MeV in the IUCF Cooler ring.

Acknowledgments

The authors acknowledge the use of specific portions of various proposals, reports and a letter of intent written by the spokespersons and contact persons listed in the heading of each experiment summarized in this paper. One of us (DWM) acknowledges travel support to present the paper by the Dr. Wilhelm Heinrich Heraeus und Else Heraeus-Stiftung.

References

1. G.P.A. Berg *et al.*, later paper presented at this Workshop.
2. H.O. Meyer *et al.*, *Phys. Rev. Lett.* **65** (1990) 2846; *Nucl. Phys.* **A539** (1992) 633.

3. W.W. Daehnick *et al.*, *Bull. Am. Phys. Soc.* **37** (1992) 1313; IUCF Sci. and Tech. Reports, May 1990 - April 1991, p.52; May 1991 - April 1992, p.56 (unpublished).
4. G.W. Hoffmann *et al.*, *Phys. Rev. Lett.* **65** (1990) 3096.
5. E.J. Stephenson, private communication.
6. W.G. Love, private communication, and in collaboration with E.J. Stephenson.
7. C.A. Miller *et al.*, *Proc. of the 7th Int. Conf. on Polarization Phenomena in Nuclear Physics* (Les Editions de Physique, Les Ulis Cedix A, France, 1990) p.595.
8. T.N. Taddeucci *et al.*, *Nucl. Phys.* **A469** (1987) 125.
9. B.D. Anderson *et al.*, *Phys. Rev.* **C31** (1985) 1147; *Phys. Rev.* **C31** (1985) 1161.
10. C. Wilkin and D.V. Bugg, *Phys. Lett.* **154B** (1985) 243; *Nucl. Phys.* **A467** (1987) 575.
11. W.P. Alford *et al.*, *Nucl. Phys.* **A514** (1990) 49.
12. M. Ericson, in *Spin Excitations in Nuclei*, edited by F. Petrovich *et al.*, (Plenum Press, New York, 1984), p.27.

COULOMB-HADRONIC INTERFERENCE AT COSY ENERGIES

R. JAKOB[1], P. KROLL

Fachbereich Physik, Universität Wuppertal,
Gaußstr.20, Postfach 100127, D-5600 Wuppertal 1,
Fed. Rep. Germany

The theory of Coulomb-hadronic interference for the scattering of polarized protons is discussed. At intermediate energies it is favourable to introduce Bethe phases for each of the amplitudes. The values of the Bethe phases as well as the magnitudes of other correction terms are estimated on the basis of amplitudes reconstructed from current phase shifts. Suitable parametrizations are proposed for various observables. Examples of such observables are the polarization and the spin correlation parameter A_{LL}. The parametrizations are optimized for the COSY energy region.

1. Introduction

We are going to report on a investigation carried out recently by us [1] in which we have reconsidered the theory of Coulomb-hadronic interference (CHI) with polarized protons. Particular emphasis is placed on the application of the theory to the analysis of high precision data at intermediate energies such as provided by COSY. In contrast to Buttimore et al. [2] who have first studied CHI for the spin case we have introduced a phase for each amplitude which is the generalization of the well-known Bethe phase for the spinless case [3]. These Bethe phases take into account higher order electromagnetic corrections. The introduction of the Bethe phases is an appropriate concept in the energy region of interest.
With the cooled beam at COSY and an internal jet target, both the beam and the target

[1]Supported by the Deutsche Forschungsgemeinschaft.

eventually polarized, high precision measurements in the CHI region can be performed. The progress in precision which can be expected may be guessed from the recent analogue measurement of proton-antiproton scattering in the CHI region carried out by the E760 group with the Fermilab cooled antiproton beam and a jet target. Similar progress may be expected at COSY for the polarized case.
The reason for the interest in CHI is obvious. A set of CHI experiments with polarized beams and polarized targets, combined with data on total cross-sections in pure spin states, can provide the three forward amplitudes of elastic *pp* scattering as well as the strength of the two remaining amplitudes near the forward direction. This information is of great value for phase shift analyses at intermediate energies. It can reduce the ambiguities in such an analysis since it is information on amplitudes and not on bilinear products of amplitudes as other observables provide. A reliable set of *pp* phase shifts is of utmost importance. Among other items one may solve the outstanding problem of dibaryon resonances from such set of phase shifts, a matter still being controversial. Forward dispersion relations offer another range of applications for the results of CHI analyses. High quality input data to a dispersion relation allow a precise determination of meson-nucleon coupling constants such as those of the η, ω or ϕ [4]. These coupling constants are of interest in the present discussion of the proton spin problem [5].

2. The Theory of Coulomb-Hadronic Interference

As is well known [2, 3, 6, 7] the interaction between two hadrons is represented by the set of Feynman diagrams depicted in Fig.1. Diagram a) represents the pure hadronic amplitudes ϕ_i^h, diagram b) the one-photon exchange amplitudes ϕ_i^{em}. We will use the helicity basis. Thus, i stands for a set of helicities:

$$\phi_1 = \phi_{++,++} \; ; \; \phi_2 = \phi_{++,--} \; ; \; \phi_3 = \phi_{+-,+-} \; ; \; \phi_4 = \phi_{+-,-+} \; ; \; \phi_5 = \phi_{++,+-} \qquad (1)$$

Although the electromagnetic amplitudes are of the order of the fine structure constant they dominate in the very forward region due to their singular behaviour for $t \to 0$ (t is the usual momentum transfer variable). For large $|t|$, on the other hand, the hadronic

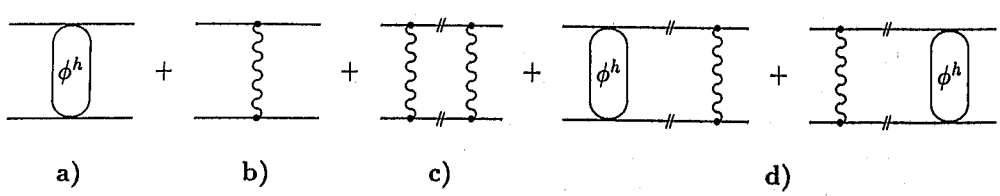

Figure 1: Set of diagrams contributing to the interaction of two hadrons: a) the pure hadronic interaction; b) one-photon exchange; c) imaginary part of the two-photon exchange; d) electromagnetic contamination of the hadronic amplitude. Primed lines are on the mass shell.

amplitudes are dominant. The region where the hadronic and the electromagnetic amplitudes are of comparable magnitude, is called the interference region. It is located at very small values of $|t|$, typically at $10^{-3} - 10^{-2}\ GeV^2$. In pp scattering there are also contributions from the crossed one-photon exchange diagram. In the small $|t|$ region these contributions can safely be neglected.
Diagram c) represents the imaginary part of the two photon exchange contribution. It provides infrared divergent corrections to the electromagnetic amplitudes. According to Yennie, Frautschi and Suura [8] the infrared divergent corrections exponentiate in QED if higher order diagrams are taken into account as well. The exponentiation leads to the well-known Coulomb phase. The sum of the contributions from diagrams b) and c) can be cast into the familiar form

$$\phi_i^{em}(s,t) \exp\left[-i\alpha\eta \ln\left(\frac{|t|}{\lambda^2}\right)\right] \tag{2}$$

where

$$\eta = \frac{s-2m^2}{\sqrt{s(s-4m^2)}} \tag{3}$$

is a kinematical factor and λ is a finite photon mass introduced to regulate the infrared divergencies. Finally the two diagrams d) give rise to electromagnetic contaminations of the pure hadronic amplitudes. The diagrams d) are evaluated with the internal lines on their mass shells. The sum of contributions from diagrams a) and d) is referred to as the contaminated amplitudes.[1]
The set of diagrams shown in Fig.1 is not complete but represents a reasonable approximation to the interaction between two hadrons. Thus for instance QED vertex and mass corrections have been neglected. The infrared divergencies of these corrections are known to cancel against the infrared divergencies of real soft photon emissions in observables. The remaining contributions as well as off-shell contributions from diagrams c) and d) are infrared finite. The effect of these contributions is, however, negligible as has been shown in [7]. Diagrams for which the photon is not solely attached to the external lines are ignored. They lead to further electromagnetic corrections which are still contained in the pure hadronic amplitudes ϕ_i^h. At present it is not possible to calculate such corrections. The diagrams d) can only be calculated by means of a model. Buttimore, Gotsman and Leader [2] have proposed an eikonal approach which is particularly suitable for processes involving particles with spin. The helicity amplitudes $\phi_{\lambda\mu,\lambda'\mu'}(s,t)$ are transformed to the impact parameter representation by

$$\hat{\phi}_{\lambda\mu,\lambda'\mu'}(s,b) = \frac{2}{\sqrt{s(s-4m^2)}} \int_0^\infty J_{|\nu_1-\nu_2|}(b\sqrt{|t|})\ \phi_{\lambda\mu,\lambda'\mu'}(s,t)\ \sqrt{|t|}\ d\sqrt{|t|} \tag{4}$$

where J_n is the Bessel function of order n. $\nu_1 = \lambda - \mu$, $\nu_2 = \lambda' - \mu'$, i.e. n is the net helicity flip. In the impact parameter representation the contributions from diagrams d) are given by a product of electromagnetic and hadronic amplitudes summed over the

[1] Buttimore et al. [2] have proposed to determine the contaminated amplitudes in a CHI analysis, leaving for a second independent step the extraction of the pure hadronic amplitudes. We dont follow this strategy.

internal helicities

$$\Delta\hat{\phi}_{\lambda\mu,\lambda'\mu'}(s,b) = \frac{i}{2}\sum_{\lambda''\mu''}\left[\hat{\phi}^{em}_{\lambda\mu,\lambda''\mu''}(s,b)\hat{\phi}^{h}_{\lambda''\mu'',\lambda'\mu'}(s,b) + \hat{\phi}^{h}_{\lambda\mu,\lambda''\mu''}(s,b)\hat{\phi}^{em}_{\lambda''\mu'',\lambda'\mu'}(s,b)\right] \quad (5)$$

Using the inverse of (4), $\Delta\hat{\phi}$ can be transformed back to the t-representation. The approach proposed by Buttimore et al. is reminiscent to the non-relativistic concept of adding eikonals. It is expected to be valid at small $|t|$.
To carry out the integral transforms it is appropriate to use a parametrization of the hadronic amplitudes. Since only the small $|t|$ region is of relevance the following parametrization suffices for this purpose ($i = 1,2,3$)

$$\begin{aligned}
\phi^h_i(s,t) &= s\Big\{(C_i(s) + t\,D_i(s))\exp(\bar{b}_i t) + i(A_i(s) + t\,E_i(s))\exp(b_i t)\Big\} \\
\phi^h_4(s,t) &= s\frac{|t|}{m^2}\Big\{C_4(s)\exp\left(\bar{b}_4 t\right) + iA_4(s)\exp(b_4 t)\Big\} \\
\phi^h_5(s,t) &= s\frac{\sqrt{|t|}}{m}\Big\{C_5(s)\exp(\bar{b}_5 t) + iA_5(s)\exp(b_5 t)\Big\} \qquad (6)
\end{aligned}$$

In contrast to previous authors we have allowed for terms linear in t. This modification is motivated by the fact that for proton-proton scattering some of the amplitudes are expected to have zeros or maxima (minima) near the forward direction, namely $Re\phi_i, i = 1,2,3$ and $Im\phi_2$. At intermediate energies this expectation is confirmed by recent phase shift analyses [9, 10].
Using the ansatz (6) as well as the well known electromagnetic amplitudes (with the electromagnetic formfactors parameterized as exponentials) one is in the position to calculate the contribution from diagram d) by means of Eq.(5) and the inverse of the Fourier-Bessel transform, Eq.(4). The results can be arranged into a sum of infrared singular terms and a regular rest which we term $\Delta\phi^c_i(s,t)$. Assuming a similar exponentiation of the contributions of diagrams a) and d) as for the electromagnetic case (diagrams b) and c)), one observes that both the contributions, the hadronic one and the electromagnetic one, have in common the famous infrared-singular Coulomb-phase $\exp(i\alpha\eta\ln\lambda^2)$. This phase represents an overall phase factor which is irrelevant for observables and can therefore be dropped. What remains is a set of infrared regular amplitudes

$$\Psi_i = \phi^{em}_i + Re\left(\phi^h_i + \Delta\phi^c_i\right)e^{-i\delta^r_i} + iIm\left(\phi^h_i + \Delta\phi^c_i\right)e^{-i\delta^i_i} \qquad (7)$$

where δ^r_i, δ^i_i are the generalizations of the usual Bethe phase to the spin case. These phases have the form

$$\delta^r_i = -\alpha\eta\ \{C + \ln[|t|(2\beta_1 + \bar{b}_i)]\} \qquad \delta^i_i = -\alpha\eta\{C + \ln[|t|(2\beta_1 + b_i)]\} \qquad (8)$$

where β_1 arises from the parametrization of the electromagnetic form factor F_1 as an exponential. In the spinless case there is only one phase of the type (8) as has been shown by the authors of [6, 7]. Here, in the spin case, one has different phases for each of the real and imaginary parts of the helicity amplitudes.

It turns out that all the phases are very small in the interference region (see Sect. 3). Therefore, one may cast (7) into the more convenient form

$$\Psi_i = \phi_i^{em} + \phi_i^h - i\, Re\phi_i^h\, \sin\delta_i^r + Im\phi_i^h\, \sin\delta_i^i + \Delta\phi_i^c + O(\alpha^2) \tag{9}$$

The full amplitudes Ψ_i are represented by a sum of electromagnetic and hadronic amplitudes plus corrections arising from diagrams c) and d), namely those from the Bethe phases and from the infrared regular remainders of the diagrams d) ($\Delta\phi_i^c$).

3. Elastic Scattering of Polarized Protons in the CHI Region

Let us now discuss in some detail the correction terms in (9) for pp elastic scattering at intermediate energies. We estimate the magnitude of these terms from amplitudes reconstructed from current sets of pp phase shifts [9, 10]. We fit the ansatz (6) to these amplitudes and to supplementary information on forward scattering from data on total cross-sections in pure spin states and from dispersion relations [11]. Thus we end up with a set of parameters $A_i, C_i, D_i, E_i, b_i, \bar{b}_i$ which represent the five hadronic amplitudes for pp scattering at small $|t|$. As a characteristic kinetic energy we choose 800 MeV. In the following this set of amplitudes will be referred to as the test amplitudes. Since we are interested in an estimate of $O(\alpha)$ terms, which are not enhanced by the $1/t$ behaviour of the electromagnetic amplitudes, the accuracy of the phase shifts is sufficient for the determination of the test amplitudes. In any case, making use of different sets of phase shifts, we get an indication of the uncertainties. Only if these uncertainties are so large that they matter in an actual CHI analysis we will mention them. Otherwise the numerical values quoted below are averages over different set of phase shifts. In Tab.1 we list the values of the slope parameters $b_i, \bar{b}_i$ and of the constants $e^C(\beta_1 + b_i(\bar{b}_i))$ appearing in the Bethe phases (8). The uncertainties of these values are typically 5-10%.
Let us now turn to the discussion of the correction term $\Delta\phi_i^c$. Writing the contributions from the diagrams d) explicitly in the impact parameter representation(cf. (5)) , one finds

$$\Delta\hat{\phi}_1(s,b) = i\hat{\phi}_i^{em}\hat{\phi}_i^h + i\hat{\phi}_{i+1}^{em}\hat{\phi}_{i+1}^h + 2i\hat{\phi}_5^{em}\hat{\phi}_5^h \qquad i = 1,3 \tag{10}$$

$$\Delta\hat{\phi}_i(s,b) = i\hat{\phi}_{i-1}^{em}\hat{\phi}_i^h + i\hat{\phi}_i^{em}\hat{\phi}_{i-1}^h + 2i\hat{\phi}_5^{em}\hat{\phi}_5^h \qquad i = 2,4 \tag{11}$$

$$\begin{aligned}\Delta\hat{\phi}_5(s,b) = \frac{i}{2}\big[&(\hat{\phi}_1^{em} + \hat{\phi}_3^{em})\hat{\phi}_5^h + \hat{\phi}_5^{em}(\hat{\phi}_1^h + \hat{\phi}_3^h) \\ &+(\hat{\phi}_2^{em} + \hat{\phi}_4^{em})\hat{\phi}_5^h + \hat{\phi}_5^{em}(\hat{\phi}_2^h + \hat{\phi}_4^h)\big]\end{aligned} \tag{12}$$

The first term in each of these expressions, being proportional to either $\hat{\phi}_1^{em}$ or $\hat{\phi}_3^{em}$ (or to $\left(\hat{\phi}_1^{em} + \hat{\phi}_3^{em}\right)/2$ in the case of $\hat{\phi}_5^{em}$), generates the relevant Bethe phases. The other terms contribute only to the $\Delta\phi_i^c$'s. From numerical studies on the basis of the test amplitudes we find that with the Bethe phases the major contributions from the diagrams d) are taken into account. To a very good approximation, the $\Delta\phi_i^c$'s can be neglected at intermediate energies. This is not generally true at higher energies.
The next step is to find practicable parametrizations of proton-proton observables in

Table 1: Numerical values of the slope parameters and of the constants appearing in the Bethe phases (8) at 800 MeV.

	$\bar{b}_i\ (GeV^{-2})$	$b_i\ (GeV^{-2})$	$e^C(2\beta_1+\bar{b}_i)\ (GeV^{-2})$	$e^C(2\beta_1+b_i)\ (GeV^{-2})$
ϕ_1^h	4.49	3.63	16.8	15.3
ϕ_2^h	8.14	3.89	23.9	15.7
ϕ_3^h	5.62	5.05	18.8	17.8
ϕ_4^h	7.23	3.76	21.7	15.5
ϕ_5^h	5.01	2.62	17.7	13.5
$\phi_1^h+\phi_3^h$	5.12	4.44	17.9	16.7
$\phi_1^h-\phi_3^h$	1.38	7.73	11.3	22.6

the CHI region which are optimized for the intermediate energy region. The following strategy for finding such parametrizations has been adopted: As usual any observable is decomposed into three pieces

$$O = O_{em} + O_I + O_h \tag{13}$$

where O_{em}, O_I, O_h are the electromagnetic, interference and hadronic contributions, respectively. The Bethe phases appearing in the interference terms are regarded as known (cf. Tab.1). According to the above discussion the terms $\Delta\phi_i^c$ are neglected throughout. The test amplitudes are used in order to estimate the relative magnitudes of various other terms appearing in the interference and hadronic parts of the observables. The dominant hadronic amplitudes are considered as free parameters to be determined from the CHI analysis if they are not known to a high precision from sources other than phase shifts (e.g. from total cross-sections). Smaller contributions to O_I and O_h are absorbed into constants τ_i. Such contributions to the τ_i's are neglected which, according to the test amplitudes, are very small as compared to the dominant hadronic contributions (typically less then a few percent). Therefore, the constants τ_i have a rather simple interpretation in most cases. It is convenient to use the ansatz (6) for the hadronic amplitudes. The slope parameters appearing in it are taken from Tab.1. For the observables the slopes of the various contributions are taken to be equal to that of the dominant hadronic contribution. Although in general the other contributions have different slopes, the errors induced by this identification are tiny. The use of different slopes would lead to additional contributions, which are $\propto t^n$ (where $n \geq 1$) and are therefore suppressed in the CHI region.
In [1] parametrizations for several observables (differential cross-section, polarization, spin correlation parameters) have been proposed. Similar parametrizations can be given for other observables. The practicability of the proposed parametrizations has been demonstrated in [1] by analysing existing data with them. Here in this report we will present only two examples namely the polarization P and the spin correlation parameter A_{LL} for longitudinal polarized protons in the initial state.

i) The spin correlation parameter A_{LL}

In terms of helicity amplitudes the parameter $A_{LL}\,\frac{d\sigma}{dt}$ reads

$$A_{LL}\,\frac{d\sigma}{dt} = \frac{2\pi}{s(s-4m^2)}\left(|\phi_1|^2+|\phi_2|^2-|\phi_3|^2-|\phi_4|^2\right) \tag{14}$$

The interference and the hadronic parts are parameterized as

$$A_{LL}\frac{d\sigma}{dt}\bigg|_I = \frac{s-2m^2}{s-4m^2}\,\frac{\alpha}{4t}\,{F_1}^2(t)\,\Delta\sigma_L\,\left(\rho_3+\sin\delta_1^i\right)\,e^{\bar{B}t} \tag{15}$$

$$A_{LL}\frac{d\sigma}{dt}\bigg|_h = 2\pi\frac{s}{s-4m^2}\left\{\frac{\sigma_{tot}\,\Delta\sigma_L}{32\pi^2}(1+\rho_1\rho_3)+\tau_L^{(0)}+t\,\tau_L^{(1)}\right\}\,e^{2\bar{B}t} \tag{16}$$

where

$$\rho_3 = \frac{Re(\phi_1^h(0)-\phi_3^h(0))}{Im(\phi_1^h(0)-\phi_3^h(0))} \tag{17}$$

$\Delta\sigma_L = \frac{8\pi}{s}\,Im\,(\phi_1(0)-\phi_3(0))$ is the total cross-section for longitudinal polarized protons. $\bar{B}$ is the average slope of $Im(\phi_1^h+\phi_3^h)$ and $Im(\phi_1^h-\phi_3^h)$ ($\bar{B}=6.1\ GeV^{-2}$ at 800 MeV, see Tab.1). The Bethe phase δ_1^i with $b_1 = 3.63\ GeV^{-2}$ (see Tab.1). The constants $\tau_L^{(0)}$ and $\tau_L^{(1)}$ are given by (cf. (6))

$$\tau_L^{(0)} = {A_2}^2+{C_2}^2+\alpha\,\frac{s-2m^2}{s}(D_1-D_3) \tag{18}$$

$$\tau_L^{(1)} = 2(D_1C_1-D_3C_3)+2({A_2}^2+{C_2}^2)\,(b_2-\bar{B}) \tag{19}$$

From the test amplitudes we estimate that $\tau_L^{(0)}$ amounts to about 0.8 GeV^{-4}. The CHI contribution to $\tau_L(0)$, generated by the terms required by the zero of $Re(\phi_1^h-\phi_3^h)$, is about 10%. However, the importance of this term increases with s. $\tau_L^{(1)}$, dominated by the contributions from ϕ_1^h and ϕ_3^h, amounts to about $30-40\ GeV^{-6}$ as we estimate from the test amplitudes.

In order to get a reliable fit to the 800 MeV data we have to reduce the number of free parameters in (15), (16) to two. This is achieved by fixing $\tau_L^{(0)}$ at 0.8 GeV^{-4} and using $\rho_1 = 0$ in agreement with the result obtained from a CHI analyses of th differential cross-section data of [12] and in agreement with dispersion relations [11]. The fit, shown in Fig.2, provides $\rho_3 = -1.39\pm0.4$ and $\tau_L^{(1)} = 44\pm15\ GeV^{-6}$. Within errors ρ_3 is in agreement with the results found in [13] and with the predictions from dispersion relations [11]. $\tau_L^{(1)}$ is found to be in accordance with the estimate from the test amplitudes. This internal consistency is a clear signal for a strong t-dependence of $Re\phi_1^h$ and $Re\phi_3^h$ in the near forward direction. The use of purely exponential t-dependence would lead to a misinterpretation of $\tau_L^{(1)}$. One would conclude that $|\phi_2^h(0)|^2$ is very large in contradiction to the $\Delta\sigma_T$ data and to forward dispersion relations.

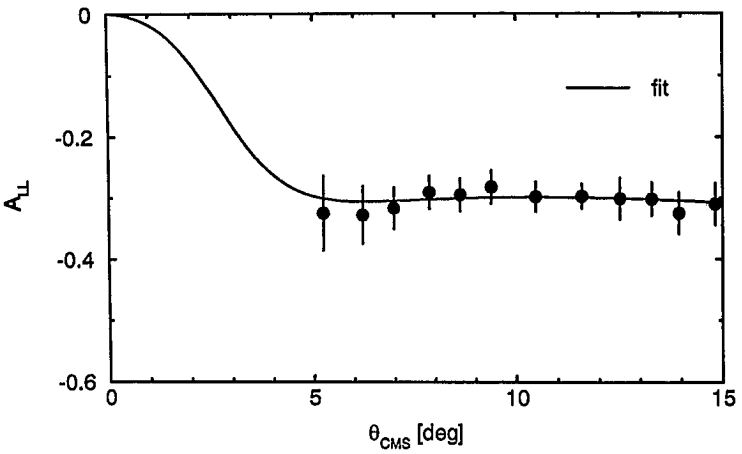

Figure 2: $A_{LL}\ d\sigma/dt$ vs. the *cms* scattering angle at 800 MeV. Data are taken from [13]. The solid line represents the fit using the parametrization ((14)-(19)).

ii) The polarization

The polarization or rather the polarization multiplied with the differential cross-section is expressed in terms of helicity amplitudes by

$$P\,\frac{d\sigma}{dt} = \frac{-4\pi}{s(s-4m^2)}\,Im[\phi_5^*(\phi_1+\phi_2+\phi_3-\phi_4)] \tag{20}$$

The purely electromagnetic contribution $P\,\frac{d\sigma}{dt}\Big|_{em}$ is zero. For the interference part and for the hadronic part the following parametrizations are proposed:

$$\begin{aligned} P\,\frac{d\sigma}{dt}\Big|_I &= -\sqrt{\frac{s}{s-4m^2}}\,\frac{\alpha}{\sqrt{|t|}}\,\sigma_{tot}\,\left(\frac{m}{s-4m^2}{F_1}^2(t)-\frac{\kappa}{2m}F_1(t)F_2(t)\right)\,e^{Bt} \\ &\quad -\frac{8\pi}{m}\,\frac{s-2m^2}{s-4m^2}\,\frac{\alpha}{\sqrt{|t|}}{F_1}^2(t)\,\left(A_5-C_5\sin\delta_5^T\right)\,e^{b_5 t} \end{aligned} \tag{21}$$

$$P\,\frac{d\sigma}{dt}\Big|_h = -\frac{s}{s-4m^2}\,\frac{\sqrt{|t|}}{m}\,\sigma_{tot}\,(C_5+A_5\rho_1+\tau_P)\,e^{(B+b_5)t} \tag{22}$$

where F_1 and F_2 are the usual Dirac and Pauli form factors of the proton and $\kappa(=1.79)$ its anomalous magnetic moment. B is the slope of the differential cross-section and $\sigma_{tot}=\frac{4\pi}{s}\,Im\,(\phi_1(0)+\phi_3(0))$ is the total cross-section. The quantity

$$\tau_P = \frac{C_5A_2-A_5C_2}{A_1+A_3} \tag{23}$$

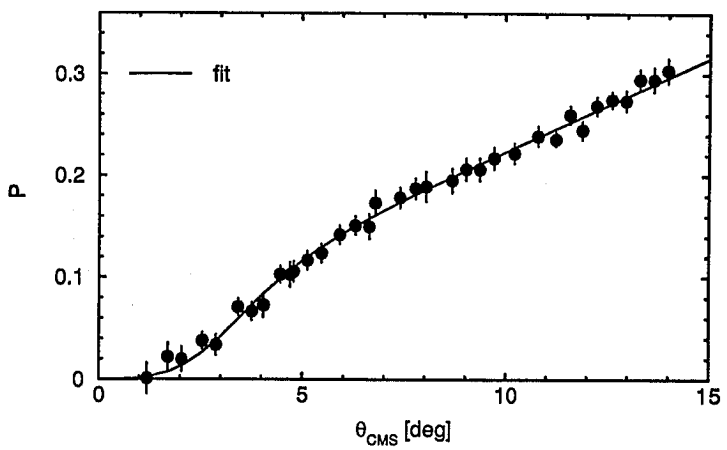

Figure 3: $P\ d\sigma/dt$ vs. the *cms* scattering angle at 800 MeV. Data are taken from [11]. The solid line represents the fit with the parametrizations ((21)-(23)).

is a contribution in which also the double flip amplitude ϕ_2^h appears. The test amplitudes yield $\tau_P = 0.02$, i.e. τ_P is small and can be neglected. With increasing energy τ_P becomes even less important. Since $\rho_1 \approx 0$ at 800 MeV the second term in (22) can also be neglected. Taking $B = 4.1\ GeV^{-2}$ and $B + \bar{b}_5 = 9.1\ GeV^{-2}$ from Tab.1, only two parameters are left free in (21) and (22), namely A_5 and C_5. A fit to the data of Pauletta et al. [12] provides $C_5 = -2.79 \pm 0.2\ GeV^{-2}$ and $A_5 = -1.74 \pm 0.3\ GeV^{-2}$. C_5 deviates substantially from the result obtained in [12]. The reason for this discrepancy can be traced back to the fact that $\bar{b}_5$ and b_5 have been assumed to be zero in [12]. This is in contradiction to our test amplitudes. In the CHI region the t-dependence of ϕ_5^h is not simply given by $\sqrt{|t|}$. An additional exponential is definitely needed with a slope even somewhat larger than that of $Im(\phi_1^h + \phi_3^h)$ (cf. Tab.1).
While C_5 is in good agreement with predictions from phase shift analyses, the result for A_5 does not agree with these predictions but is roughly in accordance with the result found in [12]. The reason for the discrepancy to phase shift information is unknown, the neglect of b_5 and $\bar{b}_5$ alone is certainly not responsible for that discrepancy. In Fig.3 the $P\frac{d\sigma}{dt}$ data are compared with the fit.

4. Summary

We have discussed the theory of CHI for polarized protons. In order to take into account higher order electromagnetic corrections it appears favourable to introduce Bethe phases for each of the amplitudes separately. These phases are generalizations of the usual Bethe

phase in the spinless case.
Specializing to proton-proton scattering at intermediate energies, we have estimated the Bethe phases and other higher order electromagnetic corrections ($\Delta\phi_i^c$) from a set of test amplitudes reconstructed from current phase shifts. The test amplitudes are also used to decide which hadronic contributions to observables are large and which are small. On the basis of these numerical studies we have proposed parametrizations of $\vec{p}p \to pp$ observables valid at intermediate energies. Typically these parametrizations include two quantities which may be considered as free parameters to be determined from a CHI analysis. One of these parameters is the hadronic quantity of interest, e.g. a ρ_i parameter. The other one, τ_i, is a constant which absorbs small terms from other hadronic amplitudes and from CHI terms. With one exception, the τ_i have simple interpretations. The practicability of the proposed parametrizations has been checked by actual fits to existing data.
Precise data on the above-mentioned observables in the CHI region supplemented by data on total cross-sections may therefore lead to a precise determination of the three forward amplitudes. In turn this information may be used in a new phase shift analysis performed at a later stage. This kind of iterative procedure may provide improved sets of phase shifts. Precise knowledge of the forward amplitudes is also of great value for other applications such as dispersion relations.
Measurements and analyses of the various observables in the CHI region constitute therefore an interesting task for COSY.

References

[1] R. Jakob and P. Kroll, *Z. Phys.* **A344** (1992) 87.
[2] N.H. Buttimore, E. Gotsman and E. Leader, *Phys. Rev.* **D18** (1978) 694.
[3] H.A. Bethe, *Ann. Phys.(N.Y.)* **3** (1958) 190.
[4] W. Grein and P. Kroll, *Nucl. Phys.* **A338** (1980) 332; P. Kroll, *πN newsletters*, Vol.**2** (1990) 87.
[5] H. Fritzsch, *Mod. Phys. Lett.* **A5** (1990) 625; H. Rollnik, *Proceedings of the 9th Intern. Symp. on High Energy Spin Physics*, eds. K.-H. Althoff, W. Meyer (Springer, 1991).
[6] M.P. Locher, *Nucl. Phys.* **B2** (1967) 525 .
[7] G.B. West and D.R. Yennie, *Phys. Rev.* **172** (1968) 1413.
[8] D.R. Yennie, S.C. Frautschi and H. Suura, *Ann. Phys. (N.Y.)* **13** (1961) 379.
[9] R.A. Arndt et al., *Phys. Rev.* **D28** (1983) 97; R.A. Arndt et al., *Phys. Rev.* **D35** (1987) 128 and private communication.
[10] J. Bystricki, C. Lechanoine-Leluc, F. Lehar, *J. Physique* **48** (1987) 199; *ibid.* **48** (1987) 1273 and private communication.
[11] W. Grein and P. Kroll, *Nucl. Phys.* **A377** (1982) 505; P. Kroll, *Physics data 22-1* (Fachinformationszentrum Karlsruhe, 1991).
[12] G. Pauletta et al., *Phys. Rev.* **C27** (1983) 282.
[13] G. Pauletta et al., *Phys. Lett.* **B211** (1988) 19.

COSY SYNCHROTRON AND STORAGE RING FOR MEDIUM ENERGY PHYSICS

R. MAIER

Institut für Kernphysik, Forschungszentrum Jülich GmbH,

Postfach 1913, D-5170 Jülich

At present the cooler synchrotron COSY a synchrotron and storage ring for medium energy physics is being commissioned at Jülich. The construction of the ring was finished during September 1992. The cooler ring will deliver protons in the momentum range from 270 to 3300 MeV/c. The phase density of the circulating protons will be increased with electron cooling at injection and with stochastic cooling at momenta between 1500 and 3300 MeV/c. High luminosity internal experiments as well as high resolution external experiments will be possible.

Details of the lattice, to match the different ion optical requirements for cooling, acceleration, internal experiments and ultra-slow extraction will be discussed. An overview of the performance of the ion sources, the injector cyclotron, the ring, the injection beamline are given. The realization status of the extraction beamlines to the external experimental area is given. The experience on the commissioning of the cooler ring complex is reported.

1. Introduction

The COSY facility consists of different ion sources, the cyclotron JULIC as injector, the injection beamline with a length of 100 m, the ring with a circumference of 184 m and the extraction beamlines to the external experimental areas. The high resolution beamline to the magnetic spectrometer BIG KARL, the beamline to the Time of Flight spectrometer and the beamline for medical therapy application[1] are under construction. In a later stage a fourth beamline will be added for polarization measurements.

The lattice of the COSY ring consists of two 52 m long 180^0 bending sections, which are separated by two 40 m long straight sections. The straights are designed as telescopic systems with a 1:1 image from the beginning to the end with a phase advance of either π or 2π. Bridged by four optical triplets one straight section is dedicated for two internal target places TP 1 and TP2. The opposite straight section provides free space for the rf cavity, the electron cooler, scrapers, Schottky pick-ups and current monitors.

The two arcs are composed of six mechanically identical periods. Each of the mirror symmetric half cells is given a QF-bend-QD-bend structure leading to a six fold symmetry of the total magnetic lattice. By interchanging the focussing and defocussing properties additional flexibility for adjusting the tune is achieved.

One of the bending arcs houses the injection and extraction devices, the stripping target, the magnet septum and bumper magnets for injection as well as the electrostatic and magnetic septa for extraction. The other arc offers space for a third internal target area TP3, which will make use of one of the ring magnets to separate 0^0 ejectiles, the diagnostic kicker and the elements for the ultra-slow extraction. The stochastic cooling pick-ups and kickers will be installed at the intersection between straight sections and arcs . The basic machine parameters are summarized in Table I, the layout of the whole facility is shown in Fig. 1.

The magnetic lattice of the ring has to match different ion optical conditions:

(i) the internal targets require low betatron functions and low dispersion
(ii) the slow extraction needs the horizontal tune near a third order resonance
(iii) the stochastic cooling demands a phase advance close to $(2n+1)\cdot\pi/2$ between the pick-up and kicker location for both planes
(iv) the electron cooler prefers low betatron amplitudes

These requirements can be fulfilled with the chosen working point. The beam and optical proporties are listed in Table II.

Table I: COSY Basic Parameters

Vacuum system	pressure	10^{-10}–10^{-11} mbar
	in the areas	rectangular 150·60 mm²
	in the straights	circular, ϕ 150 mm
RF system	cavity type/ acceleration structure	symmetric re-entrant ferrite loaded
	frequency range (h=1)	0.462–1.572 MHz
	frequency factor (at frequency)	8(400 kHz), 40(2 MHz)
	max. rate of frequency increase	4 MHz/s
	gap voltage (at duty cycle)	5 kV (100%), 8 kV (50%)
	gap voltage dynamic range	55 dB
	nominal/actual rf power	56/16 kW in push-pull
bending magnets	number	24
	radius	7 m
	angle	15^0
	field range	0.23 T–1.585
quadrupole magnets in the areas	number	24
	no. of families	6
	eff-length	0.3 m
	aperture radius	85 mm
	max. 8 radius	7.5 T/m
quadrupole magnets in the telescopes	number	32
	no. of families	8
	eff. length	0.55 m
	aperture radius	85 mm
	max. gradient	7.5 T/m
sextupole magnet	number	18
	no. of families	7
	eff. length	0.3/0.2/0.1 m
	aperture radius	85 mm
	max. strength	30 T/m²

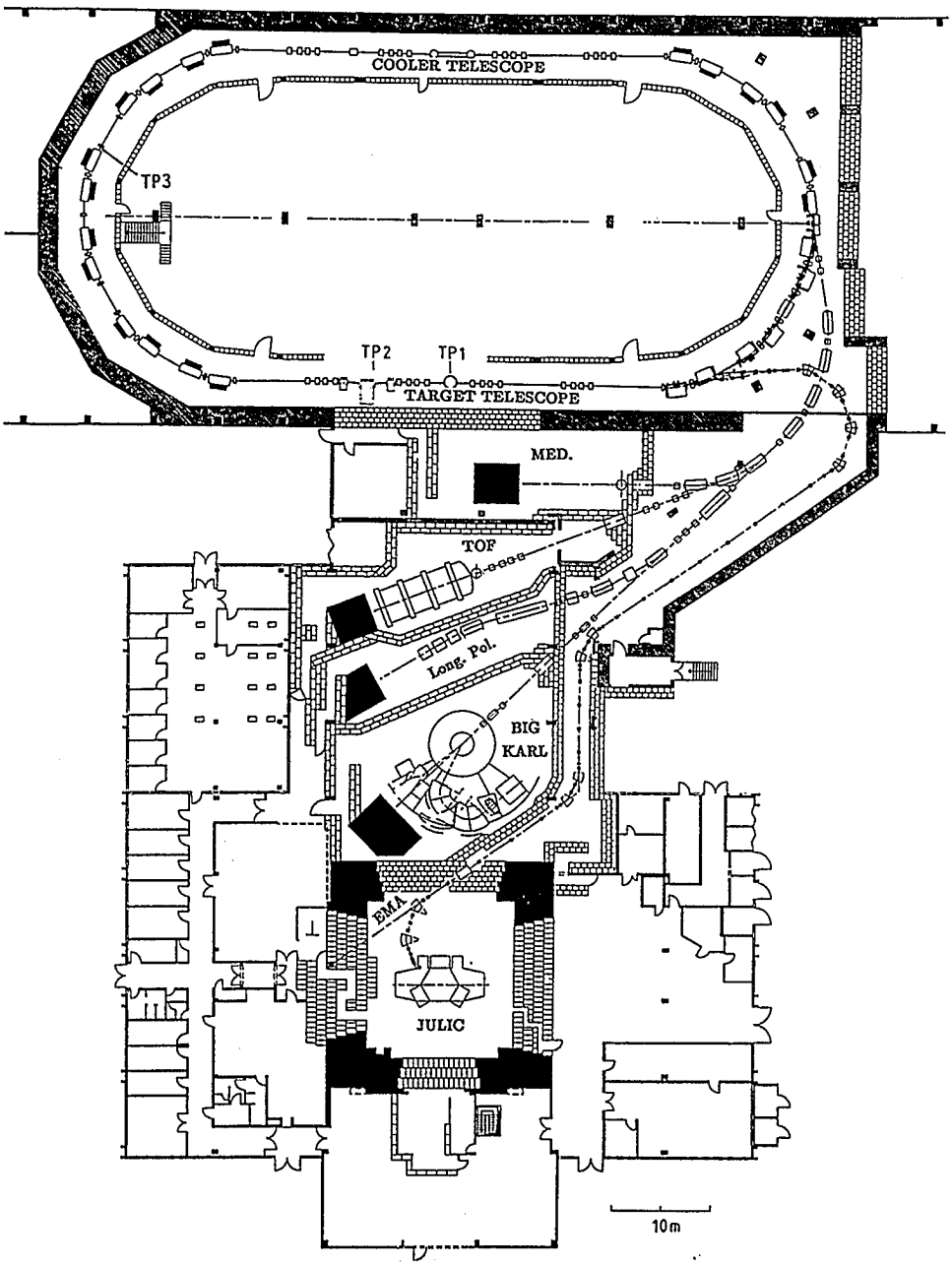

Figure 1: Layout of the COSY facility

Table II: The Beam and Optical Properties of COSY

momentum range	270-3300 MeV/c	
max. no. of stored protons	$2 \cdot 10^{11}$	
horizontal/vertical tune	3.38/3.38	
transition momentum	1860 MeV/c	
geometrical acceptance	horizontal:	130 π mm mrad
	vertical:	35 π mm mrad
	$\Delta p/p$:	$\pm$ 0.5%
nat. chromaticity hor./vert.	- 5.2/- 4.5	

lattice function at

	β_{hor}	β_{vert}	dispersion
TP1:	5.6 m	5.9 m	0 m
TP2:	1.6 m	5.1 m	0 m
TP3:	6.0 m	22.2 m	10.1 m

radii and divergences for an extracted emittance of 2.5 π mm mrad and $\Delta p/p$ of $1 \cdot 10^{-3}$ at

	x/mm	x'/mrad	z/mm	z'/mrad
medical therapy area	3.25	1.34	1.88	1.24
Time of Flight	0.56	4.90	0.72	3.47
BIG KARL	0.45	7.14	0.43	6.92

2. Accelerator Components

2.1 Injector

The injector complex consists of several ion sources, the source beam line, the isochronous cylotron Jülich as preaccelerator and the transferline between the cyclotron and the ring. The injector complex was modified and upgraded since the shutdown of the cylotron in September 1989.

Four ion sources will be available for the different particles to be accelerated in COSY. The types of sources are determinded by the fact, that the injection into the cooler synchrotron is performed by stripping. An ECR ion source for H_2^+ particles provides ion beames of 100 μA with an emittance in the order of 30 $\pi \cdot$ mm $\cdot$ mrad. With this source an H_2^+ beam of 76 MeV could be extracted from the cyclotron with a current of 10μA. To study the injection, acceleration and extraction of negative ions in the cyclotron, which is of major importance for the use of polarized particles, an H^-/D^- ion source has been installed. In the first test run in January the H^- ion source provided a

beam of 100 μA. This H^- beam could be accelerated to 45 MeV and extracted from the cylcotron with a current of 3μA.

The polarized ion source is being realized in a collaboration of the universities Bonn, Erlangen and Köln. All subsystems have been tested separately and are ready for installation. It is planned to assemble the polarized source at the cyclotron Jülich in spring 1993.
The modification and upgrading of the injector complex took about 2 years. This was mainly due to the relative time consuming dismounting of the complete former experiment installations and beam lines and, on the other hand, the course of severe interaction between the various tasks of the cyclotron itself. One was the modification of the complete rf system of the cyclotron, the second was the trim coil arrangements, which is necessary for the tuning of the isochronous magnetic field. The cyclotron was back in operation with internal H_2^+ beam in November 1991 and with extracted beam in February 1992.

For the transfer of the H_2^+ or H^- particles with an energy up to 45 MeV/nucleon a transfer beamline was constructed by Siemens Company. In March 1992 this beam line was ready to be commissioned. The beam line consists of 57 magnetic elements activated by 19 power supplies. Beam diagnostic is based on the readout of profile grids, located as pairs for both planes at 7 locations along the beamline. Each grid consists of 30 wires (wire diameter 0,1 mm, distance 1,5 mm). Slit systems, Faraday cups, viewers and pick ups for beam phase detection etc. complete the instrumentation. All subsystems are controlled by a dedicated computer which is compatible with the COSY control system. The commissioning was finished in August so that the first beam could be injected into the cooler cyclotron in September 1992.

2.2 Accelerating system h = 1

The 50 kW rf acceleration system based on a ferrite-loaded, coaxial cavity, has been developed in close cooperation, and largely under contract with the Laboratoire National SATURNE and Tompson Tubes Electroniques. The accelerating system has been installed in October 1992 into the cooler ring. A fully digital synthesis and control of the low level acceleration voltage is completely implemented[2]. The key characteristics for the high power part of the acceleration structure are given in Table I.

2.3 Injection and Ejection

The injection is a horizontal multi-turn process. Magnetic bumpers make a variable orbit deformation in the horizontal plane at the exit of the magnetic injection septum, permitting injection in successive turns.

For ejection a third order resonant extraction $3Q_h = 10$ is being considered. Phase and amplitude of the resonance will be controlled by the sextupole magnets. The first element of the extraction channel is the thin electrostatic septum adjustable both in angle and position.

The particles having been kicked by the electrostatic septum, are deflected by two magnetic septa. Table III summarizes the characteristics of the injection and extraction elements.

Table III: Characteristics of the Injection and Extraction Elements

magnetic injection septum	deflection angle	0.34 rad at 0.6 GeV/c
	magnetic field	1 T
	gap	height: 64 mm, width: 110 mm
bumper magnets	eff. length	0.35/0.7 m
	field	58 mT/29 mT
	rise time	10 ms
	flat top	10 ms
	fall time	20 ms
electrostatic ejection septum	deflection angle	3.5 mrad at 3.3 GeV/c
	eff. length	1 m
	gap height	15 mm
	max. voltage	150 kV
	foil thickness	0.1 mm
magnetic extraction septa	deflection angle	2·87.5 mrad at 3.3 GeV/c
	magnetic field	1.046 T
	gap	height: 36 mm, width: 125 mm
	length	2·969 mm

2.4 Power Supplies

The power supply system for the COSY ring is completely installed. Tests concerning feed back behaviour and stability have been made. The experiences during the last four months showed that the stability and current resolution for the DC mode (storage ring mode of the cooler synchrotron) are sufficient. In order to fit the beam through the injection parts suitable settings of current values for the dipol power supply, injection septum and the quadrupole families were found. In the COSY ring three fast bumper magnets are installed to shift the beam from the stripping to the closed orbit during the injection process. The power supplies for the bumpers are the fastest system in COSY. The range of the set values are start currents in the order of 100 A down to 0 A, ramping times in the order of 10 msec, with an maximal slope of 150 A/msec.

2.5 Vacuum System

The vacuum system is specified to operate at an averaged pressure below 10^{-10} mbar. To match this demand, each component is subject to an extended vacuum test. The procedure includes a pressure test in the 10^{-12} mbar range for sputter ions pumps, sublimation pumps and chambers. The valves and gauges are tested in the 10^{-11} mbar range. All parts have to fulfill an additional leak test. The commissioning of the COSY ring required on one hand a pressure below the 10^{-8} mbar range and on the other hand the necessity of some fast changes which require sometimes a system exposure to air. For this reason the vacuum system was operated without bakeout at a pressure of about 5×10^{-9} mbar.

2.6 Control System

The control system is hierarchically organized with distributed intelligence and autonomous operation units for each accelerator component. Data communication is performed via local area network and field bus. The host systems are UNIX based. On the field controllers a modular real time kernel RT/OS is running[3]. A first experience with the control system was gained during the commissioning of the source beamline, the cyclotron and the COSY ring itself. The usuage of a rapid prototyping tool to build intuitive graphical user interface based on object oriented design proved to be very useful.

2.7 Diagnostic Elements

At the beginning of COSY operation all beam position monitors, scrapers and screen monitors were completely at disposal concerning the hardware electronics and computer control. A wall current monitor, a beam current transformer and a strip line unit was installed and helpful measurements were carried out.

2.8 Electron Cooler

The electron cooler was ready for operation in its test position inside the COSY ring since the beginning of December 1992. On December 8th first attempts were made to produce an electron beam. The gun anode voltage was slowly increased from 10 kV to produce a beam of a few milliamperes. Observing the vacuum pressure not to exceed $2 \cdot 10^{-7}$ mbar, 400 mA was obtained after a few hours. In this time a better vacuum could not be obtained because the vacuum vessels were not baked out. After conditioning the collector overnight at 400 mA beam current the beam could be increased within the next two days. Here, a higher beam energy of 25 keV was necessary in order to increase the gun anode voltage accordingly. The beam energy was further increased in steps of 10 keV up to the design value of 100 keV. Up to now the electron cooler had operated several hours at 100 keV and 1.5 A without any high voltage problems. It should be noted that the electron beam passes through from the cathode to the collector without beam position monitoring and without using the beam steering coils besides the toroid dipol coils set according to the beam energy. To center the 2.5 cm beam at the collector entrance only small currents in the collector steerer coils were necessary.

2.9 Stochastic Cooling System

The design work on the stochastic cooling system has been finished and the manufacturing of the cooling tank as well as the production of the active rf-componends have been started. Fabrication of the tanks has been started in collaboration with the KFA Central Workshop. The active rf-components were developed in collaboration with Jansen Microwave. The completion of the transversal cooling system is expected at the end of May 1994.

3. Summary

With the beginning of fall 1992 all necessary components of the COSY cooler synchrotron had been installed to begin tests with the internal beam. Since September 1st the complete COSY facility had been restricted area. The beam position monitors, viewers, scrapers, beam current transformer and strip line unit were used as diagnostic tools to qualify the injected beam in the COSY ring.

At the 10th of September the first proton beam was observed in the COSY ring at the viewer behind the stripping target (Fig. 2).

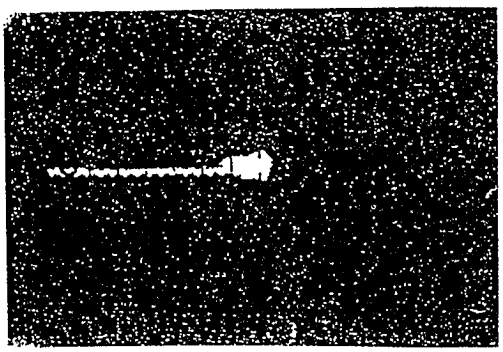

Figure 2: Beam spot on viewer 1 of the first injected proton beam in the cooler synchrotron COSY. The outgoing trace shows the moment of switching the magnetic dipol field from the rigidity of the H_2^+ beam to the rigidity of protons.

On the 21st of September 1992 the first complete turn of a focused proton beam had been achieved.

On the 7th of December 1992 four successive turns could be measured in the cooler ring. A little later the number was increased to 20. Fig. 3 shows the sum signal of a beam position monitor displaying about twenty turns.

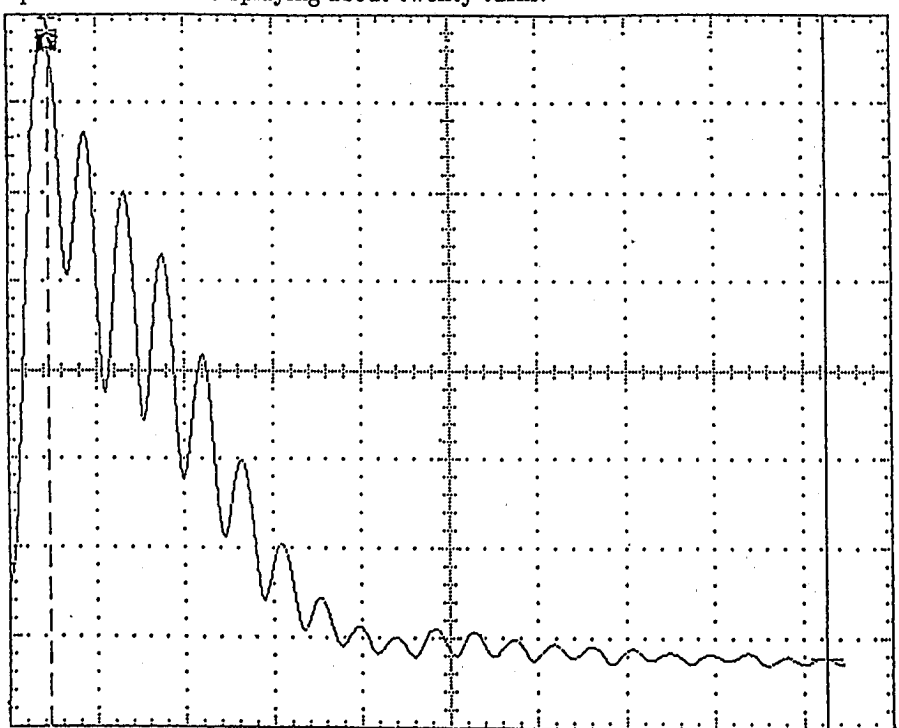

Figure 3: Sum signal of the beam position monitor showing 20 succeeding turns, measured with Tektronix-Scope TMS 520, set to: Aquisition mode: 32-fold averaged, Horizontal: 5 μsec/div., Vertical: 50 mV/div.

With a static closed orbit bump at 270 MeV/c in the ring on the 12th of January 1992 one mA could be stored with a lifetime of 1 msec. Figure 4 shows the trace of the beam current transformer from 1.3 x 10^{10} protons with a lifetime of 24 sec. In this case the accumulated current was steered aside the stripping target with the bumpers. The COSY complex is operating since September 1992 on 16/24 hour basis with a two shifts a day. Machine availability with beam was approximately 70% of total time scheduled.

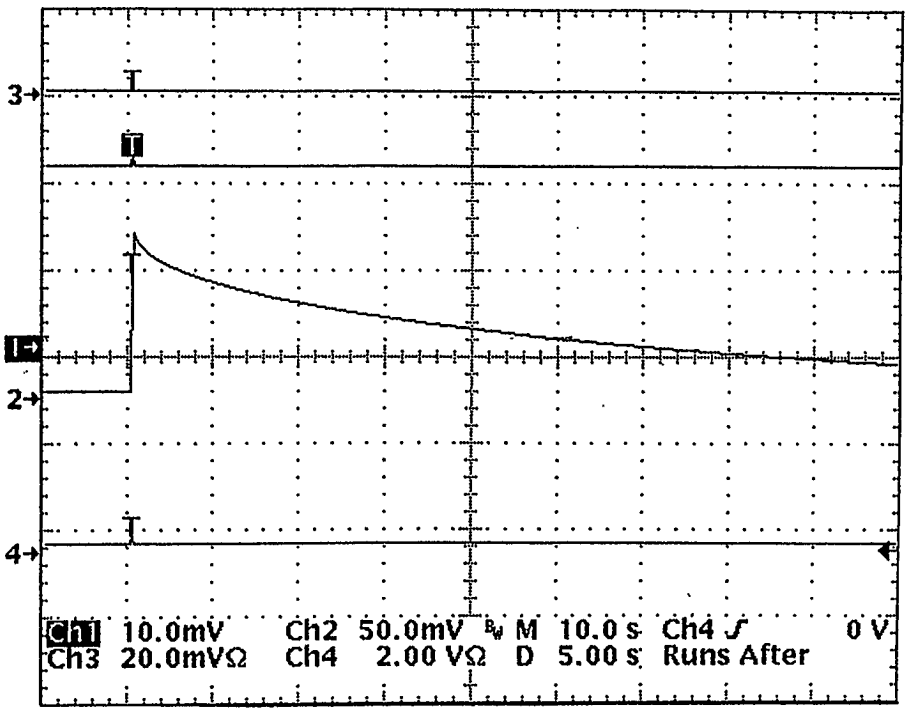

Figure 4: Signal of the beam current transformer showing about 1.3 · 10^{10} protons with a lifetime of 24 sec, measured with Tektronix-Scope TMS 520, set to: Aquisition mode: High resolution, Horizontal: 5 sec/div., Vertical 50 mV/div.

4. Acknowledgements

I would like to express my sincere thanks to the members of the machine advisory committee, the colleagues from the accellerator laboratories around the world and the CANU members.

5. References

1. R. Maier and U. Pfister, *The COSY-Jülich Project March 1992 Status*, European Particle Accelerator Conference, Berlin, March 24-28, 1992.
2. H. Meuth et al., *A Digital Synthesizer and Phase Control System for RF-Acceleration in COSY*, European Particle Accelerator Conference, Berlin, March 24-28, 1992.
3. N. Bongers et al., *The COSY-Control System. A Computer Distributed Multiprocessor System for Accelerator Control*, European Particle Accelerator Conference, Berlin, March 24-28, 1992.

THE INTERNAL CLUSTER TARGET FOR COSY

D. Grzonka*, H.Dombrowski‡, K. Kilian*, A. Khoukaz‡, W. Oelert*, R. Santo‡
* *Institut für Kernphysik KFA-Jülich, W-5170 Jülich, Germany*
‡ *Institut für Kernphysik, W-4400 Münster, Germany*

A hydrogen cluster target for internal experiments at COSY-Jülich is being built. Compared to other existing cluster targets a relatively small mechanical setup was designed. The construction of special cryopumps allows high pumping speeds which are necessary for the differentially pumping stages in cluster beam direction. The design concept and first results will be given.

1 Introduction

For an efficient use of the beam particles in a storage ring generally an internal target is desirable. The overall luminosity is comparable for internal and external target operation but at an external target each beam particle hits the target only once and is lost. For the internal target the beam particles pass through the target about 10^6 times per second. Due to nuclear reactions and scattering the beam intensity is reduced and after some time the storage ring must be filled again. The period of storing can take several hours or days. Thus the number of beam preparation phases with injection and acceleration by the power consuming ramping of the magnets can be drastically reduced. In fig. 1 the

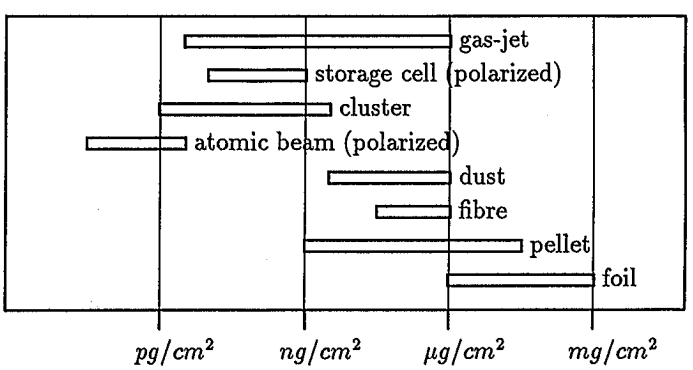

Figure 1: Survey of the possible internal targets for storage rings.

effective target mass range which is attainable by the different internal targets is shown. Two classes of internal targets are available, the solid state targets like fibre, dust and pellet, and the gaseous targets. For the solid state targets the effective target thickness can be very low because of the small overlapp between beam and target material, however, the target thickness seen by a single beam particle is in the order of mg/cm^2 which gives rise to an emittance increase of the beam. The gaseous targets again divide into two groups.

On the one side we have the gas jet and the storage cell targets with high densities but not very well defined target dimensions. The gas density is so high that collisions between gas molecules lead to an expansion of the target volume. Therefore several pumping stages in the accelerator beam direction are necessary. On the other side there are the atomic beam and cluster target. In the atomic beam target the density is so low that practically no colllisions between the gas atoms occur. In the cluster target the situation is similar with a beam of clusters consisting of up to 10^6 atoms. Thus in these targets the interaction area is well defined and pumping stages in the accelerator beam direction are not necessary. The matching to the UHV conditions in the storage ring can be made with differentially pumping stages in target beam direction.

2 Design concept

The most important part of a cluster target is the nozzle. In fig. 2 a sketch of the clustering process and the p-T diagram for hydrogen is shown. At the entrance of the

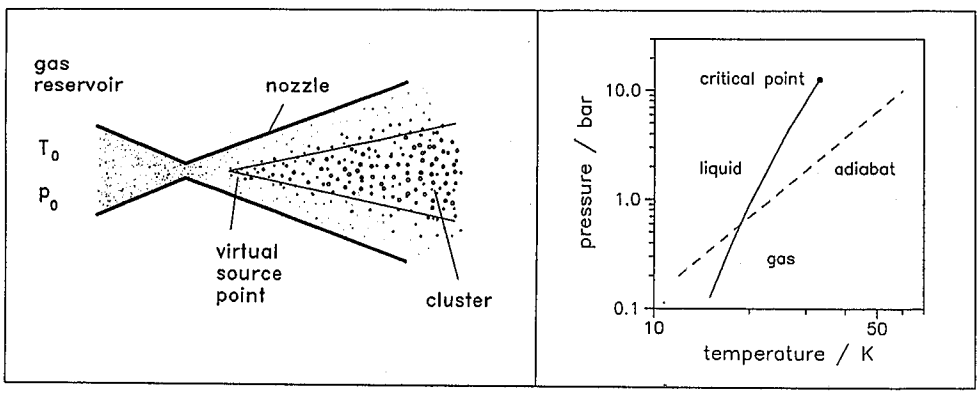

Figure 2: Sketch of the clustering process in a nozzle. On the right side the vapour pressure curve for hydrogen is shown which is crossed during the adiabatic expansion.

nozzle is a gas reservoir at a temperature T_0 and a pressure p_0. During the expansion of the gas the temperature is reduced and if the external parameters have the proper values, the vapour pressure curve is crossed and condensation starts in the nozzle resulting in a beam of gas clusters. For the description of this clustering as a function of the external parameters there exist various scaling laws [1,2,3] like equation 1.

$$N \sim p_0 T_0^{-2.4} \left(\frac{d}{tg\theta}\right)^{1.5} L^{0.2} \tag{1}$$

with N=number of atoms per cluster, p_0, T_0=pressure and temperature in the gas reservoir and L, d, θ = length, throat diameter and opening angle of the nozzle.

The equation requires low temperature and high pressure at the nozzle for optimum performance.

Now such a produced cluster beam has to be prepared for the use as a target. The situation can be described by the simple picture in fig. 3. In the nozzle the cluster beam is produced, at some distance in an UHV region the interaction with the particle beam

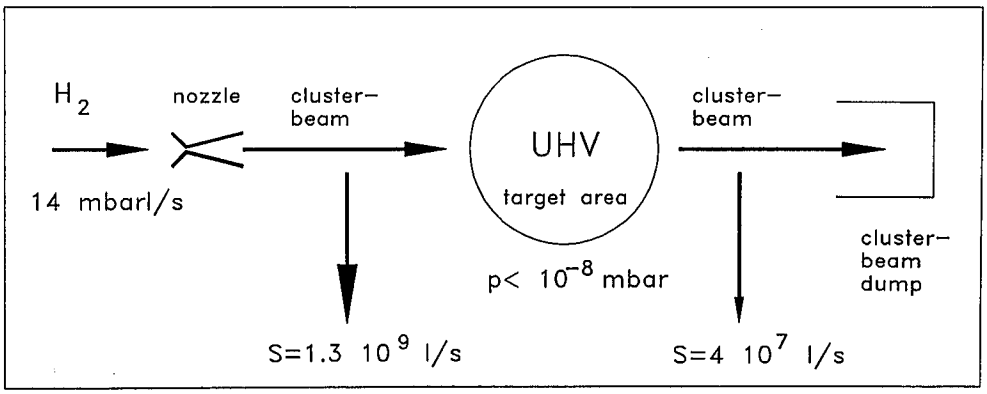

Figure 3: Situation in a cluster target setup. More than 95 % of the gas has to be pumped off which would require unrealistic pumping speeds for only one pumping stage at the source and the beam dump.

takes place and an effective beam dump is needed where the cluster beam is catched. In a typical nozzle only some per cent of the gas undergoes clustering whereby more than 95 % remains for the vacuum system at the source. Therefore for the given gas flows pumping speeds of $\sim 10^9$ l/s and $\sim 10^8$ l/s are needed at the source and the beam dump, respectively, if only one pump in each stage is used. This means in reality several differentially pumping stages in cluster beam direction are needed.

The layout of the various differentially pumping stages for the COSY cluster target can be seen in fig. 4. For each stage the pumping speed S, the pressure p and the conductance L is given.

The starting point for the layout is a maximum target diameter of 10 mm with a density of 10^{14} $atoms/cm^3$, which has been achieved in other existing cluster target setups at CERN [3,4] and at CELSIUS [5]. Using measured cluster flows as given in reference [6] for the type of nozzle which will be used, one can calculate a required gas flow of about 14 mbarl/s. With the assumption of a geometric expansion of the cluster beam the apertures between the different pumping stages are fixed. The vacuum in the target area should be not higher than 10^{-8} $mbar$. In the source part this requirement can be fulfilled with 3 stages, the skimmer stage SK, the first collimator stage K1 and a second collimator stage K2 which is UHV compatible.

In the last stage the cluster beam hits a wall, the clusters burst and a gas source of about 0.3 $mbarl/s$ has to be pumped off. Compared to the source part the conductances between the beam dump stages are relatively high due to the cluster beam divergence. Therefore in the beam dump four stages A1 to A4 are foreseen where high pumping speeds are needed.

The design of the cluster target was optimized for the COSY-11 experiment [7]. In the COSY-11 setup we install the target at a COSY dipol, which is used as a magnetic separator for the ejectiles. According to the COSY layout the target has to fit between a quadrupole and a dipole which gives some restrictions for the geometrical dimensions of the pumps.

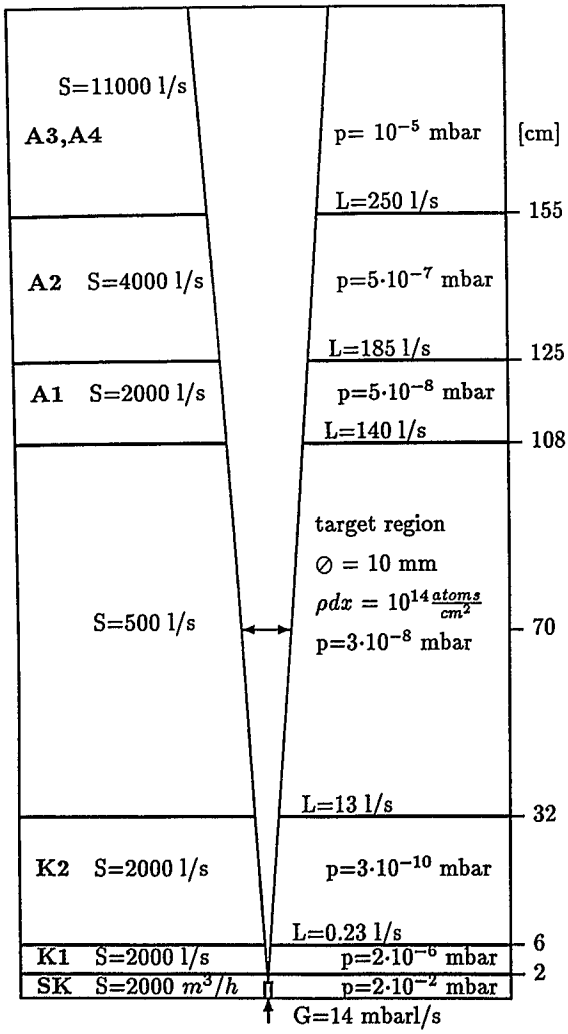

Figure 4: Layout of the cluster target for COSY with several differentially pumping stages.

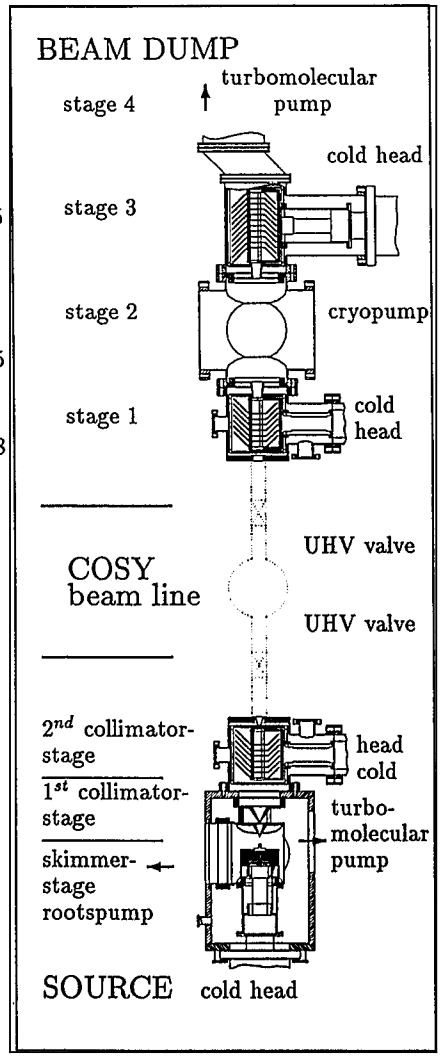

Figure 5: Realization of the layout for the cluster target.

Table 1: Data of the self constructed cryopump for the version with 5 cones for stage K2 and A1 and in brackets for the version with 7 cones for stage A3.

	H_2	N_2	He
calculated internal pumping speed in l/s	22 300 (39 000)	5 950 (10 400)	15 700 (27 600)
measured capacity in barl	29 (-)	130 (-)	- (-)
regeneration interval at p = 10^{-6} mbar	420 d	3 700 d	-

3 Cluster target setup

Now I come to the realization of the target layout in more detail. Figure 5 shows the total setup with the two main parts, the source and the beam dump. The main source parts are the nozzle, the skimmer where most of the gas is skimmed off and the two collimators. For the gas cooling we use a 2 stage refrigerator cold head. All mechanically critical parts as nozzle , skimmer, and first collimator are mounted on the cold head. With this concept the adjustment can be done very simple and de-adjustments due to the thermal shrinking are avoided. The whole skimmer chamber is fixed on the first stage of the cold head. To reduce the heat transfer stainless steel bellows are used for the coupling to the outer chamber. The nozzle is mounted on the second stage where also a heating is included.

At the skimmer stage a roots pump with a pumping speed of 2000 m^3/h is used. Measurements have shown that a cluster beam can be extracted if the pressure in the skimmer stage is lower than $10^{-1}\,mbar$. Thus to reduce the installed pumping capacity we choose a pump which is able to reach this value including a security factor of 10. At the first collimator stage two turbomolecular pumps each with a pumping speed of 900 l/s for H_2 are mounted where the skimmer stage is used as a forepump.

At the second collimator stage a special cryopump is used which allows very high pumping speeds in spite of the limited space. In our special case we have a well defined beam which should pass the chamber without disturbance and all gas particles which hit the chamber wall should be catched. The solution of this problem is a chamber filled with charcoal covered copper cones mounted on the second stage of a cold head with a hole for the cluster beam. Some data of the self constructed cryopumps are listed in table 1.

At the charcoal surface a temperature of 15.5 K was achieved which is sufficient for an efficient cryosorption of hydrogen. At this temperature an internal puming speed of about 20 000 l/s is calculated for the installed charcoal surface. The measured capacity for hydrogen amounts to about 30 barl which leads to very long regeneration intervals.

In the beam dump cryopumps are used with the exception of the last stage where a turbomolecular pump is installed. The first and the third beam dump stage is equipped with the special construction and in the second stage conventional cryopumps are foreseen because here we need the chamber volume for a cluster beam analysis system. As indicated in the drawing the turbomolecular pump in the last stage is mounted asymmetrically so that the cluster beam hits the rotor of the pump. Such an arrangement increases the pumping speed.

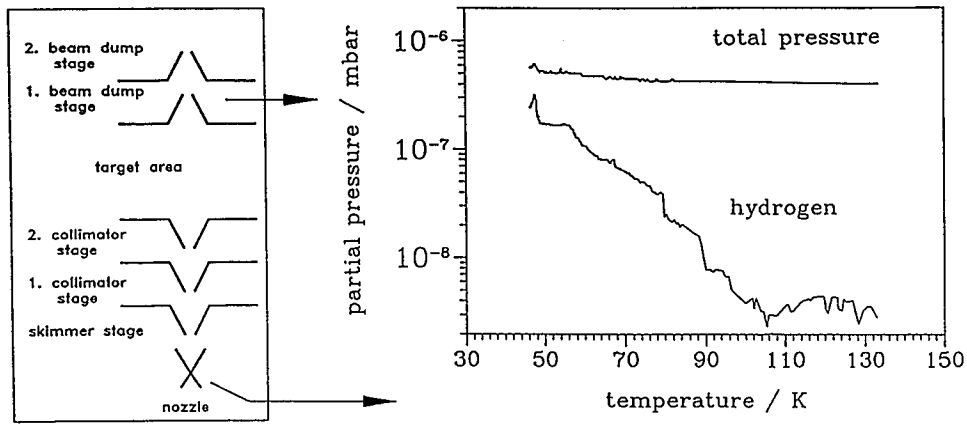

Figure 6: Measurement of the partial pressure for hydrogen in the first beam dump stage as a function of the nozzle temperature. The setup sketched on the left side was used.

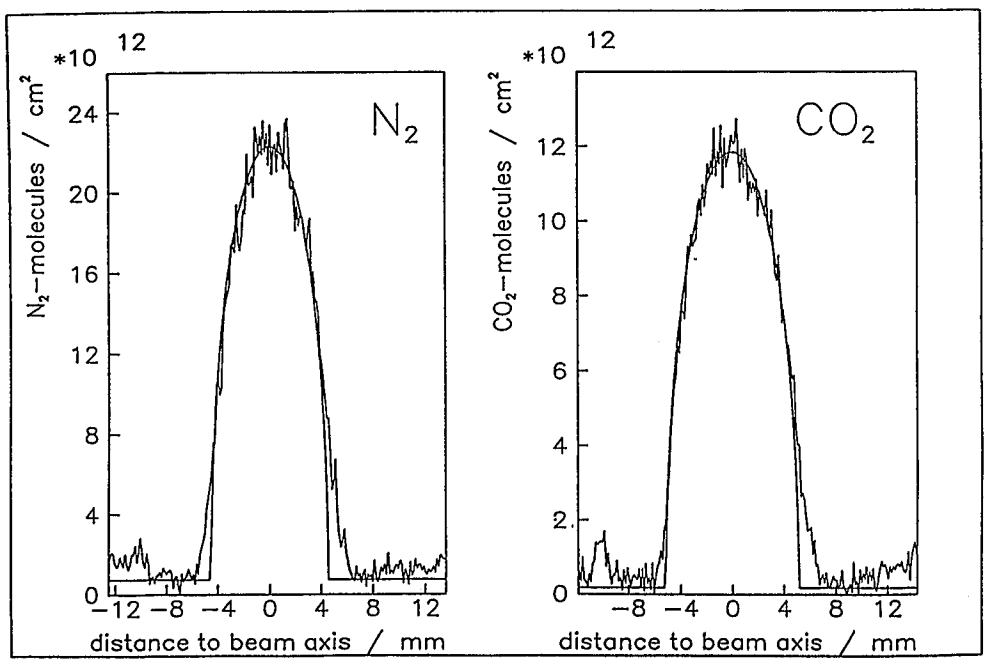

Figure 7: Cluster beam distributions, measured with elastic scattered electrons. The parabolic curve corresponds to a sharp cut density distribution.

4 First results

First measurements were done with a test setup. In the source part we used the final composition with the exception of only one turbomolecular pump being mounted. At the beam dump only two stages with turbomolecular pumps were installed. Therefore no ultra high vacuum conditions in the target region were possible which doesn't influence the studies on the hydrogen cluster jet production.

The successful production of a hydrogen cluster beam is seen in fig. 6. Using the setup sketched in the left part of this figure, we measured the partial pressure of hydrogen in the first beam dump stage as a function of the temperature at the nozzle. At high temperatures no clustering is observed and the partial pressure of hydrogen is very low. Only by clustering hydrogen can be transported to the beam dump which gives rise to a drastic increase of the hydrogen partial pressure below 100 K. Up to now target densities of $2 \cdot 10^{13}\ atoms/cm^3$ were measured, a value which will increase when using an optimized nozzle.

Of course, with the discussed system also other gases can produce cluster beams. For heavier gases, except for helium, the requirements on the vacuum system in the target setup are less severe and the necessary nozzle temperatures are not so low.

Several cluster beam production tests for heavier gases have been performed with a smaller cluster target apparatus [8]. Some typical cluster beam distributions are shown in fig. 7. There, measurements were performed by scanning an 18 keV electron beam perpendicular to the cluster beam and counting the scattered electrons. The counting rate is proportional to the length of the electron beam in the cluster beam. For a circular cluster beam with a sharp cut density distribution parabolic curves are expected as seen in fig. 7.

Presently further investigations are going on in order to increase the target density. In autumn 93 the target will be installed at the COSY ring for the COSY-11 experiment.

References

1 O. F. Hagena, W. Obert, Jou. Chem. Phys., **56**, (1972) 1793

2 O. F. Hagena, Z. Phys. D, **4**, (1987), 291

3 M. Macri, Workshop 'Internal targets for COSY' Jül-Spez-409, (1987)

4 W. Kubischta, Workshop 'Internal targets for COSY' Jül-Spez-409, (1987)

5 C. Ekström, Topical Conference on Electronuclear Physics with Internal Targets, Stanford U.S.A. 1989, World Scientific Publishing Company, (1990), 171

6 J. Gspann, Workshop 'Internal targets for COSY' Jül-Spez-409, (1987)

7 W. Oelert, see his contribution to this workshop

8 W. Bickel et al. , Nucl. Instr. & Meth., **A295**, (1990), 44

THE TIME–OF–FLIGHT DETECTOR SYSTEM FOR THE INVESTIGATION OF THE SUBTHRESHOLD K^+–PRODUCTION WITH THE 0^0 FACILITY AT COSY STATUS REPORT

R. Eßer[1], H. Ohm[1], M. Büscher[1], A. Kiselev[2], V. Koptev[2], S. Kopyto[1], S. Mikirtychyantz[2], H. Müller[3], B. Prietzschk[3], B. Rimarzig[3], G. Shcherbakov[2], K. Sistemich[1]

[1] Institut für Kernphysik, Forschungszentrum Jülich, Postfach 1913, W–5170 Jülich, Germany

[2] Petersburg Nuclear Physics Institute, 188350 Gatchina, Russia

[3] Institut für Kern– und Hadronenphysik, Forschungszentrum Rossendorf, Postfach 19, O–8051 Dresden, Germany

The 0^0 Facility[1] will separate ejectiles of reactions of the circulating proton beam with an internal target in COSY. Due to the high luminosity the 0^0 Facility allows studies of reactions with extremely low cross sections, as e.g. meson production in

$$p + {}^{12}C \rightarrow \text{Meson} + X$$

far below the free nucleon–nucleon threshold. A determination of the momentum and angular distribution of the reaction products is possible.

For the investigation of the K^+–meson production below its NN–threshold of 1.58 GeV/c as proposed in [1] the detection system requires a very efficient first–level online trigger in order to suppress the high counting rates of background protons and pions. At projectile energies of $T_p = 1$ GeV one expects a ratio of $1 : 8 \cdot 10^4 : 4 \cdot 10^5$ for the counting rates of kaons, pions and protons[2] with a momentum of 300 MeV/c. Fig. 1 shows a

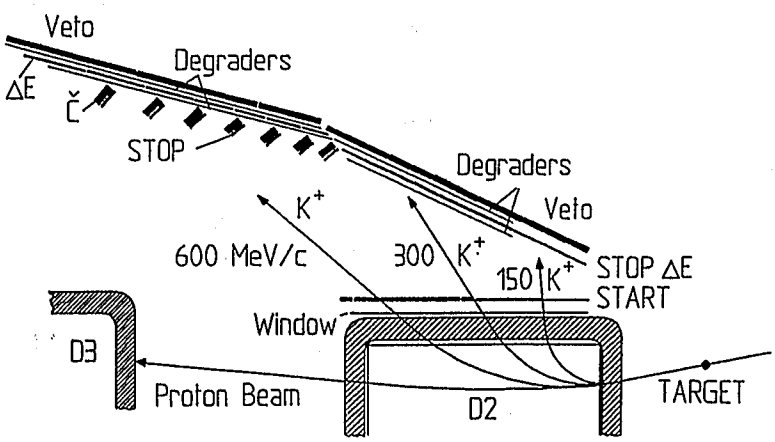

Fig. 1: View of the 0^0 Facility with the simplified detector arrangement for the investigation of subthreshold K^+–production.

simplified version of the detector arrangement. Since the wire chambers close to the magnet and close to the focal surface of the magnet are not used in the first–level trigger they are left out. The fast online trigger will use the time–of–flight (between START and STOP plastic scintillators), ΔE, Čerenkov (C) and Veto information. Simulation calculations with GEANT showed that the time–of–flight discrimination is the most efficient one with a rejection factor of at least 100 for pions. The corresponding suppression factor for protons is even higher due to the bigger time–of–flight difference. Fig. 2 shows the simulated time–of–flight spectra for particles with momenta p = 300 MeV/c ± 2.5%. The momentum spread of 5% is due to a width of 90 mm of the stop detector (see table 1). An overall time resolution of 600 ps (FWHM) has been assumed. For different momenta the $\pi^+ - K^+$ discrimination is comparable.

The thicknesses of the scintillator strips as shown in table 1 are chosen for optimum energy loss and small–angle scattering. The 'stop wall' has to be placed near the focal surface of the central magnet. The lengths of the stop scintillators have been determined by ray tracing calculations with the field map of the magnet (horizontal focusing, vertical defocusing). The identical length of all the start counters which will be placed close to the central magnet (see fig. 1) are mainly determined by the heigth of the magnet gap of about 20 cm. In consideration of the expected counting rates the use of 24 start and 32 stop scintillators is foreseen.

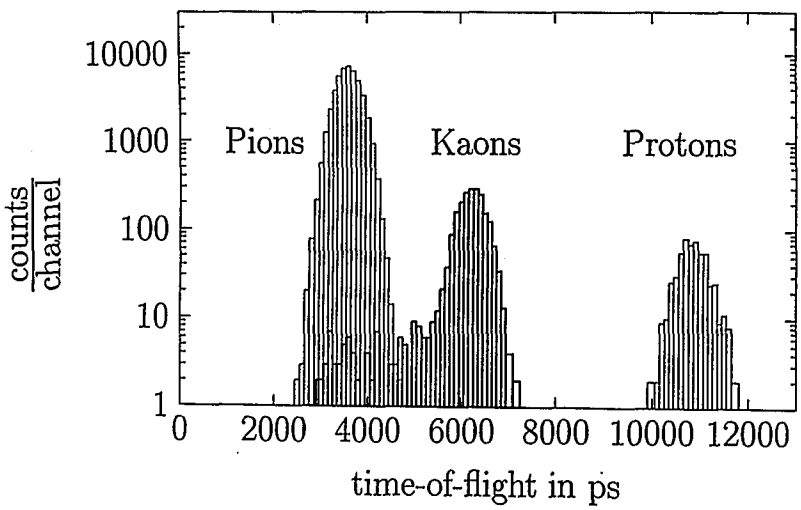

Fig. 2: Simulated time–of–flight spectrum for pions, kaons and protons with momenta 300 MeV/c ± 2.5% for the detector setup as described in fig. 1 and table 1. The simulations were performed with GEANT 3.14. Due to the limited CPU–time a ratio of $n_\pi : n_K : n_p = 10 : 1 : 1$ was chosen. The tail in the K^+–distribution is caused by kaon decay in flight.

Table 1: Dimensions of the scintillator strips (Length · Width · Thickness) for particles with various momenta.

p[MeV/c]	START [mm³]	STOP [mm³]
150	300 · 50 · 0.5	400 · 60 · 2
300	300 · 50 · 1	500 · 90 · 5
600	300 · 50 · 1	600 · 110 · 10

It should be stressed that for a fixed momentum (≡ fixed stop counter) several possible start counters can be hit. Since the flight–path lengths are different one has to combine one stop scintillator with 3 (low momentum region) to 10 (high momentum region) start detectors. A proper, remote controlled delay line system, which is necessary to use the time–of–flight information for the trigger is under development. Each detector strip has to be coupled to photomultiplier tubes at both ends. To correct for the light propagation time online a meantimer must be used. A compact meantimer to integrate in an existing discriminator is under preparation at KFA–ZEL.

In order to obtain the requested features of the time–of–flight detector system a careful selection of the components is necessary. The plastic scintillators Bicron BC420, BC408 and Nuclear Enterprises PILOT U are under discussion. Their timing relevant properties are given in table 2. Tests of a plastic scintillator made by JINR Dubna are under way.

Table 2: Physical properties of plastic scintillators under investigation.
λ_{max}: wavelength of maximum emission
L_0: attenuation length (for the scintillator of JINR measured with a 650 mm long, 50 mm wide and 5 mm thick scintillator, preliminary result)
t_D: decay time of the main component

Material	λ_{max} [nm]	L_0 [mm]	t_D [ns]
BC408	425	3800	2.1
BC420	391	1100	1.5
PILOT U	391	1000	1.4
JINR	—	540 ± 60	3.0 ± 0.5

Because of the foreseen use of lightguides one has to check if it is necessary to use a special UV–transmitting PMMA in the case of the more UV–emitting scintillator materials PILOT U and BC420 instead of the standard PMMA. We suppose that we have to use BC408 for the stop counters. The disadvantage that this material is slower is overcompensated by the higher light output due to the much longer attenuation length and the better transmission through the (standard) lightguides, as tests at the synchrocyclotron of PNPI, Gatchina showed. In order to obtain a high rejection factor of the ΔE–trigger by adding the signals of both photomultiplier tubes of each scintillator a high attenuation length is necessary especially for the long stop counters (see fig. 3).

For the stop detectors we plan to use the 2–inch Philips tubes XP2020 or XP4222B. For the start detectors the situation is more complicated because the tubes have to work in an ramped stray field of up to 0.4 T. Therefore we discuss to use smaller tubes or a channel plate from the PNPI which are easier to shield.

In several tests it turned out that dynode signals give improved timing for the time–of–flight measurements compared to the anode signals. The conversion of the analog photomultiplier signal into a logic one was performed by two leading–edge discriminators in coincidence. Single start detector modules were tested in the laboratory with ^{90}Sr ß–particles. One result – obtained with a scintillator strip of the dimensions $300 \cdot 30 \cdot 2$ mm^3 used as a start detector in a time–of–flight measurement – is shown in fig 4. The contribution of the accompanying stop scintillator to the total resolution is already subtracted. The measured time distributions were gaussian shaped down to 3 orders of magnitude from the maximum.

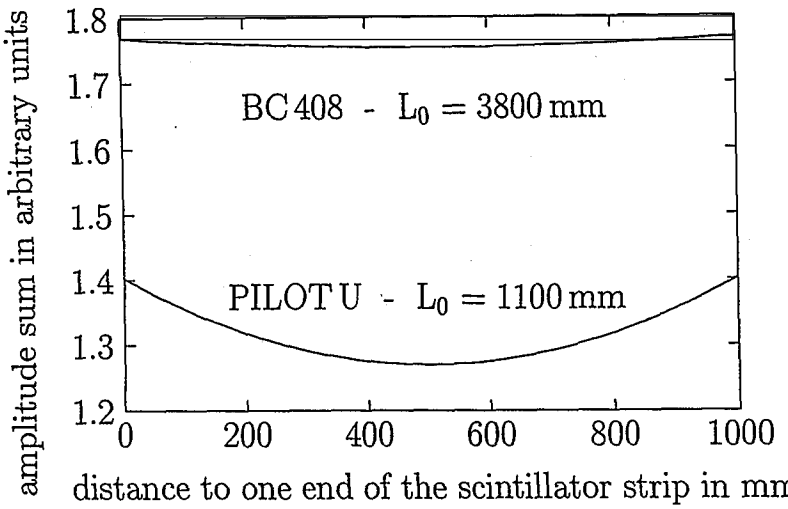

Fig. 3: Dependence of the amplitude sum from both ends of a 1000 mm long scintillator strip out of PILOT U and BC408 on the position of illumination for an (ideal–)exponential light output behaviour.

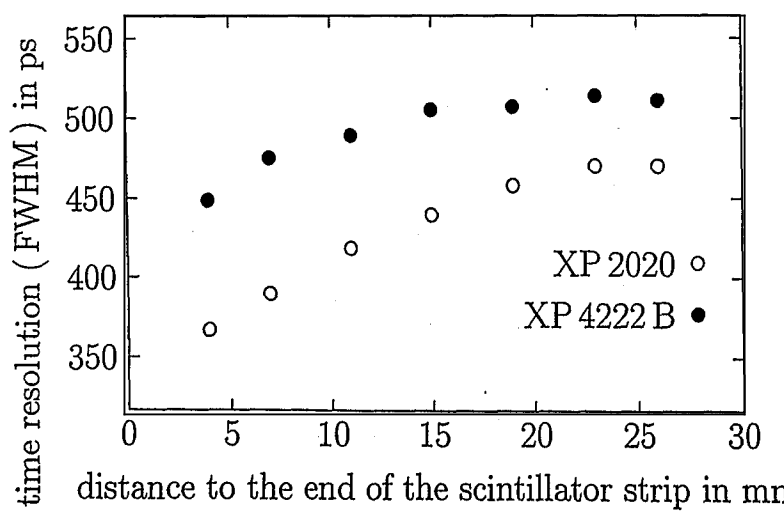

Fig. 4: Time resolution of a 300 mm long, 30 mm wide and 2 mm thick BC420 scintillator strip coupled to tubes XP2020 (o) and XP4222B (•), respectively.

In addition we tried to find an optimum voltage divider for the photomultiplier tubes by variation of the voltages between the photocathode and the focusing grid or first dynode.

The standard Philips voltage divider S563 was modified in such a way that positive high voltage was used. By use of a blue light–emitting diode the effects on the amplitude homogeneity were tested (see fig. 5). Measurements of the dependence of the signal transit time inside the tubes and the width of the time distributions from the position of the illuminated spot on the photocathode are planned. More details are given in[3].

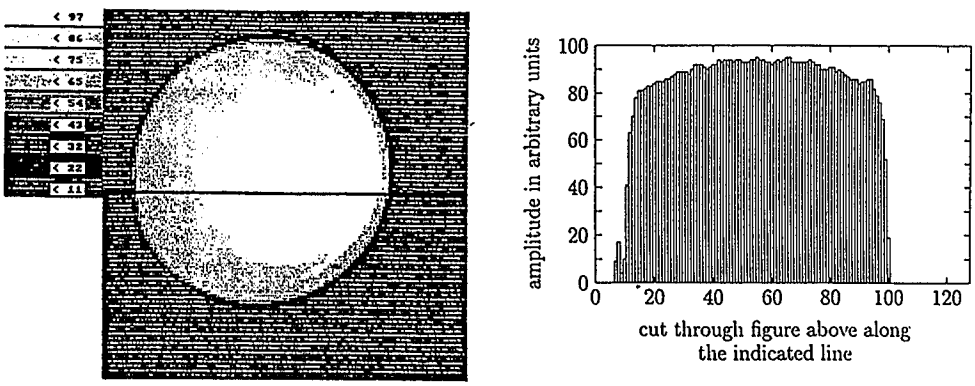

Fig. 5: Two–dimensional dependence of the photocathode sensitivity over an area of 60 · 60 mm² (left) and cut along the indicated line (right).

In order to confirm the results obtained with the ^{90}Sr source the system was tested in a secondary beam of pions and protons with a momentum of about 300 MeV/c at the synchrocyclotron of the PNPI, Gatchina. A start counter (300 mm long, 60 mm wide) and a stop counter (1000 mm long, 100 mm wide) were placed in the beam which covered them completely. A small counter consisting of a scintillator disk with 60 mm diameter operating in coincidence with the time–of–flight system was placed behind the stop counter in order to detect only those particles traversing the stop detector in a well defined position (see fig. 6). Photomultiplier tubes Philips XP2020 were coupled to both ends of each scintillator strip using fishtail lightguides out of (standard–)PMMA. The detector response was measured for different beam positions relative to the stop counter by moving the small scintillator disk.

Pulse heights for each photomultiplier, time differences between both photomultipliers of each strip counter and the time–of–flight between start and stop counter were recorded. A meantimer Struck FDMT101 was used to eliminate the effect of the different light propagation times from different irradiation positions. Data acquisiton was performed with the PC–based CAMAC system with the software package CAMDA[4].

The best resolution in the time–of–flight measurement was obtained with BC408 for both the start (4 mm thick) and the stop (10 mm thick) counter, see fig. 7. The resolution for protons and pions was 570 and 560 ps FWHM, respectively. The dependence of the time–of–flight peak position on the position of the illuminated spot on the stop detector was not more than 120 ps for beam–spot positions 60 cm apart, where the different light propagation times would have caused a 3500 ps shift without using the meantimer. First results from measurements with a very thin (1 mm) start scintillator indicate that even with this thickness as it will be used in the K^+–production studies a reasonable timing resolution is possible.

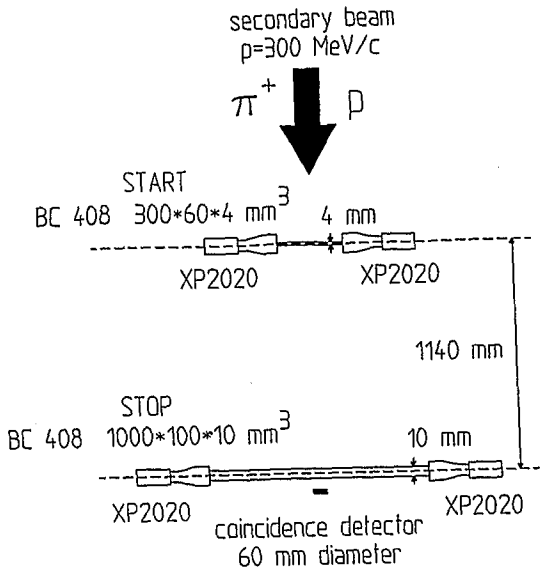

Fig. 6: Detector setup used at PNPI, Gatchina. See text for details.

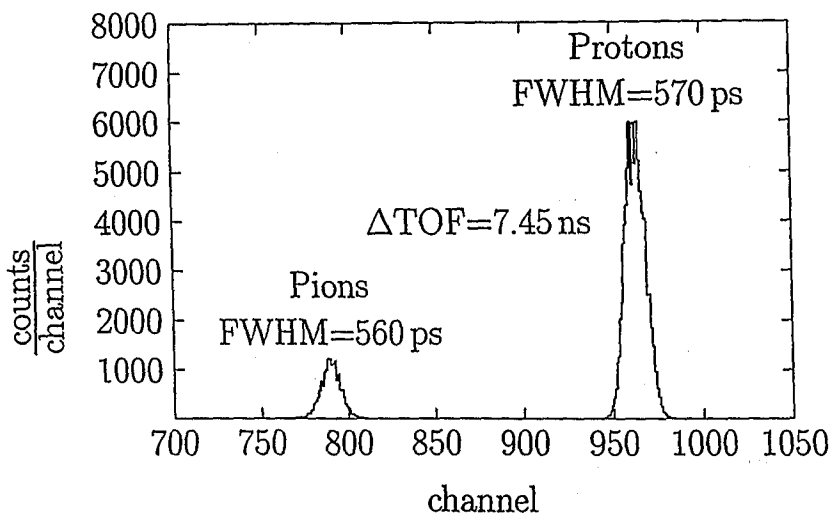

Fig. 7: Time–of–fligth spectrum for protons and pions at p = 300 MeV/c with BC408 for start and stop detector.

Fig. 8 shows the energy–loss of 300 MeV/c pions and protons where the beam was moved stepwise over the BC408 stop scintillator over a range of 75 cm. In this spectrum the intensity is plotted as a function of the sum of the amplitudes of both

photomultipliers of the strip. Though there is some broadening of the peaks due to the position dependence (see fig. 3) there is a clean separation of pions and protons. The position where the kaon peak would appear (arrow) is clearly separated from the other peaks indicating that also ΔE can be used for an efficient trigger.

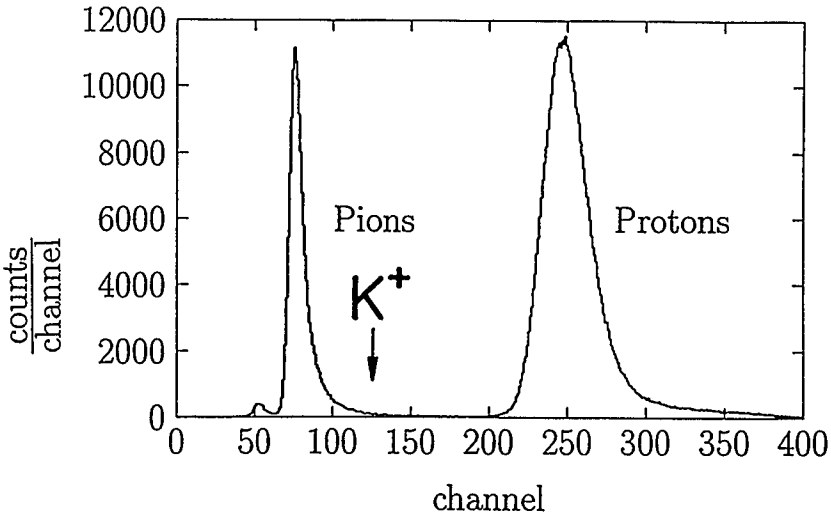

Fig. 8: Energy–loss spectrum for protons and pions at p = 300MeV/c with BC408 scintillator.

References:
1. W. Borgs et.al., COSY Proposal No. 18, 1991
2. M. Büscher, PhD–Thesis, Univ. of Cologne, Germany, 1992
3. R. Eßer, Diploma–Thesis, Univ. of Cologne, Germany, 1992
4. Physikalische Nachweisgeräte Dr. H. Stelzer, 6101 Messel, Germany

Reaction Rates in Internal Solid State Targets

H.R.Koch

Institut für Kernphysik, Forschungszentrum Jülich

The study of proton-nucleus reactions implies the use of solid state targets. For example, the investigation of K^+ production below the free NN threshold (COSY proposal no 18) will probably start with the irradiation of a thin graphite ribbon foil at the COSY internal target position TP2. In the following some basic relations concerning the time structure of the reaction rates and the mean luminosities are given.

The variation of the number of particles in COSY during one beam preparation and irradiation cycle is illustrated in fig.1. After the injection and acceleration phases the beam is bumped onto the target or the target is moved into the beam. Multiple Coulomb scattering of the beam particles at the target nuclei causes an increase of the beam emittance. The number of particles in the ring is nearly constant during the period in which the beam dimension is blown up from its value at the end of the acceleration phase to a size given by the ring acceptance. Afterwards the beam intensity decreases exponentially, if the probability of the circulating beam particles to hit the target is constant.

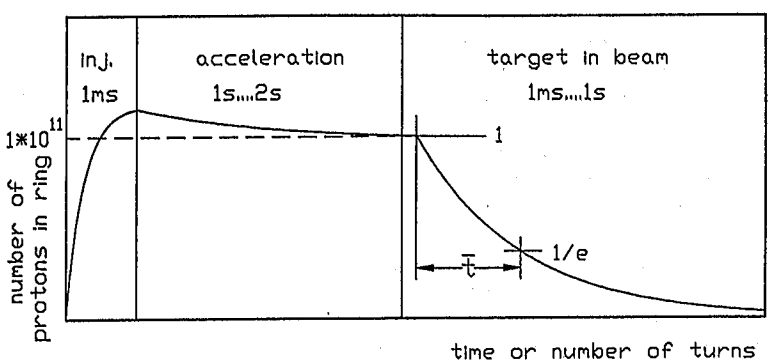

Fig.1: Number of circulating protons during one COSY cycle

For relatively thin targets (in the order of 100 $\mu g/cm^2$) the decay of the beam is best determined in simulation calculations, in which the distribution of Coulomb scattering angles is correctly reproduced, including the large angle tail far beyond the mean scattering angle. Calculations of this type have been performed for 3 proton energies and some selected target materials, covering the range of Z=1 to Z=92 (fig. 2) /1/.

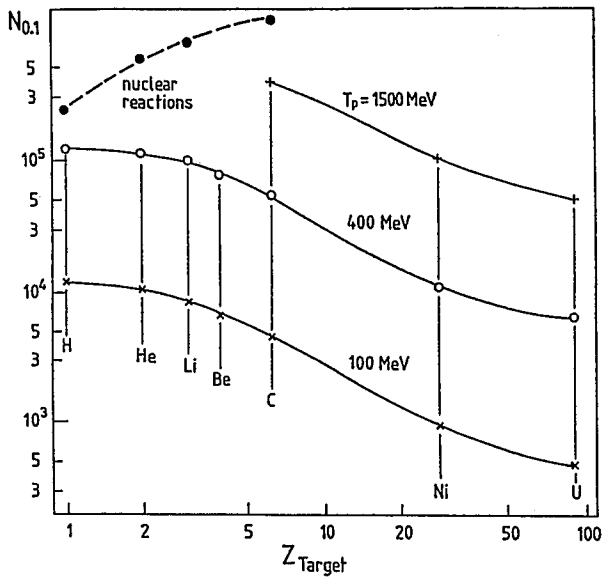

Fig.2: Lifetime of proton beam. The number of passages through targets of 100 $\mu g/cm^2$ is given which cause a decrease of the beam current to 10%. The relevant ring parameters are:
Beta function at target: $\beta_{x,z}$ = 8; 2 m
Ring acceptance: $A_{x,z}$ = 200; 50 π·mm·mrad
Figure of merit: FM = 12

These results can also be used to estimate the beam decay for other targets, energies and ring characteristics. The relation for the single Coulomb scattering angular distribution leads to the following scaling law for the mean beam lifetime $\bar{t}$ (or 1/e time for exponential decay):

$$\bar{t} = C \cdot \frac{FM}{TM/AT \cdot THP} \cdot \left(\frac{E \cdot (v/c)^2}{Z1 \cdot Z2} \right)^2$$

FM = figure of merit of storage ring
= 1 / ($\beta_X/A_X + \beta_Z/A_Z$)
β = beta functions at target / m
A = ring acceptance / π·mm·mrad
TM = target thickness/ $\mu g/cm^2$
AT = mass number of target nuclei
THP = target hit probability
E = total relativistic projectile energy T+M / MeV
v/c = projectile velocity
Z1,Z2 = atomic numbers of projectile and target

The factor C follows from insertion of the mean beam lifetime, determined for a specific experiment through simulation calculation (fig. 2), into the formula above. C is roughly constant. If the parameters are given in the units quoted above one obtains C ≈ 1 turn.

The dependence of the beam lifetime on the inverse of the target thickness, as expressed in the scaling law above, has an important consequence for the mean luminosity. The total number of target hits per cycle is given as

$$NTH = Np \cdot \bar{t} \cdot THP,$$

where Np means the initial number of beam particles. The integrated luminosity per cycle is given as

$$SL = NTH \cdot N,$$

where N is the number of target atoms/cm² (= Avog.No·TM/AT). As $\bar{t} \propto 1/N$ we obtain

$$SL \approx \text{constant (independent on target thickness).}$$

The mean luminosity becomes SL/tcycle. For solid state targets cycle times are nearly constant, as they are essentially determined by the beam preparation time:

tcycle = tprepare + tbeam, tbeam << tprepare.

The actual beam reaction time will be very roughly $tbeam \approx 3 \cdot \bar{t}$.
Consequently one obtains:

the mean luminosity is independant of the target thickness

The time dependences of the reaction rates of targets whose thicknesses differ by a factor of 2 are illustrated in fig.3. The thinner target will produce an initial reaction rate IR2 which is ½ of that related with the thicker target (IR1). However the beam life time $\bar{t}2$ related with the thinner target will be longer by a factor of 2.

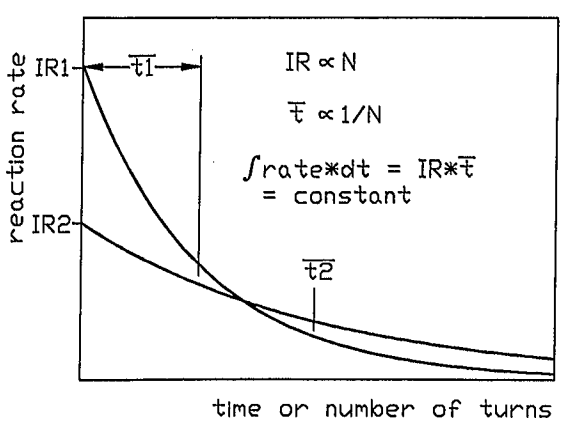

Fig.3: Reaction rates of internal targets of different thicknesses

Let us now estimate luminosities and reaction rates for a COSY internal target and the following conditions:

Tab.1: Assumed conditions for an experiment at TP2.

Number of protons per cycle:		$1 \cdot 10^{11}$
Kinetic beam energy	:	1 GeV
Revolution period	:	0.7 μs
Target	:	100 $\mu g/cm^2$ of C ($N=5 \cdot 10^{18}$)
Target hit probability	:	1
Ring parameters at TP2	:	
$\beta_{x,z}$	:	2.8; 3.2 m
$A_{x,z}$	:	130; 35 π·mm·mrad
FM	:	9
Nuclear cross section	:	100 mb
Number of reaction products:		5 per reaction

These assumptions lead to $\bar{t}$ = 55,000 turns, corresponding to 40 ms and to the following rates:

	luminosity	rate of products
Average per turn (initial)	$7 \cdot 10^{35}$ /cm²·s	$3.5 \cdot 10^{11}$ /s
Average per COSY cycle (3s)	$9 \cdot 10^{33}$ /cm²·s	$4.5 \cdot 10^{9}$ /s

The initial rate of reaction products is very high, presenting problems for any large angle detection system. Making targets thinner would help, however, target production and handling become difficult. Thus one can hardly take advantage of the achievable luminosity, if a full beam target is used.

A thin ribbon foil target as shown in fig.4a will reduce the target hit probability to values in the order of 0.02 to 0.10 and decrease the initial reaction rates. The mean luminosity would remain nearly the same. Furthermore the local restriction of the interaction region leads to well defined reaction kinematics. With the target of fig.4a we will still obtain strongly varying reaction rates, similar to those shown in fig.3. The peak at the the beginning of the irradiation should be avoided. Roughly constant reaction rates are aimed at.

The rates can be controlled in principle if the target is located outside the beam axis. Then the target can only be hit by those beam particles, which perform betatron oscillations of a certain size. The movement of the particle in the transversal (x,x';z,z')- phase space is determined by the individual particle emittance ε through the relation:

$$\varepsilon_x = (1+\alpha_x^2)/\beta_x \cdot x^2 + 2\alpha_x \cdot x \cdot x' + \beta_x \cdot x'^2 \qquad /2/.$$

α_x, α_z and β_x, β_z are Twiss parameters . $\varepsilon_x, \varepsilon_z$ are constant during the propagation of the particle through the ion optical elements of the ring. Only scattering events cause changes. However the average Coulomb scattering angles in the targets we are discussing give rise to only very small changes of these emittances after one target passage. Therefore the positions (x;z), at which a certain beam particle passes

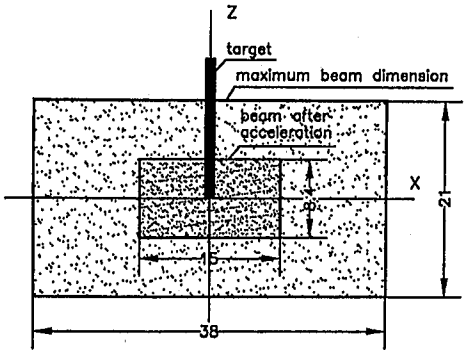

Fig.4a: Dimension of the internal COSY beam for the parameters of tab.1. The inner rectangle is the beam envelope after acceleration. The outer one refers to the beam after heating through the target has taken place.

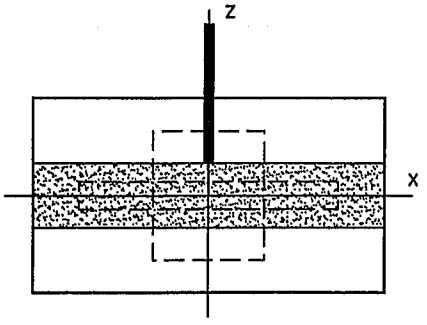

Fig.4b: Boundaries (dashed rectangles), which limit the coordinates of beam particles in the target plane. With a target at the indicated position and sufficiently long target-beam interaction the beam will cover only the dotted area (no mixing of horizontal and vertical phase space is assumed).

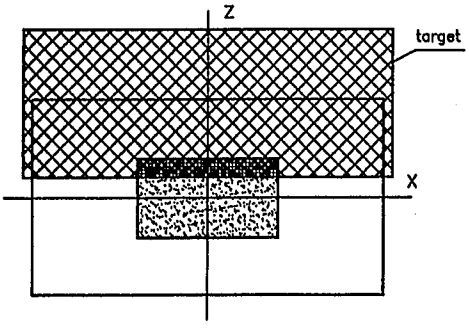

Fig.4c: Position of a wide target at the beginning of the irradiation. Lowering of the target can produce a flat rate distribution.

through the target, are located within a rectangle. Any point of the field within the rectangle can be hit. This is illustrated in fig.4b. The widths and heights of the rectangles are given as $2\cdot\sqrt{\varepsilon_x \beta_x}$ and $2\cdot\sqrt{\varepsilon_z \beta_z}$. One should not confound with the particle movement in the (x,x') or (z,z') phase space. In this representation the points at which a particle passes a certain position in the ring are located on a line: the ellipse given by the individual particle emittance and the Twiss parameters relevant for the position at the ring. We conclude, that movement of the target from the border of the beam towards the beam axis should cause gradual consumption of the beam particles. The practicability of this method for control of reaction rates will be investigated soon at the IUCF ring at Bloomington (proposal on skimmer targets, spokesman P.Pancella).

We have started to search for target shapes and displacements which are supposed to produce roughly constant reaction rates. Simulation calculations were performed for the COSY ring parameters given in tab.1. An acceptable rate distribution was obtained for a 100 $\mu g/cm^2$ carbon target. The shape and the position at the beginning of the irradiation are shown in fig.4c. At this time the target covers just the upper part of the beam. The target was then lowered at a constant speed of 1.4 cm/s. Fig.5 shows the time dependence of the reaction rate. For comparison also the rate is given, which results from a sudden movement of the target into the beam. The slow displacement reduces the maximum rate to 30 %. The studies will be continued to find procedures which produce flat rate distributions also for narrow, ribbon like targets. Further degrees of freedom have to be included: variable speed of the target displacement, triangular target shape, and targets of locally variable thickness.

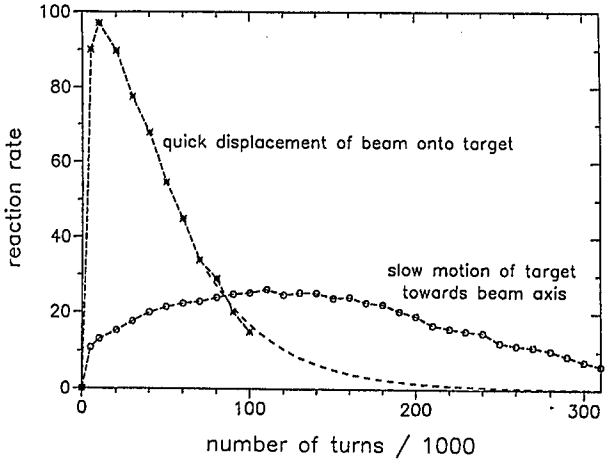

Fig.5: Effect of target motion on reaction rates

References:
/1/ H.R.Koch, O.W.B.Schult, Jül-Spez-403 (1987) 122
/2/ K.Steffen, CERN 85-19 (1985) 25

Eta Production

B.M.K. Nefkens
UCLA Physics Department
Los Angeles, CA 90024–1547

The production close to threshold of eta mesons in nuclear interactions does not conform to the conventional ideas. In a classic treatise on pion production, Gell-Mann and Watson [1] have argued that orbital angular momentum greater than $\ell\hbar$ with

$$\ell = \frac{p}{mc} \tag{1}$$

does not play an important role in production reactions. Thus, we expect S-wave production near threshold. Consider the elementary production reaction

$$p + p \rightarrow p + p + \eta. \tag{2}$$

The available cross section data just above threshold are shown in Fig. 1. They come from the SPES III collaboration at Saturne [2], these data have just become available. S-wave production would imply that the cross section increases with energy proportionaly to the phase space which means that $\sigma_t \sim \tilde{p}_\eta^2$ for reaction (1). The experiment shows differently, σ_t flattens off somewhere around Q is 2 MeV, which corresponds to $\tilde{p}_\eta > 40$ MeV/c. The dashed lines in Fig. 1 are recent theoretical predictions [3,4] for reaction (1).

An important contribution by COSY could be measurements in small energy steps of $\sigma_t(p + p \rightarrow p + p + \eta)$ near threshold with unpolarized as well as polarized beams and the determination of the Dalitz plot. The expected signal is large; this is illustrated in Fig. 2 which shows a large missing mass peak measured in the experiment of Ref [2].

Next consider the reaction

$$p + d \rightarrow {}^3He + \eta \tag{3}$$

which has been studied at Saclay also. The latest data, obtained at SPES II, [5]are shown in Fig. 3. S-wave production dictates that the total cross section is proportional to the phase space, which in this reaction means that $\sigma_t \sim \tilde{p}_\eta$. This is not observed experimentally, the cross section above $\tilde{p}_\eta \simeq 22$ MeV/c is flat up to $\tilde{p}_\eta = 75$ MeV/c. The angular distribution is isotropic as befits an S-wave production reaction. This is the case up to the maximum energy investigated, 11 MeV above threshold. Thus, the energy dependence and the angular distributions are inconsistent with one another. There is no need to remind one here that the reactions $p + p \rightarrow p + p + \pi^\circ$ and $p + d \rightarrow {}^3He + \pi^\circ$ which are similar to η production behave as expected for S-wave production.

It is of interest to look at the elementary η-production reaction by pions,

$$\pi^- + p \rightarrow \eta + n. \tag{4}$$

Recently, the available cross section data have been assigned "stars" [6] according to a series of criteria originally proposed for the assessement of the quality of the πN Data Bank [7]. Fig. 4 shows σ_t for all one- and two-star data sets, no three star experiments being available. The largest data set (20 incident pion momenta) Ref. [8] was found to be seriously in error. E.g., near $p_\pi = 687$ MeV/c the beam momentum quoted in ref. [8] is incorrect, it is too high by about 35 MeV/c which messes up the angular distribution. The πN scattering data obtained by the same group of Ref. [8] with the same setup is also in error [9–11]. The fit of $\sigma_t(\pi^- p \rightarrow \eta n)$ to a simple Breit-Wigner expression puts the peak at 1483±16 MeV, which is well below the official mass of the $S_{11}(1535)$. The data are consistent with a very small Q-value. A new detailed evaluation of the $\pi^- p \rightarrow \eta n$ reaction is needed.

It is remarkable that at the opening of the eta-decay channel in each of the three isobar families investigated thus far, the N*, Λ^*, and Σ^* families, there is a very strong S-wave, negative parity, resonance that favors the η decay channel despite a large handicap as regards the kinematically favored π- or K-decay modes, see Table I. The result for $\sigma_t(K^- P \rightarrow \Lambda\eta)$ from Ref [12] is illustrated in Fig. 5 while Fig. 6 shows $\sigma_t(K^- P \rightarrow \Sigma^\circ\eta)$ from Ref. [13].

The near-threshold η production cross section of the simplest nuclear reactions have the following values

$$\sigma_t(pp \rightarrow pp\eta) \sim 1\ \mu b,$$

$$\sigma_t(np \rightarrow d\eta) \sim 100\ \mu b,$$

$$\sigma_t(pd \rightarrow {}^3He\eta) \sim 0.4\ \mu b.$$

This suggests the importance of the neutron in η production processes. More information is needed on the η production from bound neutrons. It would be interesting for COSY to consider measurements of the reaction $p + {}^3H \rightarrow \alpha + \eta$, as well as $p + d \rightarrow p + d + \eta$. It is also important to measure carefully using the cooler ring, the cross section for $p + {}^6Li \rightarrow {}^7Be + \eta$ near threshold and to separate η production to the ground state from the first excited state of ^7Be.

Of special interest is the energy dependence of $d\sigma(pd \rightarrow {}^3He\ \eta)$ at 180° which is shown in Fig. 7 based on the data of Refs [5] and [14]. The picture defies a simple, traditional description. Particularly baffling is the flat part from 1 to 11 MeV above threshold where the angular distribution is isotropic within ten percent [5]! A bold speculation for the origin of this is the existence of quasibound η-nuclear state; this could be the result of the strong ηN attractive interaction in the S-state. There is an

urgent need for more η production near threshold in nuclear reactions to address this problem.

The necessity to discard the $\pi^- p \to \eta n$ data from Ref. [8] has some important consequences for the η decay branching ratio of different N* resonances. It turns out that the η-decay branching mode of all N* resonances except the previously discussed $S_{11}(1535)$ is determined exclusively by Baker et al [15] who based their work mainly on the data of Ref. [8]! The available data on $\sigma_t(\pi^- p \to \eta n)$, without those of Ref. [8], are shown in Fig. 8 where we have also indicated the position of the major N* resonances. Inspection of this figure leads to the conclusion that the $S_{11}(1650)$ resonance could have a sizeable η branch contrary to the 1% decay to the η channel in the eroneous assessement of Ref. [15]. There appears to be plenty of room for a sizeable η-decay of different N* resonances in support of the quark model calculations by Koniuk and Isgur [16]. Much more precise data is needed on $\sigma_t(\pi^- p \to \eta n)$, including polarization information, before the η branching ratio of the N* can be learned.

The production of η mesons near threshold may be summarized as follows. The elementary pion induced reaction $\pi^- p \to \eta n$ is dominantly an S-wave process at least up to $\tilde{p}_\eta \simeq 120$ MeV/c. The nucleon induced η production is not consistent with S-wave production especially $pd \to {}^3He\,\eta$. The nuclear environment has changed the threshold mechanism.

It is a pleasure to acknowledge the stimulating atmosphere of this Workshop, the organizational work of Otto Schult, and the hospitality provided by the WE-Heraeus-Stiftung.

This work was supported in part the the U.S. Department of Energy.

Table I Isobars with a well established η decay branch.

PDT symbol	I, J^P	spectr. notation	mass (MeV)	width (MeV)	η decay frac. (%)	Q (MeV)	R
N(1535)	$\frac{1}{2}, \frac{1}{2}^-$	S_{11}	1483±16	100–250	45–55	2±16	$\eta N/\pi n \sim 1 \pm 0.5$
Λ(1670)	$0, \frac{1}{2}^-$	S_{01}	1670±5	25–50	15–35	7±5	$\eta\Lambda/\bar{K}N \sim 1 \pm 0.5$
Σ(1750)	$1, \frac{1}{2}^-$	S_{21}	1750±20	60–160	15–55	10±20	$\eta\Sigma/\pi\Sigma > 2$

PDT = Particle Data Table, Q is the energy release, e.g., $Q = m(S_{11}) - m_n - m_\eta$
R is the ratio of branching ratios to η and π (or K) decay modes.

References

[1] M. Gell-Mann and K.M. Watson, Ann. Rev. Nucl. Sci. **4**, 219 (1954).

[2] A.M. Bergdolt et al., submitted for publication; preprint, Centre de Recherches Nucleaires, Univ. L. Pasteur, Strasbourg, France.

[3] J. F. Germond and C. Wilkin, Nucl. Phys. **A518**, 308 (1990).

[4] J. M. Laget et al., Phys. Lett. **B257**, 254 (1991).

[5] R.S. Kessler, Ph.D. thesis, UCLA, 1992, and to be published.

[6] M. Clajus and B.M.K. Nefkens in πN Newsletter #7, November 1992; preprint UCLA 10–P25–195.

[7] B.M.K. Nefkens in *Few Body Problems in Physics* Vol. II, edited by B. Zeidnitz (North Holland, p. 137, 1984).

[8] R.M. Brown et al., Nucl. Phys. **B153**, 89 (1979).

[9] J.A. Wightman et al., Phys. Rev. D **38**, 3365 (1988).

[10] R.E Cutkosky et al., Phys. Rev. D **20**, 2804 (1979).

[11] R. Koch and E. Pietarinen, Nucl. Phys. **A336**, 331(1980).

[12] D. Berley et al., Phys. Rev. Lett. **15**, 641 (1965).

[13] M.O. Jones et al., Nucl. Phys. **B73**, 141 (1974).

[14] P. Berthet et al., Nucl. Phys. **A443**, 589 (1985).

[15] R.D. Baker et al., Nucl.Phys. **B156**, 93 (1979).

[16] R. Koniuk and N. Isgur, Phys. Rev. D **21**, 1868 (1980).

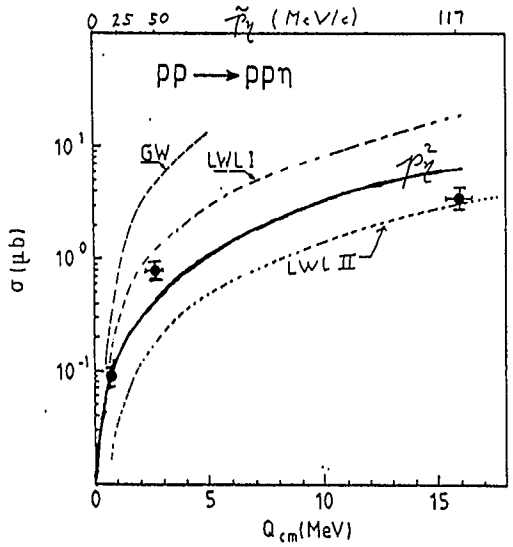

Fig. 1 $\sigma_t(pp \rightarrow pp\eta)$ from Ref. [2]. The solid line is the S-wave production arbitrarily normalized. The dashed curves are the calculations from Refs. [3 and 4].

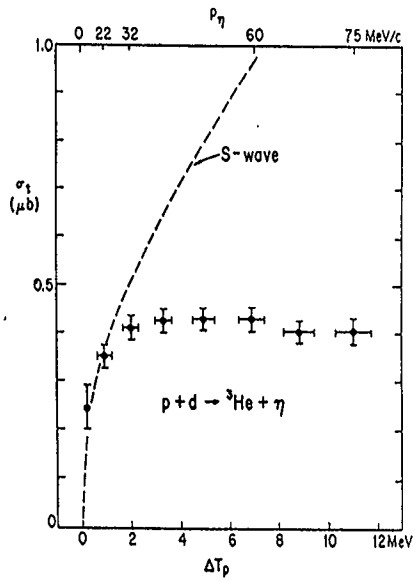

Fig. 3 $\sigma_t(pd \rightarrow {}^3He\,\eta)$ near threshold. The dots are the preliminary results from Ref. [5]. The dashed line is the prediction for S-wave production arbitrarily normalized. ΔT_p is the beam energy above threshold.

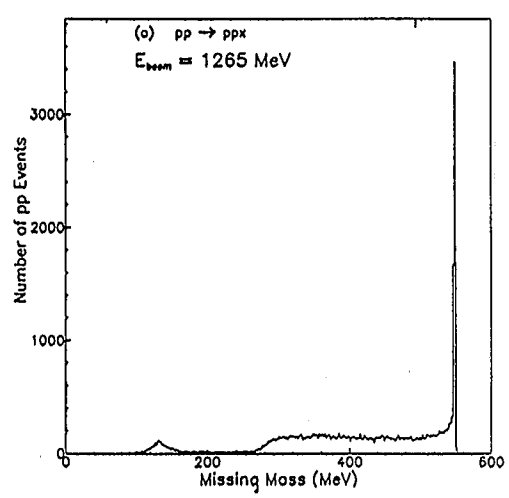

Fig. 2 Missing mass spectrum in $pp \rightarrow ppx$ measured at SPES III, Ref. [2].

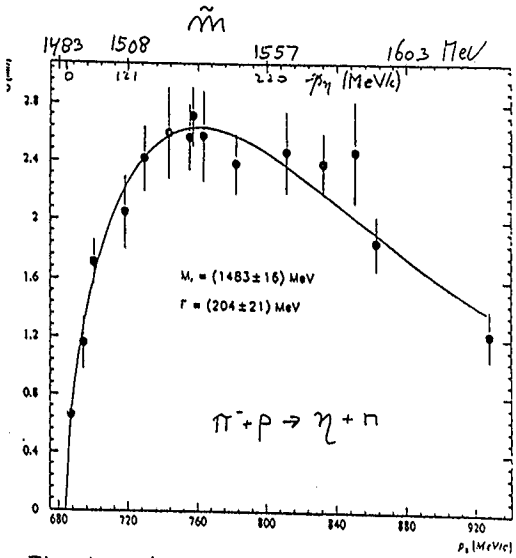

Fig. 4 $\sigma_t(\pi^- p \rightarrow \eta n)$, one- and two-star data discussed in Ref. [6]. The solid line is the fit to a Breit-Wigner type function.

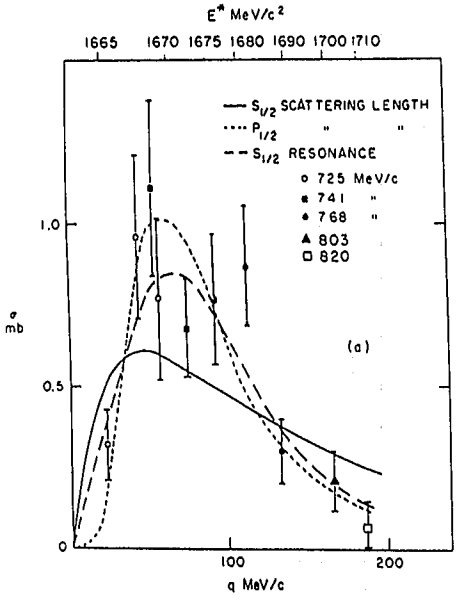

Fig. 5 $\sigma_t(K^-p \to \Lambda\eta)$ at low energy, Ref. [12].

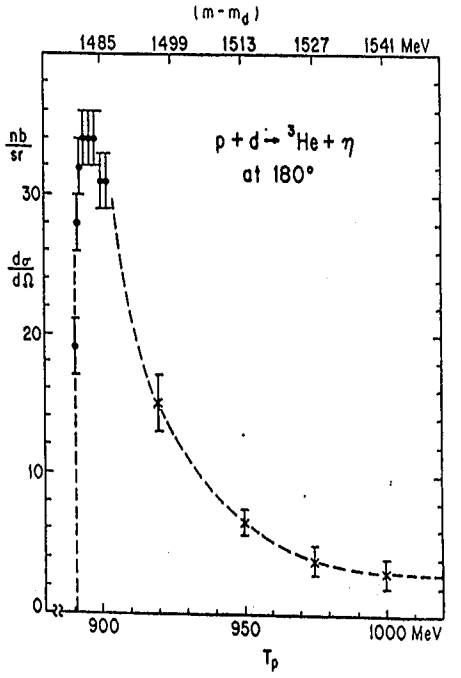

Fig. 7 $\sigma(pd \to {}^3He\,\eta)$ at 180°. Data: circles are Kessler et al. [5] (preliminary results), crosses are Berthet et al. [14].

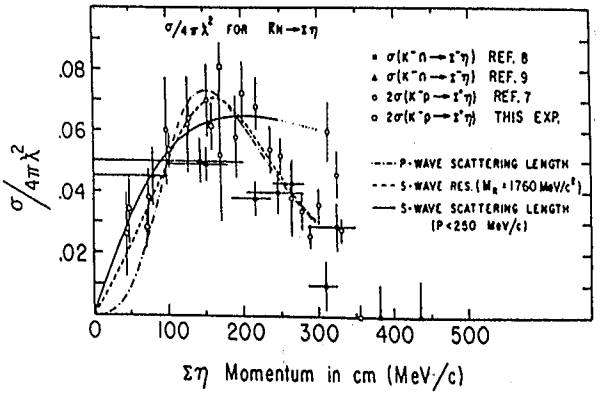

Fig. 6 $\sigma_t(K^-p \to \Sigma^\circ\eta)$ at low energy, Ref. [13].

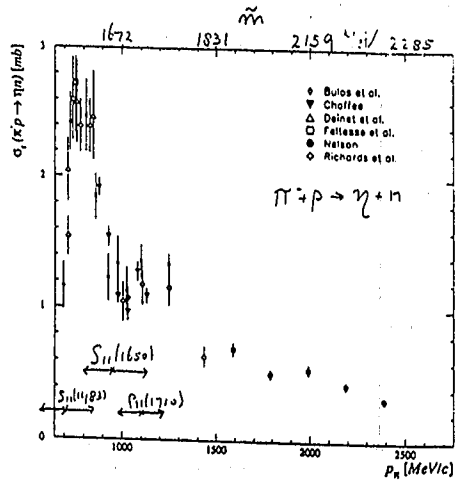

Fig. 8 $\sigma_t(\pi^-p \to \eta n)$ from Ref. [6].

STUDY OF COMPRESSIONAL MODES OF THE NUCLEON IN PROTON-NUCLEUS SCATTERING

H. Peter Morsch
Institut für Kernphysik, Forschungszentrum Jülich
D-5170 Jülich, Germany
and
Laboratoire National Saturne
F-91191 Gif-sur-Yvette Cedex, France

Abstract

Experiments are proposed to study selective excitation of negative parity baryon resonances in the nucleon in the scattering of 2 GeV protons from ^{4}He and ^{2}H targets. From these experiments spectroscopic information on important properties of the nucleon, related to the "squeezability", can be derived which is important for a crucial test of nucleon models.

The detailed experimental investigation of the properties of baryons is of large importance for the development of baryon models and thus for the understanding of the bound states of quantum chromodynamics. There are studies necessary using both hadronic and electromagnetic probes. As the electromagnetic interaction presents a vector probe acting on the baryon currents, it is well suited for the study of spin-isospin degrees of freedom as well as charge form factors. On the other side there are unique properties which can only be exploited by hadronic probes, e.g. related to the scalar structure of baryons. Studies of α-scattering have shown[1] that this probe presents a rather pure "scalar" probe (no excitation of spin and isospin degrees of freedom) which is well suited to study important aspects of the scalar structure of the nucleon, as for example the compressibility, which has been investigated in experiments at SATURNE[2]. The continuation of this program to study other important features of the nucleon, like the squeezability, appears to be a rather exciting possibility for the future. The present discussion is directly related to the earlier COSY-proposal[3] where most of the ideas are already presented.

More specifically, the dipole excitation of baryon resonances is discussed. This can be investigated in inelastic scattering from α-particles and deuterons using a proton beam of an energy in the order of 2 GeV. Apart from a small dipole excitation directly above the π^o threshold, we may expect a strong dipole excitation of the baryon resonances D_{13}(1520 MeV) and S_{11}(1535 MeV). If these resonances are excited in the scattering by α-particles, they correspond to dipole compression of the nucleon. Such effects are well known for nuclei[4,5], e.g. in the excitation of the isoscalar giant dipole resonance, the "squeezing mode" of the nucleus.

In the energy region of the D_{13} and S_{11} resonances there may be already substancial contributions from other baryon resonances, therefore it is not sufficient to perform inclusive scattering experiments. Good information should be obtained from the measurement of coincidences between protons emitted in forward direction and the recoiling target α-particle. For this measurement a magnetic divice in the form of a zero-degree spectrometer, as discussed by Sistemich et al.[6], would be well suited. Both proton and α-particle could be momentum analysed with good momentum resolution to obtain a good resolution in the reconstructed mass spectra and the missing mass of the third particle which is not detected. A simulation of the missing mass spectrum is shown in fig.1 assuming a momentum resolution of 1 % for the α-particle and 2 % for the proton. We see two well separated structures, one due to π^o production and the other due to 2π decay. If a sufficiently large magnetic gap exists for the measurement of the proton angular distribution, an unambiguous determination of the L-assignment of the excitation can be made.

The measured α and d scattering cross sections can be directly related to energy weighted sum rules and thus allow a quite model independent analysis of scalar dipole strength. It is interesting that in the constituent quark model essentially no scalar dipole strength at all exists in the D_{31} and S_{11} resonances in question. As already the P_{11}(1440 MeV) resonance is not described in this model, it would not be surprising if also for these excitations a disagreement with this model would be found. An observation of compressional dipole strength appears plausible due to the rather soft structure of the nucleon.

In the following some details of our estimates are given. If we limit ourself to the measurement of forward recoils in the angular range $\pm$ 10° where the largest cross sections are found, the proton will be emitted up to angles of about $\pm$ 50°. The vertical distribution goes up to about $\pm$ 30°. The energies of the α-particles are in the range of 30-200 MeV, the proton energy in the range of 1-1.6 GeV. If we want to use a magnetic device as discussed in ref.6 with an opening in horizontal and vertical direction of $\pm$ 10° we estimate a total efficiency of about 7-10 % in the proton detection. The differential cross section sections in the forward direction were estimated to be up to about 1 mb/sr. For an in-beam experiment at COSY with 10^{10} protons in the ring, a cycle of 2 microsec and a target thickness of 10^{14}

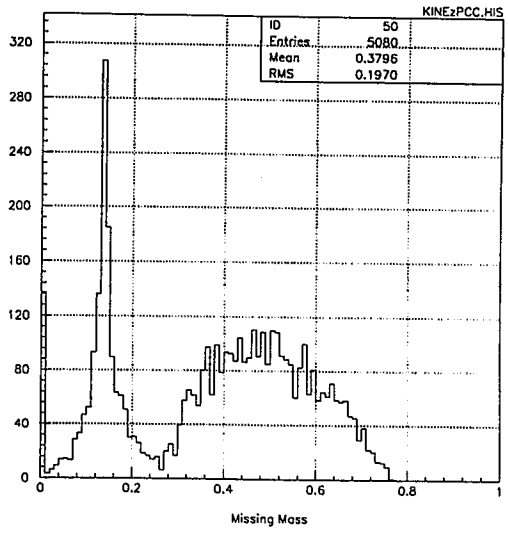

Figure 1: Simulation of the missing mass distribution for one and two pion events. The momentum resolution was 1 % for the recoiling α-particles and 2 % for the protons.

particles a simple estimate yields a coincidence rate of 500/sec. A more realistic estimate, taking into account an extended, heated beam and an efficiency cut in x-direction due to the fact, that the beam passes only a fraction of the target, gives a further reduction in the order of 15-20. Even with this we have a rather comfortable coincidence count rate in the order of 20-40 counts/sec.

The detection of the α-particles and the protons is straightforward. The α-recoils may be identified in a ΔE–E detection system with good energy resolution. For the protons we have to measure the position in either the focal plane of a spectrometer device or at two positions in a non-focussing magnet. Particle identification is obtained by a plastic detector wall.

In summary, estimates have been presented for experiments to study dipole compression effects in the nucleon. The results show that such experiments are possible in the COSY ring using a magnetic device suited for small angle studies. Such experiments can complement other exclusive experiments with an extracted beam from SATURNE and COSY. From these investigations, together with a study of the theoretical aspects of compression, we expect to get a better insight into the "scalar" properties of the nucleon.

REFERENCES:

1. H.P. Morsch, W. Spang, and P. Decowski, submitted to Phys. Lett.
2. H.P. Morsch et al., Phys. Rev. Lett. 69 (1992) 1336
3. COSY-proposal Nr.16: "Study of Selective Excitation of Baryon Resonances", 1989, Spokesman H.P. Morsch
4. H.P. Morsch, P. Decowski and W. Benenson, Phys. Lett. 101B (1981) 147
5. H.P. Morsch et al., Phys. Rev. Lett. 45 (1980) 337, and Phys. Rev. C28 (1983) 1947
6. K. Sistemich et al., contribution to this workshop

COHERENT PION PRODUCTION AT SMALL SCATTERING ANGLES

F. Osterfeld,[1] B. Körfgen,[1] P. Oltmanns,[1] and T. Udagawa[2]

[1] Institut für Kernphysik, KFA Jülich GmbH
W-5170 Jülich, Germany

[2] Department of Physics, University of Texas
Austin, Texas 78712

ABSTRACT

Charge exchange reactions to the Δ-resonance region reveal a systematic downward energy shift of the Δ peak position in nuclei as compared to the proton target. Part of this shift is caused by a coherent medium effect on the spin-longitudinal response function. The coherent effect is produced by the attractive π exchange interaction between Δ-hole states in the medium. This shift is consistent with pion total cross section data. No shift is observed in the spin-transverse channel. In order to obtain more evidence for the coherent mode, exclusive cross section data of the $^{12}C(p,n\pi^+)^{12}C(g.s.)$ reaction are analyzed. We observe a strong energy shift in the coherent pion production cross section. The coherent pions have a peak energy of E_π= 250 MeV and a strongly forward peaked angular distribution, i.e. most of the pions can be detected in the direction of the momentum transfer $\vec{q}$. High energy resolution ($\Delta E \leq 15$ MeV) is needed to separate the coherent pions from the quasi-free pπ events. This separation can be achieved at the 0° Facility being under construction at COSY.

1. Introduction

The (^{3}He,t) reactions at Laboratoire National Saturne in Paris[1,2,3] have shown that there is a substantial downward shift in the excitation energy of the Δ resonance in nuclei compared to the Δ excitation in the proton target. This phenomenon is also found to persist, although to a variable extent, at higher bombarding energies[3] and also prevails in the (p,n) reaction at E=800 MeV[4,5,6]. In fig. 1 we show an experimental zero-degree spectrum for the $p(p,n)\Delta^{++}$ reaction[5] at E=800 MeV in comparison with that of the $^{12}C(p,n)$ reaction[5,6]. The spectra are plotted versus the excitation energy ω_L in the laboratory system. For the proton target the Δ peak appears at $\omega_L \sim 365$ MeV while for the ^{12}C target the peak appears at $\omega_L \sim 295$ MeV. This shift of the Δ peak position has two different reasons: The first originates from the Fermi motion (binding) of the nucleons and of the Δ isobar in the nuclear mean field. This effect accounts for $\sim$ 40 MeV of the shift, leaving 30 MeV unexplained[7,8]. This latter part of the shift is thought to be due to a nuclear medium correlation effect on the spin-longitudinal response function[9,10,11,12,13]. In particular, recent calculations of Delorme and Guichon[11] and Udagawa *et al.*[12] performed for finite nuclei consistently show that this second part of the shift is caused by the energy (ω)-dependent π-exchange interaction in the nuclear medium. The π-exchange

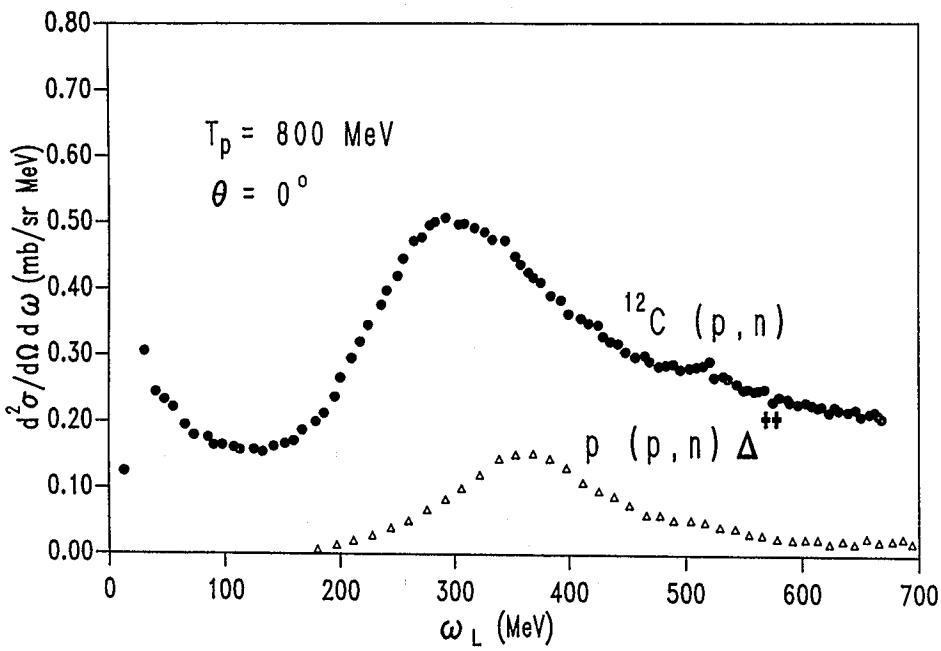

Figure 1. The experimental zero degree spectra for the $^{12}C(p,n)$ reaction (dots) and the $p(p,n)\Delta^{++}$ reaction (triangles) at $T_p = 800$ MeV incident energy. The data are taken from D. A. Lind[6].

provides a strongly attractive interaction between Δ-particle nucleon-hole (ΔN^{-1}) states in the spin-longitudinal ($\vec{S} \cdot \vec{q}\ \vec{T}$) channel leading to a lowering of the Δ mass in the nucleus. Other effects contributing to the shift come from Δ conversion processes, such as $\Delta + N \rightarrow N + N$[11,12,14] and from projectile excitation[15,16].

The inclusive charge exchange cross sections contain information on both the spin-transverse (TR) and the spin-longitudinal (LO) nuclear response functions. Experimentally the two responses can be separated by measuring photon-nucleus and pion-nucleus scattering. The photon is a purely spin-transverse probe while the pion is a purely spin-longitudinal probe. In figs. 2a and 2b total cross sections for π ^{12}C- and γ ^{12}C-scattering[17,18] in the Δ resonance region are shown[19]. The data are compared to the free cross sections ($A \times \bar{\sigma}_{\gamma N}$) and ($A \times \bar{\sigma}_{\pi N}$), respectively, where A is the nuclear mass number and $\bar{\sigma} = 1/2\,(\sigma_p + \sigma_n)$. In case of pion scattering a large energy shift is observed between the free Δ resonance and the Δ in the nucleus, while such a shift does not occur for photon scattering. This is so since the π-exchange potential couples only weakly to the TR channel. Since the (p,n) reaction is a mixed LO - TR probe, the data of this reaction consist of two parts of opposite behaviour: the LO cross section which is shifted in energy and the TR cross section which is not shifted. In this paper we shall show that the coherent pion decay, as measured in the $^{12}C(p,n\pi^+)^{12}C(g.s.)$ reaction, can be a very sensitive probe on the LO response function. To demonstrate this we make use of a microscopic model which we used previously[12] for the description of Δ excitations in the (p,n) and $(^3He,t)$ inclusive reactions.

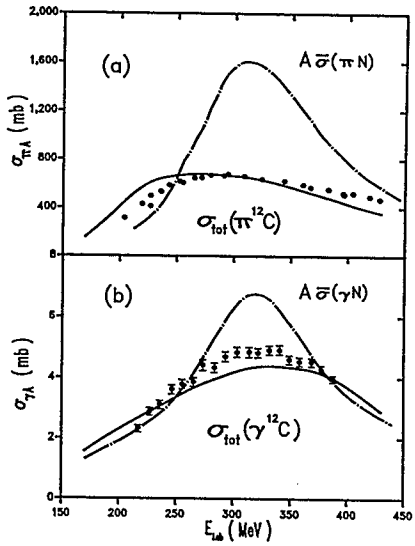

Figure 2. The photon- and pion-nucleus total cross sections for ^{12}C. The data are taken from A. S. Carroll *et al.*[17] and H. Rost[18]. The dash-dotted curve in fig. 2a represents the incoherent sum of pion-nucleon total cross sections ($A \times \bar{\sigma}_{\pi N}$), and the dash-dotted curve in Fig. 2b represents the incoherent sum of photon-nucleon cross sections ($A \times \bar{\sigma}_{\gamma N}$), respectively. The solid curves represent microscopic calculations for the total cross sections[20].

2. The Model

2.1 Inclusive Cross Sections

Our approach is based on the isobar-hole model which has been successfully used in the description of pion-nucleus[21,22] and photon-nucleus[23] scattering. In the isobar-hole model the Δ is assumed to move in a complex one-body potential. In addition, the Δ interacts with the residual nucleus B via a two-body interaction $V_{N\Delta,N\Delta}$. The wave function $\mid \psi\rangle$ describing the intermediate $(B+\Delta)$ system is then given by[12]

$$\mid \psi\rangle = G \mid \rho\rangle = \frac{1}{\omega + i\Gamma_\Delta/2 - H_B - T_\Delta - U_\Delta - V_{N\Delta,N\Delta}} \mid \rho\rangle \qquad (1)$$

where $\mid \rho\rangle$ is the doorway state excited initially by the reaction. This doorway state is characteristic for each reaction and is different for pion-, photon-, and charge exchange scattering. In eq. (1) the Green's function G describes the propagation of the $(B+\Delta)$ system. $\Gamma_\Delta(\omega)$ is the energy dependent free decay width of the Δ, H_B is the Hamiltonian of nucleus B, T_Δ and U_Δ are the kinetic energy operator and the Δ-nucleus one-body potential, respectively, and $V_{N\Delta,N\Delta}$ is the residual interaction describing the ΔN^{-1} correlations. From eq. (1) the inclusive cross section for the charge exchange reaction $A + a \rightarrow (B+\Delta) + b$ can be calculated as[12]

$$\frac{d^2\sigma}{dE_b d\Omega_b} = \frac{E_a E_b E_A E_{B+\Delta}}{(2\pi\hbar^2 c^2\sqrt{s})^2} \frac{p_b}{p_a} \frac{1}{\pi} Im(-\langle \rho \mid \psi\rangle), \qquad (2)$$

where E_i is the total energy of particle i ($i = A, B+\Delta, a, b$), p_a (p_b) is the momentum of particle a (b), and $\sqrt{s}$ is the total energy of all particles in the center of momentum system.

2.2 Exclusive Cross Section for Coherent Pion Decay

Using the wave function $\mid \psi\rangle$ of eq. (1) we can also calculate the transition amplitude T_{fi} for the coherent pion decay process $A+a \rightarrow (B+\Delta)+b \rightarrow A+\pi+b$. This amplitude is given by

$$T_{fi} = \sqrt{2E_{A'}2E_b}\,\langle \varphi_A, \phi(\vec{p}_\pi) \mid \frac{f_{\pi N\Delta}}{m_\pi} S \cdot \vec{\kappa}_\pi F(\kappa_\pi^2) T_\mu \mid \psi\rangle \sqrt{2E_A 2E_a}. \tag{3}$$

It describes the de-excitation of the $(B+\Delta)$ system to the target ground state $\mid \varphi_A\rangle$ by emission of a coherent pion of four-momentum $(E_\pi, \vec{p}_\pi)$. In eq. (3) the $\pi N\Delta$ coupling is expressed in terms of the variables of the Δ rest frame (involving the spin- $(\vec{S})$ and isospin- $(\vec{T})$ transition operators and the relative pion-nucleon momentum $\vec{\kappa}_\pi$); $F(\kappa_\pi^2)$ is the $\pi N\Delta$ form factor. Note that the pion wave function $\phi(\vec{p}_\pi)$ in eq. (3) is a plane wave. In spite of this fact, the pion distortion in the final channel is taken into account via the π-exchange interaction in $V_{N\Delta,N\Delta}$ which is included in eq. (1). The threefold differential cross section for the $A(p, n\pi^+)A(g.s.)$ reaction is then given by

$$\frac{d^3\sigma}{dE_b d\Omega_b d\Omega_\pi} = \frac{1}{(2\pi)^5 16\sqrt{\lambda(s, M_a^2, M_A^2)}} \frac{p_b p_\pi}{\mid (E_A+\omega) + \frac{E_\pi}{p_\pi}(p_b \cos\theta_{b\pi} - p_a \cos\theta_{a\pi}) \mid} \times \frac{M_a}{E_a}\frac{M_b}{E_b} \overline{\sum} \mid T_{fi} \mid^2 \tag{4}$$

where M_i stands for the mass of particle i ($i = A, B, a, b, \pi$) and $\overline{\Sigma}$ denotes the average over initial spin orientations and the sum over final spin orientations of both the projectile and target. The full three body kinematics in the final channel is included, i.e. $(E_a, \vec{p}_a) + (E_A, \vec{p}_A) = (E_b, \vec{p}_b) + (E_\pi, \vec{p}_\pi) + (E_{A'}, \vec{p}_{A'})$. The prime on A indicates that the nucleus A recoils in the π decay.

2.3 The $t_{NN,N\Delta}$ Transition Operator

In case of the charge exchange reaction A(a,b)B the doorway state entering eq. (1) is explicitly given by

$$\mid \rho\rangle = (\chi_b^{(-)}\varphi_b \mid t_{NN,N\Delta} \mid \chi_a^{(+)}\varphi_a\varphi_A\rangle \ , \tag{5}$$

where $\chi_a^{(+)}$ and $\chi_b^{(-)}$ are the projectile distorted wave functions in the incident and exit channel, respectively, φ_a and φ_b are the intrinsic wave functions of a and b, and φ_A is the initial target wave function. The effective $NN \rightarrow N\Delta$ transition operator is denoted by $t_{NN,N\Delta}$. The following simple ansatz for $t_{NN,N\Delta}$ (in momentum representation) was made[12]

$$t_{NN,N\Delta} = t'_{N\Delta} J_{\pi N\Delta} \left(\frac{\Lambda_\pi'^2 - m_\pi^2}{\Lambda_\pi'^2 - t}\right)^2 \left[(\vec{\sigma}_1 \cdot \hat{q})(\vec{S}_2^\dagger \cdot \hat{q}) + (\vec{\sigma}_1 \times \hat{q}) \cdot (\vec{S}_2^\dagger \times \hat{q})\right] \ \vec{\tau}_1 \cdot \vec{T}_2^\dagger \tag{6}$$

with $J_{\pi N\Delta} = 4\pi\hbar c f_{\pi NN} f_{\pi N\Delta}/m_\pi^2 \approx 800$ MeV fm^3, $t'_{N\Delta} = 0.60$, and $\Lambda'_\pi = 650$ MeV. Despite of its simple structure, the $t_{NN,N\Delta}$ operator of eq. (6) allows for an explanation

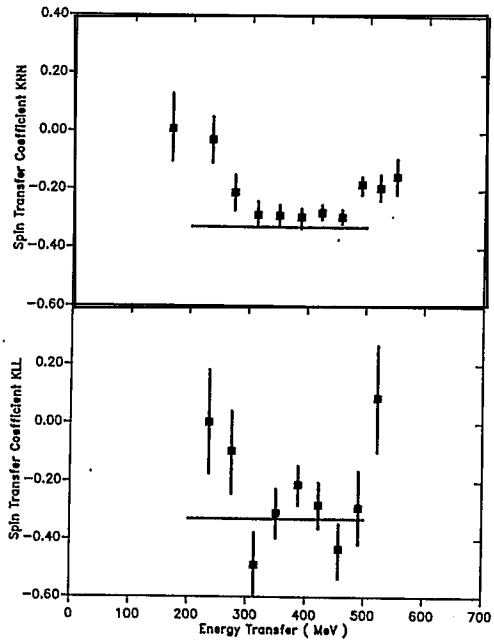

Figure 3. Calculated spin transfer coefficients K_{LL} and K_{NN} for the $p(p,n)\Delta^{++}$ reaction at $T_p = 800$ MeV in comparison with the experimental data[24].

of the $p(\vec{p},\vec{n})\Delta^{++}$ data[24] and the $p(\vec{d},2p)\Delta^0$ data[25]. This concerns not only the cross section[12,26], but also the spin observables[26,27,28]. In fig. 3 we compare our calculated spin transfer coefficients K_{NN} and K_{LL} for the $p(\vec{p},\vec{n})\Delta^{++}$ reaction with the data[24]. It is interesting to note that the predicted values of $K_{NN}=K_{LL} = -1/3$ simply come from the fact that the strengths of the LO and TR terms in $t_{NN,N\Delta}$ are equal. This ratio of LO/TR also explains the observed tensor analyzing power data of the $p(\vec{d},2p)\Delta^0$ reaction[27]. In addition, these data require that $t_{NN,N\Delta}$ is nearly constant in the $(\omega,\vec{q})$-range relevant to the Δ-resonance region[26]. Both conditions are satisfied by the $t_{NN,N\Delta}$ of eq. (6). The spin observables do not fix the absolute magnitude of $t'_{N\Delta}$. This value is determined from the basic $p(p,n)\Delta^{++}$ cross section data[6,12].

2.4 The Δ-Nucleus Interaction

The Δ is assumed to move in a complex one-body potential. This potential is taken as a complex Woods-Saxon potential, $U_\Delta = V_\Delta + iW_\Delta$, with radius parameter $R = 1.1A^{1/3}$ fm and diffuseness $a = 0.53$ fm. The depths for the real and imaginary potential are $V_\Delta = -35$ MeV and $W_\Delta = -40$ MeV, respectively. Note that V_Δ is assumed to be the sum of the Δ-nucleus single particle potential (depth=-65 MeV) and of the real part of the Δ-spreading potential (strength=+30 MeV). W_Δ represents the imaginary part of the spreading potential[22]. The spreading potential accounts in a phenomenological way for the increase of the Δ width in nuclei due to decay channels such as $\Delta N \to NN$.

The ΔN^{-1} interaction, $V_{N\Delta,N\Delta}$, is assumed to consist of the π and ρ exchange po-

tentials with an additional short range interaction. In the momentum representation, $V_{N\Delta,N\Delta}$ may be given as a sum of LO and TR components

$$V_{N\Delta,N\Delta} = [V^L_{N\Delta,N\Delta}(\vec{S}_1 \cdot \hat{q})(\vec{S}_2^{\dagger} \cdot \hat{q}) + V^T_{N\Delta,N\Delta}(\vec{S}_1 \times \hat{q}) \cdot (\vec{S}_2^{\dagger} \times \hat{q})]\vec{T}_1 \cdot \vec{T}_2^{\dagger}, \tag{7}$$

where

$$\begin{aligned} V^L_{N\Delta,N\Delta}(\omega,q) &= 4\pi\hbar c \frac{f_\pi^2(t)}{m_\pi^2}\left[g'_{\Delta\Delta} + \frac{q^2}{\omega^2 - q^2 - m_\pi^2 + i\epsilon}\right] \\ V^T_{N\Delta,N\Delta}(\omega,q) &= 4\pi\hbar c \frac{f_\pi^2(t)}{m_\pi^2}\left[g'_{\Delta\Delta} + \frac{m_\pi^2}{f_\pi^2(t)}\frac{f_\rho^2(t)}{m_\rho^2}\frac{q^2}{\omega^2 - q^2 - m_\rho^2 + i\epsilon}\right] \end{aligned} \tag{8}$$

In eq.(8), the $f_i(t = \omega^2 - \vec{q}^{\,2})$ are the meson-baryon vertex form factors which we assume to be $f_i(t) = f_{iN\Delta}\ (\Lambda_i^2 - m_i^2)/(\Lambda_i^2 - t)$ $(i = \pi,\ \rho)$, and m_i and Λ_i are the mass and cut-off mass of the meson i, respectively. The various parameters are fixed as follows: $f^2_{\pi N\Delta} = 0.324, f^2_{\rho N\Delta} = 16.63, m_\pi = 0.14$ GeV, $m_\rho = 0.77$ GeV, $\Lambda_\pi = 1.20$ GeV, and $\Lambda_\rho = 2$ GeV. The Landau-Migdal parameter $g'_{\Delta\Delta}$ describes the short range correlations for $\Delta N^{-1} \to \Delta N^{-1}$ transitions. In the present calculations, we use the minimal $g'_{\Delta\Delta}$ that cancels out the δ-function like piece of the π-exchange potential. Then the Landau-Migdal parameter $g'_{\Delta\Delta} \approx 0.33$ (in units of $J_{\pi\Delta\Delta} = 4\pi\hbar c f_{\pi N\Delta} f_{\pi N\Delta}/m_\pi^2 \approx 1600$ MeV fm^3). Note that this parameter depends on the choice of U_Δ. Its accurate value is finally fixed from the requirement to reproduce the peak position of the Δ resonance in the medium.

The LO interaction $V^L_{N\Delta,N\Delta}(\omega,q)$ has a singularity at $q = q_{pole} = \sqrt{\omega_{CM}^2 - m_\pi^2}$ in case that the excitation energy ω_{CM} (in the center of mass system) is larger than m_π, whereas the ρ-exchange potential in the TR channel has no singularity in the energy region of interest. The LO interaction is schematically plotted in figs. 5a and 5b for fixed energy transfer $\omega_{CM} = 215$ MeV (solid curves). Note that $V^L_{N\Delta,N\Delta}$ is repulsive for $q < q_{pole}$, but attractive for $q > q_{pole}$. We shall discuss the effect of the pole on the energy shift in more detail in section 3.2.

3. Results and Discussions

3.1 Pion and Photon Total Cross Sections

Using the isobar-hole model we first analyzed the pion and photon total cross sections in the Δ resonance region, as shown in figs. 2a und 2b. The isobar-hole calculation for the total pion-nucleus cross section describes the data in fig. 2a rather well. In particular, it reproduces the shift in the peak position of the total pion cross section. This shift can only be obtained if the attractive π-exchange potential is included in the residual interaction. The total photon-nucleus cross section in fig. 2b is also described well. The theoretical curve indicates that the $V_{N\Delta,N\Delta}$ is somewhat too repulsive in the spin-transverse channel since the peak position of the resonance appears at too high an excitation energy. This is an effect of the repulsive, short range part of $V_{N\Delta,N\Delta}$, which, on the one hand, is needed to compensate for the too attractive π-exchange potential in the LO channel. We remark that in order to reproduce the experimental total photon-nucleus cross section data we included besides the pure 3-3 resonance excitation a phenomenological non 3-3 background which is almost constant in the Δ resonance region[20].

3.2 Inclusive (p,n) Cross Sections

In fig. 4a we show the previously[12] calculated inclusive cross section for the 0-degree spectrum of the ^{12}C(p,n) reaction at 800 MeV incident energy in comparison to the experimental data[6]. The theoretical cross sections are calculated within the distorted wave impulse approximation (DWIA) using eq. (2). The calculation underestimates the data by a factor of $N = 1.2$. This is due to the fact that the Δ-resonance is located on top of a large continuum (background). The background is the result of various processes the importance of which varies with excitation energy: On the high energy side of the resonance ($\omega_L \geq 350$ MeV) the background is mainly produced by projectile excitation where the proton is excited to a Δ^+ which subsequently decays into a $n + \pi^+$. The cross section on the low energy side may be produced by nucleon-knockout, by multi-step processes, and by projectile excitation[29].

In fig. 4a we also show the correlated LO and TR cross sections separately. The peak position of the LO spectrum is lowered by ~ 60 MeV in energy in comparison with the TR spectrum. This is due to the attractive π-exchange interaction in the LO channel[11,12,13]. To explain this effect in more detail, we show in fig. 5 the momentum (q) dependence of the ΔN^{-1} residual interaction in the LO channel (full curve), along with the square of a typical ($J^\pi = 1^+$) ΔN^{-1} transition density (dashed curve). The square of the transition

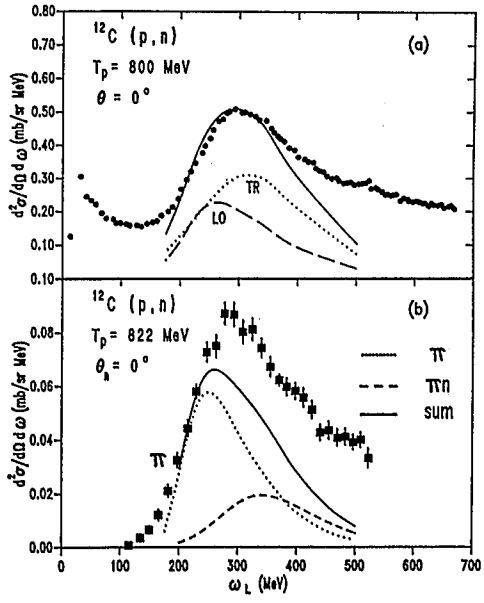

Figure 4. Inclusive and exclusive $^{12}C(p,n)$ cross sections. (a) Calculated zero degree neutron spectra for the ^{12}C(p,n) reaction at $T_p = 800$ MeV in comparison with the experimental data of D. A. Lind *et al.*[6]. The spin-longitudinal and spin-transverse cross sections are shown separately. (b) Pion coincidence spectrum for the $^{12}C(p,n)$ reaction at $T_p = 822$ MeV. The data are taken from J. Chiba *et al.*[31]. The data are compared to the calculated zero degree coherent pion production cross section (dotted curve) and to the π^+n coincidence (dashed curve) cross section[30]. The sum of both cross cross sections is represented by the full curve.

density is defined by

$$M_L(q) = \int d\hat{q} < \widetilde{\psi_J} \mid \exp(-i\vec{q}\cdot\vec{r})\, \vec{S}^{\dagger}\cdot\hat{q}\, T^{\dagger}_{\mu=-1} \mid 0 > \\ < 0 \mid -T_{\mu=+1}\, \vec{S}\cdot\hat{q}\, \exp(i\vec{q}\cdot\vec{r}) \mid \psi_J > \qquad (9)$$

where ψ_J is the ΔN^{-1} wave function for the multipolarity J^{π}. $< \widetilde{\psi_J} \mid$ is the conjugate state of $\mid \psi_J >$. The square of the transition density enters the calculation of the energy shift as

$$\Delta E_J \equiv \langle \psi_J \mid V_{N\Delta,N\Delta} \mid \psi_J \rangle = \frac{1}{(2\pi)^3} \int dq\, q^2 (V^L_{N\Delta,N\Delta}\, M_L(q) + V^T_{N\Delta,N\Delta}\, M_T(q)\,). \qquad (10)$$

Here the energy shift has been split into LO and TR components. The expression for $M_T(q)$ is obtained from $M_L(q)$ by replacing $(\vec{S}\cdot\hat{q})$ with $(\vec{S}\times\hat{q})$. From fig. 5 one observes that by folding $V^L_{N\Delta,N\Delta}$ with $q^2 M_L(q)$ a net attractive energy shift is obtained. In the present case of a $J^{\pi} = 1^+$ state, the attraction is larger for the (p,n) charge exchange reaction (fig. 5a) than for pion scattering (fig. 5b) since in the latter case a relatively large cancellation takes place between the contributions to ΔE_J in eq. (10) coming from the left- and right-hand side of the pole. The transition density for $^{12}C(p,n)$ scattering peaks at larger momenta than that for $\pi\,^{12}C$ scattering since in the former case the pion propagating through the nucleus is a *virtual* pion while in the latter case it is a *real* pion. Therefore in pion-nucleus scattering the momentum distribution of the pion wave function should peak near the pion pole, as can be seen in fig. 5b.

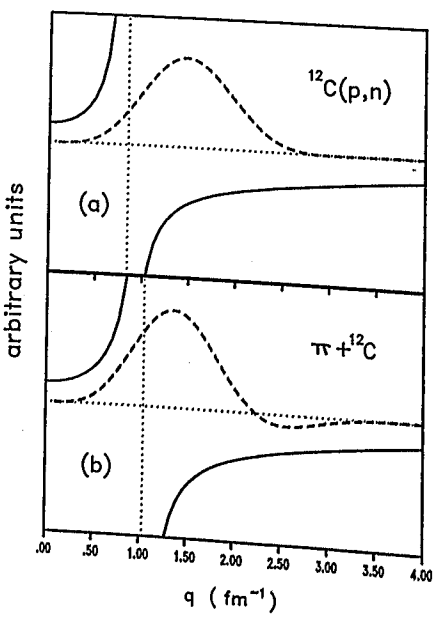

Figure 5. The ΔN^{-1} residual interaction (full curves) and the square of the transition density ($q^2 M_L(q)$) for the $J^{\pi} = 1^+, L = 0$ state (dashed curves) in the spin longitudinal channel as function of momentum transfer q. In (a) the square of the transition density for the $^{12}C(p,n)$ reaction is shown and in (b) the corresponding transition density for the pion scattering process is plotted. Both transition densities are calculated at the center of mass energy $\omega_{CM} = 215$ MeV.

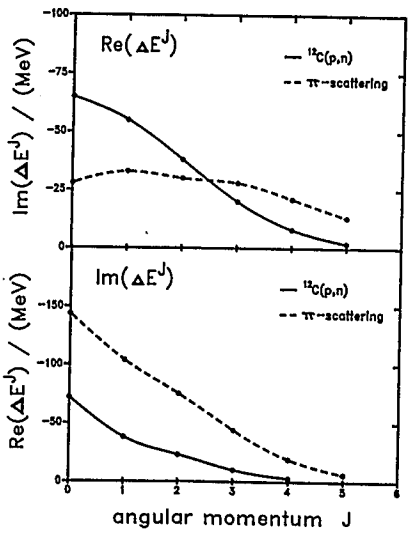

Figure 6. The real and imaginary parts of the energy shift ΔE_J as function of the pion nucleus total angular momentum J.

The different behaviour of real and virtual pions in the medium shows up in the energy shift ΔE_J. To illustrate this, we present in fig. 6 the real and imaginary parts of ΔE_J calculated for both virtual (full lines) and real (broken lines) π absorption as function of the pion nucleus total angular momentum J. The imaginary part ΔE_J^{Im} comes from the pole term in $V^L_{N\Delta,N\Delta}$ and describes the coherent π production events. Note that the imaginary part is significantly smaller for virtual π absorption as compared to real π absorption. This is opposite for the real part, where ΔE_J^{Re} is larger for ^{12}C(p,n) than for real π absorption at $J \leq 2$. Thus the (p,n) data provide different information on the π correlation effect than π nucleus scattering data.

3.3 Spin Observables

The relative shift between the LO and TR responses can be experimentally tested by measuring the spin observables. In fig. 7 we show the calculated spin transfer coefficients K_{NN} and K_{LL} for the $^{12}C(\vec{p},\vec{n})$ - reaction at $E = 800$ MeV incident energy. The calculations were performed in two different ways, namely once by inclusion of the ΔN^{-1} residual interaction (full curve) and once without its inclusion (dashed curve). One can notice that in the case where no $V_{N\Delta,N\Delta}$ is included, the spin transfer coefficients K_{LL} and K_{NN} are unchanged as compared to the corresponding observables in the $p(\vec{p},\vec{n})\Delta^{++}$ reaction (fig. 3). The inclusion of $V_{N\Delta,N\Delta}$, on the other hand, leads to a significant change in the values of K_{NN} and K_{LL}, in particular in the excitation energy region near $\omega_L = 250$ MeV. The enhancement of the LO response in this excitation energy region leads to higher values for K_{LL} and to lower values for K_{NN}, relative to the uncorrelated response. The opposite effect can be seen in the high ω region. Presently the corresponding spin transfer measurements are performed at LAMPF.

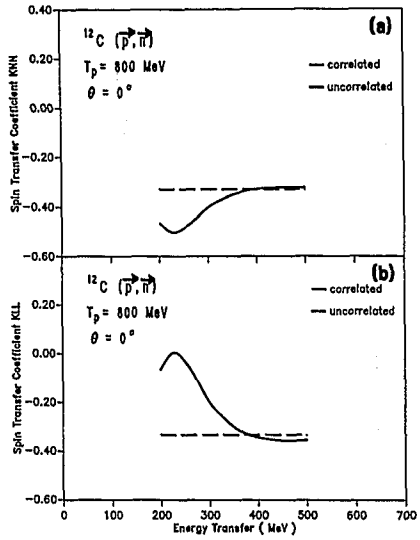

Figure 7. Calculated spin transfer coefficients (a) K_{NN} and (b) K_{LL}. The theoretical results with and without inclusion of $V_{N\Delta,N\Delta}$ are shown by the full and dashed curves, respectively.

It should be remarked at this stage that with a similar motivation a measurement of the tensor analyzing power has been made for the ^{12}C($\vec{d}$,2p) reaction at E_{lab}=2 GeV at SATURNE[25]. We have recently analyzed the data[27], finding that the data at extreme forward angles (0° data particularly) were not reproduced very well, particularly not in the excitation energy region where the pion correlations play an important role, i.e. at lower excitation energies. We believe that this problem may be due to the fact that in this excitation energy region other reaction mechanisms, e.g. one- and two-step nucleon-knockout and various other two-step mechanisms, may play an important role. The fact that both the tensor analyzing power data and the inclusive cross section data consistently defy explanation seems to support this view. Just as in the $(\vec{d}, 2p)$ reaction, contributions from different mechanisms other than one-step Δ excitation might also contribute to the (p,n) reaction and thus distort the experimental spin transfer coefficients.

3.4 Coherent Pion Decay

In fig. 4b we compare the $^{12}C(p, n\pi^+)^{12}C(g.s.)$ coincidence cross section (dotted curve) calculated[30] by means of eq. (4) with the measured data of Chiba *et al.*[31]. The theoretical coincidence cross section peaks at an excitation energy of ω_L =250 MeV. This is in line with the peak position of the LO cross section in fig. 4a, and with a previous calculation[14]. The absolute magnitude of the calculated cross section has not been readjusted, i.e no normalization factor N is included. Thus it is important that the coherent pion production cross section describes the slope of the data on the low-energy side correctly. In addition, the calculation shows that a large fraction of the experimentally observed pions are coherent pions. The cross section which is not described by the coherent pion production can arise from other processes, such as πn events or πp events where the proton has not been measured due to the acceptance of the detector (The detector FANCY

at KEK accepts charged particles in the angular range $15° \leq \theta \leq 141°$ [31]). Other pions can come from projectile excitation events, i. e. where the projectile is excited to a Δ^+ which decays into $n+\pi^+$. In fig. 4b we also show the theoretical cross section contribution from target $\pi^+ n$ events (dashed curve). This cross section has its peak at much higher excitation energy ($\omega_L \sim 350$ MeV) than the coherent pion production cross section. This added contribution leads to an improvement in the description of the data (full curve). If also the other two contributions, i. e. the $\pi^+ p$ - events (with the proton missing the detector) and the projectile excitation events, were taken into account correctly, then the data should be described reasonably well.

In fig. 8 we show the angular distribution of the pion coincidence cross section, separated for LO and TR excitation as function of the scattering angle θ_π between $\hat{q}$ and $\hat{k}_\pi$. The angular distribution resulting from the TR excitation of the nucleus has a characteristic shape with a minimum at $\theta_\pi = 0°$ and a maximum at $\theta_\pi \approx 30°$. This is very similar to the shape of the angular distributions in coherent pion-photoproduction (fig. 10). The reason for this is that the spin structure of the excitation $(\vec{S}^\dagger \times \vec{q})$ and de-excitation $(\vec{S} \cdot \vec{k}_\pi)$ operators occuring in pion-photoproduction is exactly the same as that of the TR excitation of the nucleus by (p,n) reactions. The product of excitation and de-excitation operators is proportional to $\mid \vec{q} \times \vec{k}_\pi \mid = q k_\pi \sin\theta_\pi$ which vanishes for θ_π=0° and peaks for θ_π=90°. However, an additional factor comes from the target transition matrix element in eq. (3). This matrix element becomes the larger, the smaller the scattering angle θ_π. This is due to the dependence of the matrix element on the recoil momentum $\mid \vec{q} - \vec{p}_\pi \mid$ transferred to A' in the coherent π decay process. This recoil momentum is smallest for $\vec{q}$ parallel $\vec{p}_\pi$, making the matrix element largest for θ_π=0°. Thus the observed TR angular distribution with its peak at $\theta_\pi = 30°$ is the result of two competing effects, one coming from the spin structure of the transition operators and the other coming from the target transition matrix element.

The LO angular distribution in fig. 8 is very strongly forward peaked, i.e. most of the pions can be detected in the direction of the momentum transfer $\vec{q}$. This shows that there is an intimate relation between LO coherent pion production on the one hand and elastic pion-nucleus scattering on the other hand. In the former case an initially off-mass shell pion is converted into an on-mass shell pion by the multiple scattering in the nucleus. This conversion process is possible since the nucleus as a whole can pick up the recoil momentum needed to lift the pion on its mass shell. In the $^{12}C(p,n\pi^+)^{12}C(g.s.)$ reaction the recoil momentum amounts to $\Delta q \approx 0.5$ fm^{-1} at $\omega_L = 250$ MeV corresponding to a recoil energy of $\Delta\omega_L \sim 0.5$ MeV for the ^{12}C nucleus.

In fig. 9 we compare the calculated angular distribution of the (^{3}He,tπ^+) reaction with count rates of this reaction taken at LNS[32]. In these data only events with triton angles larger than 2° and inside an energy window of 50 MeV around the ground state were considered. Therefore, these data can only very carefully be compared with our calculation. For the sake of comparison, we have normalized the overall magnitude of the experimental count rates, so that they agree with the calculated cross section at $\cos\theta_{t\pi} = 1$. We can see that these experimental data are in good agreement with the calculation for forward angles up to $\cos\theta_{t\pi} = 0.8$. The fact that there is only a mismatch for higher angles $\theta_{t\pi}$ is an indication that the experimental data considered in this cut consist to a great extent of coherent pions. The deviation at higher angles is, however, possibly due to incoherent pions, especially those from $p\pi^+$ and $n\pi^+$ events.

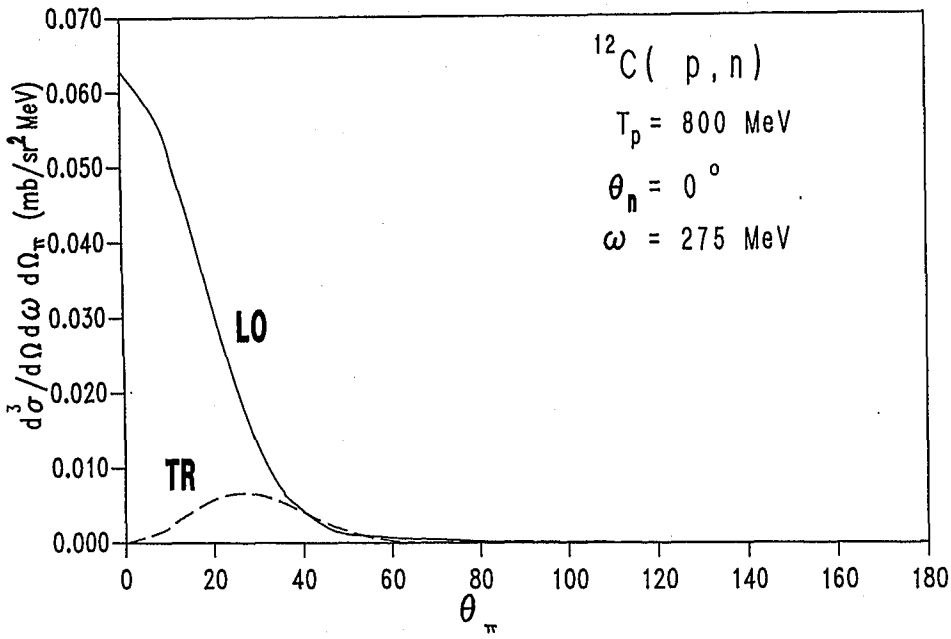

Figure 8. Calculated angular distribution for the coherent pion production process, separated for spin-longitudinal (full curve) and spin-transverse (dashed curve) excitation.

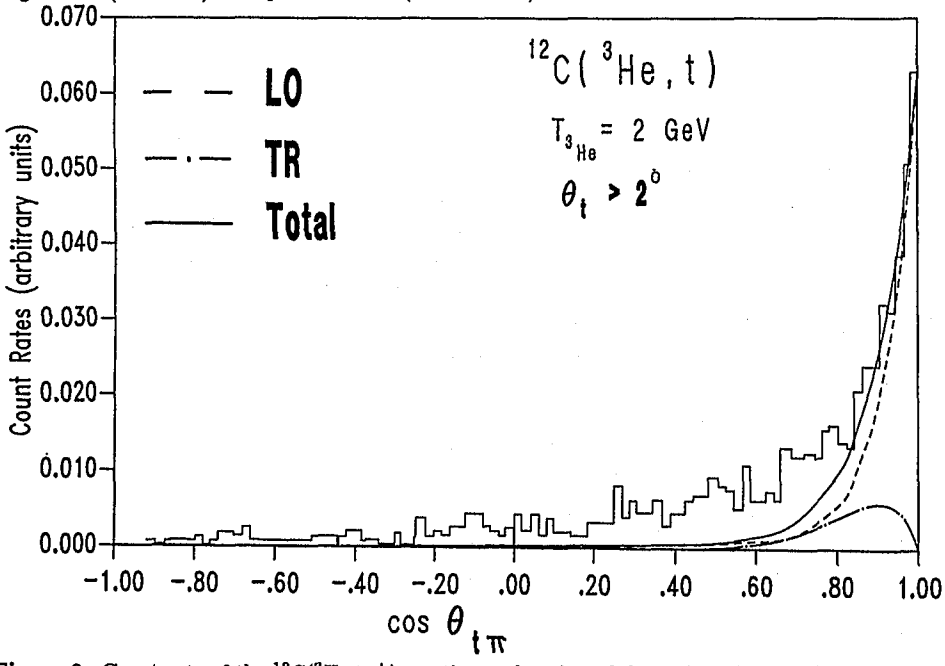

Figure 9. Count rate of the $^{12}C(^3He,t\pi^+)$ reaction as function of the cosine of $\theta_{t\pi}$, which is the angle between the outgoing π^+ and t. The data are taken from M. Roy-Stephan[32]. The theoretical curves are explained in the text.

In order to make an estimate of count rates for the coherent pion production cross section to be measured at the 0° FACILITY at COSY, we have calculated the integrated cross section for the $^{12}C(p,n\pi^+)^{12}C(g.s.)$ reaction at $T_p = 800$ MeV. The integration has been performed for an energy transfer between 250 and 300 MeV and for pion and neutron angles between 0° and maximum angles as listed in table 1. We find that the integrated cross sections are in the μbarn region if we allow for neutron angles up to 3°, whereas they are in the 0.1 μbarn region, if we only allow for neutron angles up to 1°. The various estimated cross sections are given in table 1.

Table 1. Theoretical estimates of coherent pion production cross sections integrated over various neutron and pion scattering angles

	σ [μb]	
	$\theta_\pi \leq 8°$	$\theta_\pi \leq 5°$
$\theta_n \leq 7°$	6.0	2.5
$\theta_n \leq 5°$	4.0	1.5
$\theta_n \leq 3°$	1.5	0.7
$\theta_n \leq 1°$	0.2	0.1

In fig. 10 we compare the calculated differential pion-photoproduction cross section at two different incident photon momenta with the data[33]. The full and dashed curves represent calculations with and without inclusion of the residual interaction $V_{N\Delta,N\Delta}$. One

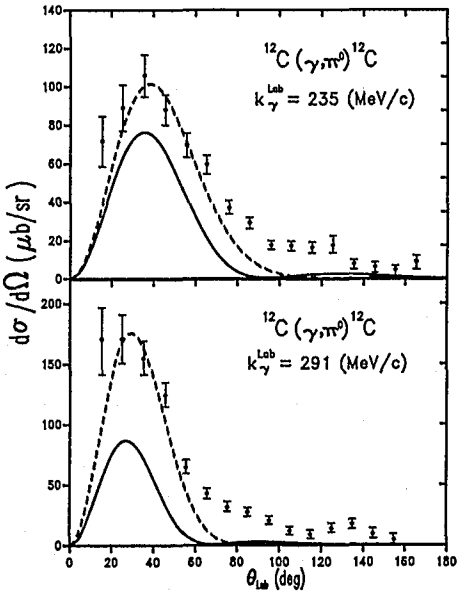

Figure 10. Differential cross section for coherent π^0-photoproduction on ^{12}C at $E_\gamma = 235$ MeV and $E_\gamma = 291$ MeV. The data are taken from J. Arends *et al.*[33]. The full curves show the theoretical results with inclusion of $V_{N\Delta,N\Delta}$, the dashed curves without inclusion of $V_{N\Delta,N\Delta}$, respectively.

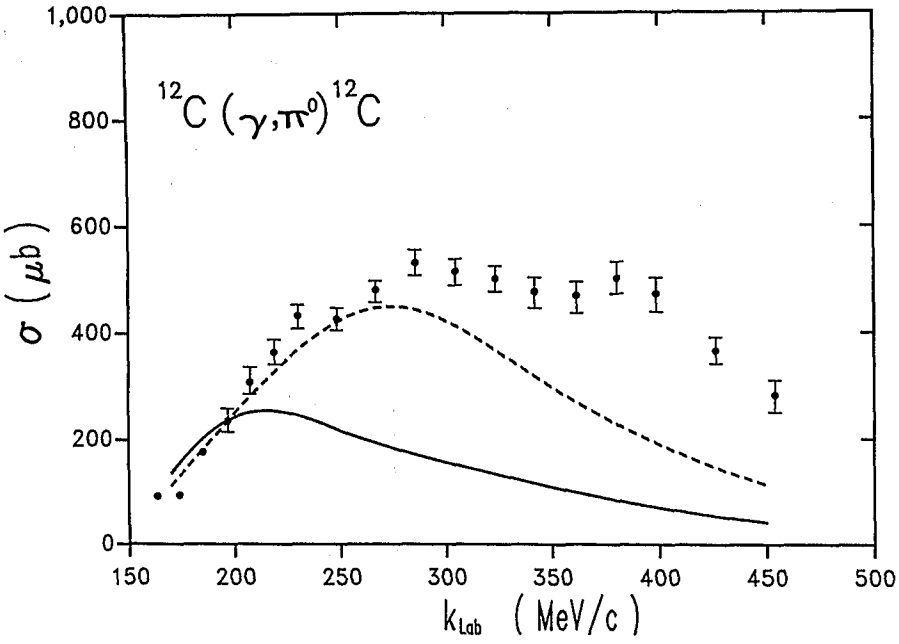

Figure 11. Total cross section for coherent π^0-production on ^{12}C from J. Arends *et al.*[33] in comparison with the theoretical results. The calculations with and without inclusion of $V_{N\Delta,N\Delta}$ are shown by the full and dashed curves, respectively.

can recognize that both calculations describe the shape of the experimental angular distributions rather well. The calculations with inclusion of $V_{N\Delta,N\Delta}$, however, underestimate the absolute magnitude of the cross sections by a factor of $\sim$ 2. The reason for this underestimate is twofold: On the one hand we have neglected various background contributions to the excitation process in the calculations. On the other hand the experimental data include besides the coherent pions also pions from other reaction processes where the final nucleus is left in an excited state. This is due to the experimental energy resolution which amounts only to $\sim$ 15 MeV[33]. In fig. 11 we compare the calculated excitation energy spectra for the $^{12}C(\gamma,\pi^0)^{12}C(g.s.)$ reaction with the data[33]. One can notice that the calculations with and without inclusion of $V_{N\Delta,N\Delta}$ differ in magnitude and shape. The reduction in the calculation including the residual interaction (solid curve) relative to that without $V_{N\Delta,N\Delta}$ (dashed curve) is an effect of the pion distorsion which is automatically included in the complete ΔN^{-1}-calculation. The peak position of the solid curve is shifted down in energy relative to the dashed curve by $\sim$ 80 MeV. This shift is an effect of the attractive residual interaction in the spin-longitudinal channel. Although the photon excites the nucleus spin-transversely, there is a mixing between the spin-transverse and spin-longitudinal channel due to the finiteness of the nucleus. The peak position of the coherent pion-photoproduction cross section is lowered in comparison to that of the $^{12}C(p,n\pi^+)^{12}C(g.s.)$ reaction by $\sim$ 30 MeV (see fig. 4b). This is so because the pion-photoproduction involves larger momentum transfers than the charge exchange reaction. Therefore the nuclear form factor suppresses the cross section in the former case.

4. Conclusions

In summary, we have shown that the shift of the Δ-peak position observed in the (p,n)- and (^{3}He,t)-reactions at intermediate incident energies is due to the strongly attractive correlations in the isovector LO channel. The same shift is also observed in the pion-nucleus total cross section. The attraction comes from the energy-dependent π-exchange interaction in the medium. No significant energy shift is found in the TR channel. This is in agreement with what is observed in the electro-excitation of the Δ, e. g. in the photon-nucleus total cross section, as discussed in this paper.

Furthermore, we have shown that for charge exchange reactions the pion coincidence cross section is an excellent tool to study the LO response function. In the $^{12}C(p, n\pi^+)^{12}C(g.s.)$ reaction the peak position of the coherent pion component is significantly shifted towards lower excitation energies by the ΔN^{-1} correlations. In addition, it is shown that the pions are strongly forward (in the direction of $\hat{q}$) peaked. Both effects, the energy shift and the forward peaking of coherent pions, should give a clear signature on the existence of the nuclear pionic mode. A more accurate interpretation of the π^+ events requires a thorough investigation of both the angular distribution of the $p\pi^+$ - events and of the π^+ events originating from projectile excitation. Such investigations can be performed at the 0° FACILITY to be built at COSY.

Acknowledgements

This work is supported in part by the Studienstiftung des deutschen Volkes, by the Graduiertenkolleg "Die Erforschung subnuklearer Strukturen der Materie" at the University of Bonn and by the U.S. Department of Energy under Contract DE-FG05-84-ER40145.

References

1. For reviews on the experimental and theoretical situation of Δ's in nuclei see for example:
   C. Gaarde, Ann. Rev. Nucl. Sci. **41** (1991) 187;
   J. Delorme and P. A. M. Guichon, Proc. of the 10^{th} Biennale de Physique Nucleaire,
   p. C.4.1, Aussois, 1989, Lycen 8906;
   F. Osterfeld, Rev. Mod. Phys. Vol. **64**, (1992) 491.
2. D. Contardo *et al.*, Phys. Lett. **B 168** (1986) 331.
3. V. G. Ableev *et al.*, Sov. Phys. JETP. Lett. **40** (1984) 763.
4. C. G. Cassapakis *et al.*, Phys. Lett. **B 63** (1976) 35.
5. B. E. Bonner *et al.*, Phys. Rev. **C 18** (1978) 1418.
6. D. A. Lind, Can. J. Phys. **65** (1987) 637.
7. B. K. Jain and A. B. Santra, Nucl. Phys. **A 519** (1990) 697.
8. H. Esbensen and T.- S. H. Lee, Phys. Rev. **C 32** (1985) 1966.
9. G. Chanfray and M. Ericson, Phys. Lett. **B 141** (1984) 163.
10. V. F. Dmitriev and T. Suzuki, Nucl. Phys. **A 438** (1985) 697.
11. J. Delorme and P.A.M. Guichon, Phys. Lett. **B 263** (1991) 157.
12. T. Udagawa, S. W. Hong, and F. Osterfeld, Phys. Lett. **B 245** (1990) 1.
13. M. Ericson, Nucl. Phys. **A 518** (1990) 116.

14. S.-W. Hong, F. Osterfeld, and T. Udagawa, Proc. of the Intern. Conf. on *Nuclear Collective Motion and Nuclear Reaction Dynamics*, eds. K.-I. Kubo *et al.*, World Scientific, 1991, p.261.
15. E. Oset, E.Shiino, H.Toki, Phys. Lett. **B 224** (1989) 249.
16. P. F. de Cordoba and E. Oset, Nucl. Phys. **A 544** (1992) 793.
17. A. S. Carroll *et al.*, Phys. Rev. **C 14** (1974) 635.
18. H. Rost, Bonn Report IR-80-10 (1980).
19. T. E. O. Ericson and W. Weise, *Pions in Nuclei*, Oxford University Press, 1988.
20. B. Körfgen, Berichte des Forschungszentrums Jülich, 2540 (1991).
21. M. Hirata, J. H. Koch, F. Lenz, and E. J. Moniz, Phys. Lett. **B 70** (1977) 281; M. Hirata, J. H. Koch, F. Lenz, and E. J. Moniz, Ann. of Phys. **120** (1979) 205.
22. Y. Horikawa, M. Thies, and F. Lenz, Nucl. Phys. **A 345** (1980) 386.
23. J. H. Koch, E. J. Moniz, and N. Ohtsuka, Ann. of Phys. **154** (1984) 99.
24. G. Glass *et al.*, Phys. Lett. **B 129** (1983) 27.
25. C. Ellegaard *et al.*, Phys. Lett. **B 231** (1989) 365.
26. P. Oltmanns, Berichte des Forschungszentrums Jülich, 2510 (1991).
27. F. Osterfeld, B. Körfgen, P. Oltmanns, and T. Udagawa, in: Proc. of the Workshop on *Meson Production, Interaction and Decay*, Cracow, Poland, May 6 - 11 1991, eds. A. Magiera *et al.*, World Scientific, Singapore, 1991, p. 116.
28. T. Udagawa, F. Osterfeld, P. Oltmanns, Proc. of LAMPF Workshop on *N-N and N-Nucleus Scattering*, Los Alamos, New Mexico, to be published.
29. P. F. de Córdoba *et al.*, to be published.
30. P. Oltmanns, F. Osterfeld and T. Udagawa, Phys. Lett. **B 299** (1993) 194.
31. J. Chiba *et al.*, Phys. Rev. Lett. **67** (1991) 1982.
32. M. Roy-Stephan, invited talk at *International Nuclear Physiscs Conference INPC92*, Wiesbaden, 26 July - 1 August 1992.
33. J. Arends *et al.*, Z. Phys. **A 311** (1983) 367.

ZERO DEGREES CENTIGRADE - OR THE d + d → α + 2π REACTION IN CELSIUS

CHR. BARGHOLTZ[1], KJ. FRANSSON[1], L. HOLMBERG[1], A. JOHANSSON[2], K. LINDH[1], D. PROTIC[3], G.RIEPE[3], L. SANDBERG[1], P.-E. TEGNÉR[1], P. THÖRNGREN-ENGBLOM[1] and G. WEISS[1]

[1]Department of Physics, Stockholm University, Box 6730, S-113 85 Stockholm, Sweden

[2]The Svedberg Laboratory, Uppsala University, Box 533, S-751 21 Uppsala, Sweden

[3]Institut für Kernphysik, Forschungszentrum Jülich, Postfach 1913, D-5170 Jülich, Germany

A simple spectrometer has been built for charged particles emitted in forward directions from the cluster-jet target in CELSIUS. It consists of a ΔE-E telescope of high-purity germanium which can be inserted into the CELSIUS ring in the bend following the target straight section. We study the reaction d + d → α + 2π close to threshold as a means of investigating the production and rescattering of isospin, I=0, pion pairs at low energy. The double-differential cross section for the production of alpha particles in forward directions is measured. In June of 1992 an exploratory measurement using a 570 MeV deuteron beam was made. With an integrated luminosity of 8.8 x 10^{33} cm^{-2}, 10 events were identified as due to the α+2π reaction. A second experiment was performed in December with an increased luminosity. A short description is given of the experiments including the performance of the spectrometer, and some preliminary results are presented.

1. Introduction

With the introduction of so called cooler rings into intermediate energy physics the possibility has been opened up to investigate the threshold behaviour of meson producing reactions with low background and good energy resolution. In the CELSIUS ring at The Svedberg Laboratory in Uppsala a variety of light-ion and light heavy-ion beams are now available for experiments. The maximum proton energy is 1.36 GeV.

A characteristic feature of fusion or near fusion reactions close to threshold is that the resulting nuclear system emerges from the reaction at an angle very close to zero degrees in the laboratory. That means that in the absence of any bending field the heavy reaction product essentially stays within or very close to the primary beam. In order to detect such heavy reaction products we have constructed and installed a low-cost spectrometer at the CELSIUS ring in Uppsala. The spectrometer utilizes the bending field of the ring itself to separate the heavy reaction products from the circulating beam. The heavy particles are detected in a solid state ΔE-E detector telescope.

In a first experiment we study the d + d → ^{4}He + 2π reaction at a center-of-mass energy 29 MeV above the 2π^0 threshold (570 MeV beam energy). In this reaction the pion pair is created in a pure isospin, I=0, state. Studies of the π-π interaction at low energy show that there is attraction in the I=0, L=0 channel[1]. The attraction is insufficient to bind pairs of real pions (except for the pionium atom). However, pion properties are modified in the presence of nuclear matter and it has been suggested that bound two-pion states may appear inside nuclear matter[2]. An earlier investigation of the d + d → ^{4}He +

2π reaction[3] showed that at beam energies above 780 MeV the missing mass spectrum deduced from the detected alpha particles is dominated by the so called ABC-effect for masses around 300 MeV/c^2.

In this note we describe briefly the zero degree spectrometer and report on a first set of measurements.

2. The zero degree spectrometer

2.1 Description

The zero degree spectrometer is an integrated part of the CELSIUS ring cf. Fig. 1. Its main element is a ΔE-E telescope of high-purity germanium. The telescope is mounted on a moving arm allowing it to be inserted into the main vacuum chamber of CELSIUS at a position 40% into the second dipole magnet following the cluster-jet target station. The arm is operated via the CELSIUS main computer system allowing its movement in a

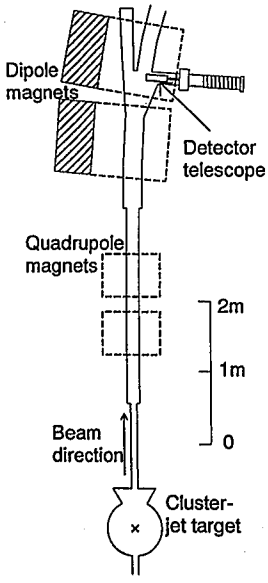

Figure 1. Part of the fourth straight section and the fourth bend of CELSIUS, showing the cluster gas-jet target station and the zero degree spectrometer.

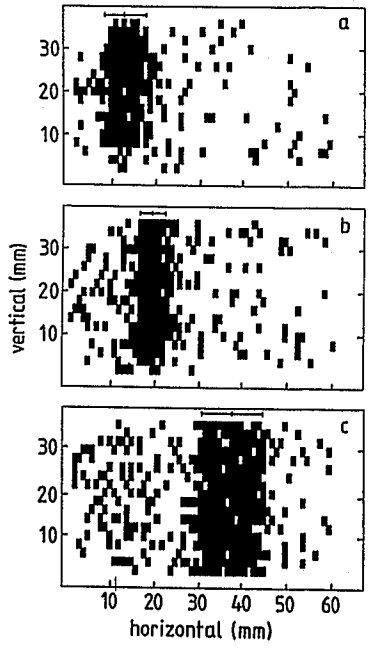

Figure 2. Spectra showing the position distribution on the ΔE detector element for protons from d+p reactions at 90 MeV. The spectra correspond to protons with a momentum relative to that of the beam centered at a) 56.15%, b) 54.75% and c) 51.95% in 0.20% wide intervals. Above each distribution is indicated the expected range for protons emitted within 10 mrad around zero degrees in the horizontal plane. The center of the beam is located approximately 178 mm to the left of the center of the detector elements shown.

straight forward manner to be synchronized with the acceleration cycle. During an experiment the telescope can be withdrawn from the beam pipe during injection, acceleration and dumping of the beam in order to protect the detector elements from excessive numbers of scattered beam particles. The time needed to bring the detector telescope from the so called "parking" position to the measuring position is approximately 5 s.

The detector telescope is made of high-purity germanium. The ΔE element is 1.4 mm thick and position sensitive with 66 stripes on the front surface, each 1 mm wide, for the horizontal position and 18 stripes on the rear surface, each 2 mm wide, for the vertical position. In order to limit the number of connectors leading out of the ring vacuum the position information is read out by means of charge division, i.e. for each detector surface there is a resistor chain fitted next to the ΔE detector inside the high vacuum to which each stripe is connected. Both ends of the chains are connected to pre-amplifiers outside of the vacuum approximately 30 cm away from the detector. The circular E-detector used in this experiment has a thickness of 14.9 mm and a diameter of 60 mm.

The detector elements are cooled by circulating LN_2 through a cold head on which the telescope is mounted. If the detector elements become radiation damaged during an experiment the detector telescope is withdrawn from the CELSIUS vacuum chamber into an outer chamber which is then sealed off from the ring vacuum and where the detector elements can be annealed before continuing measurements.

In its present position 6.1 m away from the target the detector telescope can be reached by particles provided they are emitted within 10 mrad of 0°. Changing the radial position of the detector telescope, particles can be detected with a rigidity between approximately 0.42 and 0.77 of that of the circulating beam. Using the information on particle energy and the position on the detector in conjunction with ray trace calculations, the direction of emission of the particle from the target can be determined. With a beam emittance of 1π mm mrad, the angular resolution (FWHM) for particles with a relative rigidity of 0.50 is better than 2 mrad and the acceptance ($\Omega\Delta p/p$) is approximately 6 x 10^{-5} sr.

2.2 Results of tests

The performance of the spectrometer was checked with protons from d+p reactions using a 90 MeV, cooled, deuteron beam. At this beam energy protons elastically scattered to zero degrees have an energy of 80 MeV and are fully stopped in the detector telescope. For these 80 MeV protons the energy resolution for the summed energy deposited in both detectors was 300 keV.

Protons from breakup reactions reach the detector telescope with a continuous spectrum of energies. These protons were used to check the results of ray trace calculations. Hit patterns on the detector were obtained for protons within narrow gates in momentum, $\Delta p=0.2\%$ of the momentum of the circulating deuteron beam. In Fig. 2 such hit patterns, for three different momenta, are compared to the approximate limits of acceptance expected from ray trace calculations. It can be seen that a horizontal focus lies close to the detector for a momentum approximately 55% of that of the circulating beam.

The approximately homogeneous distribution of hits on the detector outside of the expected limits of acceptance are most probably due to a background of protons

originating from scattering of beam particles against the walls of the vacuum chamber. Although this background is small compared to the number of particles reaching the detector telescope from the target it constitutes a major problem, to be discussed below, when extracting the very small cross sections of near threshold reactions.

3. First experiments

The first experiment aims at a study of the $d + d \rightarrow {}^4He + 2\pi$ reaction at a center of mass energy 29 MeV above the $2\pi^0$ threshold. A first test run was made in June of 1992. Most of what is reported below refers to that run. The analysis of data from the second experimental run in December has just begun.

3.1 Beam and target

A cooled beam of 570 MeV deuterons was let to interact with a deuterium cluster jet. The CELSIUS cycle, i.e. the time between two successive injections, was chosen to be 900 s. Deuterons were injected at t = 7 s at an energy of 24 MeV, then accelerated to 570 MeV between t = 8 and 30 s and then cooled. At t = 870 s the beam was dumped and the bending field ramped down to make CELSIUS accept a new injection. During flat top (t = 30 to 870 s) the intensity of the beam remained essentially constant.

The 8 mm thick and 4 mm wide deuterium cluster jet provided a target thickness of approximately 10^{14} atoms/cm^2. During the test run in June the resulting average luminosity during flat top was 10^{29} cm^{-2}s^{-1}. In the December run a preliminary evaluation indicates that the luminosity may have been a factor of five higher than that.

3.2 Measurements

During injection, acceleration and beam dumping, the detector telescope was "parked" with its center approximately 300 mm away from the the nominal beam center. For the measurements two positions were used. In the first one, used for calibration purposes, the center of the detector was 136 mm away from the nominal beam center. In this position the detector telescope was reached by particles with rigidities between 0.45 and 0.65 of that of the beam. In the second measuring position, 176 mm away from the beam, particles with rigidities between 0.40 and 0.54 of that of the circulating beam were detected.

Variations in the luminosity were monitored by detecting elastically scattered deuterons. For this purpose a detector telescope consisting of a 5 mm thick plastic scintillator and a 300 mm thick CsI scintillator was positioned at 35° relative to the beam 385 mm from the target.

For each hit in the detectors of the zero-degree spectrometer the following information was stored on tape: four pulse heights from the ΔE detector (two from the front side and two from the rear side charge divider), the pulse height from the E detector and the time difference between the hits in the two detectors. In addition, information concerning detector position, time in the cycle, beam current and horizontal beam position in the target straight section was stored.

Figure 3 shows a ΔE-E spectrum from the detector telescope of the zero-degree spectrometer obtained in the 136 mm position. Five main contributions can be seen. The

two characteristically bent distributions correspond to low-energy protons and deuterons that are stopped in the thicker detector. These particles cannot have reached the detector telescope from the target. Instead they belong to the background most likely due to scattering of beam particles on the walls of the CELSIUS vacuum chamber. Particles in the background may have a spectrum of energies extending essentially all the way up to the full beam energy. Protons or deuterons with energies in excess of 84 or 113 MeV respectively pass both detectors and deposite only a fraction of their energy in the detector telescope. Such events fall within the massive distribution running from the lower end of the bent distributions towards the origin. During the experiment in June the total background due to protons and deuterons caused less than a few hundred counts per second in the telescope and did not by itself constitute a major problem. However, scattering of beam particles in the walls of the ring could produce alpha particles as well. Even a small number of such background particles reaching the detector telescope may interfere severely with a determination of (the very small) cross section for alpha particle production in d + d reactions. A first estimate of the particle background during the experiment in December indicates that the background of low energy protons and deuterons was much lower at that time.

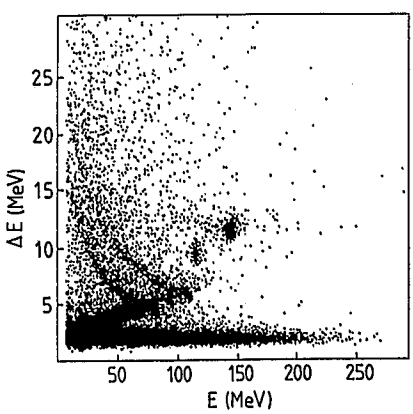

Figure 3. ΔE-E spectrum from the detector telescope of the zero degree spectrometer. The telescope was centered 130 mm away from the nominal beam center, cf. text.

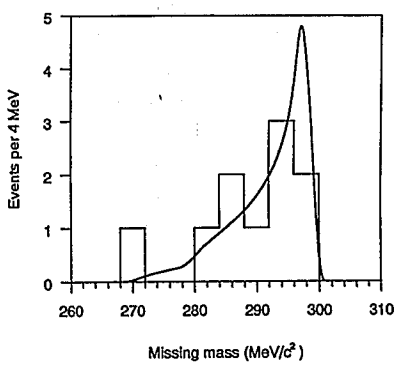

Figure 4. Measured missing mass spectrum from the d(d,X)^{4}He reaction. The smooth curve corresponds to the expected distribution (arbitrary units).

The dominating distribution in the lower left corner of Fig. 3 corresponds to high-energy protons from break-up reactions. These protons pass through the telescope and deposite only a small fraction of their energy. The long tail extending up to approximately 250 MeV is due to such protons inducing nuclear reactions in the E detector which may result in most of the original energy staying in the detector. In addition two peaks are seen (just below the diagonal) corresponding to ^{3}He particles from the d(d,n)^{3}He and d(d,π)^{3}He reactions For both reactions the particles pass through the telescope and deposit only part of their energy. The ^{3}He particles from the (d,n) reaction have a higher energy and thus leave less energy in the detectors. In connection with the experiment in

December we made a run with a 300 MeV deuteron beam. At this somewhat lower energy the ^{3}He particles from the (d,n) reactions are stopped in the telescope and can be used for calibration.

In the 176 mm position we no longer detect ^{3}He particles from the d(d,n)^{3}He reaction. It is in this position, however, that we expect to detect alpha particles from the d(d,2π)^{4}He reaction.

3.3 Analysis and preliminary results

At a beam energy of 570 MeV the alpha particles from the (d,2π) reactions are fully stopped in the detector telescope. By putting a gate in the ΔE-E spectrum, 4 MeV wide in ΔE, in the region where alpha particles are expected in the data from the June experiment, 16 events were selected with a total energy between 220 and 330 MeV. Some of these events, if truly alpha particles from the target, would correspond to emission angles larger than the limits of acceptance. Removing these events we obtain the missing mass spectrum in Fig. 4 from the remaining 10 events. Missing masses in a 29 MeV wide range starting at $2m_\pi c^2$ (=270 MeV) are expected. The smooth curve in Fig. 4 shows the shape of the missing mass spectrum expected based on the spectrometer acceptance and the low-energy π–π scattering parameters of Ref. 1 neglecting any rescattering from the alpha particle and any influence from production dynamics.

The integrated luminosity was estimated from the observed number of events due to the d(d,$\mathcal{N}\pi$)^{3}He reaction. The cross section for this reaction has been measured by Chapman *et al.*[4]. At a deuteron energy of 650 MeV a cross section of 2.2 mb/sr, at 0° in the laboratory, was determined. Assuming that this cross section varies with phase space alone when extrapolating it down to 570 MeV, the total integrated luminosity in the June experiment would be 8.8 x 10^{33} cm^{-2}. The 10 accepted events from the d(d,2π)^{4}He reaction then correspond to a total cross section of approximately 70 nb, assuming isotropy in the center of mass frame.

A much more precise result will hopefully be available when the analysis of the December experiment has been completed. Those data are based on an integrated luminosity approximately ten times greater than that obtained in June.

4. Conclusion

Extrapolating down to the present energy the result of Chapman *et al.*[5] for the total cross section of the d(d,2π)^{4}He reaction at 650 MeV, we obtain a value of approximately 66 nb in good agreement with the estimate above. Due to the marginal statistics, however, no real conclusions can been drawn from this apparent agreement. However, we want to point out that if the result of the December experiment goes in the same direction it could mean that the ABC effect which is so prominent in the missing mass spectrum at higher energies (and varies rapidly with beam energy[3]) does not greatly influence the cross section at beam energies below 650 MeV. This would be an interesting result which might shed light on the still obscure question concerning the mechanism responsible for the ABC effect. If the ABC effect is not present at this low energy then the (d,2π) reaction may be an ideal tool to study the modifications of the π–π interaction inside nuclear matter. To this end we are investigating the possibility to study the ^{14}N(d,2π)^{16}O reaction with the same spectrometer using a ^{14}N beam in CELSIUS.

Acknowledgements

The authors wish to thank the CELSIUS group and the personnel of the detector laboratory at Forschungszentrum Jülich, whose efforts made these experiments possible. This work was supported in part by the Swedish Natural Science Research Council.

References

1. O. Dumbrajs, R. Koch, H. Pilkuhn, G. C. Oades, H. Behrens, J. J. DeSwart, and P. Kroll, *Nucl. Phys.* B216 (1983) 277.
2. P. Schuck, W. Nörenberg, and G. Z. Chanfray, *Z. Physik* A330 (1988) 119.
3. J. Banaigs, J. Berger, L. Goldzahl, L. Vu Hai, M. Cottereau, C. LeBrun, F. L. Fabbri, and P. Picozza, *Nucl. Phys.* B105 (1976) 52.
4. K. R. Chapman, J. D. Jafar, G. Martelli, T. J. Macmahon, H. B. Van Der Raay, D. H. Reading, R. Rubenstein, K. Ruddick, D. G. Ryan, W. Galbraith, and P. Sharp, *Nucl. Phys.* 57 (1964) 499.
5. K. R. Chapman, J. D. Jafar, G. Martelli, T. J. Macmahon, H. B. Van Der Raay, D. H. Reading, R. Rubenstein, K. Ruddick, D. G. Ryan, W. Galbraith, and P. Sharp, *Phys. Lett.* 21 (1966) 465.

K^+ PRODUCTION IN PROTON–NUCLEI INTERACTIONS BELOW 1 GEV

V.P. Koptev
High Energy Physics Department, Petersburg Nuclear Physics Institute,
188350 Gatchina, St. Petersburg district, Russia

In this paper the experiments on K^+ production in different target nuclei at the 1 GeV proton beam in PNPI are described. Mainly those results are presented which were not published in international journals.

The kaon production program at the 1 GeV proton synchrocyclotron in Gatchina started fifteen years ago when the hypernuclear physics was in the peak of its development. The questions of the Λ–binding energy in nuclei, excited states of hypernuclei, lifetime of strange particles in nuclear matter were under serious discussions. The process $pA - K^+(A+1)$ could be one of the reactions used for hypernuclear production. The cross sections for this reaction were not measured and theoretical calculations predicted very low values of the cross sections (much less than 1 nb/sr). To study the reaction, a spectrometer with the good resolution and the large solid angle was needed. The spectrometer should have a small length because of the small kaon lifetime, and strong criterions for kaon–pion separation were necessary.

To get some experimental estimates of cross sections we started with the reaction $pA \rightarrow \pi^+(A+1)$. Cross sections for this reaction above 200 MeV were also not known but could be measured with a much simpler technique, using the existing pion channel as the spectrometer with the momentum resolution of 0.2%. From the measured π^+ spectra (fig. 1) we understood that the cross section for the $pA \rightarrow K^+(A+1)$ reaction would be not larger than 10 pb/sr. In principle, that was not so bad since for the proton beam intensity of $2 \cdot 10^{12}$ p/s, for the solid angle of 0.01 sr and for the thickness of the ^{9}Be–target of 1 cm it gave a count rate equal to 40 K^+/s in the ^{10}Be ground state peak. This count rate was not less than the count rate of Λ–hypernuclei production in the most promising $\pi^+A \rightarrow K^+A$ reactions. But the kaon spectra would be measured in the momentum region $600 - 650$ MeV/c which was close to the maximum of the pion spectra. The pion background would be extremely huge: $N_{\pi^+}/N_{K^+} \geq 10^8$.

We did not find the solution of the background problem and started to do the second, simpler part of the kaon program: measurements of the cross sections for the inclusive K^+ production in the reactions $pA \rightarrow K^+ \ldots$ at the projectile energies $T_p \leq 1$ GeV. Since the proton energy of 1 GeV was much less than the threshold energy for $pN \rightarrow K^+\Lambda N$ reactions we would have a chance to study nucleon–nucleon interactions at small distances in nuclei, receiving an information either on the high momentum component of the internuclear nucleons or on short range correlations of nucleons in nuclei. There was no experimental information on $pA \rightarrow K^+$ reactions below 2 GeV and our first theoretical calculation based on direct $pN \rightarrow K^+\Lambda N$ interactions and on the one–nucleon Hartree–Fock wave function predicted discouragingly low cross sections. That is why we

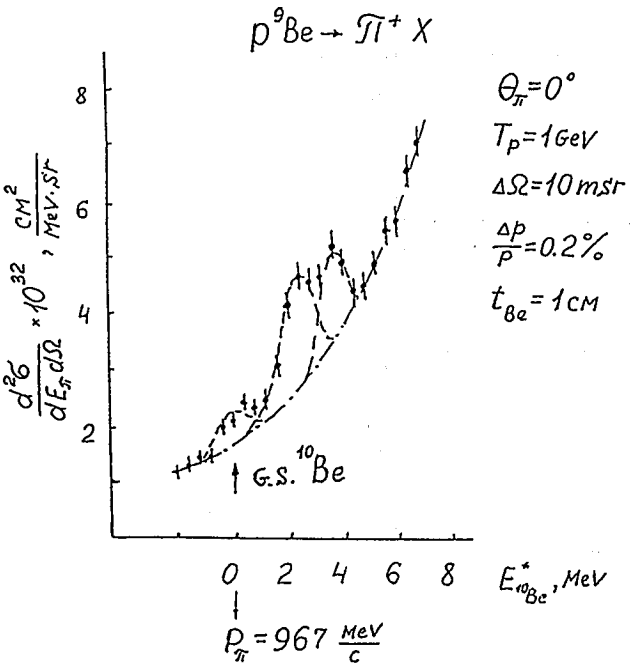

Fig. 1: The pion spectra from p⁹Be interaction close to the upper kinematical limit.

started our measurements with the rather simple but powerful method [1] which not only gave the possibility to measure the total cross section of the K^+–meson production in $pA \to K^+ ...$ reactions, but also left the door open for lifetime measurements of kaons stopped in matter.

We did not record the K^+–mesons, but detected muons from the decay ($K \to \mu\nu$) of K^+ mesons stopped in the very same target. We selected monoenergetic muons ($p = 236$ MeV/c) by the magnetic spectrometer ($\Delta p/p = 4\%$) and separated muons from the background of pions and electrons by the $\Delta E,E$ method. To reject the muon background from π^+–decay in fight, the discrete temporal structure of synchrocyclotron proton beam was used as a time criterion. During short microbunches (5 ns) kaons were produced and stopped in the target. Between these microbunches (75 ns) the $K^+ \to \mu^+\nu$ decays happened. It was very important that there existed the time interval $\Delta t \approx 35 - 40$ ns with a very low level of the background ($\sim 10^{-4}\%$). That helped us not only to identify the events with kaons but to measure precisely (as a by–product) the lifetime of K^+–mesons (fig. 2) [2].

By this method we measured the total cross section of the K^+ production in the $pA \to K^+ ...$ reaction for the proton energy below 1 GeV (fig. 3) and different targets. The data were analyzed mainly in the frame of two models: the direction mechanism of K^+ production and the two–stage mechanism wherein a fast pion was produced ($pN \to \pi NN$) at the first stage.

The directed mechanism predicted cross sections which were three orders of magnitude less than the data if no short range nucleon–nucleon correlations were taken into account. The two–nucleon correlations gave only a factor of ten higher values of the precided cross sections. The data could be described in the frame of the direct mechanism if a phenomenological nuclear nucleon momentum distribution was considered (solid lines in the fig. 3).

The two–stage mechanism, applied in the frame of the Fermi–gas cascade model calculation, gave a satisfactory agreement with the data.

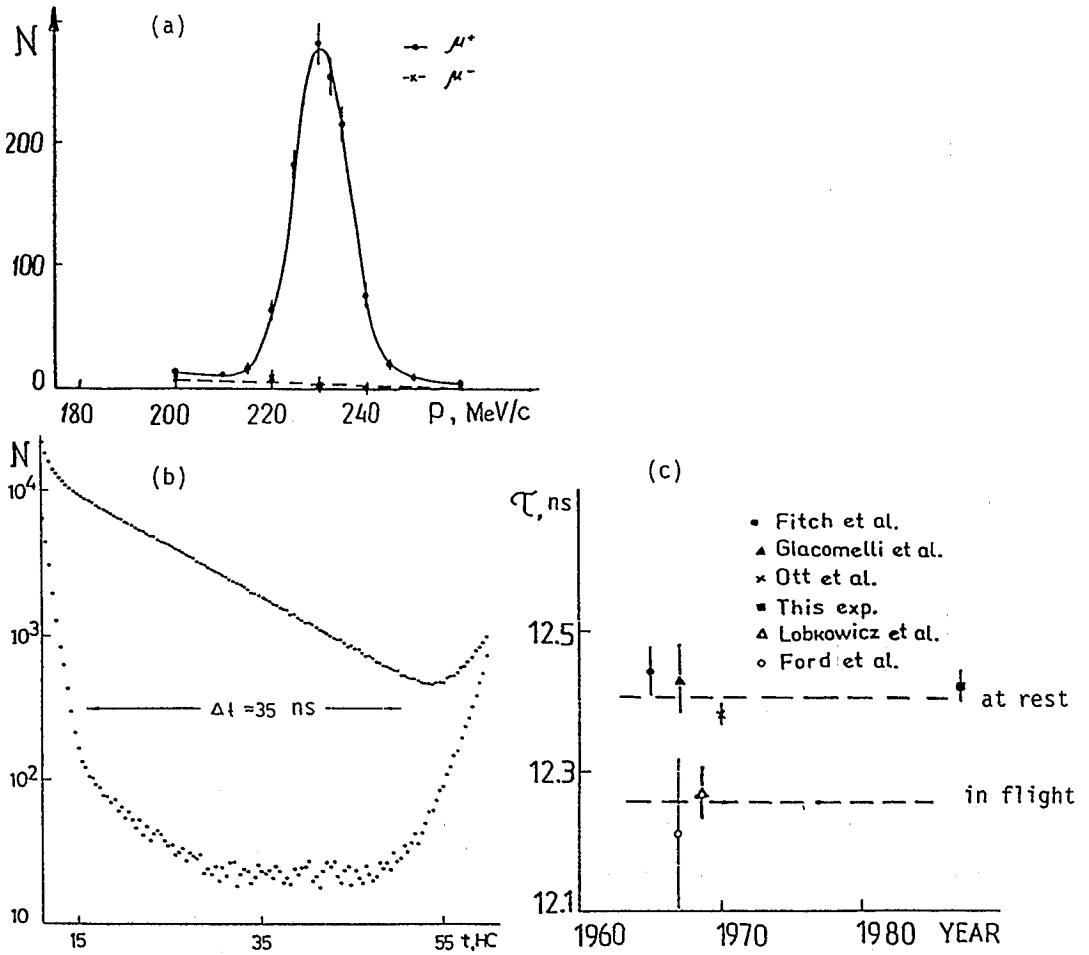

Fig. 2: The results of K^+–meson lifetime measurements [2].
a) Momentum distribution of μ^+–mesons, detected during the Δt–time interval.
b) Time–of–flight spectrum for μ^+–mesons with P = 230 MeV/c (upper points) and background spectrum measured at P = 210 MeV/c and P = 260 MeV/v.
c) Comparison of data received in this work with published data.

Recently, these two mechanisms were precisely studied and applied by W. Cassing et al. [3].

We considered also cluster (fluctons, quark bags, coloured strings) mechanisms. Since these mechanisms had more parameters (a probability of a cluster formation and a momentum distribution of the clusters), it was difficult to understand their importance for the kaon production.

Additional experiments which can separate different reaction mechanisms are necessary. One of them is the experiment on kaon production in pion–nucleus interactions ($\pi^+ A \rightarrow K^+ ...$) at pion energies below the threshold of the elementary reaction

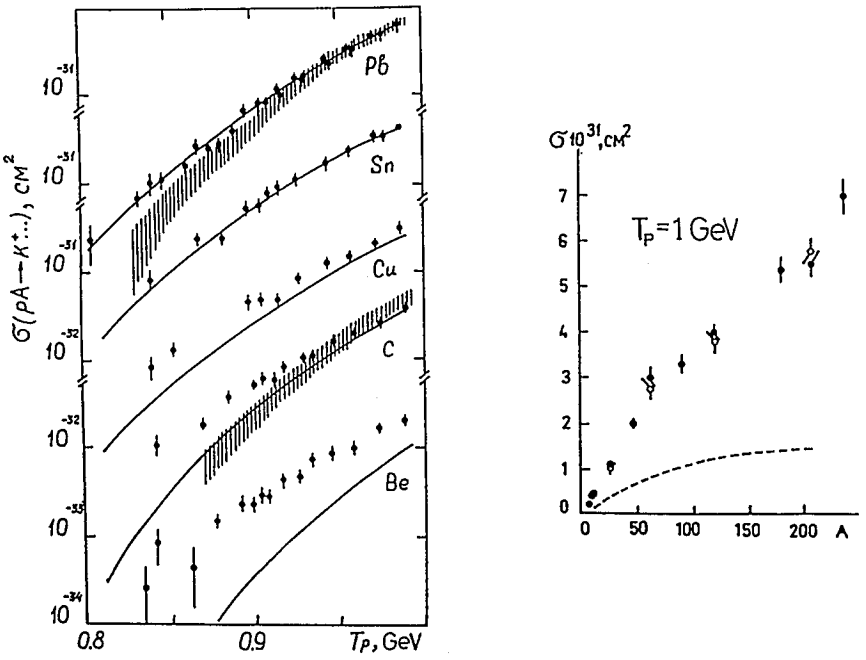

Fig. 3: The total cross section of K^+ production. The open points and shadowed areas are the results of the two–stage cascade model calculations. The dashed line presents the part of σ_{tot} connested with the intermediate deuteron production. The solid lines are the result of the direct model calculations [1].

$\pi^+p \to K^+\Lambda$. At the pion energies below 650 MeV even the total cross sections became strongly sensitive to the high momentum component of nuclear nucleons (in fig. 4a the dashed line corresponds to the Fermi gas momentum distribution). In principle, as it was pointed out by W. Cassing, the two stage mechanism is also possible when in the first stage a Δ–isobar is produced. Kaons are generated in the second stage in ΔN interactions.

The kaon angular distribution (fig. 4b) and double differential cross sections [4] will help to separate different mechanisms, especially at small angles.

A K^+d–correlation experiment in $pA \to K^+d$ reactions seems to be very attractive. If the two stage mechanism is a reality then in the first stage, deuterons will be produced in the reactions $pN \to \pi d$ (in 25% of the events at $T_p = 1$ GeV and in 65% of the events at $T_p = 0.9$ GeV). Deuterons escape the nuclei ($60 - 40\%$ from Be and $2 - 3\%$ from Pb) at small angles and form a rather narrow peak in the deuteron spectra (fig. 4c).

An expected count rate of K^+d correlations will be 200 events per hour at $T_p = 1$ GeV for the 0^0–Facility [5]. This measurement will be interesting at lower energies where only the highest momenta (dashed lines in fig. 4d) of the Fermi–gas momentum distribution

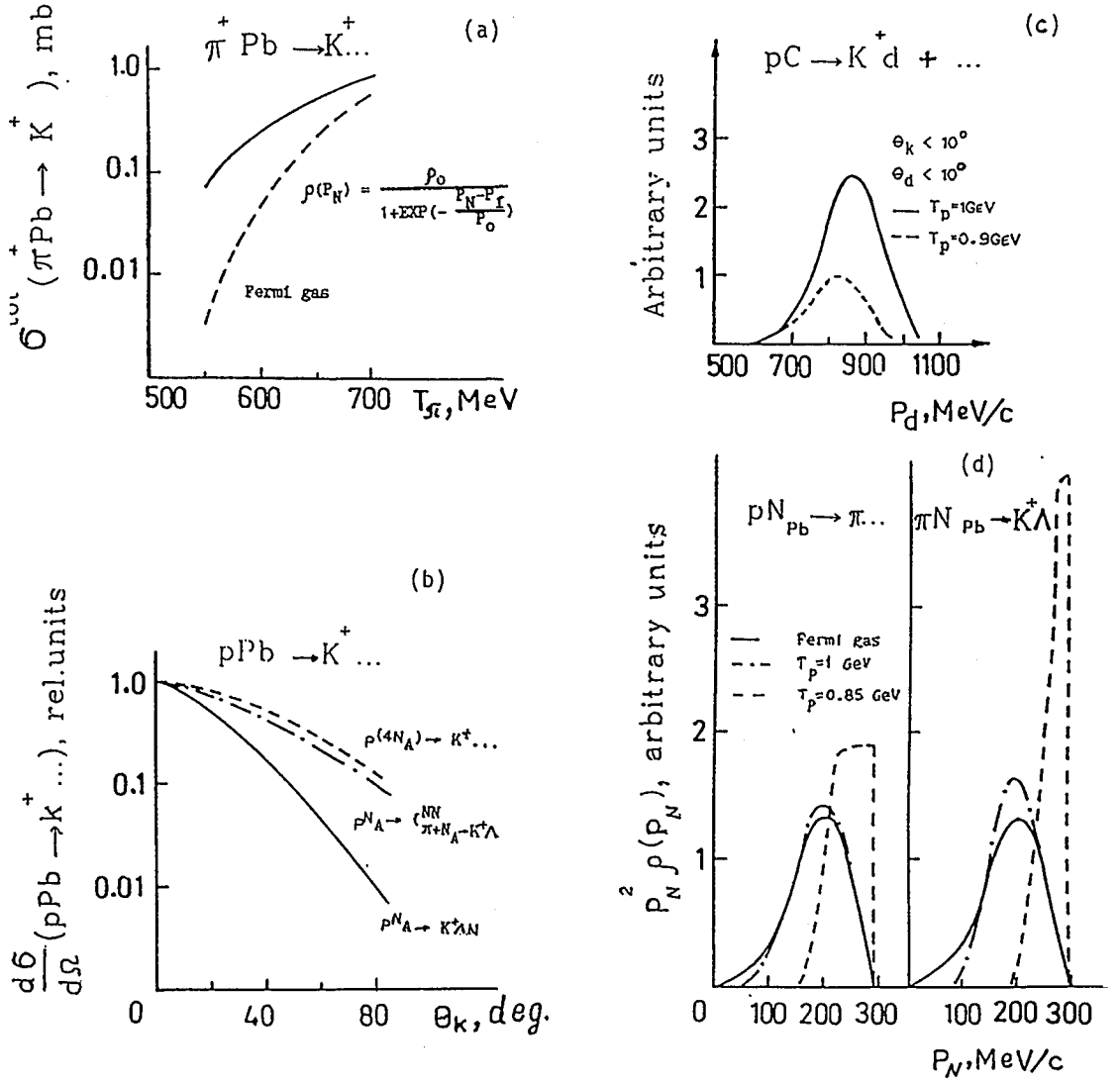

Fig. 4: The prediction for

a) the total cross when the Fermi gas (dashed line) or the phenomenological nuclear nucleon momentum distributions are used in the one step $\pi^+ N_A \to K^+\Lambda$ mechanism;

b) angular distributions for different mechanisms;

c) the momentum distribution of deuterons correlated with kaons from the two–step mechanism;

d) the momentum distribution of nuclear nucleons realized at both stages of the two–step mechanism for different projectile energies [1].

(solid lines in fig. 4d) are realized in the calculated total cross sections of K^+–meson production. The momenta higher than 300 MeV/c must be taken into account to achieve better agreement with the experimental data.

As it is seen, the pion production in proton nucleon interaction can be very important for the kaon production in proton–nucleus interactions below 1 GeV. A variety of the inclusive and exclusive experiments on the total, differential and double differential cross sections for π production has been already done at polarized and not polarized proton beams. Most of these data are explained by interactions happening in the peripheral nucleon region with rather low transferred momenta (t^2/m^2). For example, inclusive proton spectra at any angle are the result of the integration over the large region of t^2/m^2 (fig. 5a) for the cases when both the projectile (1) and the target (2) nucleons are excited. The values of the cross sections received at any proton momentum are defined mostly by t^2/m^2 less than 5.

The results of calculation, presented in figs. 5–6, are done in the frame of OPEM [6]. The off–shell πN–amplitude corrections and the NN final state interactions are taken into account.

The dipole pionic form factor (fig. 5c) was chosen to describe most of the NN $\rightarrow \pi$NN data below 1 GeV at unpolarized beams. The shadowed area shows the uncertainty of the linear A–α dependence from the normalization to the total cross sections. With this calculation one can choose the kinematics where only the high transferred momenta are necessary. That can be realized at the 0^0 Facility.

The proton spectra from the forward–backward pion–proton correlations are shown in fig. 5b. The left side and right side broad peaks are connected with the Δ production on the target or projectile protons, respectively. They are mainly defined by the interactions with low transferred momenta (fig. 5d). The peaks in the middle of the spectra are caused by the final state interactions (FSI) of nucleons with low relative momenta (velocities). These peaks were studied at LAMPF [7] and it was shown that their width is mainly defined by the angular and momentum resolution of the spectrometer.

An observation of these peaks will be interesting for the investigation of reactions $pp \rightarrow K^+p\Lambda$ and for a $K^+ - p$ correlation experiment. That can be a direct way to study interactions of Λ–hyperons and nucleons at small relative velocities and to receive the ΛN coupling constant. If these measurement are done close to the threshold (e.g. $T_p \leq 1800$ MeV) then all the particles (K^+,Λ,p) will go into the forward direction and in the proton spectra ($\Theta_p = 0^0$), measured in correlation with kaons ($\Theta_k = 0^0$), there will be observed two intensive peaks corresponding to forward ($\Theta^* = 0^0$) and backward ($\Theta^* = 180^0$) Λ in the ΛK^+ center of mass system (CMS).

And at last, the FSI peak can help to decide the phenomenon of a possible pη attractive interaction. The simplest reactions where this can be studied is the $pp \rightarrow pp\eta$ process. At the 0^0 Facility, $pp \rightarrow pp\eta$ can be investigated. If this reaction is studied in the energy range 1.26 GeV $< T_p <$ 2.26 GeV (better close to the threshold, e.g. at $T_p = 1.4$ GeV, then all the three particles (p,p,η) will go into the forward direction. The pp–correlations at small angles will help to enrich pη events with small relative p and η velocities for which an enhancement connected with the pη final state interaction can be observed. There are two points in the proton ($\Theta_{p1} = \Theta_{p2} = 0^0$) spectra with $\beta_{p1} = \beta_{\eta'}$

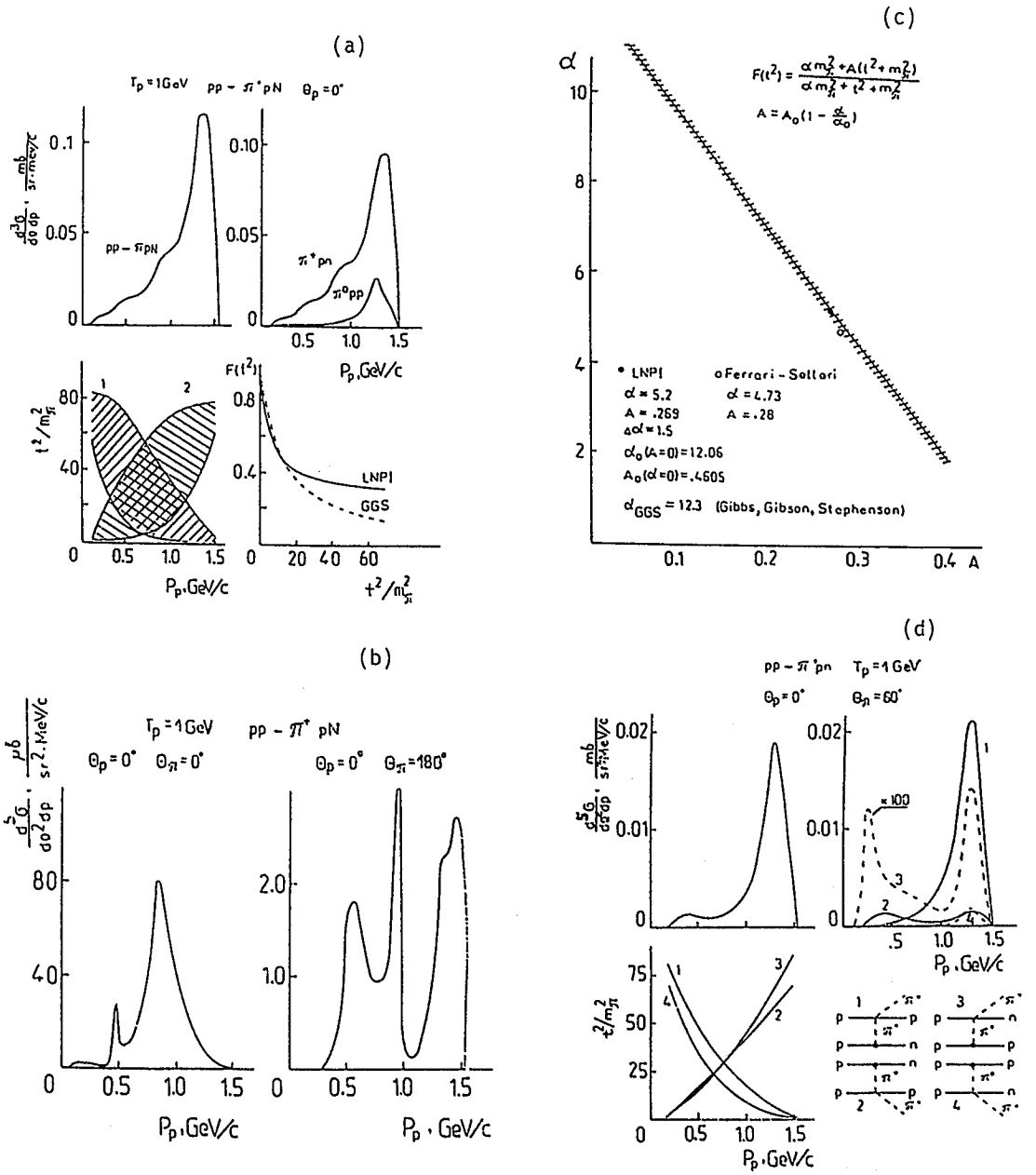

Fig. 5: Transferred momenta (t^2/m^2 in fig. a,d) and inclusive (a) and exclusive (b,d) proton spectra, calculated in the frame of OPEM with the formfactor $F(t^2)$ (a,c).

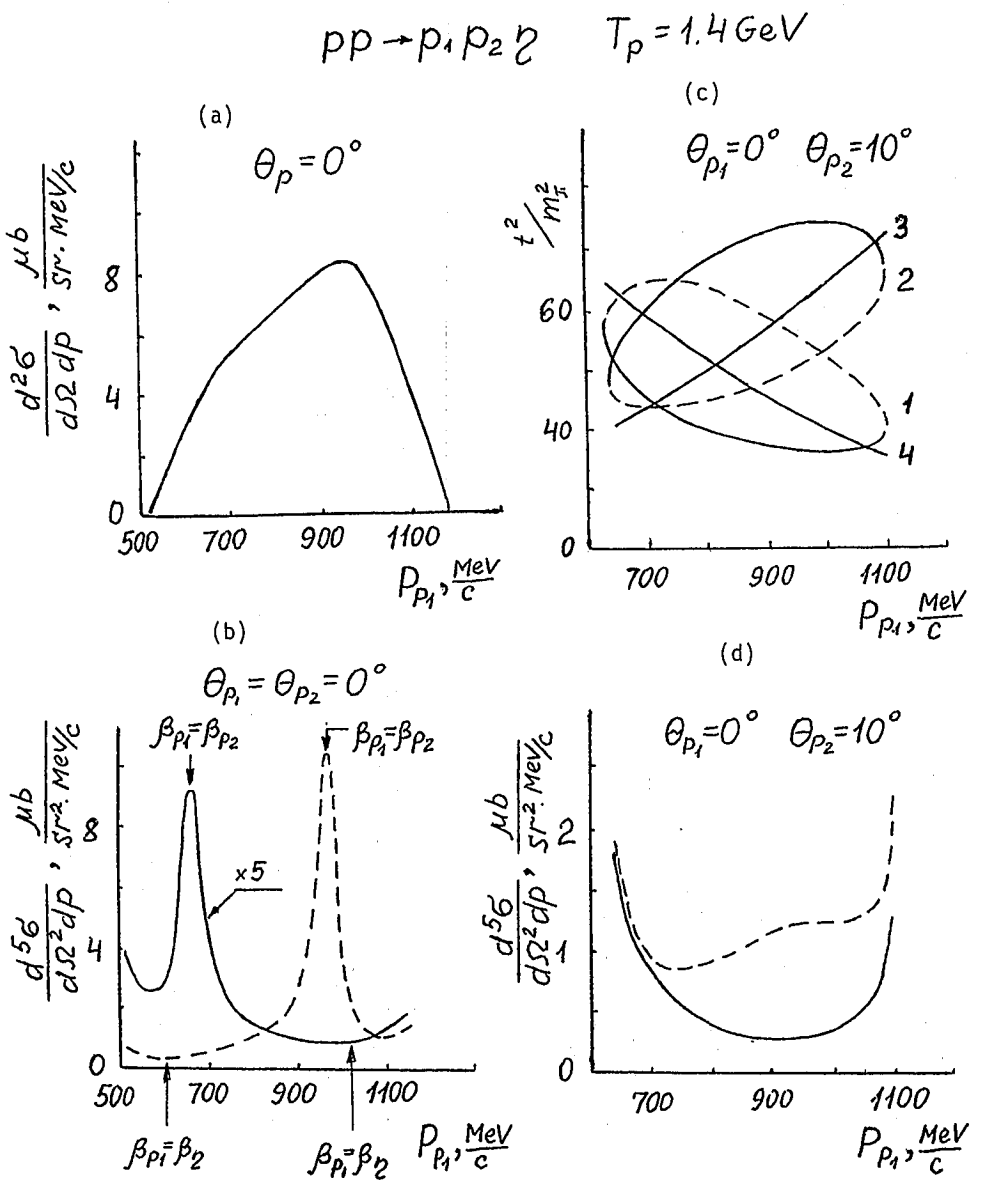

Fig. 6: Transferred momenta (c) for the four diagrams (like in Fig. 5d) and inclusive (a) and exclusive (b,d) differential cross section, received from OPEM calculations. Dashed (solid) lines correspond to forward (backward) protons in the $p_2\eta$ CMS.

corresponding to η going forward and backward in pη CMS. They are close to the pp FSI peaks and it is better to measure these two branches of the proton spectra separately (fig. 6b). As it was shown in [8], the background of $pp \rightarrow pp\pi^0$ and $pp \rightarrow pp\pi^0\pi^0$ reactions can be rejected even without a magnetic spectrometer.

To study the particle production (π^+,K^+,η) with high transferred momenta ($t^2/m^2 > 20$) one should "switch off" the final state interaction. It can be done if one works in the kinematics where the forward going protons are detected in correlations with the second charged particle at large angles (fig. 6d, 5d). This experiment will be more effective when it is done with the polarized protons beam at the polarized proton target. Then there is a chance to separate the diagrams corresponding to the cases of the projectile or the target excitation.

Returning back to the K^+ meson production, it was mentioned that NΔ interaction could be important. The experiments on studies of the Δ–isobar admixture in nuclei can also be done at the 0^0–Facility. Even inclusive measurements of the recoil spectra from the reactions $pA_z \rightarrow (A-1)_{z-1} + \Delta^{++}p$ (e.g. $p^9Be \rightarrow {}^8He\ \pi^+pn$) in comparison to the reactions $pA_z \rightarrow (A-1)_{z-2}\ \pi^+pp$ (e.g. $p^9Be \rightarrow {}^8Li\pi pp$) will give upper estimates for the Δ isobar excitation of nuclear nucleons. This experiment has recently been started in Gatchina [9]. But to understand the influence of different mechanisms it is necessary to do an exclusive experiment measuring the recoils in coincidence with the forward going protons. In this experiment, a thin target (< 1 mg/cm^2) must be used to detected the low energy recoils. The magnetic spectrometer at an internal target in cooperation with ΔE,E criteria is necessary.

References:

[1] V.P. Koptev et al., JETP 67 (1988) 2177

[2] V.P. Koptev et al., the proceeding of the international symposium on muon and pion interactions with matter, Dubna 1987, p. 447
S.G. Barsov et al., LNPI research report 1986–1987, p. 20

[3] W. Cassing et al., Phys. Lett. B238 (1990) 25

[4] W. Cassing, the report at this meeting

[5] Proposal COSY18, Study of the subthreshold K^+ production at 0^0 Facility at TP2 in COSY,
K. Sistemich et al., the report at this meeting

[6] V. Abaev, V. Koptev, unpublished

[7] J. Hudomaly–Gabitzsel et al., Phys. Rev. C18 (1978) 2666

[8] COSY proposal
D. Bour et al., Study of η and η' production and interaction

[9] A.I. Amelin et al., preprint PNPI–1748 (1991)

SUBTHRESHOLD PRODUCTION OF K^- MESONS IN PROTON-INDUCED REACTIONS AT LIGHT NUCEI

H. MÜLLER

Institut für Kern- und Hadronenphysik, Forschungszentrum Rossendorf
Postfach 19, O-8051 Dresden, Federal Republic of Germany

The energy dependence of the various particle production channels in proton-proton interactions from threshold up to about 5 GeV is satisfactorily reproduced in the framework of the modified phase-space model. This is the starting point for predicting the unknown cross sections for K^- production in the same energy region and for considering subthreshold production of K^- mesons in proton-deuteron and proton-carbon interactions. Special emphasis is put on the discussion of associated production of light fragments and the role of resonances in the production process. The predicted cross sections are a basis for estimating the counting rates, which can be expected in the planned investigation on the 0° Facility at COSY.

1. Introduction

The production of particles in proton-nucleus (pA) reactions at energies below the corresponding threshold for free nucleon-nucleon (NN) interactions is a typical cooperative nuclear phenomenon. Subthreshold production may be interpreted either in terms of high-momentum components of the nuclear wave function or by assuming that clusters consisting of several nucleons participate in the interaction process. Clusters, in their turn, may exist as an intrinsic property of nuclei or they may be formed dynamically during the interaction by distributing the transferred energy and momentum between the participants. It is of principal importance for a correct description of nuclear reactions at relativistic energies to understand the mechanism of subthreshold production. The kinematical regions where a "high degree of collectivity" is needed for the production process to take place are especially conclusive. That is the case if the energy approaches the absolute proton-nucleus threshold and, in particular, if the production of heavy particles is investigated. Due to strangeness conservation each K^- is accompanied by a K^+ meson and the produced mass amounts to nearly 1 GeV. This value is considerably larger than in the case of pion or K^+ production what makes the K^- channel especially interesting at subthreshold energies.

A distinguishing feature of K^- production consists in the fact that the K^- may be created via resonances. A well-established resonance of this kind is the Φ meson with a mass of 1.02 GeV which decays with nearly 50 % probability into a K^+ and a K^- meson. Other candidates are the $f_o(975)$ and the $a_o(980)$ mesons the nature of which is vividly discussed at present. Are they usual $q\bar{q}$ quark model states, $K\overline{K}$ molecules or candidates for glueballs? For more details see ref.[1] and references therein. K^- production via these states must be sensitive to the underlying structure, and an experimental investigation will surely help to clarify this problem. By mesuring K^+ and K^- mesons in coincidence

it can be determined to which degree the K^- mesons are decay products of primarily produced resonances and to which degree K^+K^- pairs are created directly. This yields additional information on the subthreshold production mechanism and the nature of the involved resonances.

A further interesting channel to be investigated proceeds in two steps via the $\Lambda(1520)$ resonance. First the K^+meson is produced together with the $\Lambda(1520)$ and the K^-meson arises then from the decay of the $\Lambda(1520)$. It is, however, difficult to determine the yield of this particular production channel by measuring the decay products of the $\Lambda(1520)$, because a large uncorrelated background must be expected.

As argued in Ref.[2], the cross section for K^- production should be sensitive to the sea-quark distribution in nuclei, because the K^- meson consists of quarks ($\overline{u}s$), which are not present as valence quarks in the initial channel. The question whether the sea-quark distribution changes if the nucleons are embedded in a nucleus is controversely discussed in the literature. Thus, the investigation of subthreshold K^- production may also yield new knowledge in this respect, although higher incidence energies are shurely better suited for solving this problem.

In a recent paper[3] subthreshold production of K^+ mesons has been considered in the framework of the modified phase-space model. The integrated cross sections measured by Koptev et al.[4] at energies between 0.8 and 1.0 GeV were well reproduced. Here, these investigations are extended to the production of K^- mesons. There are no data for K^- production, neither for elementary proton-proton (pp) nor pA interactions. Therefore, after a short description of the main features of the model in Sect. 2, we begin in Sect. 3 with a study of the various pp-reaction channels in the threshold regions in order to fix the parameters of the model. On this basis the energy dependence of the cross section for the K^--production channel is predicted. Proton-induced production of K^- mesons at light target nuclei (deuteron and carbon) is then considered in Sect. 4. Conclusions are summarized in Sect. 5.

2. Basic assumptions of the modified phase-space model

A detailed description of the model can be found in refs.[3,5,6]. Here, only the basic assumptions and a few new features are discussed. As in ref.[5], a pp interaction is described by a two-step picture. In the first step translational energy is converted into internal excitation energy of the two colliding protons. An excited subsystem is pictured as consisting of the valence quarks of the initial particles and additional quark-antiquark pairs created during the collision. In the second stage of the reaction the available quarks recombine randomly into baryons and mesons according to the rules of quark statistics[7] populating in this way all possible final channels allowed by conservation of internal quantum numbers. The relative probability of populating a definite channel is calculated as the product of the Lorentz-invariant phase-space factor with the square of an empirical matrix element, which describes the dynamics of the interaction. As schematically depicted in Fig. 1b, the phase-space factor is decomposed[8] in such a way that the underlying physical picture of the reaction process is reflected. The integral over the invariant masses of the two excited subsystems emerging from the first step of the interaction is modified by that part of the

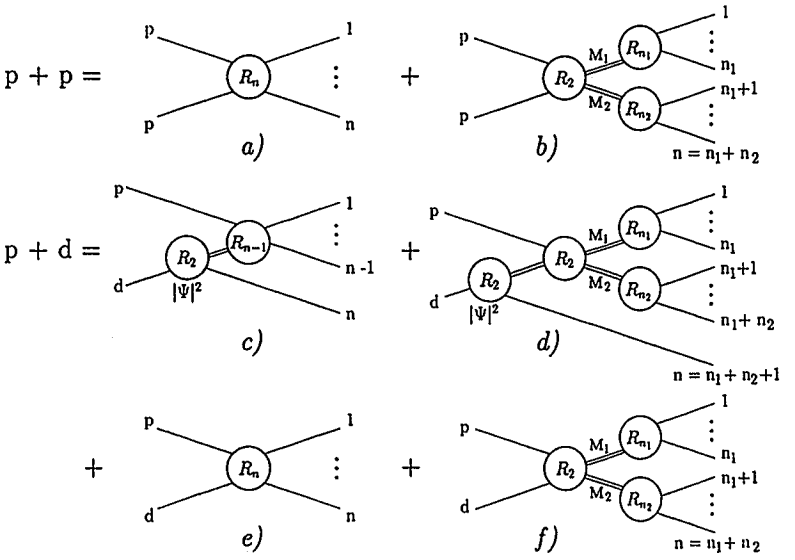

Figure 1: Phase-space decomposition for *pp* (graph a-b) and *pd* (graph c- f) interactions. The phase-space factor for i particles or particle groups is denoted by R_i.

matrix element containing a parameter Θ, which is similar to a temperature (for details see refs.[5],[6]). For the present considerations in the threshold region an energy dependence of this parameter is used in the form

$$\Theta = \Theta_o[1 - \exp(-E_{ex}/\overline{E_{ex}})] \tag{1}$$

with $\Theta_o = 320$ MeV and $\overline{E_{ex}} = 1.5$ GeV. Eq.(1) approaches asymptotically the value of Θ used so far[5]. The value of $\overline{E_{ex}}$ is chosen such that a good overall description of the various particle production channels is achieved. In (1), $E_{ex} = \sqrt{s} - 2m_p$ denotes the energy available for excitation of the interacting particles given by subtracting the two proton masses m_p from the c.m. energy $\sqrt{s}$. It is surely a reasonable assumption that temperature Θ and available energy are correlated, however, the function (1) should be considered only as a first guess. Further investigations are necesssary.

A second modification of the model is shown in Fig. 1a. At low energies the translational energy between the two excited subsystems may become comparable to their internal excitation energy. Then, a description as a single excited system seems to be more reasonable. Therefore, the two processes from Fig. 1a and 1b are taken into consideration in the present version of the model.

There are two further parameters. The value of the volume parameter R=1.2 fm is taken from ref.[5] and that of the strangeness suppression factor $\lambda = 0.1$ from the compilation of Wroblewski[9]. Up, down and strange quarks are sampled according to the ratio $u : d : s = 1 : 1 : \lambda$, and the parameter R arises from the integral over coordinate space.

Proton-deuteron (*pd*) interactions are described analogously. In the case of quasi-free

interactions (diagrams c) and d) in Fig. 1) the deuteron is assumed to dissociate into the participant, which interacts with the projectil, and the spectator, whose momentum distribution is given by the Paris[10] deuteron wave function $|\Psi|^2$. Additionally, the interaction of the whole deuteron with the incoming proton (diagrams e) and f) in Fig. 1) is considered, too.

3. Production of mesons in proton-proton collisions

In the framework of the modified phase-space model hadron-hadron, hadron-nucleus and nucleus-nucleus collisions are treated in a unified way based on the same principal assumptions[3]. Results of model calculations can be compared to elementary as well as nuclear cross sections. In this section we begin with a consideration of *pp* collisions.

With regard to cross sections for K^- production in *pp* collisions there is no possibility to check the model with experimental data, because no measurements exist. Therefore, the available data for production of other meson types in the energy region of interest are confronted with model calculations with the aim to adapt the model parameters in such a way that reliable predictions for unknown channels become possible. The result is shown in Fig. 2. It can be seen that the majority of the data is well reproduced. Only the channels with production of three pions and the η production far above the threshold cause some difficulties. It will be examined whether an adjustment of the radius parameter R or the use of an energy dependence for Θ different from (1) can still improve the situation.

In the present context, the channels with strangeness production are of special interest. They are satisfactorily reproduced. The production of two neutral kaons can be expected to be similar to the creation of a K^+K^- pair due to the like masses of the involved particles. Since the calculated curve for $2K^o$ production is in excellent agreement with the data points, it can be hoped that the prediction made for the energy dependence of inclusive $pp \rightarrow K^-X$ production is not so far from the reality. The K^- production channel will be more thoroughly discussed in the next section.

4. Production of K^- mesons in proton-nucleus collisions

After having verified that meson production in the elementary *pp* process can be reasonably described in the framework of the modified phase-space model, we consider in a next step K^+K^- production in *pA* collisions. We concentrate on the lightest nuclear target, the deuteron, and compare the results to an additional calculation for carbon.

In Fig. 3 the calculated inclusive K^+K^- cross sections at hydrogen and deuterium are plotted. We see that the cross section shows the expected steep decrease when the energy approaches the threshold for the considered reaction. For the deuterium target the region between the *pd* threshold at 1.7 GeV and the *pp* threshold at 2.5 GeV is the so-called subthreshold region, which can be populated only via nuclear effects. The Fermi motion of the nucleons is taken into account by applying the Paris deuteron wave function[10] to describe the momentum distribution of the spectator in quasi-free collisions. The other principal reaction mechanism is, in the present approach, called cluster excitation and includes all processes with both nucleons of the deuteron participating in the interaction. Such processes may proceed, for example, via multiple NN collisions, the appearance of

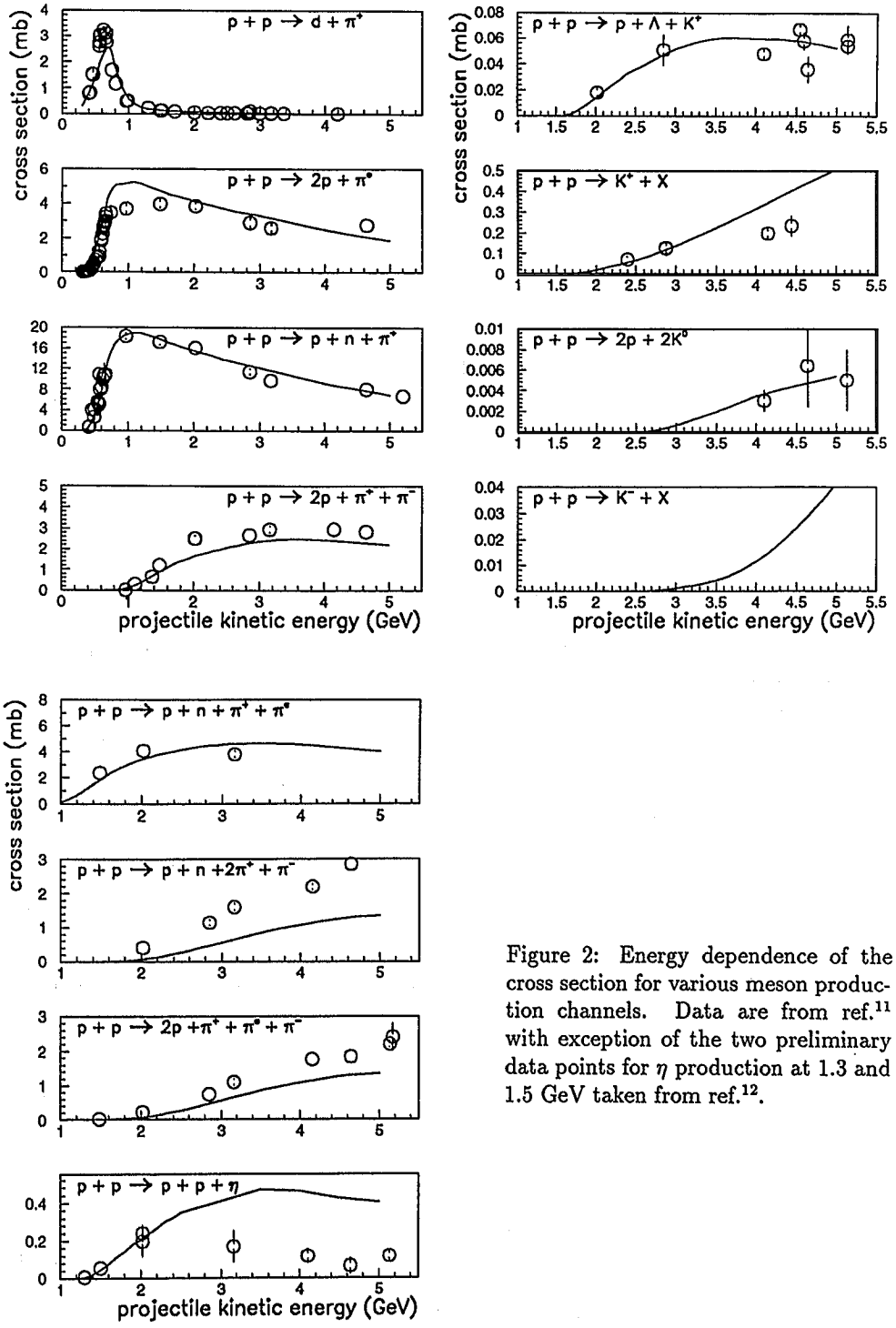

Figure 2: Energy dependence of the cross section for various meson production channels. Data are from ref.[11] with exception of the two preliminary data points for η production at 1.3 and 1.5 GeV taken from ref.[12].

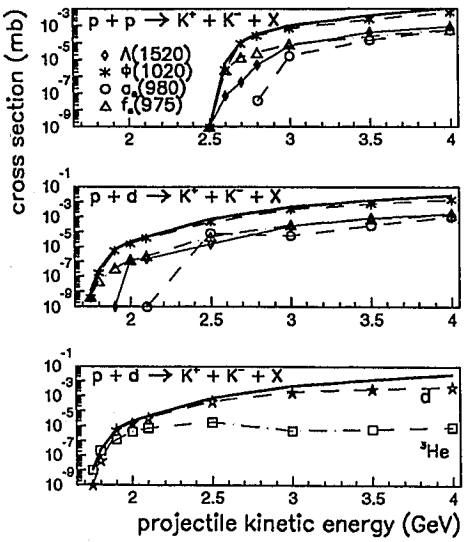

Figure 3: Energy dependence of the cross section for inclusive production of K^+K^- pairs in pp and pd reactions. Additionally, in the upper two figures the partial cross sections for K^+K^- production via resonances, and in the lower figure the cross sections for associated production of light fragments are plotted.

virtual particles in intermediate states or due to the presence of a six-quark component in the deuteron wave function. An exact treatment of such processes is rather involved and connected with many uncertainties. Therefore, all these details are neglected and a cluster of nucleons is treated as an entity, which interacts in the same way as a hadron.

Among the many aspects of subthreshold reactions we want to discuss here the associated production of light fragments and the production of K^- mesons via resonances. Recent measurements[13] of the threshold excitation function in the $pd \rightarrow {}^3HeX$ reaction at Saturne show a clear enhancement at the Φ threshold and small signals at the $K\overline{K}$ thresholds. These investigations are restricted to the threshold region. It would be interesting to measure the correlation between the K^+K^- pair and light fragments in a larger energy range. From the calculation presented in the lower part of Fig. 3 it can be expected that up to about 100 MeV above the threshold there is a large probability that the produced K^+K^- pair is accompanied by a ${}^3He$, while at higher energies the deuteron becomes the dominating particle. The production of the $K\overline{K}$ pair consumes so much energy that no energy is left for the relative motion of the remaining particles, and a bound state is favoured. A more refined inclusion of dynamical aspects of the production process may be expected to modify the strength of the effect. Thus, a measurement of the excitation function of K^+K^- production correlated with light fragments is of great interest for the understanding of the subthreshold reaction mechanism.

Another interesting point is the question whether the $K\overline{K}$ pair is created directly or via resonances. This question becomes even more difficult, because the nature of the involved resonances is not well established at present. This concerns especially the $f_o(975)$ and the $a_o(980)$ resonances. In agreement with the latest particle review[1] these two resonances

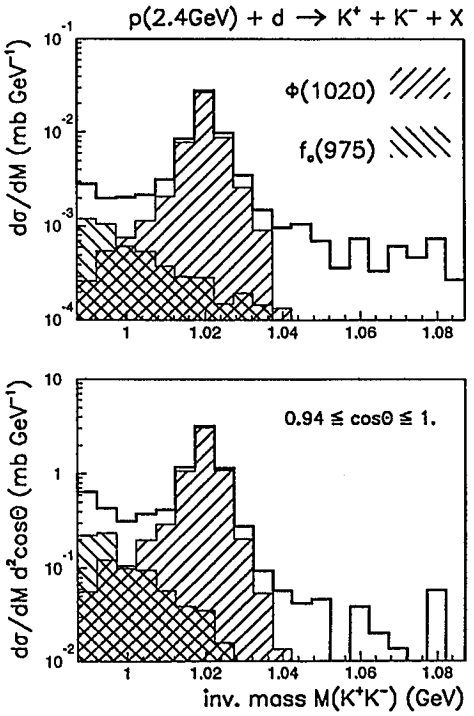

Figure 4: Invariant mass spectrum of K^+K^- pairs produced in pd interactions at 2.4 GeV.

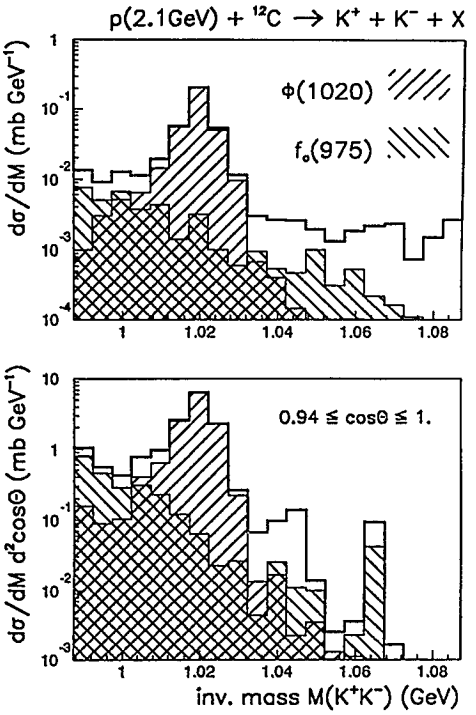

Figure 5: Invariant mass spectrum of K^+K^- pairs produced in pC interactions at 2.1 GeV.

are treated as usual $q\bar{q}$ quark-model states. For the estimate of the total cross sections this uncertainty is not so important, because K^+K^- production via the $\Phi(1020)$ meson yields the main contribution to the $pp \to K^+K^-X$ as well as to the $pd \to K^+K^-X$ cross section (see Fig. 3). In the vicinity of the threshold about 80-90% of the K^+K^- pairs are created via resonances ($a_o, f_o, \Phi, \Lambda(1520)$). This portion decreases to about 60-70% around 4 GeV.

In order to prove these theoretical estimates the invariant-mass spectrum must be measured. This is a task for which the planned 0° Facility[14] at COSY is well suited. In the Figures 4 and 5 model predictions are shown, where pd interactions at 2.4 GeV are compared with pC interactions at 2.1 GeV, and a "4π geometry" is contrasted with a "forward" geometry similar to that of the 0° Facility. In all cases the Φ peak is well pronounced sitting on a background from the broad f_o resonance. Large invariant masses are cut in the forward geometry, but the resonance region remains undisturbed.

In the case of the K^- production via the $\Lambda(1520)$ resonance an experimental verification of the yield of this channel is difficult, as demonstrated in Figs. 6 and 7. The signal from the decay of the $\Lambda(1520)$ into K^-p is weak compared to the associated production of K^- and p via all the other channels.

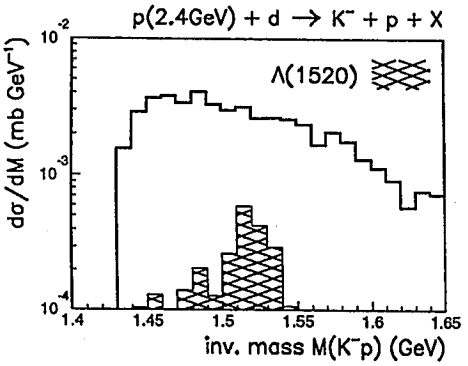

Figure 6: Invariant mass spectrum of K^-p produced in pd interactions at 2.4 GeV.

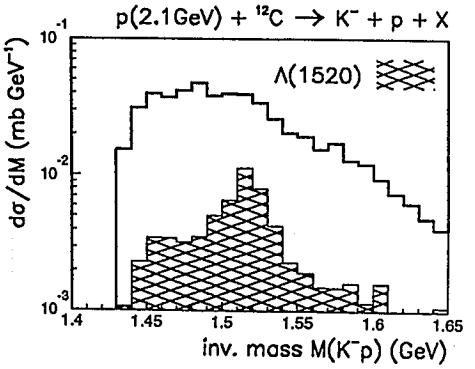

Figure 7: Invariant mass spectrum of K^-p produced in pC interactions at 2.1 GeV.

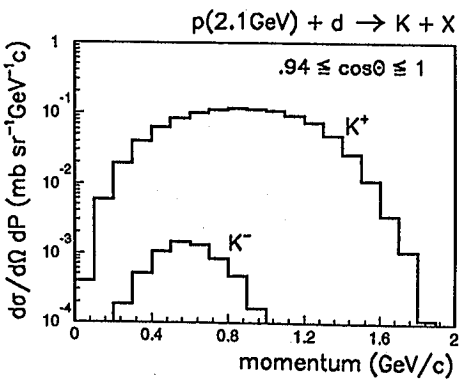

Figure 8: Inclusive momentum spectrum of K^+ andK^- mesons produced in pd interactions at 2.4 GeV.

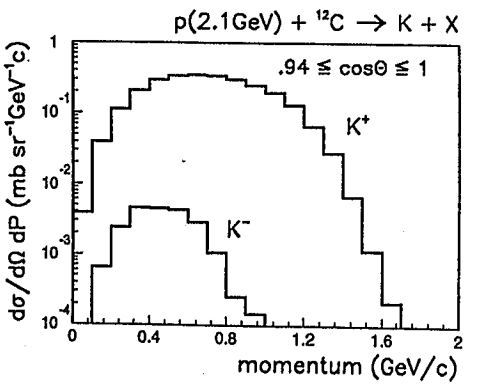

Figure 9: Inclusive momentum spectrum of K^+ andK^- mesons produced in pC interactions at 2.1 GeV.

In conclusion, in Figs. 8 and 9 examples of calculated momentum spectra for K^+ and K^- mesons are shown. Such cross sections are necessary for an estimate of the expected counting rate at a given incidence energy. Moreover, it is expected that an investigation of subthreshold K^- production at the 0° Facility will be started by measuring this type of spectra.

5. Conclusions

At the planned 0° Facility a simultaneous measurement of positive and negative particles emitted in forward direction will be possible. This is a prerequisite to the investigation of subthreshold production of K^+K^- pairs. Interesting questions are the associated production of light fragments and the production via resonances. The use of the lightest nuclear target, the deuteron, offers the best chance to understand the reaction mechanism.

Cross sections for the planned measurements are predicted in the framework of the modified phase-space model, which is implemented such that complete events are sampled. These events can be used as input in a detector response package like GEANT in order to optimize the experimental arrangement. Such calculations will be carried out in near future.

References

1. M. Aguilar-Benitez et al., *Phys. Rev.* **D45** (1992) Part 2
2. A.V. Efremov et al., *Yad. Fiz.* **47** (1988) 1364
3. H. Müller and K. Sistemich, *Z. Phys.* **A344** (1992) 197
4. V. P. Koptev et al., *Zh. Ehksp. Teor. Fiz.* **94** (1988) 1
5. H. Müller, *Z. Phys.* **336** (1990) 103
6. H. Müller, *Z. Phys.* **339** (1991) 409
7. V.V. Anisovich, V.M. Shekhter, *Nucl. Phys.* **B55** (1973) 455
8. E. Byckling, K. Kajantie, *Particle kinematics* (New York, London, Sydney: Wiley 1973)
9. A. Wroblewski, *Acta Phys. Pol.* **B16** (1985) 379
10. M. Lacombe et al., *Phys. Lett.* **101B** (1981) 139
11. V. Flamino et al., *Preprint CERN-HERA* **84-01** (Geneva 1984)
12. E. Chiavassa et al., *Sixiémes Journées d' Études Saturne* (Mont Sainte Odile, 1992)
13. R. Wurziger, *Sixiémes Journées d' Études Saturne* (Mont Sainte Odile, 1992)
14. W. Borgs et al., *COSY Proposal #18* (1991)

THRESHOLD MEASUREMENTS AT THE EXPERIMENT COSY - 11

Walter Oelert*

Institut für Kernphysik, Forschungszentrum Jülich, D - 5170 Jülich, Germany

* *representing the COSY - 11 collaboration (1) at COSY-Jülich*

Abstract

COSY - 11 is an internal target experiment presently being installed at the cooler ring COSY-Jülich, using a cluster target in front of one of the C - type dipole magnet. The magnetic field separates and momentum analyses reaction products from the circulating beam.
It is proposed to scan relevant momentum regions via the pp $\rightarrow$ ppX reaction and to observe the structure of resonances by missing mass determination. A detection of decay particles from particular resonances (e.g. $f_0(975)$) should support its identification and enable to determine its internal structure.
The vanishing relative momenta between the reaction products make threshold studies an ideal tool to investigate meson-meson, meson-baryon, and nucleon-baryon final state interactions. The special emphasis of the COSY - 11 experiment is the observation of narrow resonances especially in the 1 GeV/c^2 mass range where flavour strangeness becomes important.

I. Introduction

A proton cooler ring like COSY-Jülich (2) permits investigations on meson production and meson spectroscopy, reaction dynamics and final state interactions among mesons and nuclei in their ground state and/or excited states, decay features and two step reaction processes in the nuclear target.

In the Standard Model of particle physics the major difficulty arises due to the self coupling of the gluon force field resulting in the fast running coupling constant. At high four-momentum transfer this coupling constant leads to the asymptotic freedom, whereas at low momenta QCD predicts a strong increase of the coupling constant resulting in infrared slavery. Thus, confinement prevents an unburdened insight into that part of physics which is of special interest, since nature is made out of hadrons which are subject to forces with ranges in the order of hadronic dimensions.
Beyond the naive quark model, QCD theory expects that other quark - gluon combinations should exist as hybrids, glueballs and $q\bar{q}\,q\bar{q}$ states. Thus mesonic objects with quantum numbers as $J^{PC} = 0^{--}$ or 1^{-+} or charge $Q = 2$ would indicate exotic hadronic structures. However, in the search for such exotic hadrons it should be re-

alized that the simple meson spectroscopy as evaluated in the u, d, and s - quark antiquark triplet of flavour SU(3) can tell us much about the nature of quark confinement.

In the conventional picture two spin s = 1/2 quark antiquark objects combine, generally described in the framework of a phenomenological potential derived within the QCD, to spin S = 0 or S = 1 which couples to the orbital angular momentum L between these two quarks, forming the meson. Thus, parity and charge conjugation of mesons are assigned to: $P = (-1)^{L+1}$ and $C = (-1)^{L+S}$
restricting these particles to the low quantum numbers as:

pseudo-scalar mesons:	$J^{PC} = 0^{-+}$	L = 0, S = 0
vector mesons:	$J^{PC} = 1^{--}$	L = 0, S = 1
scalar mesons:	$J^{PC} = 0^{++}$	L = 1, S = 1
axialvector mesons:	$J^{PC} = 1^{+-}$	L = 1, S = 0

The pseudo-scalar meson - and the vector meson nonet are experimentally confirmed and in textbooks interpreted as members of $q\bar{q}$ multiplets. Indications arose that this conventional interpretation might be too simple; employing an effective quark model description Krewald et.al. (3) recently pointed out that the neutral ρ meson for instance is dominated by a $\pi^+\pi^-$ final state interaction and that the ϕ meson might have as little as only 50% $s\bar{s}$ content. In addition, the quark or even gluon contents of the η and η' mesons are still under discussion.
The p-wave multiplets are even less understood. The f_0 (975) and a_0 (980) mesons are controversially discussed as either being $q\bar{q}$ scalar mesons or being two-quark - two-antiquark states or even being of $K\bar{K}$ molecule structure.
It is essential that more work is needed to firm the picture of mesons and mesonic states and their type of interactions. COSY-Jülich with protons of momenta up to $\simeq$ 3.3 GeV/c and with high precision due to phase space cooling is predestined for such kind of studies. In proton proton interactions single mesons or few meson combinations with masses up to the ϕ meson (1.02 GeV/c^2) can be observed via their production, reaction dynamics and decay. Heavier mass target-projectile combinations allow for heavier mass meson production and might in some cases have the advantage of a clean isospin selection. On the interpretation level of basic reaction dynamics, however, the additional nucleon degrees of freedom complicate the interpretation.
A further attractive feature of high precision cooler ring beams is the threshold production reaction, where the full center of mass phase space is pushed into a small laboratory angle cone. This allows a limited forward detection of ejectiles for a complete exclusive measurement. In addition, threshold studies are limited to only a few partial waves which might result in an easier interpretation; though, in general, threshold cross sections are rather small.
Free of contamination windowless internal targets (atomic beam or cluster targets) as thin as $\simeq 10^{14}$ atoms/cm^2 can be used in cooler rings, still providing high luminosities up to a few 10^{31}cm^{-2}s^{-1}. This advantageous feature of low target density and high luminosity results in the possibility of studying both atomic electromagnetic and nuclear strong interaction physics (it is known that long range Coulomb interaction can give valuable information about the strong interaction with its much

shorter range). Experiments without the danger of secondary reactions in the target are possible under these circumstances. The development of pellet targets (4) promises even higher luminosities which seem to be essential for rare decay studies. The disadvantage of the beam pipe in an internal target experiment, where no reaction ejectiles can be registered at low angles, might be diminished by using a magnetic dipole system as suggested by the COSY - 11 experiment and as more comfortable available when realizing the 0° - facility (5) at COSY-Jülich.

II. Motivation for Experiments at Small Angles

Based on the concept of Yukawa the baryon - baryon interaction can be described by exchange of mesons. The long range part of the interaction is determined by the π exchange whereas mesons with heavier masses contribute significantly to the

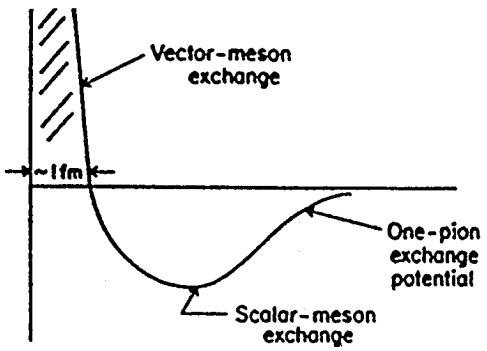

Figure 1:

Schematic view of the nucleon - nucleon potential

interaction at shorter distances, as shown in Fig. 1. At sufficient total energies $\sqrt{s}$ the otherwise virtual exchange-mesons can be produced as real particles on the mass shell. They might propagate between the baryons and/or they can leave the interaction zone consuming the available center of mass (excitation) energy and be observed in an appropriate detector system. Reactions like $pp \rightarrow pp\pi^0$ or $pp \rightarrow pn\pi^+$ or $pn \rightarrow pp\pi^-$ have attracted considerable interest for such investigations (6,7,8) at the new cooler accelerators. Presently, a widely unknown research field of questions opens here, as for instance the determination of the meson - nucleon coupling constants $f^2(i)$, which both experimentally and theoretically (Chew - Low theory) seems to be rather well known for the π - meson (9) but insufficiently known for other mesons.

Furthermore, the heavier mesons determine particularly the short range forces of the strong interaction, a regime where the dualism of one-meson exchange on the one side and quark - gluon descriptions on the other side is still in discussion. Sufficient high beam energies or beam momenta are needed in order to cross the particular meson production thresholds, see Table I. In various models the π, ρ, and ω-mesons are frequently regarded as exchange mesons in the N-N interaction.

In the COSY - 11 experiment we want to restrict ourselves to the study of the threshold behaviour of the (i) "few π mesons", (ii) heavier mesons at about 1 GeV/c^2, and (iii) mesonic state - hadronic and possibly electromagnetic - production, states or resonances with very small widths.

Table I **Masses and threshold parameters for particle production in pp interactions**

meson(s)	mass	threshold P_{beam}	E_{beam}	
	(GeV/c^2)	(GeV/c)	(GeV)	
π^0	0.135	0.777	0.280	
$\pi^\pm$	0.140	0.792	0.290	
$\pi^+\pi^-$	0.279	1.219	0.600	
$\pi^+\pi^-\pi^0$	0.419	1.617	0.931	
η	0.549	1.986	1.258	
$\pi^+\pi^-\pi^+\pi^-$	0.558	2.012	1.283	
($K^0\pi^0$	0.633	2.227	1.478	)*
($K^\pm\pi^\mp$	0.634	2.229	1.480	)*
$\eta\ \pi$	0.688	2.390	1.629	
$\pi^+\pi^-\pi^+\pi^-\pi^0$	0.698	2.418	1.655	
ρ	0.770	2.632	1.856	
ω	0.783	2.670	1.892	
$\eta\ \pi\ \pi$	0.828	2.807	2.021	
$\pi^+\pi^-\pi^+\pi^-\pi^+\pi^-$	0.837	2.836	2.048	
$\rho\ \pi$	0.905	3.043	2.246	
$\omega\ \pi$	0.918	3.083	2.285	
η'	0.958	3.208	2.404	
f_0	0.975	3.263	2.457	
$\pi^+\pi^-\pi^+\pi^-\pi^+\pi^-\pi^0$	0.977	3.269	2.463	
a_0	0.983	3.288	2.481	
K^+K^-	0.987	3.302	2.494	
K^0K^0	0.995	3.327	2.519	
ϕ	1.020	3.404	2.593	

* *due to strangeness conservation not directly producable in* pp → ppX *reactions see chapter II. e.*

Especially two-meson objects are of particular interest, since they are the simplest systems involving the interaction between hadrons. These two-meson $q\bar{q}$ - $q\bar{q}$ combinations open just one additional degree of quark structure complication over the single $q\bar{q}$ meson or qqq baryon.
In the following paragraphs motivations of the planned threshold studies at the COSY - 11 experimental set-up will be briefly presented.

II. a. Meson Production via the Reactions pp → pp+ Meson

Scanning through the excitation function of hadronic collisions the reaction mechanism is intimately connected to the coupling of nuclear degrees of freedom. With

increasing momentum heavier mesons become more and more important as exchange particles mediating the short range part of the strong interaction force. The interpretation of experimental data from IUCF (6) on the basic pion production reaction $pp \rightarrow pp\pi^0$ is directly related to the pion - nucleon dynamics. Calculations of the $pp \rightarrow pp\pi^0$ total cross section at threshold with the final nucleons in a relative S-state including pion rescattering in the πN S-wave and in the P-wave through the Δ (1232) resonance in addition to the direct production underestimate the experimental results by a factor of three to four (10). Similar problems arise from the precise data of $pp \rightarrow pn\pi^+$ measurements (7). Further discussions on this point were given by D. Miller during the present seminar.
The large cross section for the η production in the $pd \rightarrow {}^3He\eta$ reaction observed at SATURNE (11) governed different reaction mechanism speculations. Considerably stronger than in the case of π-production the elementary η production process near threshold is expected to be dominated by the $N^*(1535)$ S_{11} resonance whereas the non-resonant contribution to the η-production is regarded as being negligible on the basis of the weak $NN\eta$ coupling constant. Additional experiments on investigations of this reaction are presently being performed (12) or in preparation (13,14).

The question arises to which extent the meson production is a cooperative process where the available energy is at least partly (at threshold totally) converted into the meson mass. In the nuclear collision such cooperative effects might be due to both nucleon correlations and quark dynamical effects in coherent productions via gluonic intermediate states. In the nucleon collision "only" the quarks of the two nucleons act in producing a new meson. In this framework investigations of production strength and production dynamics of heavier mesons are of special interest, since they probe the elementary $q\bar{q}$ production including different flavours.
For such three body final state reactions as $pp \rightarrow ppM$ the interaction between two of the final state particles can be controlled by choosing their relative momenta in appropriate scales. This possibility should be a powerful tool to study final state interaction effects. Resulting from the PS185 collaboration at CERN such investigations have been performed via the $\bar{p}p \rightarrow \bar{\Lambda}\Lambda\pi^0$ reaction, as shown in Fig. 2 (15).

Though the set-up of the COSY - 11 experiment is certainly optimum for meson production close to threshold, the interesting field of meson decay studies should at least be mentioned here as a further experimental extension at COSY-Jülich.
Isgur (16) pointed out that within the constituent quark model the transition rate between ground states of vector meson and pseudo-scalar meson nonets as

$$\rho \rightarrow \pi\gamma \text{ or } \rightarrow \eta\gamma, \qquad \omega \rightarrow \pi\gamma \text{ or } \rightarrow \eta\gamma, \qquad \phi \rightarrow \pi\gamma \text{ or } \rightarrow \eta\gamma \text{ or } \rightarrow \eta\gamma$$

should be firmly predictable in QCD theory on lattice calculations. Relevant investigations of these transitions are regarded to be especially important since the transition amplitudes determine the relative meson quark contents. Nefkens (17) gives a strong pledge on the opportunities being available for probing the Standard Model of particle physics and testing chiral perturbation theory of low energy QCD by measuring decay modes of light mesons with high precission.

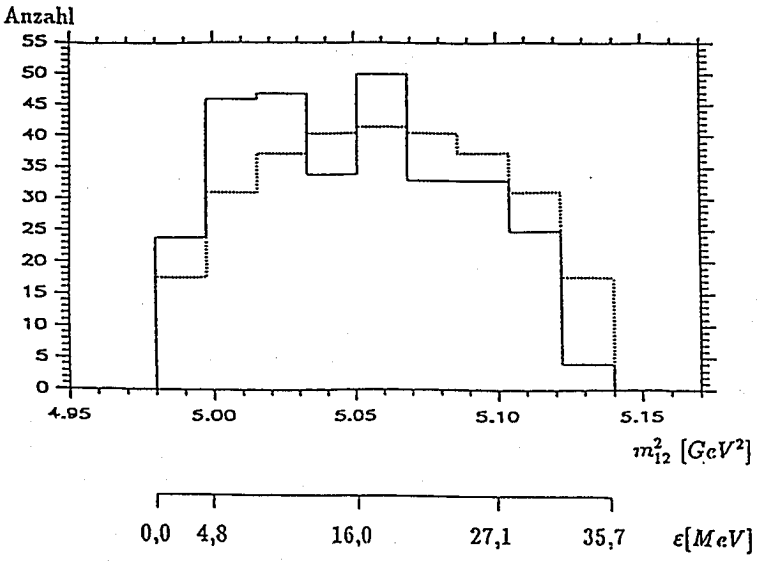

Figure 2:
Experimental data (solid line) and phase space calculations (dotted line) of the $\bar{p}p \rightarrow \bar{\Lambda}\Lambda\pi^0$ reaction at 1.919 GeV/c antiproton momentum. An enhancement of production yield over the phase space distribution is observable at excess energys $\varepsilon \leq$ 12 MeV/c^2

II. b. Production of Mesonic States

The repulsive core of the nucleon-nucleon system complicates the exploration of its full six quark structure due to quark exchange effects (18). Thus, an understanding of rather simple two-quark - two-antiquark object as the simplest non-natural hadronic system would be a challenge in low energy hadron physics. In addition, Isgur (16) pointed out that the $qq\bar{q}\bar{q}$ system is a more readily accessible variety since e.g. the $\pi^+\pi^+$ and $\pi^+\pi^-$ combinations have very different quark exchange characteristics.

Reaction mechanisms for double pion production are displayed in Fig. 3, and can either involve two Δ isobars, or an N* having reasonably large probability for $N\pi\pi$ decay fractions like the P_{11} (1440 MeV) resonance (30 - 50 %).

Figure 3:
Reaction mechanisms for double pion production

In case the $\pi\pi$ interaction is considered to be of largest interest, those kinematical situations should be selected where the relative pion momenta are minimal. In addition, the low energy $\pi\pi$ interaction seems to have some strong attractive but non-resonant components, since enhancements of low invariant $\pi\pi$ mass pairs have been reported in various experiments, including the "ABC"-effect (19) and meson decays as $\eta' \rightarrow \eta\pi^+\pi^-$.

II. b. 1. Mesons in the Range of 1 GeV/c²

The mesons η', f_0, a_0 and ϕ are of special interest, since their structure of valence quarks involves strange quarks, and since they decay strongly into two mesons:

$\eta' \rightarrow \pi^+\pi^-\eta$ (44.1 %) $\qquad$ $f_0 \rightarrow \pi\,\pi$ (78.1 %), $K\overline{K}$ (21.9 %)

$a_0 \rightarrow \eta\,\pi$ (seen), $K\overline{K}$ (seen) $\qquad$ $\phi \rightarrow K^+K^-$ (49.1 %), $K^0_LK^0_S$ (34.4 %), $\rho\pi$ (12.9 %)

Thus the production dynamic of these mesons is of fundamental nature. Especially, investigations of the meson production at the reaction threshold appears to be appropriate in view of the sea-quark structure and its dynamical contribution to the nucleon.

Interpretations suggest that the f_0 meson (former notation S*) is in reality two close and narrow states where one of them contains $s\bar{s}$ - quarks, the other should be a flavour singlet which couples to $\pi\pi$ and $K\overline{K}$ with similar strengths. The discussion on possible gluonium candidates is still alive. Thus, some of these mesons - supposed to have widths in the order of 30 MeV/c² - could well exhibit an overlay of structures with much smaller widths. Another feature of these resonances is their decay into the $K\overline{K}$ channel if $\sqrt{s}$ is larger than the equivalent center of the resonance. This fact could suggest a hadronic $K\overline{K}$ nature of the resonances which in particular couples to an atomic structure as a kaonium.

II. b. 2. Arguments in Favour of a $qq\bar{q}\bar{q}$ Interpretation

In the following we will concentrate on a particular discussion of the scalar mesons f_0 and a_0 which are difficult to accommodate as $^3P_0$ $q\bar{q}$ states. Already in 1977 Jaffe (20) deduced in the bag model from colour hyperfine interactions a low-lying "cryptoexotic" nonet of $qq\bar{q}\bar{q}$ states and suggested to identify f_0 and a_0 as members of that nonet. In Fig. 4 the picture of a deformed $q^2\bar{q}^2$ state, with colour representations and vectors of angular momenta, as suggested in (20) is shown.

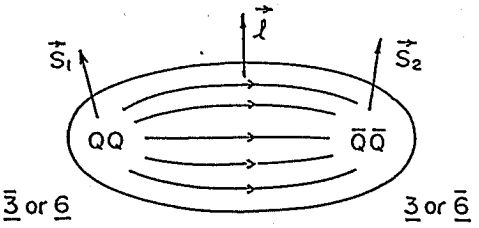

Figure 4:

Deformed $q^2\,\bar{q}^2$ state

The main argument in favour of the a_0 as a $qq\bar{q}\bar{q}$ state interpretation is its almost complete degeneracy in mass with the isoscalar $f_0(975)$, together with the observation that the $f_0(975)$ couples much more to the K-$\overline{K}$ than to the π-π system.

II. b. 3. Arguments in Favour of $q\bar{q}$ and Gluonic Nature

Close (21) summarized the discussion of the literature in this mass range that "two pieces of circumstantial evidence for a gluonic component have recently emerged. The process $\Psi \rightarrow \phi\,\pi^+\pi^-$ is doubly forbidden by the OZI rule (see Fig. 5 left) and thereby offers a good glueball signal: $\Psi \rightarrow \phi G$; $G \rightarrow \pi^+\pi^-$. The S*(975) is a sharp and clear bump in the $\pi^+\pi^-$ invariant mass spectrum.

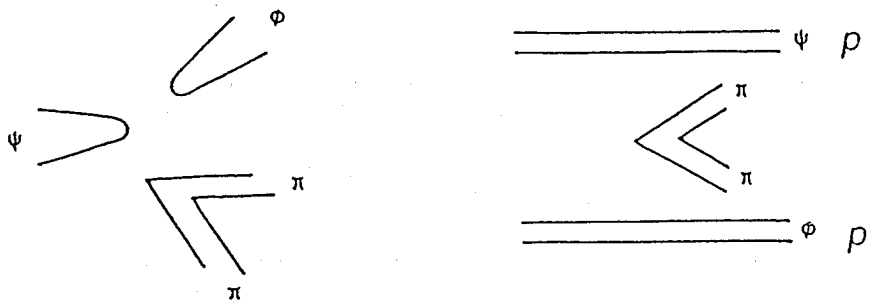

Figure 5:
OZI forbidden diagram of the process: $\Psi \rightarrow \phi\,\pi^+\pi^-$ (left)
and the suggested diagrams:
hypothetical $\Psi\phi \rightarrow \Psi\phi + \pi\pi$, realistic $pp \rightarrow pp + \pi\pi$ (right)

Twisting the diagram of Fig. 5 (left) for $\Psi \rightarrow \phi\,\pi^+\pi^-$ around one would expect similar structures to show up in the hypothetical $\Psi\phi \rightarrow \Psi\phi + \pi\pi$ diagram or the realistic central region in pp collisions: $pp \rightarrow pp + \pi\pi$(Fig. 5 right). Data on this reaction have been taken (22) and analysed by Au et al.(23). There is clear indication of the S* presence as a shoulder in the data. The data quality is such that Au et al.(23) resolve two signals in the S* region; S(988) contains $s\bar{s}$ quarks whereas S(993) is a flavour singlet (coupling to $\pi\pi$ and $K\bar{K}$ with similar strengths) and a possible gluonium candidate." In an early analysis three resonance poles were claimed in the 1 GeV/c^2 mass region resulting from a K-matrix coupled $\pi\pi$ and $K\bar{K}$ channel formalism (24). A more recent similar analysis (25) using ISR data on central π production (26) as well as DM2 and MARKII results on $J/\Psi(1S) \rightarrow \phi\pi\pi$, $\phi K\bar{K}$ and photoproduction data on $D_s \rightarrow \pi\pi\pi$ disfavours a $K\bar{K}$ molecule interpretation of the $f_0(975)$.
Albrow (27) pointed out that the former S* now $f_0(975)$ meson has been considered to be essentially a bound state of two neutral kaons, however, a recent analysis concludes that a single narrow resonance is not enough to fit the data, the f_0 should be two close and narrow states in reality. One (988) is likely to be a bound state of neutral kaons, the other (991) couples equally to pion and kaon pairs, as expected for a glueball.

II. b. 4. Arguments in Favour of $K\bar{K}$ Molecule Structure

Calculations based on variational considerations of the $qq\bar{q}\bar{q}$ state followed by a mapping onto a coupled channel meson meson scattering problem indicate a $K\bar{K}$ molecule like structure of these resonances (28). Weinstein (29) compares the Breit-Wigner line shape of a 600 MeV wide $f_0(1300)$ with a 34 MeV wide $f_0(975)$ (upper part of Fig. 6) and a 400 MeV wide $a_0(1300)$ with a 57 MeV wide $a_0(980)$ (lower part of

Fig. 6). Thus the discrepance between naive quark model considerations and the f_0 and a_0 features become clearly visible.

In addition, the elastic I = 0 $\pi\pi$ phase shift from a coupled channel equation (30) is compared to experimental data in Fig. 7 and demonstrates a good reproduction of the major experimental features.

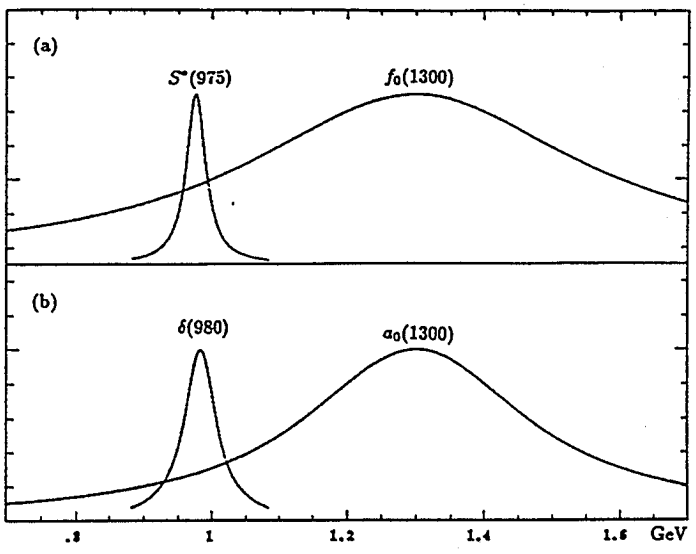

Figure 6:
Comparison of Breit-Wigner line shapes for different mesonic states, in order to demonstrate the difference between naive quark model predictions and features of the $f_0(975)$ and $a_0(980)$

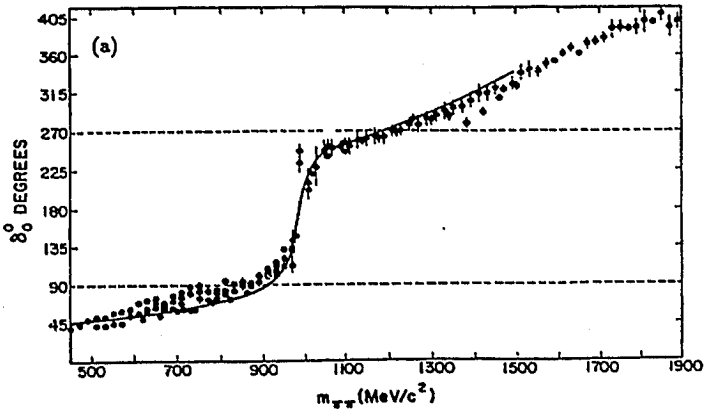

Figure 7:
The elastic I = 0 $\pi\pi$ phase shift from a coupled channel equation is compared to experimental data

Further, equivalent indications - as shown during the present seminar by Speth - result from coupled channel calculations of π-π scattering (31). Accordingly, the sharp rise of the phase shift at about 980 MeV is due to a strong coupling of the π-π to the K-$\overline{K}$ channel with an interaction via vector meson exchange.
If the 988 MeV/c^2 meson could be regarded as a bound state of neutral kaons with mass:
2 × mass K_0 = 995.44 MeV/c^2
a well separated equivalent K^+K^- bound state
mass K^+ plus mass K^- = 987.34 MeV/c^2
would be expected. More speculative, are there hadronic molecular charged combinations like $K^+\overline{K}^0$ or K^-K^0?

II. b. 5. Recently Available Data

Further arguments on the nature of scalar mesons at about 1 GeV/c^2 can be found in the Review of Particle Properties (32). Due to insufficient statistics a recent study of $f_0(975)$ production from Υ decay (33) cannot distinguish between a $q\overline{q}$ or a $K\overline{K}$ structure. Based on the presently available data arguments for both interpretations can be deduced from the data.
In addition, measurements at high momenta in γp, $\pi^{\pm}$p and $K^{\pm}$p reactions (34) result in cross section ratios relative to the corresponding ρ^0 production which according to the authors suggest the normal $q\overline{q}$ structure of the $f_0(975)$ meson.

Thus we are faced with the basic question of hadron spectroscopy to learn about the confinement mechanism of QCD and its prediction for the spectrum of mesons (hadrons) which is far richer than in the simple quark model and where even hadronic states without quark content are postulated as gluonic excitation of matter. A systematic study of the low energy meson-meson interaction is needed. These studies should produce $\pi\pi$, πK, $\pi\eta$, $\pi\eta'$, $\pi\rho$, $\pi\omega$, $K\overline{K}$, ηK etc. as isolated as possible from other hadronic states. COSY - 11 is constructed for measuring precise data on these topics. The planned physics would certainly profit from the adventure of the 0°-facility (5) due to its larger geometrical acceptance and higher flexibility.
A discovery of an additional state beyond those of the quark model - as known in the conventional nonets - would be an obvious candidate for a special state from those predicted by QCD as : four quark states, mesonic molecules, hybrids or even possibly glueballs.

Investigating reactions of the three body final state type pp → ppX might lead to X being one neutral meson or two mesons with zero net charge; whereas in the case of the pp → pnX reaction X is a positive charged system. Especially at the production threshold with two formed mesons involved in the final state, these then are distinguished by a very small relative momentum. This condition should allow to observe possible meson - meson interactions. Qualitatively similar arguments hold for the two baryons in the exit channel. In case of a π^+ production via the pp reaction the final state interaction could lead to the deuteron as a simple species of dibaryons.

In the following paragraphs some additional ideas for physics cases to be done at a low angle facility will be briefly presented.

II. c. Search for the Dibaryon d'(2.065)

Dibaryons are defined as hadronic objects with baryon number B = 2. On the quark - gluon level of the constituent quark model such structures should have six valence quarks leading to different types of dibaryons with increasing exotic degrees:

(i) bound states of two B = 1 baryons as: N, N*, Δ, Λ, ..., Ω, ...
(ii) objects containing six valence quarks in clusters as: q^6, q^5q^1, ... $q^2q^2q^2$ where the single clusters need not to be colour neutral
(iii) objects containing valence quarks and antiquarks with the difference between them being six as: $q^{6+n}\,\bar{q}^n$.

During the last decade searches for dibaryon resonances have been extensively performed; their existence has been claimed several times and has been disclaimed with nearly the same frequency (35).
At COSY-Jülich two experimental activities are in preparation reentering these studies. In the kinetic energy range of 250 - 600 MeV and 1.5 - 2.5 GeV spin-averaged and spin-dependent cross sections of the pp interaction are proposed to be measured in small energy steps by the EDDA (COSY - 5) collaboration (36).
A Letter of Intent (37) suggests to examine the threshold range of a dibaryon proposed to exist resulting from interpretations of low energy double charge exchange reactions ($\pi^+\pi^-$) on nuclei. In these experiments an unexpected energy dependence has been observed near the kinetic energy $T_{\pi^+} \simeq 50$ MeV, as displayed in Fig. 8. Furthermore the single charge exchange reaction on ^{14}C reveals an increasing differential cross section, whereas the one for double charge exchange is decreasing in the kinetic energy range T_{π^+} from $\simeq$ 20 MeV to $\simeq$ 100 MeV (38).

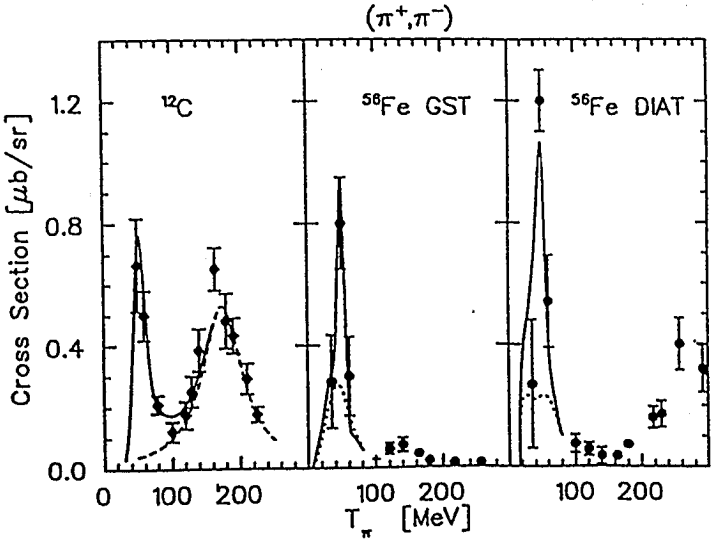

Figure 8:
Double charge exchange reaction ($\pi^+\pi^-$) cross sections on different nuclei

The data imply the existence of a $J^P = 0^-$, $I \neq 1$ resonance at 2.065 MeV (d') with a total width of $\Gamma = 5$ MeV (39). It is suggested to search for the d' dibaryon production in an exclusive measurement at the COSY-TOF spectrometer (40) via the $pp \rightarrow d'\pi^+ \rightarrow pp\pi^-\pi^+$ reaction and to determine the invariant πNN mass.
At COSY - 11 the inclusive measurement $pp \rightarrow d'\pi^+ \rightarrow ppX\pi^+$, where X is not detected but reconstructed by missing mass after measuring the four-momentum vectors of the three charged ejectiles, appears to be promising. Due to the narrow width of the predicted d' resonance the low angle experimental set-up using a COSY dipole should be optimum for measuring the pp excitation function in the d' mass range. The non-resonant background $pp \rightarrow pp\pi^+\pi^-$ is very strongly rejected due to the small geometrical acceptance.

II. d. ρ^+ Production Rate via the $pp \rightarrow d\rho^+$ Reaction

At a Workshop on "Meson Production, Interaction and Decay" Nefkens (17) pointed out the strong importance of studying the reaction $pp \rightarrow d\rho^+$ including the decay of the ρ^+ to $\pi^+\gamma$ in an exclusive measurement. The rate of this particular radiative decay of the (deuteron tagged positive charged) vector meson to a pseudo-scalar meson, a quark spin flip $\rho \rightarrow \pi$ transition, is directly proportional to the magnetic moment of the quarks and thus would measure the (non)-mixing between ρ and ω. Such investigations could contribute to the determination of up and down quark mass differences.
The idea is to produce the ρ^+ via the $pp \rightarrow d\rho^+$ reaction using the Jacobian peak method at 0^0. The ρ^+ should be detected via the decay $\rho^+ \rightarrow \pi^+\pi^0$ which gives a monochromatic π^+ in the C.M. frame. Considering portions of the ρ mass (M = 768 MeV, Γ = 152 MeV) between 700 MeV and 850 MeV one would study the ρ^+ production at the following "threshold" conditions:

$pp \rightarrow d\rho^+$(700 MeV)	at $P_\rho \simeq$ 2.4 GeV/c
$pp \rightarrow d\rho^+$(768 MeV)	at $P_\rho \simeq$ 2.6 GeV/c
$pp \rightarrow d\rho^+$(840 MeV)	at $P_\rho \simeq$ 2.8 GeV/c

Knowing the incident beam four-momentum proton vector and measuring the recoil four-momentum deuteron vector, the invariant ρ^+ mass and its four-momentum vector is determined. These predisposing measurements can be perfectly done at the COSY - 11 apparatus without changes.
The decay of interest $\rho^+ \rightarrow \pi^+\gamma$ again gives a monochromatic π^+ and γ in the C.M. frame, however, a large acceptance π^+ and γ detection must be foreseen for such a study. The background Bremsstrahlung $pp \rightarrow d\pi^+\gamma$ is supposed to have a very small cross section and a $\frac{1}{E_\gamma}$ dependence.

II. e. Are Kπ Final States Observable at COSY?

As discussed above in the two-meson production section, the observation of Kπ final state interaction would be of particular interest.

In strong interactions the K mesons can be produced in the associated strangeness production, as suggested for the COSY-TOF (40) spectrometer. For the production of a Kπ pair the following reaction types can be envisaged:

pp	$\rightarrow$	p	Λ^0	$K^+\pi^0$	with the threshold at P_p = 2.74 GeV/c
pd	$\rightarrow$	pp	Λ^0	$K^+\pi^-$	with the threshold at P_p = 2.13 GeV/c
pp	$\rightarrow$	p	Σ^+	$K^+\pi^-$	with the threshold at P_p = 2.98 GeV/c

Such reactions most likely will suffer from low cross sections, e.g. at 3.47 GeV/c a total cross section of 19μb was reported for the last listed reaction (41).

In the present phase COSY - 11 does not foresee a neutral particle detection in the target region and thus the π^0 will not be measured. The decay of $\Lambda^0 \rightarrow p\pi^-$ will have rather limited geometrical acceptance, but at least in the second reaction it could be reconstructed via a missing mass evaluation.

II. f. Heavier Target - Projectile Combinations

The use of a cluster target would in principle allow for measurements with heavier nuclei, e.g. N_2, CO_2, CH_4, and Ar target beams have been produced (42). In addition, COSY-Jülich will be able to accelerate at least deuterons. This option should be recognized, since some meson production studies can preferably be done in interactions between target-projectile combinations heavier than the pp system. Such studies offer special possibilities to single out some isospin states in the meson-meson system.
Examples of such possibilities are for instance:

$pd \rightarrow {}^3He\pi^0\pi^0$	with isospin I = 0
$pd \rightarrow {}^3He\pi^+\pi^-$	with isospin I = 0 or 1
$pd \rightarrow {}^3H\pi^+\pi^0$	with isospin I = 1
$dd \rightarrow {}^4He\pi^\pm\pi^\mp$	with isospin I = 0

These reaction isospin selection could preferentially be employed when different excitation contributions from resonances should be disentangled in baryon spectroscopy. For illustration the density of baryon resonances is shown in Fig. 9 as taken from Isgur(16).

Another approach for using heavy targets has been suggested by Johansson (43). The ^{12}C nuclear target should be used performing a proton capture experiment resulting in the ground state of ^{13}N. Since this nucleus does not have a particle stable excited bound state the recoil measurement of p(^{12}C, ^{13}N)X is unique for the production of mesons like η(549) and η'(958). In addition to the interest in the production cross section itself, a η and η' decay study via secondary reactions on nucleons of the target, as suggested by Roderburg on a deuteron target in the COSY - 12 experiment (13), could help to disentangle the quark content of these SU(3) octet singlet pseudoscalar meson quark antiquark combinations.

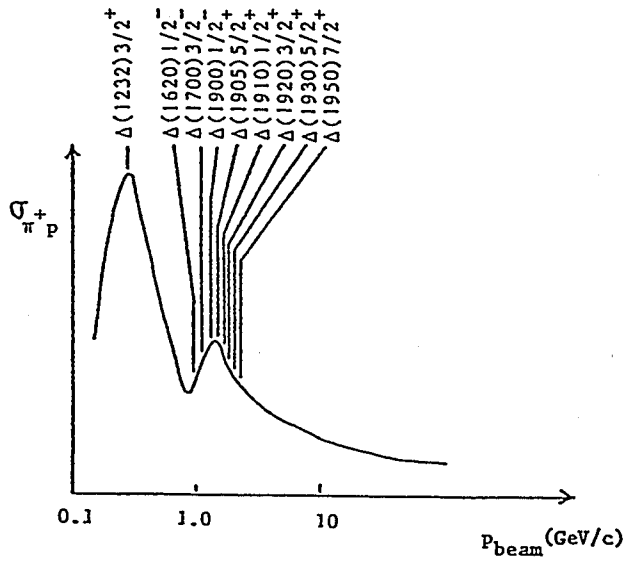

Figure 9:

One of the lessons of baryon spectroscopy as seen by Isgur (16)

II. g. Electromagnetic Interaction Forming Two-Meson Atomic States

Opposed to the hadronic meson-meson interaction experimental observation of two-meson atomic states has not been reported (44). From antiprotonic atoms it is well known that shifts and broadening of low lying atomic energy levels and changes of their life times can be mediated by the short range strong interaction and thus giving valuable informations.
Traditionally, π-π scattering has been studied indirectly via final state interactions in the $\pi N \rightarrow \pi\pi N$ reaction. Probably due to the intrinsic difficulty of such measurements it is observed that different experiments are not always consistent and furthermore that the extracted informations are model dependent.

Recently ideas have been discussed (45,46) to produce pionium $(\pi^+\pi^-)$ in the $pd \rightarrow {}^3He\ (\pi^+\pi^-)_{atom}$ reaction. Predominantly the $\pi^+\pi^-$ atom decays to $\pi^0\pi^0$ and with much less probability to $\gamma\gamma$. Wycech and Green (47) evaluated signals relevant for a production of atomic states as pionium $(\pi^+\pi^-)$, kaonium (K^+K^-) and a $K^+\pi^-$ system, distinguishing between production in S- and P-wave states.
A recoil energy distribution measurement for identifying the atomic state has been suggested (45). A single ^{3}He spectrum should be able to distinguish between the free $\pi^+\pi^-$ pair production (threshold energy at 430.492 MeV) and the $(\pi^+\pi^-)^{1S}$ pair production (threshold energy at 430.489 MeV), since the energy of the recoiling ^{3}He nucleus changes rapidly, close to threshold in the $pd \rightarrow {}^3He\pi^+\pi^-$ reaction. For both processes all of the ^{3}He particles will recoil into a very small forward cone of $\leq \pm 0.1°$(45). As we learned by Miller during the present workshop, the experimental plans tend to change in the sense of measuring additionally the $(\pi^+\pi^-)_{atom}$ decay into two π^0's which then decay into $\gamma\gamma\ \gamma\gamma$.

Under very optimistic experimental conditions with a resolution of 70 keV the signal to $\pi^0\pi^0$ background ratio (48) would only be $\simeq$ 1% due to the few eV pionium line width. As discussed above, the $K^+\pi^-$ atomic state is very difficult to be generated. Whereas the width of $\pi\pi$ and $K\pi$ atoms is supposed to be about 0.2 eV the KK width is 480 eV, making the possibility of observing K^+K^- atoms somewhat larger (48). In addition, the basic mechanism for creating the K^+K^- atom is enhanced, since it appears via scalar $f_0(975)$ and $a_0(980)$ resonances.

III. Principle of the Experimental Set-up

Several features of the COSY ring installation serve for a measurement of the production reaction pp $\rightarrow$ ppX at threshold, with X being one or a few mesons. The high beam quality in a cooled beam mode operation together with the C-type dipole magnet allows the use of an internal target station in front of the magnet.

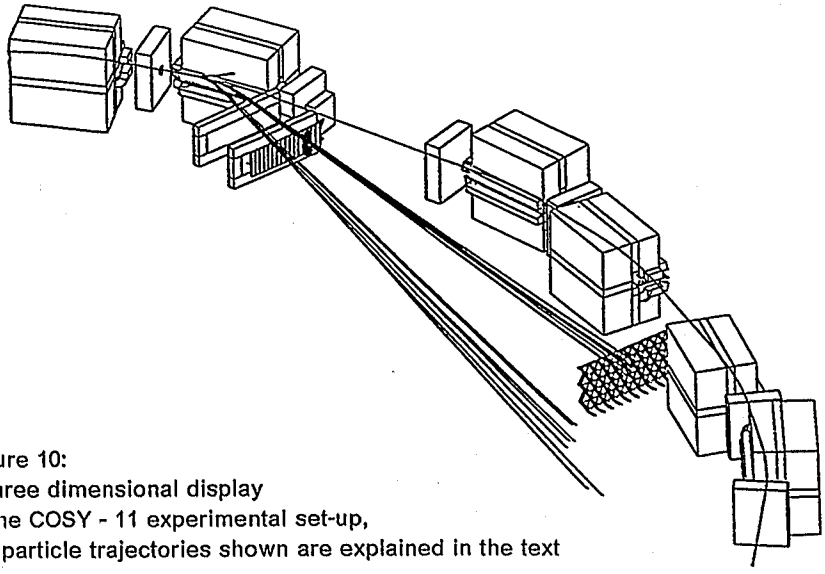

Figure 10:
A three dimensional display
of the COSY - 11 experimental set-up,
the particle trajectories shown are explained in the text

Resulting from compromises between the need of measuring at 0°, the need of high luminosity employing thin targets, and the need of optimizing available resources the COSY - 11 collaboration proposed to use a regular COSY dipole for both separating the ejectiles from the beam and using the dipole for the determination of momenta of reaction ejectiles. Certainly these compromises lead to restrictions which are less severe using the more flexible 0°-facility (5) foreseen to be built at COSY, as presented during the present seminar. In fact, it is envisaged that the COSY - 11 physics case will be continued at the 0°-facility when being available.

In the following single components of the COSY - 11 set-up will be presented briefly. Depending on the sign of their charge the reaction products will be bent out of the COSY beam trajectory as shown in the three dimensional Fig. 10. The reaction

$pp \rightarrow ppK^+K^-$ is chosen as an example, the calculations have been performed with a beam momentum 2 MeV/c above the threshold at 3.3016 GeV/c. The separation of the four ejectiles p, p, K^+, and K^- to

(i) K^- with short tracks leading into the magnet
(ii) K^+ with tracks passing through two drift chamber stacks and a scintillation detector arrangement just behind the second stack, and
(iii) the two protons with tracks again passing through the two drift chamber stacks, the scintillation detector arrangement behind them providing a start signal and (after 9 meters) a large scintillation detector providing a stop signal, in order to measure the time of flight

is clearly displayed.

Figure 10 shows only partly the essential components of the COSY - 11 experiment, these are: the magnet, the vacuumchamber, the cluster target, the detector system, and the data acquisition; in addition, the beam conditions at the target station and the geometrical acceptance will have significant influences on the features of the expected data.

III. a. Magnet

In the COSY - 11 experiment the magnetic field of a regular COSY dipole is used for ejectile separation. Consequently, the field cannot be adjusted to the optimum conditions for a particular reaction, a feature which is foreseen at the 0^0-facility (5), but has to be used as given by the accelerator conditions. Since the field will be used for reconstructing the particle four-momentum vectors its precise knowledge is essential. Figure 11 shows field mappings for three different amplitude values perpendicular to the beam direction (49), together with the center beam pipe part of the magnetic set-up at the top of the figure. In the chosen coordinate system the beam center circulates at position $x = 0$ mm, at $x = -215$ mm is the end of the iron yoke and the coils range up to $x = -370$ mm. In the gap between the upper and lower coil an average fringe field of $\geq 0.3 \times B_0$ still exists. In a later stage the collaboration intends to fill this volume with gas wire counters depending on experiences with the presently foreseen set-up.

III. b. The Vacuum Chamber

A major technical challenge is the construction and production of the vacuum chamber. Inside of the chamber the ultra high vacuum is required for beam preparation, whereas the particle detectors are placed outside in normal atmosphere. The separating window should be as thin as possible. Figure 12 shows the drawing (50) of the arrangement in a top view between the two quadrupoles before and after the dipole in use. The vacuum chamber has four places for particle detection: a) a thin foil called "Kunststoffolie" for positively charged particles leaving the magnetic field on its long side, b) a thin foil called "Metallfolie" for positively charged particles leaving the magnetic field in forward directions close to the beam pipe, c) a foil called "Metallfolie" for negatively charged particles leading into the magnet, this foil is fol-

lowed by scintillation and silicon detectors, and d) a foil close to the cluster target for measuring the recoil protons of elastically scattered protons in the pp-interaction, in order to calibrate and align the whole COSY - 11 detector arrangement. Presently the vacuum chamber is under construction and should be finished in late summer 1993.

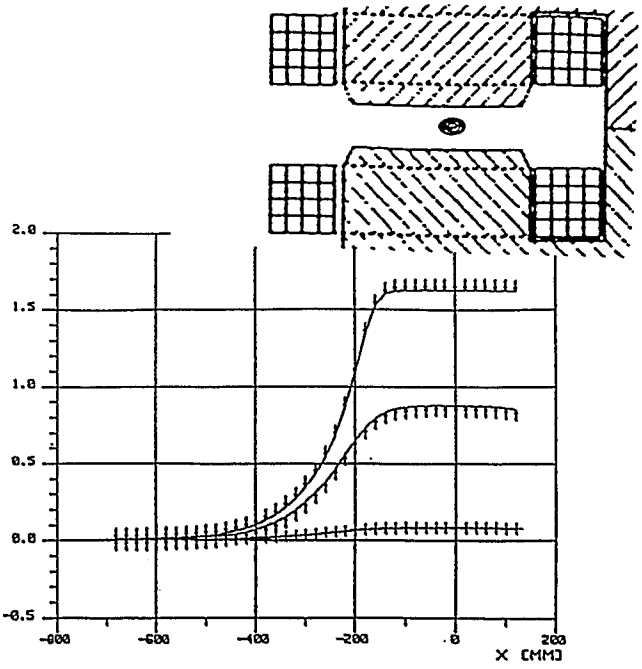

Figure 11:
Magnetic field mappings perpendicular to the beam direction for three different field settings, where the field is measured in Tesla. The COSY beam area center part of the magnetic set-up is shown in the upper part of the figure.

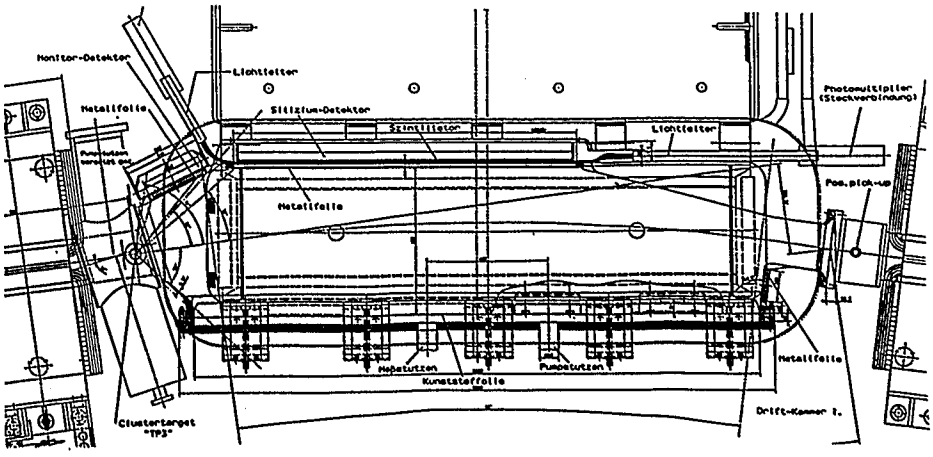

Figure 12: Technical drawing of the COSY - 11 vacuum chamber

III. c. The Cluster Target

The cluster target is under construction (42) and basically finished. Test measurements are presently being performed, details were given at this seminar by D. Grzonka.

III. d. The Detectorsystem

The following detector system will be used, see Fig. 10:

a) Two stacks of each six drift chambers planes separated by 70mm for measuring the direction of positively charged particles, similar detectors have been constructed for the focal plane of the Big Karl magnetic spectrometer. An extensive description of these detector chambers is given in Ref. (50).

b) The drift chambers are followed by an array of 16 scintillation counters each 100 mm wide and 4 mm thick. A further array of ten movable scintillation counters each 12 mm wide and 2 mm thick should be placed thereafter for separate observation of two particles close to each other. For two even closer charged particles a discrimination via signal amplitude is foreseen.

c) After a distance of nine meters a scintillator wall will be placed, designed according to ideas developed at the Physics Institut, University of Bonn (51), which will provide a stop signal for time of flight measurements of the two baryons in the $pp \rightarrow ppX$ reaction.

d) For negatively charged particles two detectors are foreseen inside the magnetic yoke, (i) a long scintillation counter and (ii) a silicon pad array (52) with the dimensions of 4.5×23 mm^2. For the construction of the pad detector we could profit from experience at CERN (53) regarding both the counters and the front-end electronics. Measurements at the test beam of CERN demonstrated the perfect functioning of the system to be used.

e) For particles undergoing less bending in the magnetic field a micro counter set-up is planned placed close to the beam pipe at the front end of the magnet.

f) Finally, for calibration purposes a silicon pad detector arrangement will be installed in order to measure elastically scattered events.

g) In a later stage a neutral particle detector at the front end of the magnet should complete the experimental set-up.

III. e. The Beam Conditions

At the target place TP3 where COSY - 11 will be installed, a cooled beam with $\varepsilon = 1$ πmm mrad is expected (54) with $x_{rms} = 2.9$ mm and $y_{rms} = 3.8$ mm. Since the cluster target beam diameter can be varied between 10 mm and 1 mm the experimental conditions should be optimized for either high luminosity or high resolution.

In agreement to calculations, experience from the Jetset experiment at LEAR/CERN teaches that at a beam momentum of $\simeq$ 1 GeV/c and a target density of 3×10^{13} atoms/cm^2 a beam loss rate of 50 % is observed after 12 h of running.

III. f. Geometrical Acceptance

Due to the experimental set-up in front of a space limiting gap of the dipole a 100 % acceptance will be observed up to an excess energy which is equivalent to $\simeq$1 MeV/c^2 additional mass for the reaction pp $\rightarrow$ pp M only. The produced meson or meson-system M will be identified via the missing mass technique. Further, both negative and positive charged mesons will be analysed depending on the particular conditions with limited acceptance. Figure 13 presents a geometrical acceptance calculation for the case of the pp $\rightarrow$ ppϕ reaction, where the ϕ decays into K^+ and K^- and the beam momentum being 20 MeV/c above the production threshold.

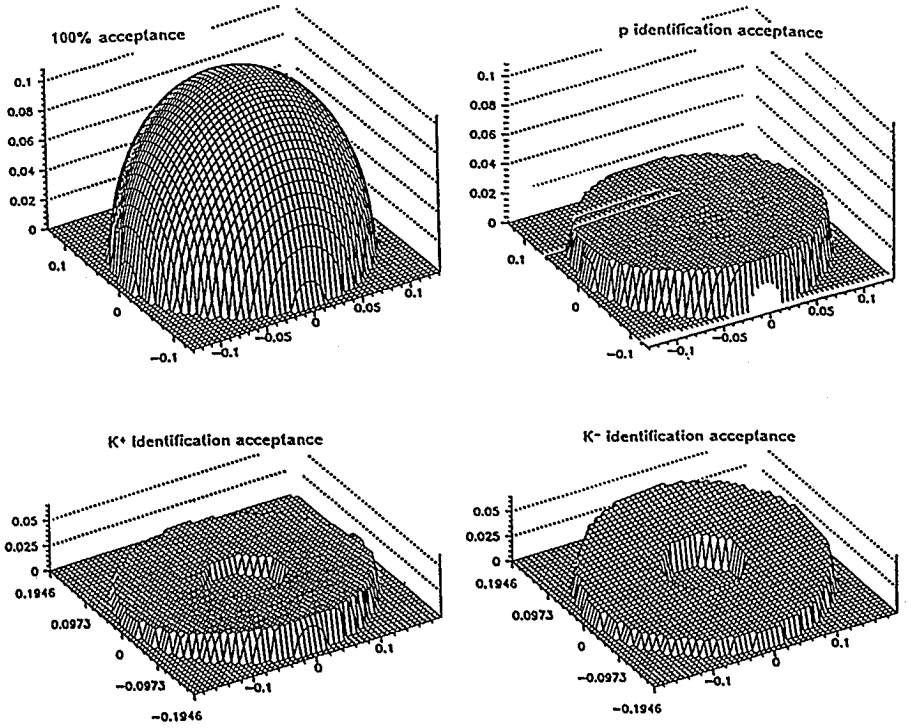

Figure 13:
Monte Carlo calculations of the reaction pp $\rightarrow$ ppϕ $\rightarrow$ ppK$^+$K$^-$ at P_p = 3.42 GeV/c for the geometrical momentum acceptance distribution in the c.m. system, vertical P_y, horizontal P_x, and P_z; see text for further details

The Monte Carlo calculations were performed as follows: at the target the ejectiles start with the maximum possible momentum components, a sphere in momentum space, which is transfered to the detector for 100% acceptance. Due to the limiting dipole gap, for beam momenta well above threshold, only a part of this sphere is transfered to the detectors.

III. g. Data acquisition

The data acquisition system will be based on regular bus-standards. The data digitalization will be performed in FASTBUS and CAMAC (ADC's, TDC's, and DRAMS), the event building and event saving onto magnetic tape will be performed in VME. The different systems are interconnected via a VIC-bus (VME-Intercrate-Connection). Experiment control, on-line sort and event display will be done on an ULTRIX Work-station which is connected via Ethernet (TCP/IP) with the VME event building crate. On-line sort and display will use the CERNlib software programs HBOOK, KUIP, and PAW++. Generally normalized structures and use of international standards were employed in the development of interfaces between VIC bus and Fastbus/CAMAC performed by the ZEL-Jülich together with C.E.S. and STRUCK.

Outlook

An internal experiment at COSY-Jülich is presently being prepared, to study the production of mesons and mesonic states, especially to observe the f_0 and a_0 meson range, where structure speculations ranging from normal $q\bar{q}$- and mesonic-molecules interpretations to even gluonic matter considerations are still alive. Several other physics cases have been presented which could be done at a small angle facility in storage rings.
Installation of the COSY - 11 experiment is foreseen in fall 1993 with consecutive calibration work and data taking.

Acknowledgments

The support of the Dr. Wilhelm Heinrich Heraeus und Else Heraeus-Stiftung is gratefully acknowledged. I would like to thank Prof. Dr. O. Schult and Prof. Dr. E. Rössle for organizing the interesting and fruitful seminar.

References

(1) *Members of the COSY - 11 collaboration:*
D. Grzonka, K. Kilian, P. Moskal, W. Oelert, E. Roderburg, M. Rook, Th. Sefzick, P. Turek; IKP 1, Forschungszentrum Jülich
M. Köhler; ZEL, Forschungszentrum Jülich
H. Dombrowski, A. Khoukaz, R. Santo, M. Wolke; IKP, Universität Münster
J. Balewski, L. Jarczyk, B. Kamys, M. Kistryn, J. Smyrski, A. Strzalkowski; IKP, Jagellonica University Cracow
A. Budzanowski, M. Ziolkowski; Institut of Nuclear Physics, Cracow
for support in all fields of the preparation of the experiment COSY - 11, we would like to thank especially:
V. Drüke, D. Drochner, D. Filges, H. Hadamek, A. Hardt, M. Heczko, M. Karnadi, F. Klehr, S. Martin, J. Majewski, A. Misiak, R.D. Neef, R. Nellen, D. Prasuhn, U. Rindfleisch, G. Stollwerk, K.H. Watzlawik, P. Wüstner, K. Zwoll

(2) Cooler Synchrotron COSY-Jülich, User Guide, May 1990, IKP KFA Jülich
(3) S. Krewald et al.; Phys. Lett. B272 (1991) 190 and private communication
see also: H. J. Lipkin Phys. Lett. 179B (1986) 278
(4) H. Calen et al.; AIP Conference Proceedings, No. 221, Nashville, in 1990
Edts.: Nann and Stephenson, p 13
(5) K. Sistemich; COSY Proposal No. 18, IKP KFA Jülich
(6) H.O. Meyer et al.; Phys. Rev. Lett. 23 (1990) 2846
(7) W.W. Daehnick; Prodeedings of the Workshop on Meson Production, Interaction
and Decay, Cracow, 6-11 May 1991, Edts.: Magiera, Oelert, Grosse, p 279
(8) H. Schmitt et.al.; Third LEAR Workshop Tignes, 1985, Editions Frontieres,
(9) P. Kroll; contribution to this 105. WE-Heraeus-Seminar
(10) J.A. Niskanen, 10th Nordic Meeting, Gräftavallen, January 1993, unpublished
(11) F. Plouin; Production and Decay of Mesons, Paris 1988, Edt.: P. Fleury, p 114
(12) PROMICE Collaboration at CELSIUS, Uppsala
(13) E. Roderburg et al.; COSY Proposal No. 12, IKP KFA Jülich
(14) H. Machner et al.; COSY Proposal No. 24, IKP KFA Jülich
(15) G. Decker; PhD Thesis, Forschungszentrum Jülich Jül-2645
(16) N. Isgur; Proceedings from Ref. (11), p 3.
(17) B. Nefkens; Prodeedings from Ref. (7), p 40.
(18) K. Maltman and N. Isgur; Phys. Rev. D29 (1984) 952
(19) A. Abashian et al.; Phys. Rev. 132 (1963) 2296
(20) R.L. Jaffe; Phys. Rev. D15 (1977) 267 and 281; and Phys. Rev. D17 (1978) 1444;
R.L. Jaffe and F.E. Low; Phys. Rev. D19 (1979) 2105
R.L. Jaffe and K. Johnson; Phys. Lett. 60B (1976) 201
(21) F. Close; Rep. Prog. Phys. 51 (1988) 833
(22) T. Akesson et al.; Nucl. Phys. B264 (1986) 154
(23) K. Au et.al. Phys. Lett. 167B (1986) 229
(24) K.L. Au et al.; Phys. Rev. D35 (1987) 1633 and Phys. Lett. 167B (1986) 229
(25) D. Morgan and M.R. Pennington; Phys. Lett. 258B (1991) 444
(26) D. Morgan and M.R. Pennington; Rutherford Appleton Laboratory RAL-92-070
(27) M. Albrow CERN Courier, January/February 1987
(28) J. Weinstein and N. Isgur; Phys. Rev. D27 (1983) 588 and D41 (1990) 2236
(29) J. Weinstein; Hadron '89, Ajaccio, 1989, Edts.: Binon, Frere, Peigneux, p 233
(30) two contributions to Meson-Workshop: J. Weinstein p 89, J. Speth p 129
Jülich 1990, Jül-2469, Edt.: W. Oelert and Th. Sefzick
(31) D. Lohse et al.; Phys. Lett. 234B (1990) 235
(32) Review of Particle Properties, Phys. Rev. 45D 1992
(33) A. Lindner; PhD thesis 1992, unpublished
(34) R.J. Apsimon et al.; OMEGA Photon Collaboration, CERN-PPE/92 - 135
(35) K.K. Seth; Proceedings Intern. conf. Medium and High Energy Physics,
Taipei, Taiwan May 1988, World Scientific, Singapore
(36) J. Bisplinghoff, F. Hinterberger; COSY Proposal No. 5, ISKP Bonn
(37) R. Bilger et al.; Letter of Intend for COSY-Jülich
(38) B. Brinkmöller; Arbeitstreffen Mittelenergiephysik, Manderscheid, 1992, p567
(39) M. Schepkin; talk given at the Conference Particle Production Near Threshold,
Uppsala 1992, to be published in Physica Scripta 47 (1993)
(40) P. Turek; COSY Proposal No. 15, IKP KFA Jülich
(41) HERA CERN Compilation III (1984)

(42) *W. Bickel et al.; Nucl. Inst. & Meth. A295 (1990) 44*
H. Dombrowski et al.; Verhandlungen der DPG VI 28 (1993) 689
(43) *T. Johansson; Workshop, Jül-Spez-409 (1987), Edt. by W. Oelert*
(44) *L.G. Afanasyev et al.; Phys. Lett. 255B (1991) 146*
(45) *H. Nann; Prodeedings from Ref. (7), p 100.*
(46) *B. Höistad, T. Johansson et.al., Proposal to the Celsius Cooler Facility (1992)*
(47) *S. Wycech; Proceedings from Ref. (7), p 65.*
(48) *S. Wycech and A.M. Green; preprint HU-TFT-93-9, 15 February 1993*
(49) *M. Rook; Diplomarbeit, Forschungszentrum Jülich, Jül-2407, 1990*
(50) *B.Gugulski et al.; KFA-IKP(i) - 1992 - 3*
(51) *G. Anton et al.; Nucl. Instr. Meth. A310 (1991) 631*
(52) *Silicon Pin-Diode Pad Detectors, Senter for Industriforsking, Forskingsveien 1, Norwegen*
(53) *E. Beuville et al.; Nucl. Instr. & Meth. A288 (1990) 157*
E. Chesi and P. Martinengo; PS202 Note 15.1.1988
(54) *R. Maier; beam quality numbers given at the 5th COSY-PAC meeting, 1992*

STRANGENESS PRODUCTION WITH PROTONS AND PIONS

Carl B. Dover

Physics Department
Brookhaven National Laboratory
Upton, New York 11973

ABSTRACT

We discuss the spectrum of physics questions related to strangeness which could be addressed with intense beams of protons and pions in the few GeV region. We focus on various aspects of strangeness production, including hyperon production in pp collisions, studies of hyperon–nucleon scattering, production of hypernuclei in proton and pion–nucleus collisions, and spin phenomena in hypernuclei.

1. Introduction and Motivation

Nucleon–nucleon (NN) interactions in the multi–GeV energy range produce a number of final states. Most often pions are produced, but also strange particles emerge from such collisions, for instance Λ, Σ or Ξ baryons, or kaons ($K^{\pm}$, K_L, K_S). In the present talk, we emphasize the various aspects of the strangeness production mechanism, as well as the study of secondary hyperon–nucleon collisions as a means of shedding light on the SU(3) structure of baryon–baryon interactions. We also consider the production of hypernuclei (Λ bound to a nuclear core) in proton–nucleus (pA) collisions, and via the (π, K) associated production reaction.

This paper is organized as follows: In Section 2, we review the existing data on strangeness production in pp collisions, focusing on the ΛpK^+ and ΣNK^+ final states. In Section 3, the status of our knowledge of low energy hyperon–nucleon (YN) scattering is reviewed, with an emphasis on the spin dependence of the interaction and tests of SU(3) symmetry. The formation of hyperfragments ($_{\Lambda}$A) in pA collisions is examined in Section 4. Some comments on hypernuclear production with pion beams is given in Section 5, emphasizing polarization phenomena.

2. Strangeness Production in pp Collisions

The lowest–lying threshold for strangeness production in pp collisions corresponds to a lab momentum $p_L = 2.34$ GeV/c for the reaction $pp \to \Lambda p K^+$. As p_L rises above threshold, the total cross section for the $pp \to \Lambda p K^+$ reaction first rises rapidly, attains a peak of 50–60 μb near 5–6 GeV/c, and then drops off slowly. The inclusive cross section for Λ production, on the other hand, continues to rise, attaining values of 4–5 mb above 100 GeV/c, roughly 10% of the pp total cross section. This behavior is shown in Fig. 1, taken from Baldini *et al.* [1]. As the energy increases, the three–body $\Lambda p K^+$ final state represents a smaller and smaller part of the total Λ production. For instance, we have

$$\frac{\sigma\,(pp \to \Lambda p K^+)}{\sigma\,(pp \to \Lambda X)} \approx \begin{cases} 0.04 & (12 \text{ GeV/c}) \\ 0.02 & (24 \text{ GeV/c}) \end{cases} \tag{1}$$

The three–body $K^+\Lambda p$ and $K^+\Sigma N$ final states are of particular interest, since one can make a reasonable attempt to calculate these cross sections theoretically. The data on these processes [2,3] in the few GeV region are displayed in Figs. 2 and 3. In this medium energy regime, it is still reasonable to describe the reaction mechanism in terms of meson exchanges, as depicted in Fig. 4. Calculations of this type have been carried out by Laget [2] and Deloff [4]; the latter results are questionable, since a fit is only obtained with $g^2_{KN\Lambda} \ll g^2_{KN\Sigma}$, whereas there are numerous indications from other data that the $KN\Lambda$ coupling constant $g_{KN\Lambda}$ is much stronger than that for $g_{KN\Sigma}$. For instance, from analyses of $\overline{K}N$ disperson relations, Baillon *et al.* [5] give $g^2_{KN\Lambda} = 0.8 \pm 3.2$, $g^2_{KN\Sigma} = 21.3 \pm 3.7$. A somewhat larger ratio of Σ/Λ couplings was extracted from data on Λ and Σ production in K^-p interactions [6]. Laget [2] uses reasonable coupling constants $g^2_{KN\Sigma} = 1$, $g^2_{KN\Lambda} = 14$, in agreement with values obtained from studies of hyperon–nucleon scattering [7] and kaon photoproduction reactions [8].

The Saturne data [3] shown in Fig. 3 display characteristic enhancements just above the Λp and ΣN thresholds at an invariant mass of $W = 2.053$ GeV/c^2 and 2.131 GeV/c^2, respectively. This is due to the strong s–wave YN attraction, i.e. the final state interaction amplitude t in Fig. 4. The pion exchange graph dominates the $pp \to K^+\Sigma N$ reactions (see Fig. 2), but the kaon exchange mechanism is more important for the $K^+\Lambda p$ channel. The direct kaon emission graph (bottom of Fig. 4) plays a key rôle in reproducing the structure which appears at the ΣN threshold, which also depends sensitively on the strong coupling of the Λp and ΣN channels.

Note that the relative phase between the π and K exchange amplitudes is not fixed à priori. Laget [2] has chosen the sign which gives the maximum additive effect on the cross sections. Further data, particularly on spin observables, are needed in order to check this relative phase and also other dynamical aspects of the model (the diagonal and non–diagonal $YN \to Y'N$ couplings, for instance). Such data could be obtained with high luminosity proton beams. Some predictions for spin observables are shown in the bottom half of Fig. 3.

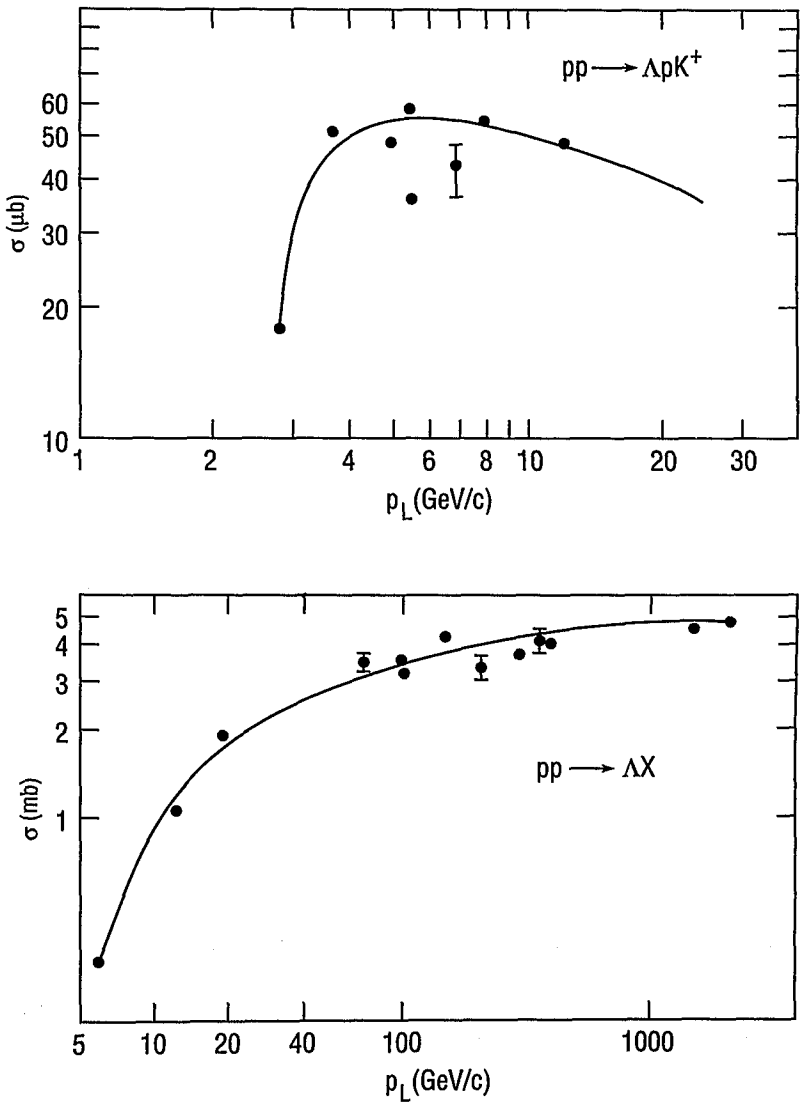

Figure 1: Total cross sections for inclusive Λ production and the three–body final state ΛpK^+ in pp collisions, as a function of lab momentum p_L, from Baldini *et al.* [1]. A few typical error bars are shown; the solid curves represent numerical fits to the data.

The meson exchange picture with $K\Lambda N$–$K\Sigma N$ coupled channels certainly makes sense in the region near threshold. As we pass to higher energies, one might ask where such a

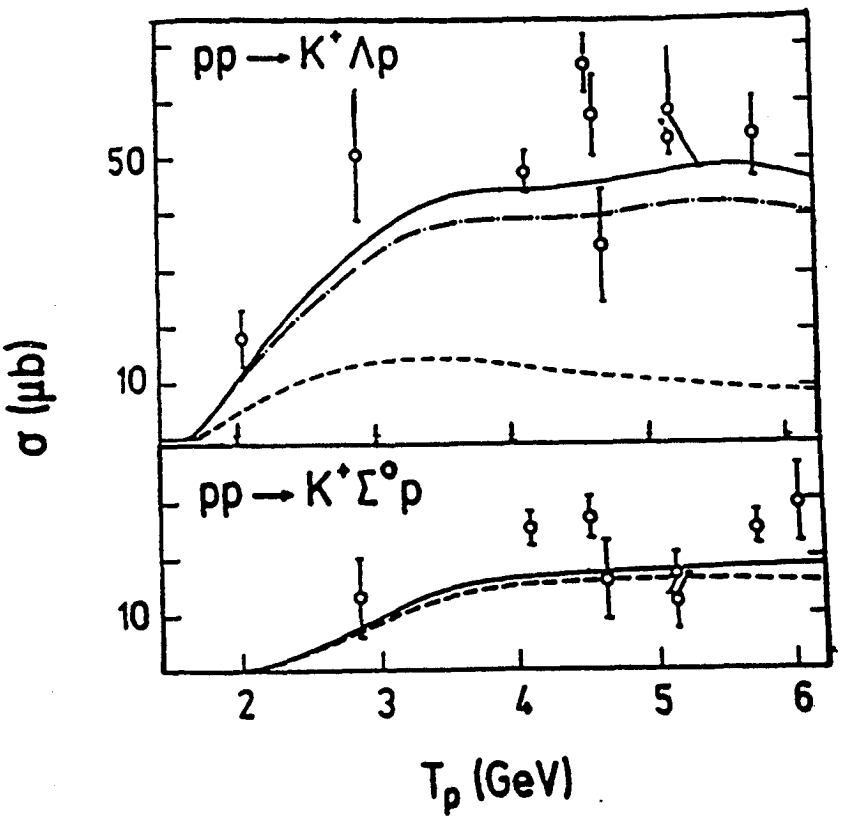

Figure 2: Total cross sections for the reactions $pp \to \Lambda p K^+$ and $\Sigma^0 p K^+$, as a function of proton lab kinetic energy in T_p. The dashed line represents the contribution of the pion exchange graph (see Fig. 4), while the solid and dash-dot lines include kaon exchange with two different values of the cutoff mass in the form factor for the meson–baryon vertex; from Laget [2].

picture breaks down, since many other reaction channels open up. The thresholds for some of these are given in Table 1.

Even though many other channels come into play above 3 GeV/c, the simple meson exchange picture works well at least up to $T_p = 6$ GeV, as shown in Fig. 2. A key ingredient in this success is the proper treatment of the energy dependence of the elastic $\Lambda N \to \Lambda N$ and $\Sigma N \to \Sigma N$ t–matrices which appear in Fig. 4. Although many channels may be energetically accessible, their effect appears only as an absorptive correction, i.e. channels

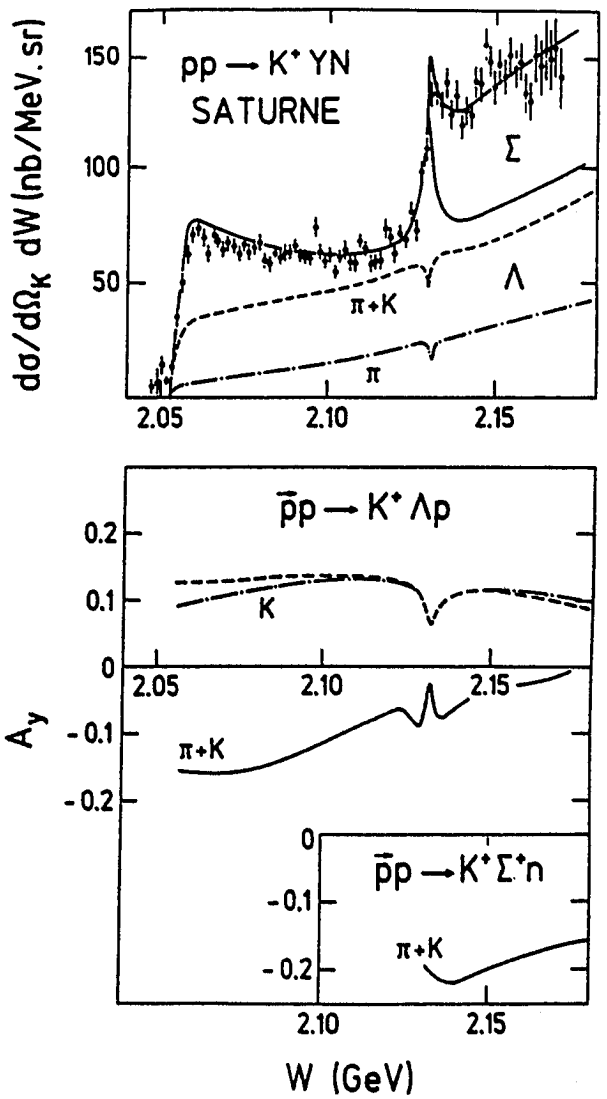

Figure 3: Top: Missing mass spectrum for the $pp \to K^+YN$ reaction at $T_p = 2.3$ GeV. The K^+ is measured at an angle $\theta_K = 10°$, and W is the invariant mass of the recoiling YN system. The data are from Frascaria *et al.* [3] and the theoretical curves are from Laget [2]. Various meson exchange contributions are indicated; the solid curve includes direct kaon emission. Bottom: Predictions [2] for the beam asymmetry A_y at 2.3 GeV. The solid curve represents the full calculation, including both pion and kaon exchange. The scale is the invariant mass W of the hyperon–nucleon system.

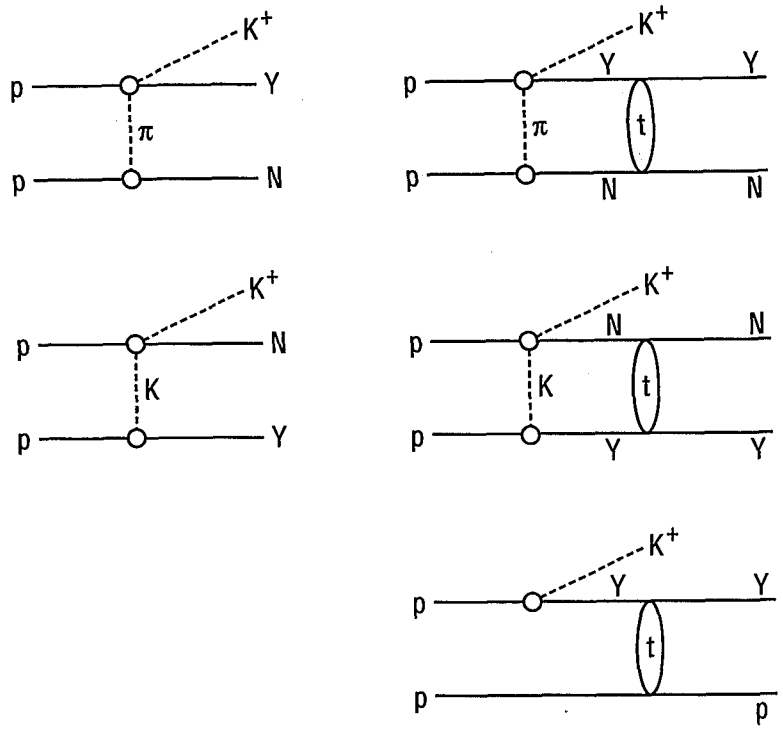

Figure 4: Meson exchange processes which contribute to the $pp \to YNK^+$ reaction. The oval labeled t stands for the YN scattering amplitude. The bottom graph represents the "direct" kaon emission, which represents a substantial contribution (see Fig. 3).

like $YN \to YN\pi$ are included in terms of the inelasticities η of the elastic partial wave amplitudes.

The further study of the $pp \to K^+YN$ reactions, in particular the spin observables, is well worthwhile. Such experiments have been proposed at SATURNE and COSY. The spin information would provide strong constraints for theoretical models.

Table 1: Threshold lab momenta p_L and lab kinetic energy T_p for various final channels produced in pp collisions.

Channel	p_L (GeV/c)	T_p (GeV)
$\Lambda K^+ p$	2.34	1.582
$\Sigma^0 K^+ p$	2.57	1.794
$\Lambda K^+ p\pi^0$	2.74	1.958
$\Sigma^0 K^+ p\pi^0$	2.97	2.174
$\Sigma^0(1385) K^+ p$	3.15	2.35
$\Lambda(1405) K^+ p$	3.22	2.413
$\Lambda K^+ \Delta(1232)$	3.24	2.436

3. Hyperon–Nucleon Scattering: Spin Observables and SU(3)

The $pp \to K^+ YX$ reaction, with K^+ detection for tagging, leads to the production of hyperons Y, which can then be scattered from a secondary proton or nuclear target, in order to study the YN interaction. In this section, we indicate the physics justification for such a program.

The existing information on hyperon–nucleon scattering is very sparse. Essentially all the low-lying total cross section data is collected in Fig. 5, taken from [9]. Compared to the NN data, the error bars for YN are rather large, and data exist only in a limited momentum range. There are also data on differential cross sections. Even at low momenta (160–170 MeV/c), the angular distributions are not isotropic, indicating a significant p–wave contribution.

The solid curves in Fig. 5 correspond to best fits in a meson exchange model for baryon–baryon scattering. The particular model shown here, due to the Nijmegen group [7], employs the exchange of nonets of mesons, namely

$$\{\pi, \eta, \eta'\}_{0^-}, \quad \{\delta, \sigma, S^*\}_{0^+}, \quad \{\rho, \omega, \phi\}_{1^-} \tag{2}$$

with a hard core cutoff at short distances. A more recent Nijmegen potential model, due to Maessen *et al.* [10], uses soft core form factors. Similar models have recently been developed by the Bonn group [11].

In the Nijmegen models [7,10], SU(3) symmetry is used to relate the coupling constants for hyperons and nucleons. For example, the coupling constants for the pseudoscalar octet $\{\pi, \eta_8, K\}$ are given by

$$g_{NN\eta_8} = (4\alpha_{PS} - 1)/\sqrt{3}, \quad g_{\Lambda NK} = -\frac{(1 + 2\alpha_{PS})}{\sqrt{3}}, \quad g_{\Sigma NK} = 1 - 2\alpha_{PS},$$
$$g_{\Sigma\Sigma\pi} = 2\alpha_{PS}, \quad g_{\Sigma\Lambda\pi} = g_{\Sigma\Sigma\eta_8} = -g_{\Lambda\Lambda\eta_8} = \frac{2(1 - \alpha_{PS})}{\sqrt{3}} \tag{3}$$

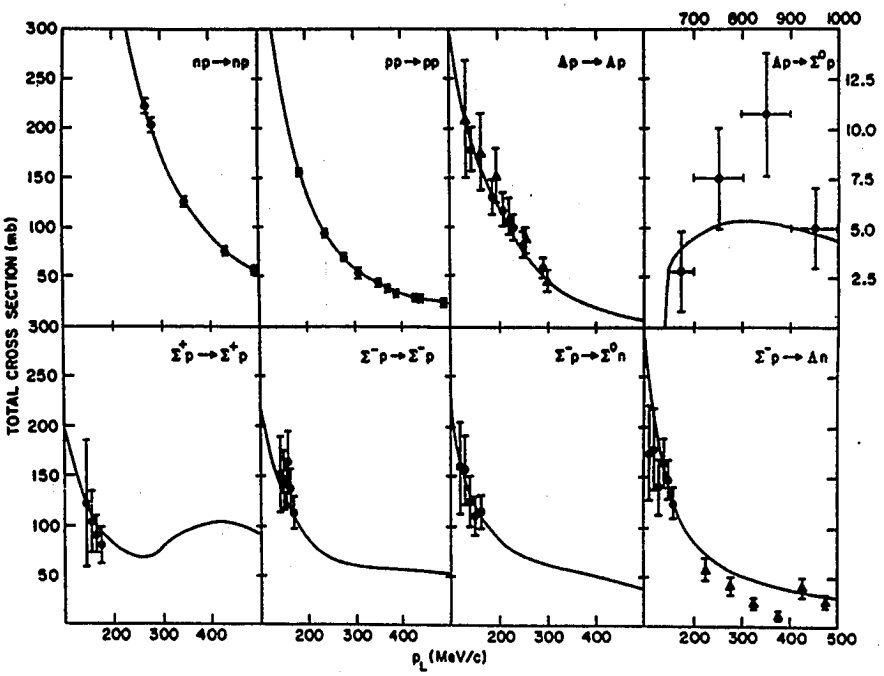

Figure 5: Total cross sections for NN and YN scattering, as a function of lab momentum p_L, from Ref. 9. The solid curves are potential model fits of the Nijmegen group (Model D, ref. [7]).

in units of $g_{NN\pi}$, where α_{PS} is the pseudoscalar F/D ratio. An angle θ_{PS} describes the octet (η_8)–singlet (η_1) mixing. In the Nijmegen models, α_{PS} is adjusted to achieve a best fit to the data ($\alpha_{PS} = 0.485$ in [7]; $\alpha_{PS} = 0.355$ in [10]). In the Bonn model [11], the SU(6) value $\alpha_{PS} = 2/5$ is picked. A unique α_{PS} cannot be determined from the baryon–baryon data, since its optimum value is intertwined with the parametrization of the short range potential. In SU(6), we predict the ratio

$$\frac{g^2_{\Sigma NK}}{g^2_{\Lambda NK}} = \frac{1}{27} \tag{4}$$

This very strong suppression of the ΣNK vertex is not seen in various production experiments, where Σ/Λ ratios of order 1/2 are measured [6]. These larger ratios can be accommodated in SU(3) with a choice $\alpha_{PS} \simeq 0.3$, but are at odds with SU(6). Thus the imposition of an SU(6) constraint on meson–baryon couplings does not appear well motivated, even though one can achieve a good fit by using a flexible multi–parameter form for the short range cutoffs.

The fits to baryon–baryon scattering are driven by the high precision NN data. The YN data by themselves can be reproduced with a wide range of models, including simple one or two term separable potentials, which have no theoretical motivation. From the data of Fig. 5, we note that the charge exchange cross sections ($\Sigma^- p \to \Sigma^0 n$, Λn), which require isovector meson exchange, are of the same order as $\Sigma^- p$ or $\Sigma^+ p$ elastic scattering. Thus it is clear from the data that the ΣN potential must have a strong isospin ($\vec{t}_\Sigma \cdot \vec{\tau}_N$) dependence, which is naturally generated by π and ρ exchange. The degree of spin dependence is not so clear, since only spin averaged cross sections have been measured. In fact, the various models predict quite different spin dependences. For instance, Nijmegen Models D and F have

$$a\left({}^1\mathrm{S}_0\right) \approx a\left({}^3\mathrm{S}_1\right) \tag{5}$$

for the ΛN singlet and triplet scattering lengths, whereas the soft core model [10] suggests a significant spin dependence:

$$a\left({}^1\mathrm{S}_0\right) \simeq -2.8 \text{ fm}, \quad a\left({}^3\mathrm{S}_1\right) \simeq -1.4 \text{ fm} \tag{6}$$

Further, the models predict a strong spin dependence for ΣN reactions. For instance, Models D, F [7] at low energies lead to

$$\begin{aligned} &{}^3\mathrm{S}_1 \text{ dominance for } \Sigma^- p \to \Sigma^- p,\ \Lambda n \\ &{}^1\mathrm{S}_0 \text{ dominance for } \Sigma^+ p \to \Sigma^+ p \end{aligned} \tag{7}$$

Different models which give equivalent fits to spin–averaged cross sections predict significantly different spin separated cross sections $\sigma_0({}^1\mathrm{S}_0)$ and $\sigma_1({}^3\mathrm{S}_1)$. Thus the main motivation of future experiments on YN scattering is to measure spin observables. The simplest of these is the elastic polarization $P(\theta)$, which is sensitive to the baryon–baryon spin–orbit couplings. Note that for YN interactions, there exist both symmetric $[(\vec{\sigma}_Y + \vec{\sigma}_N) \cdot \vec{L}]$ and antisymmetric $[(\vec{\sigma}_Y - \vec{\sigma}_N) \cdot \vec{L}]$ spin–orbit terms, whereas for the NN system the antisymmetric coupling drops out because of the requirements of the Pauli principle. From Λ–hypernuclear spectra, there is evidence [12] that the one–body Λ–nucleus spin–orbit strength V_{LS}^Λ is very small compared to the value V_{LS}^N for a nucleon. Polarization data on Λp scattering would be invaluable in clarifying the relation between the two–body ΛN and many–body Λ–nucleus spin–orbit potentials. With respect to experiments with protons in the few GeV region, some questions to consider are: i) Can we make use of the polarization of the Λ's from the primary $pp \to K^+ \Lambda p$ reaction?; ii) Is it necessary to tag Λ production by detecting the K^+?; iii) What are the virtues/disadvantages of a polarized proton target for Λp studies?.

Another issue pertaining to hyperon–nucleon scattering studies is the degree to which SU(3) symmetry is broken. In the SU(3) limit, we can write the baryon–baryon scattering amplitude as

$$T = a + bF^2 + cG^3 \tag{8}$$

in terms of the quadratic (F^2) and cubic (G^3) Casimir operators of SU(3). Here $\{a, b, c\}$ are functions of spin, energy and momentum transfer. An amplitude of the form [8] implies the following cross section relations [9]:

$$\sigma_0\left(\Sigma^+ p \to \Sigma^+ p\right) = \sigma_0\left(np \to np\right) \tag{9a}$$

$$\sigma_0\left(\Sigma^- p \to \Lambda n\right) = \frac{1}{3}\sigma_0\left(\Sigma^- p \to \Sigma^0 n\right) \tag{9b}$$

$$\sigma_0\left(\Lambda p \to \Lambda p\right) = \frac{1}{6}\left[5\sigma_0\left(\Sigma^+ p \to \Sigma^+ p\right) + \sigma_0\left(\Sigma^- p \to \Sigma^- p\right) - \frac{5}{3}\sigma_0\left(\Sigma^- p \to \Sigma^0 n\right)\right] \tag{9c}$$

$$\sigma_1\left(\Lambda p \to \Lambda p\right) = \frac{1}{2}\left[3\sigma_1\left(\Sigma^- p \to \Sigma^- p\right) + 3\sigma_1\left(\Sigma^- p \to \Sigma^0 n\right) - \sigma_1\left(\Sigma^+ p \to \Sigma^+ p\right)\right] \tag{9d}$$

It is understood that these relations apply after differences in kinematical phase space factors are removed [9]. In potential models, SU(3) is broken not only by baryon mass differences, but also by those of the exchanged mesons. Since the π, η and K masses are very different, one might expect SU(3) breaking effects to be huge. However, the SU(3) relations are predicted [9] to be satisfied at the 30% level in the Nijmegen potential model.

In order to verify the SU(3) relations of Eq. (9), spin separated cross sections $\sigma_{0,1}$ are required. This provides motivation for ΛN and ΣN scattering experiments with polarized hyperon beams or a polarized hydrogen target (or both).

4. Production of Hypernuclei with Proton Beams

Most hypernuclear research has been done with kaon (K^-) and pion (π^+) beams [12]. Some of the basic reactions for Λ and Σ production are

$$K^- n \to \pi^- \Lambda \tag{10a}$$

$$\pi^+ n \to K^+ \Lambda \tag{10b}$$

$$K^- p \to \pi^+ \Sigma^- \tag{10c}$$

The process (10a) involves small momentum transfer q at small angles, so a slow Λ is produced which readily sticks to a nuclear core, yielding a bound hypernucleus ${}_\Lambda$A. Reaction (10b) involves $q \geq p_F$, even at small angles, and thus tends to populate hypernuclear states of the highest available spin [13]. The reaction (10c) produces Σ hyperons, which also experience attractive forces capable of binding them to a nuclear core. Due to the strong conversion $\Sigma N \to \Lambda N$, Σ states are generally expected to be broad, although specific mechanisms have been proposed which may suppress their width to values $\Gamma \leq 5$

MeV, where they become observable as quasiparticle excitations [14]. The existence of Σ hypernuclei remains controversial.

Progress in hypernuclear structure physics requires experiments of much higher energy resolution than currently available ($\Delta E \simeq 3-5$ MeV). Such experiments are eventually planned at CEBAF, where the process

$$\gamma p \rightarrow K^+\Lambda \tag{11}$$

will be used with virtual or real photons. The kinematics of the electroproduction reaction (11) is similar to (10b), but (γ, K^+) has a large spin flip amplitude, whereas (π^+, K^+) does not (at small angles). Thus different hypernuclear states are preferentially populated in (γ, K^+) and (π^+, K^+) reactions; see [15] for a detailed discussion. Future prospects for high resolution hypernuclear structure studies have been discussed at a previous workshop [16].

Meson or photon beams are the method of choice for exploring the properties of hypernuclei, but it is also possible to produce hyperfragments with proton beams, and this method merits further study. The basic process is $pN \rightarrow K\Lambda N$, followed by the sticking of the Λ or ΛN to a nuclear fragment. Reactions to consider are

$$p + A_Z \rightarrow {}_\Lambda\mathrm{A}'_{Z'} + X \tag{12a}$$

$$p + A_Z \rightarrow K^+ + p' + {}_\Lambda\mathrm{A}_{Z-1} \tag{12b}$$

$$p + A_Z \rightarrow K^+ + {}_\Lambda(\mathrm{A}+1)_Z \tag{12c}$$

Since the Λ is generally produced with a sizeable momentum in the lab frame, the sticking probability is always small. In (12a), the hypernucleus is detected through the weak decay $\Lambda \rightarrow p\pi^-$. The experimental data on hypernuclear yields in pA and π^-A collisions have been reviewed by Lyukov [17]. Some results are shown in Fig. 6. The yield of hyperfragments in pA interactions does not exceed 2×10^{-3} or so, with a broad maximum centered around 50 GeV/c. The frequency of observed mesonic decays is an order of magnitude smaller ($1 - 3 \times 10^{-4}$ from 10–50 GeV/c). The charge distribution of observed hyperfragments is centered around $Z = 2$, and decreases rapidly for $Z > 3$. Thus only rather light fragments are observed by this method; in heavier hypernuclei, the dominant weak decay mode is non–mesonic ($\Lambda N \rightarrow NN$), since the $\Lambda \rightarrow p\pi^-$ mode is Pauli blocked.

The solid curves in Fig. 6 represent theoretical expectations based on a simple coalescence model [17], in which the bound hypernucleus is formed only when the Λ is produced with a small momentum relative to the nuclear core. Although the coalescence picture leads to the correct order of magnitude for the hyperfragment yield, the existing data are not precise enough to test the detailed form of the predicted energy dependence.

The reactions (12b) and (12c) involve a large momentum transfer (defined as $p_L - p_{K^+}$ for a K^+ at 0°). The three–body final state of (12b) will have a larger cross section than that for the two–body channel (12c), since the momentum transfer is shared between the

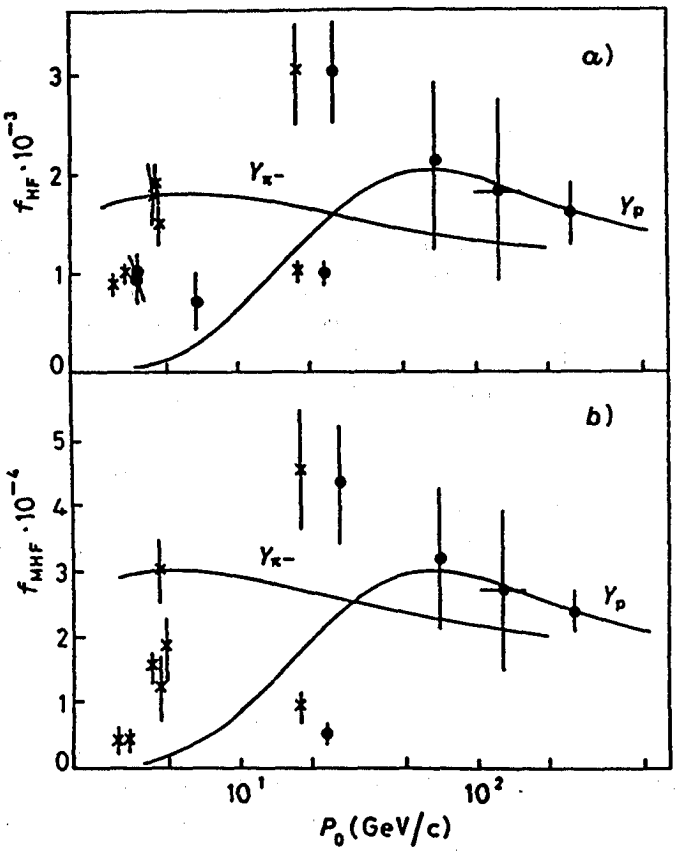

Figure 6: In a) we show the measured yields f_{HF} in units of 10^{-3}, for hyperfragments obtained in π^- or p–nucleus collisions, as a function of the incident particle momentum P_0. Theoretical expectations are shown as the solid curves Y_{π^-} and Y_p. Circles refer to pA and crosses to $\pi^- A$ interactions. In b), we indicate the frequency of observation f_{MHF} (in units 10^{-4}) of mesic decays ($\Lambda \rightarrow p\pi^-$) of hyperfragments. The plot is taken from Lyukov [17].

K^+ and p'. However, in (12b), one must detect both the K^+ and p' in order to construct the missing mass spectrum for the hypernucleus, so the advantage in cross section is lost. Recently, there have been experiments at Saturne, due to Boivin *et al.* [18], to search for the two–body reactions

$$p + {}^3\mathrm{He} \rightarrow K^+ + {}^4_\Lambda\mathrm{He} \qquad (13a)$$

$$p + {}^4\mathrm{He} \rightarrow K^+ + {}^5_\Lambda\mathrm{He} \qquad (13b)$$

at a proton kinetic energy of 2.1 GeV and a kaon lab angle $\theta_{K^+} = 7°$. The momentum transfer here is about 500 MeV/c and the missing mass resolution is 1.5 MeV. From other data, ${}^{4}_{\Lambda}$He is known to have a 0^+ ground state and a bound 1^+ excited state at 1.1 MeV; ${}^{5}_{\Lambda}$He has a single $1/2^+$ bound state. No clear signal of bound state formation was observed, leading to upper limits

$$\left(\frac{d\sigma}{d\Omega_L}\right)_{7°} < \begin{cases} 3 \text{ nb/sr} & \text{for (13a)} \\ 1.7 \text{ nb/sr} & \text{for (13b)} \end{cases} \tag{14}$$

The observed limits (14) are within the range of theoretical estimates [19,20]. Because the momentum transfer is large, the rôle of short range correlations is extremely important. Such correlations enhance the high momentum components in the single particle momentum distribution of the target nucleus, and greatly increase the cross section above the value obtained with uncorrelated Gaussian wave functions. With correlations, Shinmura [19] predicts $\sim$ 2 nb/sr for reaction (13b) at small angles, comparable to the observed limits (14). This prediction is very model dependent, however.

The message here is the following: the (p, K^+) reaction is a good probe of the reaction mechanism for hypernuclear production in high momentum transfer processes. However, the cross sections are very small ($\lesssim$ 1–2 nb/sr) near 2 GeV and one is unlikely to attain a sufficiently high energy resolution to perform detailed spectroscopic studies. A more promising direction of research is the study of the strangeness production mechanism itself in proton–nucleus collisions. Some data [21,22] at 10 GeV indicate that the production of high energy K^+ and K^- mesons in pA collisions is described by the same structure function f of the nucleus as the production of other particles. This universality, observed for K^- mesons which consist only of sea quarks ($s\bar{u}$), may indicate [22] that the nucleus contains a hard quark–antiquark sea differing from the soft sea present in the nucleon.

5. Hypernuclear Physics with Pion Beams: Polarization Phenomena

The (π^+, K^+) reaction on nuclear targets has enormous potential for studies of hypernuclear structure [12,13,16]. Pion beams near 1 GeV/c are optimal, with a premium on intensity for high resolution studies. In the momentum range 1–1.2 GeV/c, we straddle the peak of the cross section for the elementary process $\pi^+ n \to K^+\Lambda$, by which a neutron is converted into a Λ hyperon, which can then bind to a nuclear core to produce a hypernucleus of strangeness $S = -1$. The formation of the hypernucleus is tagged by the detection of the strange K^+ meson. A high π^+ intensity would enable us to perform coincidence experiments involving strong, electromagnetic or weak decays of various hypernuclear states. Since the (π^+, K^+) reaction at finite angles can produce significant hypernuclear polarization, weak decay studies would further elucidate the properties of

the nucleon–catalyzed Λ weak decay amplitudes, i.e. $\Lambda N \to NN$. Studies of γ decays of hypernuclear excited states provide us with precise information on the spin dependence of the effective lambda–nucleon (ΛN) interaction in the nuclear medium. High energy resolution (π^+, K^+) experiments ($\sim$ 200 keV resolution is desirable) can directly resolve the fine structure of the hypernuclear spectrum in favorable cases. Thus far only coarse resolution (typically 3 MeV) hypernuclear experiments have been possible. The first (π^+, K^+) experiments at the Brookhaven AGS and KEK [23] have served to clarify the single particle properties of the Λ, i.e., the properties of the Λ–nucleus mean field [24]. To approach the level of precision of non–strange nuclear spectroscopy, a high resolution capability is clearly necessary.

At non-zero angles, the (π^+, K^+) reaction can be used to produce *polarized* hypernuclei. [25-27] In the elementary pseudoscalar meson-baryon process, the amplitude t and the Λ polarization P_Λ are of the form

$$\begin{aligned} t =& f + ig\vec{\sigma}\cdot\hat{n} \\ P_\Lambda =& 2Im\left(fg^*\right) / \left(|f|^2 + |g|^2\right) \end{aligned} \tag{15}$$

where $\vec{\sigma}$ is the baryon spin and $\hat{n}$ is the normal to the scattering plane. In the regime of $p_\pi \approx 1 - 1.1$ GeV/c, P_Λ is quite substantial for $\theta_L \geq 5°$. This offers the attractive possibility of producing polarized hypernuclear states. As we shall see, the polarization varies in an interesting way, depending on the quantum numbers of the initial and final states. There is also an interplay between two sources of hypernuclear polarization [26], namely the f-g interference in the elementary amplitude and the effects of meson distortion in the medium, i.e., the difference between the absorption experienced by mesons passing on the near-side or far-side of the nucleus.

Consider a transition $J_i M_i \to J_f M_f$, induced by the (π^+, K^+) reaction. The matrix element is

$$\begin{aligned} M\left(J_i M_i; J_f M_f\right) = \Big\langle J_f M_f \Big| \int d^3r \chi^{(-)*}\left(\vec{p}_K, \vec{r}\right) \chi^{(+)}\left(\vec{p}_\pi, \vec{r}\right) \\ \sum_{k=1}^{A} U_-(k)\, \delta^{(3)}\left(\vec{r} - \vec{r}_k\right) \left[f + ig\vec{\sigma}_k \cdot \hat{n}\right] \Big| J_i M_i \Big\rangle \end{aligned} \tag{16}$$

where $\chi^{(\pm)}$ are meson distorted waves, and U_- is the U–spin lowering operator which generates the $n \to \Lambda$ transition. The cross section is proportional to $\sum_{M_f} |M(M_f)|^2$, while the polarization P_f of the hypernuclear state $|J_f\rangle$ is defined as

$$\begin{aligned} P_f =& \frac{1}{J_f} \sum_{M_f} M_f P\left(M_f\right) \\ P\left(M_f\right) =& \sum_{M_i} |M\left(J_i M_i; J_f M_f\right)|^2 / \sum_{M_i, M_f} |M\left(J_i M_i; J_f M_f\right)|^2 \end{aligned} \tag{17}$$

The polarization P_f is a measure of the population asymmetry with respect to the reaction plane.

For the special case of a $J_i = 0$ target and a pure particle-hole hypernuclear state, the polarization assumes a simple analytic form. For example, consider the configurations in ${}^{12}_{\Lambda}\mathrm{C}$:

$$\begin{aligned} &\left[{}_{\Lambda}S_{1/2} \otimes {}_{n}P^{-1}_{3/2}\right]_{1^-,2^-} \\ &\left[{}_{\Lambda}P_{3/2} \otimes {}_{n}P^{-1}_{3/2}\right]_{0^+,1^+_1,2^+_1,3^+} \\ &\left[{}_{\Lambda}P_{1/2} \otimes {}_{n}P^{-1}_{3/2}\right]_{1^+_2,2^+_2} \end{aligned} \tag{18}$$

For the 1^- ground state of ${}^{12}_{\Lambda}\mathrm{C}$, we have

$$\begin{aligned} P_{1^-} &= (P_{PW} + P_A)\,/\,(1 + P_{PW}P_A) \\ P_{PW} &= -\,4\,\mathrm{Im}\,[fg^*]\,/\,(4|f|^2 + |g|^2) \\ P_A &= -\,2\sqrt{2}\,\mathrm{Im}\,[I^*(0)\,I(1)]\,/\,(|I(0)|^2 + 2|I(1)|^2) \end{aligned} \tag{19}$$

where

$$I(m) = \langle \phi_\Lambda \parallel \tilde{j}_{1m} \parallel \phi_n \rangle \tag{20}$$

and $\tilde{j}_{1m}$ is obtained by expanding the product $\chi^{(-)}\chi^{(+)}$ in partial waves [26]; in PWA, $\tilde{j}_{1m}$ reduces to $j_1(qr)\delta_{mo}$, and $P_{1^-} = P_{PW}$. Meson absorption effects provide the physical origin of P_A. In most cases, particularly for $\theta_L \leq 15°$, the influence of P_A is relatively minor, and we have $P \approx P_{PW}$. In plane wave approximation (PWA), one obtains simple analytic formulae for the polarization. For instance, for the 1^- ground state of ${}^{12}_{\Lambda}\mathrm{C}$, we have

$$P_{1^-} = -4\,\mathrm{Im}\,[fg^*]\,/\,(4|f|^2 + |g|^2) \approx -\frac{P_\Lambda}{2} \tag{21}$$

for small θ_L, since here $|g|^2 \ll |f|^2$. The cross sections for the unnatural parity states peak in the vicinity of $\theta_L \approx 15°$, at the $0.5 - 1\ \mu b/sr$ level for 2^- and 3^+. In this angular region, the 1^- and 2^+ cross sections have dropped to the $5\ \mu b/sr$ level, so a high resolution experiment could probably separate the 3^+ and 2^+ levels, thus providing information on the spin dependence of the ΛN interaction.

The polarization expected for unnatural parity states is negligible. However, for the natural parity 1^- and 2^+_2 states, P is very substantial near $\theta_L = 15°$, where the cross section is still large enough to be measurable. When configuration mixing of the 2^+_1 and 2^+_2 states is included, the polarization pattern could be strongly modified. Thus polarization measurements offer another promising spectroscopic tool for pinning down the ΛN interaction.

Ejiri *et al.* [25,27] have shown that polarized hypernuclear states may be populated through nucleon and γ decays of highly excited compound systems. Polarized hypernuclei

are particularly useful when combined with coincidence measurements of decay particles. For instance, the asymmetry of weak decay pions [28] provides information on hypernuclear structure and pion distortions inside the nucleus. A polarized hypernucleus could also be used to obtain a measurement of the Λ magnetic moment in a hypernucleus. Finally, we note that the angular distribution of nucleons from the non-mesonic weak decay of a polarized hypernucleus reveals interference terms between parity-conserving and parity-violating weak amplitudes.

If a polarized hypernucleus decays, the angular distribution of the nucleon has the form

$$W(\theta) = A_0 + A_1 P_\Lambda P_1 (\cos\theta) \tag{22}$$

where P_Λ is the polarization of the Λ and A_1 is given by an interference of parity–conserving ${}^3S_1 \rightarrow {}^3S_1 - {}^3D_1$ and parity–violating ${}^3S_1 \rightarrow {}^3P_1$ amplitudes for the $\Lambda N \rightarrow NN$ weak process. The first measurements of such weak decay angular distributions were recently performed at KEK by Ejiri and his collaborators [29]. Because of the rather coarse energy resolution, however, one cannot make detained comparisons with theoretical expectations.

6. Final Remarks

What contribution could a few GeV cooled proton facility make to strange particle physics? The key word in this discussion is SPIN. In the elementary production processes $pp \rightarrow K\Lambda N$, $K\Sigma N$, KY^*N, spin observables are crucial in probing the reaction mechanism. There are currently no spin data, although several proposals exist. The meson exchange approach, which rules at energies up to a few GeV, must break down at some point, to be supplanted by a picture involving explicit quark dynamics. If we study the secondary collisions of Λ or Σ hyperons produced in primary pp collisions, we can qualitatively improve our knowledge of YN scattering phenomena. To make progress, it is essential to measure the polarization P for ΛN and ΣN scattering, as well as the spin–separated cross sections $\sigma_{0,1}$. A closer look at spin observables in inclusive hyperon production is also warranted, as well as a global investigation of the strangeness production mechanism in proton–nucleus collisions. Finally, definitive measurements of cross sections for Λ hypernuclear production in pA interactions would provide useful tests of coalescence models (for inclusive ${}_\Lambda$A production) or short range correlations in two–body reactions at high momentum transfer.

Acknowledgments

This work supported by the US Government, Department of Energy under contract number DE–AC02–76–CH00016. I would like to thank Otto Schult for his kind invitation to the Bad Honnef Workshop, and for the many productive discussions which ensued.

REFERENCES

1. Baldini *et al.*, Landolt–Börnstein New Series 1/12b, p. 162.
2. J.M. Laget, Phys. Lett. B259, 23 (1991).
3. R. Frascaria *et al.*, Nuoco Cim. 102A, 561 (1989).
4. A. Deloff, Nucl. Phys. A505, 583 (1989).
5. P. Baillon *et al.*, Phys. Lett. 50B, 383 (1974) and Nucl. Phys. B134, 31 (1978).
6. E. Hirsch, U. Karshon and H.J. Lipkin, Phys. Lett. 36B, 385 (1971).
7. M.M. Nagels, T.A. Rijken and J.J. deSwart, Phys. Rev. D15, 2547 (1977) and D20, 1633 (1979).
8. R.A. Adelseck and B. Saghai, Phys. Rev. C42, 108 (1990).
9. C.B. Dover and H. Feshbach, Ann. Phys. 198, 321 (1990).
10. P.M.M. Maessen, T.A. Rijken and J.J. deSwart, Phys. Rev. C40, 2226 (1989).
11. B. Holzenkamp, K. Holinde and J. Speth, Nucl. Phys. A500, 485 (1989).
12. R.E. Chrien and C.B. Dover, Ann. Rev. Nucl. Part. Sci. 39, 113 (1989).
13. C.B. Dover, L. Ludeking and G.E. Walker, Phys. Rev. C22, 2073 (1980).
14. C.B. Dover, D.J. Millener and A. Gal, Phys. Rep. 184, 1 (1989).
15. C.B. Dover and D.J. Millener, *Electroproduction of Strangeness*, in Modern Topics in Electron Scattering, Eds. B. Frois and I. Sick, World Scientific, Singapore (1991), pp. 608–44.
16. LAMPF Workshop on (π, K) Physics, AIP Conf. Proc. No. 224, Particles and Fields Series 43, Eds. B.F. Gibson *et al.*, American Inst. of Physics, New York (1991).
17. V.V. Lyukov, Nuovo Cim. 102A, 583 (1989).
18. M. Boivin *et al.*, *Upper Limits for Light Hypernuclei Production Rates in the* (p, K^+) *Reaction*, Saclay preprint (1991).
19. S. Shinmura, Nucl. Phys. A450, 147c (1986); Prog. Theor. Phys. 76, 157 (1986).
20. M.G. Huber, B.C. Metsch and H.G. Hopf, Lecture Notes in Physics, Vol. 242, p. 499, Springer (1986).
21. D. Armutliiski *et al.*, Sov. J. Nucl. Phys. 47, 473 (1988).
22. S.V. Boyarinov *et al.*, Sov. J. Nucl. Phys. 50, 996 (1989).
23. P.H. Pile *et al.*, Phys. Rev. Lett. 66, 2585 (1991).
24. D.J. Millener, C.B. Dover and A. Gal, Phys. Rev. C38, 2700 (1988).
25. H. Ejiri *et al.*, Phys. Rev. C36, 1435 (1987).
26. H. Bandō, T. Motoba, M. Sotona and J. Žofka, Phys. Rev. C39, 587 (1989).
27. T. Kishimoto, H. Ejiri and H. Bandō, Phys. Lett. B232, 24 (1989).
28. T. Motoba, K. Itonaga and H. Bandō, Nucl. Phys. A489, 683 (1988).
29. S. Ajimura *et al.*, Phys. Rev. Lett. 68, 2137 (1992) and Phys. Lett. 282B, 293 (1992).

HADRON PRODUCTION IN PROTON-NUCLEUS COLLISIONS [1]

W. CASSING

Institut für Theor. Physik, Heinr.-Buff-Ring 16
D-6300 Giessen, Germany

Abstract

The production of K^+, η or ω mesons in proton-nucleus reactions is analysed with respect to primary nucleon-nucleon ($NN \to N\Lambda K^+$ or $NN\eta, NN\omega$), Δ-nucleon ($\Delta N \to N\Lambda K^+$, $NN\eta, NN\omega$) and secondary pion-nucleon ($\pi N \to K^+\Lambda$, $\omega N, \eta N$) production channels on the basis of Hartree-Fock groundstate momentum distributions and free on-shell production processes. Whereas for K^+ or ω production in proton-nucleus reactions the secondary channel πN clearly dominates at subthreshold energies, η mesons arise from primary and secondary processes with roughly the same order of magnitude. Furthermore, detailed VUU calculations for nucleus-nucleus collisions show that the relative weight of the various channels is quite different as compared to the proton-nucleus case especially for the role of the Δ N channel such that simple extrapolations from $p+A$ data to $A+A$ cross sections are not legitimate. In addition, the production of hypernuclei in $p+^{238}U$ reactions is calculated for various bombarding energies and found to be above 1 μb for laboratory energies $T_{lab} \geq 1.3$ GeV.

1. Introduction

The production of heavy mesons at bombarding energies far below the free nucleon-nucleon threshold is of specific interest [1-5] as one hopes to learn either about cooperative nuclear phenomena or about high momentum components of the nuclear many-body wavefunction. While a lot of models have been proposed for K^+ production in proton-nucleus and nucleus-nucleus collisions [5-12], only few efforts have been invested for η-production [13,19,22,25] where first experiments are available by now [14,20]. On the other hand, ω production has not yet been studied in p + A reactions so far.

In this contribution we use a folding model for primary and secondary production processes based on Hartree-Fock initial groundstate momentum distributions [15,16]. We briefly recapitulate the folding model in Section 2 and present results for η, K^+ and ω mesons for $p+^{12}C$ reactions. In section 3 we compare the results of the folding model with those from semiclassical VUU simulations that are applied to K^+ production in nucleus-nucleus collisions, too. In Section 4 we present estimates for the formation of hypernuclei in $p+^{238}U$ reactions while Section 5 is devoted to a summary and discussion of open problems.

2. Primary and Secondary Reaction Channels

We briefly recall the assumptions of the folding model which is described in more detail in [15,16]. The underlying picture is sketched in Fig. 1 for a $p+^{208}Pb$ collision

[1]Supported by BMFT, GSI Darmstadt and Forschungszentrum Jülich

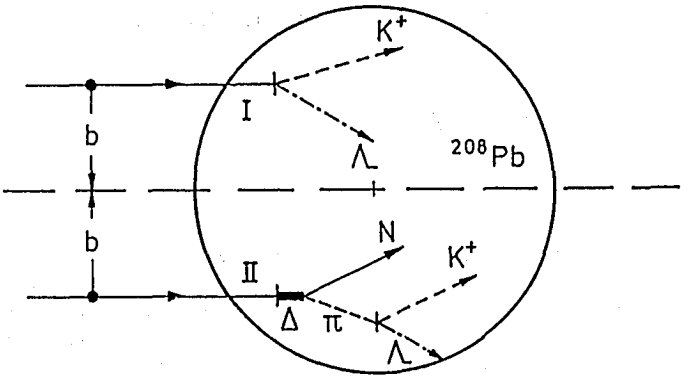

Fig. 1: Illustration of a $p + ^{208}Pb$ collision at impact parameter b for primary and secondary production of a $K^+\Lambda$ pair.

at finite impact parameter b : A proton impinging on a nucleus at a bombarding energy $T_{lab} > 400$ MeV is decelerated by the optical potential in the interior of the nucleus by about $U_{opt} \approx 40$ MeV due to the momentum dependence of the effective in-medium nucleon-nucleon force [17,18] before colliding with another nucleon. The first collision then happens at an average distance $\lambda_1 \approx (\sigma_{NN}\rho_0)^{-1} \approx 1.5\ fm$ from the 'nuclear surface'. Apart from elastic scattering the proton may produce a heavy meson x with momentum k_x in the first collision. The Lorentz-invariant differential cross section to produce a meson in a primary proton-nucleon (pN) collision is then given by

$$\{E_x \frac{d^3\sigma_x^{NN}}{d^3k_x}\}_{prim.} = \int d^3p\ \{E'_x \frac{d^3\sigma_x^e(\sqrt{s})}{d^3k'_x}\}\ \rho(\mathbf{p}) \tag{1}$$

where the Pauli-blocking factor for the final nucleon states has been neglected since kinematically the nucleons end up in an unoccupied regime in momentum space. In eq. (1) $\rho(\mathbf{p})$ stands for the target momentum distribution (normalized to 1) whereas the primed indices denote meson momenta in the individual nucleon-nucleon cms frame which have to be Lorentz-transformed to the detection frame, respectively. The quantity $\sqrt{s}$ is the invariant energy of the individual NN system.

The ansatz (1) physically implies that for primary production channels only the nuclear momentum distribution $\rho(\mathbf{p})$ is of relevance and thus involves an off-shell picture with respect to stationary single-particle states. The latter assumption is the basic conjecture of the present approach.

The elementary differential cross section $E_x d^3\sigma_x^e(\sqrt{s})/d^3k_x$ in (1) is parametrized as a function of the maximum momentum $k_{\max}(\sqrt{s})$ as [5]

$$E'_x \frac{d^3\sigma_x^e(\sqrt{s})}{d^3k'_x} \approx \sigma_{pNx}(\sqrt{s}) \frac{3E'_x}{(\pi\ k_x'^2 k_{\max})}(1 - \frac{k'_x}{k_{\max}}) \cdot (\frac{k'_x}{k_{\max}})^2 \tag{2}$$

where $k_{\max}$ is given by

$$k^2_{\max} = (s-(2m+m_\eta)^2)\cdot(s-(2m-m_\eta)^2)/(4s)\ for\ \eta's$$
$$k^2_{\max} = (s-(m+m_\Lambda+m_K)^2)\cdot(s-(m+m_\Lambda-m_K)^2)/(4s)\ for\ K^+$$
$$k^2_{\max} = (s-(2m+m_\omega)^2)\cdot(s-(2m-m_\omega)^2)/(4s)\ for\ \omega's, \tag{3}$$

the cross sections $\sigma_{pNx}(\sqrt{s})$ by [5]

$$\sigma_{pp\eta}(\sqrt{s}) \approx 0.17/GeV\cdot(\sqrt{s}-\sqrt{s_0})/[0.253\ GeV^{-2}+(\sqrt{s}-\sqrt{s_0})^2][mb],$$
$$\sigma_{pp\omega}(\sqrt{s}) \approx 0.33/GeV\cdot(\sqrt{s}-\sqrt{s_0})/[1.05\ GeV^{-2}+(\sqrt{s}-\sqrt{s_0})^2][mb],$$
$$\sigma_{pNK+}(\sqrt{s}) \approx 0.8(k_{\max}/(GeV/c))^4[mb] \tag{4}$$

with $\sqrt{s_0}$ denoting the individual threshold energies. As indicated by recent experimental data [20] we use $\sigma_{pn\eta} \approx 7\ \sigma_{pp\eta}$ closely above threshold. Furthermore, we adopt $\sigma_{pn\omega}(\sqrt{s}) \approx 3\ \sigma_{pp\omega}(\sqrt{s})$. In general one should note that the elementary cross sections $\sigma_{pNx}(\sqrt{s})$ are not known properly especially close to threshold which introduces a quite sizeable uncertainty in the following calculations. The expressions for the differential pion cross sections $\sigma_{pN\pi}(\sqrt{s})$ are well known and taken from an experimental data analysis of Ver West and Arndt [21].

Apart from the elementary differential cross section $d^3\sigma^e_x/d^3k$ the quantity (1) is determined by the momentum distribution $\rho(\mathrm{p})$ describing the available momentum components in a nucleus. We evaluate $\rho(\mathrm{p})$ in the mean-field limit, *i.e.* Hartree-Fock, thus neglecting the extreme momentum components due to residual two-body correlations.

In order to obtain the inclusive differential cross section in a proton-nucleus reaction we have to multiply the differential cross section (1) by the number of first-chance collisions $N_1(A)$ which is evaluated within the Glauber approximation ($N_1 \approx 7.3$ for ^{12}C). The resulting mesons yields for $p+^{12}C$ are shown in Fig. 2 (dashed lines) as a function of the proton laboratory energy T_{lab}. Here, the first collision approximation clearly misses the experimental data for K^+ production by Koptev et al. [12] by at least an order of magnitude and indicates that higher order processes [27-29] or even cluster production [30] might play an important role.

Apart from the primary reaction channels described above, the first p N collision may also lead to the excitation of a Δ- resonance or even higher baryon resonances (e.g. N(1440), N(1535) ..) which due to their short lifetime of 1 - 2 fm/c decay to nucleons and mesons prior to collisions with another nucleon. However, the contribution especially of $N\Delta$ channels for meson production in nucleus-nucleus collisions was found to be quite substantial in case of heavy-ion reactions [34,37] (cf. Section 3) such that this specific subchannel has to be reanalyzed for proton-nucleus reactions.

Here we concentrate on the latter channel and first calculate the differential probability

$$\frac{d^4\ P^{NN}_\Delta}{d^3k_\Delta dM_\Delta} = \int d^3p\ \frac{d^4\sigma_\Delta(\sqrt{s})}{d^3k'_\Delta dM'_\Delta}\sigma_{tot}(\sqrt{s})^{-1}\ \rho(\mathrm{p}) \tag{5}$$

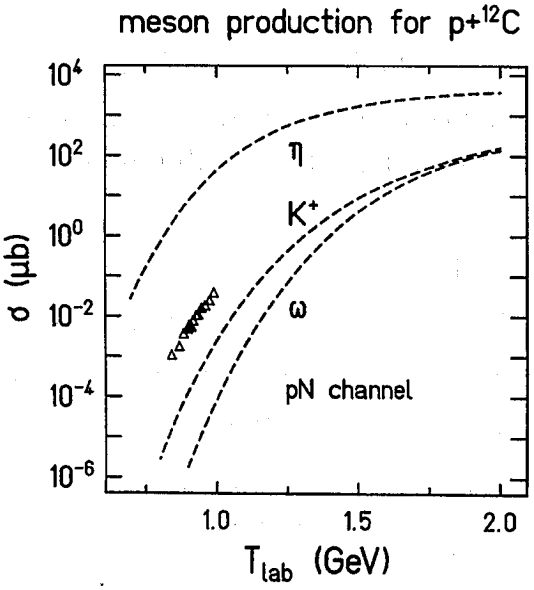

Fig. 2: The calculated K^+, η and ω cross section from primary pN collisions as a function of the bombarding energy for $p + ^{12} C$. Also shown are the experimental data for K^+ production from Koptev et al. [12] (open triangles).

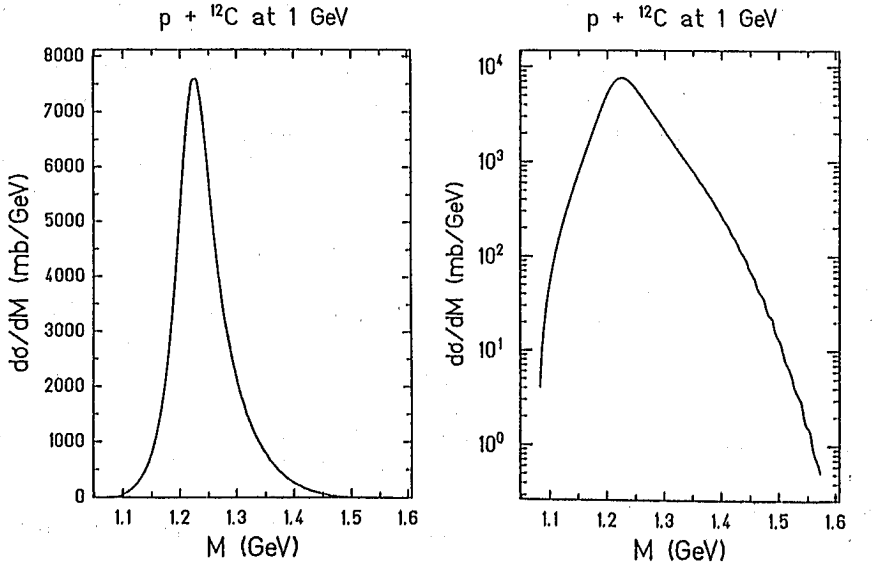

Fig. 3: Differential multiplicity dM_Δ/dM for p + ^{12}C at 1 GeV in linear and logarithmic representation.

to produce a Δ resonance with momentum k_Δ and mass M_Δ in a proton-nucleon collision averaged over the momentum distribution of the target. The primed indices denote quantities in the individual nucleon-nucleon cms that have to be Lorentz transformed to the actual detection frame of reference while $\sigma_{tot} \approx 42\ mb$ stands for the total proton-nucleon cross section. The differential cross section $\sigma_\Delta(\sqrt{s})$ is again adopted from Ver West and Arndt [21]. For the details of the isospin specific reaction channels and the explicit parametrization of the angular distribution we refer the reader to refs. [24-26].

Summing over isospin, the differential probability to produce a Δ resonance of mass M in a p + ^{12}C reaction at 1 GeV bombarding energy by first chance pN collisions is shown in Fig. 3. It clearly exhibits the well known resonance peak at 1.232 GeV, however, shows a substantial amount of high mass Δ's, too. The momentum distribution of these Δ's is displayed in terms of cluster plots in Fig. 4 for the same reaction as a function of M_Δ (given in GeV). Simply due to kinematics the Δ's of low mass show a broader distribution in momentum space than those of high mass. The forward-backward asymmetry of the Δ's in momentum is a result of the nonisotropic angular distribution for the process $N + N \rightarrow N + \Delta$.

In order to evaluate K^+, η or ω production by the Δ-nucleon channel we fold the primary Δ probability (5) with the nucleon momentum distribution $\rho(\mathrm{p})$ and the invariant production cross section, *i.e.*

$$\{E_x \frac{d^3\sigma_x}{d^3k}\}_{\Delta N} = \sum_\tau \int dM \int d^3k \int d^3p$$

$$\{E'_x \frac{d^3\sigma_{\Delta N \rightarrow x}(\mathrm{p},\mathrm{k},M)}{d^3k'}\} \rho(\mathrm{p}) \frac{d^4P_\Delta^{NN}}{d^3k dM} \frac{R(M)}{R(M)+\Gamma(M)} \tag{6}$$

where $\sum_\tau$ denotes the summation over isospin. For the elementary differential cross sections $d^3\sigma_{\Delta N \rightarrow x}(\sqrt{s})/d^3k'$ we use the same parametrizations as for the NN channels at the same invariant energy $\sqrt{s}$, since these cross sections cannot be determined experimentally. We note that the latter recipy has been proven quite successful for meson production in nucleus -nucleus collisions [5,36,37].

The quantity $R(M)/(R(M)+\Gamma(M))$ in (6) describes the probability for a Δ resonance of mass M to collide with another nucleon before decaying into the πN channel with a partial width $\Gamma(M)$ given approximately by

$$\Gamma(M) = \Gamma_0(\frac{M_0}{M})\ (\frac{q}{q_0})^3(\frac{v(q)}{v(q_0)})^2$$

$$v(q) = \frac{\alpha^2}{\alpha^2 + q^2}$$

$$\Gamma_0 = 110MeV;\ M_0 = 1232MeV;\ \alpha = 300MeV/c;\ q_0 = 227MeV/c \tag{7}$$

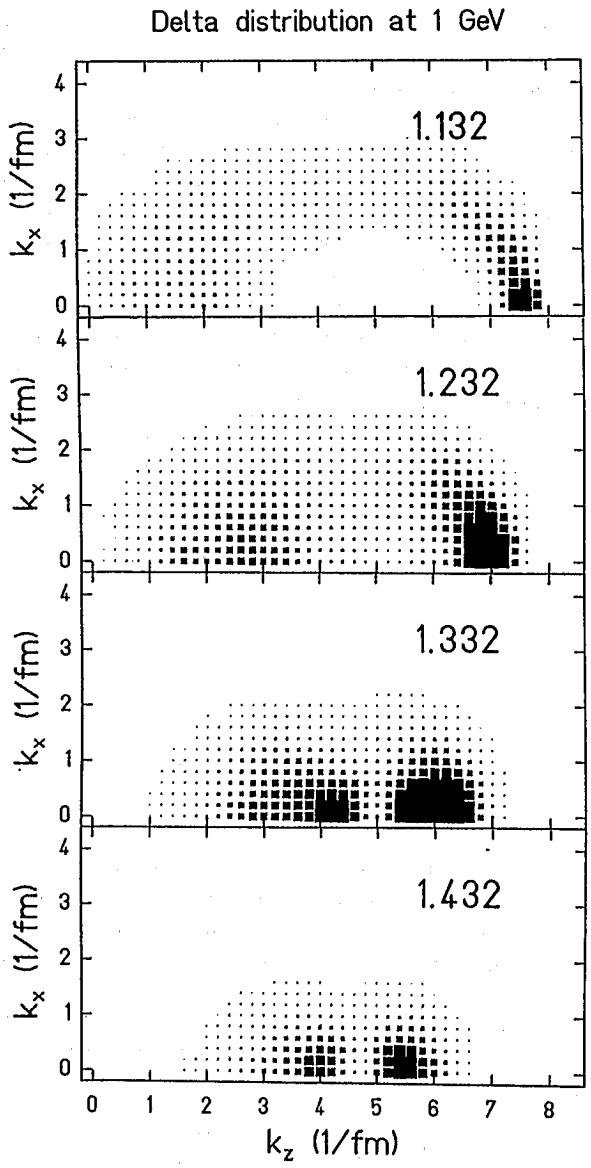

Fig. 4: Differential multiplicity $dM_\Delta/dMdk_zdk_x$ for p + ^{12}C at 1 GeV in terms of cluster plots for various Δ masses M (in GeV).

where q denotes the cms momentum in the πN channel. The quantity R(M) is the partial width for $\Delta - N$ scattering

$$R(M) = \hbar < \beta > \sigma_{\Delta N}\rho_0 \tag{8}$$

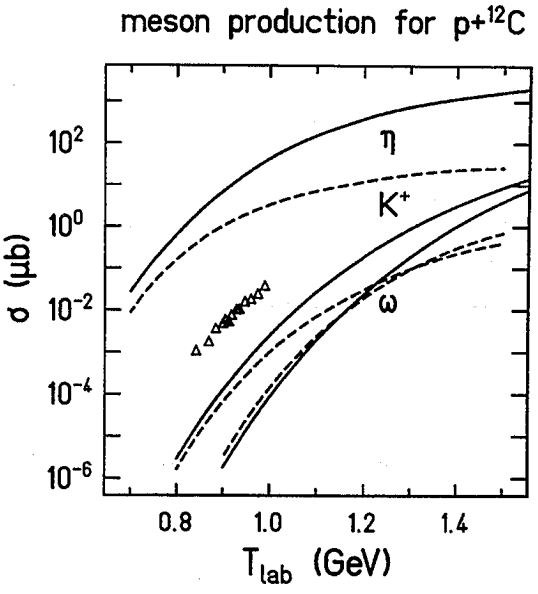

Fig. 5: The calculated K^+, η and ω cross section from primary pN collisions (full lines) as a function of the bombarding energy for $p+^{12}C$ in comparison to the contribution from the $\Delta - N$ channel (dashed lines). The triangles represent the experimental data for K^+ production from Koptev et al. [12].

where $< \beta >$ is the average velocity in the $\Delta - N$ collision, $\sigma_{\Delta-N} \approx 25mb$ and $\rho_0 \approx 0.16fm^{-3}$. Inserting $< \beta > \approx 0.8$ and $\Gamma(M) \approx 120MeV$, we find that about 34 % of the energetic Δ's may collide with another nucleon - thus contributing perturbatively to meson production - in p + A reactions before decaying into the πN channel. The situation, however, is quite different in A + A reactions since here R(M) can be larger than $\Gamma(M)$ due to the much higher densities involved [37] (cf. Section 3).

The expected contribution for inclusive meson yields from the $\Delta - N$ channel for p + ^{12}C is shown in Fig. 5 (dashed lines) in comparison to the contribution from primary pN collisions (full lines). At far subthreshold energies both contributions are approximately the same while at higher energies the Δ induced production channel plays a minor role in p + A collisions.

The differential pion multiplicity $f_\pi(\mathrm{k}_\pi)$ as emerging from Δ decay can now easily be evaluated from the isotropic two-body decay of the resonance. The results for $p+^{12}C$ at 1 GeV are presented in Fig. 6 in terms of contour lines increasing by a factor of 10 from line to line and show a substantial amount of pions with rather high momenta.

In order to evaluate the $K+$ yield from $\pi N \rightarrow K^+\Lambda$ collisions (cf. Fig. 1) we fold the pion distribution $f_\pi(\mathrm{k}_\pi)$ again with the nucleon momentum distribution $\rho(\mathrm{p})$ and the invariant production cross section, *i.e.*

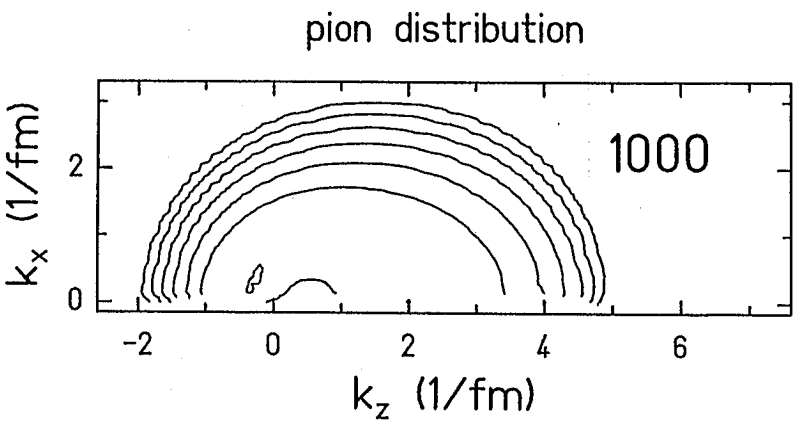

Fig. 6: The differential pion distribution $f_\pi(\mathrm{k}_\pi)$ as resulting from Δ decays for p + ^{12}C at 1 GeV. The contour lines increase by a factor of 10.

$$\{E_K \frac{d^3\sigma_K}{d^3k}\}_{\mathrm{sec.}} = \sum_\tau \int\int d^3p\; d^3k_\pi$$

$$\{E'_k \frac{d^3\sigma_{\pi N\to\Lambda K^+}(\mathrm{p},\mathrm{k}_\pi)}{d^3k'}\}\rho(\mathrm{p}) f_\pi(\mathrm{k}_\pi) \frac{\Gamma(M_0)}{(R(M_0)+\Gamma(M_0))} \tag{9}$$

taking into account the partial decay probability $\Gamma/(R+\Gamma)$ at resonance of the Δ to decay into the πN channel. In (9) $\sum_\tau$ denotes the summation over the intermediate pion channels allowed by charge conservation. In case of K^+ production this includes the channels $\pi^+ n \to K^+\Lambda$ and $\pi^0 p \to K^+\Lambda$. For η or ω mesons we only have to substitute the index K by η,ω in eq. (9) and to consider the channels $\pi^+ n \to \eta(\omega)p$, $\pi^0 p \to \eta(\omega)p$, $\pi^0 n \to \eta(\omega)n$ and $\pi^- p \to \eta(\omega)n$. The (isospin averaged) differential cross section for secondary η production is approximated by $\sigma_{\pi N\to\eta N} \approx 1/2\; \sigma_{\pi^- p\to\eta n}$ whereas the latter is parametrized by

$$\sigma_{\pi^- p\to\eta n}(\sqrt{s}) \approx 13.07\; GeV^{-0.5288} \cdot (\sqrt{s}-\sqrt{s_0})^{0.5288} [mb] \tag{10a}$$

for $\sqrt{s_0} = 1.486 < \sqrt{s} < 1.58906$ GeV,

$$\sigma_{\pi^- p\to\eta n}(\sqrt{s} \approx 0.14486\; GeV^{1.452426}/(\sqrt{s}-\sqrt{s_0})^{1.452426} [mb] \tag{10b}$$

for $\sqrt{s} \geq 1.58906$ GeV which represents a fit to the well known experimental data for $\pi^- p \to \eta n$ [31] up to $\sqrt{s} = 4$ GeV. In case of K^+ and ω production the respective cross sections are taken from Cugnon et al. [7,23].

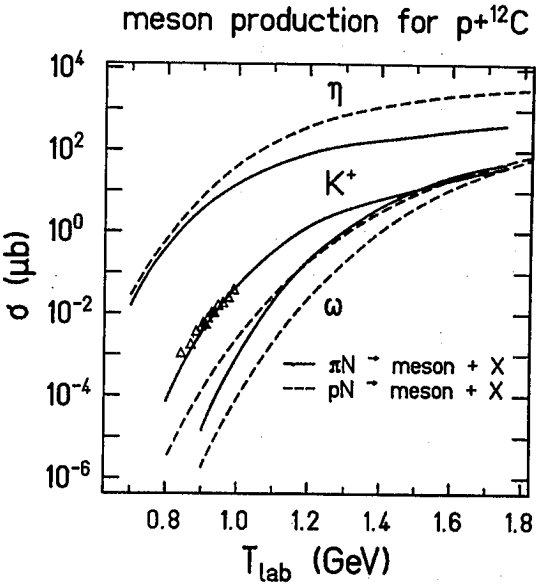

Fig. 7: The calculated K^+, η and ω cross section from primary pN collisions (dashed lines) for $p+^{12}C$ in comparison to the contributions from the secondary πN channels (solid lines). The triangles represent the experimental data for K^+ production from Koptev et al. [12].

In order to calculate the production cross sections for $p+A$ reactions from the secondary pion induced reaction channel, we again adopt the Glauber model which implies to multiply the folded cross sections (9) by the number of πN collisions. We recall that the number of first-chance nucleon-nucleon collisions $N_1(A)$ in this approximation gives $N_1(A) \approx A^{0.785}$ for $A \geq 15$ which is expected to hold with roughly 20% accuracy at the bombarding energy of interest. Furthermore, the number of events leading to meson production in secondary processes is approximated by $N_1(A) \cdot C(A)$, where the factor $C(A)$ accounts for the probability that a pion (produced in the first collision via the formation and decay of a Δ resonance) rescatters in the finite volume of the target. We assume the pion creation point for fixed impact parameter b to be displaced from the nuclear surface by $(\sigma_{pN}\rho_0)^{-1}$. Since the most energetic pions (that might produce an η, ω or K^+ meson in a πN collision) approximately move in beam direction, too, they propagate additionally by $(\sigma_{\pi N}\rho_0)^{-1}$ before a secondary collision takes place (cf. Fig. 1). This limits the impact parameter to $b^2 < R^2 - \lambda^2/4$, where λ is given by

$$\lambda = \{\sigma_{pN}\rho_0\}^{-1} + \{\sigma_{\pi N}\rho_0\}^{-1} \approx 3.5\ fm \tag{11}$$

when inserting experimental values for the cross sections σ_{pN} and $\sigma_{\pi N}$ at the energies of interest ($\rho_0 \approx 0.16\ fm^{-3}$). Integration over b and normalization then yields the probability [15]

$$C(A) = (R^2 - \lambda^2/4)/R^2, \tag{12}$$

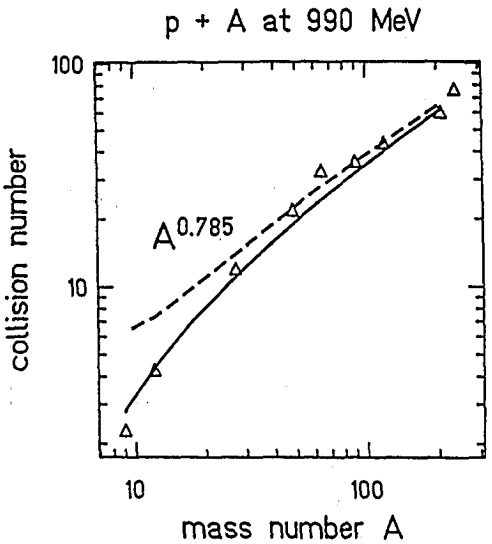

Fig. 8: The number of first-chance nucleon-nucleon collisions $N_1(A)$ as a function of the target mass number A (dashed line). The solid line denotes the effective number of secondary processes according to (12). The triangles represent the experimental data [12] at 990 MeV each divided by 9.1 nb.

where $R \approx 1.2\ A^{1/3}\ [fm]$ is the radius of the target with mass number A.

The resulting cross sections for η, K^+ and ω production in $p+^{12}C$ reactions are shown in Fig. 7 by the solid lines. We find that the K^+ data from Koptev et al. [12] are well reproduced when accounting for the secondary reaction channels. As in case of K^+ mesons also the ω mesons are essentially produced by secondary πN collisions while for $\eta's$ the primary and secondary reaction channels are approximately of the same order of magnitude at far subtreshold energies. Please note that η and ω reabsorption is not taken into account in the global overview in Fig. 7. For further details on η reabsorption we refer the reader to refs. [16,20].

The conjecture that at energies below 1 GeV the kaons are primarily produced by the πN channels is supported by the mass dependence at $T_{lab} = 990$ MeV, which is shown in Fig. 8 by the tringles where we have divided the experimental data [12] by $\sigma = 9.1\ nb$ which is the calculated K^+ cross section per pion-nucleon collision at this energy. The first-chance collision number $N_1(A)$ (dashed line) sincerely misses the A-dependence for low masses whereas the number of secondary collision events $N_2(A) \approx N_1(A) \cdot C(A)$ (solid line) quite nicely reproduces the experimental trend. We are thus confident that our approach is realistic enough to allow for further extrapolations and especially predictions (cf. Section 4).

3. Comparison to VUU Simulations

The simplicity of the folding model (Section 2) allows for a rather fast evaluation of differential meson cross sections in $p + A$ reactions and thus provides a more global

view on systematics with respect to mass A and projectile energy T_{lab} provided that it is also supported by more microscopic calculations *e.g.* of the VUU type [5,32]. Since a detailed description of particle production in the framework of transport approaches has been given in the review [5] we do not present any further equations and discussion of numerical implementations. The only quantities of interest are the parametrization of the elementary process $pN \to N\Lambda K^+$, $\pi N \to \Lambda K^+$, which we take to be the same for the comparison, and the initial condition for the target momentum distribution $\rho_{VUU}(\mathbf{p})$ in the VUU simulation. As described in [5] the distribution $\rho_{VUU}(\mathbf{p})$ — that is adopted in the initialization — is very close to Hartree-Fock results for momenta $p \leq p_F$ (Fermi momentum), however, lacks high momentum components $p > p_F$ in line with the semiclassical approximations performed in the derivation of the transport theory. We thus expect differences to appear especially for low bombarding energies.

3.1 Proton-Nucleus Collisions

Since at very low subthreshold energies the cross sections of the relevant elementary processes are very small, we propagate $N's$ and $\Delta's$ but treat pions perturbatively, *i.e.* a pion is produced in given nucleon-nucleon collision with a differential probability according to the Ver West and Arndt prescription [21] in the same way as in the folding model (Section 2). The only difference thus is a discrete (space-time localized) description of NN collisions in the VUU approach. The second step reactions $\pi N \to \Lambda K^+$ are treated by folding the individual pion probability $f_i(\mathrm{k}_\pi)$ from each individual NN collision i over all discrete nucleon momenta $\mathrm{k_N}$ in a volume of 33 fm^3 around the creation point $\mathrm{r_i}$ of

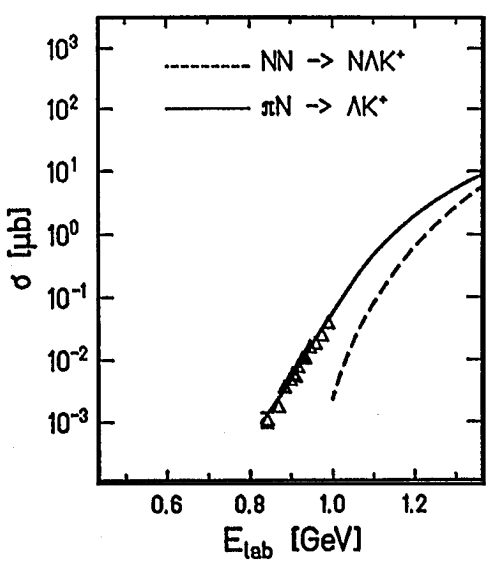

Fig. 9: Results of VUU calculations for K^+ production in $p+^{12}C$ reactions for primary (dashed line) and secondary channels (solid line) in comparison to the data [12].

the pion. The volume of 33 fm^3 corresponds to a sphere of radius 2 fm which reflects the pions average mean-free-path $\lambda_\pi = (\sigma_{\pi N} \cdot \rho^0)^{-1} \approx 2\ fm$. We, furthermore, have neglected the fact that the pion is produced by the decay of a baryonic resonance which propagates in the nuclear medium by about 0.5-1 fm and accidentally might decay outside the nucleus in case of very light nuclei. For the purposes of the present investigation we only note that the final K^+ cross section from πN reactions changes by at most 20% when changing the radius parameter by a factor of 2 for $A \geq 12$. The numerical results for $p + ^{12} C$ [33] are shown in Fig. 9 in comparison to the data of Koptev et al. [12] and demonstrate the dominance of the πN channels for K^+ production in the same way as the folding model. Note that due to the lack of higher momentum components there are no kaons from the primary channel below 1 GeV. This restriction, however, does not seriously change the result for the secondary channel since here the Fermi motion is exploited twice.

3.2 K^+ Production in Nucleus-Nucleus Collisions

Since the VUU approach has been especially developed for heavy-ion reactions at intermediate and high bombarding energy [5,32], we can use the same approach for $A + A$ collisions and study the contribution of the various channels as a function of bombarding energy. The numerical results for $^{40}Ca + ^{40} Ca$ from 0.6 to 1.6 GeV/u are shown in Fig. 10 where the dashed line reflects the K^+ yield from πN reactions which is small at all bombarding energies compared to the baryon-baryon production channels (solid line) [34,35]. As noted before, this result is essentially due to the fact that the Δ resonance more likely collides with another nucleon at high density than to decay into the πN channel.

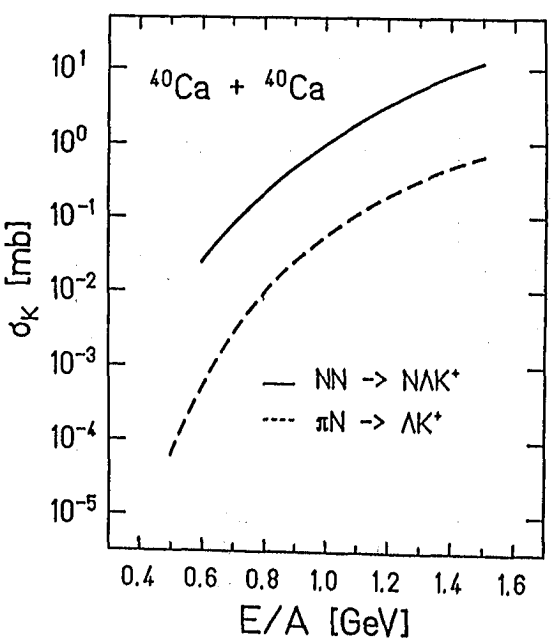

Fig. 10: Calculated K^+ cross section for $^{40}Ca + ^{40} Ca$ as a function of bombarding energy for baryon (solid line) and pion (dashed line) induced production channels.

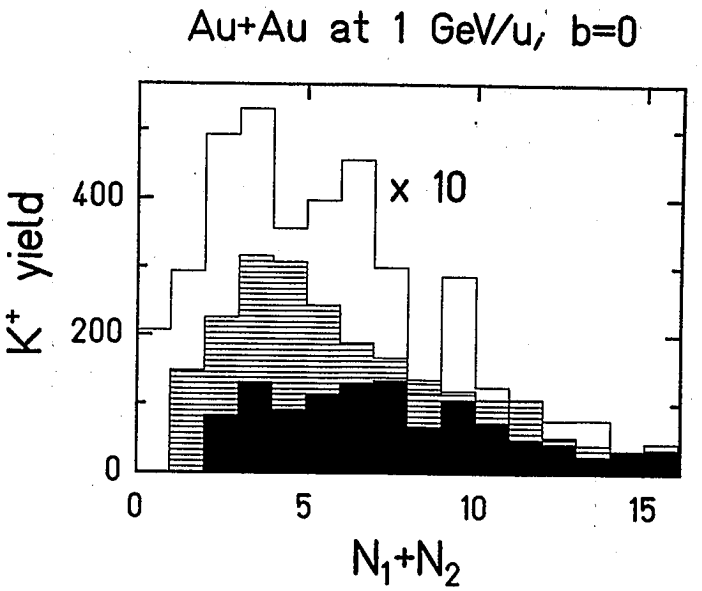

Fig. 11: Baryonic decomposition of the collisions producing a K^+ for $Au + Au$ at 1 GeV/u and $b = 0$. Open histograms: nucleon-nucleon collisions (x10); hatched histogram: nucleon$-\Delta$ channel; filled histogram: $\Delta - \Delta$ channel.

The baryonic decomposition for K^+ production channels is shown in Fig. 11 for a central collision of $^{197}Au + ^{197}Au$ at 1 GeV/u as a function of the collision number $N_1 + N_2$ that the baryons have experienced before producing the kaon. Two observations are evident: First, there are not only primary and secondary reaction channels; in A + A reactions multiple collisions play a dominant role! Second, the $\Delta - N$ channel gives the largest contribution to the $K+$ yield at subthreshold energies since at high density of the baryonic system a substantial amount of energy is stored in internal excitations of the nucleons [37].

4. Production of Hypernuclei

Since the production of a K^+ meson at the low bombarding energies considered here is associated with the production of a Λ particle, we simultaneously obtain the differential cross section for $\Lambda's$ from the dominant processes $\pi N \rightarrow K^+\Lambda$. The numerical results for $d^3\sigma_\Lambda/d^3k_\Lambda$ and bombarding energies of 1, 1.2 and 1.4 GeV are presented in Fig. 12 in terms of contour lines that increase by a factor of 10 from line to line.

As is well known the $\Lambda's$ are bound in heavy nuclei by $U_\Lambda \approx 25$ MeV such that all $\Lambda's$ with kinetic energy less than U_Λ are trapped within the target nucleus in the mean-field limit. This constrains the momenta to

$$(k_\Lambda^2 + m_\Lambda^2)^{1/2} - m_\Lambda \leq |U_\Lambda| \tag{13}$$

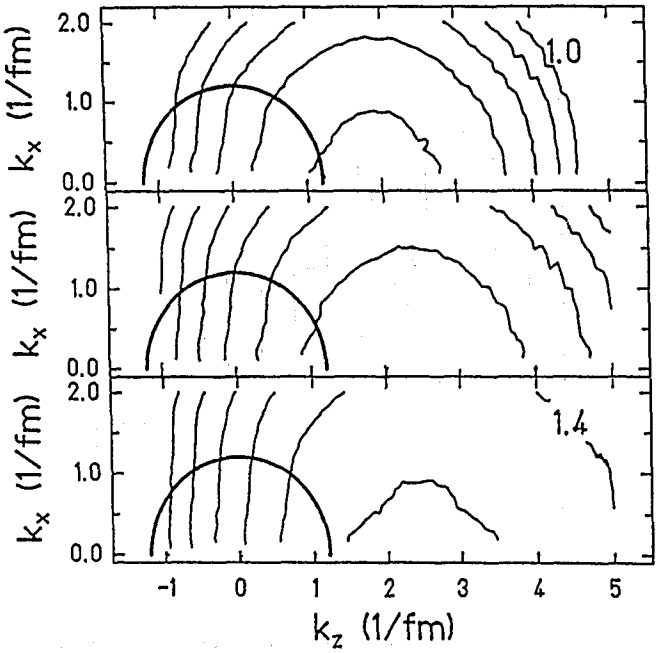

Fig. 12: Differential multiplicities of Λ particles in $p+^{238}U$ collisions at 1.0, 1.2 and 1.4 GeV. The contour lines increase by a factor of 10 from line to line. The thick-solid half-circle indicates the fraction of Λ particles that are trapped in the mean field of the target nucleus.

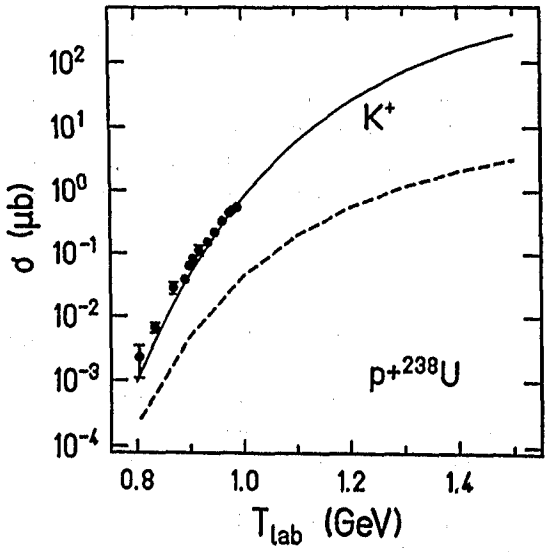

Fig. 13: Calculated K^+ cross section (solid line) for $p+^{238}U$ as a function of bombarding energy in comparison to the calculated cross section for hypernucleus formation (dashed line) and the K^+ data for $p+^{208}Pb$ [12].

when transforming k_Λ to the rest-frame of the recoiling nucleus. In case of heavy nuclei like ^{238}U the recoil momentum per nucleon is small and can be neglected for a first estimate of hypernuclei formation. Thus all $\Lambda's$ with momenta inside the thick solid lines in Fig. 12 are trapped and lead to a heavy hypernucleus. A trapping probability P_c then is defined by the fraction of $\Lambda's$ inside the solid sphere normalized to the total number of Λ particles.

The resulting hypernucleus cross section for $p+^{238}U$ is shown in Fig. 13 by the dashed line involving the processes $\pi^0 p \rightarrow K^+\Lambda$ and $\pi^+ n \rightarrow K^+\Lambda$ together with the associated total K^+ cross section (solid line) that is compared with the data of Koptev et al. [12] for $p+^{208}Pb$. We note that the K^+ cross section is well described and that the cross section for hypernuclei formation presents a conservative estimate which should be considered as a lower limit since Λ rescattering in the nucleus has not been taken into account. In fact, the ΛN cross sections are quite high [38] and a sizeable fraction of $\Lambda's$ with momenta larger than 200 MeV/c ($\approx$ 1 fm^{-1}) are expected to be trapped as a consequence of residual scattering. Furthermore, also the reaction $\pi^0 n \rightarrow K^0\Lambda$ should contribute to hypernucleus formation such that the dashed line in Fig. 13 should additionally be scaled by $r = 1 + \sigma_{K^0}/\sigma_{K^+}$.

The resulting cross sections thus are expected to be larger than 100 nb above $T_{lab} = 1.1$ GeV and even in the order of 1 μb for $T_{lab} \approx 1.3$ GeV. The trapping or capture probability P_c(*i.e.* the ratio of the dashed to the solid line in Fig. 13) is about 3.2% at 1.1 GeV and drops to 1.1% at 1.5 GeV since the kinematical matching becomes more unfavourable with increasing bombarding energy. However, these trapping probabilities are still large enough to open up a new branch of studies with heavy hypernuclei.

5. Summary

In this contribution we have presented calculations for K^+,ω and η production in p-nucleus reactions based on on-shell scattering processes and uncorrelated Hartree-Fock momentum distributions. This approach quite accurately reproduces pion as well as K^+ yields in proton induced reactions and compares well with VUU calculations for these reactions [16]. Whereas in case of η production primary and secondary channels are roughly of the same order of magnitude at far subthreshold energies, the production of K^+ or ω mesons is found to be dominated by the secondary πN channel. The latter result is essentially due to the fact that via secondary reactions one can exploit the internal Fermi motion twice and thus shift the production threshold substantially to lower energies. Furthermore, the pion induced production cross sections are large compared to the nucleon induced cross sections above threshold.

The secondary reaction mechanism is furthermore supported by the experimental mass dependence of the K^+ inclusive cross sections. This becomes striking especially for light targets such as ^9Be or ^{12}C. On the other hand, one can not simply extrapolate K^+ cross sections from $p + A$ reactions to nucleus-nucleus collisions since the reaction channels are quite different. Detailed VUU calculations even show that in lowest order the pion induced production channels in $A + A$ collisions can be neglected, since the ΔN channel contributes dominantly. On the other hand, the latter channel is insignificant in $p + A$ reactions.

Besides kaons especially the associated production of Λ particles and — in case the $\Lambda's$ get trapped by the target nucleus — the formation of heavy hypernuclei is of specific interest. Very conservative estimates indicate trapping probabilities in the order of a few percent from 1 to 1.5 GeV which yields cross sections for hypernuclei in the order of μb in $p + {}^{238}U$ reactions at about 1.3 GeV and above. This opens up the possibility for a new branch of hypernuclear physics especially at COSY in the next years.

in collaboration with: A. Lang, U. Mosel, T. Vetter, K. Weber, Gy. Wolf (Univ. of Giessen), O.W.B. Schult, W. Borgs, D. Gotta, A. Hamacher, H.R. Koch, H. Ohm, J. Pfeiffer, R. Riepe, H. Seyfahrt, K. Sistemich, V. Drüke, D. Filges, K.H. Watzlawik, R. Nellen, M. Karnadi, H. Stechemesser, G. Stollwerk (Forschungszentrum Jülich), B. Kamys, St. Kistryn, L. Jarczyk, P. Zolnierczuk, K. Pysz, J. Smyrski, A. Strzalkowski, B. Styczen (Univ. of Cracow) and P. von Brentano (Univ. of Köln)

References

1. P. Grimm and E. Grosse, *Prog. Part. Nucl. Phys.* 15 (1985) 339
2. P. Braun-Munzinger and J. Stachel, *Ann. Rev. Nucl. Part. Sci.* 37 (1987) 1
3. H. Nifenecker and J. A. Pinston, *Prog. Part. Nucl. Phys.* 23 (1989) 271
4. R. Shyam and J. Knoll, *Nucl. Phys.* *A*426 (1984) 606; A483 (1988) 711
5. W. Cassing et al., *Phys. Rep.* 188 (1990) 363
6. J. Randrup and C. M. Ko, *Nucl. Phys.* *A*343 (1980) 519; A411 (1983) 537
7. J. Cugnon and R. M. Lombard, *Nucl. Phys.* *A*422 (1984) 635
8. W. Zwermann and B. Schürmann, *Nucl. Phys.* *A*423 (1984) 525
9. W. Zwermann, *Mod. Phys. Lett.* *A*3 (1988) 251
10. S. V. Efremov, M. V. Kazarnovsky, E. Ya. Paryev, *Z. Phys.* *A*344 (1992) 181
11. J. Aichelin and C. M. Ko, *Phys. Rev. Lett.* 55 (1985) 2661
12. V. P. Koptev et al., *Sov. Phys. JETP* 67 (1988) 2177
13. A. L. De Paoli et al., *Phys. Lett.* 219B (1989) 194
14. E. Chiavassa et al., *Z. Phys.* *A*342 (1992) 107
15. W. Cassing et al., *Phys. Lett.* 238B (1990) 25
16. W. Cassing et al., *Z. Phys.* *A*340 (1991) 51
17. S. Hama et al., *Phys. Rev.* *C*41 (1990) 2737
18. K. Weber et al., *Nucl. Phys.* *A*539 (1992) 713
19. Ye. Golubeva et al., *preprint* INR-774 92
20. E. Chiavassa et al., *Nucl. Phys. A*, in press
21. B. J. Ver West and R. A. Arndt, *Phys. Rev.* *C*25 (1982) 1979
22. Ye. S. Golubeva et al., *preprint* INR-773 92;
    A. A. Sibirtsev, *preprint* 1992
23. J. Cugnon, P. Deneye and J. Vandermeulen, *Phys. Rev.* *C*41 (1990) 1339
24. Gy. Wolf et al., *Nucl. Phys.* *A*517 (1990) 615
25. Gy. Wolf, W. Cassing and U. Mosel, *Phys. Lett.* *B* 271 (1991) 43
26. Gy. Wolf, W. Cassing and U. Mosel, *Nucl. Phys.* *A*545 (1992) 139c

27. V. I. Komarov et al., *Nucl. Phys.* *A*326 (1979) 397
28. M. M. Nesterov and N. A. Tarasov, *Sov. Phys. JETP* 59 (1984) 226
29. N. A. Tarasov et al., *Pis'ma Zh. Eksp. Teor. Fiz.* 43 (1986) 217
30. H. Müller, *Z. Phys.* *A*339 (1991) 409;
H. Müller and K. Sistemich, *Z. Phys.* *A*344 (1992) 197
31. Landolt-Börnstein, Vol. NS *I*/12, ed. by O. Madelung, Springer 1988
32. G. F. Bertsch and S. Das Gupta, *Phys. Rep.* 160 (1988) 189
33. W. Cassing et al., *Nucl. Phys.* *A*519 (1990) 357c
34. G. Batko et al., *Proc. of the Intern. Workshop on Gross Properties of Nuclei and Nuclear Excitations XVIII*, Hirschegg, Austria, 1990, *p.* 174
35. L. Xiong et al., *Phys. Rev.* *C*42 (1990) 2231
36. W. Cassing and U. Mosel, *Prog. Part. Nucl. Phys.* 25 (1990) 235
37. A. Lang et al., *Nucl. Phys.* *A*541 (1992) 507
38. B. Holzenkamp et al., *Nucl. Phys.* *A*500 (1989) 485

THE pp→dπ$^+$ EXCITATION FUNCTION AT SMALL ANGLES

F. Hinterberger
Institut für Strahlen- und Kernphysik der Universität Bonn
Nussallee 14-16, D-5300 Bonn 1, Germany

Abstract

Besides the elastic scattering the pp→dπ$^+$ reaction is the only two-body reaction of the proton-proton system. The paper considers the possibility to study this reaction as a function of energy over a wide energy range. The feasibility is discussed with respect to the planned zero-degree facility at the cooler synchrotron COSY.

1 Introduction

The aim and purpose of the paper is (i) to emphasize the physics questions which are related to a study of the pp→dπ$^+$ excitation function at higher energies, (ii) to sketch the experimental situation, (iii) to discuss the kinematics and a possible szenario with respect to the zero degree facility at COSY [1] and (iv) to consider the method of internal target excitation functions in connection with the zero degree facility.

It will be shown that the zero degree facility is an ideal extension of the EDDA detector system [2]. The EDDA experiment is planned to measure simultaneously the excitation functions pp→pp and pp→dπ$^+$. Unpolarized differential cross sections, analyzing powers and the polarization correlation parameters A_{nn}, A_{ss} and A_{ls} will be measured as a function of energy. The EDDA detector covers the angular range $\theta = 10° - 72°$. The zero degree facility covers the missing angular range $\theta = 0° - 10°$ and $\theta = 72° - 180°$.

2 Physics questions

The pp→dπ$^+$ reaction is the only two-body reaction coupled to the pp→pp elastic scattering channel. A detailed investigation of the proton-proton excitation spectrum makes it necessary to study pp→pp excitation functions as well as pp→dπ$^+$ excitation functions. In view of the spin structure of the reactions it is necessary to measure unpolarized differential cross sections as well as polarization observables as a function of energy.

The study of the pp→dπ$^+$ reaction is related to the fundamental problems of the nucleon-nucleon interaction. Below the pion threshold this interaction is well studied, both experimentally and theoretically. Modern meson-theoretical potentials like e.g. the Bonn potential [3] or the Paris potential [4] provide very efficient model descriptions. These models can be extended to higher energies (e.g. 800 MeV, see refs. [5], [6]). An

important question in going to higher energies is the transition from the meson-nucleon picture to the quark-gluon picture [7].

A still open problem is the existence of dibaryons. Until now, the experimental search for such resonances was concentrated at rather low energies, that means below c.m. energies of about 2300 MeV. This search was motivated by theoretical predictions on the basis of bag models [8]. However, these calculations neglected the energy shift which is due to the coupling of the internal quark-gluon wave functions to the external nucleon-nucleon continuum wave functions. Taking this energy shift into account, Lomon [9] for instance predicts the lowest singlet dibaryon in the proton-proton system at a c.m. energy of about 2700 MeV.

3 Experimental situation

Concerning the pp→dπ^+ reaction, there are many data below 800 MeV. This is true for differential cross sections as well as for polarization observables. Also the inverse reaction dπ^+→pp has been investigated in great detail at lower energies [10].

Above 800 MeV data are scarce. Using the polarized proton beam of SATURNE and the spectrometer SPES4 angular distributions of analyzing powers have been measured at seven incident proton energies between 1200 and 2300 MeV [11]. The angular distributions show pronounced structures with considerable variations from the lowest to the highest energy. The data plotted as a function of the c.m. energy for t=0, u=0 and $\theta_{cm} = 90°$ show rapid variations at $\sqrt{s} = 2.65$ GeV.

In a recent measurement [12] these results were confirmed. Besides analyzing powers also differential cross sections have been measured at six incident proton energies between 1300 and 2400 MeV. The excitation functions of the differential cross section at t=0 and $\theta_{cm} = 90°$ also show deviations from a monotonic behavior at $\sqrt{s} = 2.65$ GeV.

The c.m. differential cross sections are on the order of 2 to 15 μb/sr that means roughly a factor 1000 smaller than the pp→pp elastic scattering cross sections.

4 Kinematics and the zero degree facility

In fig.1 the kinematical ellipses for the emission of a deuteron and a pion are plotted for an incident proton energy of 2500 MeV. The small angle range below 10° and the backward angle range above 72° is not covered by the EDDA detector.

Pions near 0° in coincidence with deuterons near 180° in the c.m. system can be separated from the proton beam using the zero degree facility. A possible scenario is shown in fig.2. The momenta of the corresponding pions and deuterons are rouhghly 2/3 and 1/2 the beam momentum, respectively. Concerning the high-momentum deuterons near 0° and the low-momentum pions near 180° c.m. angle a possible scenario is shown in fig.3. As first level trigger one can use the kinematical coincidence between pion and deuteron as well as the ratio of the specific ionizations. Detector systems consisting of scintillating fiber hodoscopes and plastic scintillator arrays can be used for that purpose.

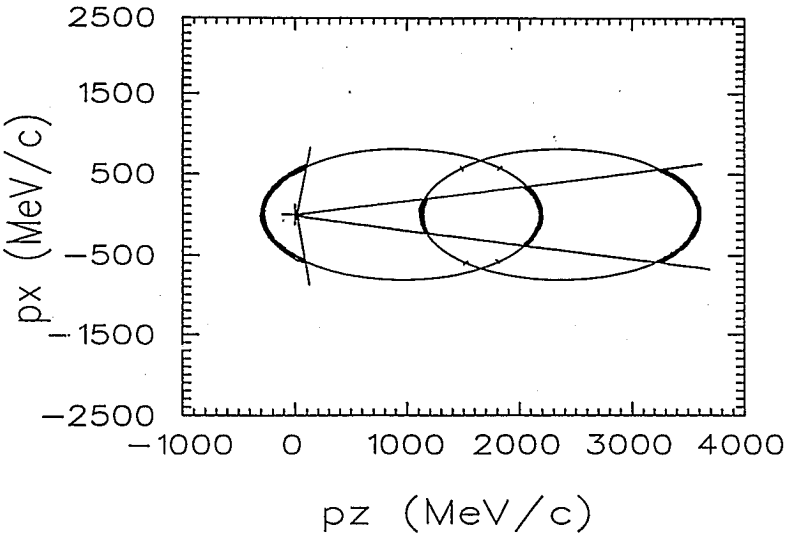

Figure 1: The kinematical ellipses of the reaction $pp \rightarrow d\pi^+$. The kinetic energy of the proton beam is 2500 MeV. The angular acceptance of the EDDA detector (10°-72°) is indicated in the figure.

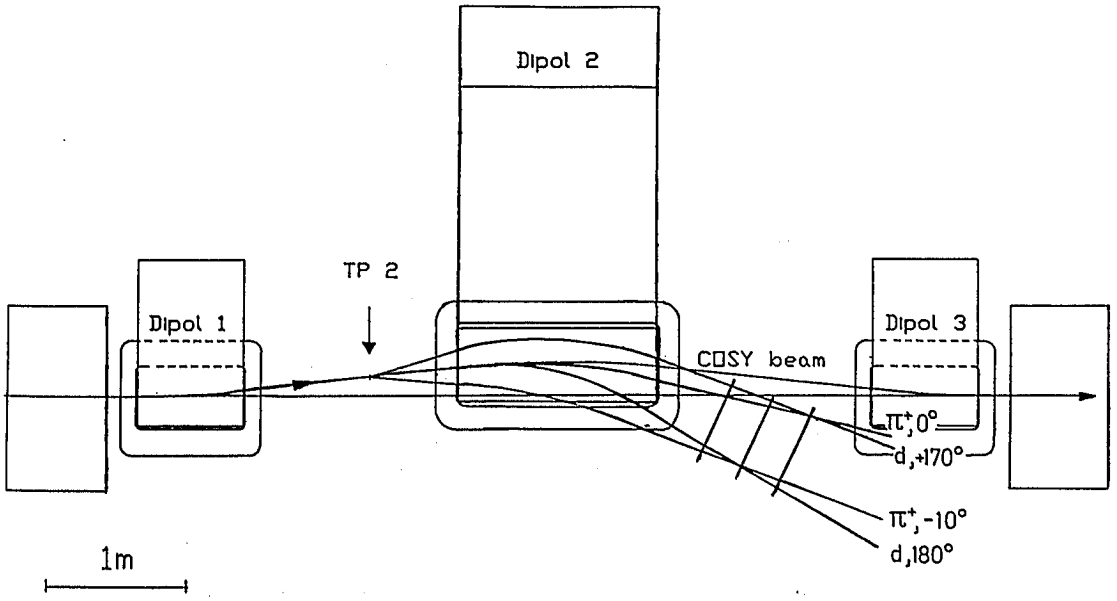

Figure 2: Scheme for detecting pions near $\theta_{cm} = 0°$ in coincidence with deuterons near $\theta_{cm} = 180°$.

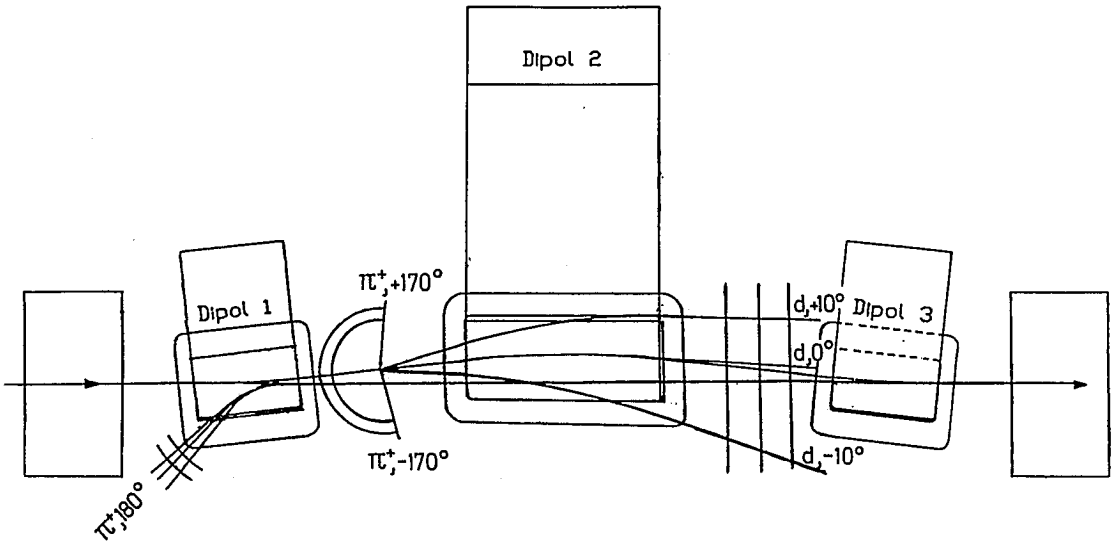

Figure 3: Scheme for detecting deuterons near $\theta_{cm} = 0°$ in coincidence with pions near $\theta_{cm} = 180°$.

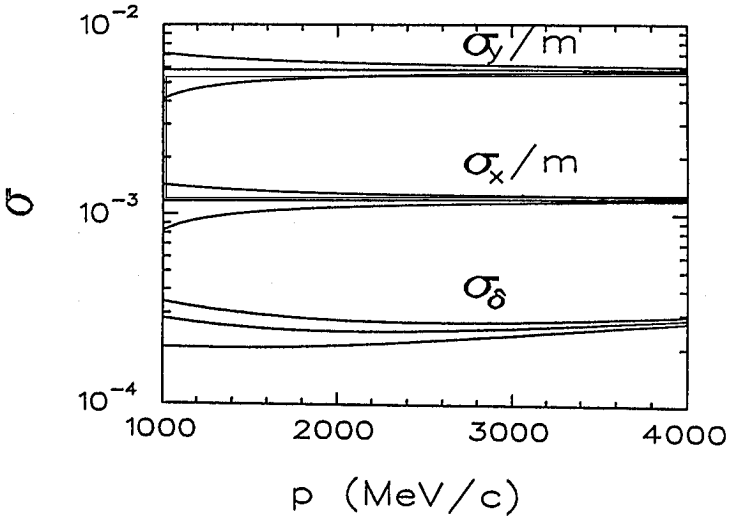

Figure 4: The beam spot at the target position TP2 with an 8μm thick internal CH_2 fiber target. The equilibrium emittances (ϵ_x = 1.0 mm mrad and ϵ_y = 5.0 mm mrad) yield a constant beam width of σ_x =1.2 mm and σ_y =6.0 mm, respectively.

5 Internal target excitation functions

In order to measure excitation functions with a high relative accuracy one has to have a fast and automatic beam energy variation. Human control should be avoided as much as possible. Then, one can also apply the multipass technique, that means, one can measure the same excitation many times in order to get rid of accidental instabilities. In addition, one has the advantage that a measurement can easily be repeated.

With an external beam the fast and automatic beam energy variation is difficult to achieve. In contrast, with an internal target one can use the standard acceleration ramp of the synchrotron and a very fast and automatic energy variation is possible.

A further benefit of this method is the adiabatic damping of the beam emittances which is due to the conservation of phase space (Liouville's theorem) during the acceleration of the beam particles. This adiabatic damping effect can be used to compensate the beam heating effects due to the internal target. The average increase of transverse and longitudinal beam emittance, $\Delta\epsilon_{target}$, is caused by the small angle Coulomb scattering and the energy loss straggling in the target, respectively. Simple analytic formulas for $\Delta\epsilon_{target}$ can be found in ref. [13]. The adiabatic damping is proportional to the actual emmittance ϵ and the relative momentum increase per turn $\Delta p/p$. The resulting change of beam emittance per turn, $\Delta\epsilon$ is given by the following equation [14].

$$\Delta\epsilon = +\Delta\epsilon_{target} - \epsilon\frac{\Delta p}{p} \tag{1}$$

It is even possible to compensate exactly the target heating and to operate with constant emittances. As an example fig. 4 shows the result of calculations [14] for an 8 μm thick CH_2 fiber target at the target station TP2 of COSY . It is possible to prepare the beam such that the resulting beam spot at the target position has the following one standard deviation values: horizontally 1.2 mm and vertically 6.0 mm. The energy straggling can also be compensated approximately. The resulting relative momentum deviation is about 210^{-4} in the given example.

6 Summary and conclusion

A detailed study of the pp$\rightarrow$dπ^+ excitation functions is important in view of the open questions of the nucleon-nucleon interaction at higher excitation energies. The zero-degree facility is well suited for the small angle excitation function measurements. It is possible to measure differential cross sections, analyzing powers as well as three polarization correlation parameters. As internal target one can use either a CH_2 fiber target or a hydrogen cluster target for the unpolarized differential cross section measurements and a polarized atomic beam target for the polarization observables. The method of measuring excitation functions with internal targets has the great advantage of a fast and automatic energy variation and the benefit of the adiabatic damping of the beam emittances.

References

[1] W. Borgs et al., AIP Conf. Proc. 221 (1991) 299

[2] J. Bisplinghoff and F. Hinterberger, AIP Conf. Proc. 221 (1991) 312

[3] R. Machleidt, K. Holinde and Ch. Elster, Phys. Rep. 149 (1987) 1

[4] M. Lacombe, B. Loiseau, J. M. Richard, R. Vinh Mau, J. Cote, P. Pires and R. de Tourreil, Phys. Rev. C21 (1980) 861

[5] Ch. Elster,W. Ferchländer, K. Holinde, D. Schütte and R. Machleidt, Phys. Rev. C37 (1988) 1647

[6] Ch. Elster,W. Ferchländer, K. Holinde, D. Schütte and R. Machleidt, Phys. Rev. C38 (1988) 1828

[7] R. Vinh Mau, C. Semay, B. Loiseau and M. Lacombe, Phys. Rev. Lett. 67 (1991) 1392

[8] P. J. Mulders and A. W. Thomas, J. Phys. G9 (1983) 1159

[9] P. Gonzalez, P. LaFrance and E. L. Lomon, Phys. Rev. D35 (1987) 2142

[10] M. P. Locher, M. E. Sainio and A. Svarc, Adv. in Nucl. Phys. 17 (1986) 47

[11] R. Bertini, G. Roy, J. M. Durand, J. Arvieux, M. Boivin, A. Boudard, C. Kerboul, J. Yonnet, M. Bedjidian, E. Decroix, J. Y. Grossiord, A. Guichard, J. R. Pizzi, Th. Hennino, and L. Antonuk, Phys. Lett. B203 (1988) 18

[12] J. Yonnet, R. Abegg, M. Boivin, A. Boudard, G. Bruge, P. Couvert, G. Gaillard, M. Garcon, L. G. Greeniaus, D. A. Hutcheon, C. Kerboul and B. Mayer, Colloque de Physique C6 (1990) C6-379 and submitted to Nucl. Phys. A

[13] F. Hinterberger and D. Prasuhn, Nucl. Instr. and Meth. A279 (1989) 413

[14] F. Hinterberger and D. Prasuhn, Nucl. Instr. and Meth. A321 (1992) 453

AN INTERNAL HIGH-DENSITY STORAGE CELL TARGET FOR POLARIZED HYDROGEN

Kirsten Zapfe

Deutsches Elektronen-Synchrotron, Notkestraße 85, D-2000 Hamburg 52, Germany
(for the HERMES-FILTEX target group)

A high-density target of polarized atomic hydrogen was produced by injection of atoms from an atomic beam source into a T-shaped storage cell. The target was installed in the Heidelberg test storage ring (TSR). The target polarization and target thickness were measured by means of an electron-cooled beam of 27 MeV α-particles. A target thickness of 1.1 $\times 10^{14}$ polarized hydrogen atoms/cm^2 (2 hyperfine states) was achieved cooling the cell to 80 K. The target polarization was $P_T = 0.82$ and $P_T = 0.45$, when state 1 or states 1+2 were selected, respectively, or 90 % of the maximum possible value.

1. Introduction

Discussions in the last years[1] showed considerable interest in studies of spin physics using internal polarized hydrogen or deuterium gas targets in electron and proton rings. So far, experiments with polarized hydrogen gas targets are limited to one experiment with a polarized deuterium target at the electron storage ring VEPP-3 in Novosibirsk[2]. Proposed experiments include, for instance, the study of deep inelastic scattering of high energy electrons by polarized hydrogen und deuterium to study the spin structure functions of the nucleon (HERMES experiment at HERA)[3] as well as antiproton spin physics (e.g. FILTEX experiment to polarize a circulating beam of antiprotons)[4].

For these kinds of experiments a target thickness in the order of 10^{14} $\vec{H}$/cm^2 is required. A jet of polarized atoms, e.g. from an atomic beam source, provides at best a target thickness of the order 10^{12} $\vec{H}$/cm^2 [2,5]. The available target thickness can be improved by more than two orders of magnitude by injecting the polarized gas into a thin walled, T-shaped storage cell[6,7] as indicated in Fig. 1.

Compared to polarized solid targets, the polarized gas targets have the following advantages:

- high effective polarization ($\approx$ 80 %), as they have practically no dilution by unpolarized nucleons;
- rapid reversal of polarization at frequencies in the order of 1 Hz.

Here we report the installation of a storage cell target in the Heidelberg test storage ring (TSR) und measurements of the target polarization und target thickness by means of an electron-cooled beam of 27 MeV α-particles of intensity up to 0.3 mA. The de-

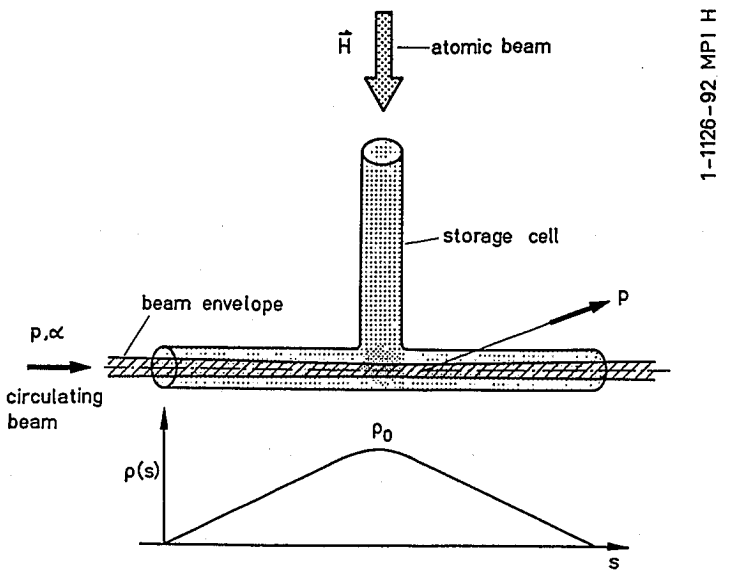

Fig. 1. Principle of a storage cell target and density profile along the ion beam axis. The cell consists of a straight beam tube and a feed tube. Polarized gas from a source is injected into the feed tube and trapped due to the small conductance of the tubes.

velopment of this target was motivated by the FILter Target EXperiment (FILTEX)[4], which aims to polarize a stored beam of antiprotons by spin selctive attenuation in a polarized target and to study the spin-dependece in the antiproton-proton interaction at low momenta using the same target, surrounded by detectors. With the target described here, a first proof of principle of the new methode to polarize stored ions has recently been performed with 23 MeV protons[8].

2. The Polarized Hydrogen Gas Target

2.1 Storage Cell

As sketched in Fig. 1 the T-shaped storage cell consists of a long narrow tube through which the circulating beam passes and a feed tube, e.g. under right angle, into which polarized atoms are injected.

Assuming a triangular density distribution of the hydrogen gas along the cell, the target areal density is given by

$$n = \frac{I}{C_{tot}} \cdot \frac{l_b}{2} \quad . \tag{1}$$

Here I is the intensity of the injected atomic beam, l_b the length of the beam tube and C_{tot} the total gas conductance from the center outwards. The total conductance of the

cell is given by

$$C_{tot} = C_f + 2 \cdot C_{b/2} \tag{2}$$

with C_f and $C_{b/2}$ beeing the conductance of the feed and half beam tube, respectively. To get a high density, the conductance of the cell must be minimized.

In the molecular flow regime, the conductance of a short cylindrical tube is determined by the molecular weight M, the temperature T [K], the diameter d [cm] and the length l [cm] according to:

$$C = 3.8 \cdot \sqrt{\frac{T}{M}} \cdot \frac{d^3}{l + \frac{4}{3}d} \,. \tag{3}$$

Combining Eq. 1 and 2 the target thickness n depends strongly on the tube diameter and lenght:

$$n \sim \frac{l^2}{d^3} \,. \tag{4}$$

The acceptance of the storage ring should not be limited by the cell. Therefore the cell diameter should be in the order of 10–15 σ of the beam size. With

$$\sigma(s) \sim \sqrt{\epsilon \cdot \beta(s)} \,, \tag{5}$$

where ϵ is the emittance of the beam and $\beta(s)$ the β-function at the position s, the target density is proportional to:

$$n \sim \frac{l^2}{\beta^{3/2}} \,. \tag{6}$$

The strong dependence of the target thickness on the cell diameter respectivly the beam size makes a low value of the β-function at the target of greatest importance, as indicated in Fig. 2. Working in a low energy ion storage ring, continuous electron cooling must be applied to compensate for the emittance blow-up and decelaration of the beam due to the interaction with the target.

The cell used for the measurements reported here consists of a T-shaped aluminum tube of 0.2 mm wall thickness, 11 mm in diameter and 250 mm in length[9,10]. The feed tube is 100 mm long with a diamter of 10 mm. The cell was made in two halves ("clam shell cell"), so that it could be opened for beam injection. The two sealing surfaces of each half tube are enlarged by 10 mm wide lips to reduce the leakage rate out of the cell. A small opening opposite to the feed tube allows for diagnostics with a quadrupole mass spectrometer. The cell can be cooled to 80 K to increase the target thickness.

The injected atoms diffuse slowly out of the cell performing about 400 wall bounces. Studies of wall depolarization at Heidelberg[11] and Wisconsin[12] in hydrogen storage cells have shown, that especially wall coatings of Fomblin oil and Teflon inhibit recombination and depolarization of the hydrogen atoms. In our case the cell is coated with Teflon.

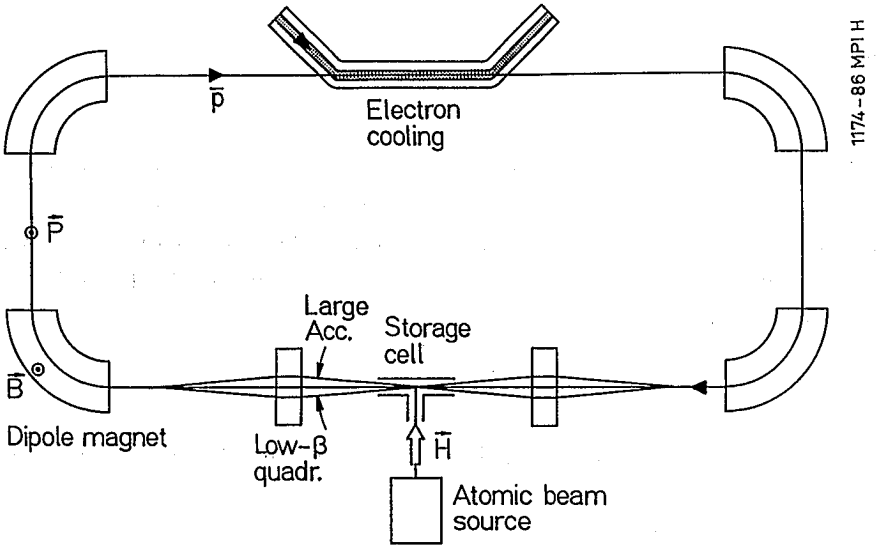

Fig. 2. Scheme of a storage ring with an internal target in the low-β section and electron cooling.

2.2 Atomic Beam Source

The atomic beam source developed for this project[13] is based on the well-known Stern-Gerlach separation of thermal atoms by a strong inhomogenous magnetic field according to their spin projection. A schematic representation of the atomic beam source and target chamber is shown in Fig. 3. The source consists of a dissociator with a cooled nozzle, a beam formation system with two skimmers and a system of permanent sextupole magnets with a pole tip field of 1.5 T[14]. The last magnet is installed within the target chamber (see Fig. 3). The distance between the exit of this magnet and the feed tube of the storage cell is 40 mm. The clean vacuum system based on turbomolecular and cryogenic pumps is designed for high gas flow. The base pressure is about 10^{-8} mbar in order not to pollute the UHV system of the storage ring. The geometry of nozzle, skimmers and separation magnets are emperically optimized for minimum attenuation of the beam.

The sextupole magnets focus the two hyperfine components with electron spin $m_j = +1/2$, while the two components with $m_j = -1/2$ are defocussed. For the experiments described here a weak guide field of 5 G in the vertical direction is applied over the target region to define the polarization axis. Under these conditions, the theoretical maximum nuclear polarization for the two yperfine states (1+2) is $P = 0.5$. Using a RF-transition between sextupole magnets 2 and 3, one hyperfine substate (1) with maximum nuclear polarization $P = 1.0$ can be selected. It should be noted, that working in a strong magnetic holding field (e.g. in the case of HERMES) two substates

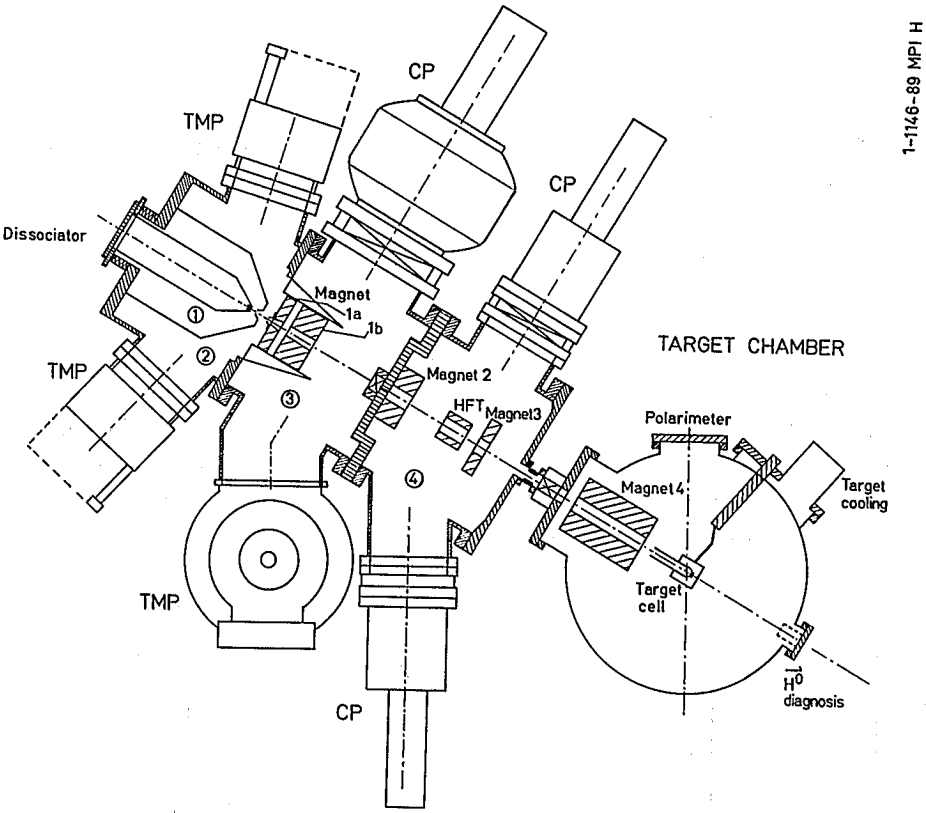

Fig. 3. Schematic representation of the FILTEX source and target chamber. The tilt angle of 30° has been chosen for reasons of experiment geometry in order to leave the horizontal and vertical plane free for the detectors.

can be used to get a maximum nuclear polarization of P = 1.0, as proton and electron spin are decoupled.

After a recent improvement of the magnet system by using conical magnets, i.e. magnets with diameter increasing along the beam axis, which have better focusing properties compared with cylindrical magnets, an intensity of $I = 8.1 \times 10^{16}$ atoms/s in two substates is obtained routinely. This is about a factor of four higher than the intensity reported for cold sources following the Zürich design[15,16]. With our intensity we expect according to Eq. 1 a target thickness for the FILTEX target cell at 80 K of about 1.0×10^{14} atoms/cm^2.

2.3 Target Section

The target chamber[17], comprising the cooled storage cell, a high-capacity cryogenic pump and the detection system, was located in the low-β section of the TSR. With three differential pumping stages on each side the pressure outside the target section was kept

in the 10^{-10} mbar range. The recoil protons were detected by four vertical, 1 mm thick, 50 mm wide and 250 mm long scintillation counters symmetrically arranged left and right of the beam axis. The detectors are separated by circular (250 mm diameter), 125 μm thick Kapton windows from the target chamber vacuum.

3. Measurements with the Target

The storage cell target together with the atomic beam source has been tested in 1991[18] by passing a 35 MeV beam of α-particles from the Heidelberg MP tandem accelerator through the cell and measuring the left-right asymmetry of recoil protons near $\theta_{lab} = 21°$. The target polarization was found to be $P = 0.42 \pm 0.04$ compared to the maximum possible value for hyperfines states 1+2 in a weak magnetic field (5 G) of $P = 0.5$. The measurements were difficult because of a large background from scattering of beam halo by the cell wall as shown in the left hand side of Fig. 4.

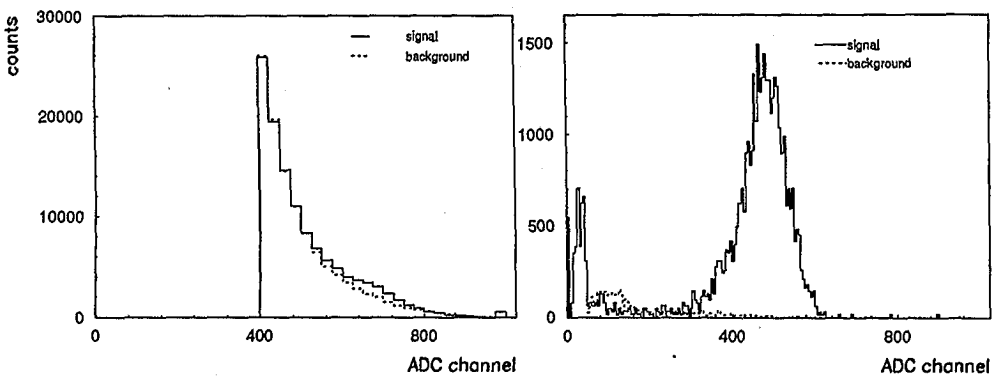

Fig. 4. Pulse height spectra of the signal and the background with external beam (left) and with stored beam (right).

Already the first tests of the target with a stored beam in the TSR showed excellent energy spectra of the recoil protons, with a background of less than 1 % (Fig. 4, right). Background measurement were made by replacing the hydrogen gas in the target cell by an amount of oxygen sufficient to cause the same amount of beam loss by scattering. Since beam injection was readily achieved with closed cell, a new cell consisting of a simple cylindrical tube of 11 mm inner diameter and 25 cm length was installed replacing the clam shell cell

The target polarization und the target thickness were measured using an electron-cooled beam of 27 MeV α-particles of intensity up to 0.3 mA. The lifetime of the stored beam with target cell in place was 1 h without gas and about 11 min with polarized gas. The target polarization was reversed by reversing the 5 G guide field over the target.

During the tests, the target cell was cooled down to 80 K in order to increase the target density.

3.1 Target Polarization

The target polarization was extracted from the count rate asymmetries with spin up and down for each counter. Fig. 5 shows a spectrum of the recoil protons at a laboratory angle of 21° for target spin up and down. The target polarization could be measured to an accuracy of 1 % in a few minutes. The value of the p-α analyzing power in the angular range used here is large and well known[19].

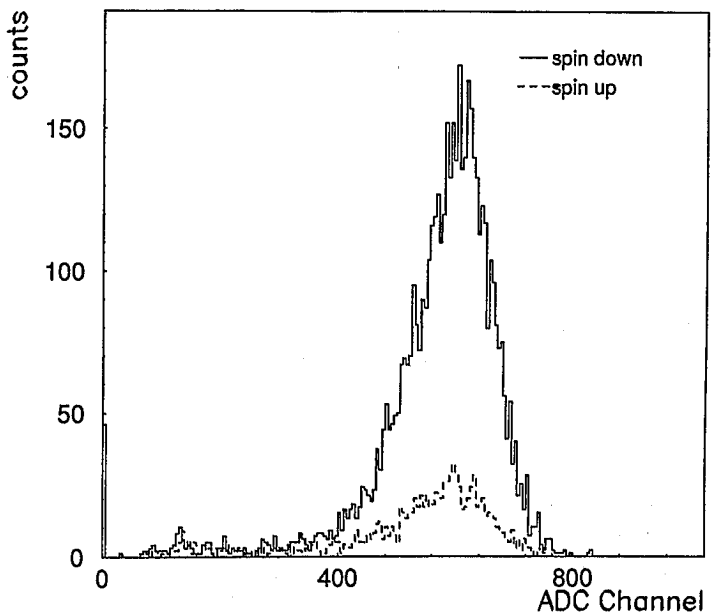

Fig. 5. Pulse height spectrum produced by recoil protons at 21° for target spin up (- - -) and down (——). in the bombardment of the polarized hydrogen target by 27 MeV α-particles circulating in the storage ring. The spectra shown were obtained by selecting a single spin state. The results indicate a target polarization of P = 0.826 ± 0.004 (statistical error). The run time was 6 min.

Measurements of the polarization as a function of the cell wall temperature are shown in Fig. 6. The open and closed circles refer to measurements with the RF-transition between the sixtupoles of the atomic beam source turned off (2 substates) and on (1 substate), respectively. The target polarization is constant for wall temperatures between 80 K und 300 K. Below 60 K a significant decrease in polarization is observed. The observed average values for T $\geq$ 80 K are 0.45 with RF-transition off, and 0.82 with RF-transition on. Tracking calculations for the sixtupole system and the efficiency of

the RF-transition (95 %) gave ideal values of 0.49 and 0.88, respectively. In both cases the measured polarization amount to more than 90 % of the ideal value, leaving little room for polarization losses by wall depolarization. It should be mentioned, that the results may still undergo small changes in the final data analysis.

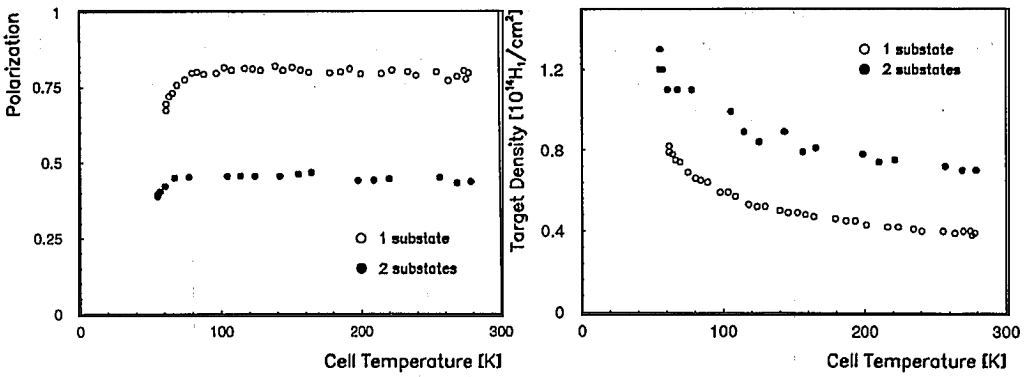

Fig. 6. Measured target polarization (left) and target thickness (right) as a function of the cell wall temperature. Open and closed circles refer to measurements with the RF-transition in the atomic beam source turned off and on, respectively.

Another important result was, that after several weeks of running with alpha beam currents between 0.05 and 0.3 mA and proton beams of up to 1 mA no aging effects of the cell coating and therefore no deterioration of the target polarization have been observed.

3.2 Target Thickness

The target thickness was calculated from the spin-averaged count rates and the known cross section, detector geometry and beam current. As an independent method the deceleration rate of the beam with electron cooling switched off has been used to determine the target thickness. The right hand side of Fig. 6 shows the decrease in target thickness from rejection of state 2 atoms, as well as the expected increase in target thickness with decreasing cell wall temperature ($n \sim 1/\sqrt{T}$). At the optimum working temperature of 80 K a density of $n = 1.1 \times 10^{14}$ atoms/cm^2 has been measured with two substates of hydrogen, and a density of $n = 0.65 \times 10^{14}$ atoms/cm^2 with one substate. This is in agreement with the values calculated from the atomic beam flux and the cell geometry using Eq. 1.

4. Conclusions

A storage cell target for polarized hydrogen has been installed in the Heidelberg test storage ring. At a cell temperature of 80 K a target thickness of $n = 1.1 \times 10^{14}$ atoms/cm^2 with a polarization of $P_T = 0.45$ have been measured with two substates of hydrogen, and $n = 0.65 \times 10^{14}$ atoms/cm^2 with $P_T = 0.82$ for one substate. The observed target thickness is about 30 times larger than the recently reported value for the Phase II deuterium target in use at the VEPP-3 ring in Novosibirsk[20]. It is important to note, however, that in applications, where a strong magnetic field is applied over the target, high polarization and high target thickness can be obtained at the same time by use of two spin states.

Due to the very short time of about 10 min for one run, several aspects like the dependence of the target parameters on the cell wall temperature, or the long-term stability, could be studied for the first time with high precision.

The achieved target polarization and flux of target atoms are more than sufficient to meet the requirements of the HERMES proposal[3]. At present the atomic beam source is modified for the HERMES experiment to provide a polarized hydrogen as well as a polarized deuterium beam. The results show that a polarized storage cell in a storage ring is a reliable and highly efficient tool for future experiments.

Acknowledgement

This work was done in collaboration with B. Braun, W. Brückner, M. Düren, D. Fick, H.-G. Gaul, G. Graw, W. Haeberli, M.T. Lin, Ch. Montag, B. Povh, M. Rall, K. Rith, F. Rathmann, P. Schiemanz, E. Steffens, J. Stenger, F. Stock and J. Tonhäuser.

The skilful operation of the TSR facility by the Accelerator Group und interesting discussions, in particular with M. Grieser are gratefully acknowledged.

References

1. e.g. Proc. 9th Int. Symp. in High Energy Spin Physics, Bonn 1990, Vol. I: Conference Report, eds. K.H. Althoff and E. Meyer (Springer, Heidelberg, 1991).
2. R. Gilman et al.; Phys. Rev. Lett **65** (1990) 1733.
3. HERMES-Kollaboration; Proposal DESY PRC-90/01 (1990).
4. H. Döbbeling et al.; Proposal CERN/PSSC/85/80 (1985), and Addendum (1986).
5. J.S. Dunham et al.; Nucl. Instr. and Meth. **219** (1984) 46.
6. K.P. Schüler; Proc. in High Energy Physics with Polarized Beams and Polarized Targets, Lausanne 1990, Experientia, Suppl. **38** (1981) p. 460.
7. W. Haeberli; Proc. Workshop on Nucl. Phys. with Stored, Cooled Beams, Indiana 1984, eds. P. Schwandt and H.O. Meyer, AIP Conf. Proc. **128** (1985) p. 251.
8. E. Steffens: *Test of Spin Filter for stord Protons and Implications to polarize An-*

tiprotons, Proc. 10th Int. Symp. in High Energy Spin Physics, Nagoya 1992, in prep.
9. K. Zapfe; Ph. D. Thesis, Universität Heidelberg, 1991, unpublished.
10. K. Zapfe; Proc. Workshop on Polarized gas Targets for Storage Rings, Heidelberg 1991, eds. H.-G. Gaul, E. Steffens and K. Zapfe, MPI für Kernphysik, Heidelberg (1992) p. 135.
11. W.S. Luck; H. Jänsch, D. Fick, H.T. Duong and E. Steffens, Proc. 7th Int. Conf. on Polarization Phenomena in Nuclear Physics, Paris 1990, eds. A. Boudard and Y. Terrien, Colloq. de Phys. **C6** (1990) p. 209.
12. W. Haeberli; Proc. 9th Int. Symp. in High Energy Spin Physics, Bonn 1990, Vol. II: Workshops, eds. E. Meyer, E. Steffens and W. Thiel (Springer, Heidelberg, 1991) p. 194.
13. W. Korsch; p. 168 of ref. 12.
14. P. Schiemenz, A. Ross and G. Graw; Nucl. Instr. and Meth. **A305** (1991) 15.
15. A.A. Nagvi and M. Raashid; Nucl. Instr. and Meth. **A320** (1992) 32.
16. V. Derenchuk et al.: *Performance and Status of the IUCF High Intensity Polarized Source*, Preprint IUCF (1992).
17. K. Zapfe; p. 222 of ref 12.
18. M. Düren et al.; Nucl. Instr. and Meth. **A322** (1992) 13.
19. P. Schwandt, T.B. Clegg and W. Haeberli; Nucl. Phys. **A163** (1971) 432.
20. D.M. Nikolenko; p. 13 of ref. 10.

TWO MESON PRODUCTION IN HADRONIC SCATTERING

J.M. LAGET

Service de Physique Nucléaire, Centre d'Etude de Saclay
F91191, Gif-sur-Yvette CEDEX, France

Among the various strangeness production reactions, two Kaon production channels deserve a particular attention. Figure 1 shows the threshold excitation function of the $pd \rightarrow {}^3HeX$ reaction [1] recently measured at SATURNE. Beside the η' and the ϕ meson peaks, characteristic enhancements appear at the K^+K^- and K^0K^0 thresholds, above the multipion emission background. The study of these channels is interesting for two reasons. On the one hand, the coupling between the two pion and the two kaon channels [2] may induce interesting structures which would correspond to S-wave $K\overline{K}$ molecules. Such molecules are also predicted in quark models [3,4]. On the other hand, two gluon exchange mechanisms are expected to play a role, besides more conventional meson exchange ones, in the production of ϕ meson since it is primarily made of a $s\overline{s}$ pair

As the $pd \rightarrow {}^3He\,\eta$ reaction [5] and the $pd \rightarrow {}^3He\,\pi^0$ reaction [6], the $pd \rightarrow {}^3He\,\phi$ reaction is expected to be dominated by the three body mechanisms schematically depicted in Figure 2 : the high momentum transfer is more likely shared by three rather than two nucleons. In that picture, the problem reduces to finding a good description of the $\pi N \rightarrow \phi N$ elementary reaction. However, the corresponding cross section is small, since the OZI rule is violated : box diagrams are the more likely candidates. One example is given in Figure 2 : the corresponding cross section has been computed [7]. But it accounts for only one fourth of the cross section which was measured near threshold [8]. In the meantime, it has been found [9] that the $\phi \rightarrow \rho\pi$ branching ratio is significant —of the order of 15%. The rho exchange mechanism could be a good candidate, but this remains to be checked. If such a three body mechanism appears to be suppressed, one would have to consider one loop two body mechanisms of which an example is given in Figure 2. But again, due to the loop integration, they are also expected to be suppressed. However, the contribution of all these meson exchange mechanisms remains to be evaluated. Whether enough room will be left for other hard mechanisms is still an open question.

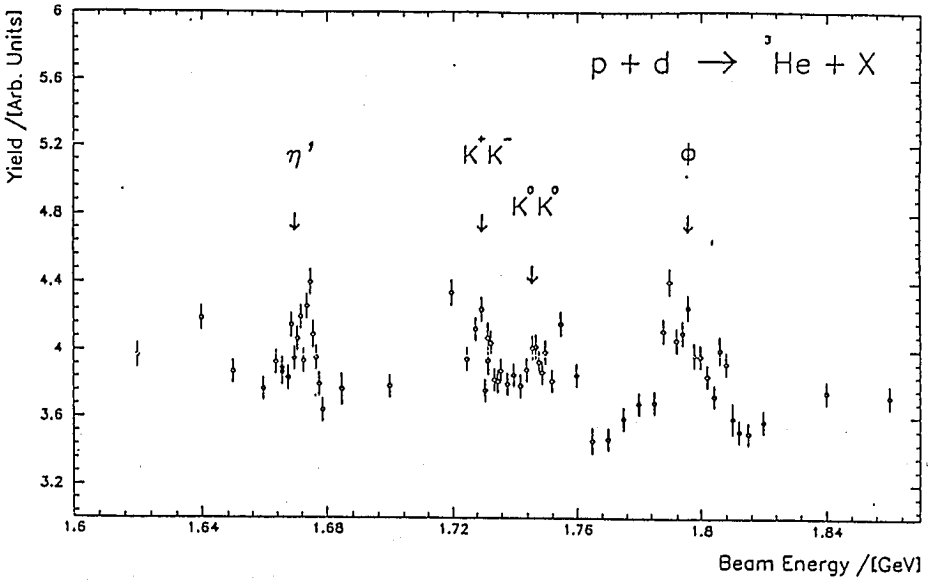

Figure 1: *The SATURNE threshold excitation function of the reaction* $pd \rightarrow {}^3HeX$ *reaction [1].*

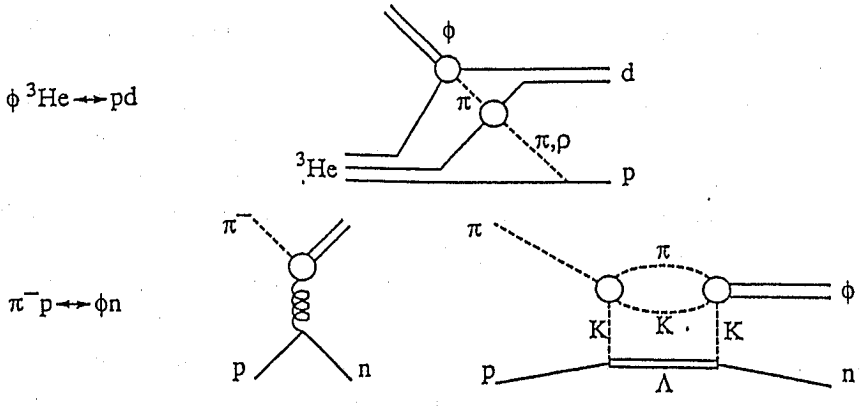

Figure 2: *Possible meson exchange mechanisms for the* $pd \rightarrow {}^3He\,\phi$ *and* $\pi N \rightarrow \phi N$ *reactions.*

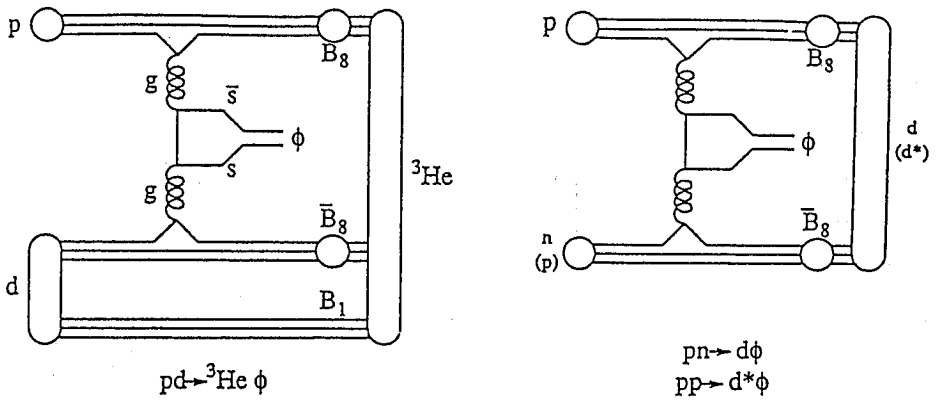

Figure 3: *Possible hard mechanisms for the* $pd \rightarrow {}^3He\,\phi$ *and* $NN \rightarrow NN\phi$ *reactions.*

Possible hard mechanisms are depicted in Figure 3. Since its coupling to a gluon changes the color of a quark, two gluons have to be exchanged in order to conserve the color of the $s\bar{s}$ pair in the ϕ meson. In exclusive processes, or below the inelastic threshold, each gluon must couple to a colored cluster in the nuclear wave function and connect it to physical asymptotic state. Such a study of the hidden color component of the nuclear wave function will complement its study with the electromagnetic probe. This is really the domain of KAON, but it could be likely that, due to the expected suppression of the meson exchange mechanisms, SATURNE and COSY would be already able to put some constraints on such hard mechanisms.

The same problematic arises in the analysis of the two meson production channels. In a mesonic picture, the $\pi N \rightarrow \phi N$ amplitude in Fig. 2 should be replaced by the $\pi N \rightarrow \pi\pi N$ or $\pi N \rightarrow KKN$ amplitudes. Assuming that they proceed through a pion exchange mechanism, the cross section of the $pd \rightarrow {}^3He\,X$ reaction is expected to reflect the variations of the $\pi\pi \leftrightarrow KK$ elementary reaction cross section, as depicted schematically on Fig. 4. On top of the P-wave two pion and the three pion production smooth contribution, the S-wave two pion production cross-section is expected to exhibit a dip just at the K^+K^- threshold. Here the $\pi\pi \rightarrow KK$ channel strong coupling forces the corresponding $\pi\pi$ phase shift [10] to go quickly through 180°. This dip should be filled by the contribution of the K^+K^- channel : the resulting cross-section migth be flat here !. However, the $K^\circ K^\circ$ contribution should clearly appear as a peak near the corresponding threshold. Whether room will be left for more exotic mechanisms is still an open question whose answer require to complete the analysis along these lines.

In any case a more exclusive study of these two channels ($\pi\pi$ and KK) would be particularly welcome. It must be undertaken at SATURNE and COSY.

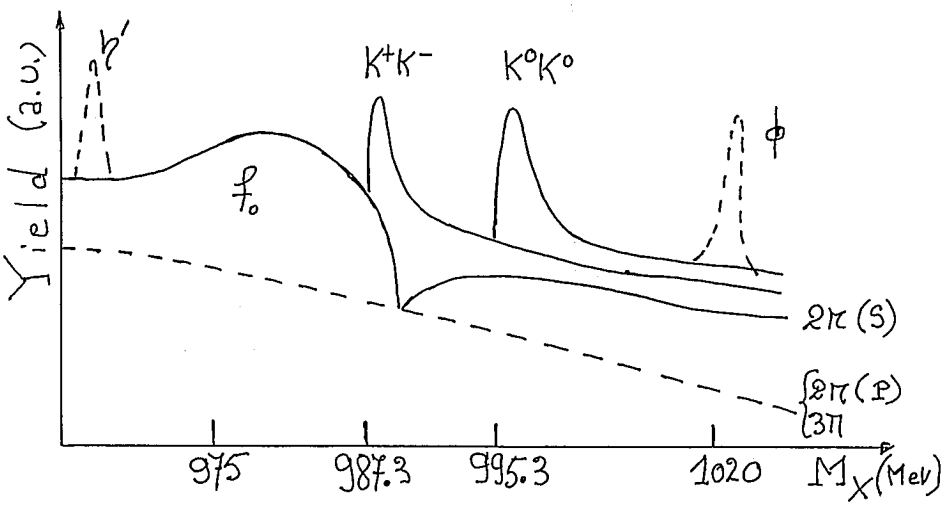

Figure 4: *A schematic decomposition of the* $pD \rightarrow {}^3HeX$ *reaction cross-section.*

References

[1] R. Frascaria, in *Baryon spectroscopy and the structure of the nucleon.* H.P. Morsch and M. Soyeur Eds., (Research Center Julich, 1992) p.291.

[2] F. Cannata, J.P. Dedonder and L. Lesniak, *Z. Phys.* **A334** (1989) 457.

[3] J. Weinstein and N. Isgur, *Phys. Rev.* **D41** (1990) 2236;
Phys. Rev. **D43** (1991) 95.

[4] R. Jaffe, *Phys. Rev.* **D15** (1977) 267.

[5] J.M. Laget and J.F. Lecolley, *Phys. Rev. Lett.* **61** (1988) 2069.

[6] J.M. Laget and J.F. Lecolley, *Phys. Lett.* **B194** (1987) 177.

[7] E.L. Berger and C. Sorensen, *Phys. Lett.* **B62** (1976) 303.

[8] H. Courant *et al., Phys.Rev.* **D16** (1977) 1.

[9] G. Parrour *et al., Phys. Lett.* **B63** (1976) 362.

[10] K.L. Au, D. Morgan and M.R. Pennington, *Phys. Rev.* **D35** (1987) 1633.

Subthreshold Strangeness Production

A.A.Sibirtsev*

Institut für Kernphysik, Forschungszentrum Jülich,
Postfach 1913, W-5170 Jülich, Germany
*permanent address: Institute of Theoretical and Experimental Physics,
Cheremushkinskaya 25, 117259, Moscow, Russia

February 2, 1993

Abstract

The strange particle production at projectile energies below the free nucleon-nucleon threshold in proton-nucleus collisions is studied. We analyzed the contribution from different reaction channels to this process. The features of K^+d and K^+p correlations were discussed in order to propose experimental measurements which allow to distinguish the mechanisms analyzed. Subthreshold double strangeness production in proton-nucleus collision is discussed.

1 Introduction

Particle production in proton-nucleus collision at bombarding energies below the threshold for the reaction on free nucleon is of considerable interest for several reasons. First, the lack of incident proton energy to produce the particle forces one to attract the ideas on collective interaction physics or the internal nuclear motion. At collision energies far below the NN-threshold the account for the standard Hartree-Fock groundstate momentum distribution is not enough to create required energy and the extreme momentum components is necessary. The nature of the high momentum component of the nuclear wave function is of a special interest because the arguments for it existence are based on the assumption about the residual two-body correlations or multi-quark bags inside the nucleus. Really, the suggections about the high momentum component overlap the hypotheses about the collective phenomena. Thus the study of the subthreshold particle production can get important information about the nuclear structure at very short distances.

Second, at collision energy just enough to produce the particle the interaction picture seems to be quite simple to reconstruct the reaction mechanism. Generally we consider the direct production mechanism as well as two-step process that are responsible for the subthreshold phenomena [1-4]. However this consideration about the production dynamics is still a theoretical poin of view and one need the clear experimental evidence on it. The subthreshold particle production is an excellent tool to study the collision dynamics.

The particle production off nuclei is considered through the two essential stages. The first stage is the production dynamics that operates with the different reaction mechanisms and assumptions about the collision pictures and particle formation. The attemption to understand the interaction picture forwards us to analyze the contribution of possible reaction mechanisms and to make precise calculations on them. The second stage considers the particle propagation inside the nucleus. This process seems to be not so interest but, by the other hand, it is very complicated to be described in detail. The accuracy of the calculation on particle propagation is about the factor of two.

It is obvious that a particle produced inside the nucleus iteracts in the nuclear medium. If this is the case, the secondary interactions of the produced particle significantly distorts the information about the production dynamics. Because of the large cross section for the interaction of pions, etas, antikaons and antiprotons with nucleons, these hadrons are rescattered strongly in the nucleus. This is why there is special interest on kaons which have a large mean free path in the nuclear medium at normal density. It has, therefore, been suggested that the kaons can serve as carrier of the information about the production dynamics deep inside the nucleus.

In this paper we use a folding model for primary and secondary production processes in order to analyze subthreshold K^+-production. We concentrate on the features of K^+d and K^+p correlations in order to propose experimental measurements at COSY which allow to distinguish the processes discussed. The contribution of the reaction channels to the subthreshold double strangeness production in proton-nucleus collision is studied.

2 Primary and secondary K^+ production

We consider the following interaction pictures for subthreshold K^+-production in proton-nucleus collision.

The K^+-meson is produced in the first collision of the incident proton with a nuclear nucleon due to the internal nuclear motion

$$p + N \rightarrow K^+ + \Lambda + N \tag{1}$$

The standard way to describe the internal motion of the nucleons is to use the Hartree-Fock groundstate momentum distribution. In order to analyze the particle production at bombarding energies far below the NN-threshold it is necessary to take into account the high momentum component of the nuclear wave function.

A different model to explain the production of mesons at subthreshold energies is the two-step reaction picture. The production of pion in a first collision of the incident proton with a nuclear nucleon followed by a pion-nucleon interaction is assumed

$$p + N_1 \rightarrow N + N + \pi \tag{2}$$

$$p + N_2 \rightarrow \Lambda + K^+ \tag{3}$$

The importance of the secondary pion-nucleon production process for subthreshold kaon and eta-meson production in proton-nucleus collision was found by Cassing et al. [1,5].

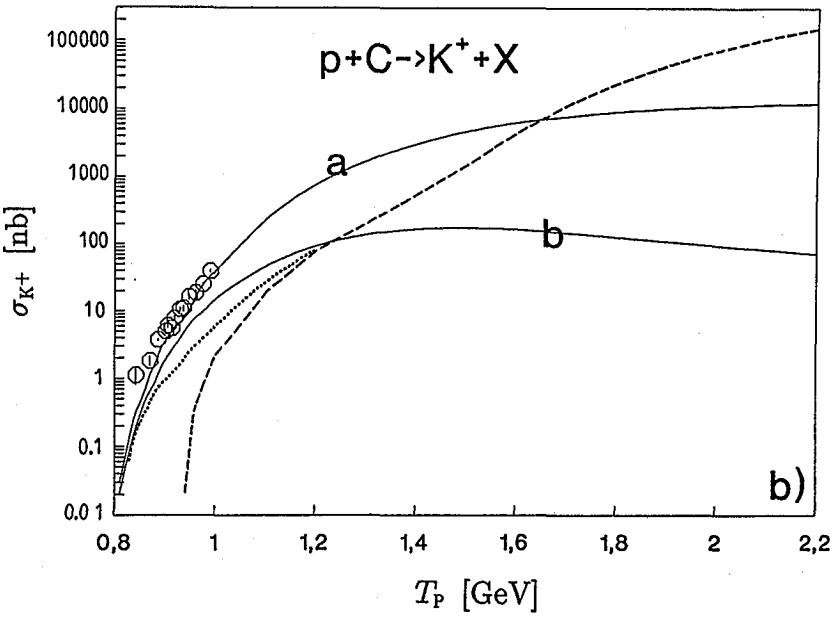

Figure 1: K^+ production cross section. The experimental data from Ref.8. The FCM results are shown by dashed line. The solid lines represent the TSM results for p+N→N+N+π (a) and p+N→d+π (b) channels.

The cross section for the K^+-production in the first collision of incident proton with nuclear nucleon is calculated in the framework of the First Collision Model (FCM) as

$$E_{K+}\frac{\mathrm{d}^3\sigma_{pA\to K+X}}{\mathrm{d}^3p_{K+}} = N_1\int \mathrm{d}^3q\ \Phi(q)E'_{K+}\frac{\mathrm{d}^3\sigma_{pN\to K+\Lambda N}(\sqrt{s})}{\mathrm{d}^3p'_{K+}} \qquad (4)$$

where $\Phi(q)$ is the momentum distribution of the nucleons, N_1 is the number of first chance collisions, $\sqrt{s}$ is the invariant energy of the incident proton-nucleon system and primed indices denote the K^+ momentum and energy in this p+N system, q is the nucleon momentum. In formula (4) $\mathrm{d}^3\sigma_{pN\to K+\Lambda N}(\sqrt{s})/\mathrm{d}^3p_{K+}$ stands for the elementary K^+ differential cross section in collisions of protons with free nucleons [6]. The effective number of first chance collisions N_1 is calculated by the Glauber approximation [7].

The results for the cross section of K^+-meson production in p+ ^{12}C collisions calculated with FCM taking into account the Hartree-Fock initial groundstate momentum distributions are shown in Fig.1 (dashed lines) as a function of the proton laboratory energy. We also perform the experimental data by Koptev et al [8]. It can be seen that direct mechanism does not contribute significantly to the K^+-production cross section up to proton energies of 1 GeV. The production of kaons in the collision of secondary pions with the nucleons is considered in the framework of the Two Step Model (TSM). The K^+-production cross section in two-step processes

taking into account the internal motion of the nucleons is given by:

$$E_{K^+}\frac{\mathrm{d}^3\sigma_{pA\to K^+X}}{\mathrm{d}^3p_{K^+}} = \iint \mathrm{d}^3q\ \mathrm{d}^3p_\pi\ F(p_\pi)\ W(p_\pi,A)\ \Phi(q)\ E'_{K^+}\frac{\mathrm{d}^3\sigma_{\pi N\to K^+\Lambda}(\sqrt{s})}{\mathrm{d}^3p'_{K^+}} \quad (5)$$

where $W(p_\pi,A)$ is the probability that pions produced in the first collision are rescattered in the target nucleus [5], $F(p_\pi)$ is the spectrum of pions produced in the first proton-nucleon collision, $E_{K^+}\ \mathrm{d}^3\sigma_{\pi N\to K^+\Lambda}(\sqrt{s})/\ \mathrm{d}^3p_{K^+}$ is the elementary differential cross section for K^+ production in pion-nucleon collisions [8] and $\Phi(q)$ is the nucleon momentum distribution.

The pion spectrum in Eq.5 is calculated in the framework of FCM as

$$F(p_\pi) = \int \mathrm{d}^3q\ \Phi(q)E'_\pi\frac{\mathrm{d}^3\sigma_{pN\to NN\pi}(\sqrt{s})}{\mathrm{d}^3p'_\pi}\frac{1}{\sigma_{tot}(p+N)} \quad (6)$$

where $E_\pi\mathrm{d}^3\sigma_{pN\to NN\pi}(\sqrt{s})/\mathrm{d}^3p_\pi$ is the elementary pion differential cross section and $\sigma_{tot}(p+N)$ is the total proton-nucleon cross section.

The pion-production cross section was taken from the compilation of experimental data by Flaminio et al. [10] and the differential cross section is assumed to be isotropic in the p+N center of mass system and completely determined by energy and momentum conservation.

The resultant cross sections for K^+ production in p+^{12}C collisions are shown in Fig.1 by a solid line (curve a). The results calculated by TSM reproduce the experimental data much better than the FCM results.

We also take into consideration the secondary-pion production in the reaction

$$\mathrm{p} + \mathrm{N} \to \mathrm{d} + \pi \quad (7)$$

The result of the calculation using Eq.5 with the pion spectrum $\mathrm{F}(\mathrm{p}_\pi)$ for reaction (7) is also shown in Fig.1 (curve b).

The experimental K^+-production cross section is well reproduced when accounting for the secondary reaction channels (TSM) since the sum of the curves a and b match the data. For subthreshold K^+ production the primary reaction channel (FCM) is by at least an order of magnitude less than the secondary reaction channel. The contribution from TSM with deuterons accounts for about 30% of the total experimental K^+-production cross section below the incident proton energy of 1 GeV. At higher bombarding energies the contribution from TSM with deuterons decreases because of the pN$\to$dπ cross section.

3 K^+-deuteron and K^+-proton correlations

Below we discuss the features of K^+d and K^+p correlations in order to propose experimental measurements which allow to distinguish the production channels.

One of the possible ways to identify experimentally the K^+-production channel with an intermediate pion and deuteron (p+$N_1\to$d+π, π+$N_2\to$ Λ+K^+) is to measure the deuteron-momentum spectrum in coincidence with the K^+. This proposal was suggested by Sistemich et al [11] for an experimental study of the subthreshold K^+ production at the Proton Synchrotron COSY-Jülich.

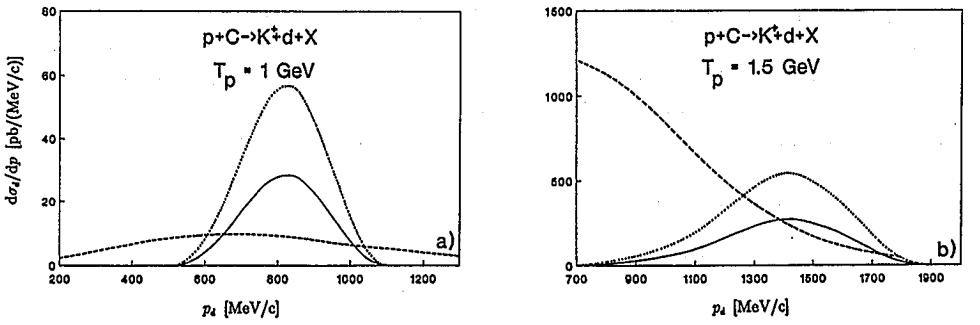

Figure 2: The spectra of deuterons associated with K^+ mesons calculated for p+^{12}C collisions at 1 (a) and 1.5 GeV (b). The curves denote results for direct deuterons without (dotted) and with reabsorption (solid) and for coalescent deuterons (dashed).

The original deuteron momentum spectra calculated by TSM for p+^{12}C collisions at 1 and 1.5 GeV are shown in Fig.2 by the dotted curves. The momenta of the deuterons are high enough to separate them from the evaporated deuterons ($p < 300$ Mev/c). The original deuteron signal seems clear and evident enough to identify this K^+-production channel. It is obvious that deuterons produced in the first collision of the incident proton with a nucleon undergo rescattering inside the nucleus. In this case the deuteron spectrum is distorted and the total deuteron yield is decreased by the nuclear reabsorption via deuteron breakup.

Another problem is concerned with the fast deuteron background that can contribute to the original deuteron momentum spectrum. Experimental studies on the fast deuteron production in proton-nucleus collisions at bombarding energies from 500 MeV to 10 GeV provided deuterons with momenta up to 1 GeV/c [12,13].

In order to evaluate the deuteron reabsorption inside the nucleus we made calculations using the 3-dimensional cascade model COMIC described in detail in Ref.14. The following reactions were considered

$$\begin{aligned} \mathrm{p+N \to d+\pi} \;\; ; \;\; \pi + \mathrm{N} \to \Lambda + \mathrm{K^+}; \\ \mathrm{d+N \to N+N+N} \;\; ; \;\; \mathrm{d+N \to d+N} \end{aligned} \tag{8}$$

The total deuteron-nucleon cross section was calculated by the Franko and Glauber [15]. At the deuteron momenta of interest the deuteron reabsorption factor equals 0.5 for a carbon target and 0.15 for lead. In Fig.2 by the solid curve we present the deuteron momentum spectrum distorted by reabsorption.

In order to analyze the fast deuteron background by means of the COMIC cascade model we consider the following reactions

$$\begin{aligned} p+N \rightarrow N+N+\pi \quad &, \quad \pi+N \rightarrow Y+K^+ \\ N+N \rightarrow N+N \quad &, \quad Y+N \rightarrow Y+N \end{aligned} \tag{9}$$

It is important to take into account all possible rescatterings of secondary particles because we consider the fast deuteron production via the coalescence of neutron-proton pairs with small relative momenta. We applied the coalescence model for deuteron formation described in details in Ref.16. This approach was very useful in the analysis of experimental data on fast deuteron production in pA and $\bar{p}$A collisions and allows to reproduce the fast deuteron yields as well as the deuteron spectra.

The deuteron production cross section is given by

$$\frac{d^3\sigma_{p+A\rightarrow d+X}}{d^3Q} = \sigma_A \int d^3q \; f(q) g_{np}(q,Q) \tag{10}$$

where σ_A is the inelastic cross section for proton-nucleus interaction, $f(q)$ is the squared deuteron wave function and $g_{np}(q,Q)$ is the density matrix for the neutron-proton states with total momentum Q and relative momentum $2q$. We use the parameterization of the deuteron wave function by Alberi et al [17]. The density matrix was calculated by the cascade model taking into account the reactions (9).

The deuteron spectra calculated for p+ ^{12}C collisions at 1 GeV and 1.5 GeV are shown in Fig.2 by the dashed curve. The direct deuteron spectrum seems very clear for an incident proton energy of 1 GeV and is superimposed by the background at 1.5 GeV. At bombarding energies higher than 1 GeV the contribution from the p+N$\rightarrow\pi$+d channel significantly decreases (see Fig.1). For this reason the rate of the fast deuteron background from the p+N$\rightarrow\pi$+N+N channel increases and prevailes over the direct deuteron rate. Thus, the total deuteron spectrum which is the sum of the direct and background deuterons seems very difficult to analyze in order to select different K^+-production channels at bombarding energies higher than 1 GeV.

Other way to identify the direct K^+-production in the reaction p+N$\rightarrow$N+Λ+K^+ is to analyze the missing-mass spectrum of the Λ-particles. At energies below the NN threshold for direct K^+ production the missing-mass distribution reflects the internal momentum distribution of the nucleons. Without the internal motion one would expect a sharp peak at the free hyperon mass in the missing-mass spectrum. In Fig.3 we show the missing-mass distribution calculated by means of FCM for p+^{12}C collisions at 1 and 1.5 GeV. The spectra have a sharp drop-off at the free hyperon mass. The missing-mass distributions for two-step processes calculated by TSM are shown also in Fig.3. At a proton energy of 1 GeV we predict two clear signals corresponding to the different production mechanisms. At an energy of 1.5 GeV the spectra become unseparated due to the width of the TSM distribution. This method seems useful for investigation of the production mechanisms and, what is more attractive, it provides very clear and evident signals to detect.

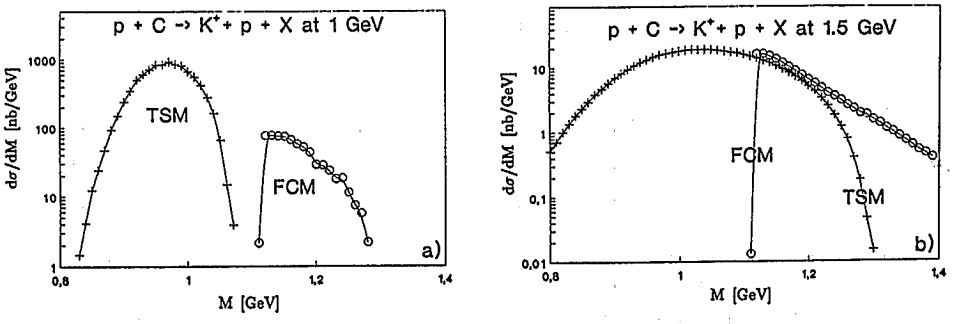

Figure 3: Missing-mass spectra for the K^+p-system calculated for p+^{12}C collisions at 1 (a) and 1.5 GeV (b).

4 Double strangeness production

The study of multi-strange hadronic matter is of special attention because of the number of motivations. The production of doubly strange hypernuclei, which consist of two Λ hyperons bound to a nuclear core is discussed by Dover [18]. Rafelski enphasized the double strangeness production as a signature of quark-gluon plasma formation [19]. Considerable interest is the six-quark H dibaryon of Jaffe [20]. One of the possible signature for these extraordinary phenomena is the observation of two K^+ mesons in the final states. However, to make conclusion about the dubious, but quite interest multi-strange states we have to understand the problem by the assumptions based on the conventional processes for double strangeness production.

Below we discuss the standard mechanisms for two K^+ production in proton-nucleus collision. We concentrate on subthreshold process because of the following reasons. First, to form doubly strange $\Lambda\Lambda$ hypernuclei one need to produce enough slow hyperons in order to stick them in nucleus. Thus the energy of the incident proton should be close to the threshold or below it. Second, to get a strong trigger and large efficiency for the process we suggest to detect two K^+ mesons at very forward angles in laboratory. In order to calculate two K^+ production cross section we onsider the following reactions

$$p + N \rightarrow K_1^+ + K_2^+ + \Lambda + \Lambda \tag{11}$$

$$p + N_1 \rightarrow K_1^+ + N + \pi + \Lambda \tag{12}$$

$$\pi + N_2 \rightarrow \Lambda + K_2^+ \tag{13}$$

T	2.7	2.8	2.9	3.0	3.1	3.2	3.4	3.7	4.0	5.0
FCM		0.07	1.2	4.3	9.1	15	33	65	100	213
TSM	2.5	3.4	5.3	8.3	11	16	35	80	138	371
Cascade	45	68	116	132	174	223	306	452	609	870

Table 1: The calculated cross sections (nb) for K^+K^+ production in p+^{12}C collisions at proton energy T (GeV).

$$p + N_1 \rightarrow N + N + \pi_1 + \pi_2 \quad (14)$$
$$\pi_1 + N_2 \rightarrow \Lambda + K_1^+ \quad (15)$$
$$\pi_2 + N_3 \rightarrow \Lambda + K_2^+ \quad (16)$$

We calculate the cross section of the direct two K^+ production in p+^{12}C by means of FCM and show the results in Tab.1. The threshold incident proton energy for K^+K^+ production on free nucleon is 3.62 GeV. The cross section for two K^+ production in two-step process was calculated in the framework of TSM. The process (14-16) was calculated by means of the cascade model [14].

In Tab.1 we show the results calculated for different bombarding proton energies for carbon target. At proton energies below 3 GeV the contribution of FCM is negligible. The cascade contribution significantly prevailes the two-step one. It is noticeable that two K^+ production cross section at incident proton energies below the threshold is large enough to be measured.

5 Summary

We have analyzed subthreshold K^+ production in proton-nucleus collisions in order to find the features of the different production channels. We concentrate on evident distinctions between the reaction mechanisms and attempt to give a basis for their experimental identification. The analysis of kaon-deuteron correlations proved the possibility of an experimental study of the two-step reaction channel (p+N$\rightarrow \pi$+d, π+N$\rightarrow$Y+K^+). Despite of the strong deuteron reabsorption inside the target nucleus and the fast deuteron background the selection of the kaon-production channels is possible at incident proton energies below 1 GeV. At higher bombarding energies the fast deuteron background prevailes over the direct deuteron rate.

The K^+-proton correlations are very attractive and clear to understand the subthreshold K^+-production mechanism. We discussed the missing-mass spectrum of the K^+p-system and found it very promising to clarify the K^+-production channel. It is important that the analysis of the missing-mass spectrum is theory-independent and seems to be free of speculation.

We estimate the cross section for two K^+ production and found it large enough to measure. The study of two K^+ production is very important to understand the multi-strange hadronic matter and to evaluate the probability for doubly strange hypernuclei formation.

Acknowledgments

It is a pleasure to thank O.W.B. Schult and K.Sistemich for helpful discussions and comments. I would like to thank M. Büscher for his collaboration on many aspects of the work reported here.

References

1. W.Cassing et al., *Z.Phys.* **A340** (1991) 51
2. A.Shor et al., *Nucl.Phys.* **A514** (1990) 717
3. A.A.Sibirtsev, *Sov. J. Nucl. Phys* **53** (1993) (to be published)
4. A.A.Sibirtsev and M.Büscher (to be published)
5. W.Cassing et al., *Phys.Lett.* **238B** (1990) 25
6. W.Zwermann, *Mod.Phys.Lett.* **A3** (1988) 251
7. R.J.Glauber and G.Mattia, *Nucl.Phys.* **B21** (1970) 135
8. V.P.Koptev et al., *JETP* **94** (1988) 1
9. J.Cugnon et al., *Nucl.Phys.* **A422** (1984) 635
10. V.Flaminio et al. in *Compilation on cross sections CERN-HERA-3* (1979)
11. K.Sistemich et al., *COSY Proposal 18* Juelich (1990)
12. J.Ero et al., *Preprint KFKI-23/A* Budapest (1990)
13. S.V.Boyarinov et al., *Yad.Fiz.* **47** (1988) 942
14. A.A.Sibirtsev, *Sov. J. Nucl. Phys.* **55** (1992) 541
15. V.Franco and R.J.Glauber, *Phys.Rev.* **142** (1966) 1195
16. G.A.Lobov and A.A.Sibirtsev, *Preprint ITEP-72* Moscow (1990)
17. G.Alberi et al., *Phys.Rev.Lett.* **34** (1975) 503
18. C.B.Dover, *Nucl.Phys.* **A547** (1992) 27c
19. J.Rafelski, *Phys. Lett.* **B307** (1988) 371
20. R.L.Jaffe, *Phys. Rev. Lett.* **38** (1977) 195

Folding model predictions of proton-K^+ coincidence spectra for K^+ production in p+^{12}C collisions at proton energies below the free nucleon-nucleon threshold

B. Kamys (+),

Institute of Physics, Jagellonian University, PL-30059 Cracow, Poland

The production of particles in proton-nucleus collisions at energies below the free nucleon-nucleon threshold is expected to be very sensitive to details of the nuclear many-body wave function since it can occure only due to cooperative nuclear phenomena. K^+ production might be of special interest in this context because it offers a possibility to obtain undisturbed information on the reaction due to large mean free path of positively charged kaons in nuclear matter.

The available at present experimental data on the subthreshold K+ production in proton-nucleus collisions are very scarce. They consist only of results of inclusive measurements of Koptev et al. [1] in which total cross sections were obtained.

As it was discussed by Cassing, Koptev and Sistemich during the present seminar, the inclusive measurements do not allow to unambiguously decide the mechanism underlaying the K^+ production. Exclusive measurements are necessary to distinguish contribution of one-step process ($N+N \Rightarrow K+N+\Lambda$) from competing, two-step mechanism ($N+N \Rightarrow \pi+N$, $\pi+N \Rightarrow K+\Lambda$). For example, Cassing et al. [2] emphasized a different shape of angular distributions of kaons originating from one- and two-step processes what can be used as a mean to disentangle contributions of both mechanisms.

In the present contribution a possibility is discussed to distinguish different production mechanisms via studying kaon-proton coincidence spectra. The two-step mechanism is expected to produce smooth coincidence spectra covering the whole available phase space, presented in Fig. 1., due to the fact that all directions of the pion momentum participate,. The one-step process should be more selective, populating only limited parts of phase space.

Folding model of Cassing et al. [2] was extended in the present work to allow for evaluation of coincidence cross sections $d^6\sigma/d^3p(P)\, d^3p(K)$. The dynamics of the one-step K^+ creation was incorporated by folding the elementary K^+ production cross section (in the nucleon-nucleon system) with the momentum distribution of target nucleons. Since the coincidence spectra below the free nucleon-nucleon threshold

may be strongly influenced by kinematical constraints arising from momentum and energy conservation, one has to treat them with utmost care. To assure explicitely energy and momentum conservation the following procedure was applied; It was assumed that the recoiled nucleus plays a role of the spectator only and consequently its momentum is antiparallel to the Fermi momentum of the interacting target nucleon and has the same value. Within such an approximation the dynamical part of the one-step cross section was multiplied by the appropriate factor of the four-body (p+K^++Λ+recoil nucleus) phase space density and integrated over momenta of not observed particles.

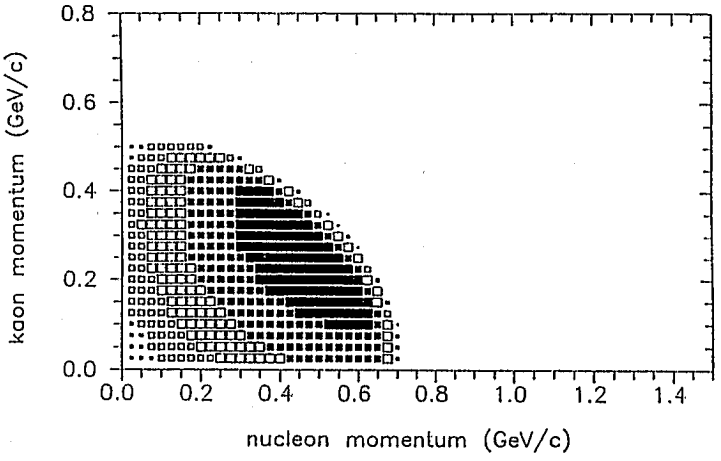

Fig. 1

The model was used to evaluate coincidence spectra of protons and K+ originating from the reaction (p+^{12}C -> K^++p +Λ + recoil nucleus) at several proton energies below the free nucleon-nucleon threshold. Results of the calculations are presented in Fig. 2 for protons and kaons detected both at zero degree (beam direction). Very characteristic dependence of the coincidence spectra on the beam energy may be observed. At the lowest energy (T(p)=0.95 GeV) only one, well separated peak is present which at higher energy (T(p)=1.1 GeV) becomes broader and separates into two peaks at still higher energies. This energy dependence as well as populating only a small part of the available phase space, shown in Fig. 1 for the lowest beam energy, seems to be a specific feature of one-step mechanism, thus it can be used for selection of contributions of one-step and two-step mechanisms. In Fig. 3 an angular dependence of the coincidence spectrum is presented for one-step production mechanism, evaluated for a beam energy of T(p)=1.4 GeV. The kaons are emitted in forward direction (0 deg.) while the direction of the detected

Fig. 2

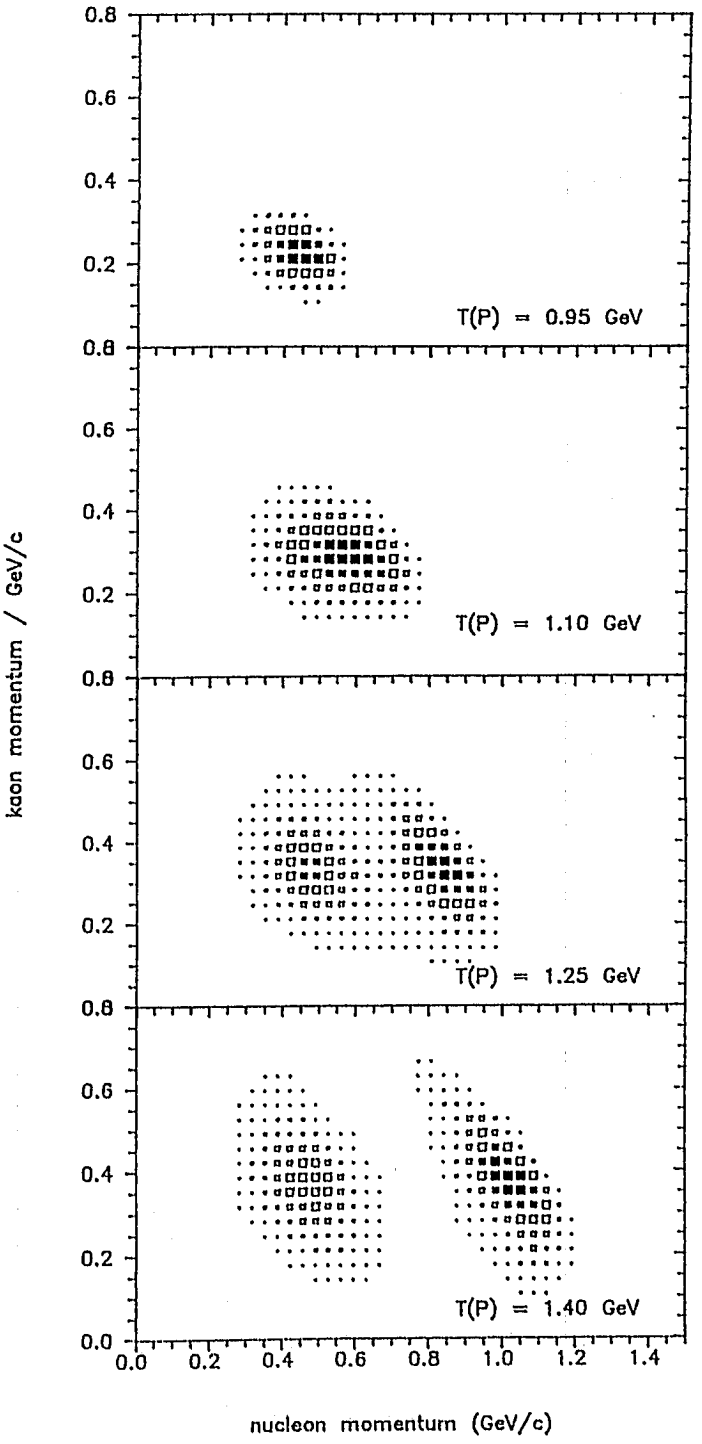
T(P) = 0.95 GeV
T(P) = 1.10 GeV
T(P) = 1.25 GeV
T(P) = 1.40 GeV
kaon momentum / GeV/c
nucleon momentum (GeV/c)
0.0
0.2
0.4
0.6
0.8
1.0
1.2
1.4

Fig. 3

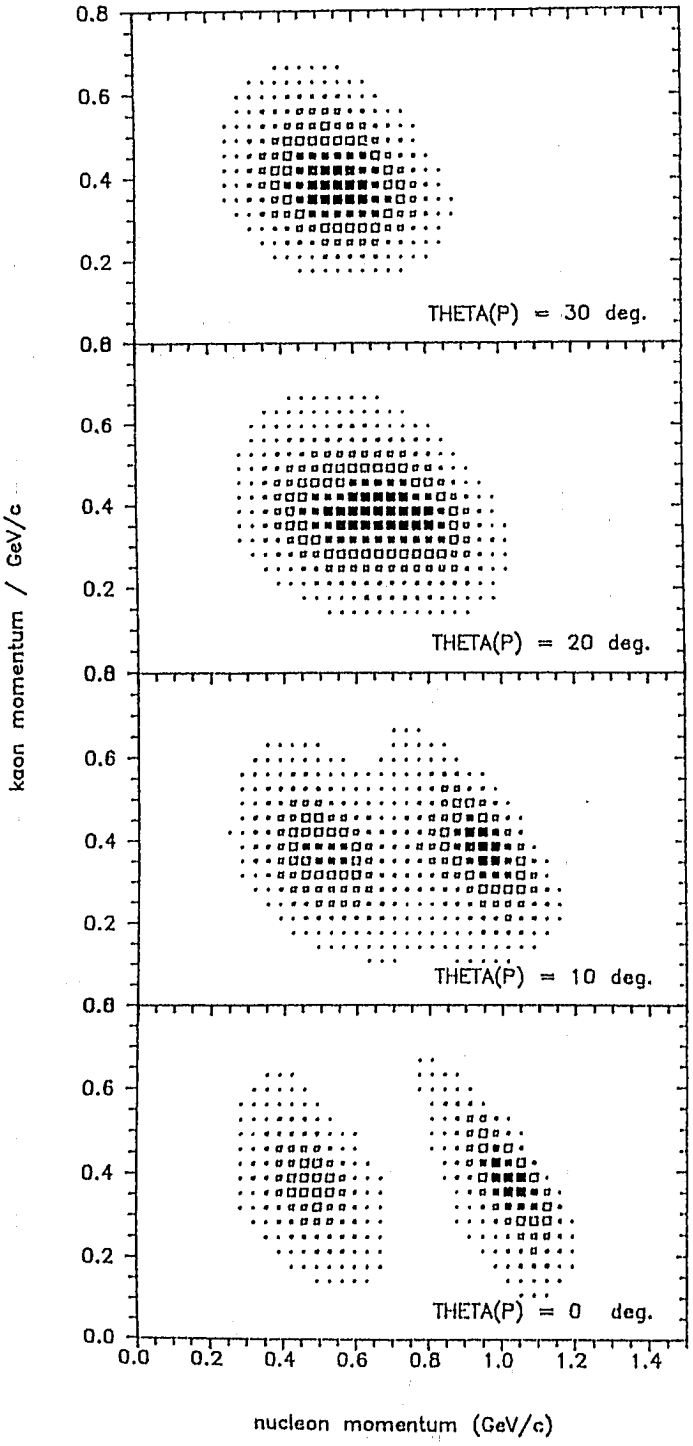
THETA(P) = 30 deg.
THETA(P) = 20 deg.
THETA(P) = 10 deg.
THETA(P) = 0 deg.
kaon momentum / GeV/c
nucleon momentum (GeV/c)
0.0
0.2
0.4
0.6
0.8
1.0
1.2
1.4

proton momentum changes from 0 deg. (lowest part of the figure) to 30 deg.. Again very specific behaviour of the coincidence spectra is observed. The two peaks visible in the spectrum for forward direction of the proton momentum (0 deg.) tend to unify into one peak at larger angles.

In conclusion, a distinct signature of the production mechanism is observed in the proton-K^+ coincidence spectra. It may be used to differentiate the one-step and two-step contributions to the production cross section.

(+) In collaboration with W. Cassing (Giessen University), L. Jarczyk (Cracow University), O. W. B. Schult (KFA Jülich), K. Sistemich (KFA Jülich), A. Strzalkowski (Cracow University)

[1] V. Koptev et al., JETP **67** (1988) 2177
and contribution to the present seminar,
[2] W. Cassing et al., Phys. Lett. **B238** (1990) 25
and contribution to the present seminar,
B. Kamys, W. Cassing, L. Jarczyk, O. Schult, K. Sistemich, A. Strzalkowski, Annual Report 1991, KFA, Juel-2590, p. 30

MESON SCATTERING AND THE STRUCTURE OF MESONS

J. SPETH and B.C. PEARCE
Institut für Kernphysik, Forschungszentrum Jülich,
D-5170 Jülich, Fed. Rep. Germany

ABSTRACT

We investigate the effects of a coupled channel model of $\pi\pi$ and $K\bar{K}$ scattering on the time-like scalar and electromagnetic formfactors of the pion and nucleon within the meson-exchange framework. A unified picture results of the pion, kaon and nucleon formfactors, $\pi\pi$ and $K\bar{K}$ scattering. We find a large scalar root mean square radius for the nucleon of 1.25 fm corresponding to a 15 MeV contribution to the sigma term. We begin by reviewing the $\pi\pi - K\bar{K}$ model that serves as input to the form factor calculations.

1. Introduction

Despite it being generally accepted as the correct theory of the strong interactions, its non-perturbative nature has meant that QCD has still failed to provide us with detailed descriptions of phenomena in the low energy ($\sim$ 1 GeV) region. Hence the abundance of models of strong interaction physics. However, there are indications[1] that most of the dynamics in this regime can be understood in terms of colour-neutral objects, namely nucleons, mesons and isobars. This is the basis of the success of the meson exchange models of medium energy nuclear physics.

It is obvious that such a description must eventually break down. At some energy scale, the quark and gluonic degrees of freedom must become important. The question is, at what energy does this occur. Clearly, this is connected to the size of the quark confinement region. Since the radii of physically observed hadrons is given by the meson cloud as well as the confining region, the range of applicability may be larger than thought from naive estimates based on physical sizes.

One of the strengths of the meson exchange models is that they enable the (possibly strong) effects of the meson cloud to be analysed. In many models based on quarks and gluons these effects are ignored. For example, the quark model[2] describes states only in terms of valence quarks. In that model, the ρ meson is entirely $q\bar{q}$, yet presumably in nature it must have a component that is $qq\bar{q}\bar{q}$. In the effective meson picture, this component arises from the two pion self energy correction to the ρ and gives rise to its width for decay to two pions. Calculations of the decay width within the quark model exist but the effect of the self energy diagrams on the real part of the mass is ignored on the assumption that it can be accounted for by a renormalisation of the parameters of the model. It is interesting that, to describe the $f_0(975)$ and $a_0(980)$

mesons within the quark model, it is necessary to first project out an effective meson type potential and then proceed in a similar vein to the meson exchange picture.[3]

In this contribution we will show how the meson exchange model can be applied to calculations of the nucleon sigma term[4] and the pion electromagnetic form factor . We begin by reviewing the application to $\pi\pi$ and $K\pi$ scattering developed recently by the Jülich group.[5]

2. The model

The meson exchange model is obtained by (a) writing down the Lagrangian describing the basic meson-meson-meson and meson-meson-baryon vertices, (b) defining phenomenological form factors for each vertex (parameterised in terms of a cutoff mass) to account for the omitted underlying quark-gluon structure, (c) constructing a potential V by computing as many of the resulting two-particle-irreducible meson exchange diagrams as possible, (d) summing all of the two-particle diagrams by solving a Bethe-Salpeter — Lippmann-Schwinger type integral equation with V as the driving term.

The exact solution to the field theory would be obtained by solving the Bethe-Salpeter equation with a complete kernel (i.e., including *all* two-particle irreducible diagrams in step (c) above). This is of course impossible in practice so we make two approximations. First, the infinite set of two-particle irreducible diagrams constituting the potential is truncated to include only t- and s-channel meson exchanges. Secondly, we utilise either the Time Ordered Perturbation Theory (TOPT) or Blankenbeclar-Sugar (BbS) approaches to reduce the dimensionality of the integral equation from four to three, which makes it more amenable to solution.*

The integral equation that we solve for the t-matrix, T, is expressed in operator form as

$$T = V + VGT, \tag{1}$$

where G is the two-body propagator. This is to be understood as a 2×2 matrix equation to account for couplings between the $\pi\pi$ and $K\bar{K}$ channels.

The details of how this is applied to the $\pi\pi - K\bar{K}$ system already appears in Ref. 5. In this contribution we will try to concentrate more on a description of the physics involved.

To completely specify the calculation we require an effective meson Lagrangian to constrain the vertices. For this purpose we use the Lagrangian of Bando *et al.*[6] In this model, the ρ meson emerges as the gauge boson of a hidden local gauge symmetry in the non-linear sigma-model. After gauge fixing, this model is identical to the Weinberg Lagrangian.[7] For us, the important ingredients of the model (after

*Reference 5 utilised the TOPT approach. However, in order to obtain the correct analytic behaviour of the scalar form factor in the unphysical region, it was necessary to redo the calculation using BbS. Both methods gave similar results in the physical region after some readjustment of cutoff parameters. In particular, the conclusions regarding the nature of the $f_0(975)$ were unchanged.

extension to SU(3)) are that it incorporates the well known symmetries of QCD and nature (e.g. chiral symmetry) and provides us with psuedoscalar–psuedoscalar–vector vertices in which the coupling constants are constrained by the symmetry. It also allows inclusion of couplings to the photon in a natural way.

The relevant t-channel meson exchange diagrams that will contribute to V are (a) ρ exchange between $\pi\pi$ and $\pi\pi$ states, (b) $K^*(890)$ exchange between $\pi\pi$ and $K\bar{K}$ states, and (c) ρ, ω and ϕ exchange between $K\bar{K}$ and $K\bar{K}$ states. These are illustrated in Figs. 1(a)–1(c). To these we must also add s-channel pole diagrams as

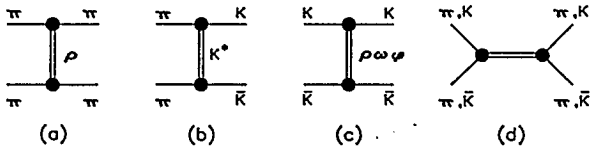

Figure 1. Meson exchange contributions to the coupled $\pi\pi - K\bar{K}$ system. (a)–(c) t-channel. (d) s-channel.

illustrated in Fig. 1(d). These correspond to the genuine $q\bar{q}$ states while the t-channel exchanges provide the (possibly strong) background. In solving the integral equation, many diagrams are generated that renormalise both the mass and coupling constants of these s-channel poles (this can be seen by iterating Eq. (1) with the potential of Fig. 1). One example of such a diagram is given in Fig. 2. Hence, the physically

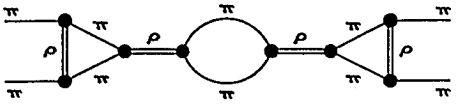

Figure 2. An example of a diagram generated by solving Eq. (1) that renormalises Fig. 1(d)

observed state is a combination of bare $q\bar{q}$ state and two-meson dressing. Rather than explicitly calculating the mass shift and change in the coupling constant due to renormalisation, we introduce the bare mass and bare coupling constant as free parameters which are adjusted to fit the resonant phases.

3. $\pi\pi$ scattering

We begin by considering the partial waves with $I^G(J^{PC}) = 2^+(0^{++})$ and $2^+(2^{++})$ since they provide tight constraints on some of the parameters. There are no experimentally observed resonances in these channels, so the phase shifts are completely determined within the model by the t-channel processes. Also, isospin 2 means there is no coupling to the $K\bar{K}$ channel. As seen in Fig. 3 it is possible to achieve excellent agreement with the data.

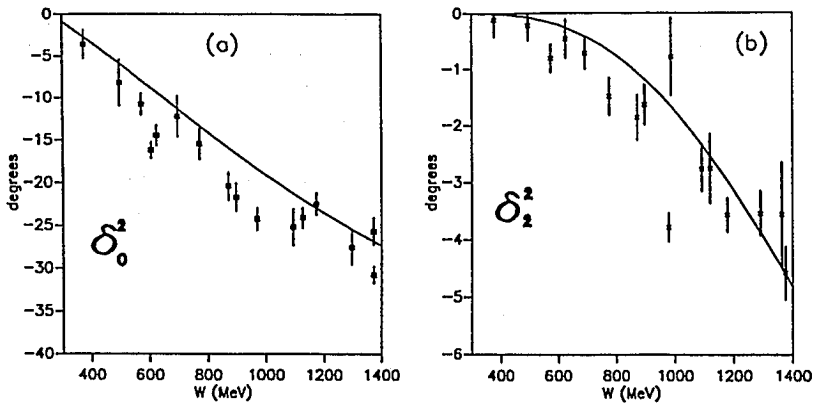

Figure 3. Results for the non-resonant, $I = 2$ partial waves. (a) $I^G(J^{PC}) = 2^+(0^{++})$ and (b) $2^+(2^{++})$. For references to the data, see Ref. 5.

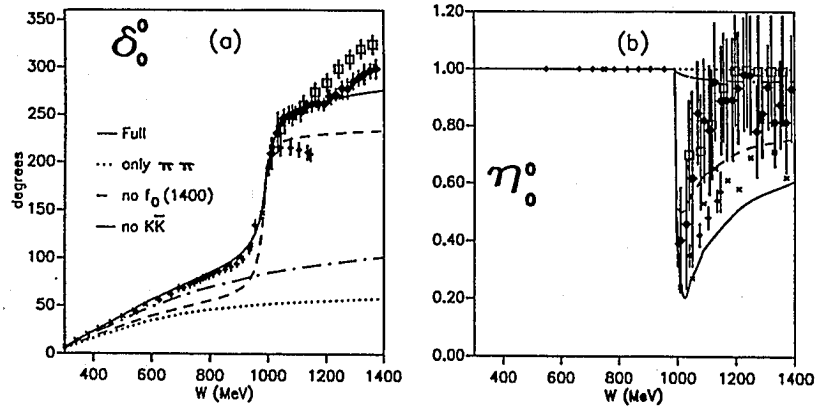

Figure 4. Results for the phase shifts (a) and inelasticity (b) in the $I^G(J^{PC}) = 0^+(0^{++})$ partial wave. For references to the data, see Ref. 5.

With the parameters of the t-channel ρ-exchange diagram of Fig. 1(a) constrained, we now turn to the scalar-isoscalar channel with quantum numbers $I^G(J^{PC}) = 0^+(0^{++})$. This channel contains a narrow resonance, the $f_0(975)$ which was once identified as a member of the scalar $q\bar{q}$ nonet, but it is now generally agreed that its mass and decay properties are inconsistent with that assignment.

The phase shifts and inelasticities resulting from the meson-exchange coupled-channel calculation for this partial wave are shown in the solid curves of Fig. 4.

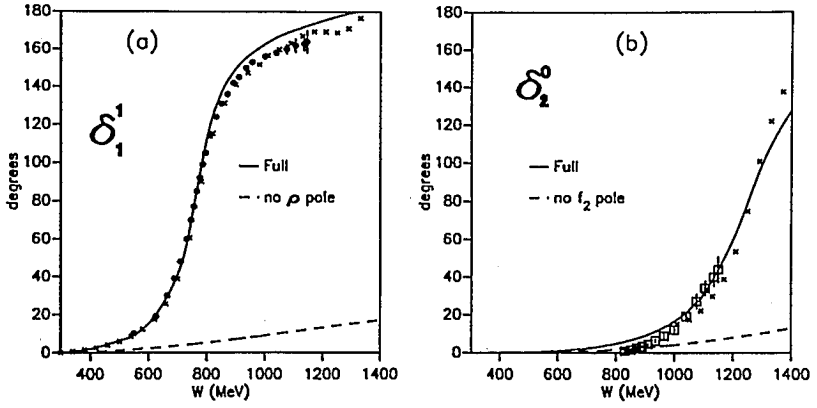

Figure 5. Results for the resonant (a) $I^G(J^{PC}) = 1^+(1^{--})$ and (b) $0^+(2^{++})$ partial waves. For references to the data, see Ref. 5.

If the coupling to the $K\bar{K}$ channel is omitted then we have a single-channel problem with the potential given by ρ exchange (Fig. 1(a)). This results in the dotted curve. If the channel coupling is turned on by including the diagrams of Figs. 1(b) and (c) then resonant structure at the $f_0(975)$ energy is immediately obvious in the dashed curve. In fact, if we calculate $K\bar{K}$ scattering with the potential given only by Fig. 1(c) (i.e., no coupling to the $\pi\pi$ channel) then we find typical bound state phase shifts. This confirms that the structure observed in Fig. 4 is due to a bound $K\bar{K}$ state. It comes about because the ρ, ω and ϕ exchange contributions of Fig. 1(c) are each attractive, providing enough attraction to bind. To obtain complete agreement with the empirical $\pi\pi$ phase shifts, it is necessary to include an s-channel pole corresponding to the broad $f_0(1400)$. The bare mass and coupling constant are taken as free parameters which are adjusted to fit the data, resulting in the solid curve. The dash-dotted curve is the result of turning off the diagram of Fig. 1(c), which, since Fig. 1(c) is the mechanism for creating the bound state, illustrates the strong background to the $f_0(975)$ provided by t-channel exchanges and the $f_0(1400)$.

The scalar nonet requires two non-strange, isoscalar states (a mixture of the singlet and octet representations) although we have only included one. We should, in principle, also include the $f_0(1590)$ but we have omitted it at this stage since it is at a mass where effects of coupling to the $\rho\rho$ and $N\bar{N}$ channels may become important.

Results for the partial waves $1^+(1^{--})$ and $0^+(2^{++})$ are shown in Fig. 5. These waves contain the ρ and the $f_2(1270)$ respectively, which both decay predominantly to $\pi\pi$. In both cases it was necessary to include an s-channel pole (corresponding to a genuine $q\bar{q}$ state) in order to reproduce the data. The results of just the t-channel processes are indicated in the figures by the dashed lines.

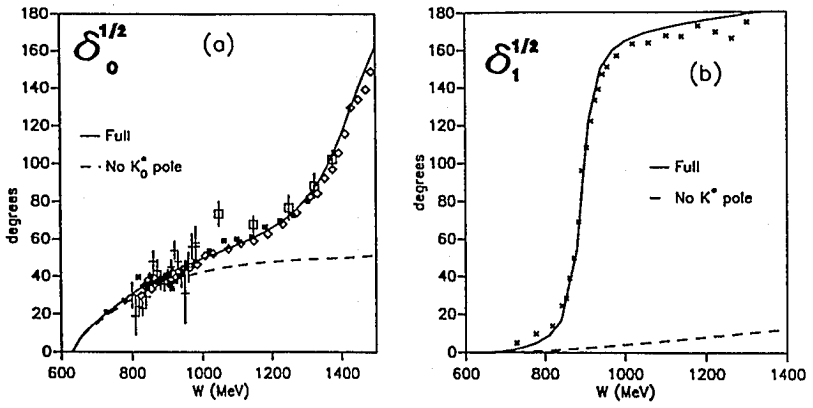

Figure 6. Results for the resonant (a) $I(J^P) = \frac{1}{2}(0^+)$ and (b) $\frac{1}{2}(1^-)$ partial waves of the $K\pi$ system. For references to the data, see Ref. 5.

4. $K\pi$ scattering

It is straightforward to extend the model of the $\pi\pi$ system to the $K\pi$ interaction. Since all of the t-channel exchange processes are completely determined by the $\pi\pi$ system, it provides a useful consistency check of the model. Only the bare masses and coupling constants of the s-channel poles remain to be adjusted in the cases where they are necessary. This system is somewhat simpler than the $\pi\pi$ case since there are no coupled channels to consider in the energy region of interest.

In Fig. 6 we show the results for the resonant partial waves, $I(J^P) = \frac{1}{2}(0^+)$ and $\frac{1}{2}(1^-)$. These correspond respectively to the $K_0^*(1430)$ and $K^*(892)$ states listed by the Particle Data Group. The dashed curves are the results using only the t-channel exchange driving terms while the solid curves include s-channel states (with bare masses and couplings adjusted to reproduce the data as usual). The $K_0^*(1430)$ is of special interest since it is a member of the lowest lying scalar nonet which we have just demonstrated should not contain the $f_0(975)$. In fact, as can be seen, the model requires a genuine $q\bar{q}$ state in order to agree with experiment. However, the t-channel exchanges provide a strong, non-negligible background. Similarly, the $\frac{1}{2}(1^-)$ requires an s-channel pole term in order to reproduce the vector $K^*(892)$, although the background is much less in that case.

The non-resonant partial waves provide a useful check of the self-consistency of the model. In this case, all the parameters are determined in the $\pi\pi$ sector. As can be seen in Fig. 7, the results are very reassuring.

It is clear that the model described is very successful at describing the low-lying states that couple strongly to $\pi\pi$ and $K\pi$. The $f_0(975)$, about which there is some controversy, emerges as a $K\bar{K}$ bound state (or molecule). This interpretation agrees

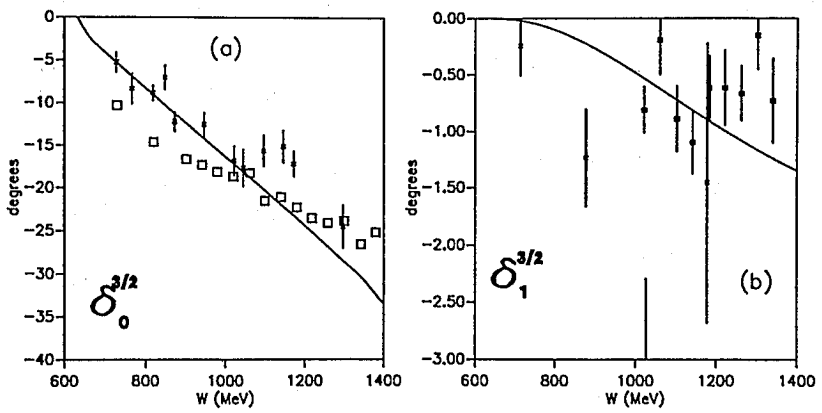

Figure 7. Results for the non-resonant (a) $I(J^P) = \frac{3}{2}(0^+)$ and (b) $\frac{3}{2}(1^-)$ partial waves of the $K\pi$ system. For references to the data, see Ref. 5.

in spirit (although not in the details) with the non-relativistic quark model calculation of Weinstein and Isgur[3] but is at variance with the analysis of Morgan and Pennington.[8] All other resonance states examined ($\rho(770)$, $f_2(1270)$, $K_0^*(1430)$ and $K^*(892)$) required the inclusion of s-channel poles. It was also necessary to include a state corresponding to the $f_0(1400)$. To extend the calculation to higher energies it will be necessary to include coupling to other channels (for example, $\rho\rho$ and $N\bar{N}$).

5. Scalar form factors and the nucleon σ term

The nucleon σ term, $\sigma(t)$, can be defined in terms of the matrix element[9]

$$\sigma(t)\bar{u}(p')u(p) = \frac{m_u + m_d}{4m_N}\langle p'|(\bar{u}u + \bar{d}d)|p\rangle \tag{2}$$

A low energy theorem relates $\sigma(t)$ defined in this way, to the isospin even πN amplitude $\tilde{D}(t)$ at the Cheng-Dashen point[10]

$$\sigma(2m_\pi^2) \approx f_\pi^2 \tilde{D}(2m_\pi^2)\,(\equiv \Sigma)\,. \tag{3}$$

The interest in the σ term was generated when analysis of the πN data revealed $\Sigma = 64 \pm 8$ MeV[11] yet naive estimates based on baryon mass differences gave $\sigma(0) \approx$ 30 MeV. It was recently pointed out[9] that the strong s-wave $\pi\pi$ interaction produces a significant t dependence of $\sigma(t)$. That is, the usual assumption that $\sigma(2m_\pi^2) \approx \sigma(0)$ may not be valid.

To investigate this effect using the $\pi\pi$ model discussed above, we consider $\sigma(t)$ to be given by

$$\sigma = \sigma_B + \Gamma_B G\mathcal{V} + \Gamma_B GTG\mathcal{V}. \tag{4}$$

Here, σ_B represents the "bare nucleon" σ term. We do not attempt to calculate this contribution, concentrating instead on the t dependence of the remaining pieces. The next two terms involve the matrix element of $\bar{u}u + \bar{d}d$ between pion (kaon) states. The bare part (i.e., without $\pi\pi(K\bar{K})$ rescattering which we put in explicitly) of this process is denoted by Γ_B. The pions (kaons) then connect to the nucleon directly or via multiple scattering. The elementary $\pi\pi(K\bar{K}) \to N\bar{N}$ amplitude is denoted by $\mathcal{V}$. For the elementary pion (kaon) matrix elements (Γ_B) we simply couple the two pseudoscalar fields to a scalar with a pointlike vertex. The coupling constants of these vertices account for the strength of the matrix elements they represent and are taken as parameters (we describe how they are fixed next).

Equation (4) is represented graphically in Fig. 8. The dotted line does not represent

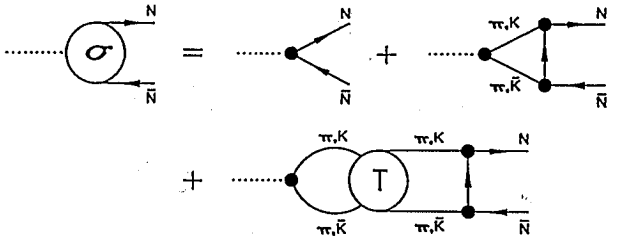

Figure 8. Pionic corrections to the nucleon σ term

a particle line but represents the operator $\bar{u}u + \bar{d}d$ appearing in Eq. (2). We have drawn it as a line to draw the obvious parallel between this and the electromagnetic form factor which we discuss in the next section.

Embedded in Eq. (4) is the σ term of the pion (kaon), $\Gamma(t)$, which is given in this model by

$$\Gamma = \Gamma_B + \Gamma_B G T. \tag{5}$$

This is illustrated in Fig. 9. For $t = 0$ this can be expressed as derivatives of the pion

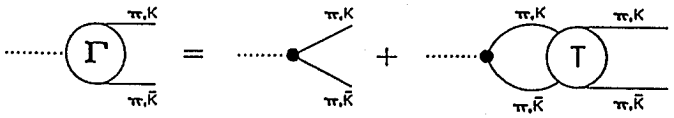

Figure 9. The pion (and kaon) scalar form factor

(kaon) masses with respect to the quark masses.[12] By requiring that the solution of Eq. (5) agrees with these predictions at $t = 0$ we are able to fix the two coupling constants mentioned above. This means we have no free parameters in the calculation.

The result for the pion form factor $\Gamma_\pi(t)$ is shown in the solid curve of Fig. 10(a).

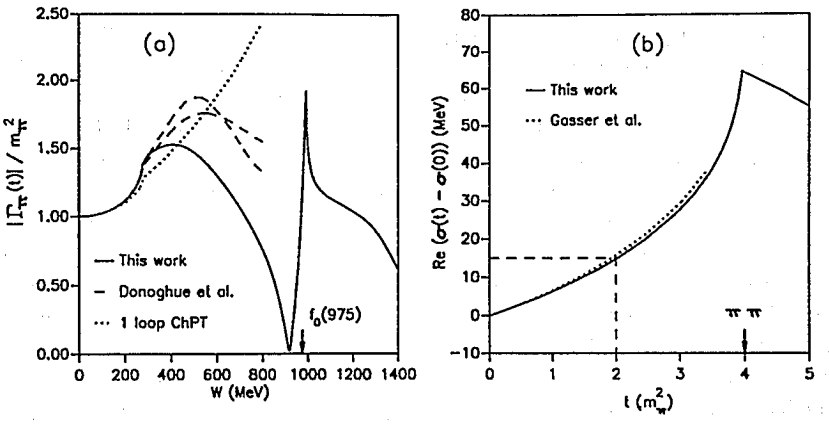

Figure 10. (a) The pion scalar form factor. The dashed and dotted curves are from Ref. 12. (b) t dependence of the nucleon σ term. The dotted curve is from Ref. 9.

The effect of the $f_0(975)$ is clearly evident. The r.m.s. radius is 0.75 fm. For comparison, we also show the results of a one-loop chiral perturbation theory calculation[12,9] (dotted curve) and, in the dashed curve, a recent calculation by Donoghue, Gasser and Leutwyler.[12,9]

The latter calculation uses a dispersion relation approach using the empirical $\pi\pi$ phase shifts (solving the Muskhelisvili–Omnes equations) to impose unitarity on $\Gamma(t)$. In a sense, our calculation is a close parallel of theirs. It differs in that we use the solution of the scattering integral equation to impose unitarity rather than dispersion theory, and we use a dynamical model of the $\pi\pi - K\bar{K}$ system that includes off-shell effects rather than the empirical phase shifts. We use the same method to fix the two coupling constants described above as they use to fix the two subtraction constants in their analysis and the same unitarity relation they use is automatically embedded in Eq. (5). It is interesting that our calculation agrees with theirs below threshold but differs beyond that.

Having fixed the coupling constants and confirmed that our calculation of $\Gamma(t)$ is sensible, we can proceed to the nucleon σ term. In Fig. 10(b) we show the difference $\sigma(t) - \sigma(0)$ in the vicinity of the Cheng-Dashen point (assuming the contribution of the "bare nucleon" σ term, σ_B is approximately a constant function of t). Our results are in almost exact agreement with the dispersion relation calculation of Gasser, Leutwyler and Sainio[9] (dotted curve) throughout the range of their calculation. (Again, embedded in our calculation is the same unitarity relation that drives their dispersion integrals.) In particular, we confirm their result that there is a strong t dependence of $\sigma(t)$ near the Cheng-Dashen point, giving rise to a 15 MeV contribution to $\sigma(2m_\pi{}^2) - \sigma(0)$ and a scalar r.m.s. radius of 1.25 fm.

6. Pion electromagnetic form factor

Effective meson Lagrangians can easily be extended to include couplings to photons,[6] enabling us to compute, for example, the electromagnetic form factor of the pion. The important new ingredient for us is a diagram in which the photon transforms to a ρ-meson. In the usual vector dominance picture, the pion electromagnetic form factor would then be obtained from the photon transforming to a ρ which then decays to two pions. By using a Breit-Wigner propagator for the ρ to account for its width and adjusting the overall strength, one can obtain agreement with the data in the ρ resonance region but it is not possible to simultaneously fit the ρ resonance and the normalisation requirement $F_\pi(t=0)=1$. However, in the model of the $\pi\pi$ system just described, the $\pi\pi$ self energy corrections to the ρ means that the physical ρ propagator is more complicated than a simple Breit-Wigner.

If we write $\Gamma_{\gamma\rho}$ for the amplitude arising from the Lagrangian for the process $\gamma \to \rho$, d for the bare ρ propagator and f_B for the bare $\rho \to \pi\pi$ vertex, then, up to appropriate normalisations, the π electromagnetic form factor is written (in operator form) as

$$F_\pi = \Gamma_{\gamma\rho} d f_B + \Gamma_{\gamma\rho} d f_B G T, \tag{6}$$

where T is the coupled channel t-matrix discussed earlier and G is the two-body propagator. This equation is illustrated diagramatically in Fig. 11. The first term is

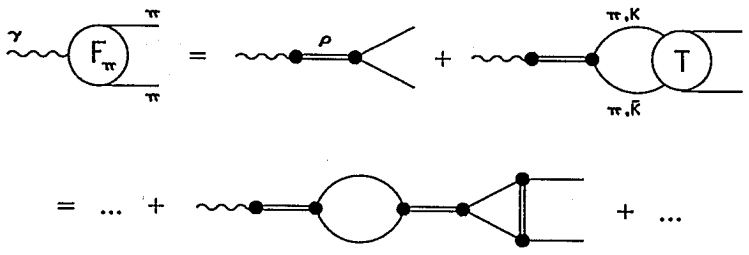

Figure 11. The equation for the π electromagnetic form factor.

just the diagram usually written down in the vector dominance picture, except that now the ρ propagator is simply the Feynman propagator for the bare ρ appearing in the Lagrangian. The second term is the final state interaction that dresses this bare ρ giving it its physical mass and width. The second line in Fig. 11 gives an example of a diagram that is included by applying the final state interaction.

Since we take the $\gamma \to \rho$ interaction to be pointlike (i.e., it has no form factor associated with it) the only new parameter introduced is the $\gamma \to \rho$ coupling constant. This is fixed by requiring $F_\pi(0)=1$. However, it turns out that the $\pi\pi$ results are somewhat insensitive to the bare $\pi\pi\rho$ cutoff mass. This is illustrated in Fig. 12(a), where we show the $\pi\pi$ phase shifts in the ρ channel for four values of the monopole cutoff mass Λ. In each case, the bare ρ mass is readjusted to fit the data but all

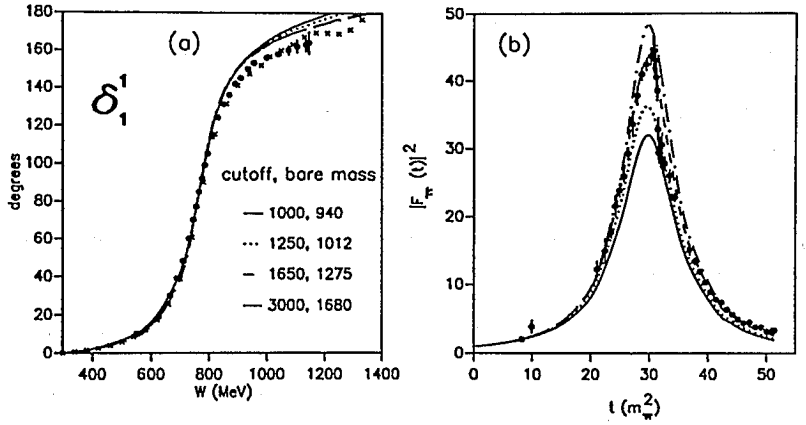

Figure 12. (a) The dependence of the $\pi\pi$ phase shifts on the $\pi\pi\rho$ cutoff mass. (b) Corresponding dependence of the electromagnetic form factor.

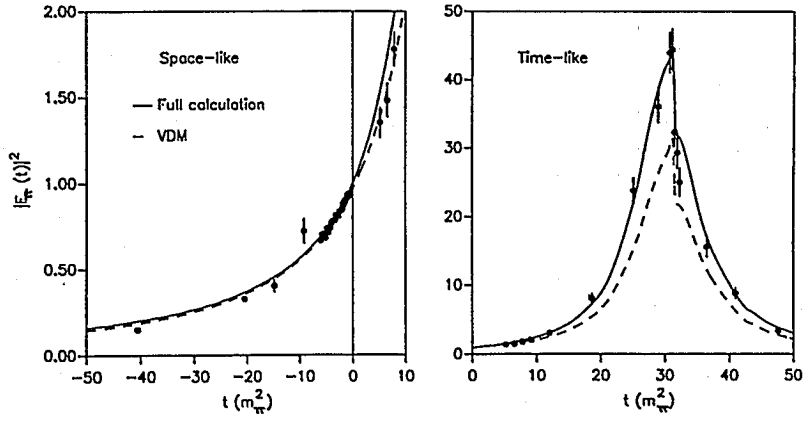

Figure 13. Results for the pion electromagnetic form factor including the ω contribution. The solid curve is the full calculation; the dashed curve is the vector dominance model.

other parameters are kept fixed. In Fig. 12(b) we show the corresponding results for the electromagnetic form factor, where we see a strong dependence on the $\pi\pi\rho$ cutoff mass. Hence, the electromagnetic form factor provides a measurement of the off-shell $\pi\pi\rho$ vertex. In Fig. 13 we show the results for both the space- and time-like regions using the optimal value of the cutoff mass (1650 MeV). The curves include the addition of a $\rho - \omega$ mixing contribution obtained by adding to the calculation the usual Breit-Wigner vector (ω) dominance contribution. The coupling constants

for this piece are fixed by known decays ($\omega \to \pi\pi$ and $\omega \to e^+e^-$), with only the phase adjusted to fit the data. The dashed curve is the results of the naive vector dominance model with inclusion of the $\rho-\omega$ mixing contribution. The full calculation results in an r.m.s. radius of 0.647 fm. This is closer to the experimental value[13] of 0.66 ± 0.01 fm than the value 0.62 fm obtained using the vector dominance model.

It is an assumption of the meson exchange approach that the form factors that are introduced are a means of parametrising the underlying quark-gluon structure of the hadrons. Since the electromagnetic form factor seems to be so sensitive to the form factor at the vertex where two pions couple to a *bare* ρ, it is tempting to interpret this as a measure of the size of the confining region. Yeilding to such temptation, the required cutoff mass of 1650 MeV would imply an r.m.s. radius of 0.29 fm. However, in the analysis so far we have kept the parameter a defined in the Lagrangian of Bando *et al.* [6] fixed at the "vector dominance" value of 2. This means the photon does not couple directly to the π but only via the ρ. Relaxing this constraint introduces some ambiguity, making such a prediction less reliable.

7. Conclusions

The model of the $\pi\pi - K\bar{K}$ system[5] we have reviewed is driven by s- and t-channel meson exchanges with the vertices obtained from an SU(3) symmetric Lagrangian. Only the well-established mesons (ρ, ω, ϕ, $K^*(892)$) are used in the t-channel driving terms. The $f_0(975)$ then emerges as a $K\bar{K}$ bound state. All other resonances considered (ρ, $f_2(1270)$, $K^*(892)$ and $K_0^*(1430)$) required the introduction of s-channel poles corresponding to genuine $q\bar{q}$ states. It was also necessary to include a state corresponding to the $f_0(1400)$.

The scalar form factors basically agree with those derived from dispersion theory by Gasser *et al.* [9] with excellent agreement obtained for the nucleon form factor. We obtain a 15 MeV contribution to the nucleon σ term arising from the difference $\sigma(2m_\pi^2) - \sigma(0)$. The r.m.s. scalar radii of the pion and nucleon are 0.75 fm and 1.25 fm respectively.

We have also presented results for the pion electromagnetic and scalar form factors and the nucleon scalar form factor that utilise the $\pi\pi - K\bar{K}$ model. The electromagnetic form factor results provide tighter constraints on the bare $\rho\pi\pi$ form factor than do the $\pi\pi$ phase shifts. The value obtained for this cutoff parameter corresponds to a confinement size of about 0.29 fm, although this may change if the photon is allowed to couple directly to the pions.

References

[1] G. t'Hooft, *Nucl. Phys.* **B72** (1974) 461; E. Witten, *Nucl. Phys.* **B160** (1979) 57.
[2] S. Godfrey and N. Isgur, *Phys. Rev.* **D32** (1985) 189.
[3] J. Weinstein and N. Isgur, *Phys. Rev.* **D41** (1990) 2236.
[4] B.C. Pearce, K. Holinde and J. Speth, *Nucl. Phys.* **A541** (1992) 663.

[5]D. Lohse, J.W. Durso, K. Holinde and J. Speth, *Nucl. Phys.* **A516** (1990) 513.
[6]M. Bando, T Kugo, S. Uehara, K. Yamawaki and T. Yanagida, *Phys. Rev. Lett.* **54** (1985) 1215.
[7]S. Weinberg, *Phys. Rev.* **166** (1968) 1568.
[8]D. Morgan and M.R. Pennington, *Phys. Lett.* **B258** (1991) 444.
[9]J. Gasser, H. Leutwyler and M.E. Sainio, *Phys. Lett.* **B253** (1991) 260.
[10]J. Gasser, H. Leutwyler and M.E. Sainio, *Phys. Lett.* **B253** (1991) 252 and references therein.
[11]R. Koch, *Z. Phys.* **C15** (1982) 161.
[12]J.F. Donoghue, J. Gasser and H. Leutwyler, *Nucl. Phys.* **B343** (1990) 341.
[13]S.R. Amendolia et al., *Phys. Lett.* **B138** (1984) 445; *Nucl. Phys.* **B277** (1986) 168.

MAGNET SPECTROMETER FOR THE IUCF COOLER

G. P. A. BERG, L. C. BLAND, C. C. FOSTER, P. SCHWANDT,
K. SOLBERG, and Y. WANG

Indiana University Cyclotron Facility, Bloomington, Indiana 47405, U.S.A

A Chicane/Spectrometer system has been proposed for the IUCF Cooler Spectrometer. The system is designed to meet the special requirements of Cooler internal target experiments at very small angles. This goal is achieved with a three magnet chicane with variable chicane angle 0°-24° which will be installed in a straight section of the Cooler storage ring. For medium resolution momentum analysis a quadrupole/dipole system with an optional septum magnet is installed behind chicane magnet 2. While reaction products with rigidities close to the beam rigidity can be analyzed at angles down to 3°, those with up to 53% of beam rigidity can be analyzed down to 0°. We will present the modes, ion optics, layout and design properties of the system.

1. Introduction

The IUCF Cooler was built with one of its six straight sections dedicated to accommodate a magnet spectrometer system as shown in Fig. 1. The nuclear physics program at medium energies utilizing the special properties of the Cooler ring and the proposed chicane/spectrometer system includes a variety of reactions designed to study symmetry breaking phenomena (e.g. pd $\rightarrow$ ^{3}He($\pi^+\pi^-$), dd $\rightarrow$ $\alpha\pi^0$), proton inelastic scattering and exclusive proton-induced knockout reactions (e.g. ($\vec{p},\vec{p}'$), ($\vec{p}$,2p), ($\vec{p}$,pn)) and charge exchange reactions in the β^+ direction (e.g. ($\vec{d}$,^{2}He)). Requirements for such a magnet system are:

- Small angle and 0° capability
- Large solid angles
- Large momentum acceptance
- Large dynamical range for one momentum setting
- Wide range of momentum settings
- Medium resolution of about 100 keV
- Variable types and locations of internal and external Cooler targets

The physics objectives for the Cooler spectrometer, discussed in detail by Miller et al. [1] in another contribution to this conference, are facilitated by the unique opportunities presented by the Cooler ring, e.g. for near-threshold studies with high resolution, for experiments with internal carrier-free polarized targets, and for 0° reaction investigations. In all but one example given there (inelastic proton scattering from polarized targets), the reaction particles or recoils to be detected are of substantially lower rigidity than the beam.

The question as to whether the spectrometer system should be capable of bending full beam rigidity (3.6 Tm) was carefully considered from the outset in the physics discussions. Clearly some physics will require this capability (e.g. elastic and inelastic scattering), but it appears that it is not of major import based on the presently discerned physics program.

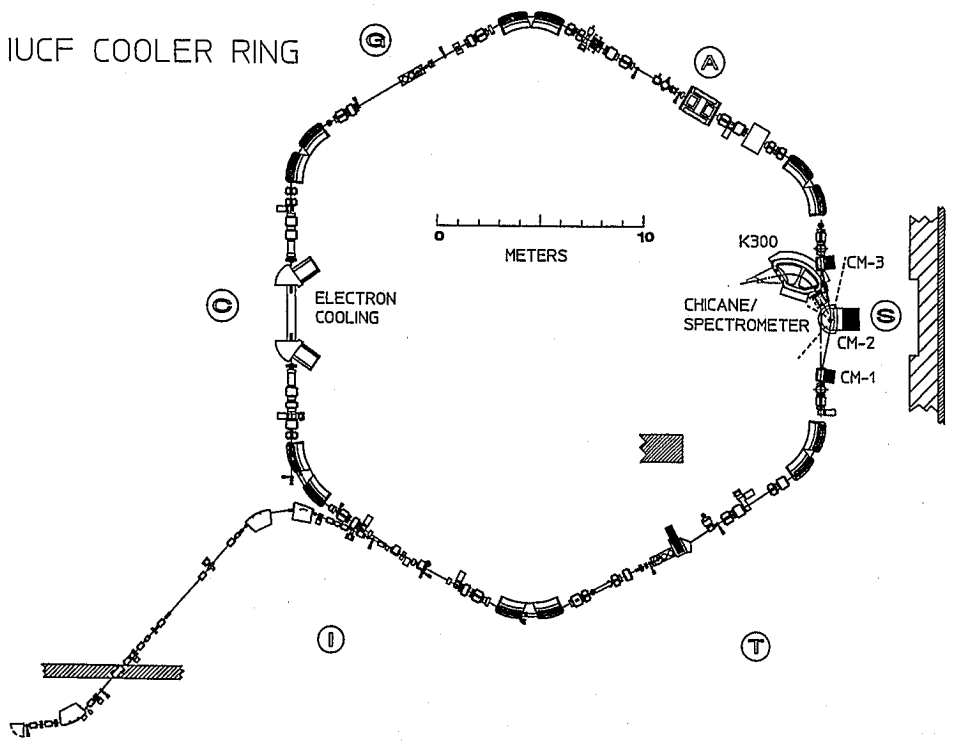

Fig. 1 IUCF Cooler ring with chicane/spectrometer system installed in the Cooler "S region" opposite the electron cooling "C region".

In the case of inelastic scattering it is important that the impulse approximation is applicable. It has been demonstrated extensively at IUCF that this is the case for incident energies above about 150 MeV. Some energy variation to permit changes of contributions from different spin-dependent parts of the effective interaction is also desirable; however, a maximum energy of 270 MeV appears to satisfy this requirement.

On the practical side, to construct a K600-size spectrometer capable of bending full beam rigidity and at the same time having a large enough solid angle to accommodate experiments like (d,^{2}He) would greatly increase the cost. In addition, such a large spectrometer would not be able to go to the very small angles in the Cooler ring demanded as an important part of the physics of elastic and/or inelastic scattering from 300-500 MeV. The existing K600 would suffer from the same small-angle limitation, and in addition it has only a modest solid angle and momentum bite, which would severely compromise a large fraction of the proposed physics. Furthermore, because the Cooler ring only takes beam from the cyclotron for a few seconds per 20-60 second Cooler cycle, the K600 in its present location can share the beam from the cyclotron to perform concurrent high-resolution experiments for incident energies up to 200 MeV.

We have reviewed several designs of large acceptance spectrometers built recently, in particular the SASP at TRIUMF and the MRS at LAMPF. In both cases the capability closely conformed to what we require, but neither appears to offer any substantial advantage over the existing K300 (which was originally conceived as a second arm spectrometer to be used in conjunction with the K600 at IUCF). When the question of cost is added, it becomes clear that any of the alternative solutions where one starts from scratch will be considerably more expensive than a solution which incorporates the K300 already on site.

The proposed chicane/spectrometer incorporating the K300 is thus our choice for the most cost-effective instrument in the Cooler ring for the large variety of experiments requiring the detection of lower-rigidity reaction products described in ref. 1. With the addition of the septum magnet it will also allow elastic and inelastic proton scattering from polarized targets up to 270 MeV to scattering angles as small as 3° in the laboratory. The proposed system provides a very good compromise in terms of energy resolution and solid angle for the diversity of physics investigations proposed. The following sections describe the details of the proposed chicane/spectrometer system making use of existing components of the K300 spectrometer.

2. Modes of Operation

Designing a spectrometer system with the above requirements coupled to a storage ring is an ion optical as well as a technical challenge. Unusual and novel designs deviating from proven spectrometer design concepts are necessary. Before describing the proposed system in detail, the different modes of operation will be outlined schematically.

In order to extract reaction particles from internal Cooler targets a chicane magnet system consisting of three dipoles CM-1, CM-2, and CM-3 will be installed in the Cooler S-region (see Fig. 1). Dipole magnet CM-1 bends the Cooler beam by angles between 0° and 12° away from the normal path. Twice this angle is called the chicane angle. The configurations in Figs. 2 and 3 show the chicane with chicane angles of 24° and 16°, respectively. Dipole magnet CM-2 bends the beam back by the amount of the chicane angle, and dipole magnet CM-3 brings the beam again on to the normal ring closed orbit. Different chicane angles between 0° and 24° can be achieved by moving CM-2 perpendicular to the unperturbed Cooler beam orbit (when all the chicane magnets have zero field).

Dipole magnet CM-2 also bends reaction products from different target locations away from the beam, as shown in Fig. 3 for reaction particles emitted at 0° and 10° and magnetic rigidities in the range from 0.2 Tm to 1.9 Tm. The highest magnetic rigidity which can be analyzed in the quadrupole dipole (QD) spectrometer system for particles emitted at 0° is 1.9 Tm, as shown in Fig. 2. The dipole in the QD system is the existing K300 magnet. By inserting a septum magnet (S) between CM-2 and Q, the smallest observation angle for elastically-scattered particles is 3°, as shown in Fig. 4. Dipole magnet CM-2 has a large gap of 15 cm both to provide large solid angles and to allow targets to be installed inside the gap. The circular field boundary provides a compromise in optimizing the ion-optical requirements for different target locations and scattering angles.

Several translational and rotational degrees of freedom need to be built into the chicane/spectrometer system. These motions of the chicane/spectrometer system are necessary for setting and optimizing the angle and momentum ranges to be measured. The

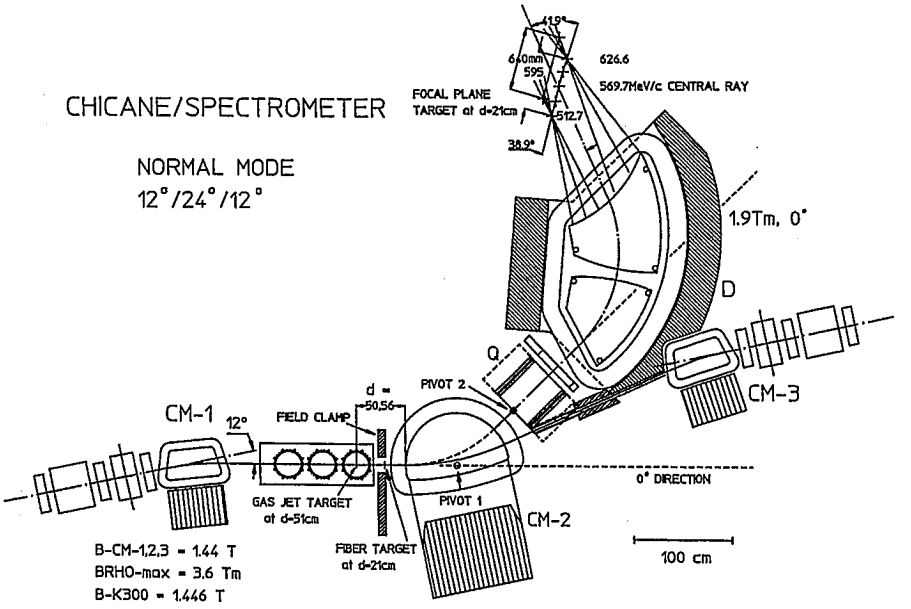

Fig. 2 Chicane at 24° and spectrometer in normal mode at its most forward angle setting. Typical target locations and a sample focal plane are indicated.

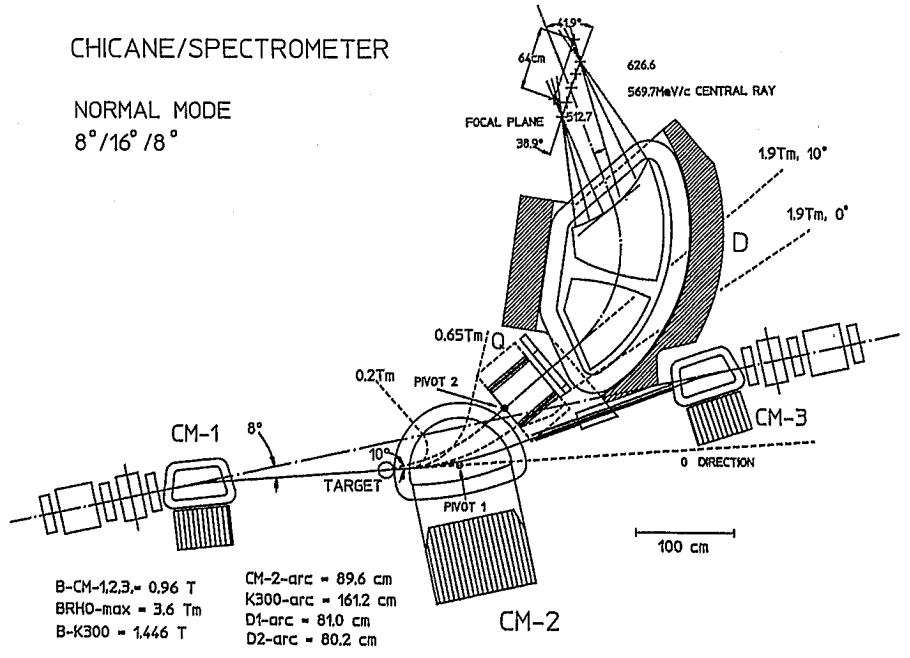

Fig. 3 Chicane at 16° where lower momentum particles are captured in the spectrometer. A fiber or skimmer target can be operated at the indicated location.

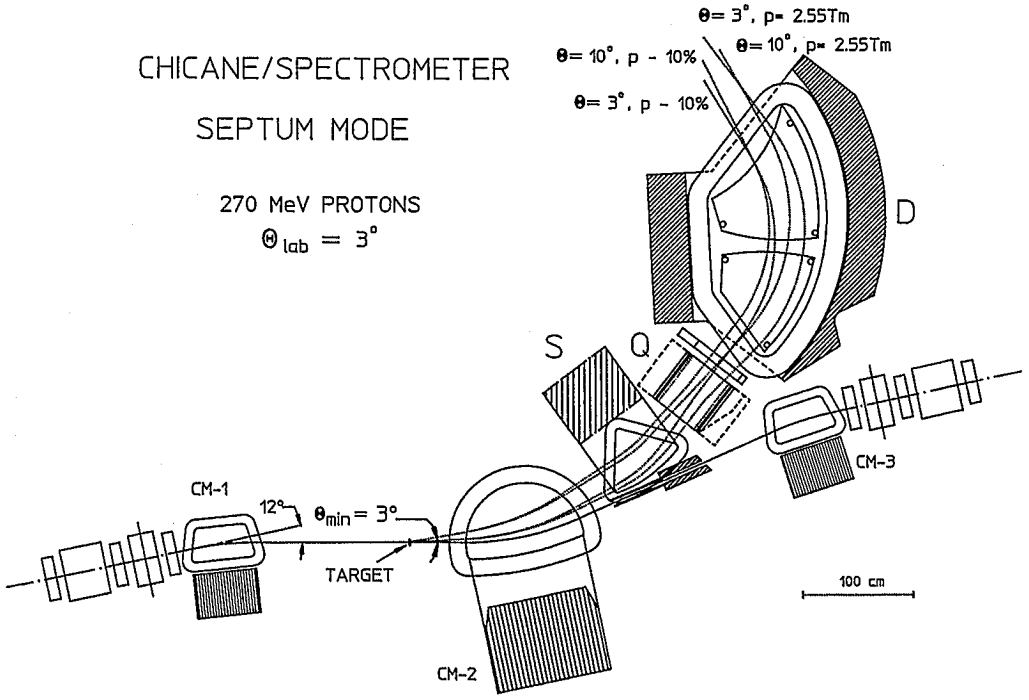

Fig. 4 Chicane/spectrometer in septum mode. The septum dipole S allows measurements of particles with full beam rigidity (up to 2.55 Tm) at angles as small as 3°.

perpendicular linear motion of CM-2 mentioned above allows the analysis of particles with different magnetic rigidities at the same exit location of CM-2. This is particularly useful if different momentum ranges of particles have to be measured with a fixed detector or at forward spectrometer locations. The spectrometer system can be rotated simultaneously around two pivots (see Fig. 5), one located at the center of CM-2 and one at the entrance of the quadrupole Q. This compound motion allows the setting and optimization of the desired angle and momentum range in the spectrometer system.

The spectrometer will be mounted on a carriage which incorporates a flexible air pad motion system (see Fig. 5) to allow unconstrained spectrometer motion, insertion or removal of the septum magnet S between CM-2 and the quadrupole Q, or removal of the spectrometer altogether for replacement with another detector system. Should the straight section be needed for other experiments or tests, it is possible to easily remove all magnets except CM-1 and CM-3. The length of the free drift space between CM-1 and CM-3 is 550 cm along the unperturbed beam path. The length of the free drift space between CM-1 and CM-2 available for target installations is about 180 cm.

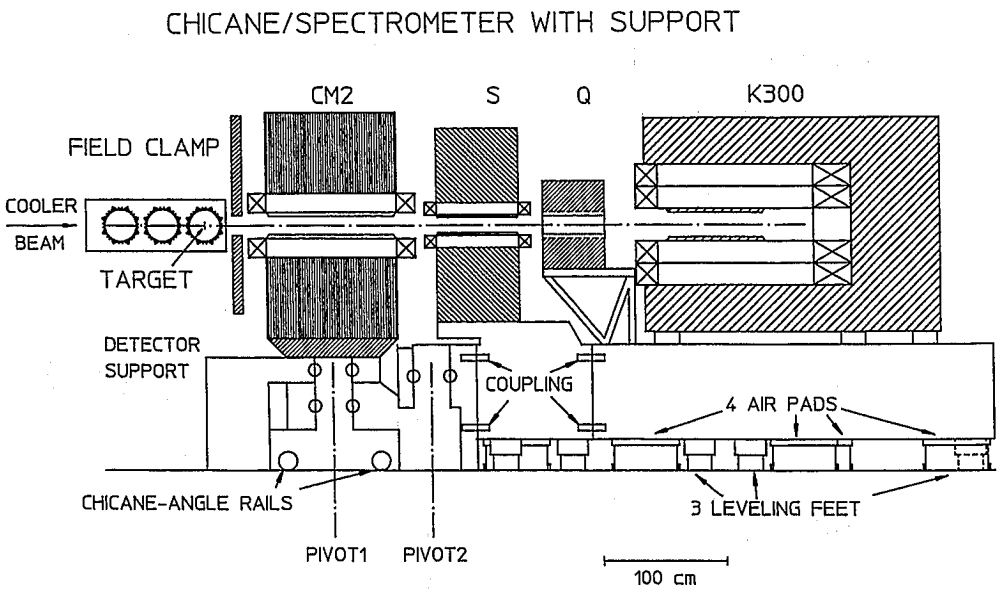

Fig. 5 Side view showing chicane magnet CM-2 and the spectrometer system in the septum mode (S,Q,K300 dipole). The support system is shown schematically with rails and pivots for mechanical adjustment. Air pads and leveling feet allow movement and positioning of the spectrometer.

The 0° extension of the beam direction entering CM-2 is kept clear to allow experiments with a secondary neutron beam. The feasibility of producing tagged neutrons by measuring protons from the (d,np) breakup reaction was studied intensively. Several modes were suggested to measure the (n,p) reaction from targets in CM-2 which would allow the reaction protons to be analyzed in the K300 spectrometer simultaneously with the tagging protons. It is also possible to use the neutron beam further downstream. In the latter location neutron detector systems with very large solid angles and moderate resolution can be installed. Since the good resolution (n,p) modes using the single spectrometer are limited in solid angle, we have kept open the option of a second-arm spectrometer for future development. Installation of a second spectrometer to detect (n,p) protons could provide an increase in the count rate by up to an order of magnitude, but a special large-target, large-solid-angle spectrometer would be needed. The Cooler experiment [1] CE10 was designed to determine the feasibility of the production of tagged neutrons. The measured absolute cross sections were encouraging for the production of a useful rate of tagged neutrons in the Cooler ring. No additional effort and cost related to the ion-optics are necessary to keep the good resolution, one or two spectrometer, tagged-neutron modes as future options.

In summary, the technical concepts of the proposed single-spectrometer design have been developed to achieve a versatile and flexible instrument for carrying out the proposed physics with the option of future development capabilities. A brief description will be given below of the different spectrometer configurations for the proposed experiments.

The application of the "normal mode" chicane/spectrometer to studies using the (d,^{2}He) reaction is shown in Fig. 2. The requirement for this reaction to measure 0° protons of magnetic rigidity Bρ = 1.9 Tm, produced by the maximum Cooler deuteron beam energy of 290 MeV (Bρ = 3.6 Tm), have determined the maximum chicane angle of 24°. This figure also shows a gas jet target location and a field clamp to reduce the fringe field of CM-2 at the target. This configuration is also required in the experiment designed to locate the isovector 0^- strength [1]. For experiments using polarized targets, a free space of 150 cm is available between CM-1 and the field clamp for installation of the target.

In Fig. 6. the chicane/spectrometer is shown set at a chicane angle of 24° to detect the ^{3}He reaction products which are to be measured in the chiral symmetry test [1]. A similar configuration will be used to measure the ^{4}He reaction products from the dd$\rightarrow \alpha\pi^\circ$ charge symmetry breaking experiment [1].

For studies of inelastic scattering of protons from polarized targets a septum magnet will be inserted between CM-2 and the spectrometer quadrupole as shown in Fig. 4. This triangular-shaped dipole magnet can separate particles with magnetic rigidities close to the beam rigidity at scattering angles as small as 3°. The maximum beam rigidity for this mode is 2.55 Tm (270-MeV protons) limited by the existing K300 dipole magnet.

Knockout reactions like (p,2p) or (p,pn) can be studied by using the spectrometer and a second detector array on the right side of the beam line. In this configuration the CM-2 magnet is removed from its support using the existing 30-ton crane. The support is adjusted in the original Cooler beam direction. The K300 spectrometer is attached to the support in its normal mode and can rotate between 25° and more backward angles when used without the septum magnet. If more forward angles are needed the septum magnet can be used. A special scattering chamber is required to accommodate the target which is located in the center of rotation of the support system. This chamber has to be attached to the K300 and needs windows to allow the detection of the second reaction particle on the right side of the beam. The separation between the Cooler ultra-high vacuum and spectrometer system vacuum will be accomplished using established foil and valve techniques [2] as is presently employed in the Cooler T-section at the 6° magnet.

Figure 7 shows the chicane/spectrometer configuration that will be employed to measure the elastic scattering of tagged polarized neutrons. An internal "skimmer" neutron production target for deuteron breakup is located inside CM-2, followed by the target to be studied with neutron elastic scattering. To measure neutron elastic scattering only moderate resolution is required. This can be achieved in a large plastic detector array on the left side of CM-2, in place of the K300 spectrometer. A neutron detector on the right side of CM-2 can cover the angular range from 0° to about 60°. For the n+p elastic scattering at backward angles, the second target would be located just downstream of CM-2, followed by a suitable detector for the elastic recoil protons. Wire chambers in the recoil proton detector stack will provide precise angle measurement.

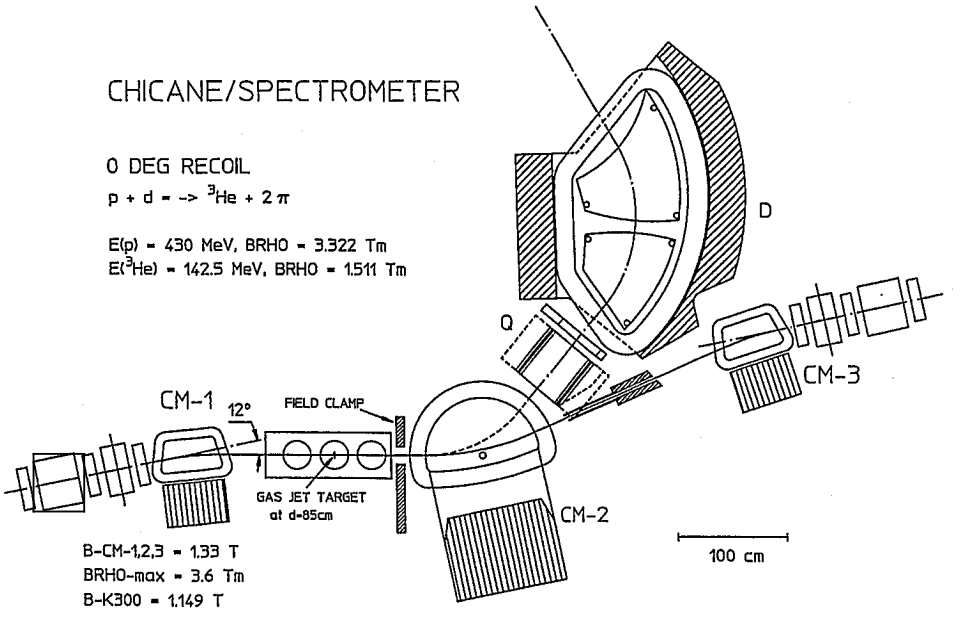

Fig. 6 Example of the recoil mode p + d → ^{3}He + 2π threshold reaction in which the spectrometer collects the complete cone of recoil particles.

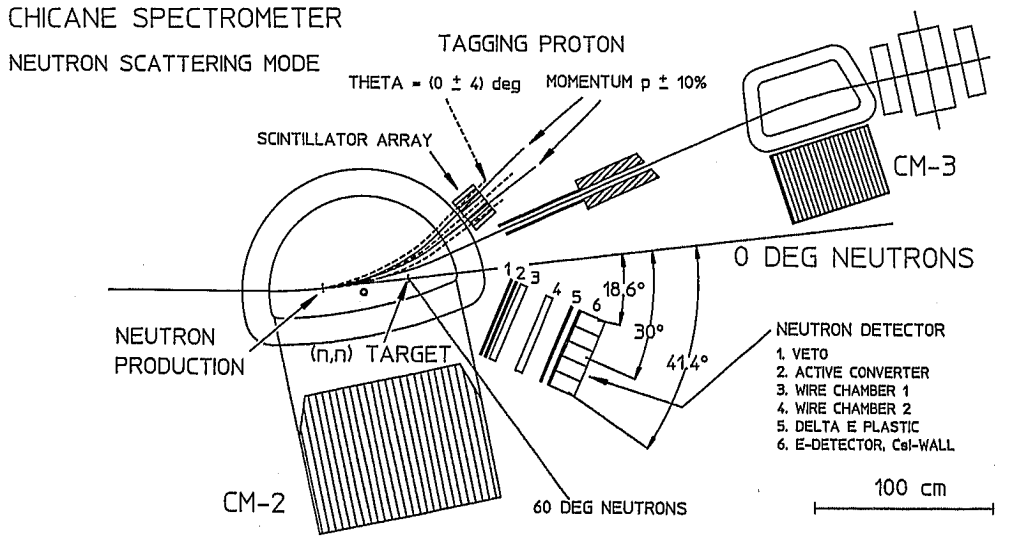

Fig. 7 Example of the chicane mode where the spectrometer is not used. In this low-resolution, large-solid-angle application, a tagged neutron beam is produced and used to study neutron elastic scattering over the angular range from 0°- 60°.

For pion production studies, the chicane/spectrometer offers two configurations. For medium resolution, moderate solid-angle requirements, the spectrometer can be used to analyze the recoil products. In the case of the $p + p \rightarrow d + \pi^+$ reaction, the spectrometer will be equipped with the septum magnet to separate the proton beam from the recoil deuterons emitted in a forward angle cone with rigidities slightly smaller than beam rigidity. For large solid angle, low resolution requirements, CM-2 can be used to bend recoils in a manner similar to that used with the 6° magnet in the Cooler T-section. The advantage of the Cooler chicane is the flexible chicane angle and the large momentum and solid angle range of CM-2. Fig. 3 shows an example of two recoils with rigidities of 0.2 Tm and 0.65 Tm for the chicane angle set at 16°. The spectrometer can be removed using the air-pad system to provide access for a separate detector stack.

3. Ion-Optical Concepts

The ion-optical concept of the Cooler chicane/spectrometer system combines the functions of a three-magnet chicane (used to separate the circulating Cooler beam from reaction products) with a flexible spectrometer system that can be configured to detect the reaction products from a wide variety of reaction processes. The variable chicane angle (0° to 24°) is designed to allow the separation of reaction products with rigidities up to 1.9 Tm at 0° when the Cooler beam has its maximum rigidity of 3.6 Tm.

This design incorporates the requirements listed in Sec. 1. The required flexibility of the system prevents the simultaneous optimization of the ion optics for all configurations. In particular the variable target location leads to different optical properties of the spectrometer such as focal plane size and location, resolving power, and angular range. The intended use of a variety of targets with very different beam-target interaction volumes will require ray tracing utilizing several detector measurements in order to achieve the required precision in observables such as resolution, scattering angle and momentum. Fiber and skimmer internal targets represent well-localized sources of reaction products. However, gas jet targets and windowless gas cells are extended sources ranging in length from a few centimeters to a few tens of centimeters along the beam direction.

Another major factor in the ion-optical design is introduced by the dispersive dipole CM-2 in front of the spectrometer quadrupole. This magnet is necessary to separate the beam from the reaction products. This dictates a horizontal orientation of the K300 dipole bend plane. It also reduces (together with the larger target distance to the quadrupole) the momentum range from 35% (in the original K300 design) to about 20%. This is still acceptable for all of the proposed experiments. A quadrupole with a 45-cm horizontal opening is needed for this momentum range as well as to maximize the solid angle. The solid angle is typically 10 msr, but the exact value depends on the target location. (It also varies as a function of the dynamical momentum and the scattering angle.)

The ion-optical code TRANSPORT [3,4] was used to fit the desired first-order properties of the system. Subsequent calculations with the code RAYTRACE [5] were used to determine and minimize the higher-order aberrations, to study details of the focal planes, and to follow individual rays of interest, as shown e.g. in Figs. 2 and 3. A plotting routine was added to the original RAYTRACE program to allow the fast evaluation of individual rays. The spectrometer system is optimized for a target location d = 23 cm in front of

the effective field boundary (EFB: d=0 cm) at the entrance of CM-2. In the quadrupole, a hexapole component of 0.03 T at 16 cm radius is required to reduce a large $(x|\phi^2)$ aberration. In the center of the focal plane the overall horizontal image is 1.6 mm in width, and is dominated by the $(x|\theta^2)$ aberration. The overall x-image increases to a total of 4.3 mm on the low momentum side and 2.6 mm on the high momentum side of the dynamical range. These aberrations can be partially corrected in software using horizontal angle measurements, and may be completely corrected if the vertical angle is also measured. Such corrections using horizontal angle and vertical position information are made routinely in the present K600 spectrometer. The quadrupole magnet will incorporate the necessary hexapole and octupole components. Other aberrations (up to the 5th order) as calculated with RAYTRACE do not contribute significantly to the horizontal image size.

For the target location at d = 23 cm, the overall vertical size of the image in the focal plane has the shape of a "bow tie" with a minimum height of 5.6 cm near the center and growing to 27 cm at the ends of the focal plane. A horizontal detector size of 60 cm is adequate for this configuration. The detector system is described in more detail in section 9. below.

4. Details of Chicane Magnets

The identical magnets CM-1 and CM-3 can provide a 0° to 12° deflection for the beam of maximum rigidity (3.6 Tm). They are each tilted by 6° relative to the straight-through path in the Cooler S-region, so that the beam orbit through them is as symmetrical as possible for different deflections (without moving these magnets). The C-magnet design for the yoke reduces the amount of iron which must be removed from the existing K300 dipole to provide clearance for CM-3 at most forward position. All three chicane magnets are laminated to avoid eddy current effects during ramping of the Cooler ring. Each of these magnets has 12° edge angles at the entrance and exit to satisfy Cooler ring focussing requirements. The pole piece dimensions are 523 mm in length by 350 mm in width. The pole gap is 60 mm to accommodate the full acceptance of the Cooler ring with β_y = 14 m and ε_y = 25 mm · mrad, as well as to provide space for the baking elements. The maximum field is 1.44 T used also in other laminated dipoles now operating in the Cooler ring. Magnets CM-1 and CM-3 will both run from the same power supply and each will require about 18 kW of power.

CM-2 is a much larger magnet than either CM-1 or CM-3. Not only does it need to bend full-rigidity beam particles by 24°, but it must also have a larger pole gap in order to allow a large acceptance solid angle for reaction particles which must pass through CM-2 before reaching the K300 spectrometer. The design gap is 15 cm, and the maximum field is again 1.44 T. CM-2 is also of a C-magnet design, leaving the low-momentum side completely open to allow the undisturbed extraction of reaction products of all momenta smaller than the beam momentum. The semicircular pole shape with a radius of 53 cm is an ion-optical compromise for beam and reaction particles with different entrance and exit angles. Particles of all rigidities leaving the target at 0° exit the magnet at normal incidence. This is particularly important for the Cooler beam. For other angles, the particles entering and exiting CM-2 do not do so normally, thus providing focussing effects which can be accommodated by adjusting quadrupole Q.

The return yoke of CM-2 is located on the high-momentum side of the beam. The exit side is shaped to allow the extraction of 0° neutrons and reaction products from targets inside the magnet at angles as far backward as about 70°. Also neutron elastic scattering studies using tagged neutrons can use a similar target location.

CM-2 has a dual function, as a Cooler dipole magnet bending the circulating beam and as the first element of the spectrometer system. Therefore CM-2 is a major magnet, much larger than conventional Cooler dipole magnets. The return yokes contain about 27 tons of soft iron, and the pole pieces will be laminated. A separate 135-kW ramping power supply will be required.

5. Details of Spectrometer System

Reaction products leaving the chicane magnet CM-2 will be momentum-analyzed with the quadrupole-dipole (QD) system as shown in Figs. 2 and 3, or with an additional septum magnet (SQD) system as shown in Fig. 4. The QD system is used for reaction products with a rigidity less than about 53% of the beam for reaction angles down to 0°, as in the (d,^{3}He) reaction. The septum magnet is required when particles with higher rigidities have to be measured at small angles, as shown in Fig. 4.

The main spectrometer dipole is based on the existing K300 dipole with split pole pieces which can analyze particles with rigidities up to 2.55 Tm. The present 10 cm gap will be enlarged to 20 cm in order to provide a solid angle of up to 10 msr. This modification of the K300 requires a second set of coils and extensions of both the vacuum chamber and the return yoke. This modified dipole along with the septum and quadrupole magnets must operate in close proximity to the Cooler beam. The return yoke of the K300 dipole will be cut away as shown in Fig. 3 in order to clear the Cooler circulating beam pipe and CM-3. In order to prevent saturation problems at high fields up to 1.7 T, the lost return iron will be added at another location. For kinematic corrections and optimization of the focal plane location, a K-coil (quadrupole coil) similar to the one used in the present K600 spectrometer will be installed on the second set of pole faces of the dipole. To power the dual set of main coils, one of two surplus power supplies recently-acquired will be used. It can provide the required 1600 A at 120 V, with only minor improvements.

The quadrupole Q, with horizontal and vertical openings of 45 cm and 15 cm respectively, will have a design similar to the present K600 entrance quadrupole. This design allows the incorporation of small hexapole and octupole components necessary to correct higher order aberrations. The main return yoke is located at the top and bottom of the magnet so that the beam can pass very close to the horizontal opening, as seen in Figs. 2 and 3. This quadrupole weighs about 2.5 tons, including 2 tons of iron and 0.5 ton of copper for the coils. A 50 kW power supply is required for its operation.

The main function of the septum magnet S is to bend particles very close to the beam rigidity into the acceptance of the quadrupole. This requires a special septum providing a sharp field drop from a maximum field of 1.7 T to an amount negligible for the Cooler beam. In addition to a special profile, a soft iron magnetic-shield tube around the beam line has been designed to protect the Cooler beam from fringe fields of all three spectrometer magnets. The gap of the septum magnet is 12.5 cm. The triangular-shaped pole faces provide the required horizontally-focussing quadrupole component. The magnet

is relatively large and requires a 200 kW power supply. It is planned to use the second surplus power supply which again needs only minor refurbishing. All of the spectrometer magnets are energized by DC power supplies since ramping is not necessary.

The spectrometer system will be coupled to CM-2 via a sliding seal or flexible port system to allow angle settings in the forward angle range up to about 25°. For more backward angles and/or for lower momenta the chicane angle can be decreased. For spectrometer angles greater than 40°, the chicane magnet CM-2 can be removed completely on the tracks to the outside of the Cooler ring.

In the spectrometer system a standard vacuum of 10^{-6} Torr will be maintained, but the vacuum in CM-2 has to meet the higher Cooler requirements of about 10^{-9} Torr. The vacuum vessels and pumping systems will be constructed corresponding to these requirements, with a separation foil similar to the ones used in Cooler experiments in the T-region [2].

6. Mounting of Chicane and Spectrometer Magnets

The advantage of using the dipole CM-2 to separate beam and reaction products unfortunately prevents the independent variation of scattering angle and momentum range commonly achieved in magnetic spectrometers. Some of this flexibility can be regained by the design of the translational motion of CM-2 and the rotation of the spectrometer around two pivot points. The mounting system is shown schematically in Fig. 5. CM-2 moves on rails which allows one to set the chicane angle or to move the magnet completely out of the ring. Attached to the support for CM-2 are pivot 1 and a short arm incorporating pivot 2. Each pivot is equipped with spherical bearings. The QD spectrometer is mounted on a sturdy carriage and is coupled to this double-pivot arm. A second detector arm is connected to pivot 1 to allow for the installation of additional detector systems.

The spectrometer carriage-to-pivot arm is designed to permit the carriage to be lifted off the floor by about 3 cm on an air-pad system in order to move it to any position within the constraints of the pivot points. Three adjustable mechanical leveling feet are provided to position the K300 at the correct height and level of the reaction plane. Suitable air-pad systems with drive mechanisms to move the spectrometer to any desired position and orientation are commercially available. Pivot 1 and 2 will be equipped with precision angle encoders to define the position of the spectrometer. The carriage motion and positioning system will be fully computer controlled.

The septum magnet, mounted on its separate support carriage and air-pad system for easy removal from the spectrometer system when not needed, can be easily inserted between the pivot arm and K300.

7. Effect of Chicane on Cooler Ring Properties

It is obvious that Cooler ring experiments with internal targets make the experiment an integral part of the accelerator. Thus an important question is whether the proposed chicane/spectrometer system will significantly alter or compromise the beam properties in the S region and/or at other points in the ring. Table 1 shows a comparison of the beam parameters at the center of the S region and the A (acceleration) region, both as the ring

is now operating ("No Chicane" column) and as calculations show it would operate with a chicane angle of 24° in the S region as proposed. These calculations represent a first iteration. In order to keep the transition energy essentially unchanged, chicane magnets CM-1 and 3 provide vertical focusing edge angles of 12° at the entrance and exit of their fields.

These changes in the Cooler ring parameters are considered acceptable. The differences indicated at the A region suggest that changes in quadrupole currents will be needed for 20 of the 36 ring quadrupoles. Further exploration may improve localization.

TABLE 1 Cooler Beam Parameters with S-Region Chicane

	No Chicane	24° Chicane
Cooler S-Region		
Aperture Functions		
β_x, β_y (meters)	0.59, 0.87	1.32, 1.32
α_x, α_y double waist	0, 0	0, 0
Dispersion η_x (meters)	4.11	4.56
Transition Energy/mc^2, γ_T	5.07	4.76
Cooler A-Region		
Aperture Functions		
β_x, β_y (meters)	2.18, 1.72	1.72, 1.08
Dispersion η_x (meters)	0	-0.0004
Tunes Q_x, Q_y	4.78, 5.10	4.88, 5.12

8. Summary of System Specifications

Table 2 shows characteristic parameters of the Cooler and the chicane/spectrometer system for the mode where the target is located at a position d=23 cm in front of the effective field boundary of CM-2. In this normal mode (DQD), the septum magnet is not used. Since several other target locations have to be accommodated for gas-jet and polarized targets (which require more space), Table 3 shows specifications for target locations d=51 cm and d = 75 cm. Also shown are the parameters for the small-angle high rigidity mode, which includes the septum magnet. All parameters shown in Tables 2 and 3 were calculated for the spectrometer in a vertical point-to-point mode at the center of the focal plane. This ensures the smallest possible vertical extent of the focal image.

The chicane magnets are designed to allow measurements at small forward scattering angles. The angular range quoted in the tables depends on the target location and can include angles up to about 25°. For larger scattering angles (up to about 90°) chicane magnet CM-2 can be removed and the spectrometer can be rotated to larger angles.

When reconstruction of the vertical scattering angle ϕ is important, as in the (d,^{2}He) reaction, an alternate focusing mode is preferable. In this (d,^{2}He) mode, the vertical image in the focal plane is larger than in the vertical point-to-point mode which allows better measurement of ϕ via the (y|ϕ) correlation.

The ion-optical properties and proper transmission through the spectrometer of all rays within the quoted solid angles were established by RAYTRACE calculations. The focal-plane detectors are designed to accept all of these rays.

TABLE 2 Parameters for Cooler, Chicane and Spectrometer

Cooler Beam Properties:		
	$p, \vec{p}$	30 - 480 MeV
	$d, \vec{d}$	20 - 290 MeV
	Emittance (cooled beam)	$\epsilon_x = \epsilon_y \sim 0.05\pi mm \cdot mrad$
	Momentum resolution, p/Δp	$\sim$ 50,000 (45 MeV p)
	Beam (at target location)	
	Spot size (cooled beam)	$2x_o = 1mm$
		$2y_o = 1mm$
	Dispersion:	$B_{16} = 4.56cm/\%$
Chicane System: CM1-CM2-CM3		
CM1, CM3:	Deflection angle	$0° - 12°$
	Max. field	$B_{max} = 1.44T$
	Max. beam rigidity	$(B\rho)_{max} = 3.6Tm$
CM2:	Beam:	
	Deflection angle	$0° - 24°$
	Max. field	$B_{max} = 1.44T$
	Max. beam rigidity	$(B\rho)_{max} = 3.6Tm$
	Reaction products:	
	Angular range	$0° - 40°$
	Magn. rigidity range	$B\rho = 0.2Tm - 1.9Tm$
DQD Spectrometer: (Target Distance d=23 cm)		
	Angular range ($B\rho = 1.9Tm$)	$0° - 40°$ (CM2 installed)
	Angular range ($B\rho = 2.55Tm$)	$> 25°$ (CM2 removed)
	Mean radius	$\rho_o = 1.31$ m
	Max. particle rigidity	$(B\rho)_{max} = 1.9Tm(0°), 2.55Tm(> 12°)$
	Max. proton energy	$160MeV(0°)$, $270MeV(> 12°)$
	Solid angle	$d\Omega \leq 9.4msr$, (elliptical)
	Acceptance angle	$d\Theta = \pm 60$ mrad, $d\Phi = \pm 50$ mrad
	Length of focal plane	$51cm$
	Momentum range p_{max}/p_{min}	1.20
	Tilt angle of focal plane	$41° \ldots 43°$
	Horizontal magnification M_x	-0.41
	Vertical magnification	-2.66
	Momentum dispersion D	$1.94cm/\%$
	Ratio	$D/M_x = 4720mm$
	Resolving power	$p/\delta p = 4720$ (for 1 mm object)
	Flight length, central ray	$538cm$

TABLE 3 Parameters for Spectrometer in Normal and Septum Modes

DQD Spectrometer: (Target Distance d=51 cm)		
	Angular range ($B\rho = 1.9Tm$)	$0° - 25°$ (CM2 installed)
	Angular range ($B\rho = 2.55Tm$)	$> 25°$ (CM2 removed)
	Solid angle (central ray)	$d\Omega \leq 7.4msr$, (elliptical)
	Acceptance angle	$d\Theta = \pm 52$ mrad, $d\Phi = \pm$ 45 mrad
	Length of focal plane	$53cm$
	Momentum range p_{max}/p_{min}	1.20
	Tilt angle of focal plane	$41° \cdots 43°$
	Horizontal magnification M_x	-0.40
	Vertical magnification	-2.59
	Momentum dispersion D	$1.96cm/\%$
	Ratio	$D/M_x = 4900mm$
	Flight length, central ray	$566cm$
DQD Spectrometer: (Target Distance d=75 cm)		
	Angular range ($B\rho = 1.9Tm$)	$0° - 20°$ (CM2 installed)
	Angular range ($B\rho = 2.55Tm$)	$> 25°$ (CM2 removed)
	Solid angle (central ray)	$d\Omega \leq 6.2msr$, (elliptical)
	Acceptance angle	$d\Theta = \pm 47$ mrad, $d\Phi = \pm$ 42 mrad
	Length of focal plane	$49cm$
	Momentum range p_{max}/p_{min}	1.20
	Tilt angle of focal plane	$41° \cdots 43°$
	Horizontal magnification M_x	-0.39
	Vertical magnification	-2.54
	Momentum dispersion D	$2.0cm/\%$
	Ratio	$D/M_x = 5130mm$
	Flight length, central ray	$590cm$
DSQD Spectrometer: (Septum Magnet, Target Distance d=51 cm)		
	Angular range ($B\rho = 1.9Tm$)	$3° - 25°$ (CM2 installed)
	Angular range ($B\rho = 2.55Tm$)	$> 25°$ (CM2 removed)
	Mean radius	$\rho_o = 1.31$ m
	Max. particle rigidity	$(B\rho)_{max} = 2.55Tm(> 3°)$
	Max. proton energy	$270MeV(> 3°)$
	Solid angle	$d\Omega \leq 4.0msr$, (elliptical)
	Acceptance angle	$d\Theta = \pm 50$ mrad, $d\Phi = \pm$ 25 mrad
	Length of focal plane	$60cm$
	Momentum range p_{max}/p_{min}	1.18
	Tilt angle of focal plane	$40°$
	Horizontal magnification M_x	-0.48
	Vertical magnification	$-$ 2.30
	Momentum dispersion D	$2.1cm/\%$
	Ratio	$D/M_x = 4375mm$
	Flight length, central ray	$618cm$

9. Detector Configuration and Readout Electronics

The detector and electronic readout system must be consistent with the resolution requirements of the chicane/spectrometer system and with applications for both single and multiple particle detection. The need for multiple particle detection places constraints on the readout electronics preventing multiplexing of the information as is currently done on the K600 spectrometer. An additional constraint on the new system is in applications where the signal of interest is contained within a large flux of background particles coming through the spectrometer. This is the mode of operation for studying the (d,^{2}He) reaction near 0° as well as in applications of the spectrometer for possible studies [1] of the π^+–π^- atomic state or studies of the isospin–forbidden reaction dd $\longrightarrow$ α π^0. The focal plane detectors must be able to handle the large singles rates expected in the above studies. In addition, there must be adequate intelligence in the first level of triggering to distinguish the signal from the background.

To obtain the resolving power of 5100 predicted from RAYTRACE calculations, a detector positioned along the focal plane must have a spatial resolution of better than 0.4 mm in the dispersion direction. Utilizing multiwire proportional chamber (MWPC) technology, this resolution can only be achieved by performing drift-time interpolations. Rays are incident on the focal plane with a range of horizontal angles from ~30° to 55°. Given this large angular range, the best solution for the focal plane position measurement is a vertical drift chamber (VDC) similar to the one presently in operation on the K600 spectrometer. Individual time-to-digital converters (TDC) will be used to encode the drift-time information from each wire. The 60 cm focal-plane length will require 105 sense wires with a spacing of 6 mm.

To achieve the optimum momentum resolution, the horizontal angle (Θ) must be measured to at least an accuracy of 8 mr, and software aberration corrections must also be made. This accuracy can be met using a second VDC positioned 12 cm downstream from the first. Utilization of a second VDC rather than a MWPC is desired to provide additional redundancy in the dispersion direction measurements.

To enable the VDC to handle the large singles rates it will be necessary to have individual preamp/discriminators for each sense wire. A total of 220 TDC channels are necessary for the drift time measurements. The best solution for reading out this information is a VME-based TDC. Since the front-end processors will also be VME based, this TDC should be the best solution for the readout.

Vertical position measurements are required to veto events which double scatter from the magnet pole faces and also to determine vertical angles at the target. The latter is particularly important in the missing mass reconstruction for multiple particle detection, as required e.g. in studies of the (d,^{2}He) reaction. Monte Carlo calculations suggest that vertical angle measurements of better than 15 mr are required to prevent loss of resolution in determining the missing mass. The angle measurements play a more important role in determining the ^{2}He mass, necessary for calibrating the detection efficiency and thus the absolute cross section.

The vertical focussing is nearly point to parallel. Thus, a measurement of the vertical position at the focal plane is crudely equivalent to a determination of the vertical angle at the target location. Utilizing MWPC detection with wire spacing of 2 mm should provide sufficient accuracy in the vertical angle measurements. Vertical angle measurements

at the focal plane are required to eliminate events which scatter from the dipole faces. These measurements can be made by adding a second MWPC. At 2 mm wire spacing, 100 wires per plane are required for the vertical position measurements.

In addition to horizontal and vertical focal-plane position measurements, multi-particle detection requires measurements to associate vertical and horizontal information for each particle. This association can be accomplished by utilizing planes of wires rotated by some angle with respect to the vertical (u,v planes). These measurements can be made with a MWPC having 3 mm spacing. For maximum redundancy, two of these planes are required. For a tilt angle of 45°, 300 sense wires per plane are necessary. Readout of the u,v, and y MWPC planes can be accomplished with the PCOS III system from Lecroy. We propose that there be two separate controllers for the two sets of u,y measurements.

The rate-capability of a conventional VDC could impose a luminosity constraint for measurements of the (d,^{2}He) reaction. At high rates, space-charge effects lower the effective field strength around a sense wire, thus reducing the wire efficiency. Accurate position measurements utilizing drift-time interpolation requires operation at low discriminator thresholds. Single-wire dead times will depend on the MWPC geometry, ionization density and discriminator thresholds. Measurements of singles rate capabilities have been carried out at IUCF with a drift chamber mounted on the K600 focal plane. Rate capabilities up to 300 kHz per wire were demonstrated. Assuming 3 wires hit in the VDC for each particle through the K300 spectrometer, the VDC would impose a limitation of ~10 MHz for the flux incident on the focal plane. This rate exceeds, by more than an order of magnitude, the largest singles rate from deuteron breakup expected within the luminosity limitations of the Cooler.

Triggering of the readout system is accomplished by two planes of scintillator located downstream of the wire chamber stacks. These scintillators also provide particle identification and relative timing information between particles for the diproton detection. Triggering for (d,^{2}He) reaction studies near 0° is the most difficult task since the two protons are virtually indistinguishable from the much larger flux of single protons resulting from deuteron breakup. A fast decision identifying a diproton event can be made by demanding that the pulse height in the trigger scintillator is twice that produced by a single proton. This technique requires a scintillator of sufficient thickness to obtain the necessary pulse height resolution so as to distinguish the energy loss of a diproton event from that of a single proton. A second level of triggering could utilize front-end electronics that inspect the encoded wire chamber data to guarantee that two tracks are observed for each event.

Segmentation of the focal-plane scintillators is required for two reasons. First, sufficient segmentation must be made to prevent the scintillators from limiting the singles rate capability of the focal-plane detection system. Assuming an upper limit of 10 MHz singles rate, an eight–fold segmentation of each scintillator plane would limit the singles rate to ~1.5 MHz in each scintillator paddle. Secondly, relative timing measurements are essential for diproton detection to distinguish "real" coincidences resulting from the (d,^{2}He) reaction from "accidental" coincidences arising from the large proton flux associated with deuteron breakup reactions. For (d,^{2}He) studies with the least negative Q–values at 0° scattering angle, it will be necessary to consider only those events which fire distinct scintillator paddles. The reals/accidentals distinction is made by measuring the relative time between the two scintillator paddles. This triggering scheme will require a minimum of 200 keV relative

energy in the diproton center of mass. This is well below the peak of the Watson/Migdal distribution. For larger relative energies, the trigger loses a constant fraction (~15%) of the diproton events contained within the K300 acceptance.

In summary, the focal–plane detector stack must meet the demands of a number of different experimental applications. Studies of the (d,^{2}He) reaction at 0° place the most stringent requirements on the detector system. A focal-plane stack consisting of a set of MWPC detectors and a two–plane segmented scintillator hodoscope meets the demands of the (d,^{2}He) studies and has sufficient flexibility for other applications of the K300/chicane. A sketch of the proposed detector configuration is provided in Fig. 8.

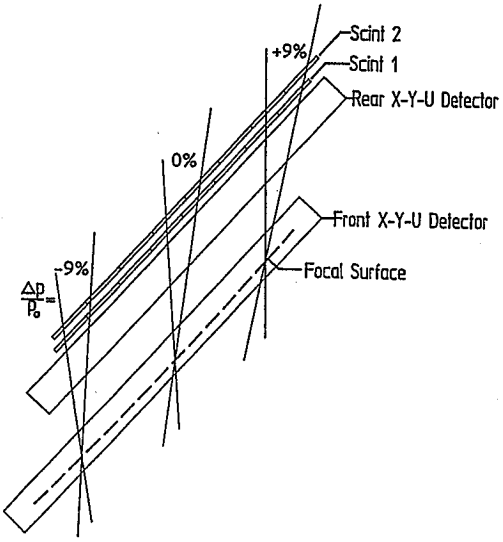

Fig. 8 Schematic drawing of the focal-plane detector to be mounted downstream of the K300 magnet in the chicane/spectrometer system. A detailed description of the properties of each detector element is given in the text.

Acknowledgments

One of the authors (GB) would like to thank Prof. Schult for the invitation and acknowledges travel support to present the paper by the Dr. Wilhelm Heinrich Heraeus and Else Heraeus Stiftung.

References

1. D. W. Miller et al., Contribution to this conference.
2. G.P.A. Berg et. al., IUCF Scientific and Technical Report, May 1990- April 1991, p. 155
3. K.L. Brown, Stanford Linear Accelerator Center, SLAC-75 (1967)
4. K.L. Brown, D.C. Carey, Ch. Iselin, and F. Rothacker. TRANSPORT, a computer program for designing charged particle beam transport systems, CERN-80-04 (Geneva 1980).
5. S. Kowalski and H.E. Enge. RAYTRACE, an ion-optical computer code to trace rays through an electromagnetic device, private communication and Internal Report MIT, Cambridge, MS July 1, 1987.

Study of pp, pd and p^{3}He Interactions in Pure Spin States at COSY

S.L.Belostotski

Petersburg Nuclear Physics Institute
St.Petesburg

Abstract
Internal gas target with a window–less storage cell in combination with the COSY polarized beam would provide an unique opportunity to study pp, pD, and p^{3}He interactions in pure spin states at advantageous experimental conditions.With this technique the double spin asymmetry Anm can be measured alongwith single spin observables both for inclusive and exclusive reactions thus providing important information on the hadrond dynamics and some aspects of nuclear physics.

Study of spin effects in the reactions with few body systems is a good way to better comprehension of the hadron dynamics. When measured polarization observables help to put additional constrains on the reaction mechanism and obtain a valuable information on nuclear and hadron structure.

It should be noted that a conventional experiment with an external polarized solid target (butanol, NH–3, etc.) is difficult sometimes because of

*) poor dilution factor (a large fraction of unpolarized nucleons) resulted in small observed asymmetries,
*) substantional background from unpolarized components,
*) low toleration to the beam energy loss in the target materials due to radiation damages and heating problem.

Another option is to use the internal polarized gas target incorporated in a storage ring. This technique has been recently upgraded by means of the arrangment which stores the polarized atoms (storage cell) [1,2]. The storage cell consists of a window–less pipe fed by the polarized source. Effective polarized gas thickness in the cell of 10^{14} atoms/cm^2 has been attained [3]. Thus for a current in the ring of 10^{17} protons/sec one gets 10^{31} 1/sec cm^2 for luminosity. This number is comparable with that for the external polarized solid target experiments in which the beam intensity has

to be usually reduced to 10^8–10^9 1/sec. There is one experiment using for several years the polarized gas (deuterium) target with the storage cell in the combination with unpolarized electron beam of VEPP–3 storage ring in Novosibirsk [4]. Dryfilm was applied as the wall–coating in the cell. Depolarization factors affected the atoms in the cell have been thoroughly investigated and shown to be small for the dryfilm coating [2]. The similar technique has been recently developed for ^{3}He polarized target mounted at the cooled proton beam of IUCF [5].

There are also several proposals in progress based upon the similar target technique combined with the polarized electron beams of the storage rings under construction now at BATES [6], DESY [7], and NIKHEF [8]. Use of the above technique provides unique opportunity for the investigations of nuclear reactions in pure beam–target spin states.However there are also some technical problems associated e.g. with admitted dimensions of the gas storage cell.

For the COSY ring we are planning installation at TP–2 the cell which would have variable dimensions (similar to that in Novosibirsk) because of large beam crossover at TP–2 at injection phaze. By our estimations the density of 10^{13}–10^{14} can be attained in the cell. Then for the expected luminosity of 10^{30}–10^{31} 1/sec cm^2 we propose to study the single and double spin asymmetries for many reactions using the polarized hydrogen, deuterium, or ^{3}He target at the advantageous conditions:

*) no dilution,

*) small background,

*)feasibility of the fast reversal and control of the beam and target polarizations,

*) high vector and tensor (for deuteron)polarizations.

The detailed physical considerations and motivations for the total bulk of the pure spin state experiments feasible with help of the above technique is out of scope of this paper.Here we will propose several selected topics being possibly regarded as of first priority experiments.We would also welcome other proposals aimed at the pure spin state investigations under above technical conditions.

1. Meson production in pure spin states.

First consider the single spin asymmetry An (analysing power) measured inclusively for the reactions

$$\vec{p} + p \rightarrow \pi^+ + X \quad \text{and} \quad \vec{p} + p \rightarrow \pi^- + X \tag{1}$$

at 13.3 and 18.5 GeV/c [9], (fig.10, p.345). Here

$$A_n = (N^+ - N^-)/(N^+ + N^-), \tag{2}$$

N+–are cross sections for the above reactions related to 'up' and 'down' polarizations of the primary beam, respectively. As one can see the both π^+ and π^- results for An are independent of the incident energy. In case of π^+ production An is increasing positive function of Xtr=Ptr/Pmax ,where Pmax is maximum pion momentum in the C.M. frame and Ptr is the transverse momentum of the pion. On the other hand, for π^- production An is close to zero. This picture is qualitatively explained in the frame of the Thomas precession model [10] predicting that $\bar{U}$ and $\bar{D}$ quarks accelerated from the sea are polarized in the directon $-\vec{n}$ ($\vec{n}=[\vec{K}i,\vec{K}f]$). In order to produce $\pi^+ = U\bar{D}$ the $\bar{D}$ quark from the see should be picked–up by the U quark of the polarized proton. If the spin of $\bar{D}$ is 'down',the spin of U should be 'up' which results in the positive analysing power. According to 'di–quark' approach the parent proton polarization is predominantly carried by the U quark of proton, the D quark being weekly polarized. Thus An for production of $\pi^- = \bar{U}D$ is found to be around zero.

This picture is maybe in conflict with the results of EMC and SLAC experiments [11,12] which show a surprisingly small contribution to the parent proton spin from ALL the valence quarks. A substantional contribution from the the sea quarks (negative), gluon component and orbital angular moment are implied [13]. It is obvious that any independent information on the spin structure of the nucleon is of great importance.

At COSY energies the most attractive are the kaon production reactions. The highest cross section (of 0.03 mb at 2.5 Gev) is related to

$$\vec{p} + \vec{p} \rightarrow p + \lambda + K^+. \tag{3}$$

The existing data are sparse in the energy region near threshold in particular for spin observables. The spin spin correlation parameter Anm (here n and m are related to the beam and target polarizations, respectively) was never measured until now.

In addition to verification of the conventual meson exchange mechanism one can try also to apply OCD considerations in order to predict Anm behaviour. For the above reaction Anm might be sensitive to the strange quark polarizations even in this low energy region, but at kinematics with high momentum transfer. According to the di–quark hypothesis and for the strange sea negatively polarized the both protons should be positively polarized in order to form $K^+ = U\bar{S}$. That means the large positive value expected for Anm. Note that for K^0 production Anm should be small because of small polarization of the D quark in the proton ($K^0 = D\bar{S}$).

Pion production. The detailed investigations of the single and double spin asymmetries for pion production have been performed in TRIUMF [14] at the energies below 0.6 GeV. The results have been compared to the theoretical model treating NN elastic and inelastic scattering in a unified way [15].

In the energy range of COSY (up to 2.5GeV) single pion production is well–known to be mostly a two step process

$$N + N \rightarrow \Delta(1232) + N \qquad \Delta(1232) \text{–>} N + \pi \tag{4}$$

Single pion production dominates up to 1GeV.At 2.5Gev the ratio of the single to double pion production is around 3/4. One pion exchange model (OPE) is in a satisfactory agreement with the cross section data at the energies about 1–2 GeV. However OPE is hardly adequate for hard collision region when Δ produced in CM frame with high Ptr (Ptr = 0.9 GeV/c) at the angles around 90 deg. In this regime an attemt can be done to predict Anm for different charge substates of Δ

$$\Delta^{++} = UUU,\ \Delta^{+} = UUD,\ \Delta^{0} = UDD,\ \Delta^{-} = DDD \tag{5}$$

proceeding from the certain polarizations of the valence quarks of the colliding protons.

It is very interesting to try to measure polarization of the produced Δ. The spin density matrix of the Δ is better experimentally reconstracted for the target

longitudinaly polarized and Δ ejected in forward direction. Density matrix is diagonlized in this case and polarization state is fixed with three parameters. One of the parameters can be defined as tensor polarization

$$\text{with} \qquad \begin{matrix} t=n(+3/2)+n(-3/2)-n(+1/2)-n(-1/2) \\ n(+3/2)+n(-3/2)+n(+1/2)+n(-1/2). \end{matrix} \qquad (6)$$

Here n(+–1/2),n(+–3/2) are the relative populations of the Δ magnetic substates. Tensor polarization t can be found by measuring the angular distribution of the nucleons or pions coming from the Δ decay in the Δ rest frame. It is given by a simple expression

$$1 - t \cdot \left[\frac{3}{2} \cos^2\Theta - \frac{1}{2} \right], \qquad (7)$$

here Θ is the angle of the detected particle(nucleon or pion) with respect to the Δ momentum (rest frame). Measurement of the vector polarization is more difficult second scattering experiment in which polarization of the nucleon emitted from the Δ is measured.

1. Study of the deuteron short range dynamics.

The polarization observables in the deuteron breakup have been proposed to study exclusively at COSY [16] in a special geometry when the slow proton emitted backward *at 180°*. is detected in coincedence with the fast proton scattered within the forward peak (approved experiment). Intermediate Δ exitation mechanism and possible other aspects of the deutron dynamics will be investigated at the favorable kinematic conditions.

Another option to try to reach high–momentum (short range) regime in the deuteron is investigation of elastic pD backward scattering. As like as for deuteron breakup in the frame of the One Nucleon Exchange mechanism (ONE) the spin observables depends on the S/D state ratio. Thus

$$Anm = \frac{3}{2} P_D \cdot P_P \cdot B(U/W) \qquad (8)$$

$$\text{where} \qquad B(U/W) = 1 - \frac{W(2W + U/\sqrt{2})}{U^2 + W^2}. \qquad (9)$$

Here U=U(q),W=W(q) are S and D states of the deutron, respectively, P_D is taget polarization, P_P is beam polarization,q is momentum of the backward scattered proton.

This simple mechanism fails to describe the cross section data at the proton beam energies around or higher 500 MeV. An addition of the OPE with intermediate $\Delta(1232)$ exitation has been proposed [17,18] in order to reproduce the behavior of the exitation function versus the primary energy.

The only hitherto investigated polarization parameter is t_{20} which has been measured at Saturne by J. Arvieux et al. [19] with help of the deuteron polarized beam in the energy range of 300–2300 MeV (150–1150 MeV for the proton beam). The behavior of t_{20} is proved to be in a rough agreement with the ONE model.

At COSY we would cover the energy range from 1 to 2.5GeV of the primary proton beam with the exitation function, t_{20}, and Anm measured for pd scattering at the angles around 180 deg. As like as for the deuteron break–up,one could expect some exotic contribution due for example to decomposition of the six–quark configuration [20]. A joint analysis of the deuteron break–up and elastic backward scattering data would be very helpful.

3. Contribution of D and S'states to the ground state of ^{3}He wave function.

To a rough approximation polarization of the ^{3}He nucleus is attributed to the single neutron whereas the pair of protons,being in the spin singlet state,do not contribute to the nuclear spin at all.In more realistic approach the ground state of the ^{3}He is not pure S–state wave function. There is a small admixture of D and S' states which results in nonzero polarization of the constituent protons. Experimental investigation of these effects is important for the few body theory and also by practical reasons because polarized ^{3}He is used as polarized 'neutron' target in particular in electron scattering experiments.

A simple way to estimate experimentally polarizations of the proton and neutron in ^{3}He is to study inclusive quasielastic polarized/unpolarized proton scattering on the polarized ^{3}He target at a given angle.The single and double spin asymmetries will be sensitive to the constituent nucleon polarizations.In Impulse Approximation (IA) these

internal polarizations can be directly deduced from the data provided the spin observables for free nucleon scattering are known at the energies under consideration. On the other hand due to absorption and rescattering effects the induced polarization arises disregarding the polarization of the parent nucleus [21,22]. In order to distinguish the induced and real constituent nucleon polarizations one has to compare effect of reversal of the target polarization with that for the beam.

The coincedence experiments p,pp and p,pn are more informative. They allow to pin down the missing momentum q which is in IA equal to the internal momentum of the knocked–out nucleon. At small q the D state contribution vanishes and the polarization observables are mostly sensitive to S' state. On the contrary,at q=200–300 MeV/c D state dominates.Thus by setting at different q–momenta one hopes to see these fine effects in the ^{3}He nucleus.

Conclusion

Double spin asymmetry Anm is the experimental observable very sensitive to reaction mechanism and, in certain cases, to internal structure of the investigated hadron/nuclear system. Several proposals for the experiments at COSY, such as K and π production in pure spin states and pD backward scattering, could be developed provided the technique of the internal gas target with a storage cell is built and installed at COSY polarized proton beam in TP–2 of the Zero Degree Facility.

References:

[1] S.I. Mishnev et al. "Polarized deuteron target in an electron storage ring", INP, Novosibirsk, 1990
[2] R.J. Holt et al. "Proceedings of the 8th Intern. Symp. on High Energy Spin Physics", Minneapolis, Ninesota, 1988, p. 1535
[3] K. Zapfe, talk in this seminar
[4] R. Gilman et al., Phys. Rev. Lett. 65, 1733 (1990)
[5] W.K. Pitts et al. "Test of gas storage cells in the cooler" proposal IUCF, 90–112
[6] F.W. Hersman et al. "Bates Large Acceptance Spectrometer Toroid" preprint BATES, 1990
[7] K. Rith et al. "The HERMES Collaboration" proposal DESY, 1990
[8] NIKHEF proposal
[9] W.T.H. van Oers "Proceedings of High Energy Spin Physics Conf." Bonn 1990, v. 1, p. 335

[10] T.A. DeGrand et al., Phys. Rev. D32, 2445 (1985)
[11] J. Ashman et al., Phys. Lett. B206 (1988) 364
[12] M.J. Alguard et al. Phys. Rev. Lett. 37 (1978) 1261
Phys. Rev. Lett. 41 (1978) 70
G. Baum et al., Phys. Rev. Lett. 51 (1981) 1135
[13] K. Rith "Proceed. of High Energy Spin Phys. Conf", Bonn 1990, v.1, p. 198
[14] C.E. Waltham et al., Nucl. Phys. A433 (1985) 649
[15] J. Dubbash, W.M. Kloet, R.R. Silbar, Nucl. Phys. A466 (1987) 573
[16] S.V. Dshemuchadze et al. "Exclusive deuteron break–up study with polarized protons and deuterons at COSY", proposal IKP, 1991
[17] Craigie and Wilkin, Nucl. Phys. B14 (1969) 477
[18] Kolybasov and Smorodinskaya, Phys. Rev. Lett. 37B (1971) 272
[19] J. Arvieux et al., Phys. Rev. Lett. 50, 19 (1983)
Nucl. Phys. A431, 613 (1984)
[20] A.P. Kobushkin "Proceed. of High Energy Spin Phys. Conf."
[21] G. Jacob, Th.A.J. Maris, C. Schneider, M.R. Teodoro, Nucl. Phys. A257 (1976) 517
[22] P. Kitching et al., Phys. Rev. Lett. 37 (1976) 1600

STUDY OF SHORT RANGE DEUTERON STRUCTURE AT COSY. THEORETICAL POINT OF VIEW

O. Grebenyuk
St.Petersburg Nuclear Physics Institute

January 29, 1993

Abstract

The well developed model of $p\vec{d} \to pp\pi$ exclusive reaction, which provides good description of recent unpolarized (TRIUMF[1], Gatchina[2]) and polarized (Saclay, [3]) experiments, is used to predict the cross sections, vector A_y and tensor A_{yy} analyzing powers under the kinematic conditions of COSY facility. Beyond Impulse Approximation, theoretical approach includes double scattering corrections and virtual pions emition graphs. Spin and isospin dependence of the input amplitudes is fully taken into account.

The results of calculations give the hope that the future experiment at COSY will be crucial test for clarifying of the reaction mechanism, which is necessary to deduce the deuteron short range structure in the experiments of such kind.

Introduction

The usual motivation for deuteron breakup experiments is the investigation of high momentum structure of deuteron. In terms of dnp vertex with one of the nucleon off-shell, which can be written as

$$D_\mu(t) = \gamma_\mu G_a(t) + \frac{1}{2}(p_v - p_s)_\mu G_b(t)\,, \qquad (1)$$

with $p_s^2 = m^2$ and $p_v^2 = m_v^2 = t$, the structure is hidden in the vertex functions $G_{a,b}(t)$. The S and D vertex functions F_S and F_D [4, 5] connect directly to non-relativistic wave functions u and w and are expressed through the functions $G_{a,b}(t)$ as

$$F_S(t) = G_a(t) + \frac{m^2 - t - 2\alpha^2}{6m} F_D(t)$$

$$F_D(t) = G_1(t) - \frac{G_c(t)}{2m}, \qquad (2)$$

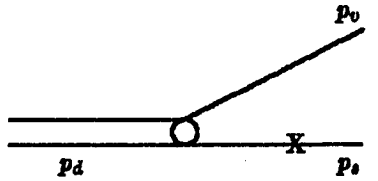

where $\alpha^2 = m(2m - m_d)$.

In the d rest frame $t = m_d^2 + m^2 - 2m_d\sqrt{m^2 + p_s^2}$ and the range of the spectator momenta $0.35 \leq p_s \leq 0.5$ GeV/c, proposed to be explored at COSY, corresponds to the range of the 'virtuality' $0.15 \leq \frac{m-m_n}{m} \leq 0.35$. From Fig.1 it is seen that the main features of *dnp* vertex at this range are rather well established. Both potentials, the Bonn [6]and Paris[7] ones (most prominent up to now), and the pole expansion fit, constrained mainly by elastic *ed* data [5], provide similar vertex functions with

> ***dominance of D wave vertex function F_D;***
> ***the node of S wave vertex function F_S, the position of which varies in rather narrow range.***

It seems like we are left with only problem to point out quantitative aspects of these features.

It is remarkable that the vertex functions, deduced from *ed* data, agree with calculated ones. For a long time there is an idea, based on peculiarity of impulse approximation (IA), to deduce the vertex functions also from the breakup reaction data. In IA, that is in the case of one nucleon exchange (ONE) graph dominance, one could deduce the vertex functions from the experimental data performing *algebraic* manipulations, provided the both polarization parameters and cross section are measured. Unfortunately along with the IA there are additional mechanisms, first of all the NN double scattering, and this competition is especially strong at the region of the interest. So we can rely only on sensitivity of the observables to *dnp* vertex. For this purpose we should choose the kinematics where IA graph affects still the observables. The proposed experiment at COSY [8] is just designed in such a way.

Collinear geometry

The kinematics in the proposed experiment is determined by protons moving one in backward (180°) and another in forward (0°) directions. The ellipses of acceptable proton momenta at different energies of projectile, provided the reaction is really $pd \to ppn$, are shown in Fig.2. In the case of proton momentum

being close to the boundary of ellipse the missing mass is equal to $m_n + m_p$, that is the second proton and the neutron compose the deuteron-like system. The maximal backward momentum increases very slowly with the energy (Fig.2) and even at the energy 2.5 GeV only $p(180°) \simeq 0.5$ GeV/c is achievable. Nevertheless there is some hope that choosing the coincidences of backward (180°) near the boundary and the forward (0°) protons reduce the contributions from the NN double scattering. Let us consider the case of maximal backward proton momentum. The pole graph with backward proton as spectator, which contribution we would like to observe in the experiment, is shown in the picture.

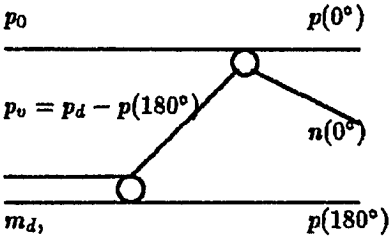

At first we have reduction of this contribution due to our intention to study the rather high $p(180°) \simeq 0.5$ GeV/c (dnp vertex does work). Besides that we have $(p(0°) + n(0°))^2 = 4m^2$, that is the considerably off-shell NN scattering occurs at the threshold. Evidently the $^1S_3$ threshold form factor related to the vertex function F_S provides additional suppressing.

The double scattering mechanism is represented by the graphs one of which is

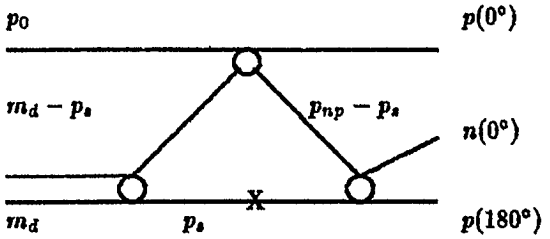

shown in the picture.

To calculate the amplitude corresponding to this graph we use, omitting for brevity spin and isospin indices, the following expression ([9], see also the next section)

$$M_{DS}(p(0°), n(0°), p(180°); p_0, m_d) = -i\, F(s_{np_s}, t)$$
$$M_{NN}(p(0°), p_{(+)}; p_0, m_d - p_{(-)}) M_{NN}(n(0°), p(180°); p_{(+)}, p_{(-)}) \,, \qquad (3)$$

where we have defined the momentum transfers $t \equiv (p_0 - p(0°))^2$ and the squared invariant mass of the np pair $s_{np_s} = p^2_{np_s}$, $p_{np_s} \equiv n(0°) + p(180°)$. The both momenta $p_{(\pm)}$ are on mass shell and $p_{(-)} + p_{(+)} = p_{np_s}$. In the d-rest frame they are equal to $\mathbf{p}_{(\pm)} = \mathbf{p}_{np_s}(\frac{1}{2} \pm \frac{E_{np_s}}{W_{np_s}} \frac{\sqrt{s_{np_s} - 4m^2}}{2p_{np_s}})$, where $W_{np_s} = \sqrt{s_{np_s}}$

(Fermi motion, see[10]). The complex factor $F(s,t)$, which may be thought at $S \simeq 4m^2$ as the transitive $d \to^1 S_3(NN)$ form factor [9], is represented in Fig.3 as functions of t for different kinetic energies of NN pair. These kinetic energies and corresponding momentum transfers for collinear geometry with maximal momentum of backward proton are shown in Fig.4 as function of projectile energy. We see that the both variables are small and correspond exactly to the large values of $F(s,t)$.

So one should not expect that this especially chosen geometry would provide the evident dominance of ONE mechanism. This conclusion is confirmed by full calculations with the model [9] shortly described in the following section.

Model

We [9] take the amplitude of the breakup reaction as the sum

$$M = M_{ONE} + M_{DS} + M_{\Delta} \,. \tag{4}$$

Amplitudes M_{ONE}, M_{DS} and M_{Δ} correspond to the graphs a, b and c shown in

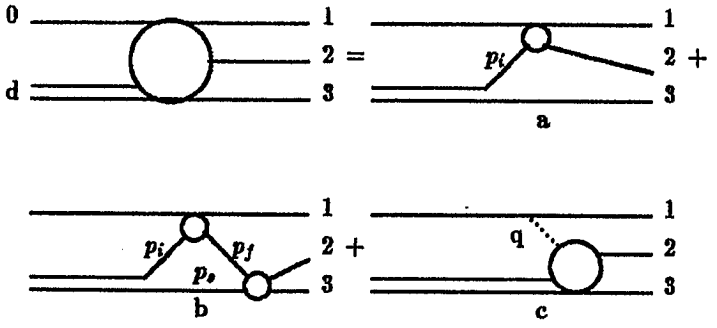

+(123→231)+(123→312)

the picture.

According to the Feynman rules we have

$$M_{ONE} = D_{dnp}\,\frac{i}{(p_i^2 - m^2)}\,M_{NN}\,, \tag{5}$$

$$M_{DS} = -i\int \frac{d\mathbf{p}_s}{(2\pi)^3 2E_s}\,\frac{D_{dnp}}{(p_i^2 - m^2)}\,M_{NN}\,\frac{1}{(p_f^2 - m^2 + i\varepsilon)}\,M_{NN}\,, \tag{6}$$

$$M_{\Delta} = \Gamma_{\pi NN}\,\frac{i}{(q^2 - \mu^2)}\,M_{\pi d \to NN}\,. \tag{7}$$

Here D_{dnp}, $\Gamma_{\pi NN}$, M_{NN} and $M_{\pi d \to NN}$ are the spin and isospin dependent amplitudes of the corresponding subprocesses. In the double scattering term

we have taken as usual the spectator on the mass shell. The definitions of the momenta are seen from the above picture.

The amplitudes M_{NN} and $M_{\pi d \to NN}$ are taken to satisfy the Pauli principle. Thus the term corresponding to the diagram *a* is antisymmetric with respect to the interchange of the first and the second nucleons and the diagrams *b* and *c* are with respect to the second and the third nucleons. To make the amplitude (4) fully antisymmetric the two more sets of the diagrams with cyclic permutated nucleons at the final state had been added to the pictured ones. These diagrams are denoted in the above picture as (123→231) and (123→312).

We have used the NN amplitudes obtained in the energy-dependent phase shift analysis (PSA) by Arndt et al. [11]. Following Everett [12] we have taken the NN amplitudes out of the loop integral (6), corresponding to the triangle diagram *b*, at some optimum Fermi momentum [10]. However in the case of the energy of the final nucleon's pair less than 400 MeV we used the form factor f for the corresponding half off shell NN amplitude $M^{off} = fM^{on}$, M^{on} being taken out of the loop integral. The threshold form factor related to the $^1S_3$-wave function of the deuteron was taken and integrated along with dnp vertex and two propagators [13, 14, 15]. The real part of the resulting integral (it is exactly $F(s,t)$ discussed in the above section) is connected with the allowing the intermediate nucleon with the momentum p_f to be off shell.

We have calculated the amplitude $M_{\pi d \to NN}$ taking into account the one-loop diagrams with the $N\Delta$ as intermediate state and the diagrams with the πN intermediate scattering in the S, P and D waves parametrized by their phase shifts. To avoid the double counting we have excluded however the one nucleon exchange diagram, which already contributes to ONE term in (4), and the P_{11}-wave (the nucleon pole in the πN amplitude is a part of the DS term). Finally, the ρ-exchange is taken into account in the $\pi d \to NN$ amplitude. The details are given in the appendix of the paper by Laget [16].

Calculations

The PSA of Arndt, which we use to calculate the NN amplitudes, is supported by the data up to the energy 1.6 GeV and besides that we have done the analytical continuation up to the 2.0 GeV by means of SAID program. Thus the reliable calculations are possible to perform now for projectile energies less than $\simeq$ 1.6 GeV and only with some caution for higher energies (we have risked up to 2.5 GeV).

In Fig.5 the predictions for tensor analyzing power A_{yy} at 1.4 GeV are presented. The solid thick line represents IA calculated with Bonn vertex. The dashed line represents the effects of inclusion of NN double scattering and the thin solid line - the full calculations including Δ excitation graphs. Three angles of forward proton, $\Theta_f = 1°,5°$ and $10°$ are tested. It is seen that the curves converge when backward proton momentum goes to its boundary and

the forward proton angle goes to zero. It might give some hope that alternative to IA mechanisms are suppressed at this regime. However one can compare in Fig.6 the results related to $\Theta_f = 1^\circ$ for Bonn and Paris vertices. If IA were valid one could discriminate them, but the corrections reduce this resolution making the final result practically insensitive to the choice of vertex. Fiq.7 displays the A_{yy} for Bonn vertex, $\Theta_f = 1^\circ$ and for two projectile energies, 1.8 and 2.5 GeV. We see here again the convergence of IA with full calculation curves. Note that NN rescattering alone does not behave so. Fig.8 reveals again, for the case of $\Theta_f = 1^\circ$ and 2.5 GeV, the insensitivity of full calculation results to the choice of vertex.

So we can conclude that apparently some convergence of full and IA calculations for A_{yy} at the maximal backward proton momenta is not caused by dominance of IA mechanism.

The above conclusion is confirmed by the predictions for the ratio of full and IA calculations of cross section. In Fig.9 these ratios are shown for $\Theta_f = 1^\circ$ and two projectile energies, 1.8 and 2.5 GeV. We see that the ratio, though decreasing when backward proton momentum goes to maximum, does not exceed the value $\simeq 5$. We see also the considerable contribution of Δ excitation mechanism. The same picture is seen in Fig.10 where the ratios with Bonn and Paris vertices at $\Theta_f = 1^\circ$ and the ratios with Bonn vertex at $\Theta_f = 1^\circ$ and 5° are compared at the projectile energy 1.4 GeV.

The predictions for vector analyzing power A_y at the 1.4 GeV are shown in Fig.11. For $\Theta_f = 1^\circ$ A_y is small and insensitive to the distinctions of vertices even in IA. The contribution of Δ is noticeable especially for larger (5°) forward proton angles.

Discussion

The main conclusion, which is possible to do *in the frame of used model*, is that even in the case of 'exotic' collinear geometry with backward proton close to kinematic boundary it would not be possible to deduce the F_S and F_D vertex functions from the data in *algebraic way*. Moreover the resolution of the cross section and polarization parameters A_y and A_{yy} with respect to the choice of vertex is small.

In spite of this skepticism we would like to stress that the used model is far from being perfect. Though we have successful description of unpolarized cross section [2] and partly of copious and precise polarization parameters measured at Saclay [3], we met still serious problems with the latter data at some kinematics. We suspect that the matter is the transitive $d \to {}^1S_3(NN)$ form factor of deuteron. It would be very useful to complete the polarization data obtained at Saclay with those at quite different kinematics of COSY.

Especially important feature manifested by these calculations is the considerable contribution of Δ excitation mechanism. This contribution is noticeable

in cross section as well as in polarization parameters which was not the case in Saclay experiment. If to believe that the NN double scattering and Δ excitation are the main competitive mechanisms to IA one, the COSY experiment would be crucial test for study of the latter mechanism.

And the last. May be it is worth to look for kinematics, using one or another model, in the vicinity of the proposed one with more preferable, with respect to IA, background.

References

[1] C. F. Perdrisat et al. *Phys. Lett.*, **156B**(1985), 38.

[2] N. P. Aleshin et al. *preprint of LNPI*, **1740**(1991).

[3] S.L.Belostotsky et al. *Phys.Lett*(1992).

[4] M.Gourdin et al. *Nuovo Cim.*, **37**(1965), 524.

[5] M.P.Locher A.Švarc. *Z.Phys.A*, **316**(1984), 55.

[6] R.Machleidt et al. *Phys.Pep.*, **149**(1987), 2.

[7] M.Lacombe et al. *Phys.Lett.*, **101B**(1981), 139.

[8] S.V.Dshemuchadze et al. *Proposal for Exclusive deuteron breakup study with polarized protons and deuterons at COSY*(1991).

[9] A.Boudard O.G.Grebenyuk J.M.Laget V.N.Nikulin. *paper in progress*(1992).

[10] G. Z. Obrant. *Sov. J. Nucl. Phys.*, **36**(1982), 504.

[11] R.Arndt et al. *SAID*, **SM89, 0-1.6 GeV**(1990).

[12] A.Everett. *Phys.Rev.*, **126**(1962), 831.

[13] V.M.Kolybasov V.G.Ksenzov. *Sov.J. Nucl.Phys.*, **22**(1976), 372.

[14] B.S.Aladashvili et al. *J.Phys.G:Nucl.Phys.*, **3**(1977), 7.

[15] J.M.Laget. *Nucl.Phys.*, **A296**(1978), 389.

[16] J.M.Laget. *Nucl.Phys.*, **A370**(1981), 491.

Figures captions

Fig.1. The vertex functions $F_{S,D}$ from Bonn [6] and Paris [7] potentials compared to those deduced from $ed \rightarrow ed$ data [5]. Thick solid lines: Bonn, dashed lines: Paris, thin solid lines: solution 1 of [5].

Fig.2. a) The ellipses of acceptable proton momenta at different energies of projectile, provided the reaction is really $pd \to ppn$
b) The maximal backward and forward momenta versus the projectile energy.

Fig.3. The transitive $d \to^1 S_3(NN)$ form factor of deuteron calculated with Bonn vertex as function of momentum transfer t at different squared invariant masses of final NN pair (the corresponding lab kinetic energies in GeV are pointed out).

Fig.4. a) The lab kinetic energy in the system of two particles, forward neutron $n(0°)$ and backward proton $p_{max}(180°)$, versus projectile energy.
b) The momentum transfer from the beam to the forward proton $p(0°)$, versus projectile energy.

Fig.5. The tensor analyzing power A_{yy} at the projectile energy 1.4 GeV for three forward proton angles $\Theta_f = 1°, 5°$ and $10°$ versus $q \equiv p(180°)$. Bonn vertex is used. Thick solid lines: IA, dashed lines: pole $+NN$ rescattering graphs, thin solid lines: full model, including Δ excitation graphs (pole $+NN+\Delta$).

Fig.6. The same as in Fig.5. Predictions with Bonn and Paris vertices for $\Theta_f = 1°$.

Fig.7. The tensor analyzing power A_{yy} at projectile energies 1.8 and 2.5 GeV for $\Theta_f = 1°$ versus $q \equiv p(180°)$. Bonn vertex is used. Thick solid lines: IA, dashed lines: pole$+NN$ rescattering graphs, thin solid lines: pole $+NN+\Delta$.

Fig.8. The same as in Fig.7 at projectile energy 2.5 GeV alone. Predictions with Bonn and Paris vertices.

Fig.9. The ratio of the corrected cross section to the cross section in IA at projectile energies 1.8 and 2.5 GeV for $\Theta_f = 1°$ versus $q \equiv p(180°)$. Dashed lines: pole$+NN$, thin solid lines: pole $+NN+\Delta$.

Fig.10. The same as in Fig.9 at projectile energy 1.4 GeV. a) $\Theta_f = 1°$. Predictions with Bonn and Paris vertices. b) $\Theta_f = 1°$ and $5°$ with Bonn vertex.

Fig.11. The vector analyzing power A_y at projectile energy 1.4 GeV for $\Theta_f = 1°$ versus $q = p(180°)$. Predictions with Bonn and Paris vertices. Thick solid lines: IA, dashed lines: pole $+NN$, thin solid lines: pole $+NN+\Delta$.

S,D vertex functions
Bonn, Paris, Locher

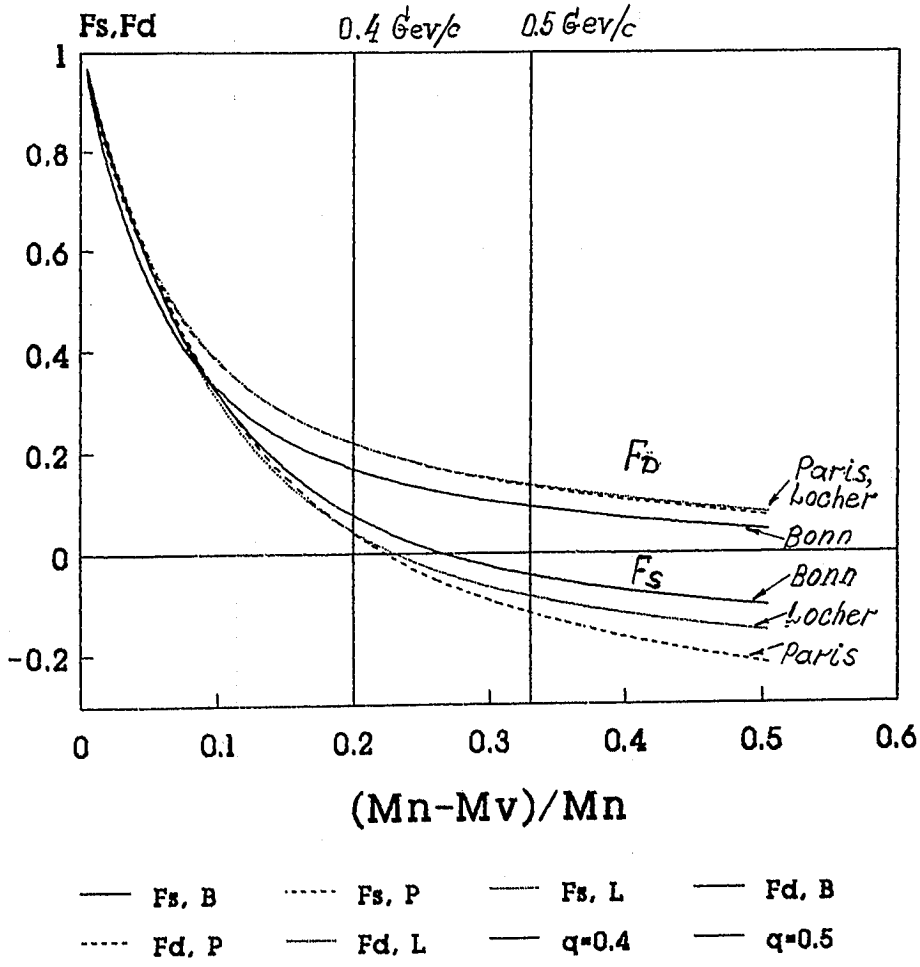

Fig.1

Proton ellipses

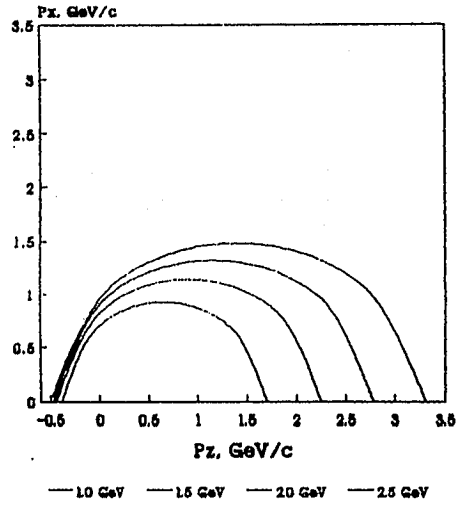

α

Max p(0), p(180)

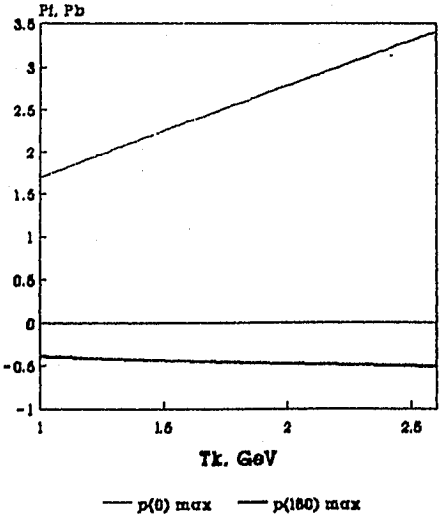

β

Fig.2

Im F(s,t)
Bonn

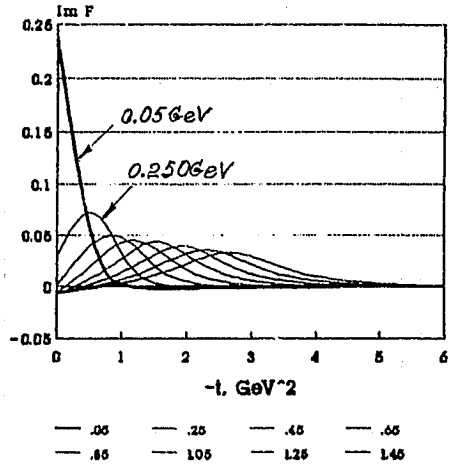

Re F(s,t)
Bonn

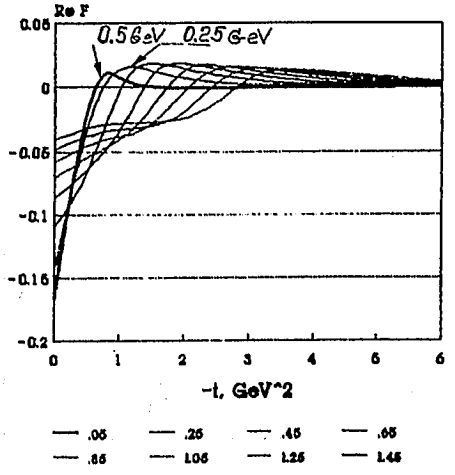

Fig.3

Tk(n pb)
Collinear geometry

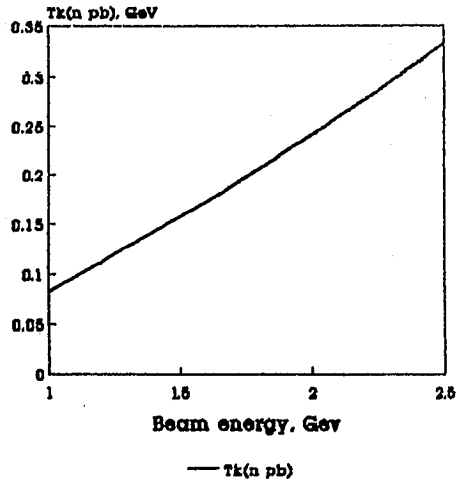

t(beam pf), GeV^2

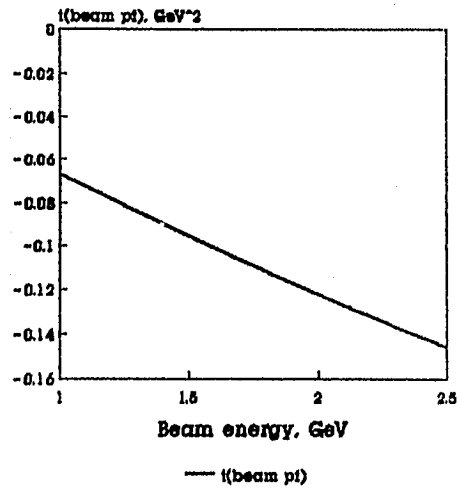

Fig.4

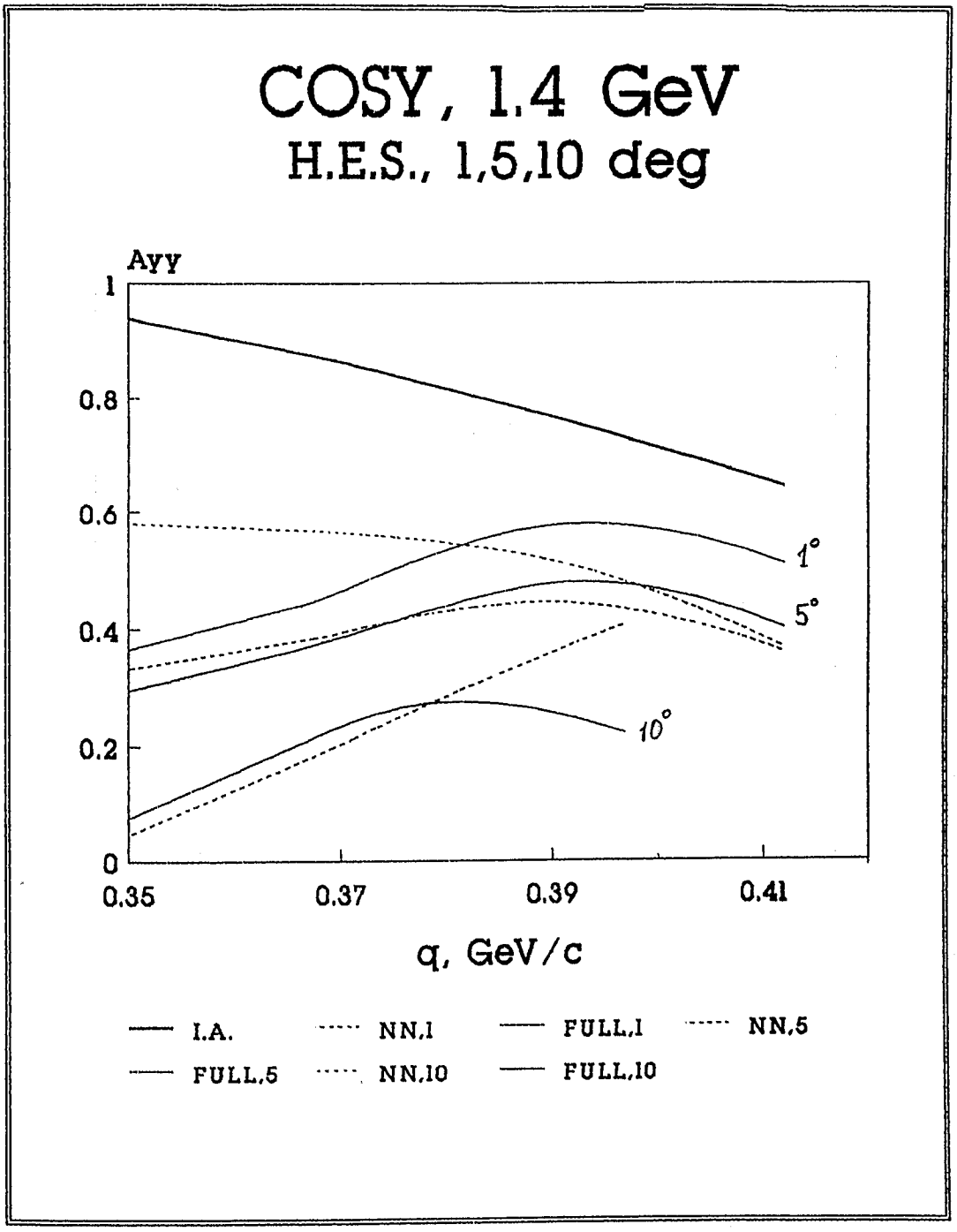
COSY, 1.4 GeV
H.E.S., 1,5,10 deg
Ayy
1
0.8
0.6
0.4
0.2
0
0.35
0.37
0.39
0.41
q, GeV/c
1°
5°
10°
I.A.
NN.1
FULL.1
NN.5
FULL.5
NN.10
FULL.10

Fig.5

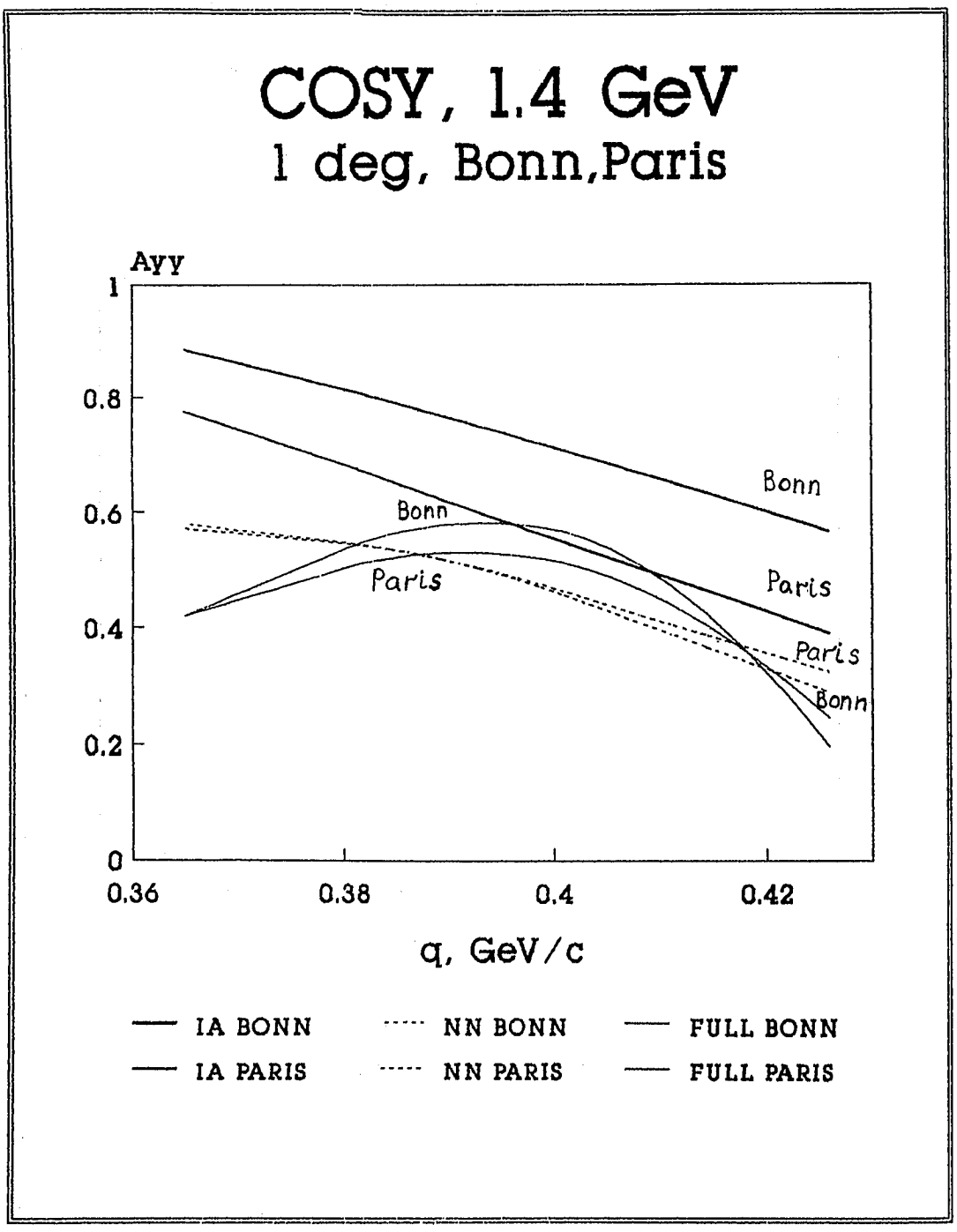
COSY, 1.4 GeV
1 deg, Bonn,Paris
Ayy
1
0.8
0.6
0.4
0.2
0
0.36
0.38
0.4
0.42
q, GeV/c
Bonn
Paris
Bonn
Paris
Paris
Bonn
IA BONN
NN BONN
FULL BONN
IA PARIS
NN PARIS
FULL PARIS

Fig.6

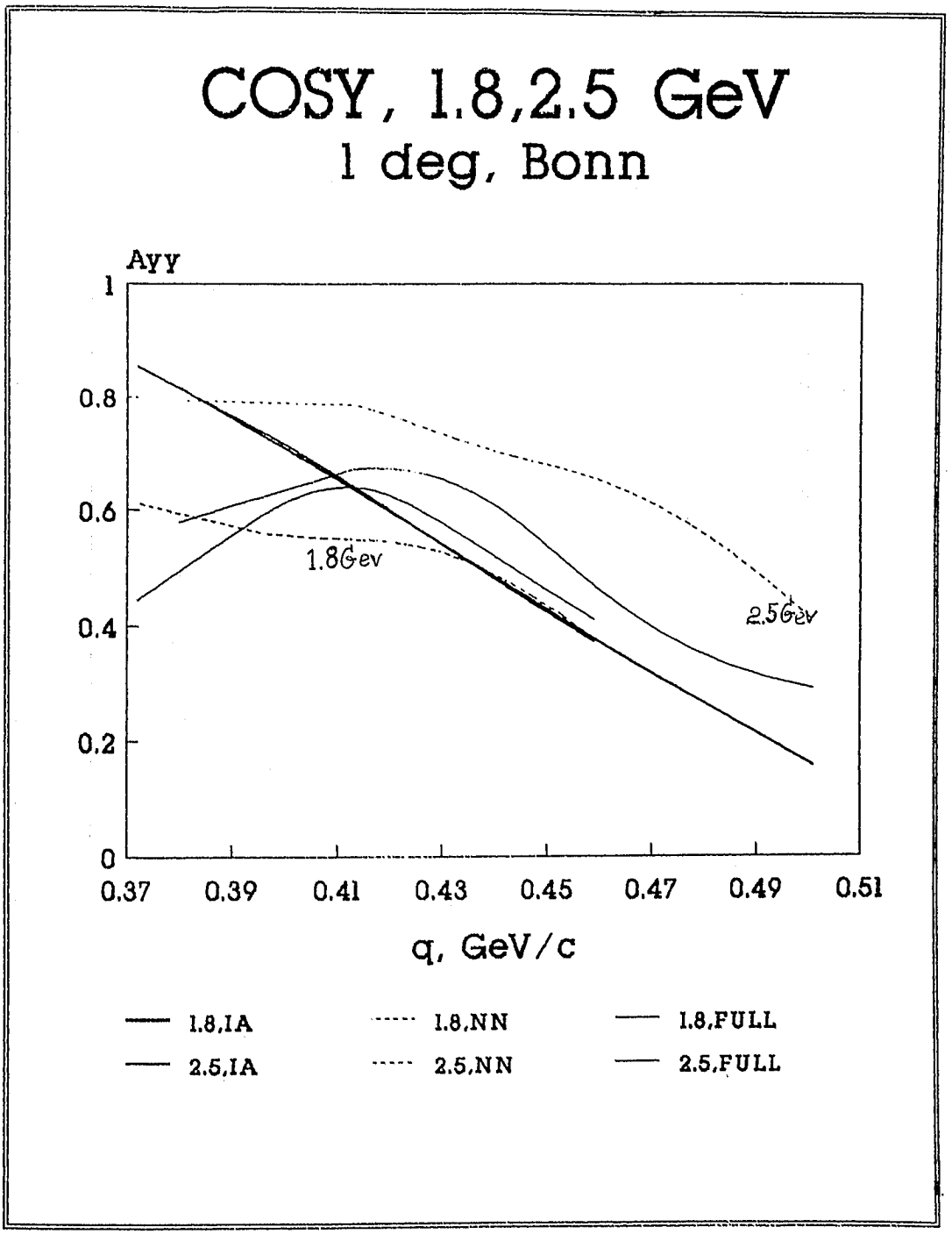
COSY, 1.8,2.5 GeV
1 deg, Bonn
Ayy
1
0.8
0.6
0.4
0.2
0
1.8Gev
2.5Gev
0.37
0.39
0.41
0.43
0.45
0.47
0.49
0.51
q, GeV/c
1.8,IA
1.8,NN
1.8,FULL
2.5,IA
2.5,NN
2.5,FULL

Fig.7

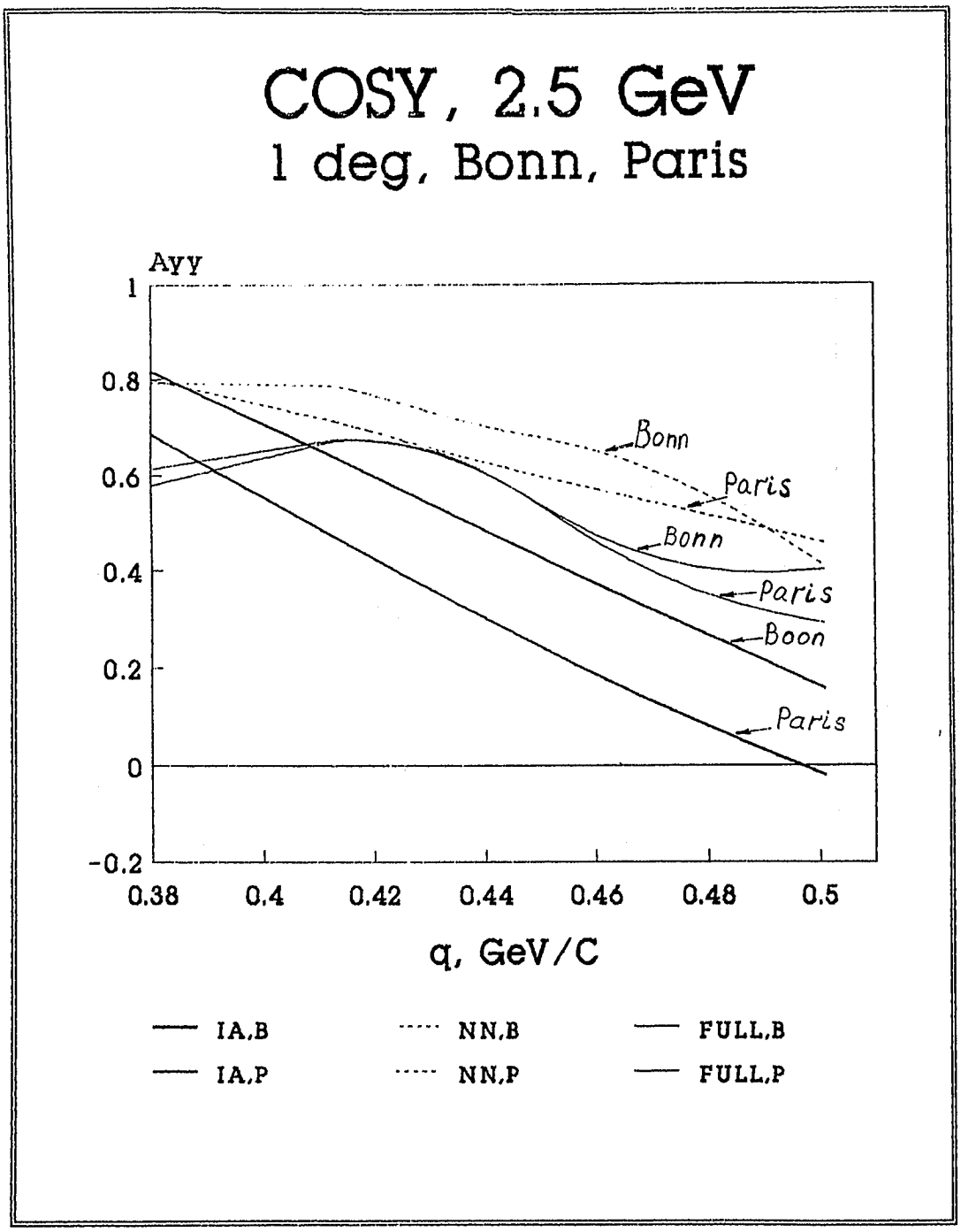
COSY, 2.5 GeV
1 deg, Bonn, Paris
Ayy
1
0.8
0.6
0.4
0.2
0
-0.2
0.38
0.4
0.42
0.44
0.46
0.48
0.5
q, GeV/C
Bonn
Paris
Bonn
Paris
Boon
Paris
IA,B
NN,B
FULL,B
IA,P
NN,P
FULL,P

Fig.8

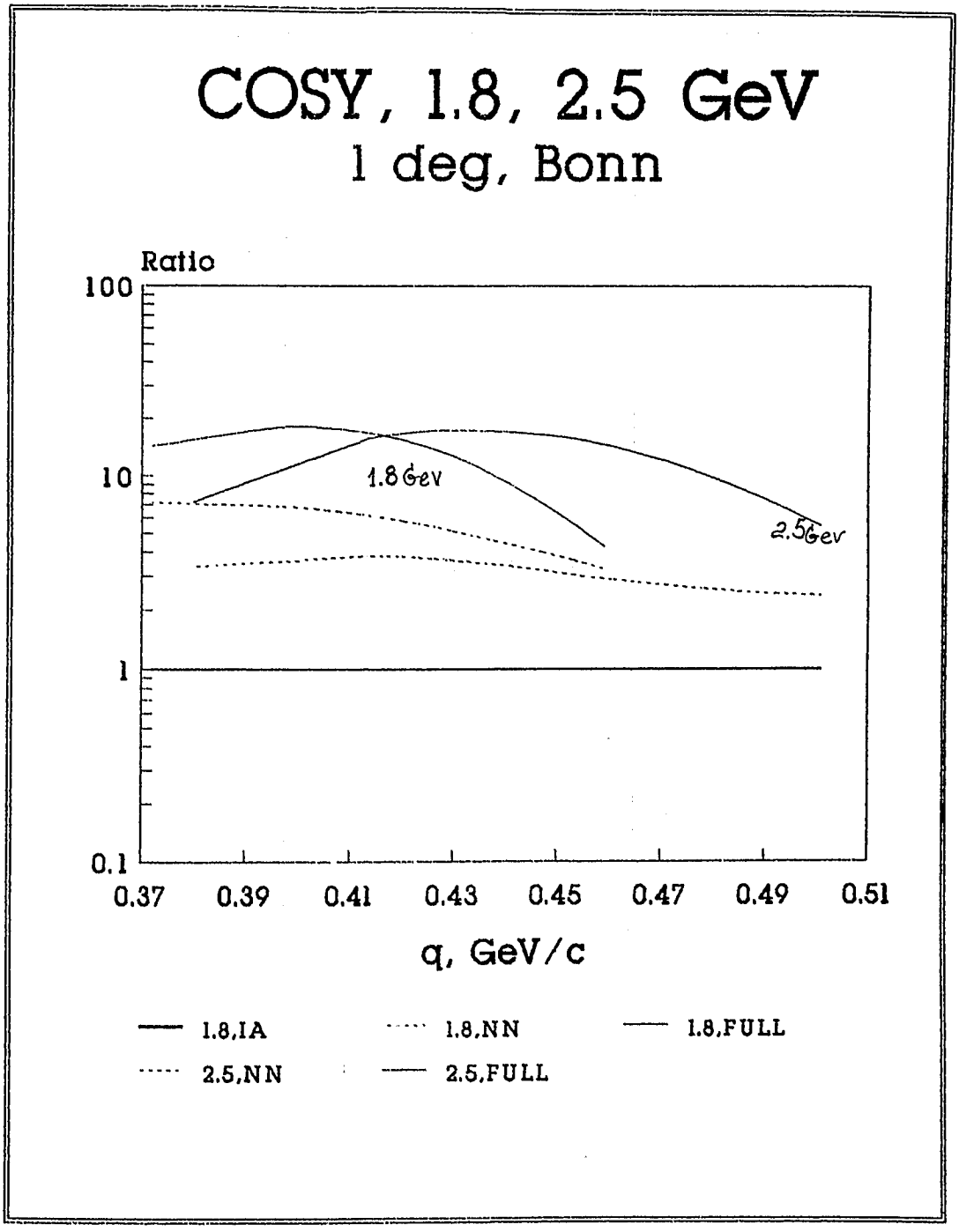
COSY, 1.8, 2.5 GeV
1 deg, Bonn
Ratio
100
10
1
0.1
1.8 Gev
2.5 Gev
0.37
0.39
0.41
0.43
0.45
0.47
0.49
0.51
q, GeV/c
1.8,IA
1.8,NN
1.8,FULL
2.5,NN
2.5,FULL

Fig.9

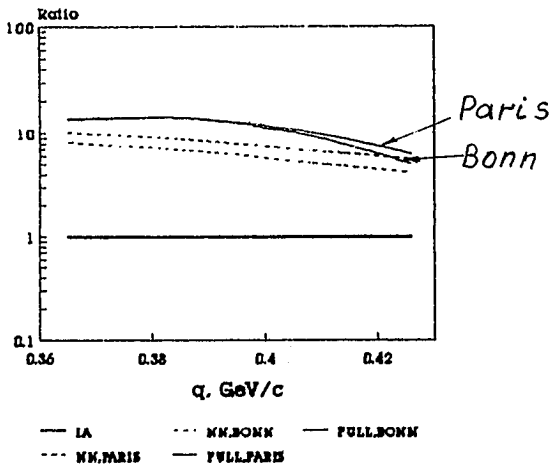
COSY, 1.4 GeV
1 deg, Bonn,Paris
Ratio
100
10
1
0.1
0.36
0.38
0.4
0.42
q, GeV/c
Paris
Bonn
IA
NN,BONN
FULL,BONN
NN,PARIS
FULL,PARIS

a

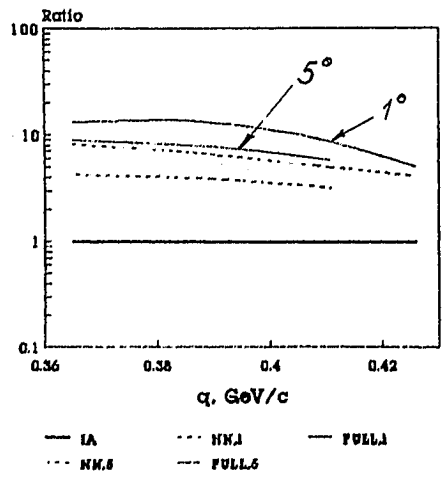
COSY, 1.4 GeV
1,5 deg, Bonn
Ratio
100
10
1
0.1
0.36
0.38
0.4
0.42
q, GeV/c
5°
1°
IA
NN,1
FULL1
NN,5
FULL,5

б

Fig.10

COSY, 1.4 GeV
1 deg, Bonn, Paris

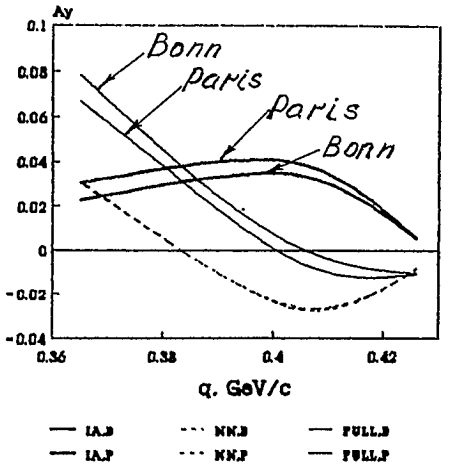

COSY, 1.4 GeV
1,5 deg, Bonn

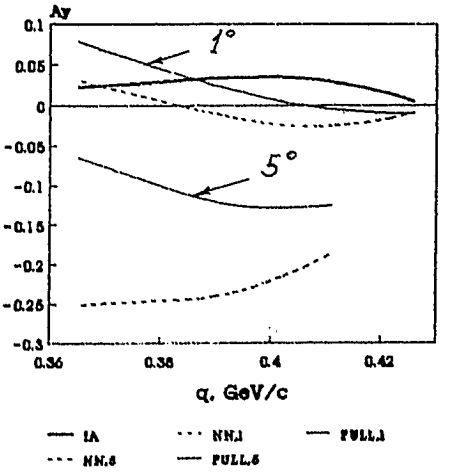

Fig.11

EXCLUSIVE DEUTERON BREAK-UP STUDY WITH POLARIZED PROTONS AND DEUTERONS AT COSY

V.I. Komarov
The Laboratory of Nuclear Problems, Joint Institute for Nuclear Research
Dubna, Moscow region, 141980, Russia

Proposal of the Dresden–Dubna–Gatchina–Juelich–Koeln–Muenster Collaboration for the deuteron break-up study using a polarized proton beam (1-2.5 GeV) and polarized deuterium target is discussed. Differential cross sections, vector and tensor analyzing power, spin-correlation asymmetry are expected to be measured. Taking advantage of a 0^0 Facility at COSY the measurements can be done exclusively in a " collinear geometry ": the protons emitted backwards close to the 180^0 angle will be registered in coincidence with the proton ejectiles near 0^0 angle. In such a geometry the deuteron S-state and D-state wave function can be investigated up to internal momentum of 0.5 GeV/c at the kinematic conditions with the spectator mechanism hopefully dominating. A set of the experimentally accessible data must be redundant for the analyses in the frame of impulse approximation. That should allow one to verify a contribution of more complicated mechanisms of the process and a role of several effects particulary caused by relativization of the wave function and by off-mass-shell behavior of the scattering amplitudes. It is attractive to check in the proposed experiments a boundary of the traditional description of the break-up process at high momentum-energy transfer to the deuteron.

1. Introduction

The aim of the talk is to discuss the reaction

$$p+d \rightarrow p+p+n \qquad (1)$$

of the deuteron disintegration by protons as a tool for investigation of the high-momentum structure of the deuteron and the possibility of studing this reaction at the 0^0 Facility[1] in COSY. The main ideas and points of the talk have been formulated in the COSY-proposal No 20 of the Dresden–Dubna–Gatchina–Juelich–Koeln–Muenster Collaboration[2].

2. Physical motivation

2.1 The process option

The processes between which one should choose with a view to the deuteron structure investigation are as a matter of fact the following:
elastic scattering of a projectile a by the deuteron

$$a+d \rightarrow a+d, \tag{2}$$

deuteron disintegration (or break-up)

$$a+d \rightarrow a+p+n, \tag{3}$$

deuteron fragmentation with a particle production

$$a+d \rightarrow a+X \tag{4}$$

with $X \equiv N+N+\pi$; $N+\Lambda+K$, etc.

The elastic scattering is to all appearance the most determined and accessible for theory interpretation process, the most selectable one of all other exclusive processes for experimental identification. However, it holds only with a bound state of the neutron-proton system and gives information essentially only on the ground state of the system. Meanwhile the ground state structure of the nucleus depending on only one kinematic variable is just a part of the complete structure, since structure functions (or response functions) of the nucleus are the functions of two substantial variables.

In that sense disintegration process (3) is preferable since it can be described at fixed energy at a two-dimensional plane, for example, the plane of four-momentum transfer squared $-q^2$ and invariant mass W of the produced proton-neutron pair. So it represents not only a spatial but also a time-dependent structure of the deuteron. On the other hand, measurement of the three-momenta of the two outgoing particles in coincidence and posessing a sufficiently high accuracy is available at the intermediate energies, providing a complete kinematic reconstruction of the events. In this connection, being richer in content, production process (4) is at a disadvantage since it hardly can be measured exclusively and so suffers in experiments from a lack of the full kinematic definiteness and even of uncertainty of the channels. Processes of the type $p + d \rightarrow He + \pi^0$ are complicated by presence of the additional nuclear system not less simple than the deuteron.

2.2 Main goals of the study

Three levels of study of the deuteron high-momentum structure in the process (1) can be roughly resolved:
The first level — the impulse approximation (IA) as a dominant mechanism of the process and the formfactors of the d→np vertex calculated in a standard way from the usual nonrelativistic deuteron wave function (DWF). The most commonly used one is the DWF (with S- and D-waves) obtained on the basis of the Reid soft-core[3], Paris[4] and Bonn[5]

potentials of the NN-interaction. That approximation is well justified for the internal momenta smaller than about 200 MeV/c. At such momenta the nucleons of the deuteron are presumably at large separation distances and the energy brought into the deuteron during the process is rather small to excite the nucleons. Nevertheless this nonrelativistic two-nucleon model combined with the single NN-scattering picture gives rather good description of the spin-averaged differential cross sections corresponding to significantly higher internal momenta up to 500 MeV/c or above. Relativization of the one-nucleon exchange approximation for the elastic backward pd-scattering and the deuteron fragmentation provides[6,7] an impressive mutual compatibility of the experimental data[7-9] and the Paris potential DWF at momenta up to about 500 MeV/c. Such facts encourage one to adopt the impulse approximation as a baseline for interpretation of the process (1) even at high momenta.

The best way to extract the DWF from experiments is to find such kinematic conditions that, at least in the frame of impulse approximation, one of the registered protons can be identified as a spectator one. Then the observed spectrum of the proton directly reflects the internal momentum distribution of nucleons in the deuteron. The most preferable in that sense is emission of the spectator proton at angles close to 180^0 in the deuteron rest frame. If one uses the 2.5 GeV proton beam, the backward proton momentum reaches the value of 0.504 GeV/c and so provides penetration into a rather high-momentum part of the DWF. At the same time the following problem inevitably arises: near this boundary the participant neutron is strongly removed from the mass-shell — its invariant mass is as small as 0.64 GeV. So the off-mass-shell behaviour of the np-scattering amplitude must be known.

It is interesting to rivet attention here on the fact that the off-mass-shell effect is the **only reason** for manifestation of a 0^0 angle scattering of the projectile proton on the neutron. For lack of a transverse momentum transfer the np-scattering manifests itself solely in leading out of the far off-mass-shell neutron to turn into the real state of the free neutron. So one can hope to study the off-mass-shell behaviour of the np-scattering by 0^0 angle proton scattering at the deuteron in accompaniment with the 180^0 proton ejectile. Of course, one must be sure that the spectator mechanism contribution is predominant indeed. The measurements under just this special geometry of 0^0 particle – 180^0 particle coincidences (and close to it) will be a subject of the following consideration here.

The same collinear geometry can be used, quite contrary, for our main topic — that is for the deuteron structure study, if the np-scattering amplitude can be derived with a necessary accuracy and reliability from other experiments and theoretical considerations. One can also use the fact that the collinear geometry gives for the break-up two kinematic branches:

$$p+d \to p(0^0,\text{fast}) + n(0^0,\text{slow}) + p(180^0) \qquad (5a)$$
$$p+d \to p(0^0,\text{slow}) + n(0^0,\text{fast}) + p(180^0), \qquad (5b)$$

differing from each other in quite a noticeably way. (For example, at $T_0 = 2.5$ GeV and $p(180^0) = 0.4$ GeV/c, one gets $p(0^0,\text{fast})$=2.9 GeV/c and $p(0^0,\text{slow})$=0.8 GeV/c.) Measurement of the cross-sections for the both branches should provide the same internal momentum distribution if the spectator mechanism holds and the np-amplitudes are taken right.

The most attractive feature of the DWF at internal momenta above 0.3 GeV/c is the expected node of the S-wave component near 0.4 GeV/c. The exact position of the node is sensitive to the S-state NN-potential used and reflects the short-range repulsion

in it. The last one is believed to be caused by the quark structure of nucleons directly, so several experiments of the last time are aimed to measure the S–wave node position. Since it is screened in the spin-averaged cross sections by the D–component contribution, only polarization experiments can help to solve the problem. The most direct way to do it consists in measurement of the tensor analyzing power A_{yy} for the break-up of the tensor-polarized (P_{yy}) deuterons by the unpolarized ($\bar{S}_p$=0) protons. As analysis in the impulse approximation shows (e.g. papers[10,11] and refs. therein), it depends only on the S– to D–state ratio χ=u/w:

$$A_{yy}(\chi) = \frac{1}{2}\frac{1-2\sqrt{2}\chi}{1+\chi^2} \quad , \tag{6}$$

and so can be measured in the collinear geometry too. For a vector-polarized (P_y) target and an unpolarized beam the cross section depends on the vector analyzing power:

$$A_y(\chi) = \frac{2}{3}P_{NN}B(\chi);\ B(\chi) = \frac{\chi^2-\chi\sqrt{2}-1}{1+\chi^2} \quad , \tag{7}$$

where P_{NN} is a free NN–scattering polarization parameter. Since the last one vanishes at zero angle, the measurement is possible only avoiding the strictly collinear geometry. Another additional and independent measurement of the function $B(\chi)$ can be realized using a combination of both beam and target polarization. Here even at zero angle the cross section depends on $B(\chi)$:

$$\sigma = \sigma_0(1 + \frac{3}{2}P_y B(\chi) S_{pi} C^{yi}), \tag{8}$$

with S_{pi} — the i-component of $\bar{S}_p$ and C^{yi} — the yi–component of a spin-correlation matrix for the NN–scattering. It shows that essential redundance of the DWF determination can be, in principle, achieved in the frame of impulse approximation. This point is extremely important since it permits checking the IA applicability and making the situation more definite when a contribution of some other mechanisms turns out to be substantial.

Meanwhile there is no doubt that such mechanisms beyond the impulse approximation are acting even in the case of the proton emission at strictly 180^0 angle. Indeed, the process (5) is converted into the backward pd elastic scattering at the maximum value of the backward proton momentum.

It means that close to this maximum value the relative momenta in the forward ejected np-pair are small and the final state interaction in it influences the cross section significantly. Moreover, the backward pd→dp scattering at energies 0.4–1.2 GeV was probably the first process investigated where dominance of the nucleon excitation in intermediate states of the hadron-nucleus scattering had revealed itself quite clearly and definitely (see refs[12–15] and the following papers). So the $\Delta(1232)$-isobar excitation during the process (5) at similar kinematic conditions is rather obvious. Therefore, the process (5) analysis, more profound than simple IA, turns out to be inevitable.

The second level — a set of several dominating mechanisms (Feynman graphs) taking into account relativization of the DWF and off-mass-shell behaviour of the elementary amplitudes.

An example of such approach is calculations performed by L.Dakhno and V.Nikonov for the proposal[2]. They used the same set of the graphs (spectator and participant contributions of the impulse approximation, elastic and inelastic screening, final state interaction) and the same technique as in ref.[16]. The result for the collinear geometry at 2.5 GeV energy demonstrates a rather high sensitivity of the A_{yy} value to the S-wave node position (K_n): e.g. for p(180^0)=0.45 GeV/c A_{yy}=0.22 at K_n=0.41 GeV/c and A_{yy}=0.54 at K_n=0.45 GeV/c.

The graphs of single and double scattering, final state interaction graphs were taken into account in the calculations[2] of O.Grebenyuk for the conditions: backward angle $\Theta_2=180^0$ and forward angle $\Theta_1=0^0,10^0,20^0$ (coplanar geometry). The calculations were performed only up to 1.8 GeV energy since there are no data on the NN–scattering phases at the higher energies. It was shown that vector analyzing power A_y is expected at values about 0.2 for $p(180^0)=0.35$ GeV/c and $\Theta_1=10^0$. As regards the components of the C_{nn}–matrix determining the spin-correlation asymmetry their values were found to be rather small at 0^0 angle, but increasing to values of 0.1–0.25 for 1.7 GeV and 10^0–20^0 c.m. angle of NN–scattering. Their tendency to increase with the energy permits one to expect a rather high sensitivity of the cross sections to the proton spin — deuteron spin orientation.

The calculations referred to were only tentative and far from systematic and consistent analysis. In particular, the study was essentially restricted by the elastic NN–interaction: for the first case the inelastic processes were taken into account only for the fast projectile during its double scattering and for the second case they were not included into consideration at all. However the role of the virtual pion exchange and rescattering for the inclusive deuteron fragmentation by protons was shown earlier in refs[17]. Behavior of the cross sections and especially the polarization observables — tensor polarization power and polarization transfer — is substantially determined by the virtual pion absorption accompanying the nucleon exchange at intermediate momenta (0.2–0.4 GeV/c) of the backward protons. Pion and nucleon rescattering on the intradeuteron nucleons gives large contribution at 0.3–0.5 GeV/c momenta. Recently calculations taking into account all these mechanisms have been also performed[18] for the exclusive process (1) in the collinear geometry and at 2.5 GeV energy. The calculation was performed using the light cone variables and the relativistic diagram technique. Description of the study was presented at the seminar[19]. At last, detailed calculations for the process (1) in collinear geometry including $\Delta(1232)$-excitation effects has been performed recently by O.Grebenyuk[20]. The important role of the final state interaction and Δ-excitation is emphasized here. A strong influence of the DWF relativization on the cross sections and the polarization observables is stressed in ref[18]. This influence is quite of the same order of magnitude as the expected influence of the six-quark contamination in the DWF. So the theory expectations demonstrate again the difficulties arising when one tries to penetrate into the high-momentum structure of the deuteron. With increasing of the intradeuteron momentum some problems become more and more important and more difficult to overcome whatever kinematic of the process we choose:

— unknown off-mass-shell behavior of the elementary amplitudes (NN, πN, ΔN, etc.);

— unresolved problem of the bound system relativization;

— large and rather indefinite number of the virtual particles (N, π, Δ, N^*, etc.) which must be taken into account;

— ambiguity of choice of the graphs which must be considered, including their interference;

— mutual distortion of the structure of the free particles at short distances between them and transformation of the systems of the separated hadrons to the common quark systems with shortening of the distances.

This trend is well seen in the development of interpretation of the backward elastic pd-scattering at intermediate energies. The main contribution to the cross-section at 0.5–1.5 GeV is made here by double scattering with $\Delta(1232)$ excitation, one-nucleon exchange and

small contribution of single scattering[21,22]. Nevertheless in spite of many efforts an ever-growing number of factors is being drawn for description of new experimental data: three-baryon resonances[23], $\Delta(1950)$-excitation[24], $N^*(1/2^+)$ and $N^*(1/2^-)$-isobar exchange[25].

So we faced the question — are these problems only of a technical character and they will be solved anyway in the course of time by increasing and complication of the calculations or are they of a fundamental kind and cannot be resolved by the numerous improvements? It is rather obvious that the traditional way of the deuteron structure description loses its sense at a sufficiently high value of the internal momenta and one will be forced to come to the next level of the deuteron description. The question is: **what values of the momentum- and energy-transfers is such change inevitable at?**

The third level — description of the deuteron in terms adopted for description of the elementary hadrons (structure functions, diffractive dissociation, etc.). This approach turns out to be widely useful in the high-energy studies (for example, deep inelastic scattering of leptons on nuclei[26]).

However the boundary energy at which the nuclei acquire hadron-like behaviour is rather uncertain. In the fragmentation processes characteristics of the fragmenting subject depend strongly on the energy transferred to it and not on the projectile energy. So one can expect very similar behavior of the nucleus fragmentation at extremely high and rather low (about 1 GeV) initial energy. Just this kind of the energy dependence is observed for the phenomena of the particle emission from nuclei in the kinematic region forbidden for a free projectile–nucleon interaction. This phenomena known as cumulative production (A.M.Baldin) or deep-inelastic nuclear reactions (G.A.Leksin) reveals very weak dependence of the cumulative particle spectra on the initial energy. This fact was interpreted in refs.[27–29] as evidence for interaction of projectile with few-nucleon systems (clusters) in nuclei at high transfer of energy:

$$E_{ex}=M^{inv}_{fin.st.}-M^{inv}_{init.st.} > 0.2 \text{ GeV} \tag{9a}$$

and momentum

$$\Delta p=|\vec{p}_0 - \vec{p}| > 0.3 \text{ GeV/c}. \tag{9b}$$

The corresponding matrix element was taken in a simple form

$$< \vec{p}_1,...\vec{p}_n|A|\vec{p}_0 >^2 \sim exp(-E_{ex}/\bar{E}_{ex}) * \exp(-(p_T/\bar{p}_T)^2) , \tag{10}$$

where $\vec{p}_0$ and $\vec{p}_1,...\vec{p}_n$ are momenta of the initial – and final-state particles respectively, p_T is transverse momentum transfer and $\bar{E}_{ex}$, $\bar{p}_T$ are parameters independent of the initial energy. The following decay of the excited and knocked few-nucleon group was assumed to occur in accordance with the random occupation of the available phase space.

This concept was developed later by H.Mueller[30] in the modified phase space model, and its ability to describe a wide range of the cumulative processes was demonstrated. In the ref[31] the model was successfully employed to reproduce the experimental data on the inclusive proton spectra for pd, dd and dC interaction at 9 GeV/c[32–34] and exclusive data for pd break-up at 1 GeV[35]. It was shown that in kinematic conditions far from quasielastic scattering a significant contribution of the deuteron interaction as a single entity should be expected.

This approach means, in fact, separation of two different kinds of the projectile–nucleus interaction: first, quasifree interactions of the projectile with the target nucleons and, secondly, all other, more complicated processes as elastic and inelastic rescattering and so on. Instead of attempts to describe these last ones by some sets of the hadron–had-

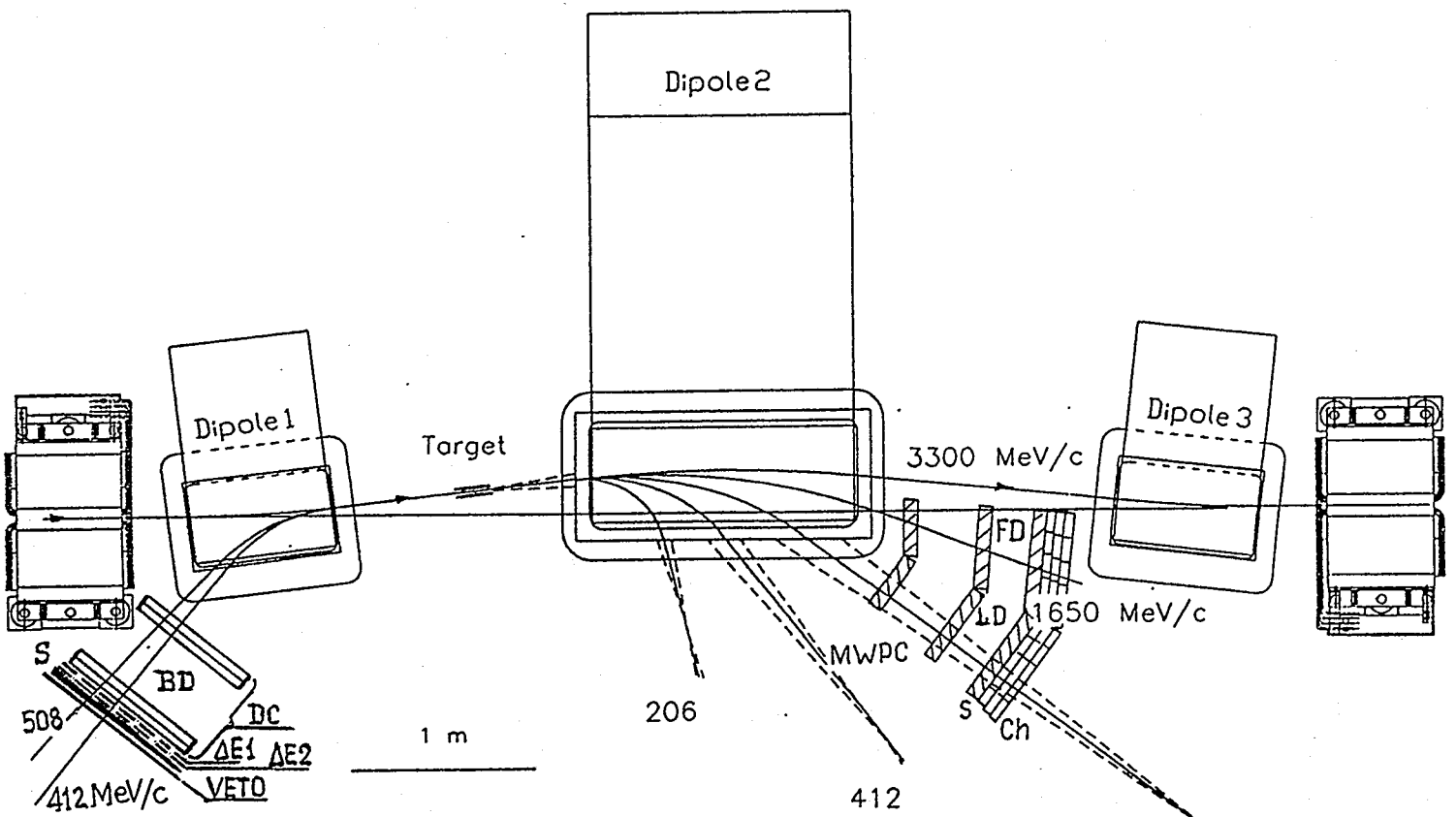

Fig.1. Scheme of the experimental arrangement. **FD, LD, BD — forward, lateral, and backward detectors respectively; DC — drift chambers, MWPC — proportional chambers; S — scintillation (Ch — cherenkov) counter hodoscopes.**

ron interactions the conversion of translational energy into internal excitation energy of cluster is considered in a phenomenological way. Decay of the excited cluster proceeds as recombination of the available quarks into baryons and mesons according to the quark statistics rules. In this connection there is no basic difference between the process of cluster excitation and inelastic diffraction of the usual hadrons. The $\bar{p}_T$-parameter, determining the transverse coherence length ($l_T \simeq \bar{p}_T^{-1}$) was found in ref[29] by fitting the experimental data as about 0.4 GeV/c. That means the transverse size of the nucleon pair participating the excitation process ($l_T \simeq 0.5$ fm) is close to the nucleon size. So the width of the peak in angular dependence of the cross section around zero degree should be close to the same for the nucleon inelastic diffraction. The longitudinal coherence length l_L occurs to be rather small in the projectile energy range of interest. Indeed, for the process (5), e.g. at 2.5 GeV and p(180^0)=0.5 GeV/c, the excitation energy amounts to E_{ex}=1 GeV and Δp=1.4 GeV/c, resulting in the value $l_L \simeq 0.14$ fm. It is too small for the diffractive dissociation of the normal hadron since in the case the coherence length must exceed the hadron dimension. So only a certain peculiarity of the few–nucleon system, for example, presence of the pure nucleon decay channel

$$[\mathrm{kN}]^* \rightarrow N_1 + N_2 + ... + N_k \ , \qquad (11)$$

being absent in the hadron case, can ensure its inelastic diffraction at such low initial energies. The diffractive dissociation of the deuteron is attractive since its analysis should be essentially simpler as compared with the deuteron dissociation by photons[36]. (The reason for that is a simpler isotopic structure of the pomeron responsible for the diffractive processes.) This situation can find an excuse only in absence of exclusive experimental data on the deuteron break-up near the collinear geometry. Even to evaluate the counting rate expected in the experiments one can use only estimations based on some kind of models. In particular, we used in the proposal[2] the earlier mentioned Dakhno–Nikonov's calculations and ones of the modified phase space model of H.Mueller, which produced rather similar results.

One can conclude that even spin-averaged exclusive differential cross sections in the proposed conditions are of noticeable interest. Measurement of the reaction (1) cross sections in the form $\mathrm{d}^2\sigma/\mathrm{d}M^2_{inv}\mathrm{d}t$, commonly used for description of the hadron diffractive dissociation, seems to be attractive for search for the hadron-like behavior of the deuteron.

To summarize this third-level consideration one should keep in mind that wide range of the experimental data on cumulative particle production clearly demonstrates quite specific features of the few-nucleon systems at high level of the momentum-energy transfer. Theoretical interpretation of this transition region between nucleon systems and quark systems is still very uncertain. So, to obtain systematic and exact experimental data, including especially informative polarization data[37], on the behavior of the most simple nucleus, accepting momentum transfer higher than $\sim$ 0.5 GeV/c and energy transfer up to 1 GeV, is an important goal of the contemporary nuclear study.

3. Experimental arrangement

The proposed experiments[2,38] are based upon the 0^0 Facility arrangement (Fig.1). They employ several essential merits of the facility:
— internal beam of the COSY, providing a luminosity $1.5 * 10^{31}$ cm^{-2}*s^{-1} sufficient for

the measurements even at small target thickness;
— TP2 target position at the COSY ring — the best one with respect to the luminosity and resolution;
— a storage cell for the polarized deuterium atomic beam, allowing about 10^{14} atoms per cm^2 target thickness;
— a special magnetic system of the dipole triplet making use of the first and the second dipoles as spectrometric ones;
— the polarized proton beam at the polarized deuterium target without any contamination of alien atoms in the working volume;
— particle detector systems and data acquisition system partly common for other experiments at the 0^0 Facility, thereby decreasing a cost of the experiments.

Some factors restrict application of the proposed arrangement:
— rather limited upper boundary of the luminosity range, hindering an access to the double scattering measurements;
— relatively small range of the available scattering angles near 0^0 and 180^0 values, impeding, in particular, high precision measurements of the vector analyzing power;
— rigidly restricted interspace between the second and the third dipoles where the forward detector system should be assembled, thereby limiting the upper boundary of the acceptable momentum range; also, time-of-flight measurements inside that base are practically impossible;
— close vicinity of the forward detectors to the primary beam, making strict requirements for the beam accompaniment after the D_2 dipole and for the forward detector ability to reject the background particles.

The main performance characteristics expected for the setup are summed in Table 1.

Table 1.

Basic parameters of the experimental setup.

Internal beam	
number of protons in the ring	10^{11}
beam width — horizontal	2.6 mm
vertical	4.5 mm
Deuteron target	
length in the beam direction	20 cm
diameter	2 cm
thickness (atoms per cm^2)	10^{14} cm^{-2}
Forward spectrometer (for T_0=2.5 GeV)	
momentum acceptance — total	from 1 GeV/c to 3.2 GeV/c
for $\Theta_1 = 0^0$	from 1.35 GeV/c to 2.35 GeV/c
angular acceptance in the vertical plane	from -2.3^0 to $+2.3^0$
angular acceptance in the horizontal plane	
– total	from -9^0 to $+9^0$
– for p_1=3.20 GeV/c	from $+2^0$ to $+8.6^0$
– for 2.35 GeV/c	from 0^0 to 6.5^0

– for 1.90 GeV/c ..... from -1.8^0 to $+4.6^0$
– for 1.35 GeV/c ..... from -6^0 to 0^0

Solid angle acceptance (for p_1=2.35 GeV/c) ..... 9 msr
momentum resolution σ(p)/p for $\Theta_1 = 0^0, p_1$=1.5 GeV/c 0.4%
p_1 =3.0 GeV/c 0.7%
momentum resolution σ(p)/p for $\Theta_1 = 6^0, p_1$ =1.5 GeV/c 3.5%
p_1=3.0 GeV/c 5.5%
angular resolution $\sigma(\Theta_1)$ for $\Theta_1 = 0^0$ ..... 0.1^0
for $\Theta_1 = 6^0$ ..... 0.8^0

Backward detector (for T_0=2.5 GeV)
momentum acceptance ..... from 0.25 GeV/c to 0.55 GeV/c
angular acceptance in vertical plane ..... from -1.9^0 to $+1.9^0$
angular acceptance in horizontal plane ..... Θ_2 from 174^0 to 180^0 and -174^0
solid angle acceptance ..... 10 msr
momentum resolution σ(p)/p for $\Theta_2 = 180^0$ 0.5%
for $\Theta_2 = 176^0$ 2%
angular resolution $\sigma(\Theta_2)$ for $\Theta_2 = 180^0$ ..... 0.2^0
for $\Theta_2 = 176^0$ ..... 1^0

A range of the ejectile angles acceptable in the forward spectrometer is governed mainly by the target-magnet dimensions and arrangement since the forward detector captures almost all the particle trajectories going out through the exit window of the D_2 magnet. That range is equal to about 6^0 in the horizontal plane and is shifted from the positive to the negative values of the angle when momentum of the forward particle decreases. Important point is that the both kinematic branches (5a) and (5b) come into the spectrometer acceptance.

A range of the acceptable backward ejectile angles is determined essentially by dimensions of the target storage-cell tube since even thin 0.5 mm aluminum walls of the tube scatter hardly the relatively slow backward protons.

The backward detector arrangement will consist of multiwire drift chambers and scintillation counter hodoscopes, providing momentum-angle determination and identification of the protons by measurement of the ionizing power.

The forward detector set will include multiwire proportional chambers, scintillation and Cherenkov counter hodoscopes. It permits momentum-angle determination and rejection of the background caused by electrons, pions and helium nuclei. Coincidence of the signals produced by the forward and backward detectors will be used for the first trigger formation. Time delay measurement between the signals of the detectors gives an additional factor for the off-line background suppression. The expected accuracy of the momentum determination for both ejectile protons is sufficient to separate the neutron in the missing-mass spectrum as follows from the Monte-Carlo simulation. The coincidence counting rate of about 0.4 s^{-1} is expected for a backward-proton momentum bin Δp_2=20 MeV/c at p_2=0.3 GeV/c and about 0.02 s^{-1} at p_2=0.5 GeV/c. That provides an accuracy of 2%-6% for the A_{yy} measurement in the same momentum bin and 0.3-0.5 GeV/c range during a ten-day run. A similar statistical accuracy can be obtained in determination of the vector polarization power and the spin-correlation asymmetry. At these measurements nonzero forward angles should be chosen, but the differential cross section of the

process is expected to decrease slowly with angular increasing near 0^0 angle: the modified phase-space model calculations[39] predict at 2.5 GeV energy a forward peak of $\sim 12^0(15^0)$ PWHM when the backward protons have a momentum 0.3(0.4) GeV/c.

The forward momentum-angle acceptance presented in Table 1 is related to the detector placed between the D_2 and D_3 dipoles. Using the additional detector (LD) at the lateral side of the D_2 magnet extends substantially the spectrometer acceptance. In particular, recording of the protons emitted at angles up to 20^0 becomes possible.

Acknowledgments

It is pleasure to thank all the participants of the COSY20 – Collaboration for common work on preparing and development of the project. I am particularly grateful to O.Schult, K.Sistemich and H.Mueller in discussions with whom the program statement has arised. I am greatly indebted to L.Belostotsky and O.Grebenyuk for development of the polarization aspect of the program. Very helpful discussions with M.Huber, M.Rekalo, B.Schoch and Y.Terrien are also gratefully acknowledged.

References

1. W.Borgs et al., Concept of the 0^0 Facility at TP2 in COSY, Ann.Rep.1991 of the IKP, KFA Juelich (1992) p.21.

2. S.V.Dshemuchadze, S.Dienel, K.W.Leege, H.Mueller, Chr.Schneidereit (IKHP FZR, Dresden); M.A.Ivanov, V.I.Komarov, G.I.Lykasov, V.S.Kurbatov, V.Z.Serdyuk, V.G.Shelkov, B.Zh.Zalikhanov, N.I.Zhuravlev, (JINR, Dubna); S.L. Belostotsky, L.G. Dakhno, O.G. Grebenyuk, V.A.Nikonov (SPINP, Gatchina); W.Borgs, M.Buescher, D.Grzonka, H.R.Koch, H.Ohm, O.W.B.Schult, H.Seyfarth, K.Sistemich (IKP, KFA Juelich); H.Dombrowski, R.Santo (IKP, Univ. Muenster), H.Paetz gen. Schieck (IKP, Univ. zu Koeln), Exclusive deuteron break-up study with polarized protons and deuterons at COSY, COSY–Proposal No.20, KFA Juelich (1992).

3. R.V.Reid, Jr. Ann. of Phys., **V.50** (1968) p.411;
G.Alberi et al., Phys.Rev.Lett., **V.34** (1975) p.503.

4. M.Lacombe et al., Phys.Lett., **B101** (1981) p.139.

5. R.Machleid et al., Phys.Rev., **V.149** (1987) p.1.

6. A.P.Kobushkin, J.Phys.G: Nucl.Phys., **V.12** (1986) p.487.

7. V.G.Ableev et al., Nucl.Phys., **A393** (1983) p.491.

8. P.Berthet et al., J.Phys.G: Nucl.Phys., **V.8** (1982) p.L111.

9. P.Bosted et al., Phys.Rev.Lett., **V.49** (1982) p.1380.

10. M.Garcon, Proc. of the 7th Int.Conf on Polariz. phenomena in nucl. phys., Colloque de physiquue, C6, Suppl. No.22, **V.51** (1990) p.61.

11. B.Kuehn, Proc. of the Int. Workshop: Dubna Deuteron-91, JINR, E2-92-95, Dubna

(1992) p.138.

12. N.G.Birger et al., Jad.Phys., **V.6** (1967) p.344.

13. N.S.Craigie, C.Wilkin, Nucl.Phys., **B.14** (1969) p.477.

14. E.T.Boschitz et al., Phys Rev.Lett., **V.24** (1970) p.236.

15. V.I.Komarov et al., Jad.Phys., **V.16** (1972) p.234.

16. L.G.Dakhno, V.A.Nikonov, Nucl.Phys., **A491** (1989) p.652;
Jad.Phys., **V.50** (1989) p.1757.

17. M.G.Dolidze and G.I.Lykasov, Z.Phys., **A336** (1990) p.339.

18. Yu.L.Dorodnykh, G.I.Lykasov, preprint INR-781/92, Moscow, (1992).

19. G.I.Lykasov, Talk at the 105.WE-Heraeus-Seminar.

20. O.G.Grebenyuk, Talk at the 105.WE-Heraeus-Seminar.

21. A.Boudard, M.Dillig, Phys.Rev., **C31** (1985) p.302.

22. O.Imambekov et al., Z.Phys., **A332** (1989) p.349.

23. L.A.Kondratyuk et al., Yad. Fiz., **V.33** (1981)1208; Proc. of the XIth Europ. Conf. on Few-Body Phys., Fontevroud, 1987, Springer-Verlag., Few-Body Systems, Suppl.2 (1987) p.242.

24. P.Berthet et al., Journ.Phys.G: Nucl.Phys., **V.8** (1982) L111.

25. Yu.N.Uzikov, Proc. of the Int. Workshop: Dubna Deuteron-91, JINR E2-92-95, Dubna (1992) p.232.

26. L.P.Kaptari et al., Particles and nuclei, **V.22** (1991) p.839.

27. V.I.Komarov and H.Mueller, Pis'ma Zh.Ehksp.Teor.Fiz., **V.29** (1979) p.501.

28. V.I.Komarov, H.Mueller, et al., ZfK-502, Zentralinstitut fuer Kernforschung Rossendorf (1983).

29. V.I.Komarov, H.Mueller, et al., Fortschritte der Physik, **V.33** (1985) p.595.

30. H.Mueller, Z.Phys., **A336** (1990) p.103.

31. H.Mueller, Proc.of the Int. Workshop: Dubna Deuteron-91, E-2-92-25, Dubna (1992) p.119.

32. S.A.Zaporozhets et al., JINR D1,2-86-668, Dubna (1986) p.341.

33. V.G.Ableev et al., Nucl.Phys., **A393** (1983) p.491.

34. L.S.Azhgirey et al., Yad.Fiz., **V.46** (1987) p.1134.

35. N.P.Aleshin et al., Phys.Lett. **B237** (1990) p.29.

36. M.P.Rekalo, Talk at the Int. Workshop: Dubna Deuteron-91.

37. S.L.Belostotsky, Talk at the 105. WE-Heraeus-Seminar.

38. V.I.Komarov, O.W.B.Schult, Proc. of the Int. Workshop: Dubna Deuteron-91, JINR, E2-92-95, Dubna (1992) p.212.

39. H.Mueller, 1991, unpublished.

PHYSICS AT SMALL ANGLES WITH THE EXTRACTED BEAMS OF SATURNE

A. Boudard

DSM–DAPNIA–SPhN
CE Saclay, 91191 Gif–Sur–Yvette
France

We will discuss the main results obtained at SATURNE in the context of measurements at small angles. The production of particles near threshold will be especially emphasized. We will show the characteristics of the extracted beams and 0^0 facilities, and discuss how they can complement or compete with internal cooled beams.

Dynamics of Two-Baryon Systems

Michael Fuchs and Bernard Metsch

Institut für Theoretische Kernphysik
der Universität Bonn
Nußallee 14-16
D-5300 Bonn
Germany

1. Introduction

It is still one of the unsettled questions in strong interaction physics whether the dynamics of multi-baryonic systems can be described in terms of locally confined hadrons (baryons and mesons) and their interactions or that it is more appropriate to invoke the full complexity of quark-dynamics to account for the properties of the intermediately excited system. Actually, this might be something that eventually even could be energy dependent or as is well known from examples in low energy nuclear physics, where collective and single-particle excitations can coexist in the same energy domain, could even be state dependent. In the present contribution we will adopt the former framework and will try to establish a relation between meson-baryon dynamics, as reflected by hadronic vertex functions and observables in various hadron-hadron scattering processes.

The number of excitations in the two-baryon system up to $E_x \cong 1$ GeV is numerous in view of all the combination of excitations of the baryons that can be conceived. As for the single baryonic excitation spectrum we have to deal with a continuum spectroscopy of broad overlapping resonances, with the additional complication, that apart from mesonic decay channels one also has to deal with the baryon-baryon scattering states. Although we consider the framework to be presented below to be general enough, we will restrict the applications to excitation energies of roughly 400 MeV, where the description can be restricted to the ΔN-excitation, coupled to the NN- and (NN)π open channels. It should be noted that this example will thus disregard one interesting issue, that is expected to occur at higher excitation energies, the mixing of various B_1B_2-configurations.

More specifically the objective of this contribution is to present an attempt to arrive

at a uniform treatment of the NN→NN, NN↔πd and the πd→πd reactions and the deuteron properties on the basis of meson-baryon-baryon vertices in the energy regime mentioned above. Since this energy range includes the pion-production threshold the description will have to account for the energy dependence of both the self-energy contributions and the baryon-baryon interactions mediated via meson exchange. This will be briefly sketched in section 2. In section 3 we will discuss the observables in NN-scattering and in section 4 some examples for the scattering with π-channels are given. Section 5 contains some concluding remarks and an outlook.

2. Meson-Baryon Dynamics.

Starting point is a Hamiltonian that reflects the Meson-Baryon dynamics through hadronic vertices:

$$H = H_0 + H_c = (H_0^B + H_0^M) + (H_+ + H_-) \tag{1}$$

where

$$H_0^B \; |Bp\rangle = E_0^B(p) \; |Bp\rangle$$

describes "bare" baryons, as e.g. from some hadronic model and

$$H_0^M \; |Mk\rangle = \omega_0^M(k) \; |Mk\rangle \; = \left(m_M^2+k^2\right)^{1/2} \; |Mk\rangle$$

describes the mesons. (Since we will neglect all meson-meson interactions, no distinction between bare and physical mesons is made here). H_+ (H_-) represents the process of meson creation (annihilation) on a baryon, parameterized through a coupling constant, a spin flavour operator and a form factor. Although also these vertex functions should eventually arise from some hadron model, we will as in the Bonn Potential [1,2] treat these as phenomenological parameters, to be determined from scattering phase shifts.

For a system with fixed baryon number (here B=2) and any number of mesons the dynamics is governed by the resolvent

$$G(z) := (z-H)^{-1} \tag{2}$$

Introducing the projection operator $\mathbb{P}_n$ on the n-Meson sub space and defining a meson-

number-conserving operator implicitly by

$$H(z) = H_0 + H_- G(z)^{-1} H_+, \quad \text{with } G(z) = \left(z\text{-}H(z)\right)^{-1} \tag{3}$$

we can express $G_{nm}(z) := \mathbb{P}_n G(z) \mathbb{P}_m$, i.e. the projections of G(z) onto the subspaces by $G(z)$:

$$G_{nm}(z) = \sum_{k=0}^{\min(n,m)} \left(G(z)H_+\right)^{n-k} G(z)\mathbb{P}_k \left(H_- G(z)\right)^{m-k} \tag{4}$$

This implies, that we can now concentrate on the treatment of $H(z)$ of Eq.(3), which still contains the full complexity of the problem. In a Born-like approximation one could write

$$H(z)^{(1)} = H_0 + H_-(z\text{-}H_0)^{-1} H_+ \tag{5}$$

but this would lead to an incorrect treatment of the particle production thresholds. In the present contribution we therefore propose an approximation for $H(z)$ as illustrated in Fig. 1:

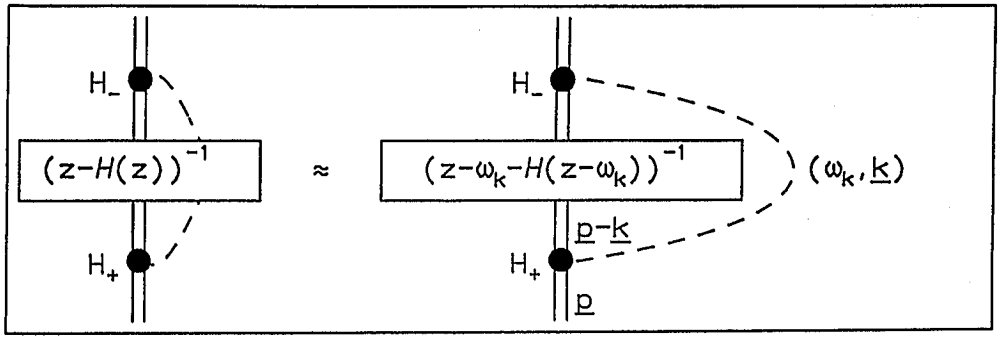

Fig. 1. Approximate treatment of $H(z)$

which essentially accounts for the fact that a baryon might be "dressed" by an indefinite number of mesons, but that neglects any mesonic interactions as well as crossed contributions. For the nucleon and Δ-resonance discussed here the approximation of Fig. 1 was used to calculate the off-shell self-energy contribution.

We can now isolate the one-body self-energy contributions

$$H(z) = (H_0+\delta H(z)) + V(z) = H_0^{(R)}(z) + V(z) \tag{6}$$

where $H_0^{(R)}$ is now the renormalized one-baryon Hamilton operator and V(z) contains baryon-baryon interactions through meson exchange. Here we will restrict the treatment to one meson exchange only. We thus arrive at the Lippmann-Schwinger equation for the n-meson subspace:

$$t_n(z) = V(z)\ \mathbb{P}_n + t_n(z)\ G_0^{(R)}(z)\ V(z) \tag{7}$$

where $G_0^{(R)} = \left(z-H_0^{(R)}(z)\right)^{-1}$.

We are now ready to write down the scattering equations for the various reactions: The transition operator is given by $T(z) = H_c + H_c(z-H)H_c$. Projection on the 0-meson subspace and subtraction of the pure self energy contributions now leads to the T-matrix for NN-scattering:

$$\mathbb{P}_0 T(z)\mathbb{P}_0 = n(z)\ t_0(z)\ n(z) \tag{8}$$

where $n(z) = (z-H_0)(z-H_0^{(R)}(z))^{-1}$ the renormalization of the asymtotic states.
In the same manner we find for πd-scattering:

$$\begin{aligned}\mathbb{P}_1 T(z)\mathbb{P}_1 = {} & n(z)u_1^L(z)\ H_+\left[G_0^{(R)}(z)+ G_0^{(R)}(z)t_0(z)G_0^{(R)}(z)\right]H_-\ u_1^R(z)n(z) \\ & + n(z)\ t_1(z)\ n(z)\end{aligned} \tag{9}$$

with $u_n^R(z) = \mathbb{P}_n + G_0^{(R)}(z)t_n(z)$ and $u_n^L(z) = \mathbb{P}_n + t_n(z)G_0^{(R)}(z)$ containing the initial and final state interactions.
The πd$\leftrightarrow$NN scattering follows from

$$\mathbb{P}_1 T(z)\mathbb{P}_0 = n(z)\ u_1^L(z)\ \left[H_+ + H_+G_0^{(R)}(z)t_0(z)\right]n(z) \tag{10}$$

Finally bound states (here the deuteron) can be calculated by solving the equation

$$H(E)\ \mathbb{P}_0\Psi = E\ \mathbb{P}_0\Psi \tag{11}$$

by expanding into a finite basis of square-integrable functions and applying the Ritz-variational principle. This concludes our scheme for the uniform treatment of the

various two-particle reactions that involve ΔN-intermediate states.

In the following we will apply this scheme to calculate the NN phase shifts by a fit of the vertex-parameters (coupling constants and cut-off masses) to empirical analysis in the energy range $T_{Lab} \leq 1$ GeV. Then we will check the treatment by comparing observables for reactions with πd-channels. We will concentrate on two versions mainly: a so called full model, where all coupling constants are fitted to NN-scattering, except for $g_{\pi NN}$ and $g_{\pi N\Delta}$, which are fixed by πN scattering; and a so called minimal model, where, apart from $g_{\pi N\Delta}$ all couplings involving the Δ-resonance are neglected. The latter, which in particular neglects all ΔN-repulsion is not considered to be a real physical alternative, but merely serves as an indicator for the relevance of ΔN-interactions.

3. Phase shifts of NN-scattering above π-production threshold.

In general the present treatment, with both the NN- and the ΔN-channels taken into account, gives an overall acceptable, though not excellent description of most phase shifts, mixing angles and inelasticities in the energy range considered. The discrepancies with respect to the experimental phase shift analyses [3-6] are mainly in the ρ-parameters of low-angular momentum partial waves, see e.g. Fig. 2. As an example we mention the $^1D_2(T=1)$ partial wave, which is the dominant contribution when pion-channels are involved. In the unbiased and automatic overall fit to the data the inelasticity comes out too low when taking the full ΔN-interaction into account, whereas neglect of especially the ΔN-repulsion, as in the second version, strongly overemphasizes the role of ΔN-intermediate states. It is hard to judge whether this reflects a serious discrepancy connected to the more basic assumptions made, such as the restriction to one-boson-exchange only and the neglect of double pion channels or that this could be cured by moderate changes in the vertex parameters. As an illustration of how the two versions mentioned above can account for observables in NN-scattering we give the angular distributions of the spin-correlation observable A_{yy} for various energies in Fig. 3. Here we also find an interesting structure at small scattering angles, the topic of the present workshop, see also the contribution by Kroll) , due to Coulomb-strong-interaction interference, that could constitute a very sensitive test of the underlying dynamics.

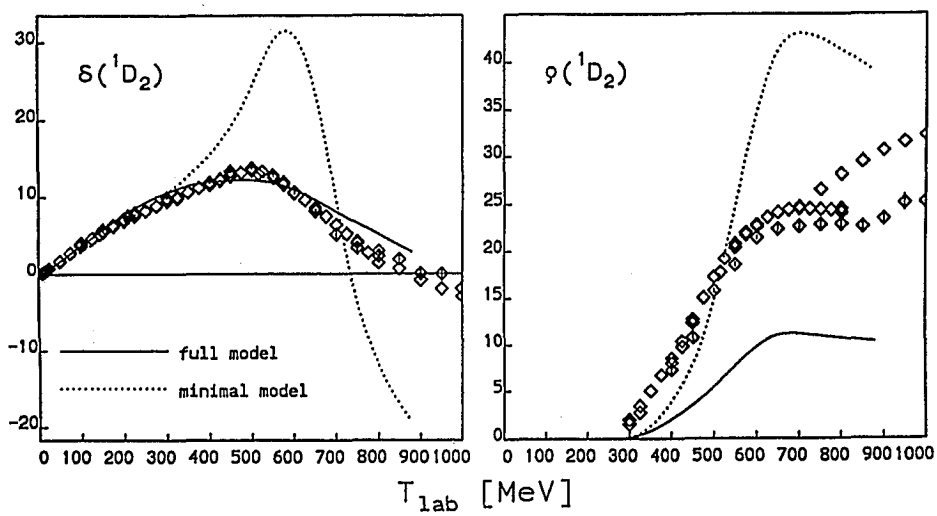

Fig. 2. $^1D_2$-(T=1) phase shift for NN-Scattering. The solid curve represents a calculation that reflects the full ΔN-dynamics, the dotted curve results from a fit where the ΔN-interaction was treated in a minimal model.

4. Two body scattering with pions.

In Fig. 4 we present the results for the differential cross section for elastic pion-deuteron scattering. Apart from the lowest energies, where π-N S-wave scattering contributions, neglected in the present treatment, might be relevant we find an acceptable description especially at backward angles only for the so called full calculation. In order to appreciate the various contributions we compare in Fig. 5 the results of some calculations with different levels of sophistication. This shows that treating the Δ-excitation only in Born-approximation is not adequate enough to account for angular dependencies of the observables, especially not for the vector polarization iT_{11}, that is positive on the whole angular range. In general we find that the parameters fitted in the full calculation to the NN phase shifts yield in general also a satisfactory description of the πd elastic scattering observables. A similar conclusion can also be drawn for the observables of the pp→πd reaction, although in general the discrepancies are larger. As a typical example see Fig. 6, where we give the spin-correlation observable $A_{zz,}$

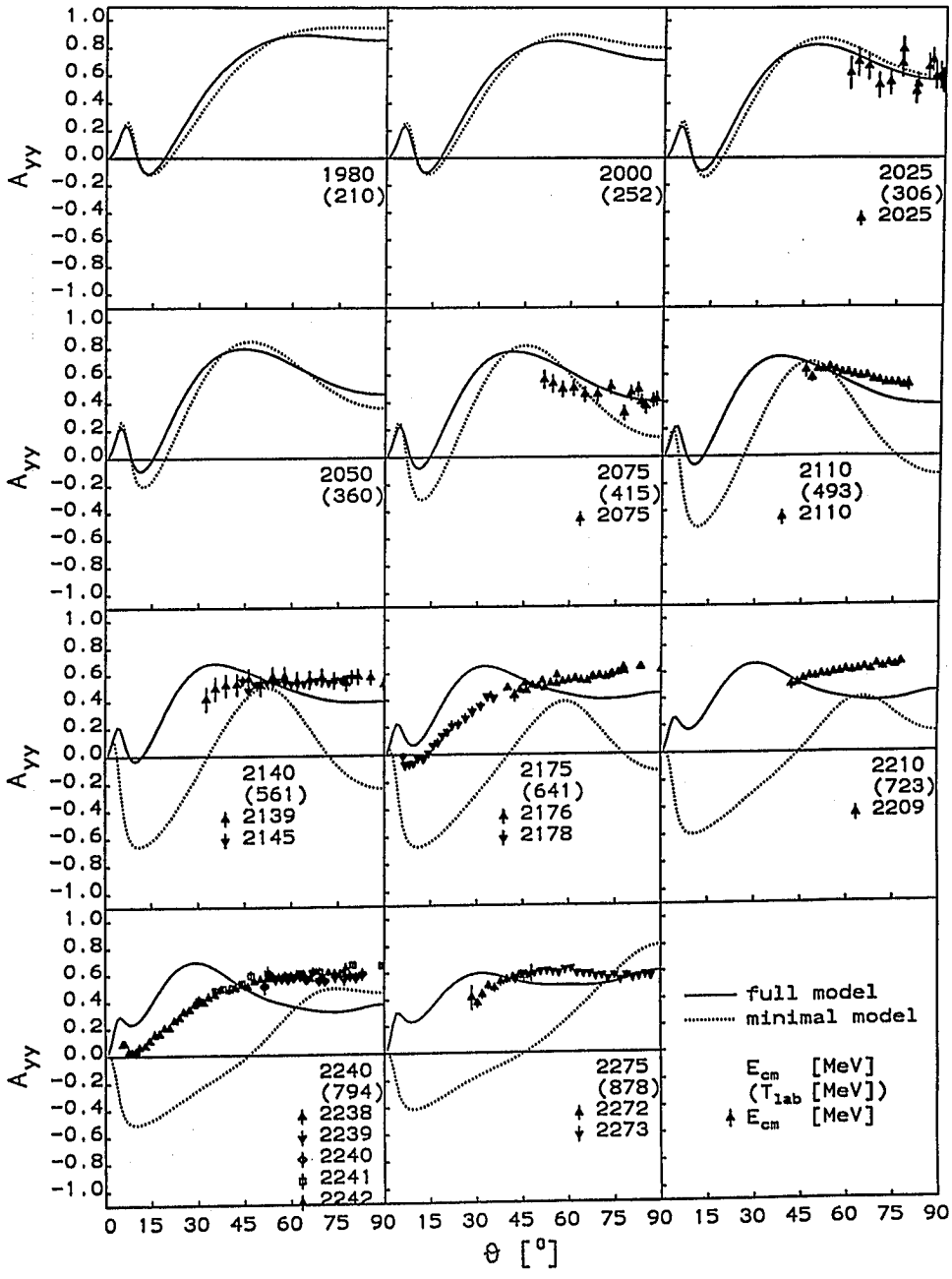

Fig. 3 Comparison of calculated and experimental spin correlation A_{yy} for pp-scattering.

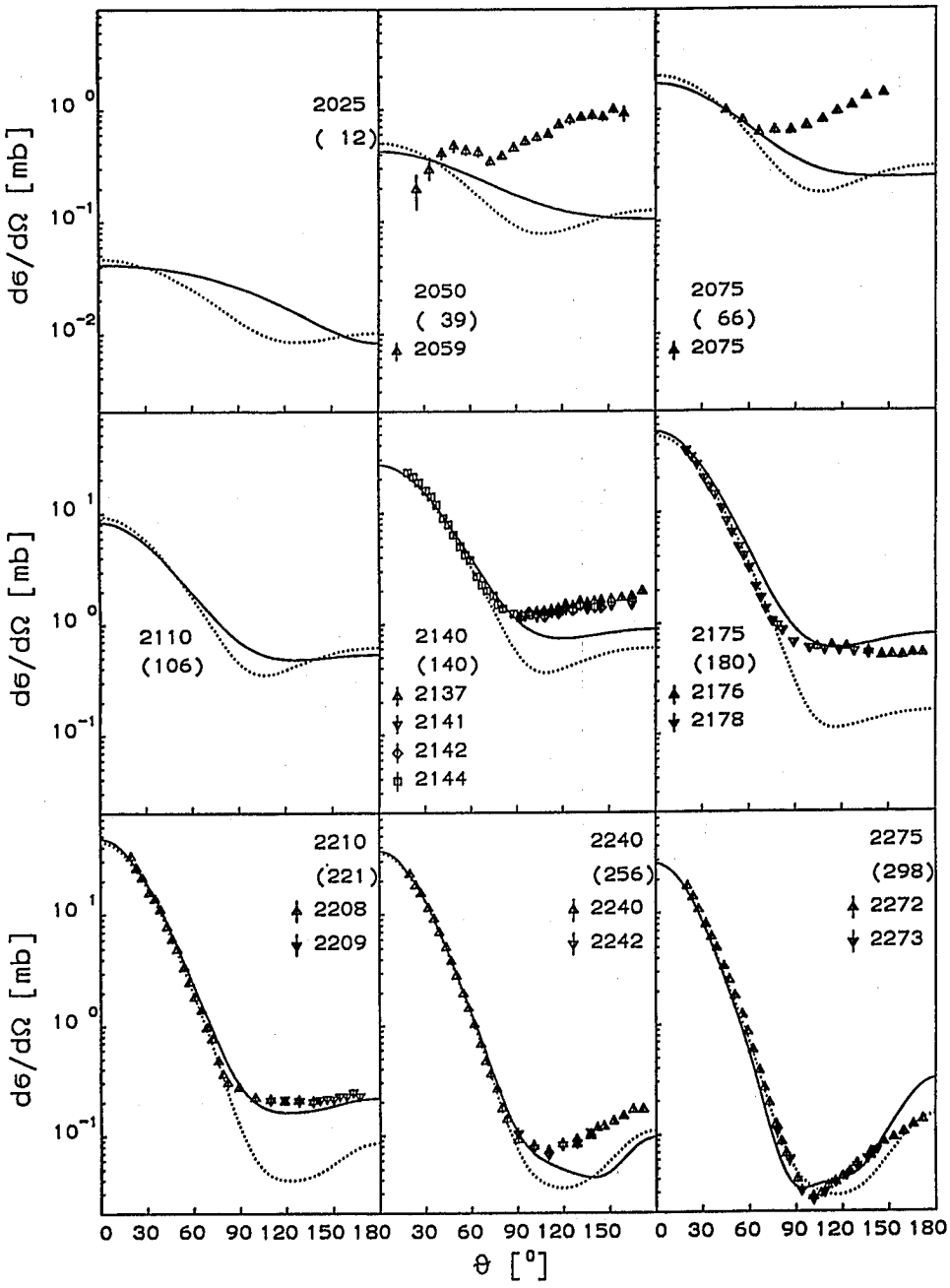

Fig. 4 Comparison of calculated and experimental differential cross sections for elastic πd-scattering (for legend see Fig. 3).

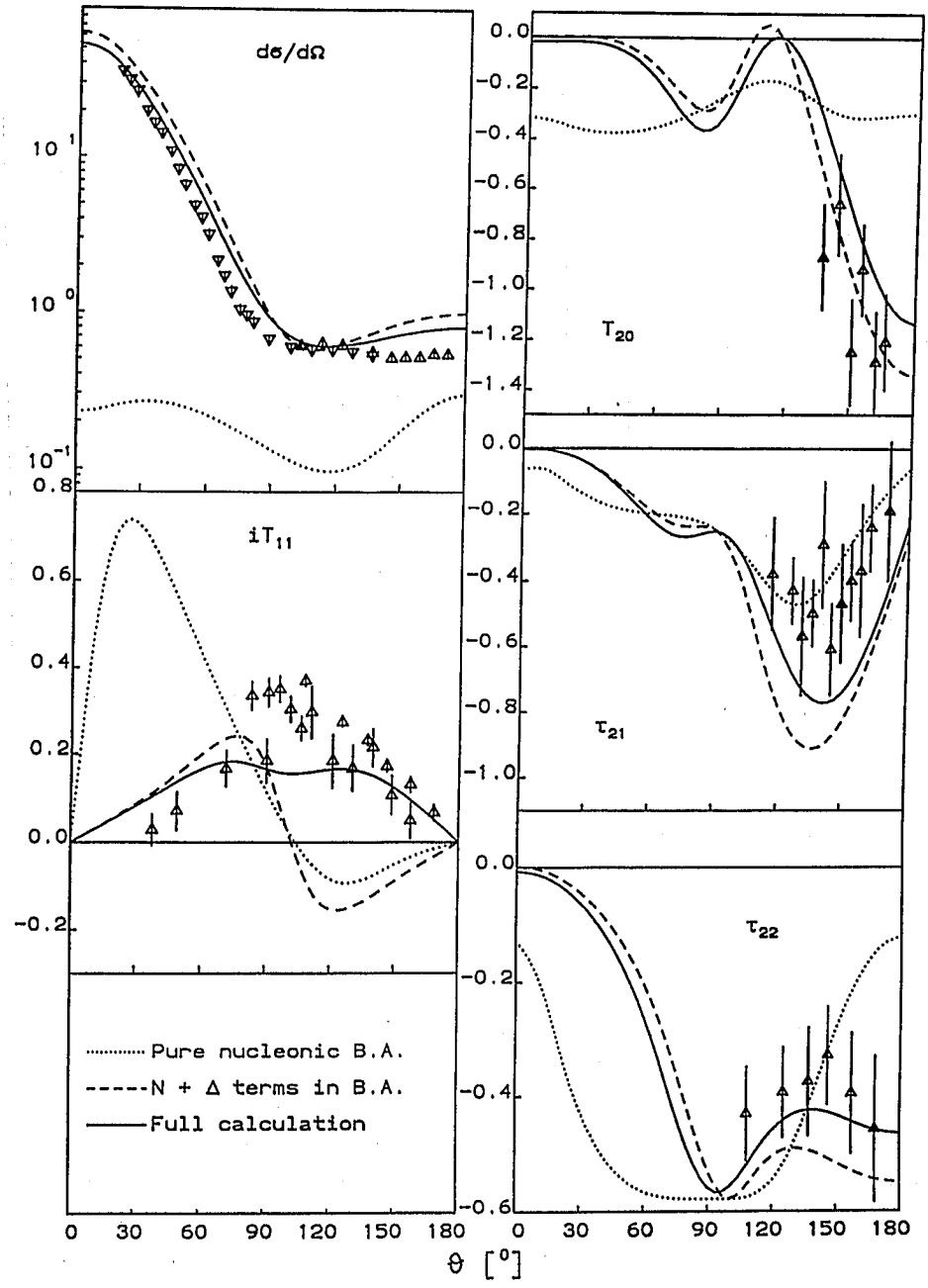

Fig. 5 Comparison of experimental and calculated angular distributions of the differential cross section, vector polarization-, and tensor polarization observables in elastic πd-scattering at the resonance energy. The solid line represents the full calculation. The dotted curve is a calculation that includes only the nucleonic contribution in Born approximation the dashed curve also includes the Δ-excitation in Born approximation.

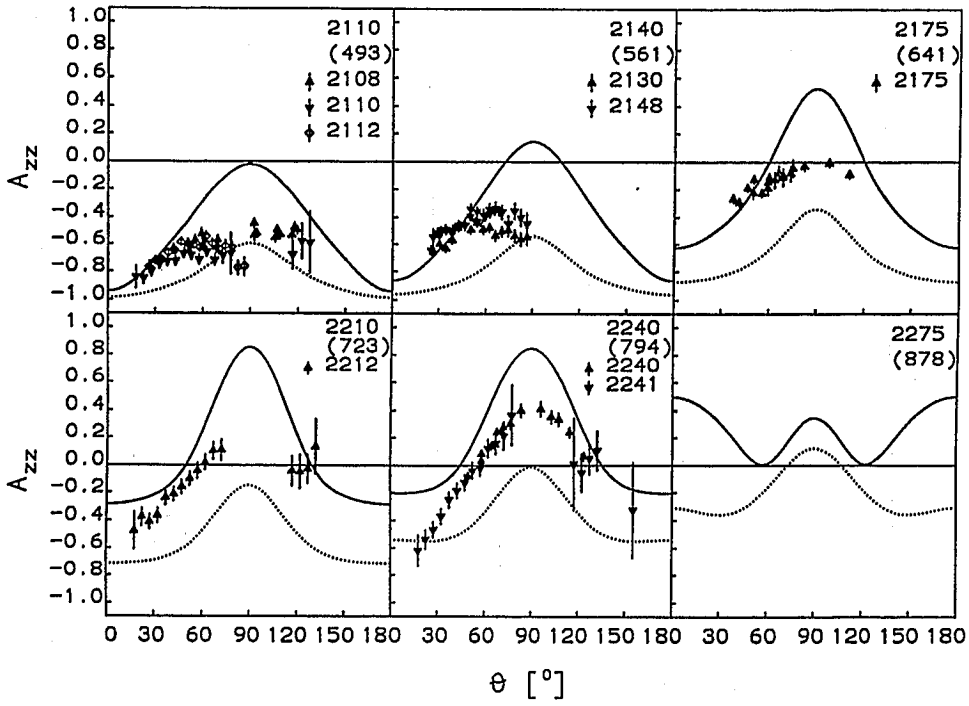

Fig. 6 Comparison of experimental and calculated longitudinal spin-correlation A_{zz}.(For legend see Fig. 4).

5. Summary and outlook.

We presented a calculational scheme that accounts for a general baryon-baryon interaction via (one) meson exchange based on baryon-baryon-meson vertices. Such a treatment allows in principle a uniform treatment of both self-energy contributions and the true interactions, which is important in an energy domain, where various scattering channels are open. As a first application we applied this to the calculation of observables in exclusive two-particle reactions with NN- and πd-channels in the region of the Δ-resonance. It should be stressed that this application is not the first (see [7-10]), nor the ultimate calculation of these scattering processes, although it is among the few that aim at uniform and consistent treatment of all the channels involved on the basis of the (in this context) basic building blocks, the hadronic vertices. In general we find an overall reasonable description of the various known scattering observables if the complexity of the NN, NΔ and πd coupled channel problem is accounted for. More specifically we have shown that details of the ΔN-interaction are relevant for a de-

scription with this quality. The preliminary conclusion of the present contribution could be, that the structure of the ΔN-system as the deuteron is determined by large attractive and repulsive contributions, that almost cancel. It should be stressed, however, that the present description of especially the dominant partial wave with J=2 and T=1 is far from ideal, the calculated inelasticity being too weak by almost a factor of two. Whether this could be cured by a modest modification of parameters without destroying the overall description is an issue which is still hard to settle. It should be stressed, that the present treatment includes one boson exchange only. Especially in view of so called crossed contributions this is not the state of the art.

The application to the ΔN-system we discussed here can be extended to include also photon- and electro-induced reactions like $\gamma d \rightarrow \pi d$. Moreover it is planned to calculate reactions with a three-body final state as $NN\pi$ and $NN\eta$. Within the same framework there are some preliminary applications to strange two-baryon systems, which are technically more involved since there exist more open channels in this case. The most interesting extension is in fact the main motivation for the present scheme: the study at higher excitation energies. This involves both the excitation of higher baryonic resonances, like $NN^*(1440)$ and $NN^*(1535)$, but also double-baryon excitations like ΔΔ. As mentioned in the introduction we may encounter here the phenomenon that different baryon-baryon configurations mix, which could be studied by exploiting the richness of various possible decay modes in the higher energy regime. In order to avoid the necessity of introducing new phenomenological parameters that describe the hadronic vertices and which are hard to fix by empirical data, it seems imperative to have an accurate and reliable model for actually computing the hadronic vertices. Although far from perfect we feel that the general framework sketched offers a suitable strategy for a systematic investigation of the dynamics of two baryon systems, a reference frame, that can be used also to appreciate possible exotic phenomena.

References

[1] R. Machleidt, K.Holinde, Ch. Elster, Phys. Rep. **149** (1987) 1.
[2] Ch. Elster, K. Holinde, D. Schütte, R. Machleidt, Phys. Rev **C38** (1988) 1828.
[3] R.A. Arndt, J.S. Hyslop III, L.D. Roper, Phys. Rev. **D35** (1987) 128.
[4] D.V. Bugg, Phys. Rev. **C41** (1990) 2708.
[5] J. Bystricky, C. Lechanoine-Leluc, F. Lehar, J. Physique **48** (1987) 199
[6] F. Lehar, C. Lechanoine-Leluc, J. Bystricky, J. Physique **48** (1987) 1273
[7] B. Blankleider, "Theory of the coupled NN-πNN system, PSI-PR-92-08
[8] G.H. Lamot, J.L. Perrot, C. Fayard, T. Mizutani, Phys. Rev. **C35** (1987) 239
[9] T.-S. H. Lee, A. Matsuyama, Phys. Rev **C36** (1987) 1459
[10] H. Pöpping, P.U. Sauer, X.-Z. Zhang, Nucl. Phys. **A474** (1987) 557.

P-D FRAGMENTATION AT INTERMEDIATE ENERGIES AND DEUTERON STRUCTURE AT SMALL N-N DISTANCES

G.I.Lykasov
Joint Institute for Nuclear Research
Head Post Office,P.O.Box 79, Moscow, Russia

and

Yu.L. Dorodnych
Institute for Nuclear Reseach, Moscow, Russia

ABSTRACT

The exclusive $pd \to ppn$ reaction at energies below 3.3(*Gev.*) is analised. The prediction for the differential cross section and the tensor analising power of deuteron T_{20} at the kinematic condions when one proton is emitted forward and another one - backword are presented. The possibility of getting a new information about the deuteron structure and off-mass shall effects of nucleons in deuteron from the analysis of this reaction at mentioned above energies is discussed. The importent role of relativistic effects in deuteron by the analysis of such processes is showed. The role of quark freedom degrees in deuteron in these reactions is discussed also.

I. Introduction

One of the basic problem in modern nuclear physics is the study of short range correlations (SRC) in nuclei. Such correlations can be investigated both in processes with large transverse momenta and in soft interactions, for example in fragmentation reactions of nuclei at high energies. In this connection the study of fragmentation reactons of deuteron on nucleons and nuclei at high energies can give more detailed information about its structure especially at small N-N distances. Besides, the analysis of the processes like elastic [1] and $h - d$ [2] scattering, deuteron brak-up by electrons [4] and protons [5] at intermediate and high energies is very interesting for the investigation of SRC.

A lot of difficulties arises in the study of this problem. First of all it is necessary to take into account the relativistic effects in deuteron if we analise the processes which occur at small N-N distances. It is know that the decay vertex of the deuteron into two nucleons is related to its wave function which is the solution of the Bethe-Salpeter equation in general case. But there is no exact simple solution of this equation therefore we must resort to diferent approximations. One is as follows. The idea of a deuteron wave function (d.w.f.) in light cone dynamics is introduced in the infinite momentum frame (IMF) [6-10]. Then it is related to the nonrelativistic (d.w.f.) depending on invariant variables [11-14]. Furthermore in the study of SRC it turns out that the analysis of such processes only in the frame of the spectator mechanism is not sufficient. It is necessary to take into account a more complete reaction mechanism.

In this paper the analysis of deuteron fragmentation processes at large and intermediate energies in the framework of of the previosly suggested approach [15-17] is presented. In addition to the spectator mechanism and the mechanism with a virtual meson in the intermediate states , which have been considered previosly , we include now the rescattering graphs of particles. The importance of including the rescattering of nucleons in $pd \to pX$ was demonstrated clearly by C.F.Perdrisat and N.Punjabi [18] and by L.Dachno and V.Nikonov [19] where however the relativistic effects in the deuteron were not taken into account. However, as was shown in refs. [15-17], the cross section and especially T_{20} are strongly sensetive with respect to the procedur of the relativisation of the deuteron dissociation vertex into two nucleons. In particular, in ref.[20] it was shown that the inclusive spectrum of protons emitted at large engles in the reaction $pd \to pX$ can't be described on the basis of a structure function obtained from nonrelativistic d.w.f. The structure function must be a function of two independent variables x and p_t describing the longitudinal and transverse motion of the constituents in deuteron respectively.

In this paper we calculate the differential cros section of the exclusive reaction $pd \to ppn$ when one proton scatters forward and another- -backword and T_{20} for this reaction. Such measurements are plained at COSY (Yuelich, Germany), therefore our results are some predictions for this experiment.

The strong sensitivity of observables (especially T_{20}) to the choise of the relativisation of the deuteron dissociation vertex was noted in our earlier papers [15-17]. In particular, in ref. [20] it was shown that the inclusive proton spectrum is not described when variational nonrelativistic d.w.f. are used.Therefore the study of relativistic effects in the deuteron is a very important task.

Our paper is organised in the following way. The general approach of the analysis of deuteron fragmentation processes in the frame of Weinberg's diagramm technique and the derivation of the amplitudes of $pd \to pX$ and $pd \to ppn$ in IMF are presented in the first section. The calculations of the differential cross section and the analising power T_{20} for the above mentioned case of $pd \to ppn$ reaction are presented in the section II. The calculation results and discussions are presented in the section III. The role of quark effects in the deuteron which can be occured in $p-d$ reactions at energies below 3.3(Gev) is discussed also in the section IY. And finaly the conclusions from the perfomed analysis and the recomendations to the planing of new experiments are presented in the section Y.

II. General formalism

a) Relativistic effects in the deuteron

As it is known, generely the deuteron vertex $d-NN$ (see fig.1) is not equialent to the deuteron dissociation into two nucleons. the annihilation $d\mathrm{N} \to \mathrm{N}$ has to much be included in this vertex. Therefore it can't be related directly to the d.w.f. in the general case. As it is known, along with the covariant formalism the noncovariant one can be used, where each Feynman graph of the n-th order is equialent to $n!$ time -ordered graphs of the old pertubative theory (OPTh). Many of these graphs vanish in the IMF, i.e., they give contributions of the order $1/P$, where P is the summed momentum of initial particles, going to infinity. Only the graphs related to the deuteron dissociation into two nucleons remain [6-9].

The Feynman graph of the process $Nd \to NNN$ (1a) and two equialent time ordered graphs of the OPTh $(1b, c)$ are presented in *fig.*1. The graph of fig 1c vanishes at large P as $1/P^2$ if the vertex N-N doesn't depend on the spin [9], and as $1/P$ when the spin dependence of the N-N vertex is taken into account [9].

Therefore the notion of the d.w.f. Ψ can be introdused, where $|\Psi|^2$ is the usual probability of the existence of two nucleons with the fraction momentum x and the transverse momentum k_t in the deuteron. However the question arises, on how many variables the relativistic d.w.f. Ψ depends and what is its form. Unfortunately there is not yet a dynamical theory which can construct the relativistic invariant form of Ψ. There is a lot of approaches for the relativisation of the $d - NN$ decay. There are the models in which this $d-NN$ decay is connected with the d.w.f.[11-14] in IMF. These models can be devided into a covariant approach [14] and a noncovariant one [11-13]. In the covariant approach [14], in which the energy in the vertex $d - NN$ is consorved, Ψ depednds on two relativistic invariant variables $\mathbf{q}^2$ and $\mathbf{n}$ where $\mathbf{q}$ is the three-momentum of the nucleon in the frame $\mathbf{k}_1 + \mathbf{k}_2 = 0$ and $\mathbf{n}$ is the direction of the light cone $\mathbf{n} = \omega/\omega_0$, see *fig.*2.

$$\mathbf{q}^2 = \frac{m^2 + k_t^2}{4x(1-x)} - m^2 \tag{1}$$

where x is the light cone variable.

In the noncovariant method [11, 12] Ψ depends on one relativistic variable $\mathbf{k}^2$ which coincides with $\mathbf{q}^2$ in the frame where $\mathbf{n} \uparrow\uparrow -\mathbf{P_d}$ (see *fig.*2). In this case the energy in the vertex $d - NN$ is not conserved and $\mathbf{k}^2$ is proportional to $P\delta E$ as it is shown in ref.[11], where $\delta E = E_d - E_1 - E_2$, here E_d, E_1 and E_2 are the energies of the deuteron and two nucleons respactively (see *fig.*2).

In both of these relativisation methods the d.w.f. Ψ is related to the nonrelativistic d.w.f. $\Psi_{N.R.}$ which depends either on two Lorenc invariant variables $\mathbf{q}^2$ and $\mathbf{qn}$ or one relativistic invariant variable [11-13]. For example, if we choose $\mathbf{n} \uparrow\uparrow -\mathbf{P_d}$, then according to refs. [10-12] the relation between Ψ and $\Psi_{N.R.}$ is written in the following form:

$$\Psi(x, k_t) = \left(\frac{m^2 + k_t^2}{4x(1-x)}\right)^{1/4} \Psi_{N.R.}(\mathbf{k}^2) \tag{2}$$

As known in ref. [14], the spin structure of d.w.f. $\Psi(\mathbf{q}^2, \mathbf{qn})$ on the light cone in the covariant approach is sufficiently complicated: it is determned by six relativistic invariant functions instead of two S- and D- waves, as in the nonrelativistic case. The increase of the number of these spin functions is explaned by the fact that the expression for the deuteron moment has diferent invariant combinations with vector $\mathbf{n}$ as well as the momentum $\mathbf{q}$. However, if we consider the deuteron stripping $dp \to pX$, when the proton is emitted forward or backward in the deuteron rest frame, the spin structure of Ψ reduces to the usual form of a nonrelativistic d.w.f. [14] because $\mathbf{n}$ is colliniar to $\mathbf{q}$. Therefore we can use the ordinal deuteron spin structure of $\Phi_{N.R.}$ and for $\Psi(x, k_t)$ we can write the following spin structure:

$$\Psi(x, k_t) = \Psi_0(x, k_t) + \frac{1}{8}\Psi_2(x, k_t) S_{np} \tag{3}$$

here $S_{np} = 3(\sigma_n \mathbf{k}^0) - \sigma_n \sigma_p$; $\Psi_0 = C_0 u$; $\Psi_2 = C_2 w$;u and w are the S and D -waves of nonrelativistic d.w.f. but depending on x and k_t^2 ; σ_n; σ_p are Pauli matrices of the neuteron and the proton respectively; $\mathbf{k}_0 = \mathbf{k}_1/|\mathbf{k}_1|$ is unit vector.

There is another approach in which the vertex $d-NN$ is not related with the d.w.f. Ψ, for example the method suggested by F.Gross [23], wich was developed later in light cone variables in ref.[24]. In this method the vertex $d-NN$ is expanded over invariants and one of the deuteron nucleons is off the mass shell. In fact there are four unknown functions in this method, which are approximated by some polinomals and its parameters are found from the description of experimental data about the electric and magnetic formfactors and the static properties of the deuteron.

An other interesting approach to the inclusion of deuteron relativistic effects is the so-called method of the dispersion integration over masses of constituent particles [25].

However we will use the relativisation method [14] where the deuteron vertex $d-NN$ is related to the d.w.f. Ψ in IMF. And as mentioned above we can use the OPTh in IMF using Weinberg's diagram technique.

b) The reaction mechanism

Let us consider now the deuteron break-up reaction $dp \to ppn$. As mentioned above and in refs.[15-19], it is unsufficient to consider the process only in pole approximation, it is necessary to take into account the full mechanism of the reaction. We will consider the reaction mechanism in the framework of Weinberg's diagram approach in IMF [6]. As is known, the idea of this method is the following: each Feynman graph of the n-th order is represented as the sum of $n!$ graphs of OPTh. In IMF a lot of graphs vanishes as $1/P$, and at large P we can neglect the contribution of these graphs.

If we consider the reaction $dp \to ppn$ for the case when the proton is emitted forward or backward in the deuteron rest frame then according to refs.[6-9] it is necessary to take into account time ordered graphs presented in $fig.3(a-d)$ of OPTh. Other time ordered pole or triangle graphs give the contributions of order $1/P$. Generally more detailed analysis is nedeed for the reaction $dp \to pX$. Therefore at large P we can restrict ourselves to the graphs of $fig.3(a-d)$ only and neglect other time ordered graphs of first and second order in hadron-nucleon $(h-N)$ interactions.

The general expression for the amplitude of the process $dN \to NNN$ corresponding to the following form:

$$F_D = C\sum_{i=1} F^{(i)} \tag{4}$$

where the following notion is introduced: $C = (2(2\pi)^3)^{\frac{1}{2}}$ is the normalisation coefficient [15]; $F^(i)$ are the amplitude parts corresponding to the graphs of $figs.3(a-d)$ [15].

$$F^{(1)} = f_{1NN}\frac{\Psi(x_1,k_t)}{\sqrt{2x_1(1-x_1)}}; F^{(2)} = f_{2NN}\frac{\Psi(x_2,k_t)}{\sqrt{2x_2(1-x_2)}} \tag{5}$$

where f_{1NN}, f_{2NN} are the amplitudes of $N-N$ interaction corresponding to the lower vertices of $fig.3a$ and $3b$ graphs; x_1, k_t corespond to the proton emitted from the upper vertex of $fig.3a$, i.e., to the spectator proton; x_2, k_t correspond to the proton emitted from the lower vertex of $fig.3b$, i.e., to the nonspectator one.

$$F^{(3,4)} = -\frac{P}{(2\pi)^3}\int \frac{\Gamma_N^{(1)}\Gamma_N^{(2)}}{4\sqrt{E(k_1)E(k_2)E(q)}}dx \int \Psi(x,k_t)G(x,k_t)d^2k_t \tag{6}$$

here $\Gamma_N^{(1)}$, $\Gamma_N^{(2)}$ are the low and upper vertieces of the $h-N$ interactionsin the graphs of $fig.3(c-e)$ respectively, $G(x,k_t)$ is

$$G(x,k_t)=\frac{1}{E_D-E(k_1)+m-E(q)-E_1-E_2+i\epsilon}$$

the two-particle Green function in terms of the variables x and k_t (see refs.[6, 9] and [16]). The expression (6), according to Weinberg's approach [6], can be written in the following form independing on the initial energy:

$$F(3,4)=\frac{1}{(2\pi)^3}\int\frac{\Gamma_N(1)\Gamma_N(2)}{4x_2'\sqrt{x_1'(1-x_1')}}dx_1'\int\Psi(x_1',k_t)G(x_1',k_t)d^2k_t;$$

where

$$G(x_1',k_{1t})=\frac{2}{s_1'+s_N-s_1-s_2+i\epsilon};$$

$$s_1'=\frac{m^2+{k_{1t}}^2}{x_1'};s_1=\frac{m^2+{p_{1t}}^2}{x_1};s_2=\frac{m^2+{p_{2t}}^2}{x_2};s_N=\frac{m^2}{x_N}$$

; and $x_2'=x_1'-x_3+x_N$; here x_1', x_2' are the fractions of momenta of the intermediate nucleons N_1 and N_2 respectively; x_N, x_D are the momenta fractions of initial nucleon and deuteron correspondentely; x_1 and x_2 are the momenta fractions of final nucleons,

$$x_d+x_N=1$$

For all graphs in $fig.3(c,d)$ $\Gamma_N^{(1)}$ corresponds either to the amplitude of elastic $N-N$ scattering (see $fig.3d$) both to the amplitude of the process $NN\to RNN$, where R is the meson in the intermediate state (see $fig.3c$). The $\Gamma_N^{(2)}$ vertex corresponds either to the absorption of a virtual meson ($fig.3c$) or to the rescattering of a nucleon on another nucleon of deuteron. For the absorption of a pseudoscalar meson by the nucleon we have: $\Gamma_N^{(2)}=gau^+(p')\gamma_5u(k_1)$, where $a=\sqrt{2}$ for π^+-meson and $a=1$ for π^--meson. If the inttredeuteron nucleons are not far from mass-shell we use the usual expression for the nucleon spinor u to obtain:

$$\bar{u}(p')\gamma_5u(k_1)=b\zeta^+(\frac{\sigma_{\mathrm{N}}\mathrm{p}'}{\mathrm{E}'+\mathrm{M}}-\frac{\sigma_{\mathrm{N}}\mathrm{k}_1}{\mathrm{E}(\mathrm{k}_1)+\mathrm{m}})\zeta \qquad (7)$$

where

$$b=\sqrt{\frac{(E(k_1)+m)(E'+m)}{4m^2}}$$

Here σ is the Pauli spinor for the nucleon.

In principle Weinberg's approach used in this paper is valid in the infinite momentum frame. However there are now experiments of deuteron sttripping at initial energies of the projectile particles, of proton or deuteron, are not very large, for example $T_p<3.3(Gev.)$, as at COSY (Juelich), then the production of vector mesons in the low vertex of the $fig.3c$ graph is very small in comparision with the pseudoscalar meson production as the experimental data show [26-27]. Therefore we can neglect the contribution of the $fig.3c$ type graph with the absorption of virtual vector mesons by nucleons and keep the graphs of $fig.3c$ with the pseudoscalar mesons in the intemediate state only.

The vertex $\Gamma_N{}^{(1)}$ in the graph of $fig.3c$ can be related to the amplitude of the real meson production in the $N-N$ interaction multiplied by the formfactor F_π that takes into account the off-shall effects of the virtual π-meson.

Note that each graph of $fig3(c,d)$ corresponds to the coherent sum of graphs taking into account all isotopic states of intermediate and final particles. Now we return to the calculation of different observables in the considered reaction.

III. Proton spectra and polarisation phenomena in $pd \to ppn$ reaction

Let us consider firstly the exclusive $pd \to ppn$ process. The expression for the spectrum $\varrho_{DN} = E_1 d\sigma/d^3p_1$ has the following expression:

$$\varrho_{dN} = C_1 \int Sp(\varrho_0 F_D{}^+ F_D)\delta^4(p_{in} - p_f)\frac{d^3p_2 d^3p_3}{2E_2 2E_3} \tag{8}$$

where

$$C_1 = 1/4\sqrt{\lambda(s_{DN}, M_D{}^2, m^2)(2\pi)^2};$$

p_2, p_3 and E_2, E_3 are three momenta and energies corresponding to scattered proton and neuteron respectively in discussed reaction; $\lambda(x,y,z) = (x-(\sqrt{y}+\sqrt{z}))(x-(\sqrt{y}-\sqrt{z}))$

The detailes of the calculation of ϱ_{dN} are presented in ref.[29]. Therefore consider now the polarisation phenomena in the discussed reaction.

According to what was mentioned above, we can take the usual nonrelativistic structure as the spin structure of relativistic dw.f. on light cone when the final proton is emitted forward and another one - backward. The general form of the deuteron matrix density ϱ_D is the following [26-28]:

$$\varrho = \frac{P_T}{3}(1 + \frac{3}{2}\wp \mathbf{S} - \frac{1}{2}\varrho_{20}(3\mathrm{S}_z{}^2 - 2) \tag{9}$$

where $\wp$ is the vector polarisation of deuteron; ϱ_{20} is its tensor polarisation; $\mathbf{S}$ is the deuteron spin operator; S_z is its z-proection.

Consider now the tensor analising power A as the average value of the spin tensor oprerator [26] $\varrho_{20} = 3S_z{}^2 - 2$, i.e., $A = <\Omega_{20}> = \sqrt{2}T_{20}$. This value can also be determined in another way [31]:

$$A = \frac{\sigma(m=+1) + \sigma(m=-1) - 2\sigma(m-0)}{\sigma(m=+1) + \sigma(m=-1) + \sigma(m=0)}$$

where $\sigma(m = +,-1,0)$ are the differential cross sections of the reaction assumed for pure spin states of the deuteron. The value of T_{20} according to the determination introduced above and to refs.[26-28], can be written in the following form:

$$T_{20} = \frac{1}{\sqrt{2}}\frac{\int Sp(\varrho_D F_D{}^+ \omega 20 F_D}{\int Sp(\varrho_D F_D{}^+ F_D)} \tag{10}$$

Consider now the anothe polarisation value, so called transfer polarisation κ. We suggest that the initial deuteron has the vector polarisation $\wp$ and some tensor polarisation, i.e., ϱ_{20} is not equal to zero, and we interested in the polarisation of final protons $\wp'$. The general expression for this polarisation has the following form [27, 28]:

$$\wp' \mathbf{n} = \frac{\int Sp(\varrho_D F_D{}^+ \sigma \mathbf{n} F_D)}{\int Sp(\varrho_D F_D{}^+ F_D)} \tag{11}$$

Return now to the discussion of the calculation results.

IV. Results and Discussion

Now we consider the calculation results of the proton spectrum and T_{20} for the exclusive reaction $pd \to ppn$ when one proton is emitted forward and the other - backward. The experimental measurements of ϱ_{dN} and T_{20} in this rection at $T_0, 3.3(Gev.)$ are planed in Yuelich (Germany). The $figs.3(a-d)$ graphs will give the contribution to the observables of this reaction.

The differential cross section $E_2 d\sigma/d^3p_2$ is presented on $fig.4a$. It is seen from this fig. that the pole mechanism (fig.3(a-b)) gives the contribution larger than one of all graphs ($fig.3(a-d)$) at $q < 0.2(Gev./c)$ and smaller than ones at $0.25 < q < 0.35(Gev./c)$). That can be explaned by the following. At small q ($q < 0.2(Gev./c)$) the interference between pole graphs and rescattering of nucleons graphs ($fig.3d$) is destructive because of final state interaction of nucleons [19, 29]. But at laregr q ($q > 0.25(Gev./c)$) the interference between all graphs of $fig.3$ is positive. The some enchancement of the spectrum at $q > 0.25(Gev./c)$ (full curve) is explained by the contributin of the triangle graph with the absorbtion of the virtual meson by the nucleon ($fig.3c$). This contribution is sufficientely large at $0.2 < q < 0.35(Gev./c)$ and initial energy $T_0 = 2.5(Gev.)$, because the reaction $NN \to \pi NN$ goes through the Δ-production in the intermediate state in this kinematic region. For the comparision the spectrum $Ed\sigma/d^3p$ of protons produced in the inclusive reaction $pd \to ppn$ at $E_0 = 4.5(Gev.)$ when the proton is emitted backward in the rest frame of deuteron [29, 31] is presented on $fig.4(b)$. It is shown from these $figs.$ that the forms of the spectra of inclusive $pd \to pX$ and exclusive $pd \to ppn$ are analogous and the difference is in the behaviour of ones at $0.2 < q < 0.35(Gev./c)$ because of different energies of initial protons.

Consider now the next result of the calculation. The tensor analising power $T_{20} = A/\sqrt{2}$ for the case of the exclusive reaction $pd \to ppn$ is presented on $fig.5a$ It is shown from this fig. that the contribution of the $fig.3(c-d)$ graphs to T_{20} is sufficientely large at $0.2 < q < 0.35(Gev./c)$ so as to the spectrum $E_2 d\sigma/d^3p_2$. For the comparision T_{20} for the inclusive rection $pd \to pX$ when proton is emitted backward is presented on $fig.5b$ [29, 31]. It is shown from these figuras that the forms of of T_{20} in the cases of the exclusive $pd \to ppn$ and inclusive $pd \to pX$ reactions are anologous.

Now we would like to consider a rather interesting problem. The so-called effect of the minimal relativisation was invented some time ago by Shapiro [33]. It was shown that in general relativistic case [33] the transformation properties of each functions of a spinless particle are different from the nonrelativistic case. The idea of the minimal relativisation is that given any non-relativistic single-time wave function in configuration space reprasentation, then the following construct:

$$\bar{\Psi}(\mathrm{p}) = \frac{1}{(2\pi)^{3/2}} \int \xi(\mathrm{p},\mathrm{r}) \mathrm{d}^3\mathrm{r} \xi(\mathrm{p},\mathrm{r}) = \frac{\omega_\mathrm{p} - \mathrm{pr_0}^{1-\mathrm{im|r|}}}{\mathrm{m}} \tag{12}$$

here $\mathrm{r_0} = \mathrm{r}/|\mathrm{r}|$ and $\omega_p = \sqrt{p^2 + m^2}$ qualifies as good candidate for the asociated relativized momentum space wave function. Indeed the function $\bar{P}si(\mathrm{p})$ has the following desirable properties:

-It transforms ireducibly under the lorentz group

-it is invariantly normalised ci34

-it reduces to the usual non-relativistic Fourier transform since $\xi(\mathrm{p},\mathrm{r}) \to \mathbf{exp(ipr)}$ as $r \to infty$

In this paper we tried to analise the sensitivity of the momentum distrubution of S-wave of d.w.f. to different transformations of $\Psi(\mathbf{r})$ (Fourier and Shapiro) . The results of the calculations are presented on $fig.6$. It is shown that the effect of so-called "minimal relativisation" gives some shift of the momentum distribution of the S-part of d.w.f. The same shift is resulted if to take into account the $6-quark$ component in deuteron in the framework of the nonrelativistic hybrid quark model [35]. From this figure one can see that the "minimal" relativisation prescription (it is a pure kinematically transformation) imitates the behaviour of d.w.f. in the hybrid nonrelativistic quark model [36-38]. Therefore it seems to be obvious that only in the case of the correct description of the inner structure of relativistic systems one can understand what is the real part of the six-quark configuration in d.w.f.

It should be noted that the Shapiro transformation of $\Psi(\mathbf{r})$ can't be the solution of the problem of the relativisation of the wave function of the bound state, however the demonstrated sensitivity of different physical observables to the different transformations of $\Psi(\mathbf{r})$ (see also [29]) shows the importance of the inclusion of relativistic effects in deuteron, especially at large q, $q > 0.4(Gev./c)$, or small r, $r < 0.5(fm.)$

V. Conclusions and Recomendations for New Experiments.

Now we can make the following conclusions from our analysis of exclusive and inclusive fragmentation p-d reactions. First of all it is unsufficient to use only the pole mechanism, i.e., the $fig.3(a,b)$ graphs, for the analysis of these processes. It is shown clearly, especially from the analysis of polarisation characteristics of $pd \to ppn$ and $pd \to pX$ (see [29]) processes that the contribution of all nonpole graphs of type $fig.3(c,d)$ is sufficiently big, especially at intermediate momentum values of final protons, $0.2 < q < 0.4(Gev./c)$ or $0.2 < q < 0.8(Gev./c)$ or $0.6 < x < 0.8$. The main contribution to the analising power T_{20} at $0.2 < q < 0.4(Gev./c)$ gives the triangle graphs with the virtual meson absorbtion as in the exclusive as and inclusive $p-d$ reactions. This type of such graphs results in especially large contribution at initial energies coresponding to the production of Δ-isobars in the intermediate state.

The comparision of T_{20} calculation in the case of the inclusive $p-d$ reaction with the experimental data [29, 31, 32] shows that it is necessary to measure this characteristic at large q more correctely, because the existing experimental data [32] have large errors at $q > 0.4(Gev./c)$. It is very interesting to analyse experimentaly T_{20} in this kinematic region in the exclusive reaction $p-d \to ppn$ at $T_0 < 3.3(Gev./c)$, what is plained at COSY in Yuelich, because the question is what is the signature of T_{20} at $q > 0.4(Gev./c)$, positive ore negative. The theory without of the quark component inclusion in the deuteron, as it was shown above and in [15, 16, 29], results in the cross of T_{20} at $q > 0.4(Gev./c)$. However the other model which takes into account the quark-gluon structure of deuteron [39] predicts the some constant behaviour of T_{20} at $q > 0.4(Gev./c)$. Therefore we would like to recomend to measure T_{20} in the descussed exclusive reaction at COSY in Yuelich more correctely at large q, $q > 0.4(Gev./c)$.

Furthermore we would like to note once more that the effect of the inclusion of $6q$-component in deuteron, as it is made in [35], can be emitaited by the inclusion of relativistic effects [29].

References

1. B.G.Arnold,C.E.Carlson,F.Gross,*Phys.Rev.* **D23**(1981)3831.
2. J.Arvieux, et al.,*Nucl.Phys.* **A431**(1984) 8131.
3. D.L.Keister,*Phys.Rev.* **C24**(1981)2628.
4. N.P.Recalo, *Proceedings of III International Symposium "Pion-Nucleon and Nucleon-Nucleon Interactions"* **2**(1989)200(16-23 April,Leningrad,1989).
5. N.S.Amelin, V.V.Glagolev, G.I.Lykasov *EPAN* **13**(1982)130.
6. S.Weinberg,*Phys.Rev.* **160**(1966)1313.
7. M.Chemtob,*Nucl.Phys.* **34**(1979)387.
8. J.B.Kogut, D.E.Soper*Phys.Rev.* **D1**(1970)2901.
9. S.J.Brodsky et et al. *Phys.Rev.* **D8**(1973)3321.
10. I.A.Shmidt, R.Blankenbecler, *Phys.Rev.* **d15**(1977)4574.
11. L.I.Frankfurt, M.I.Strikman, *Phys.Rep.* **76**(1981)215.
12. A.P.Kobushkin, L.JVizireva, *J.Phys.Nucl.Phys.* **G8**(1982)893.
13. V.B.Garsevanishvili, *XIII International Winter School of Theoretical Physics in Kappacz* **1**(1978)313.
14. V.A.Karmanov, *Nucl.Phys.* **B166**(1980)378, *Nucl.Phys.* **A362**(1981)331, *EPAN* **19**(1988)526.
15. M.G.Dolidze and G.I.Lykasov *Z.Phys.* **A336**(1990)339.
16. M.G.Dolidze and G.I.Lykasov *Proceedings of 7 International Conference on Polarisation Phenomena in Nuclear Physics* **1**(1990)50F. (July,Paris,1990); *Proceedings of X International Seminar on High Energy Physics Problems* **2** (September, Dubna, Russia, 1990)336.
17. M.G.Dolidze and G.I.Lykasov *Z.Phys.* **A335**(1990)95.
18. C.F.Perdrisat and V.Punjabi, *Phys.Rev.* **C42**(1989)1899.
19. L.G.Dachno and V.A.Nikonov *Nucl.Phys.* **A491**(1989)652.
20. L.S.Azhgirey et al. *Nucl.Phys.* **A528**(1991)621.
21. A.V.Zarubin et al. *Proc. of Intern. Workshop "Dubna Deuteron-91"* (June-1991 Dubna, Russia)214.
22. C.F.Perdrisat et.al. *Proc. of Intern. Workshop "Dubna Deuteron-91"* (June-1991 Dubna, Russia)179.
23. F.Gross *Phys.Rev.* **D100**(1979)223.
24. M.A.Braun, M.V.Tokarev *Proc. of III Intern. Symposium "Pion-Nucleon and Nucleon-Nucleon Physics"* **v.2** (April 16-22,Leningrad,1989)390.
25. V.V.Anisovich, A.V.Sarantsev *Proc.of XXY Winter School LNP*(Gatchina, Russia, 1990)42.
26. S.S.Vasan *Phys.Rev.* **D8**(1973)4092.
27. L.L.Lapidus *EPAN* **15**(1984)493.
28. D.V.Bugg and C.Wilkin *Nucl.Phys.* **A467**575(1987); *Phys.Lett.* **B152**(1985)37.
29. Yu.L.Dorodnych, G.I.Lykasov *Preprint INR* **781/91** (Moscow,1992).
30. R.V.Reid *Ann. Phys.* **50**(1968)411.
31. C.F.Perdrisat et.al. *Phys.Rev.Lett.* **59**(1987)2840.

32. V.G.Ableev et al. JETP.Lett. 47558(1988); *Proc. of 7 Intern.Conference on Polarisation Phenomena in Nuclear Physics* v.1(Paris,June,1991)40F.
33. I.S.Shapiro Dokl.akad.Nauk.,SSSR **106**(1956)647.
34. S.V.Dshemuchadze et.al. *Proposal of Deuteron Disinegration at COSY in Exclusive Experiments with Polarised Protons and Deuterons* (Dubna-Yuelich, January 1991)
35. V.G.Kadyshevski, R.M.Mir-Kasimov and N.B.Skachkov *Nuovo Cim.* A55 (1968)233.
36. V.G.Neudachin, L.T.Obuchovsky, V.I.Kukulin and N.F.Golovanova *Phys.Rev.* **C11**(1975)128.
37. A.M.Kusainov, V.G.Neudachin, I.T.Obuchovsky *Phys.Rev.* C44 (1991)2312.
38. L.G.Kislinger *Phys.Lett.* **B12**(1982)307.
39. A.P.Kobushkin Proc. of Intern. Workshop "Dubna Deuteron-91" (Dubna, Russia June, 1991)31.
40. M.Lacombe et al. *Phys.Lett.***B151**(1981)139.

Figure Captions

Fig.1. Feynman diagram of the process $dN \to NNN$ and the equivalent graphs of old pertubative theory (OLPTh).

Fig.2. Deuteron dissociation vertex.

Fig.3. The basic diagrams of $pd \to pX$ reactions with the notions explained in the text.

Fig.4a. Dependence of the exclusive spectrum at $T_p = 2.5(Gev.)$ and direction angles $\theta_1 = 0grad.$ and $\theta_2 = 180grad.$ in the reaction $pd \to ppn$. The curves correspond to the following mechanisms: dashed-contribution of the spectator graph ($fig.3a$), full-sum of all contributions ($fig.3(a-d)$).

Fig.4b. The spectrum of protons in the inclusive $pd \to pX$ reaction at $P_0 = 4.5(Gev./c)$ and direction angle $\theta_1 = 180grad.$ in the deuteron rest frame. Dott-dashed curve corresponds to the spector diagram of $fig.3a$, full one-total mechanismreaction [38]

Fig.5a. Dependence of T_{20} on the backward proton momentum p_2 in the deuteron rest frame in the exclusive reaction $pd \to ppn$ at $T_p = 2.5(Gev.)$ and detecting angles $\theta_1 = 0grad.$ and $\theta_2 = 180grad.$ Curves: 1-sum of all contributions ($fig.3a-d$) for Paris d.w.f.; 2-the same as the curve 1 but for Reid soft core d.w.f.; dashed one-contribution of the spectator mechanism ($fig.3a$) for Pris d.w.f.; 3-the same as the curve 2 but for reid soft core d.w.f.

Fig.5b. Dependence of T_{20} on the final proton momentum q in the deuteron rest frame and on the internal nucleon mpomentum k and on x. Curves:1-contribution of the spectator meechanism $fig.3a$; 2-contribution of spectator graph and absorption of π-meson by nucleon, graph of type $fig.3c$; 3-total meechanism [38]. The curves 1, 2 and 3 correspond to the calculations with Reid soft core d.w.f. The curve 4 reporesents the contribution of total mecchanism [38] but for Paris d.w.f. Curve 6-T_{20} with the complex $6q$ component included in the deuteron [17]; 5-calculation result from [24] corresponding to the relativisation of type of F.Gross [23];experimental data- from [30] and -from[31].

Fig.6. The momentum distribution of the S-wave of Paris d.w.f. Dashed curve gives the standard nonrelativistic distr4ibution; the solid one represents the relativised distribution (Shapiro transformastion) and dott-dashed curve corresponds to Paris S-wafe modified by a short range orthoogonal $6q$ part [33].

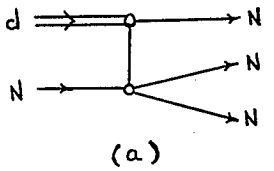

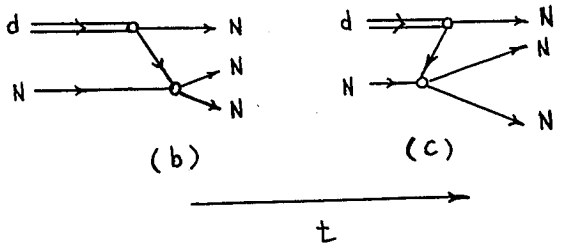

Fig. 1

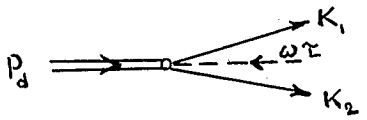

Fig. 2

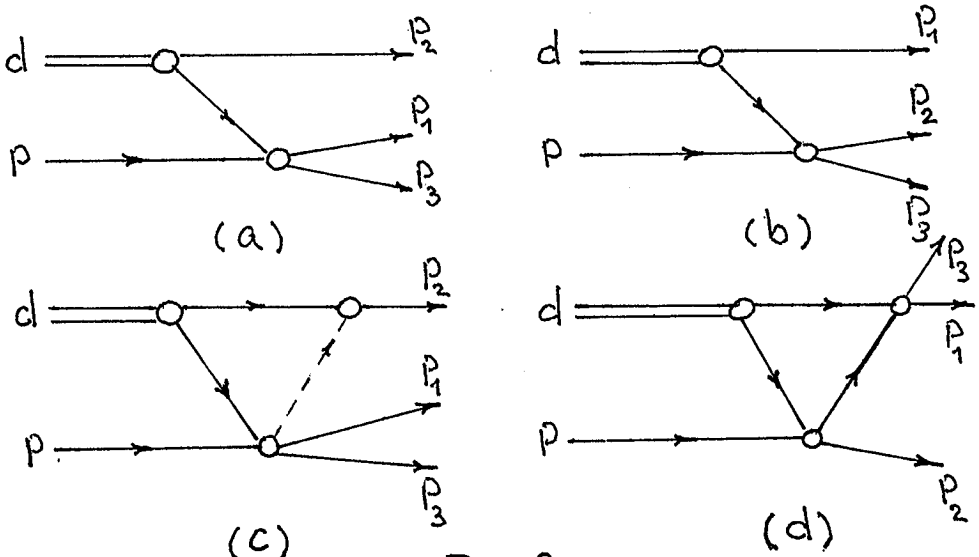

Fig. 3

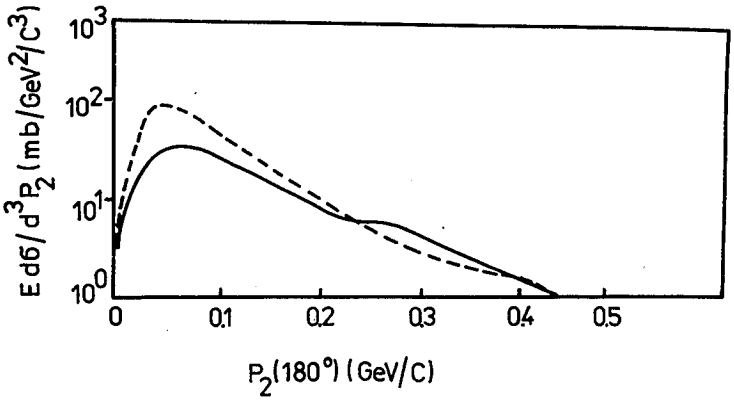
$E\,d\sigma/d^3P_2$ (mb/GeV^2/c^3)
10^3
10^2
10^1
10^0
0
0.1
0.2
0.3
0.4
0.5
$P_2(180°)$ (GeV/C)

Fig. 4a

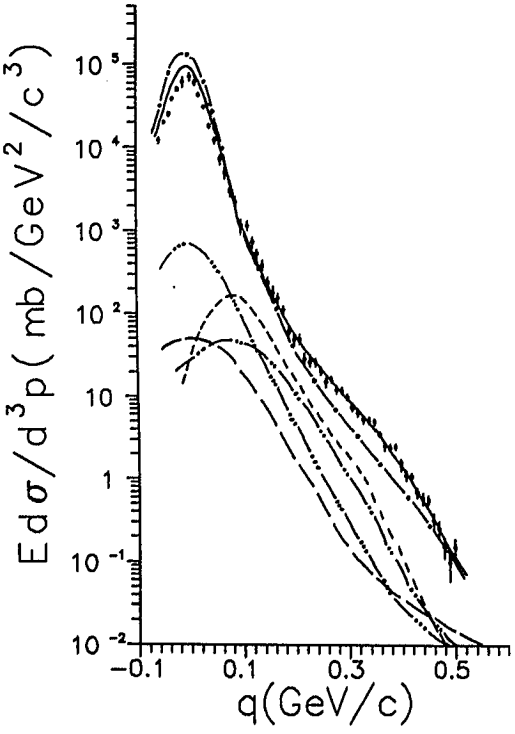
$E\,d\sigma/d^3p$ (mb /GeV^2/c^3)
10^5
10^4
10^3
10^2
10
1
10^{-1}
10^{-2}
−0.1
0.1
0.3
0.5
q(GeV/c)

Fig. 4b

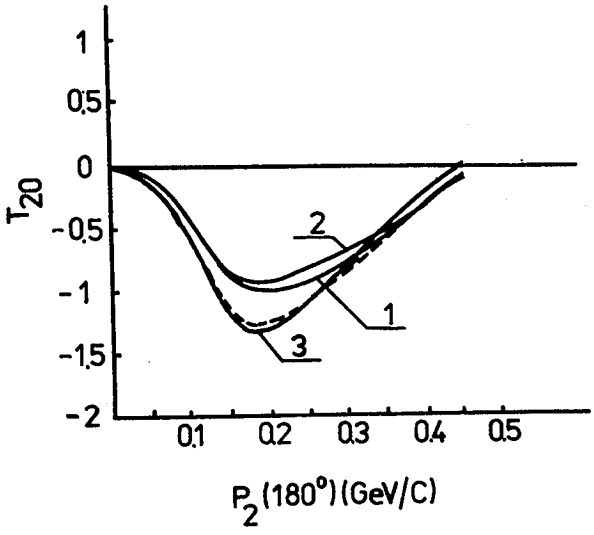
1
0,5
0
-0,5
-1
-1,5
-2
T_{20}
0.1
0.2
0.3
0.4
0.5
2
1
3
$P_2(180^\circ)$(GeV/C)

Fig.5a

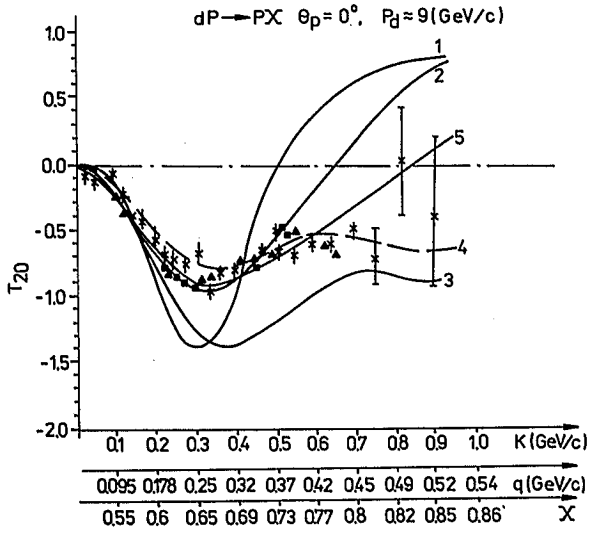
dP→PX $\theta_p = 0^\circ$, $P_d \approx 9$(GeV/c)
1.0
0.5
0.0
-0.5
-1.0
-1.5
-2.0
T_{20}
1
2
5
4
3
0.1 0.2 0.3 0.4 0.5 0.6 0.7 0.8 0.9 1.0 K(GeV/c)
0.095 0.178 0.25 0.32 0.37 0.42 0.45 0.49 0.52 0.54 q(GeV/c)
0.55 0.6 0.65 0.69 0.73 0.77 0.8 0.82 0.85 0.86 X

Fig.5b

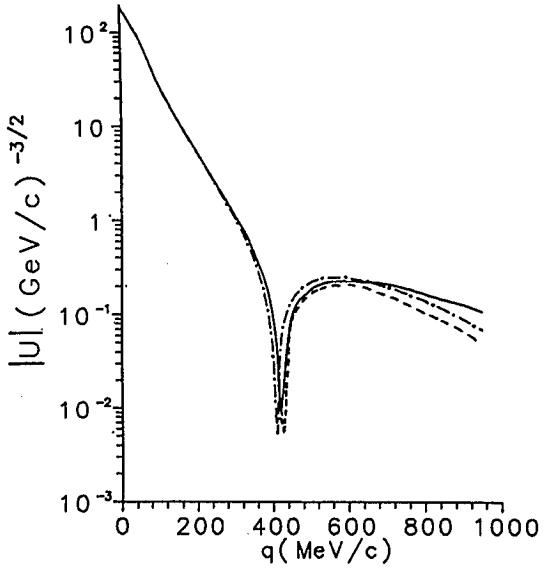

Fig.6

Participants

Prof. C. Bargholtz
Inst. of Physics
University of Stockholm
Vanadisvägen 9
S–11346 Stockholm
Sweden

Prof. S. Belostotsky
High Energy Theory Department
St. Petersburg Nuclear Physics Institute
188350 Gatchina, St. Petersburg
Russia, GUS

Dr. G.P.A. Berg
Cyclotron Facility
Indiana University
Milo B. Sampson Lane
Bloomington, IN 47405
USA

Prof. Dr. J. Bisplinghoff
Institut für Strahlen– und Kernphysik
Universität Bonn
Nußallee 14–16
W–5300 Bonn 1
Germany

Prof. A. Boudard
SPH–N, Bat 703
CEN–Saclay
F–91191 Gif–sur–Yvette Cedex
France

Dr. M. Büscher
Institut für Kernphysik
Forschungszentrum Jülich
Postfach 1913
W–5170 Jülich
Germany

Prof. Dr. W. Cassing
Institut für Theoretische Physik
Universität Gießen
Heinrich–Buff–Ring 16
W–6300 Giessen
Germany

M. Debowski
GSI Darmstadt
Postfach 11 05 52
W–6100 Darmstadt
Germany

Prof. C.B. Dover
Dept. of Physics
Brookhaven National Laboratory
Upton, L.I., NY 11973
USA

Prof. Dr. J. Ernst
Institut für Strahlen– und Kernphysik
Universität Bonn
Nußallee 14–16
W–5300 Bonn 1
Germany

R. Eßer
Institut für Kernphysik
Forschungszentrum Jülich
Postfach 1913
W–5170 Jülich
Germany

U. Faschingbauer
Max–Planck–Institut für Kernphysik
Postfach 10 39 80
W–6900 Heidelberg
Germany

Dr. D. Gotta
Institut für Kernphysik
Forschungszentrum Jülich
Postfach 1913
W–5170 Jülich
Germany

Dr. O. Grebenyuk
High Energy Theory Dept.
St. Petersburg Nuclear Physics Institute
188350 Gatchina, St. Petersburg
Russia/GUS

Prof. Dr. E. Grosse
GSI Darmstadt
Postfach 11 05 52
W–6100 Darmstadt
Germany

Dr. D. Grzonka
Institut für Kernphysik
Forschungszentrum Jülich
Postfach 1913
W–5170 Jülich
Germany

Prof. Dr. F. Hinterberger
Institut für Strahlen– und Kernphysik
Universität Bonn
Nußallee 14–16
W–5300 Bonn 1
Germany

Prof. Dr. R. Jahn
Institut für Strahlen– und Kernphysik
Universität Bonn
Nußallee 14–16
W–5300 Bonn 1
Germany

R. Jakob
Institut für Theoretische Physik
Bergische Universität Wuppertal
Gaußstr. 20
W–5600 Wuppertal 1
Germany

Prof. L. Jarczyk
Dept. of Nuclear Physics
Jagellonian University Cracow
Ul. Reymonta 4
PL–30059 Cracow
Polen

Prof. B. Kamys
Dept. of Nuclear Physics
Jagellonian University Cracow
Ul. Reymonta 4
PL–30059 Cracow
Polen

Prof. Dr. K. Kilian
Institut für Kernphysik
Forschungszentrum Jülich
Postfach 1913
W–5170 Jülich
Germany

Dr. S. Kistryn
Dept. of Nuclear Physics
Jagellonian University Cracow
Ul. Reymonta 4
PL–30059 Cracow
Polen

Prof. Dr. E. Klempt
Institut für Physik
Universität Mainz
Staudingerweg 7
W–6500 Mainz
Germany

Dr. R. Koch
Institut für Kernphysik
Forschungszentrum Jülich
Postfach 1913
W–5170 Jülich
Germany

Prof. V.I. Komarov
Laboratory for Nuclear Problems
Joint Institute for Nuclear Research
P.O.Box 79
141980 Dubna, Moscow Region
Russia/GUS

Dr. V. Koptev
High Energy Theory Dept.
St. Petersburg Nuclear Physics Institute
188350 Gatchina, St. Petersburg
Russia/GUS

Prof. Dr. S. Krewald
Institut für Kernphysik
Forschungszentrum Jülich
Postfach 1913
W–5170 Jülich
Germany

Prof. Dr. P. Kroll
Fachbereich Physik
Bergische Universität Wuppertal
Gaußstr. 20
W–5600 Wuppertal 1
Germany

Prof. J.M. Laget
Président du Comite des Experiences
Laboratoire National Saturne
CEN–Saclay
F–91191 Gif–sur–Yvette Cedex
France

Dr. G.I. Lykasov
Laboratory for Nuclear Problems
Joint Institute for Nuclear Research
P.O.Box 79
141980 Dubna, Moscow Region
Russia/GUS

Prof. Dr. U. Lynen
GSI Darmstadt
Postfach 11 05 52
W–6100 Darmstadt
Germany

Dr. H. Machner
Institut für Kernphysik
Forschungszentrum Jülich
Postfach 1913
W–5170 Jülich
Germany

Dr. R. Maier
Institut für Kernphysik
Forschungszentrum Jülich
Postfach 1913
W–5170 Jülich
Germany

Prof. Dr. R. Maschuw
Institut für Strahlen– und Kernphysik
Universität Bonn
Nußallee 14–16
W–5300 Bonn 1
Germany

Prof. Dr. T. Mayer–Kuckuk
Institut für Strahlen– und Kernphysik
Universität Bonn
Nußallee 14–16
W–5300 Bonn 1
Germany

Dr. B. Metsch
Institut für Theoretische Kernphysik
Universität Bonn
Nußallee 14–16
W–5300 Bonn 1
Germany

Prof. D.W. Miller
Cyclotron Facility
Indiana University
2401 Milo B. Sampson Lane
Bloomington, IN 47405
USA

Dr. H.P. Morsch
Laboratoire National Saturne
CEN–Saclay
F–91191 Gif–sur–Yvette Cedex
France

Dr. H. Müller
Institut für Hadronen– und Kernphysik
Zentralinstitut für Kernforschung, Rossendorf
Postfach 19
O–8051 Dresden
Germany

Prof. B. Nefkens
Dept. of Physics
University of California
405 Hilgard Ave.
Los Angeles, CA 90024–1547
USA

Dr. W. Oelert
Institut für Kernphysik
Forschungszentrum Jülich
Postfach 1913
W–5170 Jülich
Germany

Dr. H. Ohm
Institut für Kernphysik
Forschungszentrum Jülich
Postfach 1913
W–5170 Jülich
Germany

P. Oltmanns
Institut für Kernphysik
Forschungszentrum Jülich
Postfach 1913
W–5170 Jülich
Germany

Prof. Dr. F. Osterfeld
Institut für Kernphysik
Forschungszentrum Jülich
Postfach 1913
W–5170 Jülich
Germany

Dr. D. Prasuhn
Institut für Kernphysik
Forschungszentrum Jülich
Postfach 1913
W–5170 Jülich
Germany

Prof. Dr. E. Rössle
Fakultät für Physik
Universität Freiburg
Hermann–Herder–Str. 3
W–7800 Freiburg
Germany

Dr. V. Schäfer
WE–Heraeus–Stiftung
Postfach 1553
W–6450 Hanau 1
Germany

R. Schleichert
Institut für Kernphysik
Forschungszentrum Jülich
Postfach 1913
W–5170 Jülich
Germany

Prof. Dr. B. Schoch
Physikalisches Institut
Universität Bonn
Nußallee 14–16
W–5300 Bonn 1
Germany

Prof. Dr. O. Schult
Institut für Kernphysik
Forschungszentrum Jülich
Postfach 1913
W–5170 Jülich
Germany

Dr. A. Sibirtsev
ITEP
B. Cheremushkinskya 25
117259 Moscow
Russia/GUS

Prof. Dr. K. Sistemich
Institut für Kernphysik
Forschungszentrum Jülich
Postfach 1913
W–5170 Jülich
Germany

Prof. Dr. J. Speth
Institut für Kernphysik
Forschungszentrum Jülich
Postfach 1913
W–5170 Jülich
Germany

Prof. Dr. A. Strzalkowski
Dept. of Nuclear Physics
Jagellonian University Cracow
Ul. Reymonta 4
PL–30059 Cracow
Polen

Dr. P. Turek
Institut für Kernphysik
Forschungszentrum Jülich
Postfach 1913
W–5170 Jülich
Germany

Prof. Dr. J. Wambach
Institut für Kernphysik
Forschungszentrum Jülich
Postfach 1913
W–5170 Jülich
Germany

Prof. Dr. W. Weise
Institut für Theoretische Physik
Universität Regensburg
Universitätsstr. 31
W–8400 Regensburg
Germany

Dr. Kirsten Zapfe
MEA
DESY
Notkestr. 85
W–2000 Hamburg 52
Germany

Index of Authors

Konferenzen des Forschungszentrums Jülich

1 Technik und Gesellschaft
Vorträge eines Seminars veranstaltet von der
Programmgruppe Mensch, Umwelt, Technik
des Forschungszentrums Jülich GmbH
W. Fischer, L. Hennen, W. Kirstein, G. Schleser, G. Stein, Ch. Wandrey,
P.M. Wiedemann (1990)

2 Analytische Glimmentladungs-Spektroskopie
Jülich, 25.-26. April 1990, Tagungsbericht
herausgegeben von J. Rottmann (1990)

3 Die digitale Verarbeitung analoger Signale in Theorie und Praxis
KFA-Fortbildungsseminar; Jülich, im April 1989
U. Eckhardt, H. Eulenberg, F. Janßen, W. Jansen und H. Larue (1990)

4 Reduced Enrichment for Research and Test Reactors
Proceedings of the XIIth International Meeting
Berlin, 10.–14. September 1990
Arranged and edited by G. Thamm, M. Brandt (1991)

5 Kontrolle radioaktiver Abfälle
Erfahrungen mit der BMU-Richtlinie
Seminar; Jülich, 23.-24. Oktober 1990
Redaktion M. Laser (1991)

6 Intermetallische Phasen als Strukturwerkstoffe für hohe Temperaturen
Seminar; Hagen, 30.-31. Oktober 1990
herausgegeben von F.J. Bremer (1991)

7 Mikrobruchvorgänge in Al_2O_3-Keramik
DFG-Kolloquium; Jülich, 9.-10. April 1990
herausgegeben von H. Nickel, R.W. Steinbrech (1991)

8 BMFT-Workshop Klimawirkungsforschung
Auswirkungen von Klimaveränderungen
Tagungsband; Bonn, 11.-12. Oktober 1990
herausgegeben von W. Fischer, G. Stein (1991)

9 5th International Symposium on
Laser-Aided Plasma Diagnostics
Bad Honnef, 19.–23. August 1991 (1991)

10 A Regime to Control Greenhouse Gases:
Issues of Verification, Monitoring, Institutions
Proceedings of a Workshop, Bad Neuenahr, June 12-14, 1991
edited by J.C. di Primio, G. Stein (1991)

11 Hartstoffe in Werkzeugen
Seminar: Jülich, 20. und 21. Juni 1991
Redaktion: H. Prasse (1992)

12 Hadronic Processes at Small Angles in Storage Rings
105th International WE-Heraeus-Seminar, Proceedings
Bad Honnef, February 1–3, 1993
edited by E. Rössle, O.W.B. Schult (1993)

ISBN 3-89336-112-X